frontiers | Research Topics

Flare observations in the IRIS era: What have we learned, and what's next?

Edited by
Vanessa Polito, Bart De Pontieu, Adam Kowalski and Viggo Hansteen

Published in
Frontiers in Astronomy and Space Sciences

ISSN 1664-8714
ISBN 978-2-8325-3933-0
DOI 10.3389/978-2-8325-3933-0

About Frontiers

Frontiers is more than just an open access publisher of scholarly articles: it is a pioneering approach to the world of academia, radically improving the way scholarly research is managed. The grand vision of Frontiers is a world where all people have an equal opportunity to seek, share and generate knowledge. Frontiers provides immediate and permanent online open access to all its publications, but this alone is not enough to realize our grand goals.

Frontiers journal series

The Frontiers journal series is a multi-tier and interdisciplinary set of open-access, online journals, promising a paradigm shift from the current review, selection and dissemination processes in academic publishing. All Frontiers journals are driven by researchers for researchers; therefore, they constitute a service to the scholarly community. At the same time, the *Frontiers journal series* operates on a revolutionary invention, the tiered publishing system, initially addressing specific communities of scholars, and gradually climbing up to broader public understanding, thus serving the interests of the lay society, too.

Dedication to quality

Each Frontiers article is a landmark of the highest quality, thanks to genuinely collaborative interactions between authors and review editors, who include some of the world's best academicians. Research must be certified by peers before entering a stream of knowledge that may eventually reach the public - and shape society; therefore, Frontiers only applies the most rigorous and unbiased reviews. Frontiers revolutionizes research publishing by freely delivering the most outstanding research, evaluated with no bias from both the academic and social point of view. By applying the most advanced information technologies, Frontiers is catapulting scholarly publishing into a new generation.

What are Frontiers Research Topics?

Frontiers Research Topics are very popular trademarks of the *Frontiers journals series*: they are collections of at least ten articles, all centered on a particular subject. With their unique mix of varied contributions from Original Research to Review Articles, Frontiers Research Topics unify the most influential researchers, the latest key findings and historical advances in a hot research area.

Find out more on how to host your own Frontiers Research Topic or contribute to one as an author by contacting the Frontiers editorial office: frontiersin.org/about/contact

Flare observations in the IRIS era: What have we learned, and what's next?

Topic editors

Vanessa Polito — Bay Area Environmental Research Institute, United States

Bart De Pontieu — Lockheed Martin Solar and Astrophysics Laboratory (LMSAL), United States

Adam Kowalski — University of Colorado Boulder, United States

Viggo Hansteen — Bay Area Environmental Research Institute, United States

Citation

Polito, V., De Pontieu, B., Kowalski, A., Hansteen, V., eds. (2023). *Flare observations in the IRIS era: What have we learned, and what's next?* Lausanne: Frontiers Media SA. doi: 10.3389/978-2-8325-3933-0

Table of contents

frontiers | Frontiers in Astronomy and Space Sciences

TYPE Original Research
PUBLISHED 01 November 2022
DOI 10.3389/fspas.2022.999319

OPEN ACCESS

EDITED BY
Adam Kowalski,
University of Colorado Boulder, United States

REVIEWED BY
Vadim Uritsky,
The Catholic University of America, United States
Ilaria Ermolli,
INAF Osservatorio Astronomico di Roma, Italy

*CORRESPONDENCE
Markus J. Aschwanden,
aschwanden@lmsal.com

SPECIALTY SECTION
This article was submitted to Stellar and Solar Physics,
a section of the journal Frontiers in Astronomy and Space Sciences

RECEIVED 20 July 2022
ACCEPTED 13 October 2022
PUBLISHED 01 November 2022

CITATION
Aschwanden MJ and Vilangot Nhalil N (2022), Interface region imaging spectrograph (IRIS) observations of the fractal dimension in the solar atmosphere. *Front. Astron. Space Sci.* 9:999319.
doi: 10.3389/fspas.2022.999319

Interface region imaging spectrograph (IRIS) observations of the fractal dimension in the solar atmosphere

Markus J. Aschwanden[1]* and Nived Vilangot Nhalil[2]

[1]Lockheed Martin, Solar and Astrophysics Laboratory (LMSAL), Advanced Technology Center (ATC), Palo Alto, CA, United States, [2]Armagh Observatory and Planetarium, College Hill, Armagh, United Kingdom

We focus here on impulsive phenomena and Quiet-Sun features in the solar transition region, observed with the Interface Region Imaging Spectrograph (IRIS) at 1,400 Å (at formation temperatures of $T_e \approx 10^4$–10^6 K). Summarizing additional literature values we find the following fractal dimensions (in increasing order): $D_A = 1.23 \pm 0.09$ for photospheric granulation, $D_A = 1.40 \pm 0.09$ for chromospheric (network) patterns, $D_A = 1.54 \pm 0.04$ for plages in the transition region, $D_A = 1.56 \pm 0.08$ for extreme ultra-violet (EUV) nanoflares, $D_A = 1.59 \pm 0.20$ for active regions in photospheric magnetograms, and $D_A = 1.76 \pm 0.14$ for large solar flares. We interpret low values of the fractal dimension ($1.0 \lesssim D_A \lesssim 1.5$) in terms of sparse curvi-linear flow patterns, while high values of the fractal dimension ($1.5 \lesssim D_A \lesssim 2.0$) indicate quasi-space-filling transport processes, such as chromospheric evaporation in flares. Phenomena in the solar transition region appear to be consistent with self-organized criticality (SOC) models, based on their fractality and their size distributions of fractal areas A and (radiative) energies E, which show power law slopes of $\alpha_A^{obs} = 2.51 \pm 0.21$ (with $\alpha_A^{theo} = 2.33$ predicted), and $\alpha_E^{obs} = 2.03 \pm 0.18$ (with $\alpha_E^{theo} = 1.80$ predicted). This agreement suggests that brightenings detected with IRIS at 1,400 Å reveal the same nonlinear SOC statistics as their coronal counterparts in EUV.

KEYWORDS

methods, statistical -fractal dimension -sun, transition region -solar granulation -solar photosphere, fractal dimension, statistical

Introduction

There are at least three different approaches to quantify the statistics of nonlinear processes with the concept of *self-organized criticality (SOC)* and fractality: (i) microscopic models, (ii) macroscopic models, and (iii) observations of power laws and scaling laws. The microscopic SOC models consist of numerically simulated avalanches that evolve *via* next-neighbor interactions in a lattice grid (Bak et al., 1987; Bak et al., 1988), also called *cellular automatons*, which have been quantized up to

numerical limits of $\approx 10^6 - 10^9$ cells per avalanche process. The macroscopic models describe the nonlinear evolution of (avalanching) instabilities with analytical (geometric and energetic) quantities, which predict physical scaling laws and power law-like occurrence frequency size distributions. The third category of SOC approaches includes observations with fitting of power law-like distribution functions and waiting time distributions, which provide powerful tests of theoretical SOC models. A total of over 1500 SOC-specific publications have been identified with the NASA/ADS database, while the seminal paper by Bak et al. (1987) was cited over 4,000 times. For brevity, we mention a few textbooks only (Bak 1996; Aschwanden 2011; Pruessner 2012), and a recent collection of astrophysical SOC reviews, presented in the special volume *Space Science Reviews* Vol. 198 (Aschwanden et al., 2016; McAteer et al., 2016; Sharma et al., 2016; Watkins et al., 2016). Some pioneering work has been reported from fractal analysis of chromospheric network cells and (super-)granulation (Berrilli et al., 1998; Ermolli et al., 1998; Consolini et al., 1999; Criscuoli et al., 2007; Ermolli et al., 2014; Giorgi et al., 2015).

In this paper we focus on SOC modeling of impulsive events detected in the solar atmosphere, as observed with the *Interface Region Imaging Spectrograph (IRIS)* (De Pontieu et al., 2014), while solar flare events observed in hard X-rays, soft X-rays, and *Extreme-Ultraviolet (EUV)* have been compared in recent studies (Aschwanden 2022a; Aschwanden 2022b). Large solar flares observed in hard and soft X-rays show typically electron temperatures of $T_e \approx 5$–35 MK, while coronal nanoflares observed in EUV have moderate temperatures of $T_e \approx 1$–2 MK. Hence it is interesting to investigate transition region events, which are observed in a different temperature regime ($T_e \approx 10^4$–10^6 K) than coronal phenomena. In the previous study with the same IRIS data, it was found that the power law index of the energy distribution is larger in plages ($\alpha_E > 2$), compared to sunspot dominated active regions ($\alpha_E < 2$) (Vilangot Nhalil et al., 2020).

If both coronal and transition region brightenings exhibit the same SOC behavior and are produced by the same physical mechanism, one would expect the same fractal dimension and power law slope of the occurrence frequency size distribution, which is an important test of the coronal heating problem.

The content of this paper contains a theoretical modeling *Theoretical considerations*, an observational *Observations*, a discussion *Discussion*, and conclusions in *Conclusion*.

Theoretical considerations

In the following we define two theoretical definitions of the mono-fractal dimension, namely the *Mean Euclidean Fractal Dimension* (*Theoretical considerations*) and the *SOC-Inferred Fractal Dimension* (*Theoretical considerations*), which provide a test of the predicted fractal dimension.

The mean Euclidean fractal dimension

The definition of the fractal dimension D_A for 2-D areas A is also called the *Hausdorff dimension* D_{A0} (Mandelbrot 1977),

$$A_0 = L_0^{D_{A0}}, \tag{1}$$

or explicitly (normalized at $i = 0$),

$$D_{A0} = \frac{\log(A_0)}{\log(L_0)}, \tag{2}$$

where the area A_0 is the sum of all image pixels $I(x,y) \geq I_0$ above a background threshold I_0, and L_0 is the length scale of a fractal area. A structure is fractal, when the ratio D_{Ai} is approximately constant *versus* different length scales L_i and converges to a constant for the smallest length scales $L \mapsto 0$. The method described here is also called the box-counting method, because the number of pixels are counted over an area A_0 and length scale L_0.

In analogy, a fractal dimension can also be defined for the 3-D volume V,

$$V_0 = L_0^{D_{V0}}, \tag{3}$$

or explicitly

$$D_{V0} = \frac{\log(V_0)}{\log(L_0)}, \tag{4}$$

The valid range for these two area fractal dimensions is $1 \leq D_A \leq 2$ and $2 \leq D_V \leq 3$, where $D = 0, 1, 2, 3$ are all possible Euclidean dimensions.

We can estimate the numerical values of the fractal dimensions D_A and D_V from the means of the minimum and maximum values in each Euclidean domain,

$$D_A = \frac{(D_{A,min} + D_{A,max})}{2} = \frac{(1+2)}{2} = \frac{3}{2} = 1.50, \tag{5}$$

and correspondingly,

$$D_V = \frac{(D_{V,min} + D_{V,max})}{2} = \frac{(2+3)}{2} = \frac{5}{2} = 2.50. \tag{6}$$

The 2-D fractal dimension D_A is the most accessible SOC parameter, while the 3-D fractal dimension D_V requires information of fractal structures along the line-of-sight, either using a geometric or tomographic model, or modeling of optically-thin plasma (in the case of an astrophysical object observed in soft X-ray or EUV wavelengths).

We find that the theoretical prediction of $D_A = (3/2) = 1.50$ (**Eq. (5)**) for the fractal area parameter A is approximately consistent with the observed values obtained with the box-counting method, $D_A^{obs} = 1.54 \pm 0.04$ (**Table 1**).

TABLE 1 Fractal Dimension obtained from power law slope fits (PL) and from the box counting (BC) method for 12 IRIS datasets.

Dataset	Number of Events	Power law Slope fit PL	Fractal Dimension PL	Fractal Dimension BC	Fractal Dimension BC	Fractal Dimension BC	Fractal Dimension BC	Fractal Dimension BC,all
	n	a_A	D_A^{PL}	D_{A0}	D_{A1}	D_{A2}	D_{A3}	D_A
1	787	2.14	1.75	1.44	1.43	1.35	1.34	1.39 ± 0.05
2	3119	2.32	1.52	1.56	1.55	1.52	1.46	1.57 ± 0.05
3	2882	2.48	1.35	1.53	1.48	1.44	1.40	1.46 ± 0.06
4	1,614	2.83	1.09	1.67	1.66	1.58	1.53	1.61 ± 0.07
5	1,106	2.67	1.20	1.67	1.66	1.57	1.50	1.60 ± 0.08
6	65	2.47	1.36	1.66	1.64	1.62	1.54	1.62 ± 0.05
7	118	2.37	1.45	1.64	1.63	1.60	1.52	1.60 ± 0.05
8	4,412	2.50	1.33	1.56	1.55	1.48	1.40	1.50 ± 0.07
9	4,725	2.72	1.16	1.64	1.63	1.61	1.52	1.60 ± 0.05
10	3064	2.28	1.56	1.69	1.59	1.55	1.52	1.56 ± 0.04
11	1,445	2.76	1.14	1.65	1.63	1.55	1.47	1.58 ± 0.04
12	296	2.53	1.31	1.60	1.54	1.51	1.51	1.54 ± 0.04
Observations		2.51 ± 0.21	1.35 ± 0.19	1.60 ± 0.07	1.58 ± 0.07	1.53 ± 0.08	1.48 ± 0.06	1.55 ± 0.07
Theory		2.33	1.5	1.5	1.5	1.5	1.5	1.5

The SOC-Inferred fractal dimension

The size distribution $N(L)$ of length scales L, also called the *scale-free probability conjecture* (Aschwanden 2012; Aschwanden 2014), which essentially is the standard expression for the probability conservation in a power law distribution,

$$N(L)\ dL \propto L^{-d}\ dL, \tag{7}$$

where d is the Euclidean space dimension, generally set to $d = 3$ for most real-world data. Note, that this occurrence frequency distribution function is simply a power law, which results from the reciprocal relationship of the number of events $N(L)$ and the length scale L. Since the fractal dimension D_A for event areas A is defined as (Eq. 1),

$$A = L^{D_A}, \tag{8}$$

we obtain the inverse function $L(A)$,

$$L = A^{(1/D_A)}, \tag{9}$$

and the derivative,

$$\left(\frac{dL}{dA}\right) = A^{(1/D_A - 1)}, \tag{10}$$

so that we obtain the area distribution $N(A)$ by substitution of L (Eq. 9) and the derivative dL/dA (Eq. 10) into $N(L)$ (Eq. 7),

$$N(A)\ dA = N[L(A)]\left(\frac{dL}{dA}\right)dA = [L(A)]^{-d}\ A^{(1/D_A - 1)}\ dA = A^{(-\alpha_A)}\ dA, \tag{11}$$

which yields the power law index α_A, for $d = 3$,

$$\alpha_A = 1 + \frac{(d-1)}{D_A} = 1 + \frac{2}{D_A}. \tag{12}$$

TABLE 2 Parameters of the standard SOC Model, with fractal dimensions D_x and power law slopes α_x of size distributions.

Parameter	Power law Slope Analytical	Power law Slope Numerical
Euclidean Dimension	$d =$	3.00
Diffusion type	$\beta =$	1.00
Area fractal dimension	$D_A = d - (3/2) =$	1.50=(3/2)
Volume fractal dimension	$D_V = d - (1/2) =$	2.50=(5/2)
Length	$\alpha_L = d =$	3.00
Area	$\alpha_A = 1 + (d-1)/D_A =$	2.33=(7/3)
Volume	$\alpha_V = 1 + (d-1)/D_V =$	1.80=(9/5)
Duration	$\alpha_T = 1 + (d-1)\beta/2 =$	2.00
Mean flux	$\alpha_F = 1 + (d-1)/(\gamma D_V) =$	1.80=(9/5)
Peak flux	$\alpha_P = 1 + (d-1)/(\gamma d) =$	1.67=(5/3)
Spatio-temporal energy	$\alpha_{E_1} = 1 + (d-1)/(\gamma D_V + 2/\beta) =$	1.44=(13/9)
Thermal energy (h = const)	$\alpha_{E_2} = 1 + 2/D_A =$	2.33=(7/3)
Thermal energy ($h = A^{1/2}$)	$\alpha_{E_3} = 1 + 2/D_V =$	1.80=(9/5)

Vice versa we can then obtain the SOC fractal dimension D_A from an observed power law slope α_A (Table 1), by inverting $\alpha_A(D_A)$ in Eq. 12,

$$D_A^{SOC} = \frac{2}{(\alpha_A - 1)} = \frac{3}{2}. \tag{13}$$

Using the theoretical value $\alpha_A = 7/3 \approx 2.33$ (Table 2), we expect a value of $D_A^{SOC} = 1.5$ (Eq. 13), which is identical with the prediction of the mean Euclidean dimension $D_A^{ME} = 1.5$ (Eq. 5) based on the mean of the extremal maximum and minimum values. This is an alternative method (Eq. 13) to calculate the fractal area dimension, in contrast to the mean Euclidean method (Eq. 5), which we call the *SOC-inferred fractal dimension*, because it uses the (power law) size distribution of areas that are defined in SOC models.

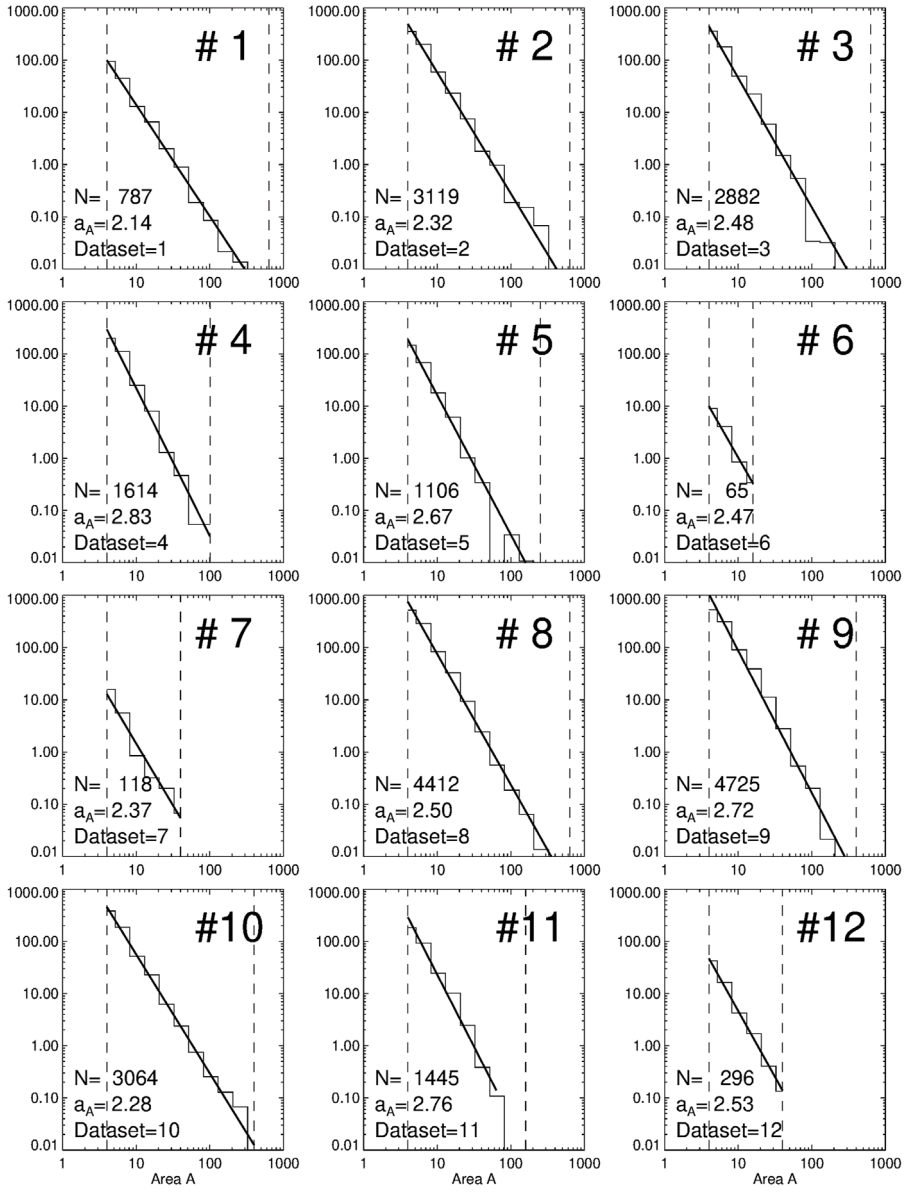

FIGURE 1
Size distributions of flare areas *A* for 12 datasets observed with IRIS SJI 1400 Å in different active regions.

Observations

This is a follow-on study of previous work, "The power-law energy distributions of small-scale impulsive events on the active Sun: Results from IRIS" (Vilangot Nhalil et al., 2020). Although both studies use the same IRIS dataset, the former study (Vilangot Nhalil et al., 2020) analyzes the power law size distributions of event energies α_E, which is important for the assessment of coronal heating requirements, while the new study analyzes the fractal dimensions D_A of impulsive events, which allows us to discriminate different physical mechanisms from the photosphere up to the transition region and corona. We call these small-scale impulsive events simply "events", which possibly could be related to "nanoflares" or "brightenings". In the previous study, 12 IRIS datasets were investigated with an automated pattern recognition algorithm, yielding statistics of three parameters, namely the event area A (in units of pixels), the event (radiative) energy E (in units of erg), and event durations or lifetimes T (in units of seconds). IRIS has pixels with a size of $0.17'' \approx 0.123$ Mm, which have been rebinned to $L_{pixel} = 0.33'' \approx 0.247$ Mm. The pixel size of areas thus corresponds to $A_{pixel} = L_{pixel}^2 = 0.247^2$

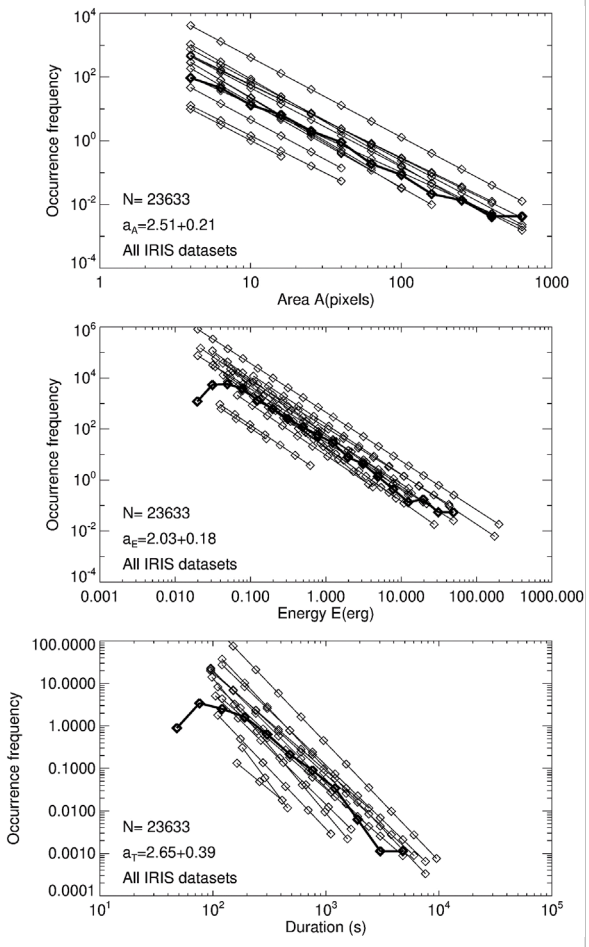

FIGURE 2
Power law fits to the size distributions of three SOC parameters: the event area *A* (top panel), the radiative energy *E* (middle panel), and the time duration (bottom panel). Individual fits to each of the 12 IRIS datasets are indicated with thin line style, while the fit to all events combined is indicated with thick line style, and the power law slopes are given in each panel.

$Mm^2 = 0.06076\ Mm^2$. The range of event areas covers $A = 4$–677 pixels, which amounts to length scales of $L = \sqrt{A} = (2-26)$ pixels, or $L = (2–26)*0.247$ Mm $\approx$ (0.5-6.4) Mm = (500-6400) km. The date of observations, the field-of-view (FOV), the cadence, and the NOAA active region numbers are listed in **Table 1** of Vilangot Nhalil et al. (2020), for each of the 12 IRIS datasets.

The automated pattern recognition code was run with different threshold levels of 3, 5, and 7 σ in the previous event detection method of Vilangot Nhalil et al. (2020), from which we use the 3-σ level here. The values in **Table 2** of the paper by Vilangot Nhalil et al. (2020) demonstrate that the fractal dimension is stable for different thresholds, as well as for noise filtering applied with diverse thresholds.

We use Slitjaw images (SJI) of the 1,400 Å channel of IRIS, which are dominated by the Si IV 1394 Å and 1,403 Å resonance lines, formed in the transition region. Vilangot Nhalil et al. (2020) compared also images from the SJI 1330 Å channel, which is dominated by the C II 1,335 Å and 1,336 Å lines, originating in the upper chromosphere and transition region at formation temperatures of $T_e \approx 3 \times 10^4$ K and $T_e \approx 8 \times 10^4$ K (Rathore and Carlsson 2015; Rathore et al., 2015).

Size distributions

Our first measurement is the fitting of a power law distribution function $N(A) \propto A^{-\alpha_A}$ of the event (or nanoflare) areas A, separately for each of the 12 IRIS datasets, as shown in **Figure 1**. The area of the event is a combination of all the spatially connected 3-σ pixels throughout their lifetime. The lowest bin was discarded in the histogram when a visible deviation from a power law was apparent. The number of events amounts to 23,633 for all 12 datasets together, varying from 65 to 4,725 events per IRIS dataset (**Table 1**). The power law slope fits vary from the lowest value $\alpha_A = 2.14$ (dataset #1) to the highest value $\alpha_A = 2.83$ (dataset #4), having a mean and standard deviation of (**Figure 2**, top panel).

$$a_A^{obs} = 2.51 \pm 0.21. \tag{14}$$

The area size distributions are shown superimposed for the 12 IRIS datasets (**Figure 2**, top panel), which illustrates almost identical power law slopes in different IRIS datasets.

Fitting the energy size distributions, $N(E) \propto E^{-\alpha_E}$, yields the following mean for all 12 IRIS datasets (**Figure 2**, middle panel),

$$a_E^{obs} = 2.03 \pm 0.18. \tag{15}$$

Fitting the duration size distributions, $N(T) \propto T^{-\alpha_T}$, yields the following mean for all 12 IRIS datasets (**Figure 2**, bottom panel),

$$a_T^{obs} = 2.65 \pm 0.39. \tag{16}$$

We will interpret these power law slopes in terms of SOC models in *Size distributions*.

The box-counting fractal dimension

The next parameter that we are interested in is the fractal dimension. A standard method to determine the fractal dimension D_A of an image is the box-counting method, which is defined by the asymptotic $(L \mapsto 0)$ ratio of the fractal area A to the length scale L, i.e., $D_A = \log(A)/\log(L)$, also called Hausdorff (fractal) dimension. We test the fractality

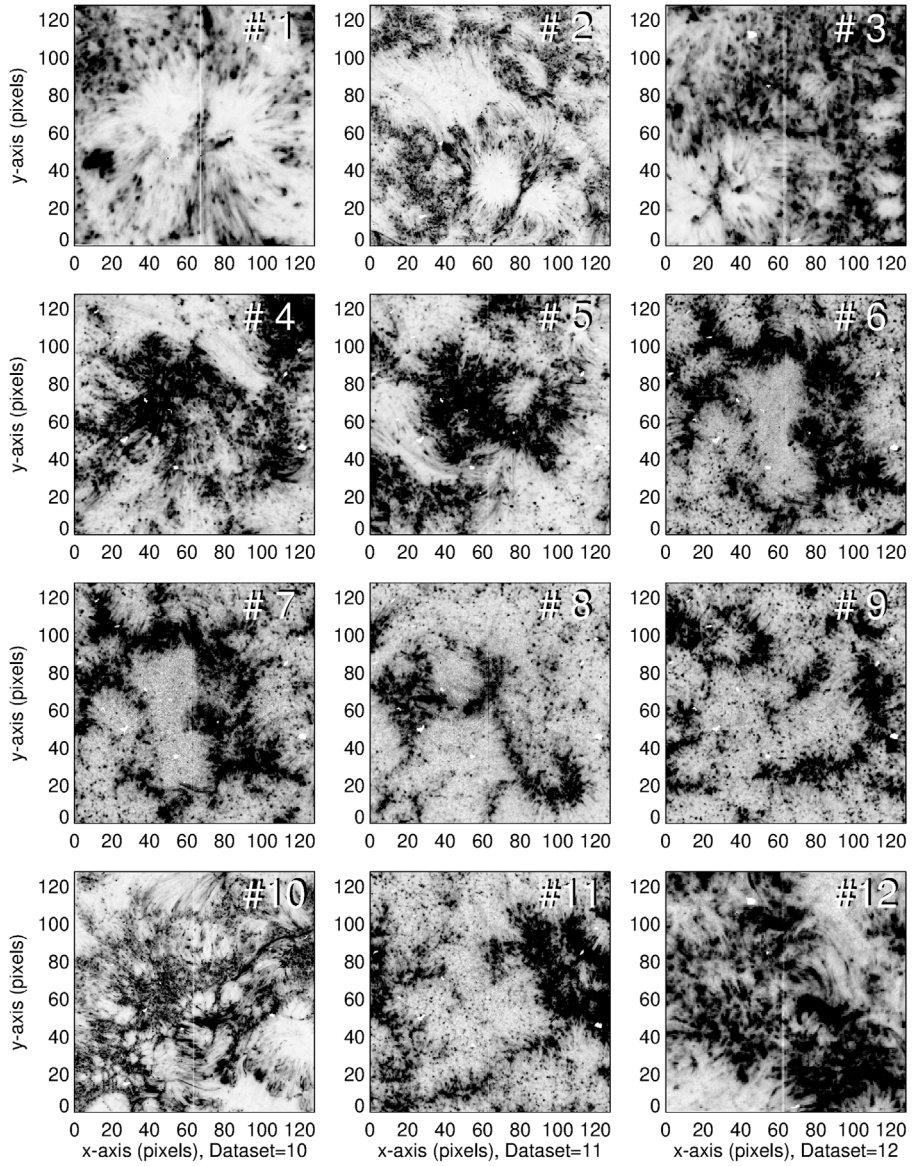

FIGURE 3
Intensity maps of 12 different active regions, observed with IRIS SJI 1400 Å. Black color indicates emission, and white color indicates the faint background.

by varying the pixel sizes (or spatial resolution) by powers of two, i.e., $L_i = 2^i = [1,2,4,8]$ for $i = [0,1,2,3]$. In order to normalize to the same number of events for each spatial resolution, the fractal (Hausdorff) dimension is defined by (e.g., Hirzberger et al., 1997),

$$D_{A,i} = \frac{\log(A_i\ 2^{2i})}{\log(L_i\ 2^i)}, \tag{17}$$

where L_i is the observed length scale, and A_i is the observed fractal area, measured at different spatial resolutions. If the fractal dimension $D_{A,i}$ stays more or less constant for different spatial resolutions $L_i = [1,2,4,8]$, then the dimension $D_{A,i}$ is said to be *"fractal"*.

It has been pointed out that the detection of small-scale impulsive events requires a careful subtraction of event-unrelated background noise in the IRIS 1400 Å data (Vilangot Nhalil et al., 2020). The main effect of background subtraction is the related change in the fractal area, which causes a sensitive bias: If too much background is subtracted, the fractal area is smaller and the resulting fractal dimension is too small, and *vice versa* when the estimated background is under-estimated. At times and locations where no impulsive

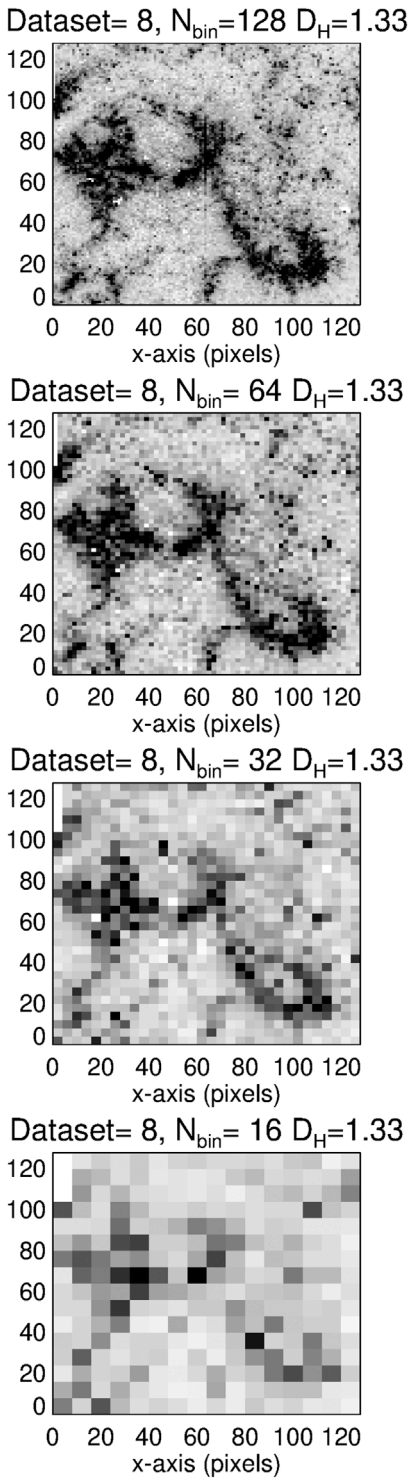

FIGURE 4
The IRIS dataset 8 is shown with different spatial resolutions of 128, 64, 32, and 16 bins, which demonstrates the scale-free definition of the Hausdorff dimension $D_H = 1.33$. Black color indicates emission, and white color indicates the faint background.

events occur, the flux distribution of an image shows a Gaussian distribution function (due to the random noise), while a heavy-tail occurs during active times (due to SOC-generated avalanches). In the case of a dominant noise component, a Gaussian can be fitted to the size distribution function, which yields a mean I_{avg} and a standard deviation I_{sig}. A 1-σ threshold can then be defined by,

$$I_{thr} = I_{avg} + I_{sig}. \tag{18}$$

which separates the linear noise fluctuations (at $I(x,y) \le I_{thr}$) from the nonlinear avalanches (at $I(x,y) \ge I_{thr}$). The calculation of a fractal dimension is then obtained from the ratio $\log(A_i 2^{2i})/\log(L_i 2^i)$ (**Eq. 17**), where the area A_i includes a count of all pixels with a flux value above the threshold, i.e., $I(x,y) > I_{thr}$, and the length scale L_i is the number of pixels that measure the length scale of a SOC avalanche.

We show the fractal dimensions measured with **Eq. 17**, for each of the 12 IRIS datasets and the 4 spatial resolutions D_{A0}, D_{A1}, D_{A2}, and D_{A3} in **Table 1**, which reveal a very narrow spread of values D_A for the fractal dimension, with a mean and standard deviation of a few percents (**Table 1**),

$$D_A^{obs} = 1.55 \pm 0.07. \tag{19}$$

Note, that the values obtained from different IRIS datasets and with different spatial resolutions are all consistent among each other and do not show any systematic dependency on the spatial resolution. Moreover, they are consistent with the theoretical expectation of the mean Euclidean dimension D_A^{ME} (**Eq. 5**) and the SOC-Inferred value D_A^{SOC} (**Eq. 13**),

$$D_A^{ME} = D_A^{SOC} = \frac{3}{2} = 1.5. \tag{20}$$

The fractal nature of the 12 IRIS datasets is rendered in **Figure 3** and **4**, where the black areas correspond to zones with enhanced emission, and the white areas correspond to the background with weak emission. The successive reduction of spatial resolution is shown in **Figure 4**.

An example of a theoretical fractal pattern with a close ressemblance to the observed transition region patterns of dataset #8 is shown in **Figure 5**, which is called the *"golden dragon fractal"* and has a Hausdorff dimension of $D_A = 1.61803$.

Fractal dimensions across the solar atmosphere

In **Table 3** we compile fractal dimensions obtained from photospheric, chromospheric, and transition region fractal features, which may be different from coronal and flare-like size distributions. The fractal dimension has been measured in photospheric wavelengths with the

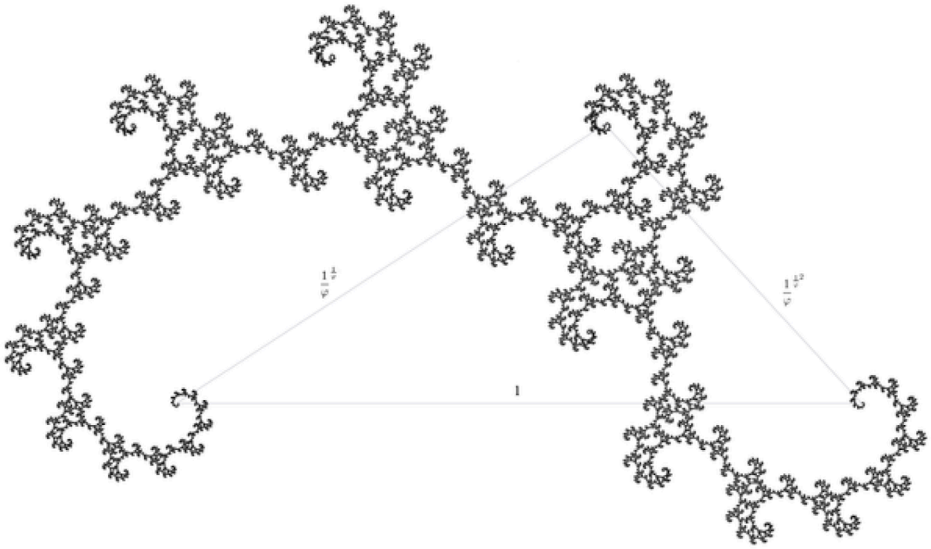

FIGURE 5
This numerically calculated fractal pattern is called a *golden dragon* and has a Hausdorff dimension of $D_A = 1.61803$. (https://en.wikipedia.org/wiki/List_of_fractals_by_Hausdorff_dimension). Note the similarity with dataset #8 in **Figure 4**.

perimeter-area method, containing dominantly granules and super-granulation features (Roudier and Muller 1986; Hirzberger et al., 1997; Berrilli et al., 1998; Bovelet and Wiehr 2001; Paniveni et al., 2005, 2010), which exhibit a mean value of (**Table 3**),

$$D_A^{gran} = 1.23 \pm 0.09. \quad (21)$$

Although this mean value is averaged from different solar features (granular cells and supergranular cells), as well as from different atmospheric heights (photospheric and chromospheric Ca II K data), the fractal dimension varies only by a small factor of ±7%. We have to be aware that photospheric emission originates from a lower altitude than any transition region or coronal feature. The relatively low value obtained for granulation features thus indicates that the granulation features seen in optical wavelengths are almost curvi-linear (with little area-filling topologies), which is expected for sparse photospheric mass flows along curvi-linear flow lines.

A second feature we consider are plages in the transition region, measured with IRIS 1400 Å (Vilangot Nhalil et al., 2020), which have formation temperatures of $\approx 10^{3.7} - 10^{5.2}$ K in the lower transition region, exhibiting a mean value of (**Table 3**),

$$D_A^{plage} = 1.54 \pm 0.04. \quad (22)$$

A third feature is an active region, observed in photospheric magnetograms and analyzed with the linear-area method (Lawrence 1991; Balke et al., 1993; Lawrence and Schrijver 1993; Meunier 1999; Janssen et al., 2003; Meunier 2004; Ioshpa et al., 2008), or with the box-counting method (McAteer et al., 2005). The mean value of fractal dimensions measured in active regions is found to be (**Table 3**),

$$D_A^{AR} = 1.59 \pm 0.20. \quad (23)$$

Apparently, active regions organize magnetic features into quasi-space-filling, area-like geometries.

Nanoflare events constitute a fourth phenomenon, which has been related to the SOC interpretation since Lu and Hamilton (1991). Nanoflares have been observed in EUV 171 Å and 195 Å with the TRACE instrument, as well as in soft X-rays using the Yohkoh/SXT (Solar X-Ray Telescope) (Aschwanden and Parnell 2002), which show a mean value of (see **Table 3**),

$$D_A^{nano} = 1.56 \pm 0.08. \quad (24)$$

Nanoflares have been observed in the Quiet Sun and appear to have a similar fractal dimension as impulsive brightenings in active regions measured in magnetograms.

For completeness we list also the fractal dimension measured in large solar flares, for M-class flares, X-class flares, and the Bastille Day flare (Aschwanden and Aschwanden 2008a), as observed in the EUV, which all together exhibit a mean value of (**Table 3**),

$$D_A^{flare} = 1.76 \pm 0.14. \quad (25)$$

This is the largest mean value of any measured fractal dimension, which indicates that the flare process fills the flare area almost

TABLE 3 The fractal dimensions of granules, plages, active regions, nanoflares, and large flares. Different methods are indicated with the acronyms (LA = Linear-area; PA = perimeter-area, and C = box counting. Mean values and standard deviations of each group are indicated with bold numbers. Studies based on the Ca II K line extend over both the photospheric and chromospheric zone.

Phenomenon	Data Method	Fractal Dimension D_A	References
Granulation (Photosphere)		**1.23 ± 0.09**	**Mean**
Granules	5750 Å, PA	1.25	Roudier & Muller (1986)
Granules	5257 Å, PA	1.30	Hirzberger et al. (1997)
Granular cells	5257 Å, PA	1.16	Hirzberger et al. (1997)
Granules	3933 Å. Ca II K	1.35	Berrilli et al. (1998)
Granules	PA	1.09	Bovelet and Wiehr (2001)
Supergranulation	MDI/SOHO, PA	1.25	Paniveni et al. (2005)
Supergranular cells	3934 Å, Ca II K, PA	1.23 ± 0.02	Paniveni et al. (2010)
Magnetic Features (Chromosphere)		**1.40±0.09**	**Mean**
Quiet Sun EUV network	CDS/SOHO	1.50 ± 0.20	Gallagher et al. (1998)
Ellerman bombs	6122 Å, Ca I	1.40	Georgoulis et al. (2002)
Magnetic features	3934 Å, Ca II K	1.32 ± 0.02	Criscuoli et al. (2007)
Plages (Transition Region)		**1.54±0.04**	**Mean**
Plages with Sunspots	IRIS 1400 Å	1.50 ± 0.09	(This work, #1-3, 10)
Plages without Sunspots	IRIS 1400 Å	1.58 ± 0.05	(This work, #4-9, 11-12)
Active regions (Photosphere)		**1.59±0.20**	**Mean**
Active regions	BBSO, LA	1.56 ± 0.08	Lawrence (1991)
	BBSO		Lawrence and Schrijver (1993)
Active region plages	6302 Å, Fe I, LA	1.54 ± 0.05	Balke et al. (1993)
Active regions	7929 Å, LA	1.86 ± 0.08	Meunier (1999)
Active regions	7929 Å, PA	1.58 ± 0.18	Meunier (1999)
Small scales	6302 Å, Fe I, PA	1.41 ± 0.05	Janssen et al. (2003)
Active regions	6768 Å, Ni I	1.80 ± 0.09	Meunier (2004)
- Cycle minimum	6768 Å, Ni I	1.31 ± 0.22	Meunier (2004)
- Cycle rise	6768 Å, Ni I	1.80 ± 0.16	Meunier (2004)
- Cycle maximum	6768 Å, Ni I	1.76 ± 0.04	Meunier (2004)
Active regions	6768 Å, Ni I, BC	1.35 ± 0.10	McAteer et al. (2005)
	5250 Å, Fe I	1.5	Ioshpa et al. (2008)
EUV nanoflares (Corona)		**1.56±0.08**	**Mean**
nanoflares	171 Å, EUV, BC	1.49 ± 0.06	Aschwanden and Parnell (2002)
nanoflares	195 Å, EUV, BC	1.54 ± 0.05	Aschwanden and Parnell (2002)
nanoflares	Yohkoh/SXT, AlMg, BC	1.65	Aschwanden and Parnell (2002)
Large solar flares (Corona)		**1.76±0.14**	**Mean**
M-class flares	171, 195 Å, EUV	1.62 ± 0.11	Aschwanden and Aschwanden (2008a)
X-class flares	171, 195 Å, EUV	1.78 ± 0.06	Aschwanden and Aschwanden (2008a)
Bastille Day flare	171, 195 Å, EUV	1.89 ± 0.05	Aschwanden and Aschwanden (2008a)

TABLE 4 Summary of solar phenomena, solar location, and range of fractal dimensions. Studies based on the Ca II K line cover both the photospheric and chromospheric zone.

Active regions (magnetograms)	photosphere	1.59 ± 0.20
Granules, super-granules	photosphere	1.23 ± 0.09
Magnetic features, networks	chromosphere	1.40 ± 0.09
Plages	transition region	1.54 ± 0.04
EUV nanoflares	corona	1.56 ± 0.08
Large solar flares	corona	1.76 ± 0.14
Bastille-Day X5.7-class flare	corona	1.89 ± 0.05

completely, due to the superposition of many coronal postflare loops that become filled as a consequence of the chromospheric evaporation process.

Thus, we can distinguish four groups with significantly different fractal properties in photospheric, chromospheric, transition region, and coronal data (**Table 4**). A first group has a very low fractal dimension ($D_A \approx 1.2$) that indicates curvi-linear features produced by super-granulation flows, a second group with chromospheric (network) features has a mean of ($D_A \approx 1.4$), a third group with intermediate fractal dimensions ($D_A \approx 1.54$) includes active region features in the photosphere, plages in the transition region, and EUV nanoflare events, and a fourth group with high values of fractal dimenions ($D_A \approx 1.8$) that includes large (M- and X-class) flares, likely to be caused by area-like topologies of magnetic reconnection and chromospheric evaporation processes.

Discussion

Basic fractal dimension measurement methods

A fractal geometry is a ratio that provides a statistical index of complexity, and changes as a function of a length scale that is used as a yardstick to measure it (Mandelbrot 1977). There are four integer values of Euclidean dimensions $d = [0, 1, 2, 3]$: zero-dimensional point-like structures ($d = 0$), one-dimensional linear or curvi-linear structures ($d = 1$), two-dimensional area-like structures ($d = 2$), and three-dimensional voluminous structures ($d = 3$). All other values between 0 and 3 are non-integer Euclidean dimensions and are called fractal dimensions.

Basic methods to measure fractal dimensions include the *linear-area (LA)* method, the *perimeter-area (PA)* method, and the box-counting (BC) method. The LA method calculates the ratio of a fractal area A to a quasi-space-filled (encompassing) quadratic area with size L^2. Similarly, the PA method yields a ratio of the encompassing curve length or perimeter length ($P = \pi r$ in the case of a circular boundary). The box-counting method uses a cartesian (2-D or 3-D) lattice grid $[x, y]$ and counts all pixels above some threshold or background, and takes the ratio to the total counts of all pixels inside the encompassing coordinate grid. These three methods appear to be very simple, but are not unique. The resulting fractal dimensions may depend on the assumed level of background subtraction, or on the spatial resolution, if not properly normalized. The encompassing perimeter depends on the definition of the perimeter (square, circle, polygon, *etc.*). Multiple different geometric patterns may cause a variation of the fractal dimension across an image or data cube. Temporal variability can modulate the fractal dimension as a function of time. Detailed discussions and examples of the topics of the background subtraction, the spatial resolution, the selection of the field-of-view, and the temporal stability are discussed in almost all references that are listed in **Table 3**. The detailed incorporation of a fractal measurement method differs in each study.

Theoretical values of fractal dimensions converge by definition to a unique value (e.g., $D_A = 1.61803$ for the *golden dragon fractal*, **Figure 5**), while observed data almost always exhibit some spatial inhomogeneity that gives rise to a spread of fractal dimension values across an image.

Granulation in photosphere

A compilation of fractal dimensions measured in photospheric, chromospheric, and coronal wavelengths is given in **Table 3**. The solar granulation has a typical spatial scale of $L = 1,000$ km, or a perimeter of $P = \pi L \approx 3000$ km. Roudier and Muller (1986) measured the areas A and perimeters P of 315 granules and found a power law relation $P \propto A^{D/2}$, with $D = 1.25$ for small granules (with perimeters of $p \approx 500$–$4,500$ km) and $D = 2.15$ for large granules (with $p = 4,500$–$15,000$ km). The smaller granules were interpreted in terms of turbulent origin, because the predicted fractal dimension of an isobaric atmosphere with isotropic and homogeneous turbulence is $D = 4/3 \approx 1.33$ (Mandelbrot 1977). Similar values ($D_A = 1.30$ and $D_A = 1.16$) were found by Hirzberger et al. (1997), Ermolli et al. (1998), and Berrilli et al. (1998). Bovelet and Wiehr (2001) tested different pattern recognition algorithms (Fourier-based recognition technique FBR and multiple-level tracking MLT) and found that the value of the fractal dimension strongly depends on the measurement method. The MLT method yielded a fractal dimension of $D_A = 1.09$, independent of the spatial resolution, the heliocentric angle, and the definition in terms of temperature or velocity. Paniveni et al. (2005) found a fractal dimension of $D_A \approx 1.25$ and concluded, by relating it to the variations of kinetic energy, temperature, and pressure, that the super-granular network is close to being isobaric and possibly of turbulent origin. Paniveni et al. (2010) investigated super-granular cells and found a fractal dimension of $D_A = 1.12$ for active region cells, and $D_A = 1.25$ for quiet region cells, a difference that they attributed to the inhibiting effect of the stronger magnetic field in active regions. Averaging all fractal dimensions related to granular datasets we obtain a mean value of $D_A = 1.23 \pm 0.09$, which is closer to a curvi-linear topology ($D_A \gtrsim 1.0$) than to an area-filled geometry ($D_A \lesssim 2.0$).

The physical understanding of solar (or stellar) granulation has been advanced by numerical magneto-convection models and N-body dynamic simulations, which predict the evolution of small-scale (granules) into large-scale features (meso- or super-granulation), organized by surface flows that sweep up small-scale structures and form clusters of recurrent and stable granular features (Hathaway et al., 2000; Berrilli et al., 2005; Rieutord et al., 2008; Rieutord et al., 2010).

The fractal multi-scale dynamics has been found to be operational in the quiet photosphere, in a quiescent non-flaring state, as well as during flares (Uritsky and Davila 2012).

The fractal structure of the solar granulation is obviously a self-organizing pattern that is created by a combination of subphotospheric magneto-convection and surface flows, which are turbulence-type phenomena.

Transition region

Measurements of the fractal dimension and power law slope of the size distribution in the transition region have been accomplished with IRIS 1400 Å observations of plages and sunspot regions (Vilangot Nhalil et al., 2020; and this work, see **Table 3**). Fractal dimensions of transition region

features were evaluated with a box-counting method here, yielding a range of $D_A \approx 1.54 \pm 0.04$ for the 12 datasets of plages in the transition region listed in **Tables 1** and **3**. The structures observed in the 1,400 Å channel of IRIS are dominated by the Si IV 1394 Å and 1,403 Å resonance lines, which are formed in the transition region temperature range of $T = 10^{4.5}$–10^6 K, sandwiched between the cooler chromosphere and the hotter corona. Apparently, the fractal dimension is not much different in plages with sunspots ($D_A = 1.58 \pm 0.05$), or in field-of-views without sunspots ($D_A = 1.52 \pm 0.09$), (**Table 3**).

One prominent feature in the transition region is the phenomenon of *"moss"*, which appears as a bright, dynamic pattern with dark inclusions, on spatial scales of $L \approx 1$–3 Mm, which has been interpreted as the upper transition region above active region plages and below relatively hot loops (De Pontieu et al., 1999). Besides transition region features, measurements in chromospheric (Quiet-Sun) network structures in the temperature range of $T = 10^{4.5}$–10^6 K yield fractal dimensions of $D_A = 1.30$–1.70 (Gallagher et al., 1998). Furthermore, a value of $D_A \approx 1.4$ was found for so-called *Ellerman bombs* (Georgoulis et al., 2002), which are short-lived brightenings seen in the wings of the Hα line from the low chromosphere. In addition, a range of $D_A \approx 1.25$–1.45 was measured from a large survey of 9342 active region magnetograms (McAteer et al., 2005). Measurements of SOHO/CDS in EUV lines in the temperature range of $T_e \approx 10^{4.5}$–10^6 revealed a distinct temperature dependence: fractal dimensions of $D_A \approx 1.5$–1.6 were identified in He I, He II, OIII, OIV, OV, Ne VI lines at $\log(T_e) \approx 5.8$, then a peak with $D_A \approx 1.6$–1.7 at $\log(T_e) \approx 5.9$, and a drop of $D_A \approx 1.3$–1.35 at $\log(T_e) \approx 6.0$ (see Figure 11 in Gallagher et al., 1998). The temperature dependence of the fractal dimension can be interpreted in terms of sparse heating that produces curvi-linear flow patterns with low fractal dimensions of $D_A \lesssim 1.5$, while strong heating produces volume-filling by chromospheric evaporation with high fractal dimensions $D_A \gtrsim 1.5$.

In recent work it was found that the concept of mono-fractals has to be generalized to multi-fractals to quantify the spatial structure of solar magnetograms more accurately (Lawrence and Schrijver 1993; Cadavid et al., 1994; Lawrence et al., 1996; McAteer et al., 2005; Conlon et al., 2008; Giorgi et al., 2015).

Photospheric magnetic field in active regions

A number of studies investigated the fractal dimension of the photospheric magnetic field, as observed in magnetograms in the Fe I (6,302 Å, 5,250 Å) or Ni I (6,768 Å) lines. Meunier (1999) evaluated the fractal dimension with the perimeter-area method and found $D_A = 1.58$ for super-granular structures to $D_A = 1.58$ for the largest structures, while the linear size-area method yielded $D_A = 1.78$ and $D_A = 1.94$, respectively. In addition, a solar cycle dependence was found by Meunier (2004), with the fractal dimension varying from $D_A = 1.09 \pm 0.11$ (minimum) to $D_A = 1.73 \pm 0.01$ for weak-field regions ($B_m < 900$ G), and $D_A = 1.53 \pm 0.06$ (minimum) to $D_A = 1.80 \pm 0.01$ for strong-field regions ($B_m > 900$ G), respectively. A fractal dimension of $D_A = 1.41 \pm 0.05$ was found by Janssen et al. (2003), but the value varies as a function of the center-to-limb angle and is different for a speckle-reconstructed image that eliminates seeing and noise.

A completely different approach to measure the fractal dimension D was pursued in terms of a 2-D diffusion process, finding fractal diffusion with dimensions in the range of $D \approx 1.3$–1.8 (Lawrence 1991) or $D = 1.56 \pm 0.08$ (Lawrence and Schrijver 1993) by measuring the dependence of the mean square displacement of magnetic elements as a function of time. Similar results were found by Balke et al. (1993). The results exclude Euclidean 2-D diffusion but are consistent with percolation theory for diffusion of clusters at a density below the percolation threshold (Balke et al., 1993; Lawrence and Schrijver 1993).

Other methods to analyze fractals in the photospheric magnetic field in active regions focus on the scaling behavior of the structure function, applied to the longitudinal magnetic field (Abramenko et al., 2002), which can discriminate between weak and fully developed turbulence. Both SOC and intermittent turbulence (IT) appear to co-exist in the solar corona, since power-law avalanche statistics as well as multi-scaling of structure functions are observed simulaneously (Uritsky et al., 2007). Moreover, stochastic coupling between the solar photopshere and the corona indicate an intimate spatial connection (Uritsky et al., 2013).

Coronal flares

Although this study is focused on the fractal geometry of transition region features observed with IRIS, we compare these results also with coronal values. The fractal dimension of coronal events has been measured for 10 X-class flares, 10 M-class flares, and the Bastille-Day flare (Aschwanden and Aschwanden 2008a; Aschwanden and Aschwanden 2008b). Interestingly, these datasets exhibit relatively large values of the fractal dimension, with a mean and standard deviation of $D_A = 1.76 \pm 0.14$. They show a trend that the largest flares, especially X-class flares, exhibit the highest values of $D_A \lesssim 1.8$–1.9 (**Table 3**). If we attribute flare events to the magnetic reconnection process, the observations imply that the flare plasma fills up the flare volume

with a high space-filling factor, which is consistent with the chromospheric evaporation process.

Phenomena of smaller magnitude than large flares include microflares, nanoflares, coronal EUV brightenings, *etc.* Such small-scale variability events are found to have a mean fractal dimension of $D_A = 1.56 \pm 0.08$ (**Table 3**), which is compatible with those found in M-class flares, but clearly has a lower fractal dimension than large flares, i.e., $D_A = 1.76 \pm 0.14$ (**Table 3**).

Self-organized criticality models

The generation of magnetic structures that bubble up from the solar convection zone to the solar surface by buoyancy, observed as emerging flux phenomena in form of active regions, sunspots, and pores, can be statistically described as a random process, self-organization with (SOC) and without (SO) criticality, percolation, or a diffusion process. Random processes produce incoherent structures, in contrast to the coherent magnetic flux concentrations observed in sunspots. A self-organization (SO) process needs a driving force and a counter-acting feedback mechanism that produces ordered structures (such as the convective granulation cells; Aschwanden et al., 2018). A SOC process exhibits power law size distributions of avalanche sizes and durations. The finding of a fractal dimension of a power law size distribution in magnetic features alone is not a sufficient condition to prove or rule out any of these processes. Nevertheless, the fractal dimension yields a scaling law between areas ($A \propto L^{D_2}$) or volumes ($V \propto L^{D_3}$), and length scales L that quantify scale-free (fractal) processes in form of power laws and can straightforwardly be incorporated in SOC-like models.

If we compare the standard SOC parameters measured in observations (**Figure 2**) with the theoretically expected values from the standard SOC model (**Table 2**), we find that the power law slopes for event areas A agree well ($a_A^{obs} = 2.51 \pm 0.21$) *versus* $a_A^{theo} = 2.33$ (**Figure 2**), while the power law slopes for the radiated energy E agree within the stated uncertainties, ($a_E^{obs} = 2.03 \pm 0.18$) *versus* $a_E^{theo} = 1.80$ (**Figure 2**), but the power law slopes for the time duration T disagree ($a_T^{obs} = 2.65 \pm 0.39$) *versus* $a_T^{theo} = 2.00$ (**Figure 2**). The latter disagreement is possibly caused by the restriction of a constant minimum event lifetime (either 60 s or 110 s) that was assumed in the previous work (Vilangot Nhalil et al., 2020). The interpretation of these results implies that transition region brightenings have a similar statistics as the SOC model, at least for active regions, nanoflares, and large flares, with a typical fractal dimension of $D_A \approx 1.54 \pm 0.04$, but are significantly lower for photospheric granulation ($D_A \approx 1.23 \pm 0.09$), which implies the dominance of sparse quasi-linear flow structures in the photosphere and transition region.

Conclusion

Our aim is to obtain an improved undestanding of fractal dimensions and size distributions observed in the solar photosphere and transition region, which complement previous measurements of coronal phenomena, from nanoflares to the largest solar flares. Building on the previous study *"Power-law energy distributions of small-scale impulsive events on the active Sun: Results from IRIS"*, we are using the same IRIS 1,400 Å data, extracted with an automated pattern recognition code during 12 time episodes observed in plage and sunspot regions. A total of 23,633 events has been obtained, quantified in terms of event areas A, radiative energies E, and event durations T. The results can be summarized as follows:

1. Fractal dimensions, measured in solar images at various wavelengths and spatial resolutions, cover a range of $D_A = 1$–2. We can organize the 7 types of solar phenomena and their range of fractal dimensions in **Table 4**, which can be subdivided into 4 non-overlapping groups: Granules and super-granules have a fractal dimension of ($D_A \approx 1.2$), chromospheric magnetic features and networks have a fractal dimension of ($D_A \approx 1.4$), active regions, plages, and coronal nanoflares have a mean fractal dimension of ($D_A \approx 1.5$), and large flares have the highest range ($D_A \approx 1.8$). Low values of the fractal dimension ($D_A \approx 1$) are consistent with curvi-linear flow patterns, while large values are consistent with space-filling features produced by chromospheric evaporation in large flares. A mean value $D_A \approx 1.5$ has been found to represent a useful approximation in standard SOC models.
2. We calculate a power law fit to the size distribution $N(A) \propto A^{-\alpha_A}$ of event areas A, and find a mean value of $a_A = 2.51 \pm 0.21$ that agrees well with the value $a_A = 2.33$ expected from the theoretical SOC model. Consequently, brightenings in plages of the transition region are consistent with generic SOC avalanches.
3. Based on the power law slope αA we derive the fractal dimension $D_A^{PL} = 2/(\alpha_A - 1)$, which yields a mean observed value of $D_A^{PL} = 1.35 \pm 0.19$ and approximately matches the theoretial mean value of $D_A = 1.5$. Alternatively, we obtain with the standard box-counting method an observed value of $D_A = 1.54 \pm 0.04$.
4. Synthesizing the measurements of the fractal dimension from photospheric, chromospheric, transition region, and coronal data we arrive at 7 groups that yield the following means and standard deviations of their fractal dimension: From these 7 groups we can discriminate four (**Table 4**) non-overlapping ranges with significantly different fractal dimensions, which imply different physical mechanisms: Low values of the fractal dimension ($D_A \approx 1.2$) indicate curvi-linear granulation flows; larger values ($D_A \approx 1.4$) align fractal

structures with chromospheric network cells; intermediate values of ($D_A \approx 1.54$) are characteristic for brightening events in the Quiet Sun and transition region; while large values ($D_A \lesssim 2.0$) are consistent with quasi-space-filling features produced by chromospheric evaporation in large flares.

The analysis presented here demonstrates that we can distinguish between (i) physical processes with sparse curvilinear flows, as they occur in granulation, meso-granulation, and super-granulation, and (ii) physical processes with quasi-space-filling flows, as they occur in the chromospheric evaporation process during solar flares. IRIS data can therefore be used to diagnose mass flows in the transition region. Moreover, reliable measurements of the fractal dimension yields realistic plasma filling factors that are important in the estimate of radiative energies and hot plasma emission measures. Future work on fractal dimensions in multi-wavelength datasets from IRIS and AIA/SDO may clarify the dynamics of coronal heating events.

Data availability statement

The raw data supporting the conclusion of this article will be made available by the authors, without undue reservation.

Author contributions

All authors listed have made a substantial, direct, and intellectual contribution to the work and approved it for publication.

Funding

This work was partially supported by NASA contract NNX11A099G "Self-organized criticality in solar physics", NASA contract NNG04EA00C of the SDO/AIA instrument, and the IRIS contract NNG09FA40C to LMSAL.

Acknowledgments

We acknowledge constructive comments of an reviewer and stimulating discussions (in alphabetical order) with Sandra Chapman, Paul Charbonneau, Henrik Jeldtoft Jensen, Adam Kowalski, Alexander Milovanov, Leonty Miroshnichenko, Jens Juul Rasmussen, Karel Schrijver, Vadim Uritsky, Loukas Vlahos, and Nick Watkins.

Conflict of interest

The authors declare that the research was conducted in the absence of any commercial or financial relationships that could be construed as a potential conflict of interest.

Publisher's note

All claims expressed in this article are solely those of the authors and do not necessarily represent those of their affiliated organizations, or those of the publisher, the editors and the reviewers. Any product that may be evaluated in this article, or claim that may be made by its manufacturer, is not guaranteed or endorsed by the publisher.

References

Abramenko, V. I., Yurchyshyn, V. B., Wang, H., Spirock, T. J., and Goode, P. R. (2002). Scaling behavior of structure functions of the longitudinal magnetic field in active regions on the Sun. *ApJ* 577, 487. doi:10.1086/342169

Aschwanden, M. J. (2014). A macroscopic description of self-organized systems and astrophysical applications. *Astrophys. J.* 782, 54. doi:10.1088/0004-637x/782/1/54

Aschwanden, M. J. (2012). A statistical fractal-diffusive avalanche model of a slowly-driven self-organized criticality system. *Astron. Astrophys.* 539, A2. doi:10.1051/0004-6361/201118237

Aschwanden, M. J., and Aschwanden, P. D. (2008b). Solar flare geometries: II. The volume fractal dimension. *Astrophys. J.* 574, 544–553. doi:10.1086/524370

Aschwanden, M. J., and Aschwanden, P. D. (2008a). Solar flare geometries: I. The area fractal dimension. *Astrophys. J.* 574, 530–543. doi:10.1086/524371

Aschwanden, M. J., Crosby, N., Dimitropoulou, M., Georgoulis, M. K., Hergarten, S., McAteer, J., et al. (2016). 25 Years of self-organized criticality: Solar and astrophysics. *Space Sci. Rev.* 198, 47–166. doi:10.1007/s11214-014-0054-6

Aschwanden, M. J., and Parnell, C. E. (2002). Nanoflare statistics from first principles: Fractal geometry and temperature synthesis. *Astrophys. J.* 572, 1048.

Aschwanden, M. J. (2022b). Reconciling power-law slopes in solar flare and nanoflare size distributions. *Astrophys. J. Lett.* 934, L3. doi:10.3847/2041-8213/ac7b8d

Aschwanden, M. J., Scholkmann, F., Bethune, W., Schmutz, W., Abramenko, W., Cheung, M. C. M., et al. (2018). Order out of randomness: Self-organization processes in astrophysics. *Space Sci. Rev.* 214, 55. doi:10.1007/s11214-018-0489-2

Aschwanden, M. J. (2011). *Self-organized criticality in Astrophysics: The statistics of nonlinear processes in the universe*. New York: Springer-Praxis, 416. ISBN 978-3-642-15000-5.

Aschwanden, M. J. (2022a). The fractality and size distributions of astrophysical self-organized criticality systems. *Astrophys. J.* 934, 33. doi:10.3847/1538-4357/ac6bf2

Bak, P. (1996). *How nature works: The science of self-organized criticality*. New York: Copernicus.

Bak, P., Tang, C., and Wiesenfeld, K. (1988). Self-organized criticality. *Phys. Rev. A* . 38 (1), 364–374. doi:10.1103/physreva.38.364

Bak, P., Tang, C., and Wiesenfeld, K. (1987). Self-organized criticality: An explanation of the 1/*f* noise. *Phys. Rev. Lett.* 59 (27), 381–384. doi:10.1103/physrevlett.59.381

Balke, A. C., Schrijver, C. J., Zwaan, C., and Tarbell, T. D. (1993). Percolation theory and the geometry of photospheric magnetic flux concentrations. *Sol. Phys.* 143, 215–227. doi:10.1007/bf00646483

Berrilli, F., Del Moro, D., Russo, S., Consolini, G., and Straus, T. (2005). Spatial clustering of photospheric structures. *Astrophys. J.* 632, 677–683. doi:10.1086/432708

Berrilli, F., Florio, A., and Ermolli, I. (1998). On the geometrical properties of the chromospheric network. *Sol. Phys.* 180, 29–45. doi:10.1023/a:1005023819431

Bovelet, B., and Wiehr, E. (2001). A new algorithm for pattern recognition and its application to granulation and limb faculae. *Sol. Phys.* 201, 13–26. doi:10.1023/a:1010344827952

Cadavid, A. C., Lawrence, J. K., Ruzmaikin, A., and Kayleng-Knight, A. (1994). Multifractal models of small-scale solar magnetic fields. *Astrophys. J.* 429, 391. doi:10.1086/174329

Conlon, P. A., Gallagher, P. T., McAteer, R. T. J., Ireland, J., Young, C. A., Kestener, P., et al. (2008). Multifractal properties of evolving active regions. *Sol. Phys.* 248, 297–309. doi:10.1007/s11207-007-9074-7

Consolini, G., Carbone, V., Berrilli, F., Bruno, R., Bavassano, B., Briand, C., et al. (1999). Scaling behavior of the vertical velocity field in the solar photosphere. *A&A* 344, L33–L36.

Criscuoli, S., Rast, M. P., Ermolli, I., and Centrone, M. (2007). On the reliability of the fractal dimension measure of solar magnetic features and on its variation with solar activity. *Astron. Astrophys.* 461, 331–338. doi:10.1051/0004-6361:20065951

De Pontieu, B., Berger, T. E., Schrijver, C. J., and Title, A. M. (1999). Dynamics of transition region 'moss' at high time resolution. *Sol. Phys.* 190, 419–435. doi:10.1023/a:1005220606223

De Pontieu, B., Title, A. M., Lemen, J. R., Kushner, G. D., Akin, D. J., Allard, B., et al. (2014). The Interface region imaging Spectrograph (IRIS). *Sol. Phys.* 289, 2733. doi:10.1007/s11207-014-0485-y

Ermolli, I., Fovi, M., Bernacchia, C., Berilli, F., Caccin, B., Egidi, A., et al. (1998). The prototype RISE-PSPT instrument operating in Rome. *Sol. Phys.* 177/1-2, 1–10.

Ermolli, I., Giorgi, F., Romano, P., Zuccarello, F., Criscuoli, S., and Stangalini, M. (2014). Fractal and multifractal properties of active regions as flare precursors: A case study based on SOHO/MDI and SDO/HMI observations. *Sol. Phys.* 289, 2525–2545. doi:10.1007/s11207-014-0500-3

Gallagher, P. T., Phillips, K. J. H., Harra-Murnion, L. K., and Keenan, F. P. (1998). Properties of the quiet Sun EUV network. *A&A* 335, 733.

Georgoulis, M. K., Rust, D. M., Bernasconi, P. N., and Schmieder, B. (2002). Statistics, morphology, and energetics of Ellerman bombs. *Astrophys. J.* 575, 506–528. doi:10.1086/341195

Giorgi, F., Ermolli, I., Romano, P., Stangalini, M., Zuccarello, F., and Criscuoli, S. (2015). The signature of flare activity in multifractal measurements of active regions observed by SDO/HMI. *Sol. Phys.* 290, 507–525. doi:10.1007/s11207-014-0609-4

Hathaway, D. H., Beck, J. G., Bogart, R. S., Bachmann, K., Khatri, G., Petitto, J., et al. (2000). *Sol. Phys.* 193, 299–312. doi:10.1023/a:1005200809766

Hirzberger, J., Vazquez, M., Bonet, J. A., Hanslmeier, A., and Sobotka, M. (1997). Time series of solar granulation images. I. Differences between small and large granules in quiet regions. *Astrophys. J.* 480, 406–419. doi:10.1086/303951

Ioshpa, B. A., Obridko, V. N., and Rudenchik, E. A. (2008). Fractal properties of solar magnetic fields. *Astron. Lett.* 34, 210–216. doi:10.1134/s1063773708030080

Janssen, K., Voegler, A., and Kneer, F. (2003). On the fractal dimension of small-scale magnetic structures in the Sun. *Astron. Astrophys.* 409, 1127–1134. doi:10.1051/0004-6361:20031168

Lawrence, J. K., Cadavid, A., and Ruzmaikin, A. (1996). On the multifractal distribution of solar magnetic fields. *Astrophys. J.* 465, 425. doi:10.1086/177430

Lawrence, J. K. (1991). Diffusion of magnetic flux elements on a fractal geometry. *Sol. Phys.* 135, 249–259. doi:10.1007/bf00147499

Lawrence, J. K., and Schrijver, C. J. (1993). Anomalous diffusion of magnetic elements across the solar surface. *Astrophys. J.* 411, 402. doi:10.1086/172841

Lu, E. T., and Hamilton, R. J. (1991). Avalanches and the distribution of solar flares. *Astrophys. J.* 380, L89. doi:10.1086/186180

Mandelbrot, B. B. (1977). *The fractal geometry of nature*. New York: W.H.Freeman and Company.

McAteer, R. T. J., Aschwanden, M. J., Dimitropoulou, M., Georgoulis, M. K., Pruessner, G., Morales, L., et al. (2016). 25 Years of self-organized criticality: Numerical detection methods. *Space Sci. Rev.* 198, 217–266. doi:10.1007/s11214-015-0158-7

McAteer, R. T. J., Gallagher, P. T., and Ireland, J. (2005). Statistics of active region complexity: A large-scale fractal dimension survey. *Astrophys. J.* 631, 628–635. doi:10.1086/432412

Meunier, N. (2004). Complexity of magnetic structures: Flares and cycle phase dependence. *Astron. Astrophys.* 420, 333–342. doi:10.1051/0004-6361:20034044

Meunier, N. (1999). Fractal analysis of michelson Doppler imager magnetograms: A contribution to the study of the formation of solar active regions. *Astrophys. J.* 515, 801–811. doi:10.1086/307050

Paniveni, U., Krishan, V., Singh, J., and Srikanth, R. (2010). Activity dependence of solar supergranular fractal dimension. *Mon. Not. R. Astron. Soc.* 402 (1), 424–428. doi:10.1111/j.1365-2966.2009.15889.x

Paniveni, U., Krishan, V., Singh, J., and Srikanth, R. (2005). On the fractal structure of solar supergranulation. *Sol. Phys.* 231, 1–10. doi:10.1007/s11207-005-1591-7

Pruessner, G. (2012). *Self-organised criticality. Theory, models and characterisation*. Cambridge: Cambridge University Press.

Rathore, B., Carlsson, M., and Leenaarts, J. (2015). The formation of *iris*diagnostics. VI. The diagnostic potential of the C II lines at 133.5 nm in the solar atmosphere. *Astrophys. J.* 811, 81. doi:10.1088/0004-637x/811/2/81

Rathore, B., and Carlsson, M. (2015). The formation of *iris*diagnostics. V. A quintessential model atom of C II and general formation properties of the C II lines at 133.5 nm. *Astrophys. J.* 811, 80. doi:10.1088/0004-637x/811/2/80

Rieutord, M., Meunier, N., Roudier, T., Rondi, S., Beigbeder, F., and Pares, L. (2008). Solar supergranulation revealed by granule tracking. *Astron. Astrophys.* 479, L17–L20. doi:10.1051/0004-6361:20079077

Rieutord, M., Roudier, T., Rincon, F., Malherbe, J. M., Meunier, N., Berger, T., et al. (2010). On the power spectrum of solar surface flows. *Astron. Astrophys.* 512, A4. doi:10.1051/0004-6361/200913303

Roudier, T., and Muller, R. (1986). Structure of the solar granulation. *Sol. Phys.* 107, 11–26. doi:10.1007/bf00155337

Sharma, A. S., Aschwanden, M. J., Crosby, N. B., Klimas, A. J., Milovanov, A. V., Morales, L., et al. (2016). 25 Years of self-organized criticality: Space and laboratory plasmas. *Space Sci. Rev.* 198, 167–216. doi:10.1007/s11214-015-0225-0

Uritsky, V. M., and Davila, J. M. (2012). Multiscale dynamics of solar magnetic structures. *Astrophys. J.* 748, 60. doi:10.1088/0004-637x/748/1/60

Uritsky, V. M., Davila, J. M., Ofman, L., and Coyner, A. J. (2013). Stochastic coupling of solar photosphere and corona. *Astrophys. J.* 769, 62. doi:10.1088/0004-637x/769/1/62

Uritsky, V. M., Paczuski, M., Davila, J. M., and Jones, S. I. (2007). Coexistence of self-organized criticality and intermittent turbulence in the solar corona. *Phys. Rev. Lett.* 99 (2), 025001. doi:10.1103/physrevlett.99.025001

Vilangot Nhalil, N. V., Nelson, C. J., Mathioudakis, M., Doyle, G. J., and Ramsay, G. (2020). Power-law energy distributions of small-scale impulsive events on the active Sun: Results from IRIS. *Mon. Not. R. Astron. Soc.* 499, 1385–1394. doi:10.1093/mnras/staa2897

Watkins, N. W., Pruessner, G., Chapman, S. C., Crosby, N. B., and Jensen, H. J. (2016). 25 Years of self-organized criticality: Concepts and controversies. *Space Sci. Rev.* 198, 3–44. doi:10.1007/s11214-015-0155-x

frontiers | Frontiers in Astronomy and Space Sciences

TYPE Original Research
PUBLISHED 16 November 2022
DOI 10.3389/fspas.2022.1040945

OPEN ACCESS

EDITED BY
Yihua Yan,
National Astronomical Observatories (CAS), China

REVIEWED BY
Mingde Ding,
Nanjing University, China
Ying Li,
Purple Mountain Observatory (CAS), China

*CORRESPONDENCE
Juraj Lörinčík,
lorincik@baeri.org

SPECIALTY SECTION
This article was submitted to Stellar and Solar Physics, a section of the journal Frontiers in Astronomy and Space Sciences

RECEIVED 09 September 2022
ACCEPTED 21 October 2022
PUBLISHED 16 November 2022

CITATION
Lörinčík J, Polito V, De Pontieu B, Yu S and Freij N (2022), Rapid variations of Si IV spectra in a flare observed by interface region imaging spectrograph at a sub-second cadence.
Front. Astron. Space Sci. 9:1040945.
doi: 10.3389/fspas.2022.1040945

Rapid variations of Si IV spectra in a flare observed by interface region imaging spectrograph at a sub-second cadence

Juraj Lörinčík[1,2]*, Vanessa Polito[1,2,3], Bart De Pontieu[2,4,5], Sijie Yu[6] and Nabil Freij[1,2]

[1]Bay Area Environmental Research Institute, NASA Research Park, Moffett Field, CA, United States, [2]Lockheed Martin Solar and Astrophysics Laboratory, Palo Alto, CA, United States, [3]Department of Physics, Oregon State University, Corvallis, OR, United States, [4]Institute of Theoretical Astrophysics, University of Oslo, Oslo, Norway, [5]Rosseland Centre for Solar Physics, University of Oslo, Oslo, Norway, [6]Center for Solar-Terrestrial Research, New Jersey Institute of Technology, Newark, NJ, United States

We report on observations of highly-varying Si IV 1402.77 Å line profiles observed with the Interface Region Imaging Spectrograph (IRIS) during the M-class flare from 18 January 2022 at an unprecedented 0.8 s cadence. Moment analysis of this line observed in flare ribbon kernels showed that the intensity, Doppler velocity, and non-thermal broadening exhibited variations with periods below 10 s. These variations were found to be correlated with properties of the Gaussian fit to a well-resolved secondary component of the line redshifted by up to 70 km s^{-1}, while the primary component was consistently observed near the rest wavelength of the line. A particularly high correlation was found between the non-thermal broadening of the line resulting from the moment analysis and the redshift of the secondary component. This means that the oscillatory enhancements in the line broadening were due to plasma flows (away from the observer) with varying properties. A simple de-projection of the Doppler velocities of the secondary component based on a three-dimensional reconstruction of flare loops rooted in the kernel suggests that the observed flows were caused by downflows and compatible with strong condensation flows recently predicted by numerical simulations. Furthermore, peaks of the intensity and the trends of Doppler velocity of the Gaussian fit to the secondary component (averaged in the ribbon) were found to correspond to one of the quasi-periodic pulsations (QPPs) detected during the event in the soft X-ray flux (as measured by the Geostationary Operational Environmental Satellite, GOES) and the microwave radio flux (as measured by the Expanded Owens Valley Solar Array, EOVSA). This result supports a scenario in which the QPPs were driven by repeated magnetic reconnection.

KEYWORDS

solar flares, solar atmosphere, solar ultraviolet emission, solar transition region, solar magnetic reconnection

1 Introduction

Spectroscopic observations of solar flare ribbons provide a wealth of information about the transfer of energy between the site of energy release in the corona and the lower atmosphere of the Sun (see e.g., the review of Fletcher et al., 2011). A typical manifestation of this process are Doppler shifts of spectral lines which formation region is affected by upflows and downflows of plasma (see e.g., Doschek et al., 1980; Canfield et al., 1987; Brosius, 2003) along magnetic field lines forming as a consequence of magnetic reconnection, the driver of solar flares (see **Section 1** in Shibata and Magara, 2011). The upflows, which can be identified as blueshifts of lines forming at coronal and flare temperatures ($\log(T\ [\mathrm{K}]) \approx 6-7$), are due to the chromospheric evaporation (e.g., Acton et al., 1982; del Zanna et al., 2006; Brosius, 2013). In this process, the deposited energy heats plasma at chromospheric heights which consequently expands at speeds sometimes reaching hundreds km s^{-1} (see e.g., the review of Milligan, 2015), and fills flare loops. The downflows, observable as redshifts of lines formed at lower temperatures in the chromosphere and the transition region ($\log(T\ [\mathrm{K}]) \approx 4-5$), are due to the process termed chromospheric condensation (e.g., Fisher et al., 1985; Warren et al., 2016; Graham et al., 2020). Chromospheric condensation occurs below the expanding region and the speeds of the downflows driven by the expansion are typically an order of magnitude lower than those of the evaporation, reaching a few to few tens km s^{-1}. Therefore, while the evaporation can in some cases lead to complete blueshifts of hot lines (e.g., Young et al., 2015; Dudík et al., 2016; Polito et al., 2016), the condensation-induced downflows are often only observed as modest redshifts or enhancements in red wings of cooler lines (Tian et al., 2015; Warren et al., 2016; Brosius and Inglis, 2018; Yu et al., 2020a; Lörinčík et al., 2022). The Doppler shifts indicative of the evaporation and condensation evolve in time. Apart from a slight delay between the visibility of the earliest traces of the condensation and the evaporation, the absolute values of the corresponding red and blue Doppler velocities drop over tens and hundreds of seconds, respectively (Graham and Cauzzi, 2015; Graham et al., 2020).

Another widely-discussed observable which traces the energization of the lower solar atmosphere is the broadening of line profiles. Apart from the thermal and instrumental broadening, line profiles are often subject to excess non-thermal broadening (e.g., Dere and Mason, 1993; Harra et al., 2013; Stores et al., 2021). In flares, the non-thermal broadening is usually attributed to unresolved turbulent motions in the emitting region or a superposition of multiple sources of Doppler-shifted emission along the line-of-sight (e.g., Milligan, 2011; Doschek et al., 2014; Warren et al., 2018). Non-thermal broadening and its origins have been studied in observations of the Interface Region Imaging Spectrometer (IRIS; De Pontieu et al., 2014) sometimes supplemented with flare simulations performed using the RADYN code (Carlsson and Stein, 1992, 1995, 1997; Allred et al., 2015). The high spectral, spatial, and temporal resolutions of IRIS are well suited to study highly-varying flare spectra (for a summary of results of IRIS see the review of De Pontieu et al., 2021). For example, Polito et al. (2019) showed that the superposition of flows alone cannot account for broad profiles of the Fe XXI 1354.1 Å line observed in flare ribbon. Jeffrey et al. (2018) discovered an increase and oscillations of non-thermal broadening of the Si IV 1402.77 Å line in a ribbon which formed during a small B-class flare. Since these occurred prior to the impulsive phase of the flare determined from the trend of the X-ray emission, the authors conclude that the turbulence contributed to plasma heating. This is supported by the observed ≈ 10 s period of the oscillations which corresponds to the timescale of the dissipation of turbulent energy predicted to range between 1 and 10 s (Kontar et al., 2017). Oscillations of both excess width and intensity of the same line of Si IV with periods between 5 and 10 s were also reported in the analysis of two microflares of Chitta and Lazarian (2020). The authors proposed that the turbulence acts as a triggering mechanism of fast magnetic reconnection. The broadened profiles are also often subject to Doppler shifts (e.g., Jeffrey et al., 2018), in some cases clearly attributed to the evaporation and condensation (e.g., Milligan, 2011; Li Y. et al., 2015; Polito et al., 2015). This indicates that these processes might act simultaneously.

The results of these studies suggest that turbulence plays an important role during the deposition of the energy released during flares in the lower solar atmosphere, possibly contributing to the heating itself. To our knowledge, in IRIS observations the signatures of the turbulence as well as high-frequency ($p < 10$ s) oscillations of properties of lines formed in the transition region have only been studied in datasets containing spectra observed during small flares (see e.g., the references above) and active region brightenings (Gupta et al., 2018). This is most-likely caused by the scarcity of major flare events observed by recent instrumentation at a cadence that would allow for the investigation of these phenomena. Thanks to the recent development of very high-cadence IRIS observing programs, new opportunities for advances in this topic are now possible as IRIS has routinely been observing transient solar activity at a sub-second cadence, starting in Fall 2021. In this work we detail high-frequency oscillations of properties of the Si IV 1402.77 Å line, including its non-thermal broadening, observed during the M-class flare from 18 January 2022.

This manuscript is structured as follows. In **Section 2** we briefly describe the investigated event. Analysis of spectroscopic and imaging data is detailed in **Sections 3**, **4**. In **Section 5** we focus on relating the time evolution of spectra observed by IRIS to features visible in SXR and microwave radio lightcurves. A brief summary of our results is provided in **Section 6**.

2 18 January 2022 flare

2.1 Data

In this paper we focus on spectroscopic observations with IRIS of the 18 January 2022 M1.5-class flare. The IRIS instrument observes solar spectra in two far ultraviolet (FUV) bands at 1,331.6 Å—1,358.4 Å and 1,380.6 Å—1,406.8 Å and a near ultraviolet (NUV) band at 2,782.6 Å—2,833.9 Å. These bands contain a multitude of lines formed across the solar atmosphere at temperatures ranging between $\log T$ [K] = 3.7 and 7. The spatial and spectral resolutions in the FUV band, containing the Si IV 1402.77 Å line that we analyze here, reach 0.33" and 0.026 Å, respectively. The pixel size of IRIS is 0.167". This flare was captured in the sit-and-stare mode with spectral and spatial summing of 2. This event is the first major (GOES-class) flare IRIS observed at an unprecedented sub-second cadence of 0.8 s. The exposure time employed in this observation is 0.3 s.

The spectrograph datacube is accompanied by a series of imaging observations from the IRIS Slit-Jaw Imager (SJI) at 2,796 Å. The analyzed flare is further studied using imaging data from the Atmospheric Imaging Assembly (AIA; Lemen et al., 2012) on-board the Solar Dynamics Observatory (SDO; Pesnell et al., 2012) and the Extreme Ultraviolet Imager (EUVI; Wuelser et al., 2004; Howard et al., 2008) on-board STEREO-A. Apart from the spectroscopic data we also investigate SXR lightcurves obtained by the Geostationary Operational Environmental Satellite (GOES) and microwave emission measured by the Expanded Owens Valley Solar Array (EOVSA; Gary et al., 2018).

2.2 Description of the event

Figure 1 presents context observations of this event. Panel (A) depicts the soft X-ray flux measured in the two passbands of the GOES-16 satellite corresponding to 0.5–4 Å (red) and 1–8 Å (blue). According to this panel, the onset of the flare corresponded roughly to 17:00 UT, its impulsive phase lasted between ≈ 17:20 and ≈ 17:40 UT when the flux peaked. At this point the flux started to drop during the gradual phase lasting roughly until 20:00 UT when another small flare elsewhere on the disk occurred.

The second row of this figure contains observations of the flare after its onset [panel (B)] as well as during its impulsive [panel (C)] and gradual [panel (D)] phases in the 171 Å filter channel of AIA which is primarily sensitive to plasma emitting at $\log T$ [K] = 5.8 (Lemen et al., 2012). The flare occurred in NOAA 12929 active region, which was located relatively close to the western limb at solar $x \approx 800$". The magnetic field configuration of this active region is outlined using the green and magenta contours in panel (B), indicating the strength of the line-of-sight (LOS) component of the photospheric magnetic field as measured by the Helioseismic and Magnetic Imager (HMI; Scherrer et al., 2012) onboard SDO. The contours correspond to ±200 G with the green contours corresponding to the positive polarity flux concentrations. During the impulsive phase of the flare [panel (C)], a pair of ribbons was observed to form, one to the south and one to the north. The comparison of panels (B) and (C) reveals that the southern ribbon was spatially coincident with the positive polarity flux concentrations while the northern one corresponded to the negative polarity flux. Here we further focus on spectra formed in the southern ribbon during the impulsive phase of the flare, also shown as observed in AIA 304 Å ($\log T$ [K] = 4.7), panel (E) when it crossed the slit of IRIS (white dashed line). **Figure 1F** shows an arcade of flare loops imaged in the AIA 131 Å ($\log T$ [K] = 7.0) which was forming at roughly the same time as shown in panel (E). The hot emission of the developing flare loop arcade is also shown in panel (G) where it is imaged in the AIA 193 Å. During flares, this channel is primarily sensitive to Fe XXIV emission peaking at $\log T$ [K] = 7.25 (see e.g., O'Dwyer et al., 2010).

A detailed view of the ribbons as well as the arcade of flare loops is provided in **Figure 2**. The structure of the ribbons is illustrated in the 2,796 Å SJI images during the time period that we focus on in this manuscript. The SJI data were averaged over five consecutive exposures to suppress the noise. An animation consisting of non-averaged full-cadence SJI observations of the ribbons is available online. The bright portion of the southern ribbon was composed of a series of small kernels. The time evolution of this ribbon, as depicted by the first row of **Figure 2** and the accompanying animation, was characterized by the motion of the kernels roughly directed from the solar east [panel (A)] towards the solar west direction [panel (E)], crossing the slit between ≈ 17:34 and ≈ 17:37 UT [panels (C), (D)]. AIA 131 Å observations of the flare arcade [panels (F–I)] show several well-defined flare loops originating from these kernels. These flare loops are further discussed in **Section 4**. The white arrow plotted in panels (D) (and (H)) points toward the kernels (and flare loop footpoints) which, when passing through the slit, led to a major increase of the intensity, Doppler velocity, and broadening of the Si IV 1402.77 Å line (**Section 3.1.1**). We discuss this in the following Section.

3 High-cadence interface region imaging spectrograph observations of the Si IV 1402.77 Å line

In this manuscript we detail characteristics of the Si IV 1402.77 Å line formed in the solar transition region. It was shown that especially in stronger flares the Si IV spectra can be affected by opacity effects (Kerr et al., 2019; Zhou et al., 2022).

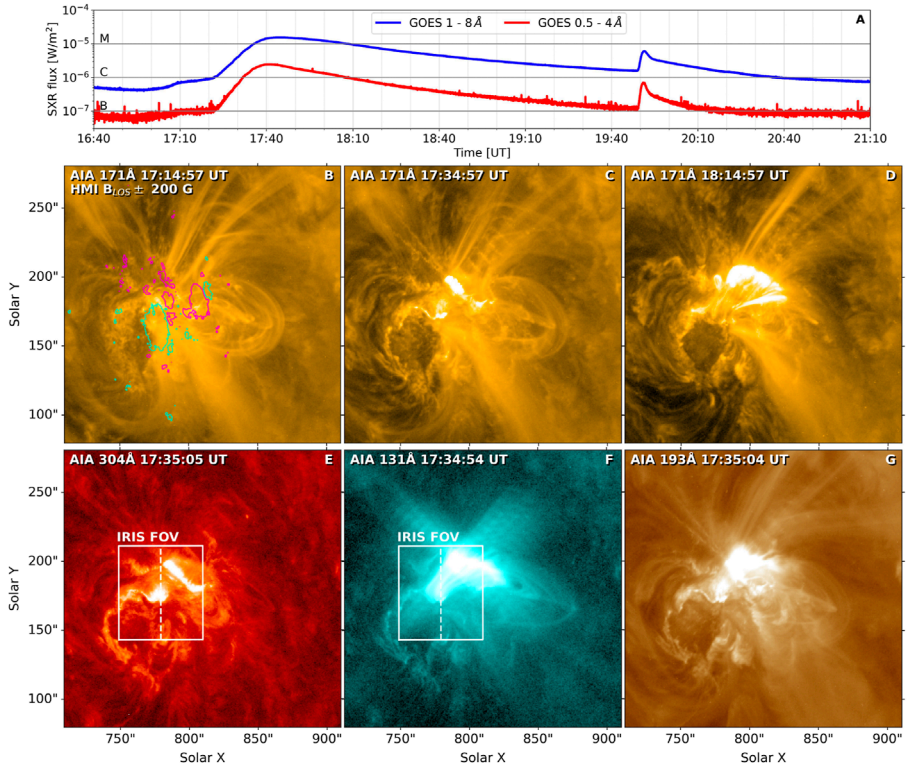

FIGURE 1
Context observations of the 18 January 2022 flare. Panel **(A)** displays the evolution of the soft X-ray flux measured in the 0.5–4 Å (red) and 1–8 Å (blue) channels of the GOES satellite. Imaging observations of the flare in AIA 171 Å during the onset, impulsive, and gradual phases of the flare is shown in panels **(B–D)**. The bottom row of the figure details the flare during its impulsive phase. Panel **(E)** shows flare ribbons observed in AIA 304 Å. Panels **(F)** and **(G)** detail hot flare emission as observed in AIA 131 Å and AIA 193 Å, respectively.

These are usually studied using the intensity ratio of the 1,402.77 Å line with the Si IV 1393.75 Å line, predicted to be ≈ 2 when Si IV is formed under optically thin conditions (see e.g., Mathioudakis et al., 1999; Gontikakis and Vial, 2018). As was recently reported by Zhou et al. (2022), this ratio is also a function of wavelength, yielding different values across profiles of the two Si IV lines and large deviations in line centroids containing dips or reversals found in flare loops. Since we focus solely on ribbon spectra in which we did not observe typical spectral features associated with strong opacity effects (see also Yan et al., 2015; Joshi et al., 2021), we assumed the line to be optically thin. The dataset we use also does not contain the Si IV 1393.75 Å line for which we could not investigate the variations of the intensity ratio of the two Si IV lines, if any.

3.1 Moment analysis

3.1.1 Maps of moments

We begin the analysis of the Si IV 1402.77 Å line by inspecting maps of the total line intensity (which is dependent on the peak intensity and the width of the profile), the Doppler velocity (v_D), and the non-thermal broadening (v_{nt}) as a function of time. These quantities were determined by calculating the moments of this line in the wavelength range of $\lambda_0 \pm 0.6$ Å which contained the entire profile even in the pixels where the Si IV line was the broadest. Prior to the calculation of the moments, the FUV continuum averaged outside of this wavelength range was subtracted from the observed spectrum. To obtain the Doppler velocities we used the reference wavelength of 1,402.770 Å (Sandlin et al., 1986). Note that in this section as well as the remainder of the manuscript we only focused on pixels where the summed intensity exceeded 10 DN. The non-thermal broadening was calculated using the formula (see e.g., Testa et al., 2016):

$$v_{nt} = \sqrt{w_{1/e}^2 - w_{inst}^2 - w_{th}^2}. \quad (1)$$

There, $w_{1/e}$ is the $1/e$ observed width of the line obtained as $\sqrt{2}\sigma$ of the fitting Gaussian, w_{inst} stands for the instrumental broadening of 3.9 km s^{-1} (De Pontieu et al., 2014), and w_{th} is the thermal broadening which, for T_{ion} = 80,000 K, equals roughly 6.9 km s^{-1} (De Pontieu et al., 2015).

These maps, shown in **Figures 3A–C**, cover the time interval between 17:24–17:44 UT when the Si IV emission in the southern

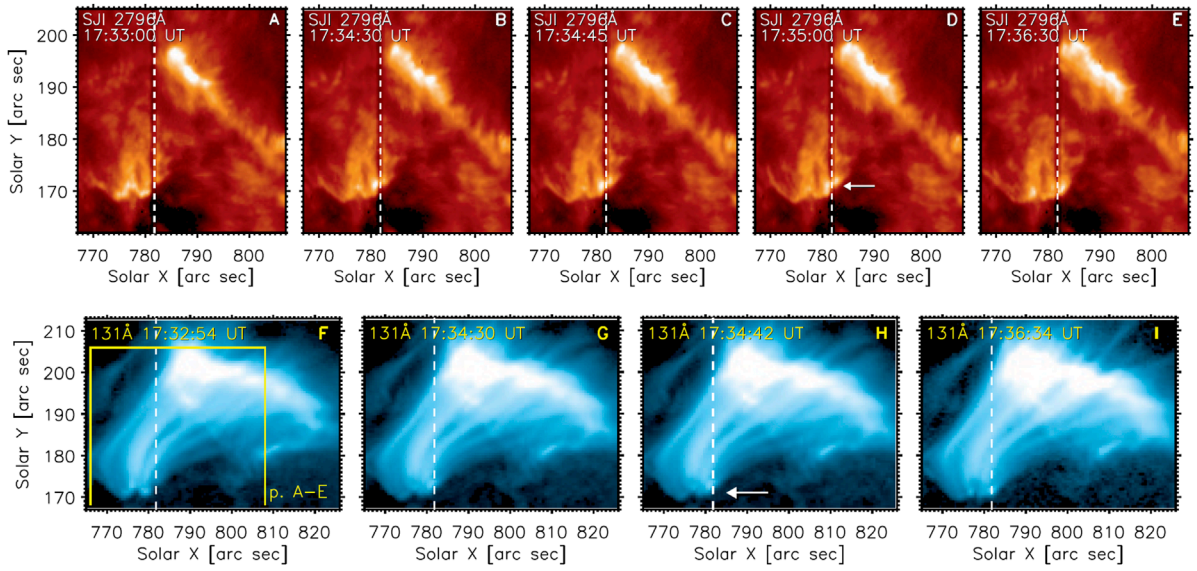

FIGURE 2
A pair of flare ribbons [panels **(A–E)**] and an arcade flare loops [panels **(F–I)**] observed in the SJI 2796 Å and AIA 131 Å during the impulsive phase of the flare. White dashed line marks the position of the IRIS slit at 17:35 UT. The white arrow plotted in panels **(D)** and **(H)** points to kernels (top row), resp. flare loop footpoints (bottom row) which spectra are analyzed in this manuscript. Animated version of the SJI observations is available online. The animation covers the period between 17:30 and 17:40 UT.

ribbon was detectable. The map of the integrated intensity [panel (A)] shows a brightening along the ribbon persisting roughly between ≈ 17:34 and ≈ 17:37 UT, corresponding to the period when the bright kernels crossed the slit of IRIS (Section 2.2). This brightening has a relatively short onset, peaks at ≈ 17:35 UT, and then diminishes gradually over the next 2 minutes. The map of the Doppler velocity [panel (B)] indicates that, in the ribbon under study, the line was usually redshifted with the highest Doppler velocities corresponding to ≈ 40 km s^{-1}. The spatial and the temporal distribution of the Doppler velocities is less homogeneous than that of the intensities. The largest redshifts are found in two regions, one visible after ≈ 17:34 UT at $Y \approx 171$" and the other approximately 3 minutes later at $y \approx 169$". These two spatio-temporal regions are even more evident in the v_{nt} map [panel (C)], suggesting that the line exhibited major non-thermal broadening in two separate episodes.

The inclusions plotted in Figures 3A–C provide zoomed-in views of the maps during their initial increase after ≈ 17:34 UT induced by the passage of the kernels through the slit detailed in Section 2.2. The grey and black arrows plotted therein indicate cuts used to investigate the time evolution of spectra at different pixels along the slit where the kernel emission was detected.

3.1.2 High-frequency variations of line moments

Figures 4A–C shows variations of the summed intensity (grey), Doppler velocity (v_D, magenta), and the non-thermal broadening (v_{nt}, green) at three slit positions corresponding to the pixels indexed 83–85 (Solar Y = 170.92–171.59") in the level 2 data cube. The time period shown corresponds to the initial increase of the intensity, and the first and second moment with a duration of roughly 80 s. These three curves exhibit an overall increase followed by a decrease, best visible in the intensity trends at the pixel positions 84 and 85. While lasting for only slightly more than a minute, in what follows this trend will be referred to as the *long-term* evolution (see Section 5).

Apart from the long-term evolution, these plots contain a pattern consisting of brief enhancements (peaks) of the three properties of the line occurring at a relatively-high frequency. This pattern, a characteristic of the *short-term* evolution, can be distinguished in all pixel positions plotted in Figures 4A–C. Unlike the long-term evolution, these enhancements are the most pronounced in the v_D (magenta) and v_{nt} (green) curves that exhibit very similar trends, with only some of them having a counterpart in the intensity curve (grey). The heights of these peaks are the largest at the pixel 84 plotted in panel (B) for the v_D curve. Magenta arrows were used to indicate some of the peaks along this curve in panel (B). The period of the variations of v_D and v_{nt} estimated by counting the peaks between 17:34:30 and 17:35:30 UT is around 7 s. The intensity exhibits fewer oscillations than the other two quantities (six as opposed to nine), leading to an estimated period of ≈ 10 s.

As stated in Section 1, quasi-periodic broadening during a flare of the Si IV 1402.77 Å line, with a period of ≈ 10 s, was first

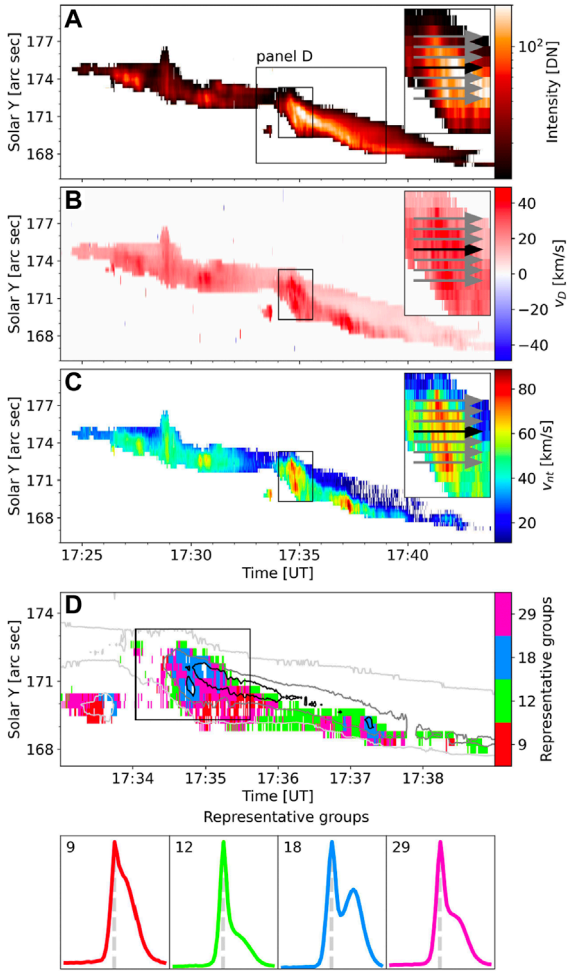

FIGURE 3
Maps of the integrated intensity [panel **(A)**], Doppler velocity v_D [panel **(B)**], and the non-thermal broadening v_{nt} [panel **(C)**] of the Si IV 1402.77 Å line resulting from the moment analysis. Arrows plotted in the zoomed-in inclusions indicate datapoints examined in **Figures 4**, **5**, with the black arrow corresponding to the pixel position 84. Panel **(D)** details the spatial distribution of Si IV line profiles which exhibited red wing enhancements. The individual pixels, color-coded according to the representative groups to which these profiles belong (displayed in the last row of the figure), are plotted atop of line intensity contours corresponding to 10 (light-grey), 70 (grey), and 140 DN (black).

reported by Jeffrey et al. (2018). A comparison of the upper panel of **Figure 3** therein and our **Figure 4B** reveals that the trends exhibited by the non-thermal broadening are very similar. In both events the non-thermal broadening of the line had grown and exhibited oscillations before the peak of the intensity. In Jeffrey et al. (2018) these oscillations also preceded the increase of the 6–12 keV X-ray flux measured by RHESSI, whereas the long-term evolution we report on (**Section 5**) was co-temporal with the increase of the SXR flux measured by GOES. The lifetime of the oscillations of v_{nt} in the event analyzed here was also longer, as they persisted even after the peak of the line's intensity (see e.g., **Figure 4B**). Another important difference in the properties of the line between the two events is that the oscillations in broadening reported by Jeffrey et al. (2018) had no counterpart in the Doppler velocity and the intensity of the line. This finding motivated us to investigate whether the short-term evolution of the curves in **Figures 4A–C** could simply be related to the motion of smaller kernels (not seen in **Figures 2A–E**) through the slit. Lightcurves produced using full-cadence 2,796 Å SJI observations at and near the location where the resolved kernels entered the slit (**Section 2.2**) however did not exhibit enhancements relatable to the short-term evolution of properties of the Si IV line (not shown). This may be caused by the fact that the emission measured in the 2,796 Å SJI filter is dominated by the chromospheric Mg II k line formed below the formation region of Si IV.

3.2 Two-component profiles of the Si IV 1402.77 Å line

Inspired by De Pontieu and McIntosh (2010), we investigated whether the oscillations could be caused by quasi-periodic appearance of strongly Doppler-shifted components in the wings of the line, and their effect on the overall moments of the spectral line. We found that a portion of profiles observed in the analyzed ribbon exhibit two well-defined components. These profiles showed a larger spectral separation than that found in more typical flare observations of Si IV profiles consisting of a superposition of near-at-rest and Doppler-shifted components (e.g., Li Y. et al., 2015; Warren et al., 2016; Yu et al., 2020a; Lörinčík et al., 2022).

A brief statistical analysis of the profiles, performed using the k-means clustering implemented in the `scikit-learn` library, revealed that approximately 35% of the profiles observed in the ribbon between 17:34 and 17:38 UT consisted of a primary component close to the rest wavelength of the line and a secondary redshifted component. The pixels where these spectra were found are plotted in **Figure 3D** atop of the intensity contours corresponding to 10, 70, and 140 DN (light-grey, grey, and black, respectively). After clustering $\approx 3 \times 10^4$ profiles into 30 representative groups we found four groups which contained a majority of these profiles. The mean spectra belonging to these groups (Nr. 9, 12, 18, 29) are displayed in the bottom row of **Figure 3**. The presence of the redshifted component was typically indicated by a pronounced red wing of the line. The strength of this component was varying in both time and space. Profiles with the strongest secondary component are found in the group Nr. 9 (red), while relatively-weaker secondary components are present in profiles in groups Nr. 29 (magenta) and 12 (green). The group Nr. 18 (blue) contains roughly 18% of the observed two-component spectra. The principal characteristic of the profiles of this group is the high separation of the two components as

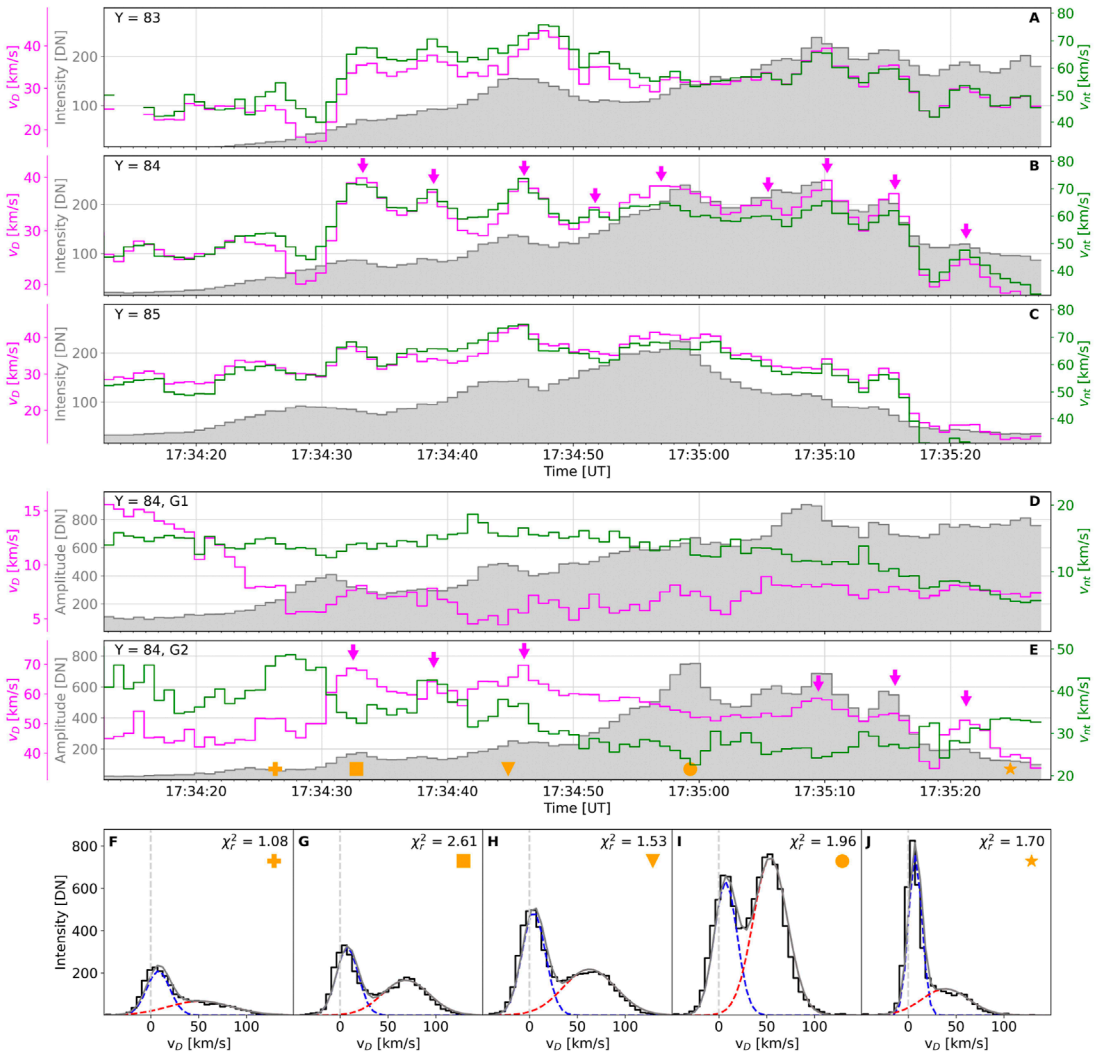

FIGURE 4
Panels **(A–E)** detail the time evolution of the total intensity (resp. intensity amplitude, grey), the Doppler velocity (magenta), and the non-thermal broadening (green) of the Si IV 1402.77 Å line. The curves plotted in panels **(A–C)** were obtained at 3 different pixel positions along the slit, 83 through 85, *via* the moment analysis. The time evolution of these quantities at the pixel position 84 (black arrow in **Figures 3A–C**) obtained via two-Gaussian fitting is detailed in panels **(D)** and **(E)**. The first Gaussian (G1) is shown in panel **(D)**, while the second Gaussian is shown in panel **(E)**. Magenta arrows in panels **(B)** and **(E)** highlight selected enhancements in the Doppler velocity determined from the moment analysis and Gaussian fitting, respectively. The orange symbols plotted in panel **(E)** mark the instants of observations of profiles displayed in panels **(F–J)**. There, the observed profiles are plotted in black, the Gaussian fits to the near-at-rest and secondary redshifted components are plotted in blue and red, respectively, and the total fit to the profiles are in grey. In top-right corner of each panel, reduced chi-squared statistic of the respective fit is listed).

well as the strength of the secondary component, in some pixels even dominating the primary one (see also **Figures 4G–I**). A comparison of **Figures 3C,D** shows that these profiles occurred in the two regions characterized by increased v_{nt}.

3.2.1 Gaussian fitting of line profiles

In order to precisely determine the properties of the spectra, the profiles observed in the ribbon were fitted using two Gaussians; one for the primary ('G1') and the other for the secondary redshifted ('G2') component. The fitting was performed using an automatic fitting routine `iris_auto_fit` included in the SolarSoft package. The time evolution of the intensity amplitudes (grey), Doppler velocities (v_D, magenta) of the centroids of the Gaussians, and their non-thermal broadening (v_{nt}, green) at the pixel position 84 (Solar $Y = 171.25$", black arrow in **Figures 3A–C**) are plotted in **Figures 4D,E**. The time interval detailed in this figure was selected to depict the short-term evolution of the parameters of the Gaussians and

corresponds to panels (A–C) of the same figure. The orange symbols in panel (E) mark instants of observations of spectra plotted in **Figures 4F–J**. These were selected as a representative sample of the spectra we analyze in this manuscript. A visual inspection of these profiles confirms that these spectra are indeed double-peaked and do not have a central reversal (c.f. **Figure 4**, Zhou et al., 2022), a manifestation of opacity effects in Si IV.

As is clear from panel (D), the redshift of the G1 (magenta) initially dropped from $v_D \approx 15$ km s^{-1} to roughly 7 km s^{-1} and stayed at this latter value during the remaining of the analyzed period. Similarly, v_{nt} (green) showed only negligible variations until ≈ 17:35 UT when it started to progressively decrease. On the other hand, the intensity amplitude (grey) exhibited an overall increase during this time interval, with a few enhancements peaking at approximately 17:34:30, 17:34:45, and 17:35:08 UT. The properties of the G2 [panel (E)] varied significantly more than those of the G1. Oscillations qualitatively similar to those of the short-term evolution of the moments of the full line can be clearly seen in the v_D curve between 17:34:25 and 17:34:50 UT, eventually reappearing ≈ 20 s later [magenta arrows in panel (E)]. During two major enhancements peaking at 17:34:33 and 17:34:46 UT, v_D reached nearly 70 km s^{-1}. This is interesting as redshifts of transition region lines in flare ribbons exceeding 50 km s^{-1} are generally rare, a few exceptions were presented e.g., by Tian et al. (2015); Zhang et al. (2016); Li et al. (2017). Note that panels (B) and (E) of **Figure 4** show that the maximal Doppler shifts resulting from the moment analysis and fitting of the redshifted component, respectively, differ by nearly 40%. This means that, because of the relative positions of centroids of the two components, the moment analysis systematically decreases the measured values of v_D (see also Tian et al., 2015; Lörinčík et al., 2022). We suggest this may be the reason why large redshifts (typically derived from moments or single-Gaussian fits) of cool lines are only rarely reported. Exceptionally high Si IV redshifts, in some cases exceeding 100 km s^{-1}, have also been reported in IRIS observations of flare loops (e.g., Tian et al., 2014; Zhou et al., 2020; Yu et al., 2022). These features are attributed to downward-oriented reconnection outflows. Since the ribbon we analyze here was not obscured by flare loops (**Figure 2**) it is very unlikely that the reconnection downflows could explain the observations we report on here. v_{nt} exhibited three clear enhancements between 17:34:25 and 17:34:50 UT, two of which had a counterpart in the v_D curve. The highest number of short-term enhancements was exhibited by the intensity amplitude. This curve also exhibits long-term evolution consisting of an initial growth approximately until 17:35 UT, later followed by its decrease, similar to the total intensity for the full profile.

On both long- and short-term scales, the parameters of the G2 follow trends comparable to those exhibited by the moments of the full spectral profile. Of particular interest is the striking similarity between the time evolution of the integrated intensity of the line (**Figure 4B**) and the amplitude of the G2 (**Figure 4E**). Similarly, the enhancements visible in v_D of the G2 can easily be associated to those exhibited by the moments. On the other hand, only two enhancements of the non-thermal broadening of the G2 show a counterpart in v_{nt} determined from the moment analysis (at 17:34:37 and 17:34:45 UT).

3.2.2 Correlation analysis

We analyzed further the dependence between the moments of the full Si IV 1402.77 Å line and the double Gaussian fits using scatter plots. Pairs of scatterplots plotted in **Figure 5** detail relations between line properties determined *via* the moment analysis of the full line shown on the vertical axes and the three parameters of the G1 and G2 shown on the horizontal axes (blue and red columns, respectively). The data points (colored dots) plotted in these panels represent spectra corresponding to all of the cuts plotted in **Figures 3A–C**, for those locations where the integrated intensity in a given pixel exceeded 10 DN. The transparency of the dots depends on the total intensity of the profile, from the weakest spectra (transparent dots) to the strongest ones (opaque dots). In each panel, the Pearson correlation coefficient (ρ) for the respective scatter plot is shown.

Panels (A–C) of **Figure 5** detail the relations between the non-thermal broadening resulting from the moment analysis ($v_{nt,\,MA}$) and the three properties of the Gaussian fits. This column of panels indicates that $v_{nt,\,MA}$ exhibits the highest correlation with the Doppler shift of the G2 with $\rho = 0.86$ [panel (A)]. $v_{nt,\,MA}$ shows a moderate correlation ($\rho = 0.56$) with v_{nt} of the G1, whereas the correlation with the v_{nt} of the G2 is weak, reaching only $\rho = 0.19$ [panel (B)]. Only a very weak linear relation ($|\rho| \approx 0.1$) between the $v_{nt,\,MA}$ and the amplitudes of the Gaussians is indicated by the scatter plots in panel (C). These results imply that the enhancements seen in the $v_{nt,\,MA}$ curve are induced by varying redshifts of the line's secondary component rather than being due to a real broadening of the profile itself. This is in analogy with the results of De Pontieu and McIntosh (2010), who proposed that quasi-periodic oscillations of intensity, velocity, and width of coronal lines, previously attributed to magnetoacoustic waves, could also be driven by quasi-periodic blueshifts induced by upflows at footpoints of coronal loops.

Regarding other notable results from the correlation analysis, the v_D values from the moment analysis show a relatively-high correlation with those of the G2 with $\rho = 0.77$ [panel (D)]. On the other hand, we found no correlation ($\rho \approx 0$) between v_D from the moment analysis and v_D of the G1. According to panel (E), v_D from the moment analysis is also moderately correlated with the non-thermal broadening of the G1 ($\rho = 0.53$). At the same time, no correlation with the broadening of the G2 was found. Finally, as seen in panel (F), the integrated intensity exhibits a slightly

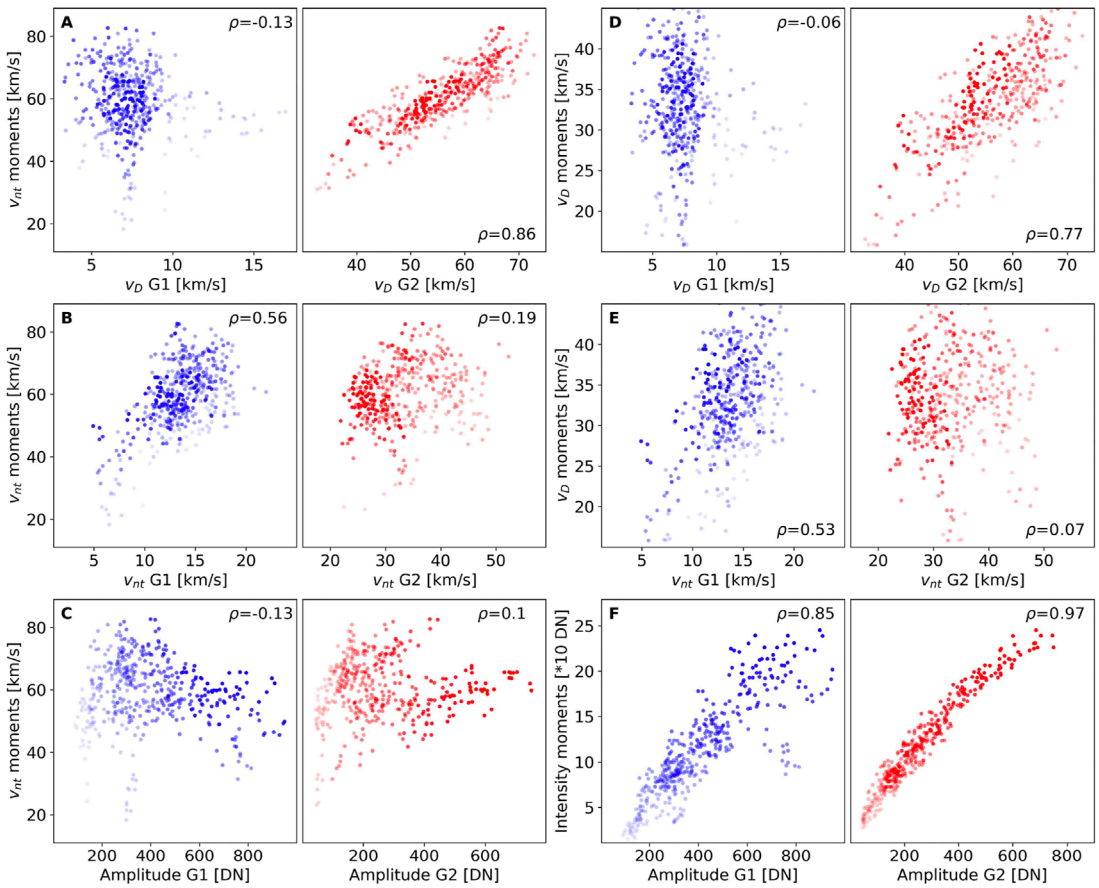

FIGURE 5
Scatterplots detailing the relation between Si IV 1402.77 Å line properties determined *via* the moment analysis (vertical axes) and the parameters of the two Gaussians fitting its spectra (horizontal axes). In each panel, the Pearson correlation coefficient calculated in the respective scatterplot is listed.

higher correlation with the amplitude of the G2 ($\rho = 0.97$) than with that of the G1 ($\rho = 0.85$).

3.2.3 Observations and modeling of double-peaked Si IV line profiles

The results of the correlation analysis presented in the previous section indicate that the short-term evolution of the Si IV 1402.77 Å line, which is characterized by quasi-periodic enhancements of its broadening as well as other properties, cannot be addressed by the presence or development of lower-atmospheric turbulences alone. We believe this is the case, despite the apparent similarity between the results of Jeffrey et al. (2018) and our observations of oscillatory signatures of the Si IV 1402.77 Å line spectra. In Jeffrey et al. (2018), the quasi-periodicity in broadening of apparently single-peaked profiles was interpreted in terms of the development of turbulence. However, in contrast to our results, the oscillatory trends reported by Jeffrey et al. (2018) were only observed in the broadening of the line. The authors concluded that time trends in which the bulk velocity does not exhibit oscillations can only be reproduced when multiple interacting Alfvén waves, representing velocity fluctuations, are present in the Si IV emitting region. We should also note that in their work individual or multiple components of the Si IV profiles were not discussed, so it is unclear whether those played a role.

Profiles qualitatively similar to those we discuss here can be found in the analysis of Brannon et al. (2015). In multiple instants detailed in their Section 3.3 and **Figure 7**, two components of the Si 1,402.77 Å exhibited a separation comparable to that we report on in **Section 3.2.1**. In Brannon et al. (2015), the component located closer to the rest wavelength showed weak Doppler shifts, in certain instants even blueshifts, which exhibit quasi-periodic variations similar to those of the secondary redshifted component analyzed therein. These are interpreted *via* elliptical waves propagating along reconnected field lines leading to minor oscillations of flare loops

along the LOS. The discussed mechanisms expected to produce such waves are the Kelvin-Helmholtz or the tearing mode instability in the flare current sheet (see also Tian et al., 2016). However, during the time period analyzed in the current paper (**Section 3.2.1** and detailed **Figure 4**), the Doppler velocity of the G1 did not exhibit short-term evolution relatable to that of the G2. This indicates that the two components of the Si IV line were not affected by a common physical mechanism such as, for example, the instability-induced oscillations of flare loops. We hypothesize that the high short-term variability (timescales <10 s) of the parameters of the G2, dominating the G1 in terms of affecting the moments of the Si IV 1402.77 Å line, suggests that the redshifted component mimicked the transient nature of Si IV spectra known from other analyses of flare ribbon emission. On the other hand, the negligible variations of v_D and v_{nt} of the G1 indicate that the primary component was less affected by the energy transport between the reconnection site and the lower atmosphere.

Double-peaked profiles of IRIS lines are consistent with recent numerical simulations (calculated with the RADYN code) of the response of a flare atmosphere to heating by accelerated (non-thermal) electrons. Kowalski et al. (2017) showed that a model atmosphere that is heated using a high non-thermal energy flux of $F = 5 \times 10^{11}$ erg cm^{-2} s^{-1} contains two emitting layers in the chromosphere, one existing due to the ongoing condensation and the second, stationary, underneath it. Even though the spectra synthesized using parameters of this atmosphere were double-peaked, we cannot immediately apply the results of this modeling to our observations. This is because, first, the authors did not provide predictions for the transition region emission and second, energy fluxes of this order of magnitude are more typical for stronger (X-class) flares (see e.g., Kennedy et al., 2015; Kleint et al., 2016; Graham et al., 2020). We plan to focus on reproducing double-peaked Si IV spectra using models with electron beam parameters constrained by HXR observations in the future. Still, these results illustrate that under specific conditions spectra of cool lines observed by IRIS might originate in two regions with distinct physical environments. Provided the Si IV line is formed under optically thin conditions, this could address the observed properties of the two-component Si IV line profiles. Recent extensions to the runs of Kowalski et al. (2017) showed that both the energy flux and the duration of the heating significantly affect the velocity profile of the chromospheric condensation in time, including its maximal velocity. As indicated in **Figure 2** of Kowalski et al. (2022), in one particular model these velocities reach up to more than 100 km s^{-1} at the maximum gas mass density. To our knowledge, no observational support for condensation speeds of this order of magnitude has yet been presented. Whether the redshifts of the Gaussian fitting the secondary component of the line observed up to 70 km s^{-1} can be related to the condensation speeds resulting from this numerical simulation is discussed in **Section 4**. According to the models, the condensing plasma cools very rapidly and the condensation speeds of this order of magnitude last only for a brief period of time (<1 s), subsequently dropping to ≈ 25 km s^{-1} during the following ≈ 9 s. The observed short-term evolution of v_D of the G2 (**Figure 4E**) consists of enhancements with a typical span between 3 and 7 time bins (2.4–5.6 s), indicating the downflow durations of the same order of magnitude as predicted by the model. We finally note that apart from the large redshifts of the secondary component, the signatures of the response of the lower solar atmosphere to non-thermal particles were likely manifested in the increased v_{nt}. During the period analyzed in **Figures 4D,E**, v_{nt} of the G2 was typically 2–3 times as large as that of the G1, what well corresponds to the observations of Brannon et al. (2015).

4 Effects of projection on observed condensation speeds

As stated in **Section 3.2.1**, the Si IV 1402.77 Å line does not typically exhibit Doppler velocities as large as those of the centroid of the Gaussian fit to the redshifted component in our observations. The occurrence of Si IV redshifts at speeds of up to ≈70 km s^{-1} is particularly interesting because the flare we report on occurred fairly close to the solar limb roughly at $\mu = 0.58$. It is thus of interest to consider whether the viewing geometry and observed velocities along the line-of-sight could be compatible with the velocities of the condensation-induced field-aligned downflows recently predicted by Kowalski et al. (2022).

We address this issue by determining the viewing angles α of the flare loops within the flare loop arcade which are rooted at or close to the kernels which crossed the slit of IRIS during the analyzed period (**Figure 2**). We define α as the angle between two vectors illustrated in **Figure 6**. The first *observer vector* points along the LOS of IRIS to the center of the disk. Since the angular distance between the kernel and the center of the disk is negligible compared to the distance between IRIS and the Sun, for simplicity we assume the vector to be pointing to the kernel itself. The second *loop vector* points from the kernel toward the closest loop coordinate above the flare loop footpoint. Essentially, the loop vector is a tangent to the lowest segment of the reconstructed loop. The calculation of the viewing angle α was done in the Heliocentric Earth Equatorial (HEEQ) coordinate system after a conversion of the heliographic loop coordinates using formula (2) in Thompson (2006).

The loop reconstruction was performed using the `ssc_measure` routine included in SolarSoft. This method is used to trace loops from imaging observations of two instruments, returning the Stonyhurst heliographic longitude, latitude, as well as the radial distance of the traced loop

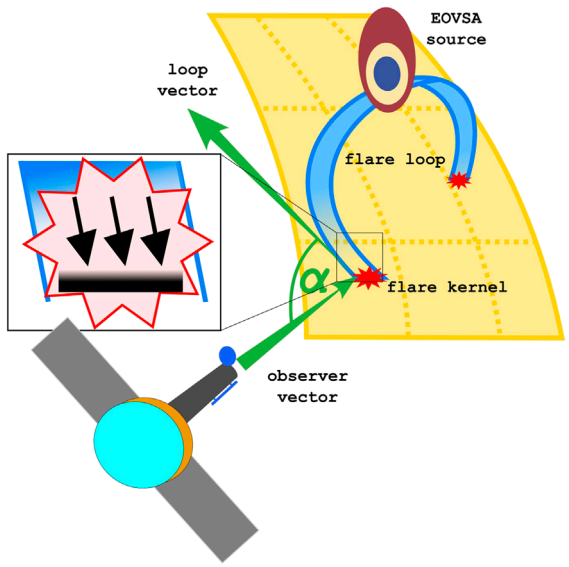

FIGURE 6
Cartoon demonstrating our definition of the angle α between the *observer vector* pointing along the LOS of IRIS to the flare loop footpoint (flare kernel, red star) and the *loop vector* directed from this footpoint to the nearest flare loop coordinate, i.e., a tangent to the loop footpoint. The zoomed inclusion on the left indicates two possible source regions of the observed spectra, one corresponding to the condensation layer (black arrows) and the other to the underlying stationary chromosphere (contoured bar). The maroon, yellow, and dark-blue contours indicate the source of the microwve emission measured by EOVSA.

coordinates (see e.g., Nisticò et al., 2013). To do so we used observations of the flare loop arcade carried out in the AIA 131 Å and EUVI 195 Å filters during the impulsive phase of the flare. Even though the EUVI 195 Å filter is primarily sensitive to plasma radiating at coronal temperatures (log T [K] = 6.2), the evolution and the morphology of the arcade of flare loops was similar to that observed in the AIA 131 Å (also compare **Figures 1F,G**). This is due to the temperature response of this channel, which, similarly as the AIA 193 Å channel, contains a secondary peak at log T [K] $\approx$7.2 (see Figure 11 in Wuelser et al., 2004). During our observation, the angular separation between SDO and STEREO-A was roughly 35°. As seen in panel **Figure 7C**, in this projection, EUVI observed the arcade at the solar limb which we also indicated in panel (B) using the yellow line. Most of the flare loops were oriented along the LOS of EUVI, which only let us use this instrument to constrain the height of the loops and their inclination from the vertical. Extracting the overall geometry of the individual loops among the arcade was thus largely contingent on the AIA 131 Å image. The AIA 131 Å data used for the tracing were therefore first averaged over 10 consecutive frames to suppress the noise and then sharpened using the Multi-Scale Gaussian Normalization (MGN; Morgan and Druckmüller, 2014). Still, portions of flare loops above their footpoints in the northern ribbon were obscured by the arcade. Even though the tracing of these loop segments was rather uncertain, this did not pose a limitation to our study as their viewing angles α are, for the most part, affected by the curvature and the orientation of the loops above the southern ribbon. Each of the loops we were able to trace was defined by 5–10 manually-selected loop coordinates which we consequently interpolated using a third-order spline interpolation. Lastly, the conversion of the heliographic loop coordinates to the coordinate frames of AIA and EUVI, necessary for the visualisation of the loops, was performed using functions for transformations of coordinate frames implemented in sunpy (SunPy Community et al., 2020).

Five flare loops traced and reconstructed in 3D using the method described above are shown in **Figure 7**. The loops are replotted on top of a blank image [panel (A)] as well as AIA 131 Å [panel (B)] and EUVI 195 Å [panel (C)] snapshots acquired at the same time as those used for tracing of the loops. In the legend plotted in panel (A), the viewing angles α of the traced loops are listed. The smallest viewing angle of 33° corresponds to the magenta loop (leftmost): its portion just above the southern footpoint seems to be tilted towards the solar east direction. The largest viewing angle is that of the red flare loop, for which the lowest segment was nearly perpendicular to the LOS of IRIS with $\alpha = 86°$. The viewing angles of the cyan, blue, and lime loops range between $\alpha = 44–52°$. Using the estimated viewing angles of the flare loops rooted in the kernel, we can now estimate the field-aligned flows along the loop legs by deprojecting the Doppler velocities obtained from the centroids of the Gaussian fits to the secondary redshifted component of the line. The field-aligned flow velocity corrected for the viewing angle of the loop can simply be obtained as $v_{\mathrm{D,corr.}} = v_{\mathrm{D}}/cos(\alpha)$. During the period detailed in **Figure 4E** the Doppler velocity of the G2 v_{D} ranged between 30 and 70 km s^{-1}. By using the average viewing angle of $\alpha = 52°$ we obtain $v_{\mathrm{D,corr.}}$ of 49–114 km s^{-1}. The upper limit of this range is close to the maximal condensation speeds recently predicted in RADYN simulations (see **Figure 2** in Kowalski et al., 2022). We note that the average value of α was significantly affected by the red flare loop with its large viewing angle that is far above the threshold of roughly 48° that would lead to a value of $v_{\mathrm{D,corr.}}$ that is within the constraints of the models.

To wrap up the analysis of the viewing angles of the flare loops, even though our 3D reconstruction of flare loops was limited by several factors such as the orientation of the flare loop arcade along the LOS of EUVI, we were still able to trace several flare loops and estimate the corresponding field-aligned flows along the legs of these loops. These were found to be possibly consistent with those predicted in RADYN simulations.

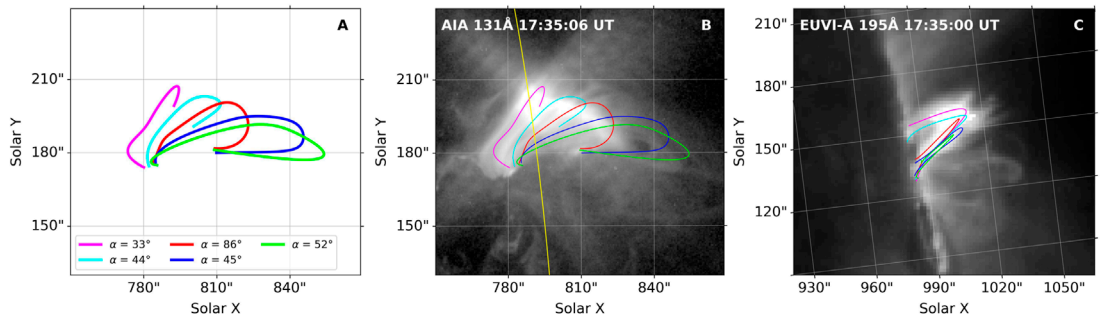

FIGURE 7
Flare loops traced using stereoscopic observations of the flare arcade from the AIA 131 Å and EUVI 195 Å during the impulsive phase of the flare. Panel **(A)** shows these loops plotted in a blank image and lists the viewing angles α of these loops. Panels **(B)** and **(C)** show the loops replotted atop of snapshots from AIA and EUVI. The yellow line plotted in panel **(B)** indicates the location of the solar limb from the observing point of the STEREO-A spacecraft.

5 Microwave and SXR emission during the 18 January 2022 flare

5.1 Sources of radio emission

The EOVSA sun-as-a-star microwave dynamic spectrum after removing the pre-flare background (**Figure 8A**) reveals several broadband impulsive bursts detected during this flare. The brightest microwave burst occurred at 17:37 UT and its flux density was over 150 sfu (solar flux units). The timing of the burst is denoted by the shaded vertical stripe in **Figure 8A**. The EOVSA images of the burst at frequencies between 3 and 18 GHz are plotted in **Figure 8C** using filled 95% contours overlaid on the AIA 1600 Å snapshot from the corresponding time. The contours were color-coded in radio frequency ν from red to blue with increasing frequency. The EOVSA sources at different frequencies appear to be distributed along a line with their higher-frequency end (blue colors) oriented toward the flare arcade.

The highest-frequency source was located at the top of the flare arcade, enclosed by the two leftmost flare loops described in **Section 4** and plotted in **Figure 7**. These loops connect the northern ribbon with the brightest kernels in the southern ribbon, where the Si IV line observed by IRIS exhibited features consistent with the reconnection-induced chromospheric condensation (**Section 3.2.3**). The location and orientation of the source in height was also consistent with the supra-arcade fan structure seen in the 131 Å image (red dashed lines in **Figures 8B,C**). The latter has been commonly regarded as an observational indication of magnetic reconnection occurring above the flare arcade (McKenzie and Hudson, 1999). The location of the microwave source can be interpreted using the standard solar flare model (Masuda et al., 1994), in which the microwave emission is produced by the flare-accelerated electrons trapped in the newly-reconnected magnetic field lines that later form flare loops. The accelerated electrons propagate downward along the flare loops and, upon colliding with the chromosphere, lead to the development of downflows (**Section 1**) with signatures such as those we report on here. The dispersion of the EOVSA sources above the flare arcade can be attributed to the decrease of the coronal magnetic strength with height (for further discussions on EOVSA microwave spectroscopy see Gary et al., 2018; Chen et al., 2020a, etc.)

The non-thermal nature of the microwave source was further affirmed by microwave spectral analysis. To investigate the nature of the microwave source, we derived the microwave brightness temperature spectrum $T_B(\nu)$ of the microwave source at 17:37 UT. In **Figure 8D**, we show the microwave spectra (red circles) derived from the red box in **Figure 8C** at 17:37 UT. Each $T_B(\nu)$ value in the spectrum represents the brightness temperature maximum within the region at a given frequency ν. The spatially-resolved microwave spectrum exhibited characteristics of incoherent non-thermal gyrosynchrotron emission produced by non-thermal electrons gyrating in the coronal magnetic field [compare our **Figures 8D,E** g. **Figure 4E** in Chen et al. (2020b), see also Bastian et al. (1998)]. We have therefore adopted the gyrosynchrotron (GS) forward fit method described in Fleishman et al. (2020) to fit the brightness temperature spectrum $T_B(\nu)$ using an isotropic non-thermal electron source with a power-law energy distribution. We restricted our spectral fit to frequencies above 2 GHz only, as the spectrum below 2 GHz contains contributions from coherent radiation (Bastian et al., 1998). From the spectral fit, we obtained the magnetic field strength of 160 G and the non-thermal power-law index of 2.8. We note that the uncertainties of the best-fit parameters are not well constrained without a more in-depth evaluation, e.g., Monte Carlo analysis, which was beyond the

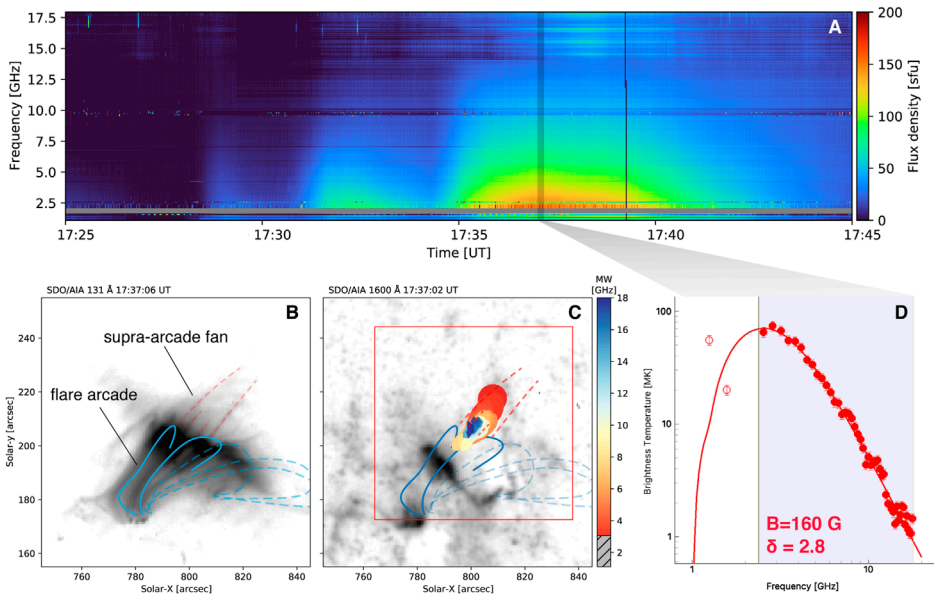

FIGURE 8
EOVSA dynamic spectroscopic imaging of the looptop microwave source of the 18 January 2022 flare. Panel **(A)** shows EOVSA total (sun-as-a-star) power microwave dynamic spectrum of the flare in 1–18 GHz. In panel **(B)**, reconstructed flare loops also shown in **Figure 7** are overplotted atop of AIA 131 Å image. The red dashed curves denote the supra-arcade fan structure. The same flare loops and fan structure are indicated in panel **(C)** with the AIA 1600 Å snapshot in the background. Between the apices of the two solid flare loops, sources of EOVSA microwave emission at 17:37 UT are plotted as contours corresponding to the 95% of the peak brightness at each frequency (decreasing from blue to red). Panel **(D)** presents the microwave brightness temperature spectrum $T_B(\nu)$ (red circles) obtained in the region denoted using the red box in panel **(C)**. Each $T_B(\nu)$ value at a given frequency ν represents the maximum brightness temperature within the region. The red solid curve is the best-fit model based on non-thermal gyrosychrontron emission. The vertical white shaded area indicates the frequency range excluded from the spectral fit. The best-fit magnetic field strength B and the power-law index δ of the non-thermal electron energy distribution are also shown.

scope of this study. Nevertheless, the microwave spectrum above 2 GHz favors a non-thermal electron source presumably associated with particle acceleration-driven energy release in the flare.

5.2 Comparison of SXR, radio, and UV lightcurves

During the time period under examination, time derivatives of the SXR and microwave radio flux exhibited several enhancements which can be related to the long-term trends exhibited by Si IV spectra observed by IRIS.

Figure 9A shows the time derivative of the SXR flux observed in the 1–8 Å channel of the GOES-16 satellite (blue) and the sun-as-a-star microwave emission measured by EOVSA averaged over frequencies between 2.4 and 5.0 GHz (orange). To suppress the noise (also see **Section 5.3**), both time derivatives were produced using data smoothed over 15 s with a moving boxcar. In the period between 17:28 and 17:42 UT, the GOES time derivative exhibits numerous enhancements (blue arrows), the most prominent one starting roughly after 17:33 UT, peaking at 17:35 UT, and decreasing until 17:36 UT. This peak, as well as peaks present at 17:28:30 and 17:31 UT, correspond to at least three enhancements visible in the EOVSA time derivative (cf. blue and orange curves). In panels (B) and (C) of the same figure, these time derivatives are compared with the properties of fits of the two components of the Si IV line. These panels detail the period between ≈ 17:33–17:39 UT when the Si IV emission was enhanced (**Section 3.1.1**) which increased the reliability of the fits to its components. The properties of the two Gaussians were averaged along the slit pixels crossing the ribbon, in this period corresponding to Solar $Y = 166$"—176".

According to **Figure 9B**, the Doppler velocity (magenta curve) exhibited a sharp increase approximately between 17:33:40–17:34:30 UT, peaking at $v_D \approx 16$ km s^{-1}. This redshift later decreased, returning to its pre-increase values ranging between 5–10 km s^{-1}. The average intensity (amplitude × width, grey curve) of the G1 started to increase after 17:33:40 UT, peaked between ≈ 17:35 and 17:37 UT, and later slowly dropped. The increase of the average intensity corresponds to that of the EOVSA time derivative and reaches the maximum simultaneously with both EOVSA and GOES lightcurves (c.f. grey, orange, and blue curves). After peaking, both EOVSA and

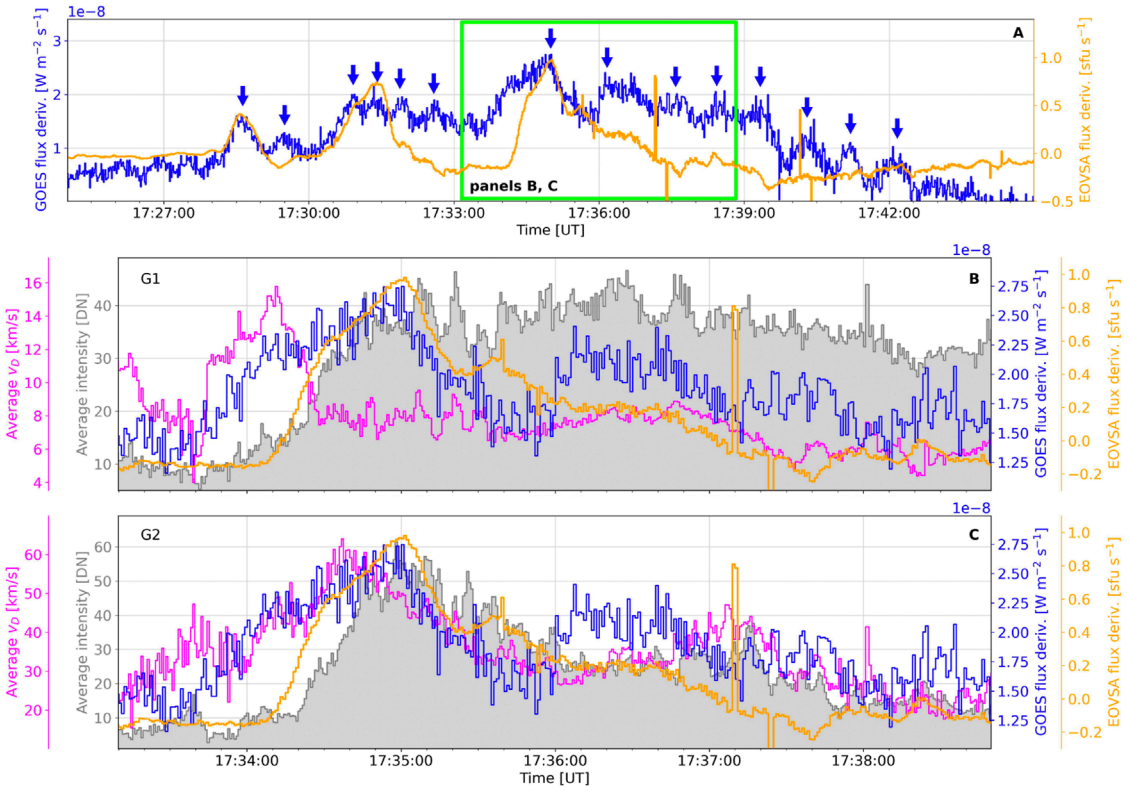

FIGURE 9
Panel **(A)** demonstrates quasi-periodic pulsations (QPPs, blue arrows) observed during the impulsive and peak phases of the flare. The blue curve is the time derivative of the GOES SXR flux in its 1–8 Å channel, while the orange curve corresponds to the microwave radio emission averaged in the range of 2.4–5 GHz observed by EOVSA. Panels **(B)** and **(C)** compare a section of these lightcurves [lime box in panel **(A)**] with properties of fits of two Gaussians fitting spectra of the Si IV 1402.77 Å line. The grey filled curve represents time variations of the observed intensity, while the magenta curve corresponds to the Doppler velocity v_D averaged in the ribbon. The GOES and EOVSA data plotted in this figure were produced using data smoothed with a 15 s boxcar.

GOES lightcurves exhibit a decrease that is not visible in the properties of the G1. The enhancement of the intensity of the G2 was relatively shorter (**Figure 9C**). After its onset after 17:34:20 UT and peak at 17:35 UT, the average intensity dropped to ≈ 50% of its peak value during the following minute, remained roughly constant until 17:37:20 UT at which point it started to decrease. The peak of v_D of this component occurred roughly 20 s prior to the peak of the intensity. In a trend similar to that of the average intensity, v_D exhibited a decrease until 17:36 UT when it slightly rose again with a minor peak at 17:37:10 UT, and finally dropped. These curves show several interesting similarities with the EOVSA and GOES lightcurves. By starting to rise at 17:34:10 UT, peaking at 17:35 UT, and progressively dropping till 17:37:40 UT, the trend of the EOVSA lightcurve well matches that of the average intensity of the G2. The initial increase of the GOES time derivative observed before 17:35 UT resembles that of v_D. On the other hand, the peak of the GOES lightcurve corresponds to the peak exhibited by the average intensity at 17:35 UT.

5.3 Quasi-periodic pulsations

Quasi-periodic enhancements are observed during flares across many passbands, typically at SXR, HXR, and microwave wavelengths. They are usually termed quasi-periodic pulsations (QPPs; see e.g., the review of Nakariakov and Melnikov, 2009, and references therein). QPPs are observed over a wide range of periods, from milliseconds to several minutes. From **Figure 9A** alone it was rather hard to estimate the period of QPPs in this flare. The QPPs visible in the GOES time derivative in **Figure 9A** exhibited four major and roughly ten minor peaks between 17:28–17:42 UT, from which we estimate their period to 1–3 min.

Numerous physical mechanisms have been associated with the generation of the QPPs (see e.g. the review of Zimovets et al., 2021). McLaughlin et al. (2018) divide these mechanisms into oscillatory and self-oscillatory processes. The oscillatory category includes for example natural MHD oscillations in flare loops and loops surrounding them or driving of periodic QPPs by external MHD waves. The self-oscillatory

processes concern for example periodic or repetitive magnetic reconnection. The duration and periods of QPPs driven by the self-oscillatory processes are given by the timescales of the energy release during the reconnection. As summarized by Hayes et al. (2019), current observations do not provide conclusive answers on the origin of the driver of QPPs, noting that various processes possibly act in different flares and their phases.

We hypothesize that the QPPs we report on, notably the prominent one peaking approximately at 17:35 UT, were most likely driven by magnetic reconnection. Our study provides twofold evidence for this scenario, in both cases dealing with signatures of non-thermal electrons in multi-wavelength observations presented in **Sections 3–5**. First, the SXR time derivative of GOES data reaches a maximum simultaneously with the time derivative of the EOVSA microwave emission which features are consistent with a non-thermal electron source (**Section 5.1**). This observable has also been reported by Yu et al. (2020b) who claimed that the correspondence between microwave and X-ray bursts supports a scenario in which the 5-min period QPPs observed therein were entirely driven by the reconnection. Second, the presence of the accelerated particles is indicated by the double-peaked Si IV 1402.77 Å spectra observed by IRIS. The peak of the intensity trend of the redshifted component, most-likely existing as a consequence of the chromospheric condensation (**Section 3.2.3**), corresponds to those of the EOVSA and GOES time derivatives. It ought to be noted that similar conclusions were reached by Li D. et al. (2015) who reported on simultaneous observations of 4-min period QPPs and peaks in redshifts as well as broadening of C I, O IV, Si IV, and Fe XXI lines observed by IRIS. We also speculate that if these QPPs were generated by MHD waves or oscillations in or near the reconnection site, the two components of the Si IV line would exhibit similar time evolution. For example, the quasi-periodic enhancements would likely be visible in the Doppler shifts of both components (as in Brannon et al., 2015) which we did not observe.

Note that apart from the long-term evolution of the two Gaussians, namely of the G2 fitting the redshifted component, we also observed oscillatory signals in the spectral properties of the Si IV line on timescales below 10 s (**Section 3**). Given the apparent correlation of the low-frequency oscillations of Si IV with the GOES and EOVSA signals, it is tempting to speculate whether such a correlation also explains the signals with shorter periods. The GOES time derivative did indeed exhibit omnipresent high-frequency oscillations, best visible in **Figures 9B,C**. However, the amplitudes of these oscillations were usually reaching a few 10^{-9} W m^{-2} s^{-1}, while σ of this curve in the same time interval was around $\approx 1 \times 10^{-9}$ W m^{-2} s^{-1}. We could thus not distinguish whether these oscillations were induced by the flare or were simply signatures of the noise (see Simões et al., 2015, for SXR irradiance noise analysis using data from older GOES satellites). Since IRIS captures only a few kernels at one time under the slit, and the flare extends over a larger FOV than IRIS can capture, it is quite possible that the full-disk GOES signal mixes information from several sources at any time, thus leading to "solar" noise that would not be expected to be correlated with the spectral properties IRIS observed in the few kernels. The relations between high-frequency oscillations in Si IV spectra and SXR flux time derivatives deserve attention of future studies, especially those analyzing flares with short impulsive phases where fast rise time of GOES SXR flux is translated into relatively-higher values of the time derivatives (although such observations would still be limited by the full-disk nature of the signal).

6 Summary and conclusion

In this manuscript we presented observations of the 18 January 2022 M-class flare, the first major flare the IRIS satellite observed at a sub-second cadence. We primarily analyzed trends exhibited by the intensity, Doppler velocity v_D, and non-thermal broadening v_{nt} of the transition region Si IV 1402.77 Å line in one of the ribbons during the impulsive phase of the flare. We paid particular attention to short-term evolution (scales of seconds) that these quantities, determined *via* the moment analysis, showed when the slit crossed the ribbon. The intensity of the line exhibited high-frequency oscillations with an estimated period of 10 s. The period of oscillations seen in v_D and v_{nt} was roughly 7 s. A substantial portion of profiles observed in the analyzed ribbon yielded double-peaked spectra. The primary component of the line observed close to its rest wavelength exhibited modest redshifts below v_D = 15 km s^{-1}. The redshifts of the secondary component were higher, temporarily reaching $v_D \approx 70$ km s^{-1}. For a brief period of time the two components showed a high separation (>60 km s^{-1}), making the components well-resolved. The time evolution of the total intensity as well as v_D and v_{nt} resulting from the moment analysis was correlated with parameters of the Gaussian fit to the redshifted component of the line. Of particular interest was a strong correlation we found between v_{nt} resulting from the moment analysis and v_D of the redshifted Gaussian. This suggests that the signatures of the oscillatory enhancements in the broadening of the line were driven by quasi-periodicities in the downward-oriented motions of plasma visible in the secondary component of the line. This result, combined with other properties of the Si IV spectra observed in this event (see below), suggests that the oscillations of line broadening do not appear to be caused by plasma turbulence in the same way as in Jeffrey et al. (2018) (**Section 3.2.3**). At the same time, the properties of the primary component did not exhibit oscillatory trends comparable to those of the secondary component. Because of the inherently different behavior of the two components we proposed that the quasi-periodic patterns were not induced by oscillations of flare loops driven by instabilities in the reconnection region, an

interpretation used by Brannon et al. (2015) for another flare that also exhibited rather rare double-peaked Si IV spectra.

Apart from the large redshifts, the likely origin of the secondary component was indicated by the broadening of the Si IV line. The fact that v_{nt} of this component exceeded that of the primary component by a factor of 2–3 suggested that the redshifted component existed due to an ongoing energization by magnetic reconnection, compatible with Brannon et al. (2015). Based on the different behaviour of both redshifts and broadening of the two components we speculate that the Si IV emission possibly originated from two regions at the flare footpoints with different physical conditions, in line with RADYN simulations of Kowalski et al. (2017). Our results appear to be compatible with a scenario in which the relatively-broader redshifted component could be linked to the condensation region and the relatively-narrower primary component to the underlying stationary region. Confirming this scenario would however require a proper simulation of the transition region emission. Nevertheless, the highest redshifts of the secondary component are consistent with the maximal velocities of chromospheric condensation ($\gtrapprox 100$ km s^{-1}) recently found in RADYN simulations (Kowalski et al., 2022). The estimated field-aligned condensation speeds were found by estimating viewing angles of flare loops anchored in the analyzed kernels based on a simple flare loop reconstruction in 3D.

Finally, we found that long-term trends (scales of minutes) of the intensity and Doppler shift exhibited by the secondary component were well matched by one of the QPPs observed in time derivatives of SXR (GOES) and microwave radio (EOVSA) fluxes. This result hints that the driving mechanism of the QPPs observed during this flare was repeated magnetic reconnection that also led to the formation of the secondary component of the Si IV line through the chromospheric condensation. Both EOVSA and GOES time derivatives also showed high-frequency oscillations. The question whether these enhancements were manifestations of high-frequency QPPs relatable to the oscillations of Si IV line properties remains to be answered in the future.

Data availability statement

Publicly available datasets were analyzed in this study. This data can be found here: https://www.lmsal.com/hek/hcr?cmd=view-event&event-id=ivo%3A%2F%2Fsot.lmsal.com%2FVOEvent%23VOEvent_IRIS_20220118_165527_4204700138_2022-01-18T16%3A55%3A272022-01-18T16%3A55%3A27.xml, https://data.ngdc.noaa.gov/platforms/solar-space-observing-satellites/goes/goes16/l2/data/xrsf-l2-flx1s_science/2022/01/sci_xrsf-l2-flx1s_g16_d20220118_v2-1-0.nc, http://ovsa.njit.edu/browser/?suntoday_date=2022-01-18.

Author contributions

The research project was led by JL. He was primarily engaged in the processing and visualization of data from IRIS, EOVSA, and GOES, as well as the preparation of the manuscript. VP and BD oversaw the progress of work on the project and primarily contributed to the interpretation of the observations. BD designed the very high-cadence IRIS observing programs and proposed the detailed study of these observations. SY was involved in the processing and analysis of radio data from EOVSA. NF was providing support necessary for processing and visualization of data in Python. All co-authors reviewed this manuscript and agreed with its submission.

Funding

This work was supported by NASA under contract NNG09FA40C (IRIS). VP also acknowledges support from NASA grant 80NSSC20K0716. SY was supported by NASA grant 80NSSC20K1283 to NJIT. NF was also supported by NASA contract NNG04EA00C (SDO/AIA).

Acknowledgments

The authors are grateful to Hugh Hudson and Paulo Simões for their insights on analysis of SXR data, Markus Aschwanden for tips on reconstruction of loops in three dimensions, Adam Kowalski for discussions regarding the chromospheric condensation, and Alberto Sainz Dalda for assistance with the k-means clustering techniques. IRIS is a NASA small explorer mission developed and operated by LMSAL with mission operations executed at NASA Ames Research center and major contributions to downlink communications funded by ESA and the Norwegian Space Centre. AIA and HMI data are provided courtesy of NASA/SDO and the AIA science team.

Conflict of interest

The authors declare that the research was conducted in the absence of any commercial or financial relationships that could be construed as a potential conflict of interest.

Publisher's note

All claims expressed in this article are solely those of the authors and do not necessarily represent those of

their affiliated organizations, or those of the publisher, the editors and the reviewers. Any product that may be evaluated in this article, or claim that may be made by its manufacturer, is not guaranteed or endorsed by the publisher.

Supplementary material

The Supplementary Material for this article can be found online at: https://www.frontiersin.org/articles/10.3389/fspas.2022.1040945/full#supplementary-material

References

Acton, L. W., Leibacher, J. W., Canfield, R. C., Gunkler, T. A., Hudson, H. S., and Kiplinger, A. L. (1982). Chromospheric evaporation in a well-observed compact flare. *Astrophys. J.* 263, 409–422. doi:10.1086/160513

Allred, J. C., Kowalski, A. F., and Carlsson, M. (2015). A unified computational model for solar and stellar flares. *Astrophys. J.* 809, 104. doi:10.1088/0004-637X/809/1/104

Bastian, T. S., Benz, A. O., and Gary, D. E. (1998). Radio emission from solar flares. *Annu. Rev. Astron. Astrophys.* 36, 131–188. doi:10.1146/annurev.astro.36.1.131

Brannon, S. R., Longcope, D. W., and Qiu, J. (2015). Spectroscopic observations of an evolving flare ribbon substructure suggesting origin in current sheet waves. *Astrophys. J.* 810, 4. doi:10.1088/0004-637X/810/1/4

Brosius, J. W. (2003). Chromospheric evaporation and warm rain during a solar flare observed in high time resolution with the coronal diagnostic spectrometer aboard the solar and heliospheric observatory. *Astrophys. J.* 586, 1417–1429. doi:10.1086/367958

Brosius, J. W. (2013). Chromospheric evaporation in solar flare loop strands observed with the extreme-ultraviolet imaging spectrometer on board hinode. *Astrophys. J.* 762, 133. doi:10.1088/0004-637X/762/2/133

Brosius, J. W., and Inglis, A. R. (2018). Localized quasi-periodic fluctuations in C II, Si IV, and Fe XXI emission during chromospheric evaporation in a flare ribbon observed by IRIS on 2017 september 9. *Astrophys. J.* 867, 85. doi:10.3847/1538-4357/aae5f5

Canfield, R. C., Metcalf, T. R., Strong, K. T., and Zarro, D. M. (1987). A novel observational test of momentum balance in a solar flare. *Nature* 326, 165–166. doi:10.1038/326165a0

Carlsson, M., and Stein, R. F. (1995). Does a nonmagnetic solar chromosphere exist? *Astrophys. J.* 440, L29. doi:10.1086/187753

Carlsson, M., and Stein, R. F. (1997). formation of solar calcium H and K bright grains. *Astrophys. J.* 481, 500–514. doi:10.1086/304043

Carlsson, M., and Stein, R. F. (1992). Non-LTE radiating acoustic shocks and CA II K2V bright points. *Astrophys. J.* 397, L59. doi:10.1086/186544

Chen, B., Shen, C., Gary, D. E., Reeves, K. K., Fleishman, G. D., Yu, S., et al. (2020a). Measurement of magnetic field and relativistic electrons along a solar flare current sheet. *Nat. Astron.* 4, 1140–1147. doi:10.1038/s41550-020-1147-7

Chen, B., Yu, S., Reeves, K. K., and Gary, D. E. (2020b). Microwave spectral imaging of an erupting magnetic flux rope: Implications for the standard solar flare model in three dimensions. *Astrophys. J.* 895, L50. doi:10.3847/2041-8213/ab901a

Chitta, L. P., and Lazarian, A. (2020). Onset of turbulent fast magnetic reconnection observed in the solar atmosphere. *Astrophys. J.* 890, L2. doi:10.3847/2041-8213/ab6f0a

De Pontieu, B., McIntosh, S., Martinez-Sykora, J., Peter, H., and Pereira, T. M. D. (2015). Why is non-thermal line broadening of spectral lines in the lower transition region of the sun independent of spatial resolution? *Astrophys. J.* 799, L12. doi:10.1088/2041-8205/799/1/L12

De Pontieu, B., and McIntosh, S. W. (2010). Quasi-periodic propagating signals in the solar corona: The signature of magnetoacoustic waves or high-velocity upflows? *Astrophys. J.* 722, 1013–1029. doi:10.1088/0004-637X/722/2/1013

De Pontieu, B., Polito, V., Hansteen, V., Testa, P., Reeves, K. K., Antolin, P., et al. (2021). A new view of the solar Interface region from the Interface region imaging spectrograph (IRIS). *Sol. Phys.* 296, 84. doi:10.1007/s11207-021-01826-0

De Pontieu, B., Title, A. M., Lemen, J. R., Kushner, G. D., Akin, D. J., Allard, B., et al. (2014). The Interface region imaging spectrograph (IRIS). *Sol. Phys.* 289, 2733–2779. doi:10.1007/s11207-014-0485-y

del Zanna, G., Berlicki, A., Schmieder, B., and Mason, H. E. (2006). A multi-wavelength study of the compact M1 flare on october 22, 2002. *Sol. Phys.* 234, 95–113. doi:10.1007/s11207-006-0016-6

Dere, K. P., and Mason, H. E. (1993). Nonthermal velocities in the solar transition zone observed with the high-resolution telescope and spectrograph. *Sol. Phys.* 144, 217–241. doi:10.1007/BF00627590

Doschek, G. A., Feldman, U., Kreplin, R. W., and Cohen, L. (1980). High-resolution X-ray spectra of solar flares. III - general spectral properties of X1-X5 type flares. *Astrophys. J.* 239, 725–737. doi:10.1086/158158

Doschek, G. A., McKenzie, D. E., and Warren, H. P. (2014). Plasma dynamics above solar flare soft X-ray loop tops. *Astrophys. J.* 788, 26. doi:10.1088/0004-637X/788/1/26

Dudík, J., Polito, V., Janvier, M., Mulay, S. M., Karlický, M., Aulanier, G., et al. (2016). Slipping magnetic reconnection, chromospheric evaporation, implosion, and precursors in the 2014 september 10 X1.6-Class solar flare. *Astrophys. J.* 823, 41. doi:10.3847/0004-637X/823/1/41

Fisher, G. H., Canfield, R. C., and McClymont, A. N. (1985). Flare loop radiative hydrodynamics. V - response to thick-target heating. VI - chromospheric evaporation due to heating by nonthermal electrons. VII - Dynamics of the thick-target heated chromosphere. *Astrophys. J.* 289, 414–441. doi:10.1086/162901

Fleishman, G. D., Gary, D. E., Chen, B., Kuroda, N., Yu, S., and Nita, G. M. (2020). Decay of the coronal magnetic field can release sufficient energy to power a solar flare. *Science* 367, 278–280. doi:10.1126/science.aax6874

Fletcher, L., Dennis, B. R., Hudson, H. S., Krucker, S., Phillips, K., Veronig, A., et al. (2011). An observational overview of solar flares. *Space Sci. Rev.* 159, 19–106. doi:10.1007/s11214-010-9701-8

Gary, D. E., Chen, B., Dennis, B. R., Fleishman, G. D., Hurford, G. J., Krucker, S., et al. (2018). Microwave and hard X-ray observations of the 2017 september 10 solar limb flare. *Astrophys. J.* 863, 83. doi:10.3847/1538-4357/aad0ef

Gontikakis, C., and Vial, J. C. (2018). Effects of resonant scattering of the Si IV doublet near 140 nm in a solar active region. *Astron. Astrophys.* 619, A64. doi:10.1051/0004-6361/201732563

Graham, D. R., and Cauzzi, G. (2015). Temporal evolution of multiple evaporating ribbon sources in a solar flare. *Astrophys. J.* 807, L22. doi:10.1088/2041-8205/807/2/L22

Graham, D. R., Cauzzi, G., Zangrilli, L., Kowalski, A., Simões, P., and Allred, J. (2020). Spectral signatures of chromospheric condensation in a major solar flare. *Astrophys. J.* 895, 6. doi:10.3847/1538-4357/ab88ad

Gupta, G. R., Sarkar, A., and Tripathi, D. (2018). Observation and modeling of chromospheric evaporation in a coronal loop related to active region transient brightening. *Astrophys. J.* 857, 137. doi:10.3847/1538-4357/aab95e

Harra, L. K., Matthews, S., Culhane, J. L., Cheung, M. C. M., Kontar, E. P., and Hara, H. (2013). The location of non-thermal velocity in the early phases of large flares—revealing pre-eruption flux ropes. *Astrophys. J.* 774, 122. doi:10.1088/0004-637X/774/2/122

Hayes, L. A., Gallagher, P. T., Dennis, B. R., Ireland, J., Inglis, A., and Morosan, D. E. (2019). Persistent quasi-periodic pulsations during a large X-class solar flare. *Astrophys. J.* 875, 33. doi:10.3847/1538-4357/ab0ca3

Howard, R. A., Moses, J. D., Vourlidas, A., Newmark, J. S., Socker, D. G., Plunkett, S. P., et al. (2008). Sun Earth connection coronal and heliospheric investigation (SECCHI). *Space Sci. Rev.* 136, 67–115. doi:10.1007/s11214-008-9341-4

Hudson, H. S., Simões, P. J. A., Fletcher, L., Hayes, L. A., and Hannah, I. G. (2021). Hot X-ray onsets of solar flares. *Mon. Not. R. Astron. Soc.* 501, 1273–1281. doi:10.1093/mnras/staa3664

Jeffrey, N. L. S., Fletcher, L., Labrosse, N., and Simões, P. J. A. (2018). The development of lower-atmosphere turbulence early in a solar flare. *Sci. Adv.* 4, 2794. doi:10.1126/sciadv.aav2794

Joshi, R., Schmieder, B., Tei, A., Aulanier, G., Lörinčík, J., Chandra, R., et al. (2021). Multi-thermal atmosphere of a mini-solar flare during magnetic reconnection observed with IRIS. *Astron. Astrophys.* 645, A80. doi:10.1051/0004-6361/202039229

Kennedy, M. B., Milligan, R. O., Allred, J. C., Mathioudakis, M., and Keenan, F. P. (2015). Radiative hydrodynamic modelling and observations of the X-class solar flare on 2011 March 9. *Astron. Astrophys.* 578, A72. doi:10.1051/0004-6361/201425144

Kerr, G. S., Carlsson, M., Allred, J. C., Young, P. R., and Daw, A. N. (2019). SI IV resonance line emission during solar flares: Non-lte, nonequilibrium, radiation transfer simulations. *Astrophys. J.* 871, 23. doi:10.3847/1538-4357/aaf46e

Kleint, L., Heinzel, P., Judge, P., and Krucker, S. (2016). Continuum enhancements in the ultraviolet, the visible and the infrared during the X1 flare on 2014 march 29. *Astrophys. J.* 816, 88. doi:10.3847/0004-637X/816/2/88

Kontar, E. P., Perez, J. E., Harra, L. K., Kuznetsov, A. A., Emslie, A. G., Jeffrey, N. L. S., et al. (2017). Turbulent kinetic energy in the energy balance of a solar flare. *Phys. Rev. Lett.* 118, 155101. doi:10.1103/PhysRevLett.118.155101

Kowalski, A. F., Allred, J. C., Carlsson, M., Kerr, G. S., Tremblay, P.-E., Namekata, K., et al. (2022). The atmospheric response to high nonthermal electron-beam fluxes in solar flares. II. Hydrogen-Broadening predictions for solar flare observations with the daniel K. Inouye solar telescope. *Astrophys. J.* 928, 190. doi:10.3847/1538-4357/ac5174

Kowalski, A. F., Allred, J. C., Daw, A., Cauzzi, G., and Carlsson, M. (2017). The atmospheric response to high nonthermal electron beam fluxes in solar flares. I. Modeling the brightest NUV footpoints in the X1 solar flare of 2014 march 29. *Astrophys. J.* 836, 12. doi:10.3847/1538-4357/836/1/12

Lemen, J. R., Title, A. M., Akin, D. J., Boerner, P. F., Chou, C., Drake, J. F., et al. (2012). The atmospheric imaging assembly (AIA) on the solar dynamics observatory (SDO). *Sol. Phys.* 275, 17–40. doi:10.1007/s11207-011-9776-8

Li, D., Ning, Z. J., and Zhang, Q. M. (2015a). Imaging and spectral observations of quasi-periodic pulsations in a solar flare. *Astrophys. J.* 807, 72. doi:10.1088/0004-637X/807/1/72

Li, Y., Ding, M. D., Qiu, J., and Cheng, J. X. (2015b). Chromospheric evaporation in an X1.0 flare on 2014 march 29 observed with IRIS and EIS. *Astrophys. J.* 811, 7. doi:10.1088/0004-637X/811/1/7

Li, Y., Kelly, M., Ding, M. D., Qiu, J., Zhu, X. S., and Gan, W. Q. (2017). Spectroscopic observations of magnetic reconnection and chromospheric evaporation in an X-shaped solar flare. *Astrophys. J.* 848, 118. doi:10.3847/1538-4357/aa89e4

Lörinčík, J., Dudík, J., and Polito, V. (2022). *Blueshifted Si IV 1402.77Å line profiles in a moving flare kernel observed by IRIS. arXiv e-prints*arXiv:2206.10114.

Masuda, S., Kosugi, T., Hara, H., Tsuneta, S., and Ogawara, Y. (1994). A loop-top hard X-ray source in a compact solar flare as evidence for magnetic reconnection. *Nature* 371, 495–497. doi:10.1038/371495a0

Mathioudakis, M., McKenny, J., Keenan, F. P., Williams, D. R., and Phillips, K. J. H. (1999). The effects of opacity in the transition region of YZ CMi. *A&A* 351, L23.

McKenzie, D. E., and Hudson, H. S. (1999). X-ray observations of motions and structure above a solar flare arcade. *Astrophys. J.* 519, L93–L96. doi:10.1086/312110

McLaughlin, J. A., Nakariakov, V. M., Dominique, M., Jelínek, P., and Takasao, S. (2018). Modelling quasi-periodic pulsations in solar and stellar flares. *Space Sci. Rev.* 214, 45. doi:10.1007/s11214-018-0478-5

Milligan, R. O. (2015). Extreme ultra-violet spectroscopy of the lower solar atmosphere during solar flares (invited review). *Sol. Phys.* 290, 3399–3423. doi:10.1007/s11207-015-0748-2

Milligan, R. O. (2011). Spatially resolved nonthermal line broadening during the impulsive phase of a solar flare. *Astrophys. J.* 740, 70. doi:10.1088/0004-637X/740/2/70

Morgan, H., and Druckmüller, M. (2014). Multi-scale Gaussian normalization for solar image processing. *Sol. Phys.* 289, 2945–2955. doi:10.1007/s11207-014-0523-9

Nakariakov, V. M., and Melnikov, V. F. (2009). Quasi-periodic pulsations in solar flares. *Space Sci. Rev.* 149, 119–151. doi:10.1007/s11214-009-9536-3

Nisticò, G., Verwichte, E., and Nakariakov, V. (2013). 3D reconstruction of coronal loops by the principal component analysis. *Entropy* 15, 4520–4539. doi:10.3390/e15104520

O'Dwyer, B., Del Zanna, G., Mason, H. E., Weber, M. A., and Tripathi, D. (2010). SDO/AIA response to coronal hole, quiet Sun, active region, and flare plasma. *Astron. Astrophys.* 521, A21. doi:10.1051/0004-6361/201014872

Pesnell, W. D., Thompson, B. J., and Chamberlin, P. C. (2012). The solar dynamics observatory (SDO). *Sol. Phys.* 275, 3–15. doi:10.1007/s11207-011-9841-3

Polito, V., Reep, J. W., Reeves, K. K., Simões, P. J. A., Dudík, J., Del Zanna, G., et al. (2016). Simultaneous Iris and*hinode*/eis observations and modeling of the 2014 october 27 X2.0 class flare. *Astrophys. J.* 816, 89. doi:10.3847/0004-637X/816/2/89

Polito, V., Reeves, K. K., Del Zanna, G., Golub, L., and Mason, H. E. (2015). Joint high temperature observation of a small C6.5 solar flare with Iris/Eis/Aia. *Astrophys. J.* 803, 84. doi:10.1088/0004-637X/803/2/84

Polito, V., Testa, P., and De Pontieu, B. (2019). Can the superposition of evaporative flows explain broad Fe XXI profiles during solar flares? *Astrophys. J.* 879, L17. doi:10.3847/2041-8213/ab290b

Sandlin, G. D., Bartoe, J. D. F., Brueckner, G. E., Tousey, R., and Vanhoosier, M. E. (1986). The high-resolution solar spectrum, 1175-1710 A. *Astrophys. J. Suppl. Ser.* 61, 801. doi:10.1086/191131

Scherrer, P. H., Schou, J., Bush, R. I., Kosovichev, A. G., Bogart, R. S., Hoeksema, J. T., et al. (2012). The helioseismic and magnetic imager (HMI) investigation for the solar dynamics observatory (SDO). *Sol. Phys.* 275, 207–227. doi:10.1007/s11207-011-9834-2

Shibata, K., and Magara, T. (2011). Solar flares: Magnetohydrodynamic processes. *Living Rev. Sol. Phys.* 8, 6. doi:10.12942/lrsp-2011-6

Simões, P. J. A., Hudson, H. S., and Fletcher, L. (2015). Soft X-ray pulsations in solar flares. *Sol. Phys.* 290, 3625–3639. doi:10.1007/s11207-015-0691-2

Stores, M., Jeffrey, N. L. S., and Kontar, E. P. (2021). The spatial and temporal variations of turbulence in a solar flare. *Astrophys. J.* 923, 40. doi:10.3847/1538-4357/ac2c65

SunPy Community, Barnes, W. T., Bobra, M. G., Christe, S. D., Freij, N., Hayes, L. A., et al. (2020). The SunPy project: Open source development and status of the version 1.0 core package. *Astrophys. J.* 890, 68. doi:10.3847/1538-4357/ab4f7a

Testa, P., De Pontieu, B., and Hansteen, V. (2016). High spatial resolution Fe XII observations of solar active regions. *Astrophys. J.* 827, 99. doi:10.3847/0004-637X/827/2/99

Thompson, W. T. (2006). Coordinate systems for solar image data. *Astron. Astrophys.* 449, 791–803. doi:10.1051/0004-6361:20054262

Tian, H., Li, G., Reeves, K. K., Raymond, J. C., Guo, F., Liu, W., et al. (2014). Imaging and spectroscopic observations of magnetic reconnection and chromospheric evaporation in a solar flare. *Astrophys. J.* 797, L14. doi:10.1088/2041-8205/797/2/L14

Tian, H., Young, P. R., Reeves, K. K., Chen, B., Liu, W., and McKillop, S. (2015). Temporal evolution of chromospheric evaporation: Case studies of the M1.1 flare on 2014 september 6 and X1.6 flare on 2014 september 10. *Astrophys. J.* 811, 139. doi:10.1088/0004-637X/811/2/139

Tian, H., Young, P. R., Reeves, K. K., Wang, T., Antolin, P., Chen, B., et al. (2016). Global sausage oscillation of solar flare loops detected by the Interface region imaging spectrograph. *Astrophys. J.* 823, L16. doi:10.3847/2041-8205/823/1/L16

Warren, H. P., Brooks, D. H., Ugarte-Urra, I., Reep, J. W., Crump, N. A., and Doschek, G. A. (2018). Spectroscopic observations of current sheet formation and evolution. *Astrophys. J.* 854, 122. doi:10.3847/1538-4357/aaa9b8

Warren, H. P., Reep, J. W., Crump, N. A., and Simões, P. J. A. (2016). Transition region and chromospheric signatures of impulsive heating events. I. Observations. *Astrophys. J.* 829, 35. doi:10.3847/0004-637X/829/1/35

Wuelser, J.-P., Lemen, J. R., Tarbell, T. D., Wolfson, C. J., Cannon, J. C., Carpenter, B. A., et al. (2004). "Euvi: The STEREO-SECCHI extreme ultraviolet imager," in *Society of photo-optical instrumentation engineers (SPIE) conference series*. Editors S. Fineschi, and M. A. Gummin (Bellingham, WA, United States: Telescopes and Instrumentation for Solar Astrophysics), 5171. 111–122. doi:10.1117/12.506877

Yan, L., Peter, H., He, J., Tian, H., Xia, L., Wang, L., et al. (2015). Self-absorption in the solar transition region. *Astrophys. J.* 811, 48. doi:10.1088/0004-637X/811/1/48

Young, P. R., Tian, H., and Jaeggli, S. (2015). The 2014 march 29 X-flare: Subarcsecond resolution observations of Fe XXI λ1354.1. *Astrophys. J.* 799, 218. doi:10.1088/0004-637X/799/2/218

Yu, K., Li, Y., Ding, M. D., Li, D., Zhou, Y.-A., and Hong, J. (2020a). IRIS Si IV line profiles at flare ribbons as indications of chromospheric condensation. *Astrophys. J.* 896, 154. doi:10.3847/1538-4357/ab9014

Yu, K., Li, Y., Hong, J., Song, D.-C., and Ding, M. D. (2022). Imaging and spectroscopic observations of the dynamic processes in limb solar flares. *Astrophys. J.* 935, 8. doi:10.3847/1538-4357/ac7e46

Yu, S., Chen, B., Reeves, K. K., Gary, D. E., Musset, S., Fleishman, G. D., et al. (2020b900). Magnetic reconnection during the post-impulsive phase of a long-duration solar flare: Bidirectional outflows as a cause of microwave and X-ray bursts. *Astrophys. J.* 900, 17. doi:10.3847/1538-4357/aba8a6

Zhang, Q. M., Li, D., Ning, Z. J., Su, Y. N., Ji, H. S., and Guo, Y. (2016). Explosive chromospheric evaporation in a circular-ribbon flare. *Astrophys. J.* 827, 27. doi:10.3847/0004-637X/827/1/27

Zhou, Y.-A., Hong, J., Li, Y., and Ding, M. D. (2022). Diagnosing the optically thick/thin features using the intensity ratio of Si IV resonance lines in solar flares. *Astrophys. J.* 926, 223. doi:10.3847/1538-4357/ac497e

Zhou, Y.-A., Li, Y., Ding, M. D., Hong, J., and Yu, K. (2020). Spectroscopic observations of high-speed downflows in a C1.7 solar flare. *Astrophys. J.* 904, 95. doi:10.3847/1538-4357/abb77c

Zimovets, I. V., McLaughlin, J. A., Srivastava, A. K., Kolotkov, D. Y., Kuznetsov, A. A., Kupriyanova, E. G., et al. (2021). Quasi-periodic pulsations in solar and stellar flares: A review of underpinning physical mechanisms and their predicted observational signatures. *Space Sci. Rev.* 217, 66. doi:10.1007/s11214-021-00840-9

frontiers | Frontiers in Astronomy and Space Sciences

TYPE Original Research
PUBLISHED 18 November 2022
DOI 10.3389/fspas.2022.1034458

OPEN ACCESS

EDITED BY
Gavin Ramsay,
Armagh Observatory, United Kingdom

REVIEWED BY
Markus Aschwanden,
Lockheed Martin, United States
Petr Heinzel,
Academy of Sciences of the Czech Republic (ASCR), Czechia

*CORRESPONDENCE
Adam F. Kowalski,
adam.f.kowalski@colorado.edu

SPECIALTY SECTION
This article was submitted to Stellar and Solar Physics, a section of the journal Frontiers in Astronomy and Space Sciences

RECEIVED 01 September 2022
ACCEPTED 28 October 2022
PUBLISHED 18 November 2022

CITATION
Kowalski AF (2022), Near-ultraviolet continuum modeling of the 1985 April 12 great flare of AD Leo.
Front. Astron. Space Sci. 9:1034458.
doi: 10.3389/fspas.2022.1034458

Near-ultraviolet continuum modeling of the 1985 April 12 great flare of AD Leo

Adam F. Kowalski[1,2,3]*

[1]Department of Astrophysical and Planetary Sciences, University of Colorado Boulder, Boulder, CO, United States, [2]National Solar Observatory, University of Colorado Boulder, Boulder, CO, United States, [3]Laboratory for Atmospheric and Space Physics, University of Colorado Boulder, Boulder, CO, United States

White-light stellar flares are now reported by the thousands in long-baseline, high-precision, broad-band photometry from missions like *Kepler*, K2, and TESS. These observations are crucial inputs for assessments of biosignatures in exoplanetary atmospheres and surface ultraviolet radiation dosages for habitable-zone planets around low-mass stars. A limitation of these assessments, however, is the lack of near-ultraviolet spectral observations of stellar flares. To motivate further empirical investigation, we use a grid of radiative-hydrodynamic simulations with an updated treatment of the pressure broadening of hydrogen lines to predict the $\lambda \approx 1800 - 3300$ Å continuum flux during the rise and peak phases of a well-studied superflare from the dM3e star AD Leo. These predictions are based on semi-empirical superpositions of radiative flux spectra consisting of a high-flux electron beam simulation with a large, low-energy cutoff ($\gtrsim 85$ keV) and a lower-flux electron beam simulation with a smaller, low-energy cutoff ($\lesssim 40$ keV). The two-component models comprehensively explain the hydrogen Balmer line broadening, the optical continuum color temperature, the Balmer jump strength, and the far-ultraviolet continuum strength and shape in the rise/peak phase of this flare. We use spatially resolved analyses of solar flare data from the Interface Region Imaging Spectrograph, combined with the results of previous radiative-hydrodynamic modeling of the 2014 March 29 X1 solar flare (SOL20140329T17:48), to interpret the two-component electron beam model as representing the spatial superposition of bright kernels and fainter ribbons over a larger area.

KEYWORDS

flares—stars, flares -sun, near-ultraviolet, habitability and astrobiology, spectroscopy

1 Introduction

Rapidly rotating, magnetically active M dwarf (dMe) stars occasionally flare with energies that are factors of 100–10,000 greater than the most energetic solar flares that have been observed in the modern era. These so-called "superflares" provide insight into the physics of extreme plasma conditions attained in stars (Osten et al., 2007; Testa et al., 2008; Osten et al., 2010, 2016; Karmakar et al., 2017) and

possibly also the young Sun (Ayres, 2015; Maehara et al., 2015; Namekata et al., 2021). Further afield, observations of these superflares are widely used in the characterization of the high-energy radiation environments in the habitable zones of low-mass stars (Smith et al., 2004; Segura et al., 2010), which are a primary target for exoplanet transit spectroscopy (e.g., Scalo et al., 2007; Belu et al., 2011; Barstow et al., 2016; Barstow and Irwin, 2016; de Wit et al., 2018; Fauchez et al., 2019) with the *James Webb Space Telescope* (JWST). The JWST and future extremely large telescope facilities provide a means to determine whether exoplanets in or around the habitable zone of low-mass stars retain atmospheres in the presence of high fluxes of stellar energetic particles and X-ray and extreme ultraviolet (XEUV) flare radiation. The evolution of the atmosphere of Mars is thought to have undergone significant mass loss due to coronal mass ejections and XEUV heating from the Sun (Jakosky et al., 2018), which motivates investigations into the evolution of exoplanetary atmospheres that are much closer to stars that are highly magnetically active for billions of years (West et al., 2008).

Segura et al. (2010) simulated the impact of a superflare event on a non-magnetic, but otherwise Earth-like, exoplanet atmosphere in the habitable zone of the dM3e flare star AD Leo. They found that planetary ozone is largely depleted due to chemical reactions (e.g., Scalo et al., 2007) that follow from incident scaled-up fluxes (Belov et al., 2005) of solar energetic protons. More recent simulations have considered the effects of repeated flaring and particle events after such a superflare has occurred (Howard et al., 2018; Tilley et al., 2019). Howard et al. (2018) and Tilley et al. (2019) discuss the role of UV-C[1] ($\lambda = 2000 - 2800$Å), and in particular the wavelengths $\lambda = 2400 - 2800$ Å, from repeated flaring in germicidal radiation surface fluxes following an ozone-depletion event. Recently, Abrevaya et al. (2020) conducted laboratory measurements of survival curves of microorganisms through exposure to a UV-C radiation flux inferred from optical observations of a superflare from the dM5.5e star Proxima Centauri (Howard et al., 2018).

The transient (Loyd et al., 2018a) and secular (Venot et al., 2016) effects on ozone biosignature photochemistry caused by ultraviolet flares is an ongoing subject of research, especially in light of the lack of direct observations of stellar energetic proton fluences and exoplanetary magnetic field properties (see discussion in Tilley et al., 2019). Loyd et al. (2018a) demonstrate that assumptions of the ultraviolet continuum shape during flares can affect ozone photolysis rates (see also Howard et al., 2020), while effects spanning several orders of magnitude on other important atmospheric constituents (CH_4, H_2O, O_2) are expected. Significant effort has been invested into the empirical characterization of the quiescent and flaring spectra of low-mass stars in the far-ultraviolet wavelength region of $\lambda = 1100 - 1800$ Å through the MUSCLES, Mega-MUSCLES, and HAZMAT treasury programs with the *Hubble Space Telescope* (Shkolnik and Barman, 2014; Loyd and France, 2014; Froning et al., 2019; Loyd et al., 2018b; France et al., 2020; Wilson et al., 2021, and see also Feinstein et al., 2022). However, much still remains unknown about the spectral characteristics of transient, impulsive-phase, near-ultraviolet (NUV) enhancements in flare radiation from $\lambda \approx 2000 - 3300$ Å (e.g., Robinson et al., 2005; Hawley et al., 2007; Brasseur et al., 2019; Fleming et al., 2022), which is thought to account for a large percentage (≈25%) of the $\lambda = 1200 - 8000$ Å radiated energy (Hawley and Pettersen, 1991). The largest X-ray solar flare of Sunspot Cycle 24 was recently studied in spatially integrated light at continuum wavelengths through a $\Delta\lambda \approx 300$ Å bandpass around $\lambda \approx 2000$ Å (Dominique et al., 2018).

Many studies of stellar flares have utilized photometry from high-precision missions of *Kepler*, K2, and TESS, which observe through broad white-light bandpasses in the optical and near-infrared. Photochemistry and habitability calculations often use extrapolations to shorter ultraviolet wavelengths by assuming a $T \approx 9000 - 10{,}000$ K blackbody spectrum (e.g., Günther et al., 2020); this assumption has also been widely employed for calculations of bolometric energies in statistical analyses (e.g., Shibayama et al., 2013; Yang et al., 2017). We refer the reader to Howard et al. (2020) and Brasseur et al., 2022, submitted to *ApJ*) for discussions about several unprecedented problems raised by recent studies of multi-wavelength broadband photometry of stellar superflares.

Very few stellar flare spectral observations exist with near-ultraviolet coverage and contemporaneous optical spectra (Hawley and Pettersen, 1991; Robinson et al., 1993; Wargelin et al., 2017; Kowalski et al., 2019b) that would facilitate detailed tests of and improvements upon blackbody modeling of flares. However, ground-based spectra suggest that the NUV flare continuum has non-negligible contributions from Balmer continuum radiation (Kowalski et al., 2010, 2013, 2016). Most recently, Kowalski et al. (2019b) analyze $\lambda \approx 2500 - 7400$ Å flare spectra and photometry over two events from the dM4e star GJ 1243. Detailed modeling demonstrates that a $T = 9000$ K blackbody fit to the blue-optical continuum at $\lambda \approx 4000 - 4800$ Å underpredicts the NUV flare flux by factors of $2 - 3$ during these two events; the discrepency was tied to a moderately-sized jump in the continuum flux around the Balmer limit, a confluence of Fe II emission lines through the

1 According to the World Health Organization, the ultraviolet is comprised of three bands: UV-C ($\lambda = 1000 - 2800$ Å), UV-B ($\lambda = 2800 - 3150$ Å), and UV-A ($\lambda = 3150 - 4000$ Å). We follow Abrevaya et al. (2020) and other recent studies of the biological impact of UV flares and denote the continuum radiation at $\lambda = 2000 - 2800$ Å as UV-C; the ultraviolet radiation at $\lambda = 1000 - 2000$ Å is also known as the very ultraviolet (VUV).

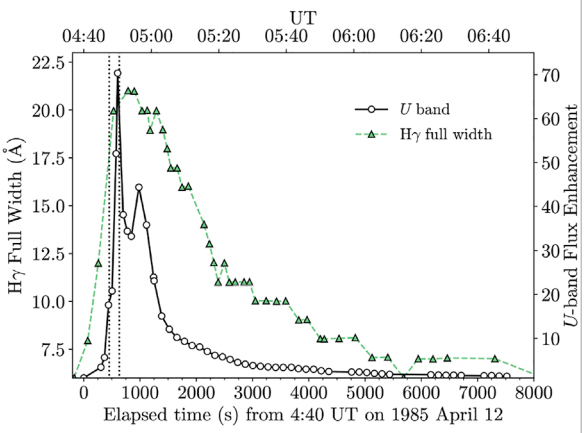

FIGURE 1
The *U*-band light curve (right axis) of the Great Flare of AD Leo and the full-width (left axis) of the Hγ emission line from Hawley and Pettersen (1991). The *U*-band flux is normalized to quiescence. The start and stop times of the exposure corresponding to the rise/peak phase spectrum is indicated with two vertical dotted lines.

NUV, and the bright Mg II *h* and *k* resonance lines (see also Hawley et al., 2007). These "hybrid flare" (HF) or "gradual flare" (GF) (see Kowalski et al., 2013) events exhibit the largest Balmer jumps that have been detected spectroscopically in dMe flares, and Kowalski et al. (2019b) argue that other dMe events that are categorized as "impulsive flare" (IF) events according to their broadband time evolution, smaller Balmer jumps, and hotter blackbody fits to the optical (Kowalski et al., 2013) and *U*-band ($\lambda = 3260 - 3940$ Å) continua (Fuhrmeister et al., 2008) yet require spectroscopic investigation at shorter wavelengths. The optical spectral properties of impulsive-type M dwarf flares are crucial in our understanding of fundamental flare physics because they are not reproduced in simulations with typical, solar-type electron beam (Allred et al., 2006) or intense XEUV radiation fields (Hawley and Fisher, 1992); large continuum optical depths are required in the flare chromosphere (e.g., Livshits et al., 1981; Kowalski et al., 2015) or photosphere.

In this paper, we present radiative-hydrodynamic model predictions of the NUV flare continuum during the Great Flare of AD Leo (Hawley and Pettersen, 1991), a particularly well-studied, impulsive-type superflare. The optical emission line data have previously been modeled in detail in Hawley and Fisher (1992) using NLTE, X-ray backwarming calculations and in Allred et al. (2006) with electron beam heating with the RADYN code. However, comprehensive models of the powerful optical continuum radiation and the broadening of the hydrogen Balmer line series have not yet been addressed. The multi-wavelength spectra of this event have been widely utilized for empirically-driven models of exoplanet photochemistry and surface UV dosages (Segura et al., 2010; Venot et al., 2016; Ranjan et al., 2017; Tilley et al., 2019; Estrela et al., 2020).

This paper is organized as follows. In **Section 2**, the AD Leo Great Flare spectrum and photometry data that are used for model fitting are briefly reviewed. **Section 3** describes the radiative-hydrodynamic flare models, which are fit to the Hγ emission line in the spectrum corresponding to the rise and peak phases of the Great Flare (**Section 4**). We calculate the Balmer line merging in the spectral region around the Balmer limit (**Section 4.3**) to further justify our two-component model fitting approach. We consider the FUV spectrum during the early impulsive phase and independently fit to the observed continuum distribution of the Great Flare in order to make a new continuum model prediction for the NUV wavelength range that was not observed during this time (**Section 4.4**). The interpretation of the results is discussed in **Section 5** in terms of the spatial distribution of intensity in an image of a well-studied solar flare; we present new calculations for habitable zone UV-C fluxes in **Section 5.2**. We conclude in **Section 6**.

2 Observations

2.1 The 1985 April 12 great flare of AD Leo

The Great Flare of AD Leo was a large-amplitude, superflare event with an energy of nearly 10^{34} erg emitted in the *U* band. The available data are the broadband *UBVR* photometry and the optical spectra covering $\lambda = 3560 - 4400$ Å at a resolving power of $R \approx 1240$. The exposure times of the spectra varied between one and 3 minutes (see Hawley and Pettersen, 1991, for details). Here, we model the spectrum that integrated over most of the rise and first peak, labeled as the "542s" spectrum in Hawley and Pettersen (1991) and "S# 36" in the analysis of Kowalski et al. (2013)[2]. The light curve of the *U* band is shown in **Figure 1** with the integration time of the rise/peak spectrum indicated.

The Great Flare exhibits all of the spectral and light curve characteristics of a highly "impulsive-type" stellar flare, according to the "IF" classification in Kowalski et al. (2013). Specifically, the blue-optical spectra were fit with a color temperature of $T \approx 11,600$ K, and the small Balmer jump in the *U* band suggests that Balmer recombination radiation is important at shorter wavelengths (Figure 9 of Kowalski et al., 2013). During the early impulsive phase, a FUV spectrum (described below) constrains the peak of the continuum to the *U* band with a turnover toward shorter

2 Segura et al. (2010) refers to the spectrum at 915 s as the peak spectrum; this is S# 39 in the labeling scheme of Kowalski et al. (2013) and corresponds to the second, lower-amplitude peak in the impulsive phase.

wavelengths that was found to be most consistent with a $T = 8500 - 9500$ K blackbody among the models that were available at the time (Hawley and Fisher, 1992). Hawley and Pettersen (1991) analyzed the highly broadened, symmetric wings of the Balmer series, which were attributed to the Stark effect. The full-width evolution of the hydrogen Balmer Hγ emission line from Hawley and Pettersen (1991) is reproduced in **Figure 1**. The rise/peak spectrum corresponds to the first observation that exhibits very broad Hγ wings.

The AD Leo Great Flare was observed with ultraviolet spectroscopy with the International Ultraviolet Explorer (IUE). A FUV spectrum was observed in the short-wavelength channel (SWP; $\lambda = 1150 - 2000$ Å), which integrated over the first 900 s of the flare (up until 4:55 UT) and included 41 min of quiescence. The fluxes in the major emission lines and in the continuum longward of 1780 Å saturated the detector. NUV spectral observations in the long wavelength band (LWP; $\lambda = 1900 - 3100$ Å) of IUE started at 5:00 UT, which is about midway during the second, fast decay phase in the *U*-band light curve in **Figure 1**. The LWP observation from 5:00–5:20 UT was split into five sub exposures, each 3 – 8 min in duration (see Figure 1 of Hawley and Pettersen (1991) for the $\lambda = 2000$ Å and 2800 Å continuum flux evolution over the first set of five sub-exposures). In the flare, some emission lines in the NUV were saturated as well (see Segura et al., 2010, for details about how these data have been utilized by interpolation and binning). Since there were no NUV spectra covering the rise and peak phases, we do not consider the IUE/LWP spectra further in this study. For detailed descriptions of the reduction and analyses of the IUE spectra, we refer the reader to Hawley and Pettersen (1991).

2.2 The 2014 March 29 X1 solar flare

The 2014 March 29 GOES class X1 flare (SOL20140329T17:48) is one of the best-observed and most-widely studied solar flares from Sunspot Cycle 24 (e.g., Heinzel and Kleint, 2014; Aschwanden, 2015; Battaglia et al., 2015; Young et al., 2015; Rubio da Costa et al., 2016; Rubio da Costa and Kleint, 2017; Woods et al., 2017; Kleint et al., 2018; Polito et al., 2018; Zhu et al., 2019). The flare was observed by the Interface Region Imaging Spectrograph (IRIS; De Pontieu et al., 2014) with FUV and NUV longslit spectroscopy (see, e.g., Kleint et al., 2016; Kowalski et al., 2017a, for detailed descriptions of these spectra). Narrow-band ($\Delta\lambda \sim 4$ Å), slit jaw images (SJI) in the NUV at Mg II 2796 (SJI 2796) and at 2830 Å (SJI 2832) are available for contextual information about the flare brightenings that cross the IRIS slit. For this study, a level-2, SJI 2832 image at 17:46 UTC is retrieved from the IRIS data archive hosted at the Lockheed Martin Solar and Astrophysical Laboratory[3]. The SJI 2832 image corresponds to the early impulsive phase of the hard X-rays at $E \geq 25$ keV and has been analyzed in Kowalski et al. (2017a). The IRIS slit location stepped through the ribbons in this flare, resulting in a cadence of 75 s for the raster and SJI 2832 images. Following previous analyses (e.g., Kowalski et al., 2017a), we convert the level-2 data in units of DN s^{-1} pix^{-1} to an equivalent, constant intensity value, $\langle I_\lambda \rangle_{\rm SJI}$, over the SJI bandpass using the time-dependent effective area curves (Wülser et al., 2018) provided by the IRIS mission.

X-ray imaging data from the Reuven Ramaty High-Energy Solar Spectroscopic Imager (RHESSI; Lin et al., 2002) were retrieved from the new RHESSI data archive[4]. We use the 6–12 keV and 50–100 keV imaging over the time-interval of 17:45:58.7 to 17:46:32.0. We refer the reader to Battaglia et al. (2015) and Kleint et al. (2016) for higher temporal and spatial resolution analyses of the RHESSI data for the 2014 March 29 flare.

3 Radiative-hydrodynamic flare models

To model the rise/peak phase spectrum of the AD Leo flare, we use results from a grid of radiative-hydrodynamic (RHD) models calculated with the RADYN code (Carlsson and Stein, 1992, 1995, 1997, 2002; Allred et al., 2015). All of the details about the simulation setup will be described in a separate paper (Kowalski et al. in preparation), but a brief summary is presented here. To simulate flare heating, we model the energy deposition from a power-law distribution (hereafter, "beam") of electrons, which is calculated in a 1D magnetic loop of half-length 10^9 cm, a constant surface gravity of $\log_{10} g/[\text{cm s}^{-2}] = 4.75$, and a uniform cross-sectional area. The effective temperature of the starting atmosphere is $T_{\rm eff} \approx 3600$ K (see the Appendix of Kowalski et al., 2017b, for details regarding the starting atmosphere). The equations of mass, momentum, internal energy, and charge are solved on an adaptive grid with the equations of radiative transfer and level populations for hydrogen, helium, and Ca II. The electron beam is injected at the loop apex with a ramping flux to a maximum value at $t = 1$ s, followed by a decrease until $t = 10$ s according to the pulsed injection profile prescription in Aschwanden (2004). The heating rate as a function of depth is determined by the steady-state solution to the Fokker-Planck equation for energy loss and pitch angle scattering due to Coulomb collisions using the module that was further developed into the

3 https://iris.lmsal.com/search/.

4 https://hesperia.gsfc.nasa.gov/rhessi_extras/flare_images/image_archive_guide.html.

FP code (Allred et al., 2020). The heating rate is recalculated at every time-step in the radiative-hydrodynamic simulation (see Allred et al., 2015). In this first generation of models, return current electric fields and magnetic mirroring forces (Allred et al., 2020) are not considered. However, hydrogen Balmer line spectra (Hα, Hβ, Hγ) are properly modeled using the Doppler-convolved, TB09 + HM88 line profile functions (Smith et al., 1969; Vidal et al., 1970, 1971, 1973; Hummer and Mihalas, 1988; Tremblay and Bergeron, 2009), which accurately capture the pressure broadening from ambient, thermal electrons and ions in the density regimes of flare chromospheres (Kowalski et al., 2017b, 2022).

Stellar flare hard X-ray emission is below current detection limits, except in the most energetic events (e.g., Osten et al., 2007, 2016), and millimeter/radio observations at optically thin frequencies have been reported only recently (MacGregor et al., 2020). The paucity of direct constraints on accelerated electrons in stellar flares thus necessitates a grid of models covering a large parameter space of electron beam heating. Our grid of M dwarf flare models includes a large range of low-energy cutoff (E_c) values: 17, 25, 37, 85, 150, 200, 350, and 500 keV. All of the selected models from the grid are calculated for injected electron beam number fluxes with hard power-law indices of $\delta = 2.5 - 4$, which are consistent with available stellar flare constraints (Osten et al., 2007; MacGregor et al., 2018, 2020, 2021). The peak injected beam energy flux densities (hereafter, "flux") span four orders of magnitude: 10^{10} (F10), 10^{11} (F11), 10^{12} (F12), and 10^{13} (F13) erg cm^{-2} s^{-1}. For this study, we select five models with maximum ("m") injected beam fluxes of 10^{13} erg cm^{-2} s^{-1} ("mF13"), low-energy cutoffs of $E_c = 37, 85, 150, 200$, and 500 keV, and a power-law index of $\delta = 3$; these are referred to as the mF13-37-3, mF13-85-3, mF13-150-3, mF13-200-3, and mF13-500-3 models, respectively[5]. These models are especially notable because they reproduce $T \approx 10{,}000$ K color temperatures in the blue-optical wavelength range and small Balmer jump ratios, as reported in many M dwarf flare spectral observations (e.g., Mochnacki and Zirin, 1980; Fuhrmeister et al., 2008; Kowalski et al., 2013, 2016). The justification for selecting these high-flux models will be discussed further in **Section 4.2**.

The mF13-37-3 model is a recalculation of the RADYN simulation from Kowalski et al. (2016) (see also Kowalski et al. (2015)) with a pulsed beam flux injection. The atmosphere in the new model follows a similar evolution with the development of a dense ($n_e = 5 \times 10^{15}$ cm^{-3}), cool chromospheric condensation at $t \approx 2.2$ s. The mF13-85-3 and mF13-150-3 models produce relatively small amounts of coronal heating and relatively fast upflows ($\approx 5 - 20$ km s^{-1}) in the flare chromosphere because most of the beam energy is deposited into the deep chromosphere. Without magnetic mirroring and return current electric field forces, long-lasting chromospheric condensations do not develop as in the mF13-37-3 model. However, large ambient electron densities ($n_e \approx 1 - 7 \times 10^{15}$ cm^{-3}) are attained due to thermal ionization of hydrogen by the beam heating in low-lying chromospheric layers (see the Appendices of Kowalski et al., 2017b, for a description of several, similar large, low-energy-cutoff models). These charge densities refer to the atmospheric (ambient/thermal) proton and electron densities that pressure broaden the hydrogen lines that we model in **Section 4.2** and **Section 4.3**. The nonthermal electron densities are many orders of magnitude smaller in the chromosphere. The large, low-energy-cutoff models represent a semi-empirical approach in the spirit of the static flare atmospheres of Cram and Woods (1982), but the RADYN models include time-dependent atmospheric thermodynamics that are calculated self-consistently with beam heating.

In addition to the F13 models, a lower beam flux that has been used to model IRIS NUV spectra of a solar flare (Kowalski et al., 2017a) and the broadening of the hydrogen Balmer series (Kowalski et al., 2022) has been injected into our M dwarf atmosphere for a duration of 15 s. The electron beam parameters ($E_c = 25$ keV, $\delta = 4$, flux of 5×10^{11} erg cm^{-2} s^{-1}) for this model ("c15s-5F11-25-4") were selected to be consistent with those that were inferred through the collisional thick target modeling of RHESSI hard X-ray data of the 2014 March 29 solar flare (Kleint et al., 2016). Similar to the analogous simulation in the solar atmosphere, a dense chromospheric condensation develops by $t \approx 4$ s with densities of $n_e \approx 5 \times 10^{14}$ cm^{-3}. We also calculate a model (m5F11-25-4) with a shorter, pulsed injection profile in the same form as for the pulsed F13 beams. Several other models that are considered in this work are two intermediate flux models (mF12-37-3 and m2F12-37-2.5) with hard power-law distributions ($\delta = 2.5$ and 3) and intermediate low-energy cutoff values ($E_c = 37$ keV). A similar model to the mF12-37-3 beam was analyzed in Namekata et al. (2020), who found satisfactory agreement between the broadening of the hydrogen Balmer α emission line in the model and in the observation of a superflare event from AD Leo.

The parameters of the RHD models that are used in the remainder of this work are summarized in **Table 1**.

4 Model spectrum analysis

We leverage the new hydrogen pressure broadening profiles that have been incorporated into RADYN to examine the models that reproduce the Balmer jump strength and blue-optical continuum color temperature. The Balmer Hγ emission

5 A corresponding grid of models is calculated using a constant beam flux injection; these models are indicated with a "c"-prefix, such as cF13-85-3.

TABLE 1 RADYN electron beam heating models.

Model	Beam Flux	$t_{1/2}$ (s)	t_{end} (s)	E_c (keV)	δ —	C4170′ (erg cm^{-2} s^{-1} Å^{-1})	$F'_{H\gamma}$ (erg cm^{-2} s^{-1})	$F'_{H\gamma}$/C4170′ (Å)	Hγ Eff. Width (Å)
mF13-85-3	max F13	2.3	10	85	3	1.14×10^{8}	1.62×10^{9}	14.2	9.1
mF13-150-3	max F13	2.3	10	150	3	1.54×10^{8}	1.16×10^{9}	7.5	10.3
mF13-200-3	max F13	2.3	10	200	3	1.73×10^{8}	6.21×10^{8}	3.6	10.4
mF13-500-3	max F13	2.3	10	500	3	1.87×10^{7}	-1.37×10^{9}	−107	−47.7
mF12-37-3	max F12	2.3	10	37	3	3.51×10^{6}	5.45×10^{8}	155.2	3.8
m2F12-37-2.5	max 2F12	2.3	10	37	2.5	1.72×10^{7}	8.65×10^{8}	50.3	5.8
mF13-37-3	max F13	2.3	10	37	3	7.94×10^{7}	2.22×10^{9}	27.9	12.1
m5F11-25-4	max 5F11	2.3	10	25	4	6.35×10^{5}	2.95×10^{8}	464.6	2.2
c15s-5F11-25-4	const 5F11	15	15	25	4	3.30×10^{6}	1.33×10^{9}	402.4	5.3

Note—$t_{1/2}$ is the full-width-at-half-maximum of the injected beam heating pulse; t_{end} indicates the end of the simulation and the duration over which the temporal averages of the model spectra are calculated. The effective width of Hγ is defined as the integral of the continuum-subtracted, peak-normalized emission line profile (Kowalski et al., 2022); note that the Hγ profile is an absorption profile in the mF13-500-3 model.

line broadening and nearby blue-optical continuum fluxes of the Great Flare are the focus of our modeling analyses (Section 4.1 and Section 4.2). In Section 4.3, we extend the detailed calculations to spectra of the entire Balmer line series.

4.1 Average model line-to-continuum ratios

We first describe a simple method that allows comparisons of 1D loop models to the Great Flare spectra, which are not spatially resolved. Over an exposure time of 180 s, we reasonably expect that many sequentially ignited, spatially distinct, $\Delta t = 10$ s pulses accumulate flare radiation in the spatially unresolved, observed flare spectrum. For each RHD model, we thus calculate a coadded spectrum from the radiative surface flux spectra at every $\Delta t = 0.2$ s by temporal averaging over the duration given by t_{end} in Table 1. These coadded spectra are used in all analyses, unless otherwise indicated.

Several coadded F13 model spectra around the Hγ emission line are normalized to the observed continuum flare-only flux averaged over $\lambda = 4155 - 4185$ Å in the Great Flare (Figure 2). With an older, less accurate prescription of hydrogen line pressure broadening, Kowalski et al. (2015) found that a coadded F13 model with a double power-law beam distribution and $E_c = 37$ keV was an adequate model of the early/mid rise phase of a giant flare from the dM4.5e star YZ CMi. As Figure 2 clearly demonstrates, the mF13-37-3 model profile with the updated hydrogen broadening is far too broad even though times when the chromospheric condensation is not extremely dense and the emission lines are relatively narrow are included in the coadd. The coadded mF13 spectra from the models with large, low-energy-cutoffs ($E_c = 85 - 150$ keV) adequately account for some or all of the flux in the Hγ wings, but these models of deep flare heating vastly under-predict the relative Hγ line-peak flux.

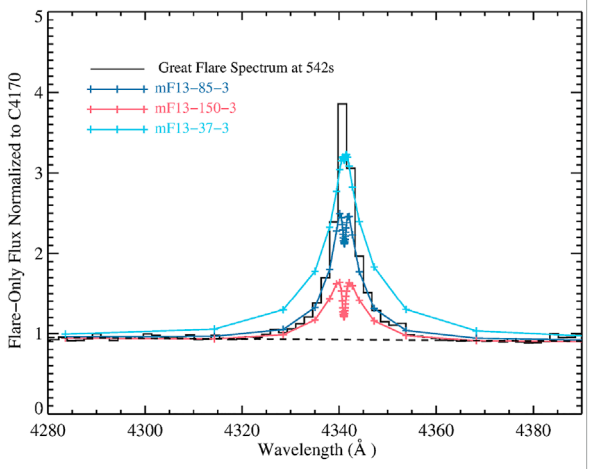

FIGURE 2
Comparisons of several F13 model spectra of Hγ directly from RADYN (and thus have relatively coarse wavelength sampling in the far wings) to the Great Flare rise/peak phase spectrum. Each model has been scaled to the observed continuum flux, C4170′. The mF13-37-3 model prediction is far too broad, while the mF13-85-3 and mF13-150-3 models do not exhibit an amount of broadening that exceeds the observation in the line wings. The dashed line shows a detailed continuum spectrum that is interpolated to the wavelengths over the Hγ line.

To quantitatively assess the models, we calculate several quantities from the detailed Hγ line profiles and the continuum spectra. Specifically, we calculate the continuum-subtracted, preflare-subtracted, line-integrated flux over the Hγ emission line (hereafter, $F'_{H\gamma}$), the preflare-subtracted flux[6] at $\lambda = 4170$ Å (hereafter, C4170′), and the ratio of these quantities (Table 1). The 5F11 and F12 models produce ratios that are far too

6 Following traditional use, we denote flare-only quantities with a prime-symbol, and we refer to an observed spectral/monochromatic/specific flux density at Earth as the "flux"; we use "spectral luminosity" to refer to the luminosity per unit wavelength.

large compared to $F'_{H\gamma}$/C4170' ≈ 20 that is calculated from the Great Flare observation (Kowalski et al., 2013), while the ratios from the F13 models with large low-energy cutoffs are too small. This motivates linear superpositions of two RHD model components–one high-flux (F13) component and one lower-flux (5F11 or F12) component–to comprehensively reproduce the observed line-to-continuum ratios, the shape of the Hγ wing broadening, and the Hγ emission line peak flux.

TABLE 2 Least-squares fitting results for Hγ.

F13 Model	X_{F13}	Lower Flux Model	X_{rel}	χ^2_{dof}
mF13-85-3	0.0028	m5F11-25-4	2.3	1.2
mF13-150-3	0.0022	m5F11-25-4	4.5	4.1
mF13-150-3	0.0019	c15s5F11-25-4	1.6	7.9
mF13-200-3	0.0017	mF12-37-3	4.9	1.9
mF13-500-3	0.0009	m2F12-37-2.5	9.6	1.7

4.2 Two-component model fits to the Hγ line in the AD Leo great flare

A linear superposition of a high flux (F13), large low-energy cutoff beam component and a lower flux (5F11, F12, or 2F12), smaller low-energy cutoff beam component is represented by the equation (Eq. 1),

$$f'_{\lambda,\mathrm{Model}} = \left(X_{F13}\, S'_{\lambda,F13} + X_{5F11}\, S'_{\lambda,5F11}\right)\frac{R^2_{\mathrm{star}}}{d^2} \qquad (1)$$

where $f'_{\lambda,\mathrm{Model}}$ is the model flux at Earth. The filling factor, X, is the exposure-time-averaged fraction of the visible hemisphere of the star that is flaring with the temporal coadd of the radiative surface flux spectrum, S_λ, calculated from each RHD model component. $R_{\mathrm{star}} = 3\times 10^{10}$ cm is the radius of AD Leo, and $d = 1.5\times 10^{19}$ cm is the distance to the star. The preflare model surface flux spectrum is subtracted to give the flare-only, model surface flux spectra, $S'_\lambda = S_\lambda - S_{\lambda,o}$, in Equation 1. To mitigate systematic errors in the far wings of the Hγ line (Figure 2), which are coarsely sampled at 31 wavelength points in the RADYN calculation, we recalculate[7] the emergent surface flux spectra using a Feautrier solver on a 327 point wavelength grid with the frequency-independent, non-LTE source function from RADYN and a four-point, third-order interpolation of the line profile opacity from the Appendix of Vidal et al. (1973). The emergent radiative flux spectra of Hγ are time-averaged over the duration of each simluation, convolved with a Gaussian with a full-width-at-half maximum that corresponds to the instrumental resolution of 3.5 Å, and binned to the wavelengths of the Great Flare spectra.

We perform an inverse-variance-weighted, linear least-squares fit of the two parameters X_{F13} and X_{5F11} to the observed spectrum around the Hγ line. The model surface flux spectra are the basis functions in the $n\lambda\times 2$ design matrix, Λ. The maximum likelihood (ML) estimates of the parameters are given by the standard matrix equation (Eq. 2),

$$\hat{\vec{X}}_{\mathrm{ML}} = \begin{pmatrix}\hat{X}_{F13,\mathrm{ML}}\\ \hat{X}_{5F11,\mathrm{ML}}\end{pmatrix} = \left(\Lambda^{\mathrm{T}} C^{-1}_{\vec{f}'_\lambda}\Lambda\right)^{-1}\left(\Lambda^{\mathrm{T}} C^{-1}_{\vec{f}'_\lambda}\vec{f}'_\lambda\right) \qquad (2)$$

where $\vec{f}'_\lambda$ is the observed $n\lambda\times 1$ flare-only flux at Earth (hereafter dropping the vector notation) as a function of wavelength and the $n\lambda\times n\lambda$ covariance matrix C is populated with independent, Gaussian uncertainties, which are estimated from the data, f'_λ. The wavelength range from $\lambda = 4320 - 4361$ Å is used in the fits, which are performed for all combinations of two models from the grid. The models in Table 1 are among the combinations with the lowest values of χ^2 and were thus chosen as the focus of this study. Figure 3 shows the result of one of the best fits with $\chi^2_{\mathrm{dof}} = 1.2$ for 21 degrees of freedom (dof). The quality of this fit is representative of many such results with two RHD component spectra consisting of a high-flux, large low-energy cutoff beam and a lower-flux, smaller low-energy cutoff beam. In the right panel of Figure 3B, we show likelihood contours for this fit to visualize typical uncertainties on the maximum-likelihood estimates of the parameters. The comparisons of the inferred filling factors of the high-flux (e.g., F13) and lower-flux (e.g., 5F11) models in each fit will be more useful in comparison to solar flare data (Section 5.3), and therefore we report values of $X_{\mathrm{rel}} = \frac{X_{5F11}}{X_{F13}}$. For the model combination in Figure 3, the best-fit parameters and standard error propagation give $X_{\mathrm{rel}} = 2.28\pm 0.08$. The value of $F'_{H\gamma}$/C4170' = 19.9 is remarkably consistent with this measured quantity from the observed flare spectrum.

The results for several representative combinations of models in Table 1 with small values of χ^2 are presented in Table 2, indicating a range of values of $X_{\mathrm{rel}} \approx 1.5 - 10$. Since these fits include only the Hγ line data for this flare, the relatively small differences in the various χ^2 values in Table 2 are not strictly indicative of a global minimum. The vast majority of all model combinations from the entire grid, however, result in χ^2 values far in excess of those shown in Table 2. We think that an exploratory approach to the model grid predictions is more productive than an effort to find one model that best satisfies all constraints from the data, given the many assumptions in the RHD modeling (e.g., specific choice of low-energy cutoff values in the grid, assumptions of constant-area loop geometry and a constant power-law index value over each pulse). The small values of χ^2 are thus most informative for limiting the vast parameter space for further comparisons of our general modeling paradigm to the multi-wavelength data of the Great Flare.

7 All analyses have been performed on both the original 31-wavelength array and the 327-wavelength array.

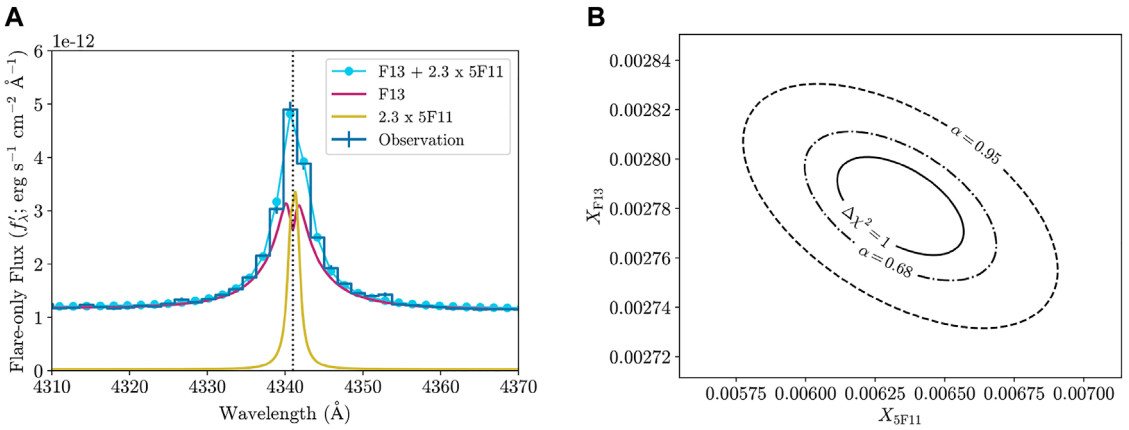

FIGURE 3
(A) A representative example of a satisfactory, two-component (mF13-85-3, m5F11-25-4) RHD model fit to the observed Hγ line profile and nearby continuum flux in the Great Flare of AD Leo. **(B)** Constant joint-likelihood contours for the model fit in the left panel. The maximum-likelihood estimates of the parameters and 1σ, Gaussian marginal uncertainties are $\hat{X}_{\mathrm{F13,ML}} = 2.78 \times 10^{-3} \pm 2 \times 10^{-5}$ and $\hat{X}_{\mathrm{5F11,ML}} = 6.34 \times 10^{-3} \pm 2.3 \times 10^{-4}$ with a correlation coefficient of $\rho = -0.53$.

4.3 Models of the balmer limit

In order to robustly extrapolate the models of this flare to the NUV wavelength range that was not observed during most of the impulsive phase, the Balmer jump strength in the observation should be satisfactorily reproduced. However, many linear combinations of two models in the RADYN flare grid produce small Balmer jump ratios that are consistent with the measured range ($\chi_{\mathrm{flare}} \approx 1.7 - 1.9$; Kowalski et al., 2013) from the spectrum of the Great Flare. For supplementary constraints, we compare the details of the merging of the Balmer series at $\lambda = 3646 - 4000$ Å. The last visible Balmer emission line is often used as an indication of the electron density, and Hawley and Pettersen (1991) discusses that the Balmer lines up to and including H15 or H16 are resolved in the Great Flare spectra. Thus, our RHD model combinations should reproduce this salient property.

We use the RH code (Uitenbroek, 2001) with a 20-level hydrogen atom and the occupational probability modifications to the bound-bound and bound-free opacities that account for level dissolution at the Balmer limit (Dappen et al., 1987; Hummer and Mihalas, 1988; Nayfonov et al., 1999; Tremblay and Bergeron, 2009). The RH calculation setup is the same as described in Kowalski et al. (2017b). These calculations are intensive because they involve a large numerical convolution at each atmospheric depth, and not every time-step in all models readily converges to a solution. To demonstrate a representative solution with the two-component modeling approach from the previous section, we use atmospheric snapshots from the mF13-150-3 simulation at $t = 0.0, 0.4, 1.0, 2.0, 4.0, 6.0, 8.0, 9.8$ s and a snapshot from the m5F11-25-4 simulation at $t = 0.8$ s. The F13 model spectra are coadded, and the preflare spectrum is subtracted from the two model components. We then use the equation (Eq. 3),

$$\left(F'_{\mathrm{H}\gamma}/\mathrm{C4170}'\right)_{\mathrm{obs}} = \frac{X_{\mathrm{rel}} \times F'_{\mathrm{H}\gamma,\,\mathrm{5F11}} + F'_{\mathrm{H}\gamma,\,\mathrm{F13}}}{X_{\mathrm{rel}} \times \mathrm{C4170}'_{\mathrm{5F11}} + \mathrm{C4170}'_{\mathrm{F13}}} \tag{3}$$

to solve for X_{rel} given $\left(F'_{\mathrm{H}\gamma}/\mathrm{C4170}'\right)_{\mathrm{obs}} = 20$. The total two-component model flux spectrum is scaled to the continuum flare flux, C4170′, in the observed spectrum. For the two-component model combination above, a value of $X_{\mathrm{rel}} \approx 3.9$ is obtained, which is close to 4.5 that is obtained from fitting the Hγ line profile (Table 2). We convolve the flare model with the spectral resolution of the data and show the result against the observations in Figure 4, which demonstrates consistency with the observed Balmer jump flux ratio, the detailed merging of the line series wings, and in the bluest visible Balmer line. Without the additional narrow-line flux from the 5F11, the highest balmer line in emission is H13, which is inconsistent with the observations. Without the continuum and Balmer wing flux from the F13 model, the Balmer jump ratio and the $F'_{\mathrm{H}\gamma}/\mathrm{C4170}'$ value from the 5F11 model are far larger (Table 2) than measured from the observed spectrum.

4.4 Broadband continuum fitting

In this section, we fit the observed continuum fluxes from the FUV to the red-optical during the early impulsive phase of the AD Leo Great Flare to compare to the results from fitting to the Hγ spectrum (Table 2) and high-order series merging (Section 4.3).

Figure 5 shows a comparison of the detailed continuum fluxes for several combinations of the models that satisfactorily

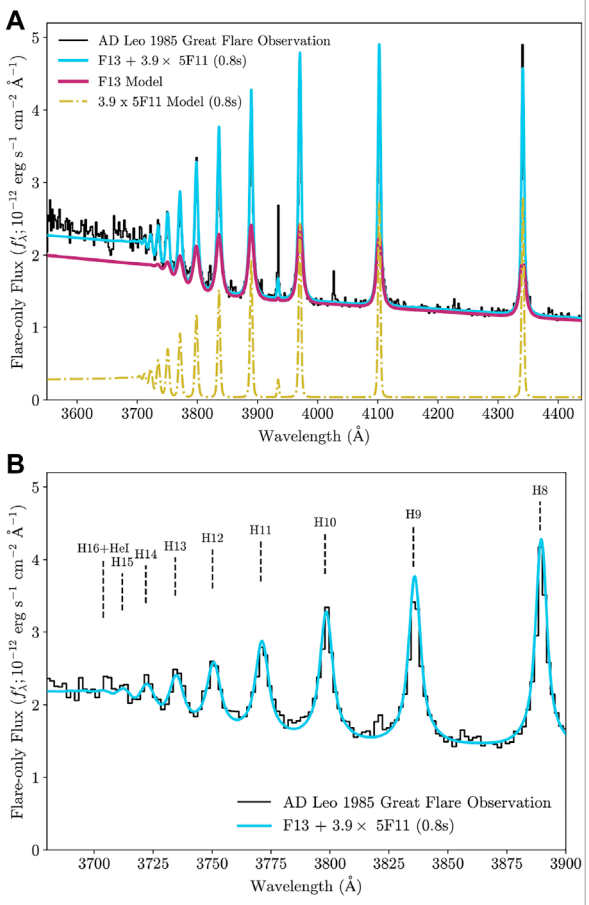

FIGURE 4
(A) RH calculations with non-ideal opacity effects at the Balmer limit. A linear superposition of the mF13-150-3 model, averaged over its duration, and the m5F11-25-4 model at $t = 0.8$ s is shown for the combination that is constrained by a value of $F'_{\mathrm{H}\gamma}/\mathrm{C4170}'$ that is measured from the observed spectrum. The individual component model calculations are shown: the m5F11 contributes to the narrow hydrogen line flux, the highest order Balmer lines, and optically thin Balmer continuum flux in addition with the optically thick Balmer continuum flux from the F13. The mF13 model accounts for nearly all of the optical continuum flux and far wing radiation. **(B)** The pseudo-continuum from the merging of the Balmer H8—H15 line wings, the dissolved level continuum between the lines, the fading of the emission line fluxes into the dissolved-level continuum at $\lambda < 3700$ Å, and the bluest Balmer line (H15) are adequately reproduced in the RHD model superposition. The wavelengths of the hydrogen series and a helium I line noted by Hawley and Pettersen (1991) are indicated.

explain the early-impulsive phase, blue-optical spectrum of the Great Flare of AD Leo. A representative RHD model combination (mF13-150-3, m5F11-25-4 ($t = 0.8$s)) from **Section 4.3** exhibits a peak at $\lambda \approx 2350 - 2400$ Å followed by a turnover toward shorter wavelengths. Qualitatively, these properties are consistent with FUV constraints of this superflare and other, smaller flares from AD Leo (Hawley et al., 2003), but the IUE/SWP observation allows a more detailed comparison. To adjust the flux calibration of the data for the different exposure times between the early-impulsive phase, IUE/SWP spectrum ($t < 900$ s in **Figure 1**) and the $\lambda > 3560$ Å ground-based spectrum ($t = 542 \pm 90$ s in **Figure 1**; see **Section 2**), we apply the relative scaling between the *U*-band and the FUV continuum flux at $\lambda \approx 1600$ Å within the first 900 s of the flare that is presented in the upper left panel of Figure 11 of Hawley and Fisher (1992). The relative scale factor (1.3) is used to adjust the lower envelope of the SWP continuum flux relative to a synthetic *U*-band flux that we calculate from the blue-optical spectrum. The scaled and original IUE/SWP spectra are shown in **Figure 5**. We also include the *V*- and *R*-band photometry from the same figure in Hawley and Fisher (1992) and apply the scaling in the same way as for the FUV continuum. We calculate two-parameter, linear least-squares fits to the seven flare-only flux measurements of the continuum in the Great Flare[8]. Minimizing χ^2 (**Section 4.2**) gives several combinations of models with very large low-energy cutoffs ($E_c = 350 - 500$) as the X_{F13} model component superimposed with the m2F12-37-2.5 model spectrum. Note, the m2F12-37-2.5 model is the only simulation in our RADYN grid with such a hard, $\delta < 3$, electron beam power-law index.

The best-fit superposition of the mF13-500-3 and m2F12-37-2.5 radiative flux spectra is shown in **Figure 5A** (top panel) with $X_{\mathrm{rel}} \approx 11.9$. Notably, this fit comprehensively accounts for the slope of the lower-envelope of the FUV flare spectrum, the Balmer jump strength, and the optical continuum constraints. The middle, left panel of **Figure 5B** shows the contributions of the individual model components to the spectral luminosity of the flare continuum from the 'panel (A). The mF13-500-3 accounts for most of the FUV continuum luminosity, whereas the Balmer jump in the m2F12-37-2.5 contributes a larger fraction in the NUV and in the *U* band. At optical wavelengths, relative contributions to the blue continuum spectral luminosity are about equal, but the lower beam-flux model is larger toward near-infrared wavelengths. The comparisons of the surface flux spectra without adjustments by the best-fit filling factors emphasize that the F13 model is the much brighter source at all wavelengths. A fit using these two model component to the observed Hγ line profile (**Section 4.2**) is shown in **Figure 5C** (bottom, right panel); the fit is excellent and, moreover, returns a similar, independent estimate for the parameter $X_{\mathrm{rel}} = 9.6$ (**Table 2**).

The fully-relativistic electron beam parameters of the mF13-500-3 beam are rather extreme, but they are not without precedent and sufficient semi-empirical necessity. Kowalski et al. (2017b) used a superposition of three RADYN

8 Instead of *U* and *B*-band photometry used for model fitting in Hawley and Fisher (1992), we use C3615', C4170', and C4400' calculated from averages of the continuum fluxes at $\Delta\lambda \approx 30$ Å around $\lambda = 3615, 4170, 4400$Å, respectively.

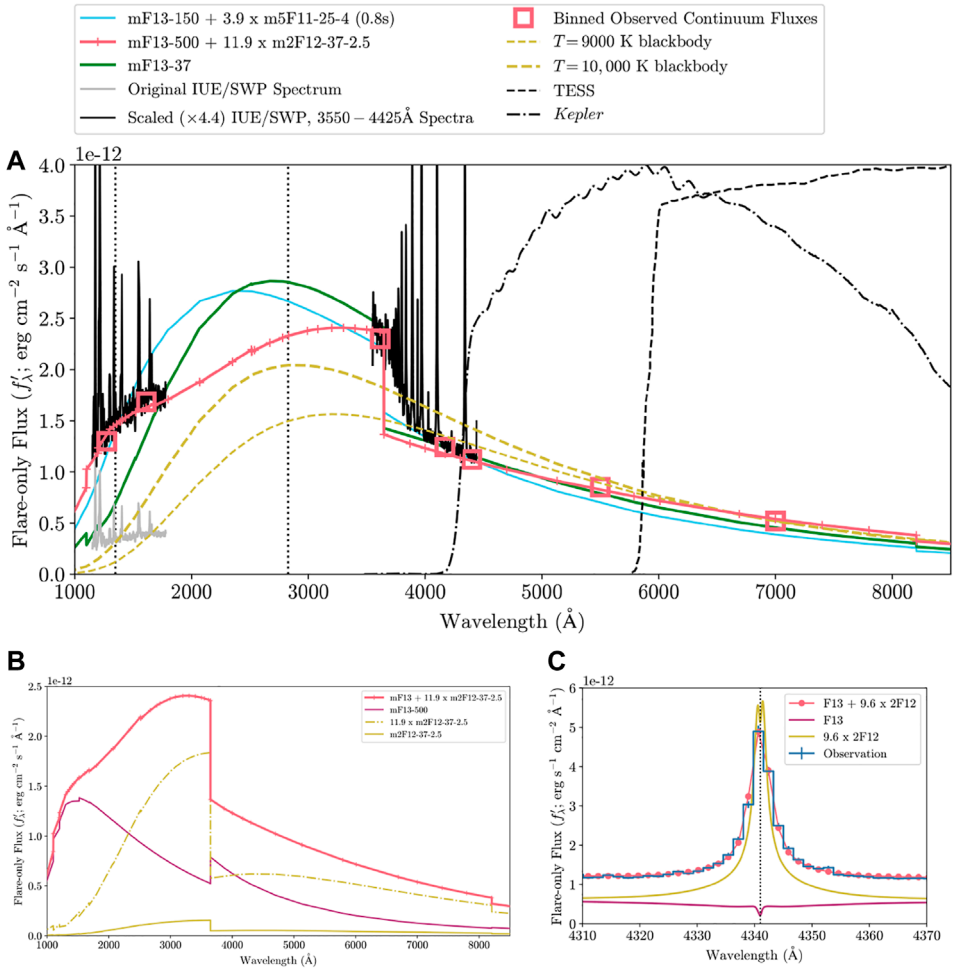

FIGURE 5
(A) Models of the early-impulsive phase broadband continuum flux distribution of the Great Flare of AD Leo compared to the IUE/SWP spectrum, optical ground-based spectrum, and broadband *V* and *R* photometry. All observed fluxes have been adjusted to the synthetic *U*-band flux according to the broadband distribution at $t = 0 - 900$ s in Figure 11 of Hawley and Fisher (1992). The wavelength-binned, flare-only fluxes that are used to fit the models are indicated by square symbols with a best-fit, two-component RHD model continuum spectrum shown as the solid red line. Other model predictions are scaled to the observations as follows: the blackbody functions are scaled to the *R* band flux observation, and the other two RHD models are scaled to the average continuum flux at $\lambda = 4155 - 4185$Å. **(B)** Individual model components in the best-fit mF13-500-3 + 11.9× m2F12-37-2.5 combination, which compares the relative contributions to the spectral luminosity of the continuum radiation in the Great Flare. The m2F12-37-2.5 model component is also shown without scaling by the best-fit filling factor to facilitate direct comparison to the radiative surface flux of the mF13-500-3. **(C)** Best-fit Hγ line profile model using the mF13-500-3 and m2F12-37-2.5 flux spectra gives a similar value of $X_{\rm rel}$ as for the fits to the broadband continuum fluxes.

simulations to model the decay phase spectra of a superflare from the dM4.5e star YZ CMi. A RADYN model with a constant electron beam energy flux injection of 2×10^{12} erg cm^{-2} s^{-1}, a low-energy cutoff of $E_c = 500$ keV, and a power-law index of $\delta = 7$ was used to explain the spectra of a secondary flare event, which exhibit features that are similar to an A-type star photospheric spectrum: namely, broad Balmer lines and a Balmer jump "in absorption" (see also Kowalski et al., 2012, 2013). Secondary flare events in the decay phase of a large flare from the young G-dwarf, EK Dra, were reported in Ayres (2015) to exhibit a response in only the FUV continuum. Finally, we note that increasing the value of $X_{\rm rel}$ after the peak flare phase may be able to explain the relatively rapid nature of the FUV continuum radiation that has been reported in other M dwarf flares (Hawley et al., 2003; MacGregor et al., 2020).

5 Discussion

5.1 Summary of fitting results

We fit the Great Flare impulsive phase (rise/peak) spectrum using simulations of electron beam heating from a new grid of RADYN flare models. The data require two, independent RHD

model components, resulting in relative filling factors ($X_{\rm rel}$) of the components between ≈1 – 10, with the lower beam flux model component exhibiting the larger filling factor. The time-evolution of the simulated atmosphere and emergent radiative flux spectra over each heating pulse is included in these comparisons to the data. Several examples of fits were presented and discussed. The shape of the Hγ line profile far into the wings and nearby continuum flux constrains combinations of a high-flux model (F13) with large low-energy cutoff values (E_c = 85 – 500 keV) and a lower-flux model (5F11–2F12) with smaller low-energy cutoff values (E_c = 25 – 37 keV). In the (mF13-85-3, m5F11-25-4) spectral luminosity, most of the Hγ wing broadening and blue-optical continuum radiation is attributed to the F13 model component. In the (mF13-200-3, mF12) model fits, most of the blue-optical continuum luminosity is due to the F13 spectrum, but much of the wing broadening can be attributed to the lower beam flux, F12, component. This is qualitatively consistent with the modeling results from Namekata et al. (2020), who found that similar F12 electron beam models produce satisfactory agreement in the broadening of the Hα line in a superflare. In their work, however, detailed comparisons to the spectra of the blue-optical continuum radiation were not possible.

We examined the prediction of one of the fits to the Great Flare Hγ line against the spectrum of the hydrogen series at the Balmer limit; there is remarkable agreement with the highest-order Balmer line in emission and with other features in the rise/peak spectrum (**Figure 4**). Models are also independently fit to the broadband photometry and spectral distribution during the first 900s of the Great Flare, and the superposition of spectra from the mF13-500-3 (or mF13-350-3) and the m2F12-37-2.5 RHD model components gives an excellent fit; moreover, this fit results in about the same relative filling factor as inferred from the Hγ line profile fitting. For this combination of models, the relative contributions to the optical continuum luminosity are comparable, but the E_c = 500 keV model dominates the FUV flare luminosity. In all model combinations, the F13 model component produces the brightest continuum surface flux.

In this section, we use the results from the fits to discuss the implications for models of the NUV radiation environment of the habitable zones of low-mass flare stars (**Section 5.2**). Then, we examine a high-spatial resolution image of a widely-studied X-class solar flare to speculate on the origin of these two spectral components in terms of solar flare phenomenology (**Section 5.3**). We show how the relative filling factors of the two model components are consistent with the relative areas of solar flare kernels and ribbon intensities, respectively, in the impulsive phase of this solar flare. In **Section 5.4**, we discuss further empirical investigation to anchor the two-component continuum and Hγ broadening models of stellar flares in reality.

5.2 The NUV radiation field in habitable zones of low-mass, flare stars

The detailed RHD models provide insight into the magnitude of the possible systematic errors for the inferred NUV radiation field in the habitable zones of low-mass flare stars. The RHD spectra in the NUV reveal that simple extrapolations from flare photometry in the red-optical and near-infrared (e.g., from the *Kepler* or TESS bands) that do not account for the Balmer jump strength, may result in rather large systematic modeling errors. We scale a T = 9000 K and T = 10,000 K blackbody to the observed R-band flux of the Great Flare in **Figure 5A** (top panel). Compared to the RHD models, the blackbody models under-predict the λ = 1800 – 3646 Å flare-only flux by factors ranging from 1.2 to 2.0. The peaks and slopes of the UV and U-band continuum spectra are largely in disagreement as well. Scaling all models to a common RHD continuum flux at a redder continuum wavelength, λ = 7810 Å, that is closer to the central wavelength of the TESS white-light band (**Figure 5**) generally results in larger underestimates of the NUV continuum flare-only flux by factors up to 2.6. The inadequacies of single-temperature, blackbody models are even more evident at λ = 1100 – 1800 Å and in the expected amount of Lyman continuum fluxes at $\lambda \lesssim$ 911 Å (not shown) that are present in the RHD model spectra.

The recent laboratory experiments of Abrevaya et al. (2020) measured survival curves of microorganisms that were irradiated by sustained fluxes of monochromatic NUV light at λ = 2540 Å. In the worst-case scenario of direct irradiation, they found that a large UV-C flux from a superflare in the habitable zone (d = 0.0485 au; Anglada-Escudé et al., 2016) of the dM5.5e star Proxima Centauri fails to terminate biological function in a small but non-negligible fraction of the initial sample. The UV-C flux[9] of 92 W m^{-2} was calculated by scaling a T = 9000 K blackbody curve to the peak magnitude change in the Evryscope g' bandpass as described in Howard et al. (2018); we refer the reader to Law et al. (2015) and Howard et al. (2019) for details about the Evryscope survey. We estimate that the peak B-band (λ = 3910 – 4890 Å) luminosity of the Great Flare of AD Leo was at least a factor of three larger than the g'-band ($\lambda \approx$ 4050 – 5500 Å) peak luminosity of the Proxima Centauri superflare. If a flare as luminous as the Great Flare (and the same in all other regards) were to occur on Proxima Centauri, the RHD models in **Figure 5** predict UV-C, impulsive-phase, habitable-zone fluxes of 800 – 1000 W m^{-2}. This range is rather similar to the habitable-zone, UV-C fluxes inferred in Howard et al. (2020) using extrapolations from much

9 For continuity with these studies, we momentarily express quantities in S.I. units.

higher temperature blackbody fits to broadband optical and near-IR photometry. As Howard et al. (2020) discuss, it would be interesting for laboratory experiments to determine whether there is an upper limit to the UV-C flux at which a microbial population achieves a steady-state survival fraction.

The pioneering study of Segura et al. (2010) combined the multi-wavelength AD Leo flare spectra for empirically-driven photochemistry and surface UV dosage modeling of an Earth-like planet in the habitable zone at $d = 0.16$ au from a dM3 star. In their approach, Segura et al. (2010) used the first IUE/LWP (NUV) spectrum available (starting at 5:00 UT in **Figure 1**) to bridge the blue-optical and IUE/SWP spectra during the early impulsive phase in the first 900 s of **Figure 1**. This approach assumes that the peak impulsive-phase NUV flare spectrum is the same as that at the end of the fast decay and start of the gradual decay phase in this event. At longer wavelengths, this assumption is not consistent with analyses of more recent, time-resolved spectra (Kowalski et al., 2013). However, we think that this approach is reasonably justified given the vagaries inherent in such spectral observations with relatively long exposure times that are not contemporaneous within the Great Flare.

Our scaling of the IUE/SWP spectrum (**Figure 5**) follows a different approach and is consistent with the relative surface fluxes at $\lambda \approx 1600$ Å and the U band that are shown in the upper left panel of Figure 11 of Hawley and Fisher (1992) and in Table 5 of Hawley and Pettersen (1991). In the IUE/LWP decay phase spectra of the Great Flare, the ratio of the $\lambda = 2800$ Å to $\lambda = 2000$ Å continuum fluxes is ≈5 (Hawley and Pettersen, 1991, see also Segura et al. (2010)), which effectively force the FUV continuum flux to a lower value relative to the fluxes at longer wavelengths in the NUV and U band. In our best-fit (mF13-500-3, m2F12-37-2.5) continuum flux model of the early impulsive phase (**Figure 5**), the $\lambda = 2800$ Å to 2000 Å continuum flux ratio is only 1.3. Thus, one expects the wavelength-integrated, UV-C flux of this model combination to be a factor of ≈1.5 larger than the empirical model of Segura et al. (2010), assuming equal top-of-the-atmosphere fluxes at $\lambda \approx 2800$ Å. However, further comparison reveals that the Segura et al. (2010) composite flare spectrum is similarly flat at $\lambda \gtrsim 2400$ Å. This effect is apparently due to the large number of blended (and saturated) Fe II and Mg II emission lines, which are generally much more prominent relative to the flare continuum radiation in the decay phase (Kowalski et al., 2019b). This coincidence is fortuitous for many follow-up studies (e.g., Venot et al., 2016; Tilley et al., 2019) that have adopted the composite NUV flare spectra from Segura et al. (2010) for photochemistry modeling: the pseudo-continuum of blended, saturated lines in the decay phase of the Great Flare mimics the shape of our RHD model continuum distribution that best reproduces the available observations in the rise and peak phases.

5.3 A solar flare "kernel + ribbon" interpretation of the great flare rise/peak phase

In this section, we argue that the results from the two-component model RHD fits are ostensibly consistent with the relative areas of high-intensity and medium-intensity sources in the impulsive phase of well-studied solar flare. The IRIS SJI 2832 image during the impulsive phase of the 2014 March 29 X1 solar flare is shown in **Figure 6**. We calculate the areas corresponding to several intensity ranges in the SJI 2832 image: $\langle I_\lambda \rangle_{\rm SJI} = 2-4\times 10^6$ erg cm^{-2} s^{-1} sr^{-1} Å^{-1} (faint threshold), $4-8\times 10^6$ erg cm^{-2} s^{-1} sr^{-1} Å^{-1} (medium threshold), and $\geq 8\times 10^6$ erg cm^{-2} s^{-1} sr^{-1} Å^{-1} (bright threshold). The bright threshold selects the pixels corresponding to the bright kernel (which is referred to as BK#1 in Kowalski et al., 2017a), and the medium threshold corresponds to the elongated ribbons on both sides of the brightest kernel[10]. In **Figure 6**, the dashed contour outlines the faint threshold area, the green-colored pixels correspond to the medium threshold pixels, and the purple and white pixels isolate the bright threshold kernel. We sum the exclusive areas within these three intensity ranges, and the equivalent circular areas that correspond to the assumed stellar footpoint geometry (**Eq. 1**) are illustrated in the bottom left of the figure. The ratios of these areas are ≈ 25:5:1 for the faint:medium:bright areas, respectively. Coincidentally, the ratio of medium:bright areas is 5:1, and the ratio of faint:medium brightness areas is also 5:1. These ratios are very similar to the areal ratios ($X_{\rm rel}$; **Table 2**) that we inferred between the higher flux and lower flux models through our spectral fitting to the AD Leo Great Flare. Thus, we attribute the two model components as representing a bright kernel–or several bright kernels–and fainter ribbons over a larger area.

The two RHD model components could also represent the faint-intensity and medium-intensity areas, respectively, which exhibit an areal ratio of 5:1. To justify this interpretation as the less plausible analogy for stellar flares, we bring in analyses of a solar, RADYN flare model ("c15s-5F11-25-4.2") from Kowalski et al. (2017a) and Kowalski et al. (2022). Kowalski et al. (2017a) synthesized the SJI 2832 intensity from this model, accounting for the emission lines and continuum response in this bandpass. At the brightest times of the 5F11 model ($t \approx 4$ s), they calculate a synthetic SJI 2832 intensity of $\langle I_\lambda \rangle_{\rm SJI} \approx 10^7$ erg cm^{-2} s^{-1} sr^{-1} Å^{-1}, which is consistent with the brightest pixels in **Figure 6**. Since this study, a detailed identification of the emission lines that contribute to the SJI 2832 data in solar flares has been presented (Kowalski et al., 2019a, see also Kleint et al., 2017), and several updates to the atomic

10 The medium threshold approximately corresponds to the "high thresh" area calculated from the excess intensity images in Kowalski et al. (2017a).

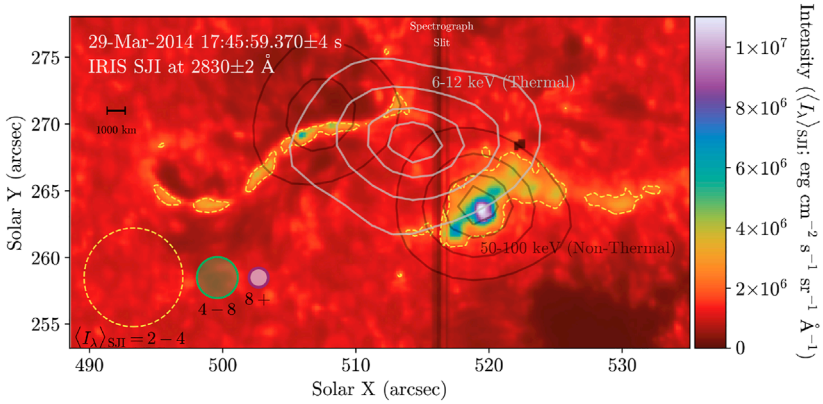

FIGURE 6
IRIS SJI 2832 image during the hard X-ray impulsive phase of the 2014 March 29 solar flare. The spatial resolution of the IRIS image is 0.″4 (0.″167 pix^{-1}; 724 km arcsec^{-1}). The projected, exclusive areas of 2.3×10^{17}, 3.9×10^{16}, and 8.6×10^{15} cm^2 correspond to the intensity ranges indicated in the figure below the equivalent circular areas. Note, an excess image formed by subtracting the image from 150 s earlier reveals much fainter emission; in this case, an excess threshold value of 6×10^5 erg cm^{-2} s^{-1} sr^{-1} Å^{-1} (Kowalski et al., 2017a) show that the faintest parts of the ribbons extend over an area of $\approx5\times10^{17}$ cm^2. The RHESSI X-ray contours are plotted at 25, 50, 75, and 90% of the maxima.

physics of Fe II have been implemented (which are to be described elsewhere in detail). The new calculations result in fainter emission line flux but similar redshift evolution of the Fe II lines. Averaging the solar c15s-5F11-25-4.2 model from Kowalski et al. (2022) over a simulated SJI 2832 exposure time of 8 s, so as to be directly comparable to the brightest pixels in the data in **Figure 6**, results in a synthetic model intensity of only $\langle I_\lambda\rangle_{SJI}\approx5\times10^6$ erg cm^{-2} s^{-1} sr^{-1} Å^{-1}. This intensity is above the medium-intensity threshold area corresponding to the green-colored ribbon pixels in **Figure 6**, but it is not nearly as bright as the most intense pixels. The IRIS raster clearly "steps over" the brightest kernel[11] in **Figure 6** (see Figure 1 in Kowalski et al. (2017a) and the discussion in Kleint et al., 2016). Thus, the 5F11 electron-beam, solar flare modeling with a small, low-energy cutoff is apparently most appropriate for the medium-intensity ribbons instead of the fainter ribbons that extend beyond the hard X-ray contours or the brightest pixels at the centroid of the hard X-ray contours. The faintest ribbon intensity in the impulsive phase[12] may correspond to locations of impulsive energy deposition by thermal conduction (Battaglia et al., 2015; Ashfield et al., 2022) and/or XEUV backheating over a large area (Fisher et al., 2012). The latter has been investigated in detail with 1D non-LTE models for the Great Flare data (Hawley and Fisher, 1992); we speculate that radiative backheating from an arcade of hot loops (e.g., Kerr et al., 2020) may account for additional Ca II K line flux in the model spectra in **Figure 4A** (top panel).

Is there evidence that a much stronger source of heating than a 5F11 beam contributes to the brightest SJI 2832 kernel pixels in this solar flare? Using an even brighter intensity threshold of $\langle I_\lambda\rangle_{SJI}=10^7$ erg cm^{-2} s^{-1} sr^{-1} Å^{-1} to mask the solar flare kernel in **Figure 6** gives an area of 3.3×10^{15} cm^{-2}, or four IRIS pixels. Dividing this area into the nonthermal electron power (8×10^{27} erg s^{-1}) above 20 keV that is inferred through standard collisional thick target modeling in Kleint et al. (2016) gives an injected electron beam flux of 2×10^{12} erg cm^{-2} s^{-1} (2F12). This is not as high as the maximum injected beam fluxes in the F13 models, but it is much larger than typically considered in solar flare RHD modeling. This line of reasoning implies that a much higher beam flux model is a more appropriate collisional thick target inference for the brightest SJI 2832 kernel in this solar flare. For these large beam fluxes, however, the standard assumptions in collisional thick target modeling of the hard X-ray footpoints are not applicable when the ambient coronal densities are small (Krucker et al., 2011). Although the RHESSI sources are largely unresolved (with a spatial resolution of 3.″6, or 5.4×10^{16} cm^2 at the Sun; Battaglia et al., 2015), the spatially integrated hard X-ray and IRIS SJI 2832 powers provide upper limits on necessitated modifications to the thick-target physics (e.g., Kontar et al., 2008; Brown et al., 2009; Kontar et al., 2012; Hannah et al., 2013; Alaoui and Holman, 2017; Allred et al., 2020) that are implemented in future modeling of the heterogeneous atmospheric response within the hard X-ray source

11 We further confirm this by inspecting the Mg II slit jaw images: though large regions of the ribbon are saturated, most of the saturation occurs away from the slit.

12 The next SJI 2832 image corresponds to the beginning of the fast decay phase of the hard X-rays, and the faint intensity threshold clearly selects a large area in the "wakes" of the bright ribbons. In these wakes, the emission lines may exhibit broad, nearly symmetric profiles as the red-wing asymmetries have coalesced with the line component near the rest wavelength (Graham et al., 2020) while the flare continuum intensity is still at a detectable level in the IRIS NUV spectra (Kowalski et al., 2017a; Panos et al., 2018; Zhu et al., 2019).

contours. Graham et al. (2020) investigated the deficiencies in chromospheric condensation model predictions of the red-wing asymmetry evolution of Fe II flare lines in IRIS spectra. Resolving the disagreements, and drawing on implications for the standard collisional thick target inferences of beam parameters, would greatly enhance the realism of the analogous stellar flare RHD component with small low-energy cutoff values.

5.4 Future observational constraints

Graham et al. (2020) used two intensity thresholds in faster-cadence SJI 2796 imaging of a different X1 solar flare to quantify newly brightened areas as a function of time. The ratios of these areas are ≈10:1, and the areal evolution is rather similar to the timing of the spatially integrated, hard X-ray emission peaks from Fermi/GBM. Further verification of the heterogeneity between kernel and the medium-brightness ribbon pixels are clearly needed from solar flare spectral observations. One such unexplored constraint is the NUV and FUV continuum evolution from IRIS flare spectra. In **Figure 5A** (top), we show the locations of two continuum windows in the IRIS spectra around $\lambda \approx$ 2826 Å and $\lambda \approx$ 1349 Å. The two spectral components obtained from our fits exhibit distinct, time-dependent C2826′/C1349′ emergent intensity ratios. A detailed investigation of the relative continuum intensities for a large sample of solar flares would help to determine the heterogeneity of the atmospheric response between the brightest kernels and nearby bright ribbons.

Reality checks could also be attained through spatially resolved characterization of the hydrogen Balmer line broadening along the slit length of observations of solar flares with the Visible Spectropolarimeter (ViSP; de Wijn et al., 2022) on the Daniel K. Inouye Solar Telescope (DKIST; Rimmele et al., 2020). Our stellar flare phenomenological modeling paradigm (**Section 5.3**) implies that the continuum-subtracted effective widths of the Hγ emission line (Kowalski et al., 2022) from the emergent intensity spectra of the brightest kernels should exhibit much larger effective widths (**Table 1**, rightmost column) than the medium-brightness ribbon component. In solar observations, the pixels with the largest Hγ effective widths should also show the brightest blue-optical continuum intensity. A statistical classification of hydrogen line spectra should reveal distinct components that correlate with timing and position along the solar flare ribbons, similar to the groupings that were reported for a large sample of Mg II flare lines in IRIS spectra (Panos et al., 2018).

On the stellar side, high-cadence spectral observations of low-mass stellar flares at $\lambda = 1800 - 3200$ Å during the impulsive phase would clarify how the NUV continuum flux peaks and turns over into the FUV in events like the Great Flare, which exhibits a small Balmer jump and a highly-impulsive, broadband temporal evolution. The Cosmic Origins Spectrograph on the *Hubble Space Telescope* provides such an opportunity: the G230L grating with a central wavelength at $\lambda =$ 3000 Å gives simultaneous spectral coverage at $\lambda = 1700 - 2100$ Å and $\lambda = 2800 - 3200$ Å, which would provide the necessary observations to test the RHD models. Recently, Kowalski et al. (2019b) reported on flare spectra from the Cosmic Origins Spectrograph (using a different central wavelength) and constrained the peak continuum flux to the *U* band. It was argued that these events are gradual-flare (GF) events with large Balmer jumps and large line-to-continuum ratios, which are in stark contrast to the measured quantities from the Great Flare optical spectra. We briefly comment that our two-component modeling can readily reproduce the properties of these gradual-type flare events as well. For example, a two-component model consisting of the mF13-150-3 and the m5F11-25-4 spectra with $X_{\rm rel} \approx$ 90 results in a Balmer jump ratio of 3.9 and a value of $F'_{\rm H\gamma}$/C4170′ ≈ 150, which are consistent with the quantities from HST-1 in Kowalski et al. (2019b). A parameter study of the detailed hydrogen line broadening and NUV spectra are planned as the subject of Paper II in that series.

6 Summary and conclusion

We have comprehensively modeled the multi-wavelength spectra during the rise and peak phase of the Great Flare of AD Leo (Hawley and Pettersen, 1991). We have shown that fitting two RHD spectral components to the detailed properties of the hydrogen series using an updated treatment of the pressure broadening, combined with a mechanism that heats deep chromospheric heights to $T \gtrsim 10^4$ K, is readily feasible with satisfactory statistical significance. This semi-empirical modeling approach accounts for the evolution of height- and wavelength-dependent emission line and continuum opacities in the flare atmosphere, which is self-consistently calculated in response to high-flux electron beam heating. A simulation (Kowalski et al., 2015, 2016) with a large electron beam flux and the largest low-energy cutoff value range ($\lesssim$ 40 keV) that is inferred from solar flare data (Holman et al., 2003; Ireland et al., 2013) produces a dense chromospheric condensation and hydrogen Balmer wings that are far too broad compared to the observation. Models that exhibit a large ($\gtrsim$ 85 keV), low-energy cutoff and high electron beam flux ($\approx 10^{13}$ erg cm^{-2} s^{-1}) are able to explain the observed continuum distribution and highly broadened Balmer line wings that are within the constraints of the Balmer Hγ–H16 emission line series. Large, low-energy cutoffs are sometimes inferred in the so-called "late impulsive peaks" in solar flares (Holman et al., 2003; Warmuth et al., 2009), and significant progress has been made to improve the hard X-ray modeling

of these events beyond the physics in the standard collisional thick target model (Alaoui and Holman, 2017).

A second, lower electron beam flux model exhibiting more similarities to nonthermal electron parameters that are typically inferred in collisional thick target modeling of hard X-ray data of solar flares (e.g., fluxes of 5×10^{11} erg cm^{-2} s^{-1}, low-energy cutoffs of $E_c \approx 25$ keV) is necessary to fit the narrower hydrogen Balmer emission peak fluxes and account for the bluest Balmer line in the AD Leo Great Flare spectrum. We suggest that this second component represents heterogeneity of nonthermal beam injection and the differences between bright, larger area ribbons and brightest kernel morphologies that are readily seen in the impulsive phase of solar flare imagery. However, further verification is needed from solar observations: specifically, comparisons of hydrogen spectra at different locations in early flare development are critical. The implementation of this two-component, semi-empirical RHD modeling approach to Balmer line profiles of other M dwarf flares with higher resolving-power, echelle observations is underway (Kowalski et al., 2022, ApJ that is currently in the bibliography; Notsu et al., 2022; in preparation) and will further constrain plausible linear combinations of RHD model spectra.

The effects of transient UV radiation during flares is a relatively new topic in the study of exoplanet habitability (e.g., surface dosages) and atmospheric photochemistry (e.g., ozone photodissociation). These studies would benefit from new NUV spectral observations of stellar flares. The semi-empirical combination of RHD model spectra that are fit to the Great Flare observations predict unexpected properties of the NUV continuum spectra of impulsive-type M dwarf flares with small Balmer jumps, highly broadened Balmer lines, and small line-to-continuum ratios. We conclude that small Balmer jumps, which appear as relatively small deviations from a $T = 9000$ K or $T = 10,000$ K blackbody fit to optical data in some flares, actually are consistent with much more energetic sources of ultraviolet radiation than previously thought were possible from solar and stellar chromospheres.

Data availability statement

The data and models supporting the conclusions of this article will be made available by the authors, without undue reservation.

Author contributions

AK contributed by analyzing the AD Leo flare data, running the RHD models, and performing the least squares fitting analysis. AK lead the analysis of the solar flare imaging, and he wrote the manuscript and produced the figures.

Funding

AK acknowledges funding support from, NASA ADAP 80NSSC21K0632, and NASA grant 20-ECIP20_2-0033. AK acknowledges publication cost support from the University of Colorado Library's Open Access Fund established through an institutional membership agreement with Frontiers.

Acknowledgments

We thank two anonymous referees for their detailed comments that helped improve this work. AK thanks Suzanne L. Hawley for many stimulating conversations about flare spectra, flare modeling, and the AD Leo Great Flare data. AK thanks Joel C. Allred and Mats Carlsson for access to and assistance with the RADYN code, and Han Uitenbroek for access to and assistance with the RH code. AK thanks Pier-Emmanuel Tremblay for access to the TB09 + HM88 hydrogen broadening profiles. Many discussions with Rachel A. Osten, Clara Brasseur, Isaiah Tristan, Ward Howard, and John P. Wisniewski about NUV and optical flare continuum radiation were important for the motivation and development of the ideas in this work. AK thanks Eduard Kontar for helpful discussions about the collisional thick target model of solar flare hard X-ray emission. AK thanks Eric Agol for suggesting ten years ago to explore large, low-energy cutoffs in flare heating models. Many discussions about Balmer jump solar flare spectra and instrumentation with Gianna Cauzzi, Hoasheng Lin, and Tetsu Anan led to refining the ideas about the solar-stellar connection presented in this work. IRIS is a NASA small explorer mission developed and operated by LMSAL with mission operations executed at NASA Ames Research Center and major contributions to downlink communications funded by ESA and the Norwegian Space Centre.

Conflict of interest

The author declares that the research was conducted in the absence of any commercial or financial relationships that could be construed as a potential conflict of interest.

Publisher's note

All claims expressed in this article are solely those of the authors and do not necessarily represent those of their affiliated organizations, or those of the publisher,

References

Abrevaya, X. C., Leitzinger, M., Oppezzo, O. J., Odert, P., Patel, M. R., Luna, G. J. M., et al. (2020). The UV surface habitability of Proxima b: First experiments revealing probable life survival to stellar flares. *Mon. Notices R. Astronomical Soc.* 494, L69–L74. doi:10.1093/mnrasl/slaa037

Alaoui, M., and Holman, G. D. (2017). Understanding breaks in flare X-ray spectra: Evaluation of a cospatial collisional return-current model. *Astrophysical J.* 851, 78. doi:10.3847/1538-4357/aa98de

Allred, J. C., Kowalski, A. F., and Carlsson, M. (2015). A unified computational model for solar and stellar flares. *Astrophys. J.* 809, 104. doi:10.1088/0004-637X/809/1/104

Allred, J. C., Alaoui, M., Kowalski, A. F., and Kerr, G. S. (2020). Modeling the transport of nonthermal particles in flares using fokker-planck kinetic theory. *Astrophys. J.* 902, 16. doi:10.3847/1538-4357/abb239

Allred, J. C., Hawley, S. L., Abbett, W. P., and Carlsson, M. (2006). Radiative hydrodynamic models of optical and ultraviolet emission from M dwarf flares. *Astrophys. J.* 644, 484–496. doi:10.1086/503314

Anglada-Escudé, G., Amado, P. J., Barnes, J., Berdiñas, Z. M., Butler, R. P., Coleman, G. A. L., et al. (2016). A terrestrial planet candidate in a temperate orbit around Proxima Centauri. *Nature* 536, 437–440. doi:10.1038/nature19106

Aschwanden, M. J. (2015). Magnetic energy dissipation during the 2014 March 29 solar flare. *Astrophys. J.* 804, L20. doi:10.1088/2041-8205/804/1/L20

Aschwanden, M. J. (2004). Pulsed particle injection in a reconnection-driven dynamic trap model in solar flares. *Astrophys. J.* 608, 554–561. doi:10.1086/392494

Ashfield, I., William, H., Longcope, D. W., Zhu, C., and Qiu, J. (2022). Connecting chromospheric condensation signatures to reconnection-driven heating rates in an observed flare. *Astrophys. J.* 926, 164. doi:10.3847/1538-4357/ac402d

Ayres, T. R. (2015). The flare-ona of EK draconis. *Astron. J.* 150, 7. doi:10.1088/0004-6256/150/1/7

Barstow, J. K., Aigrain, S., Irwin, P. G. J., Kendrew, S., and Fletcher, L. N. (2016). Telling twins apart: exo-Earths and venuses with transit spectroscopy. *Mon. Not. R. Astron. Soc.* 458, 2657–2666. doi:10.1093/mnras/stw489

Barstow, J. K., and Irwin, P. G. J. (2016). Habitable worlds with JWST: Transit spectroscopy of the TRAPPIST-1 system? *Mon. Not. R. Astron. Soc. Lett.* 461, L92–L96. doi:10.1093/mnrasl/slw109

Battaglia, M., Kleint, L., Krucker, S., and Graham, D. (2015). How important are electron beams in driving chromospheric evaporation in the 2014 March 29 flare? *Astrophys. J.* 813, 113. doi:10.1088/0004-637X/813/2/113

Belov, A., Garcia, H., Kurt, V., Mavromichalaki, H., and Gerontidou, M. (2005). Proton enhancements and their relation to the X-ray flares during the three last solar cycles. *Sol. Phys.* 229, 135–159. doi:10.1007/s11207-005-4721-3

Belu, A. R., Selsis, F., Morales, J.-C., Ribas, I., Cossou, C., and Rauer, H. (2011). Primary and secondary eclipse spectroscopy with JWST: Exploring the exoplanet parameter space. *Astron. Astrophys.* 525, A83. doi:10.1051/0004-6361/201014995

Brasseur, C. E., Osten, R. A., and Fleming, S. W. (2022). Short-duration stellar flares in GALEX data. *Astrophys. J.* 883, 88. doi:10.3847/1538-4357/ab3df8

Brown, J. C., Turkmani, R., Kontar, E. P., MacKinnon, A. L., and Vlahos, L. (2009). Local re-acceleration and a modified thick target model of solar flare electrons. *Astron. Astrophys.* 508, 993–1000. doi:10.1051/0004-6361/200913145

Carlsson, M., and Stein, R. F. (1995). Does a nonmagnetic solar chromosphere exist? *Astrophys. J.* 440, L29. doi:10.1086/187753

Carlsson, M., and Stein, R. F. (2002). Dynamic hydrogen ionization. *Astrophys. J.* 572, 626–635. doi:10.1086/340293

Carlsson, M., and Stein, R. F. (1997). Formation of solar calcium H and K bright grains. *Astrophys. J.* 481, 500–514. doi:10.1086/304043

Carlsson, M., and Stein, R. F. (1992). Non-LTE radiating acoustic shocks and CA II K2V bright points. *Astrophys. J.* 397, L59. doi:10.1086/186544

Cram, L. E., and Woods, D. T. (1982). Models for stellar flares. *Astrophys. J.* 257, 269–275. doi:10.1086/159985

Dappen, W., Anderson, L., and Mihalas, D. (1987). Statistical mechanics of partially ionized stellar plasma - the Planck-Larkin partition function, polarization shifts, and simulations of optical spectra. *Astrophys. J.* 319, 195–206. doi:10.1086/165446

De Pontieu, B., Title, A. M., Lemen, J. R., Kushner, G. D., Akin, D. J., Allard, B., et al. (2014). The Interface region imaging Spectrograph (IRIS). *Sol. Phys.* 289, 2733–2779. doi:10.1007/s11207-014-0485-y

de Wijn, A. G., Casini, R., Carlile, A., Lecinski, A. R., Sewell, S., Zmarzly, P., et al. (2022). The visible spectro-polarimeter of the Daniel K. Inouye solar telescope. *Sol. Phys.* 297, 22. doi:10.1007/s11207-022-01954-1

de Wit, J., Wakeford, H. R., Lewis, N. K., Delrez, L., Gillon, M., Selsis, F., et al. (2018). Atmospheric reconnaissance of the habitable-zone Earth-sized planets orbiting TRAPPIST-1. *Nat. Astron.* 2, 214–219. doi:10.1038/s41550-017-0374-z

Dominique, M., Zhukov, A. N., Heinzel, P., Dammasch, I. E., Wauters, L., Dolla, L., et al. (2018). First detection of solar flare emission in mid-ultraviolet balmer continuum. *Astrophys. J.* 867, L24. doi:10.3847/2041-8213/aaeace

Estrela, R., Palit, S., and Valio, A. (2020). Surface and oceanic habitability of trappist-1 planets under the impact of flares. *Astrobiology* 20, 1465–1475. doi:10.1089/ast.2019.2126

Fauchez, T. J., Turbet, M., Villanueva, G. L., Wolf, E. T., Arney, G., Kopparapu, R. K., et al. (2019). Impact of clouds and hazes on the simulated JWST transmission spectra of habitable zone planets in the TRAPPIST-1 system. *Astrophys. J.* 887, 194. doi:10.3847/1538-4357/ab5862

Feinstein, A. D., France, K., Youngblood, A., Duvvuri, G. M., Teal, D. J., Cauley, P. W., et al. (2022). AU microscopii in the far-UV: Observations in quiescence, during flares, and implications for AU mic b and c. *Astron. J.* 164, 110. doi:10.3847/1538-3881/ac8107

Fisher, G. H., Bercik, D. J., Welsch, B. T., and Hudson, H. S. (2012). Global forces in eruptive solar flares: The lorentz force acting on the solar atmosphere and the solar interior. *Sol. Phys.* 277, 59–76. doi:10.1007/s11207-011-9907-2

Fleming, S. W., Million, C., Osten, R. A., Kolotkov, D. Y., and Brasseur, C. E. (2022). New time-resolved, multi-band flares in the GJ 65 system with gPhoton. *Astrophys. J.* 928, 8. doi:10.3847/1538-4357/ac5037

France, K., Duvvuri, G., Egan, H., Koskinen, T., Wilson, D. J., Youngblood, A., et al. (2020). The high-energy radiation environment around a 10 Gyr M dwarf: Habitable at last? *Astron. J.* 160, 237. doi:10.3847/1538-3881/abb465

Froning, C. S., Kowalski, A., France, K., Loyd, R. O. P., Schneider, P. C., Youngblood, A., et al. (2019). A hot ultraviolet flare on the M dwarf star GJ 674. *Astrophys. J.* 871, L26. doi:10.3847/2041-8213/aaffcd

Fuhrmeister, B., Liefke, C., Schmitt, J. H. M. M., and Reiners, A. (2008). Multiwavelength observations of a giant flare on CN Leonis. I. The chromosphere as seen in the optical spectra. *Astron. Astrophys.* 487, 293–306. doi:10.1051/0004-6361:200809379

Graham, D. R., Cauzzi, G., Zangrilli, L., Kowalski, A., Simões, P., and Allred, J. (2020). Spectral signatures of chromospheric condensation in a major solar flare. *Astrophys. J.* 895, 6. doi:10.3847/1538-4357/ab88ad

Günther, M. N., Zhan, Z., Seager, S., Rimmer, P. B., Ranjan, S., Stassun, K. G., et al. (2020). Stellar flares from the first TESS data release: Exploring a new sample of M dwarfs. *Astron. J.* 159, 60. doi:10.3847/1538-3881/ab5d3a

Hannah, I. G., Kontar, E. P., and Reid, H. A. S. (2013). Effect of turbulent density-fluctuations on wave-particle interactions and solar flare X-ray spectra. *Astron. Astrophys.* 550, A51. doi:10.1051/0004-6361/201220462

Hawley, S. L., Allred, J. C., Johns-Krull, C. M., Fisher, G. H., Abbett, W. P., Alekseev, I., et al. (2003). Multiwavelength observations of flares on AD Leonis. *Astrophys. J.* 597, 535–554. doi:10.1086/378351

Hawley, S. L., and Fisher, G. H. (1992). X-ray-heated models of stellar flare atmospheres - theory and comparison with observations. *Astrophys. J. Suppl. Ser.* 78, 565–598. doi:10.1086/191640

Hawley, S. L., and Pettersen, B. R. (1991). The great flare of 1985 April 12 on AD Leonis. *Astrophys. J.* 378, 725–741. doi:10.1086/170474

Hawley, S. L., Walkowicz, L. M., Allred, J. C., and Valenti, J. A. (2007). Near-ultraviolet spectra of flares on YZ CMi. *Publ. Astronomical Soc. Pac.* 119, 67–81. doi:10.1086/510561

Heinzel, P., and Kleint, L. (2014). Hydrogen balmer continuum in solar flares detected by the Interface region imaging Spectrograph (IRIS). *Astrophys. J.* 794, L23. doi:10.1088/2041-8205/794/2/L23

Holman, G. D., Sui, L., Schwartz, R. A., and Emslie, A. G. (2003). Electron bremsstrahlung hard X-ray spectra, electron distributions, and energetics in the 2002 july 23 solar flare. *Astrophys. J.* 595, L97–L101. doi:10.1086/378488

Howard, W. S., Corbett, H., Law, N. M., Ratzloff, J. K., Galliher, N., Glazier, A. L., et al. (2020). EvryFlare. III. Temperature evolution and habitability impacts of dozens of superflares observed simultaneously by evryscope and TESS. *Astrophys. J.* 902, 115. doi:10.3847/1538-4357/abb5b4

Howard, W. S., Corbett, H., Law, N. M., Ratzloff, J. K., Glazier, A., Fors, O., et al. (2019). EvryFlare. I. Long-Term evryscope monitoring of flares from the cool stars across half the southern sky. *Astrophys. J.* 881, 9. doi:10.3847/1538-4357/ab2767

Howard, W. S., Tilley, M. A., Corbett, H., Youngblood, A., Loyd, R. O. P., Ratzloff, J. K., et al. (2018). The first naked-eye superflare detected from Proxima Centauri. *Astrophys. J.* 860, L30. doi:10.3847/2041-8213/aacaf3

Hummer, D. G., and Mihalas, D. (1988). The equation of state for stellar envelopes. I - an occupation probability formalism for the truncation of internal partition functions. *Astrophys. J.* 331, 794–814. doi:10.1086/166600

Ireland, J., Tolbert, A. K., Schwartz, R. A., Holman, G. D., and Dennis, B. R. (2013). Estimating the properties of hard X-ray solar flares by constraining model parameters. *Astrophys. J.* 769, 89. doi:10.1088/0004-637X/769/2/89

Jakosky, B. M., Brain, D., Chaffin, M., Curry, S., Deighan, J., Grebowsky, J., et al. (2018). Loss of the Martian atmosphere to space: Present-day loss rates determined from MAVEN observations and integrated loss through time. *Icarus* 315, 146–157. doi:10.1016/j.icarus.2018.05.030

Karmakar, S., Pandey, J. C., Airapetian, V. S., and Misra, K. (2017). X-ray superflares on CC eri. *Astrophys. J.* 840, 102. doi:10.3847/1538-4357/aa6cb0

Kerr, G. S., Allred, J. C., and Polito, V. (2020). Solar flare arcade modeling: Bridging the gap from 1D to 3D simulations of optically thin radiation. *Astrophys. J.* 900, 18. doi:10.3847/1538-4357/abaa46

Kleint, L., Heinzel, P., Judge, P., and Krucker, S. (2016). Continuum enhancements in the ultraviolet, the visible and the infrared during the X1 flare on 2014 March 29. *Astrophys. J.* 816, 88. doi:10.3847/0004-637X/816/2/88

Kleint, L., Heinzel, P., and Krucker, S. (2017). On the origin of the flare emission in IRIS' SJI 2832 filter:balmer continuum or spectral lines? *Astrophys. J.* 837, 160. doi:10.3847/1538-4357/aa62fe

Kleint, L., Wheatland, M. S., Mastrano, A., and McCauley, P. I. (2018). Nonlinear force-free modeling of flare-related magnetic field changes at the photosphere and chromosphere. *Astrophys. J.* 865, 146. doi:10.3847/1538-4357/aadc5c

Kontar, E. P., Hannah, I. G., and MacKinnon, A. L. (2008). Chromospheric magnetic field and density structure measurements using hard X-rays in a flaring coronal loop. *Astron. Astrophys.* 489, L57–L60. doi:10.1051/0004-6361:200810719

Kontar, E. P., Ratcliffe, H., and Bian, N. H. (2012). Wave-particle interactions in non-uniform plasma and the interpretation of hard X-ray spectra in solar flares. *Astron. Astrophys.* 539, A43. doi:10.1051/0004-6361/201118216

Kowalski, A. F., Wisniewski, J. P., Hawley, S. L., Osten, R. A., Brown, A., Fariña, C., et al. (2019b). The near-ultraviolet continuum radiation in the impulsive phase of HF/GF-type dMe flares. I. Data. *Astrophys. J.* 871, 167. doi:10.3847/1538-4357/aaf058

Kowalski, A. F., Allred, J. C., Carlsson, M., Kerr, G. S., Tremblay, P.-E., Namekata, K., et al. (2022). The atmospheric response to high nonthermal electron-beam fluxes in solar flares. II. Hydrogen-Broadening predictions for solar flare observations with the Daniel K. Inouye solar telescope. *Astrophys. J.* 928, 190. doi:10.3847/1538-4357/ac5174

Kowalski, A. F., Allred, J. C., Daw, A., Cauzzi, G., and Carlsson, M. (2017a). The atmospheric response to high nonthermal electron beam fluxes in solar flares. I. Modeling the brightest NUV footpoints in the X1 solar flare of 2014 March 29. *Astrophys. J.* 836, 12. doi:10.3847/1538-4357/836/1/12

Kowalski, A. F., Allred, J. C., Uitenbroek, H., Tremblay, P.-E., Brown, S., Carlsson, M., et al. (2017b). Hydrogen balmer line broadening in solar and stellar flares. *Astrophys. J.* 837, 125. doi:10.3847/1538-4357/aa603e

Kowalski, A. F., Butler, E., Daw, A. N., Fletcher, L., Allred, J. C., De Pontieu, B., et al. (2019a). Spectral evidence for heating at large column mass in umbral solar flare kernels. I. IRIS near-UV spectra of the X1 solar flare of 2014 october 25. *Astrophys. J.* 878, 135. doi:10.3847/1538-4357/ab1f8b

Kowalski, A. F., Hawley, S. L., Carlsson, M., Allred, J. C., Uitenbroek, H., Osten, R. A., et al. (2015). New insights into white-light flare emission from radiative-hydrodynamic modeling of a chromospheric condensation. *Sol. Phys.* 290, 3487–3523. doi:10.1007/s11207-015-0708-x

Kowalski, A. F., Hawley, S. L., Holtzman, J. A., Wisniewski, J. P., and Hilton, E. J. (2010). A White Light Megaflare on the dM4.5e Star YZ CMi. *Astrophys. J.* 714, L98–L102. doi:10.1088/2041-8205/714/1/L98

Kowalski, A. F., Hawley, S. L., Holtzman, J. A., Wisniewski, J. P., and Hilton, E. J. (2012). The Multiple Continuum Components in the White-Light Flare of 16 January 2009 on the dM4.5e Star YZ CMi. *Sol. Phys.* 277, 21–29. doi:10.1007/s11207-011-9839-x

Kowalski, A. F., Hawley, S. L., Wisniewski, J. P., Osten, R. A., Hilton, E. J., Holtzman, J. A., et al. (2013). Time-resolved properties and global trends in dMe flares from simultaneous photometry and spectra. *Astrophys. J. Suppl. Ser.* 207, 15. doi:10.1088/0067-0049/207/1/15

Kowalski, A. F., Mathioudakis, M., Hawley, S. L., Wisniewski, J. P., Dhillon, V. S., Marsh, T. R., et al. (2016). M dwarf flare continuum variations on one-second timescales: Calibrating and modeling of ULTRACAM flare color indices. *Astrophys. J.* 820, 95. doi:10.3847/0004-637X/820/2/95

Krucker, S., Hudson, H. S., Jeffrey, N. L. S., Battaglia, M., Kontar, E. P., Benz, A. O., et al. (2011). High-resolution imaging of solar flare ribbons and its implication on the thick-target beam model. *Astrophys. J.* 739, 96. doi:10.1088/0004-637X/739/2/96

Law, N. M., Fors, O., Ratzloff, J., Wulfken, P., Kavanaugh, D., Sitar, D. J., et al. (2015). Evryscope science: Exploring the potential of all-sky gigapixel-scale telescopes. *Publ. Astronomical Soc. Pac.* 127, 234. doi:10.1086/680521

Lin, R. P., Dennis, B. R., Hurford, G. J., Smith, D. M., Zehnder, A., Harvey, P. R., et al. (2002). The reuven ramaty high-energy solar spectroscopic imager (RHESSI). *Sol. Phys.* 210, 3–32. doi:10.1023/A:1022428818870

Livshits, M. A., Badalian, O. G., Kosovichev, A. G., and Katsova, M. M. (1981). The optical continuum of solar and stellar flares. *Sol. Phys.* 73, 269–288. doi:10.1007/BF00151682

Loyd, R. O. P., and France, K. (2014). Fluctuations and flares in the ultraviolet line emission of cool stars: Implications for exoplanet transit observations. *Astrophys. J. Suppl. Ser.* 211, 9. doi:10.1088/0067-0049/211/1/9

Loyd, R. O. P., France, K., Youngblood, A., Schneider, C., Brown, A., Hu, R., et al. (2018a). The MUSCLES treasury survey. V. FUV flares on active and inactive M dwarfs. *Astrophys. J.* 867, 71. doi:10.3847/1538-4357/aae2bd

Loyd, R. O. P., Shkolnik, E. L., Schneider, A. C., Barman, T. S., Meadows, V. S., Pagano, I., et al. (2018b). HAZMAT. IV. Flares and superflares on young M stars in the far ultraviolet. *Astrophys. J.* 867, 70. doi:10.3847/1538-4357/aae2ae

MacGregor, A. M., Osten, R. A., and Hughes, A. M. (2020). Properties of M Dwarf flares at millimeter wavelengths. *Astrophys. J.* 891, 80. doi:10.3847/1538-4357/ab711d

MacGregor, M. A., Weinberger, A. J., Loyd, R. O. P., Shkolnik, E., Barclay, T., Howard, W. S., et al. (2021). Discovery of an extremely short duration flare from Proxima Centauri using millimeter through far-ultraviolet observations. *Astrophys. J. Lett.* 911, L25. doi:10.3847/2041-8213/abf14c

MacGregor, M. A., Weinberger, A. J., Wilner, D. J., Kowalski, A. F., and Cranmer, S. R. (2018). Detection of a millimeter flare from Proxima Centauri. *Astrophys. J.* 855, L2. doi:10.3847/2041-8213/aaad6b

Maehara, H., Shibayama, T., Notsu, Y., Notsu, S., Honda, S., Nogami, D., et al. (2015). Statistical properties of superflares on solar-type stars based on 1-min cadence data. *Earth Planets Space* 67, 59. doi:10.1186/s40623-015-0217-z

Mochnacki, S. W., and Zirin, H. (1980). Multichannel spectrophotometry of stellar flares. *Astrophys. J.* 239, L27–L31. doi:10.1086/183285

Namekata, K., Maehara, H., Sasaki, R., Kawai, H., Notsu, Y., Kowalski, A. F., et al. (2020). Optical and X-ray observations of stellar flares on an active M dwarf AD Leonis with the Seimei Telescope, SCAT, NICER, and OISTER. *Publications of the Astronomical Society of Japan* 72, 68. doi:10.1093/pasj/psaa051

Namekata, K., Maehara, H., Honda, S., Notsu, Y., Okamoto, S., Takahashi, J., et al. (2021). Probable detection of an eruptive filament from a superflare on a solar-type star. *Nat. Astron.* 6, 241–248. doi:10.1038/s41550-021-01532-8

Nayfonov, A., Däppen, W., Hummer, D. G., and Mihalas, D. (1999). The MHD equation of state with post-holtsmark microfield distributions. *Astrophys. J.* 526, 451–464. doi:10.1086/307972

Osten, R. A., Drake, S., Tueller, J., Cummings, J., Perri, M., Moretti, A., et al. (2007). Nonthermal hard X-ray emission and iron kα emission from a superflare on II pegasi. *Astrophys. J.* 654, 1052–1067. doi:10.1086/509252

Osten, R. A., Godet, O., Drake, S., Tueller, J., Cummings, J., Krimm, H., et al. (2010). The mouse that roared: A superflare from the dMe flare star ev lac detected by swift and konus-wind. *Astrophys. J.* 721, 785–801. doi:10.1088/0004-637X/721/1/785

Osten, R. A., Kowalski, A., Drake, S. A., Krimm, H., Page, K., Gazeas, K., et al. (2016). A very bright, very hot, and very long flaring event from the M dwarf binary system DG CVn. *Astrophys. J.* 832, 174. doi:10.3847/0004-637X/832/2/174

Panos, B., Kleint, L., Huwyler, C., Krucker, S., Melchior, M., Ullmann, D., et al. (2018). Identifying typical Mg II flare spectra using machine learning. *Astrophys. J.* 861, 62. doi:10.3847/1538-4357/aac779

Polito, V., Galan, G., Reeves, K. K., and Musset, S. (2018). Possible signatures of a termination shock in the 2014 March 29 X-class flare observed by IRIS. *Astrophys. J.* 865, 161. doi:10.3847/1538-4357/aadada

Ranjan, S., Wordsworth, R., and Sasselov, D. D. (2017). The surface UV environment on planets orbiting M dwarfs: Implications for prebiotic chemistry and the need for experimental follow-up. *Astrophys. J.* 843, 110. doi:10.3847/1538-4357/aa773e

Rimmele, T. R., Warner, M., Keil, S. L., Goode, P. R., Knölker, M., Kuhn, J. R., et al. (2020). The Daniel K. Inouye solar telescope - observatory overview. *Sol. Phys.* 295, 172. doi:10.1007/s11207-020-01736-7

Robinson, R. D., Carpenter, K. G., Woodgate, B. E., and Maran, S. P. (1993). A search for proton beams during flares on AU Microscopii. *Astrophys. J.* 414, 872–876. doi:10.1086/173129

Robinson, R. D., Wheatley, J. M., Welsh, B. Y., Forster, K., Morrissey, P., Seibert, M., et al. (2005). GALEX Observations of an Energetic Ultraviolet Flare on the dM4e Star GJ 3685A. *Astrophys. J.* 633, 447–451. doi:10.1086/444608

Rubio da Costa, F., and Kleint, L. (2017). A parameter study for modeling Mg II h and k emission during solar flares. *Astrophys. J.* 842, 82. doi:10.3847/1538-4357/aa6eaf

Rubio da Costa, F., Kleint, L., Petrosian, V., Liu, W., and Allred, J. C. (2016). Data-driven radiative hydrodynamic modeling of the 2014 March 29 X1.0 solar flare. *Astrophys. J.* 827, 38. doi:10.3847/0004-637X/827/1/38

Scalo, J., Kaltenegger, L., Segura, A. G., Fridlund, M., Ribas, I., Kulikov, Y. N., et al. (2007). M stars as targets for terrestrial exoplanet searches and biosignature detection. *Astrobiology* 7, 85–166. doi:10.1089/ast.2006.0125

Segura, A., Walkowicz, L. M., Meadows, V., Kasting, J., and Hawley, S. (2010). The effect of a strong stellar flare on the atmospheric chemistry of an earth-like planet orbiting an M dwarf. *Astrobiology* 10, 751–771. doi:10.1089/ast.2009.0376

Shibayama, T., Maehara, H., Notsu, S., Notsu, Y., Nagao, T., Honda, S., et al. (2013). Superflares on solar-type stars observed with kepler. I. Statistical properties of superflares. *Astrophys. J. Suppl. Ser.* 209, 5. doi:10.1088/0067-0049/209/1/5

Shkolnik, E. L., and Barman, T. S. (2014). HAZMAT. I. The evolution of far-UV and near-UV emission from early M stars. *Astron. J.* 148, 64. doi:10.1088/0004-6256/148/4/64

Smith, D. S., Scalo, J., and Wheeler, J. C. (2004). Transport of ionizing radiation in terrestrial-like exoplanet atmospheres. *Icarus* 171, 229–253. doi:10.1016/j.icarus.2004.04.009

Smith, E. W., Vidal, C. R., and Cooper, J. (1969). Classical path methods in line broadening. I. The classical path approximation. *J. Res. Natl. Bur. Stand A Phys. Chem.* 73A, 389–404. doi:10.6028/jres.073A.030

Testa, P., Drake, J. J., Ercolano, B., Reale, F., Huenemoerder, D. P., Affer, L., et al. (2008). Geometry diagnostics of a stellar flare from fluorescent X-rays. *Astrophys. J.* 675, L97–L100. doi:10.1086/533461

Tilley, M. A., Segura, A., Meadows, V., Hawley, S., and Davenport, J. (2019). Modeling repeated M dwarf flaring at an earth-like planet in the habitable zone: Atmospheric effects for an unmagnetized planet. *Astrobiology* 19, 64–86. doi:10.1089/ast.2017.1794

Tremblay, P.-E., and Bergeron, P. (2009). Spectroscopic analysis of DA white dwarfs: Stark broadening of hydrogen lines including nonideal effects. *Astrophys. J.* 696, 1755–1770. doi:10.1088/0004-637X/696/2/1755

Uitenbroek, H. (2001). Multilevel radiative transfer with partial frequency redistribution. *Astrophys. J.* 557, 389–398. doi:10.1086/321659

Venot, O., Rocchetto, M., Carl, S., Roshni Hashim, A., and Decin, L. (2016). Influence of stellar flares on the chemical composition of exoplanets and spectra. *Astrophys. J.* 830, 77. doi:10.3847/0004-637X/830/2/77

Vidal, C. R., Cooper, J., and Smith, E. W. (1970). Hydrogen Stark broadening calculations with the unified classical path theory. *J. Quantitative Spectrosc. Radiat. Transf.* 10, 1011–1063. doi:10.1016/0022-4073(70)90121-4

Vidal, C. R., Cooper, J., and Smith, E. W. (1973). Hydrogen Stark-broadening tables. *Astrophys. J. Suppl. Ser.* 25, 37. doi:10.1086/190264

Vidal, C. R., Cooper, J., and Smith, E. W. (1971). Unified theory calculations of Stark broadened hydrogen lines including lower state interactions. *J. Quantitative Spectrosc. Radiat. Transf.* 11, 263–281. doi:10.1016/0022-4073(71)90013-6

Wargelin, B. J., Saar, S. H., Pojmański, G., Drake, J. J., and Kashyap, V. L. (2017). Optical, UV, and X-ray evidence for a 7-yr stellar cycle in Proxima Centauri. *Mon. Not. R. Astron. Soc.* 464, 3281–3296. doi:10.1093/mnras/stw2570

Warmuth, A., Holman, G. D., Dennis, B. R., Mann, G., Aurass, H., and Milligan, R. O. (2009). Rapid changes of electron acceleration characteristics at the end of the impulsive phase of an X-class solar flare. *Astrophys. J.* 699, 917–922. doi:10.1088/0004-637X/699/1/917

West, A. A., Hawley, S. L., Bochanski, J. J., Covey, K. R., Reid, I. N., Dhital, S., et al. (2008). Constraining the age-activity relation for cool stars: The sloan digital sky survey data release 5 low-mass star spectroscopic sample. *Astronomical J.* 135, 785–795. doi:10.1088/0004-6256/135/3/785

Wilson, D. J., Froning, C. S., Duvvuri, G. M., France, K., Youngblood, A., Schneider, P. C., et al. (2021). The mega-MUSCLES spectral energy distribution of TRAPPIST-1. *Astrophys. J.* 911, 18. doi:10.3847/1538-4357/abe771

Woods, M. M., Harra, L. K., Matthews, S. A., Mackay, D. H., Dacie, S., and Long, D. M. (2017). Observations and modelling of the pre-flare period of the 29 March 2014 X1 flare. *Sol. Phys.* 292, 38. doi:10.1007/s11207-017-1064-9

Wülser, J. P., Jaeggli, S., De Pontieu, B., Tarbell, T., Boerner, P., Freeland, S., et al. (2018). Instrument calibration of the Interface region imaging Spectrograph (IRIS) mission. *Sol. Phys.* 293, 149. doi:10.1007/s11207-018-1364-8

Yang, H., Liu, J., Gao, Q., Fang, X., Guo, J., Zhang, Y., et al. (2017). The flaring activity of M dwarfs in the kepler field. *Astrophys. J.* 849, 36. doi:10.3847/1538-4357/aa8ea2

Young, P. R., Tian, H., and Jaeggli, S. (2015). The 2014 March 29 X-flare: Subarcsecond resolution observations of Fe XXI λ1354.1. *Astrophys. J.* 799, 218. doi:10.1088/0004-637X/799/2/218

Zhu, Y., Kowalski, A. F., Tian, H., Uitenbroek, H., Carlsson, M., and Allred, J. C. (2019). Modeling Mg II h, k and triplet lines at solar flare ribbons. *Astrophys. J.* 879, 19. doi:10.3847/1538-4357/ab2238

frontiers | Frontiers in Astronomy and Space Sciences

TYPE Mini Review
PUBLISHED 09 December 2022
DOI 10.3389/fspas.2022.1041951

OPEN ACCESS

EDITED BY
Viggo Hansteen,
Bay Area Environmental Research Institute,
United States

REVIEWED BY
Graham S. Kerr,
The Catholic University of America,
United States

*CORRESPONDENCE
Katharine K. Reeves,
kreeves@cfa.harvard.edu

SPECIALTY SECTION
This article was submitted to Stellar and Solar Physics, a section of the journal Frontiers in Astronomy and Space Sciences

RECEIVED 12 September 2022
ACCEPTED 16 November 2022
PUBLISHED 09 December 2022

CITATION
Reeves KK (2022), A window into magnetic reconnection: IRIS observations of the consequences of reconnection during solar flares.
Front. Astron. Space Sci. 9:1041951.
doi: 10.3389/fspas.2022.1041951

A window into magnetic reconnection: IRIS observations of the consequences of reconnection during solar flares

Katharine K. Reeves*

Center for Astrophysics | Harvard & Smithsonian, Cambridge, MA, United States

Magnetic reconnection is a dynamic process that occurs in solar flares in a tenuous and hot environment. High-cadence, high-spatial resolution spectroscopic observations with the Interface Region Imaging Spectrometer (IRIS) have provided a unique window into the reconnection process that occurs during solar flares. IRIS has observed many consequences of the reconnection process, including detailed observations of outflows that are thought to be indicative of reconnection, possible observations of the termination shocks that are predicted by-products of reconnection, and observations of flare ribbons which are imprints of the reconnection process in the chromosphere. This paper will review these observations and put them in the context of flare models that predict reconnection signatures.

KEYWORDS

solar magnetic reconnection, solar activity, solar flares, solar flare spectra, solar ultraviolet emission

1 Introduction

The standard reconnection model of flares predicts that reconnection happens in the current sheet region above an arcade of flare loops. There are many possibly observable consequences of this process. As the magnetic fields reconfigure, outflows form emanating from the reconnection point. These flows impinge on the already reconnected flare loops below, potentially causing termination shocks. The energy released from the reconnection process is deposited in the flare ribbons, which demarcate the boundary between the closed magnetic flux of the flare loops and the open flux above.

Some manifestations of these reconnection signatures have been previously observed. Outflows due to reconnection have been identified in images (e.g., Savage et al., 2010, 2012; Yu et al., 2020) and with spectroscopic observations (e.g., Wang et al., 2007; Hara et al., 2011). Some possible evidence for a termination shock in flares has been found by the Solar Ultraviolet Measurements of Emitted Radiation (SUMER; Wilhelm et al., 1995), which observed a large blue shifted wing in the Fe XXI 1354.08 Å line in the region above the flare loops (Innes et al., 2003). The EUV Imaging Spectrometer (EIS; Culhane et al., 2007) on the Hinode mission observed similar large enhancements in the blue and red wings of the Fe XXIV line (Imada et al., 2013). These

flows were similar in magnitude and were interpreted as flows downstream of the termination shock. Flare ribbons are straightforward to observe, and their motion has frequently been used to estimate the rate of the reconnection happening in the corona (e.g., Qiu et al., 2004, Qiu et al., 2010).

The Interface Region Imaging Spectrograph (IRIS; De Pontieu et al., 2014) has unprecedented spatial resolution and temporal cadence, allowing for a clearer view of reconnection processes. IRIS obtains spectra from the chromosphere, transition region, and corona with 0.33–0.4 arcsec spatial resolution, up to two-second temporal resolution, and 1 km/s velocity resolution over a field-of-view of up to 175 arcsec × 175 arcsec. IRIS is an imaging spectrograph with a scanning slit with three spectral passbands in the ranges 1332–1358 Å, 1389–1407 Å, and 2783–2834 Å. The most useful lines for flares are the Fe XXI 1354 Å line, formed at about 10 MK, which is an ideal temperature for observing flare loops and the reconnection region, and chromospheric (Mg II h 2803 Å and Mg II k 2796 Å) and transition region (Si IV 1393.76/1402.77 Å) lines which are useful for observing flare ribbons. IRIS also has four slit-jaw imagers (SJIs), which observe in four different passbands (C II 1330 Å, Si IV Å 1400, Mg II k 2796 Å, and Mg II wing 2830 Å) with a field of view up to 130 arcsec × 175 arcsec and a spatial resolution of 0.33 arcsec/pixel. The mission's achievements can be found in a recent review paper by De Pontieu et al. (2021).

Many of the spectroscopic observations mentioned above contained blends of Doppler shifted and stationary lines, requiring careful analysis and interpretation. The high spatial resolution of IRIS means that often important features in flares, such as upflows from chromospheric evaporation, are completely separated from any stationary component, making them easier to identify. Similarly, the fast temporal cadence means that evolution of the spectra is captured in fast-moving events such as flares. Below we will review some of the IRIS observations of reconnection outflows, termination shock signatures, and flare ribbons that have increased our understanding of the reconnection process.

2 Reconnection outflows

One of the basic hallmarks of reconnection is bi-directional outflows from the reconnection point. Because of its sensitivity to the Fe XXI line, high time cadence and high spatial resolution, IRIS is capable of detailed observations of such outflows during a flare. For example, Tian et al. (2014) observed a strong redshift in the Fe XXI line during a C1.6 flare that occurred at about 17:19 UT on 2014 April 19 (SOL 2014-04-19T17:19 UT), as shown in **Figure 1**. This observation is unique in that the Fe XXI line is completely red-shifted, with no hint of a stationary component, as indicated by the green lines in **Figures 1B,E**. The location of the redshifted line is near the cusp of a hot flare loop as seen by the 131 Å channel of the Atmospheric Imaging Assembly (AIA; Lemen et al., 2012) on the Solar Dynamics Observatory (SDO), as shown in **Figure 1D**, which is also sensitive to hot plasma from the Fe XXI line. Its location strongly suggests that the redshifted Fe XXI emission is due to reconnection outflows. The initial detection of the outflows in IRIS is weak in intensity, but indicates that the redshifted velocity is as high as 300 km/s. The velocity decreases with each subsequent observation, likely because the reconnection site is moving upwards, away from the location of the slit.

Another example comes from the observation of a small eruption at the limb of the Sun that was observed by IRIS and AIA on 2014 May 1, starting at 1:35 UT (Reeves et al., 2015). As the small filament erupts, it impinges on magnetic field lines above, where coronal rain is visible pre-eruption. The IRIS slit is located such that red shifts of 100–200 km/s are observed in the Si IV 1393.76 Å line due to outflows from the reconnection between the small filament and the overlying fields. Plane-of-sky velocities of ∼300 km/s are observed in the AIA 171 Å channel. The combination of line-of-sight velocities from IRIS and plane-of-sky velocities from AIA gives a complete picture of the speed of the outflow, which works out to be 320–360 km/s. Reconnection outflows are thought to be a significant fraction of the Alfvén speed (e.g., Forbes et al., 2018), which is often taken as about 1000 km/s in the corona. Furthermore, reconnection is verified in this case by heated plasma in the region where the filament contacted the overlying field, as observed by the AIA 131 Å channel and thin-Be images from the X-ray Telescope (XRT; Golub et al., 2007) on Hinode.

A spectacular example of bi-directional outflows observed by IRIS during a reconnection event was reported by Chen et al. (2016) during a filament eruption that commenced at ∼15:35 UT on 2014 August 29. IRIS was scanning across a filament on the limb with an 8-step raster program when brightenings were observed in the 1330 Å slit jaw image during the slow rise phase of a filament eruption. Spectra of the Si IV 1393.76 Å line in raster positions 5–7 clearly show opposing flows in the region where this brightening occurred just prior to the rapid phase of the filament eruption and subsequent C4.3 flare, as shown in **Figure 2**. These outflows were interpreted as evidence of tether-cutting reconnection, where reconnection below a filament causes an instability and eruption (e.g., Moore et al., 2001). In this case, the legs of two filaments reconnected to form one filament, in the process allowing the upwards magnetic pressure to overcome the overlying magnetic tension and causing the eruption.

Even though IRIS has excellent spatial resolution, some reconnection events may create outflows at spatial scales such that IRIS is not able to separate red shifted from blue shifted flows. In this case, broadened spectral lines will be observed with IRIS. Several studies have observed broadened Si IV profiles and attributed them to superimposed bi-directional reconnection

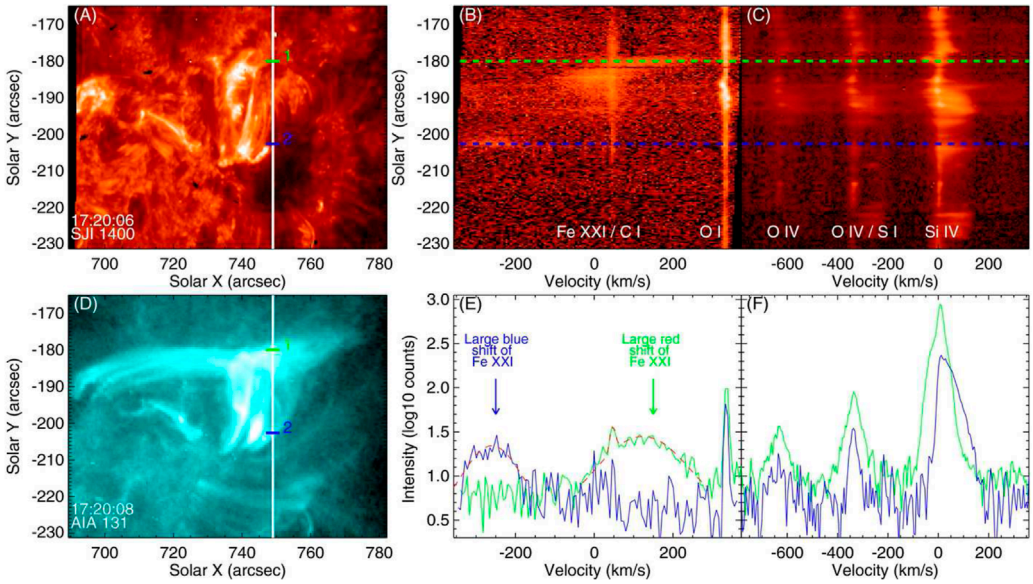

FIGURE 1
Panel **(A)** shows the 2014 April 19 flare in the IRIS 1400 Å slit jaw imager. Panels **(B,C)** show images of the spectra along the slit in various spectral windows. Panel **(D)** shows the location of the slit and points of interest superimposed on an AIA 131 Å image. Panels **(E,F)** show the spectra along the green and blue lines in the spectral windows of Panels **(B,C)**, respectively. From Tian et al. (2014).

outflows in the same pixel. A convincing example of this phenomenon was presented by Li et al. (2017), who observed broadened Si IV 1402.77 Å line profiles outside of the flare ribbons during an unusual X-shaped M2.3 flare that occurred at 15:24 UT on 2014 November 9. The line profiles in this case have relatively symmetric wings that are well fit by Gaussian functions ranging in peak velocities from ±60—± 150 km/s, as shown in **Figure 3**. These profiles are taken from locations that are in regions where separators are expected to form, according to topological modeling. The authors interpret these line profiles as being due to reconnection happening low in the solar atmosphere as the chromospheric ribbons converge on the X-point between the ribbons.

A few other examples of broadened profiles in the Si IV 1402.77 Å line indicative of reconnection have been found. One was presented by Zhang et al. (2021), who studied a jet related to a C3.4 flare that occurred at about 9:00 UT on 2015 October 16. The Si IV broadenings are made up of red and blue shifted components ranging from a few tens of km/s up to 170 km/s, and they are observed at the expected location of the reconnection current sheet that is thought to form underneath the erupting minifilament causing the jet. Another example was found by Xue et al. (2018), who studied a small scale reconnection event in AR 12571 that occurred at 2:38 UT on 2016 August 08. Two cusp-shaped loops formed, with a linear feature in between, which is interpreted as the location of a current sheet. The line profiles of the Si IV 1402.77 Å line are red shifted at the ends of the linear feature, and blue shifted in the middle. The line profiles are to be broadened along the linear feature when compared to other bright regions. This broadening is likely due to superimposed reconnection outflows, given the shape of some of the line profiles. Turbulence in the current sheet region could also contribute to the broadening of the line profiles, as shown by recent modeling (Ruan et al., 2022; Shen et al., 2022; Shibata et al., 2022). For both of the above examples, the line profiles contain clear indications that the profiles are due to multiple separable components, so an increase of spatial and spectral resolution of 2–3 times might be able to completely separate components from opposing flows.

3 Termination shocks

Termination shocks are often predicted as the consequence of reconnection outflows impinging on flare loops below the reconnection site, but clear evidence of these structures is scant. Recent modeling has suggested that IRIS should be able to observe evidence of these termination shocks. Guo et al. (2017) used a MHD model of the reconnection process to simulate IRIS Fe XXI line emission due to a termination shock in a flare located at disk center. They find that when a termination shock is present, there is enhanced emission in the red wing of the Fe XXI line because of the compressed plasma in the region downstream of the shock. The enhancements are on the order of 200–300 km/s, well within the observing capability of IRIS.

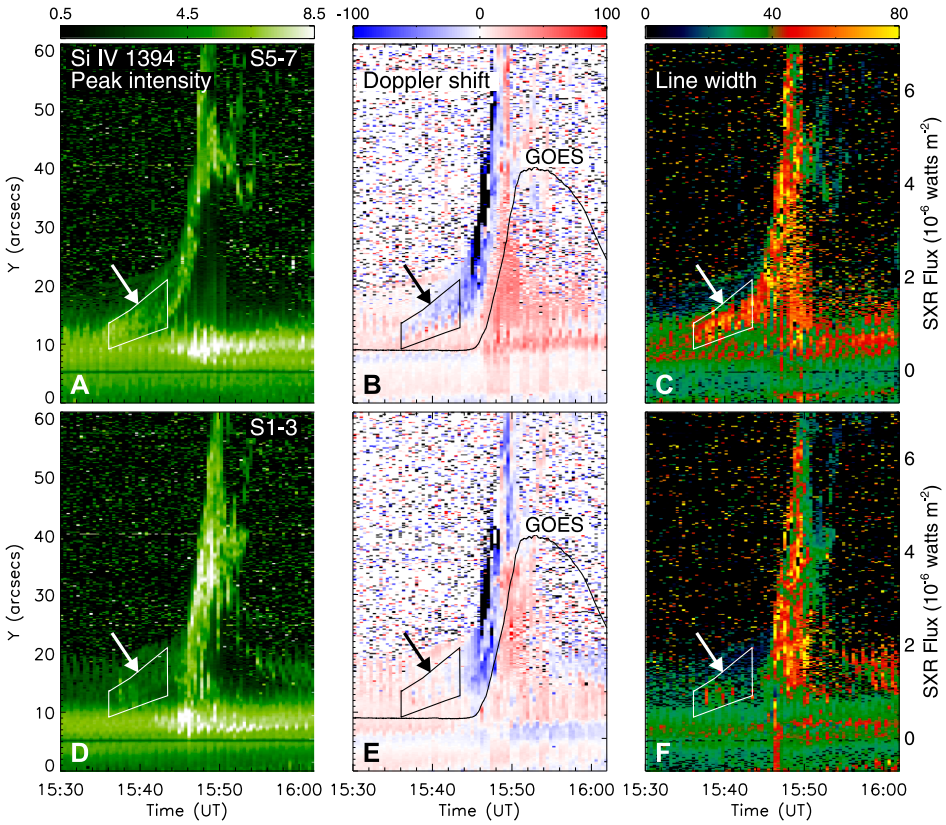

FIGURE 2
Panels **(A–C)** show the intensity, Doppler shift, and line widths, respectively, as a function of time from Gaussian fits to the Si IV 1393.76 Å line in positions 5–7 of the IRIS raster scan during a prominence eruption that occurred on 2014 August 29. Panels **(D–F)** show the same quantities, but in raster positions 1–3 for comparison. The GOES X-ray plot is shown on the panels with the Doppler shift measurements. The boxes and the arrows point to the region of interest where the opposing Doppler shifted flows are seen in raster positions 5–7. Similar signatures are not seen at raster positions 1–3. From Chen et al. (2016).

High resolution observations from IRIS have allowed for the possible detection of these predicted signatures of termination shocks in flares. Polito et al. (2018) examined an X1 flare that occurred at 17:35 UT on 2014 March 29, shown in **Figure 4**. Faint red shifts of the IRIS Fe XXI line of ~250 km/s are observed along with a strong stationary component near the tops of the flare loops, as shown in **Figure 4C**. These velocities are well within the range of those predicted by Guo et al. (2017). Some of these red shifts are accompanied by simultaneous blue shifts of a similar magnitude. Given the orientation of the flare, the authors speculate that these flows are deflection flows that are associated with a termination shock at the loop tops, as indicated in the diagram in **Figure 4**. These Doppler shifts are co-located with 30–70 keV hard X-ray sources observed by the Reuven Ramaty High Energy Solar Spectroscopic Imager (RHESSI; Lin et al., 2002), indicating that particle acceleration may be taking place, further strengthening the assertion that a termination shock is present. Similar Fe XXI line profiles were observed by Tian and Chen (2018) which may also be due to a termination shock, although the authors interpreted the flows as reconnection outflows since that was a common interpretation of red shifted flows observed in the reconnection region at the time (e.g., Wang et al., 2007; Tian et al., 2014).

A pair of studies by Cai et al. (2019) and Cai et al. (2022) examines the supra-arcade fan region in the 2017 September 10 flare, and finds possible evidence for a termination shock. The IRIS 1330 Å slit jaw data show an increase in intensity as a function of height in the supra-arcade region. The ratio of the intensities over the increase is consistent with a shock with a temperature of 7–11 MK and a Mach number of 1–2.5 (Cai et al., 2019). Additionally, a clear discontinuity in the intensity of the Fe XXI line is observed as a function of height, further indicating a compressed interface. Across the discontinuity in intensity, increases in Doppler velocity and Doppler width of the Fe XXI line as a function of height are observed. Spectroscopic data from the Hinode/EIS Fe XXIV

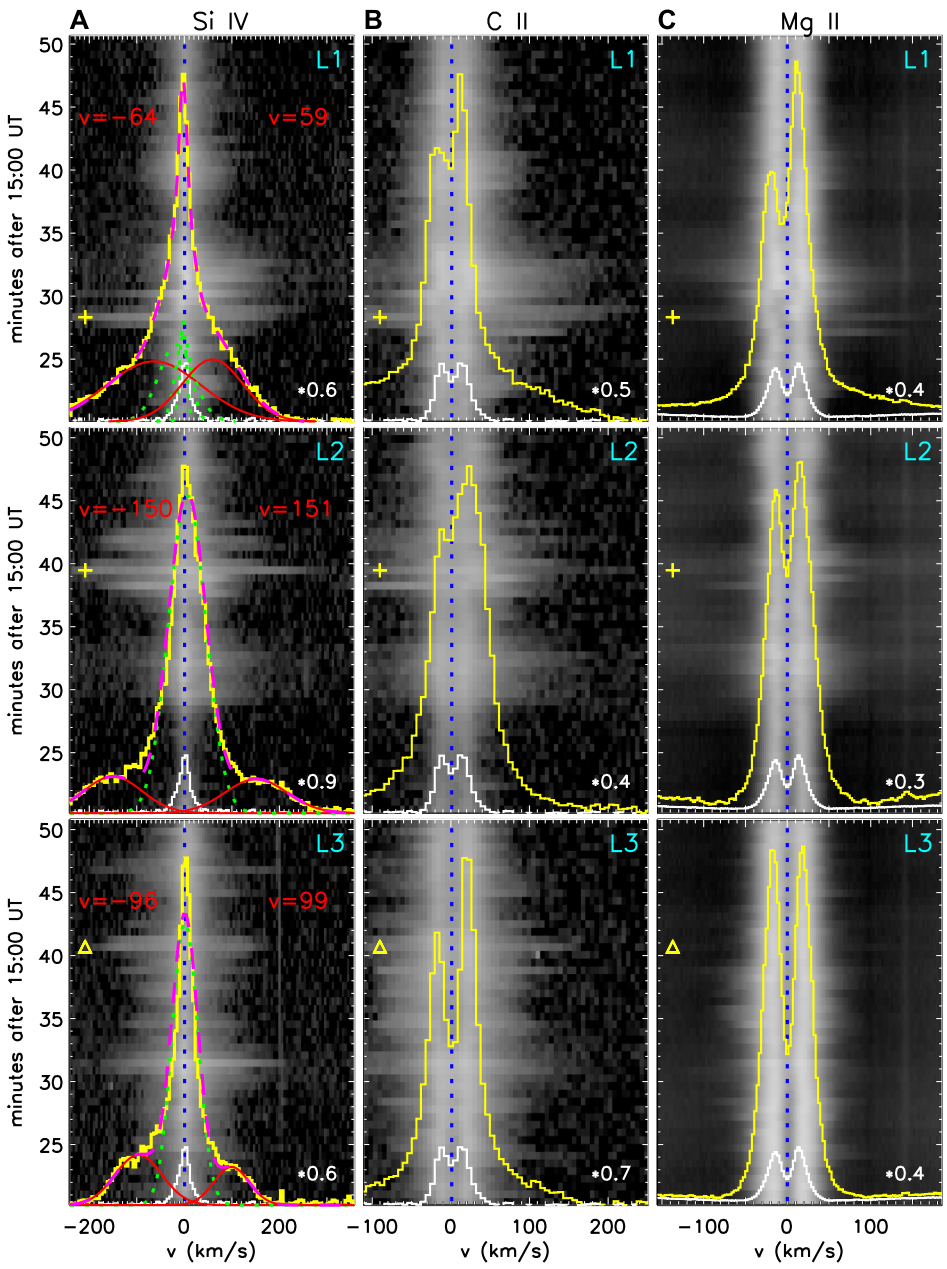

FIGURE 3
Left panels **(A)** show Si IV profiles during the 2014 November 9 flare as a function of time. Middle panels **(B)** show C II and right panels **(C)** show Mg II. Yellow profiles are from the time marked with the symbol (plus sign or triangle). White profiles are from a quiet Sun region. On the Si IV panels, red curves are Doppler shifted components, green dotted lines are stationary components, and dashed magenta lines are the total fit to the spectra. From Li et al. (2017).

255.10 Å and Fe XXIII 263.76 Å lines indicate a temperature and density discontinuity in the same location as the discontinuity seen in the Fe XXI intensity (Cai et al., 2022).

A more detailed analysis of the IRIS Fe XXI spectra in the supra-arcade region of this same event was performed by (Reeves et al., 2020). They find oscillations in the Doppler shift of the Fe XXI line at various locations above the intensity enhancement studied by Cai et al. (2019) with periods of 340–450 s. These periods are not correlated with loop length, ruling out standing slow mode waves (e.g., Wang et al., 2003) as the cause. One possible explanation for the oscillations is that they are due to the oscillating backflow from colliding termination shocks, as modeled in 2D by Takasao and Shibata (2016) and in 3D by Shibata et al. (2022).

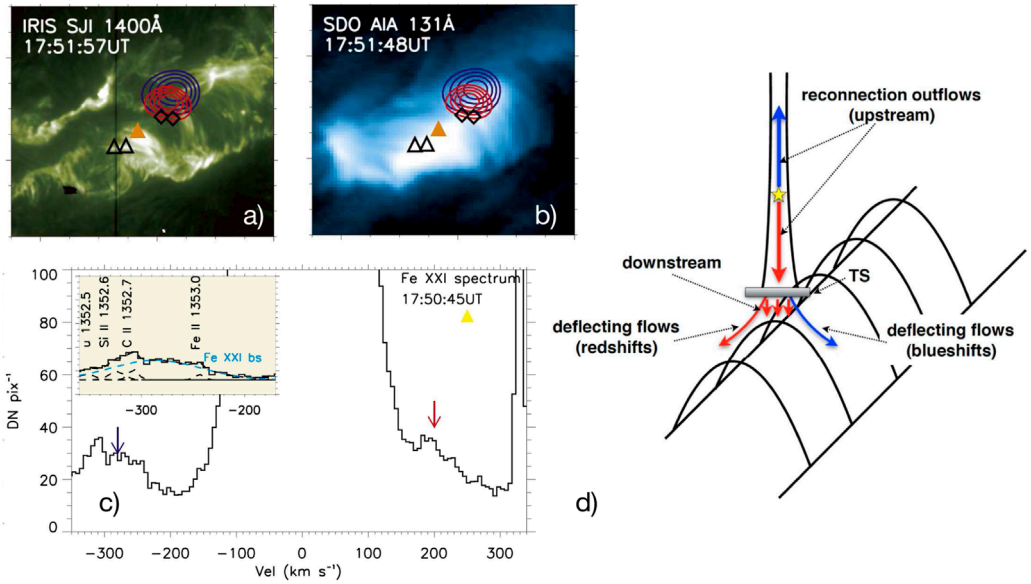

FIGURE 4
Panels **(A,B)** show the IRIS 1400 Å slit jaw image and SDO AIA 131 Å image, respectively, of the 2014 March 29 X flare. Symbols indicate locations where mainly red shifts (diamonds) or both blue and red shifts (triangles) are observed. Red and blue contours are RHESSI images formed in the 6–12 keV and 30–70 keV energy intervals, respectively. Panel **(C)** shows an example spectrum that includes both a red shift and a blue shift, from the location of the orange triangle in panels **(A,B)**. The inset shows a zoom in to the blue side of the spectrum, where line blends are identified. Panel **(D)** shows a diagram of the deflection flows around the termination shock that may be responsible for the observed Doppler shifts. Adapted from Polito et al. (2018).

4 Flare ribbon observations

IRIS is incredibly well-suited to study the ribbons formed at the footpoints of loops during flares. For example, it has been conclusively shown that IRIS can fully resolve blue shifted plasma at the flare ribbons in Fe XXI (e.g., Polito et al., 2015, 2016). Many studies have examined at the details of the energy deposition in the ribbons with IRIS (for a review see De Pontieu et al., 2021), but this section will focus on studies of ribbons that draw a direct connection between the observed emission at the flare ribbons the details of the reconnection process itself.

The high spatial resolution of IRIS means that there are many pixels that show brightenings in ribbons during flares. Thus it is possible to perform statistical studies on the spectral line profiles to obtain a clearer picture of the reconnection process. For example, Graham and Cauzzi (2015) examined the line profiles in 81 pixels encompassing the flare ribbons of an X1.6 class flare that occurred on 2014 September 10 (SOL 2014-09-10T17:45). They found that the Fe XXI line profiles along the flare ribbon show remarkably similar characteristics–completely blue shifted profiles with strong initial upflows of about 300 km/s. Line profiles of Mg II are also very similar, showing red shifts of up to 40 km/s, indicating chromospheric condensation. The brightening ribbons are a manifestation of the energy release process higher in the corona, so the fact that all of the ribbon line profiles are so similar could indicate that the energy release process occurring in the current sheet is remarkably uniform. Another possibility, however, is that the chromospheric evaporation process is somehow decoupled from the initial energy release, and is more dependent on the local conditions in the chromosphere. Recent modeling seems to indicate that the first possibility is more likely–Graham et al. (2020) found that varying the parameters of the input electron beam in simulations of this flare led to differences in the modeled spectral profiles that were not observed.

The detail provided by IRIS observations of flare ribbons allows for some interesting potential interpretations of the flare ribbon emission and its connection to the reconnection process occurring in the corona. For example, Brannon et al. (2015) analyzed the substructure in a flare ribbon observed with IRIS on 2014 April 18 that peaked at 13:03 UT. The observations have a relatively high cadence of about 10 s, and analysis of the Si IV 1403 Å line profiles indicate that there is a sawtooth pattern of alternating red shifts and blue shifts along the ribbon with a period of about 140 s. The intensity oscillates as well, out of phase with the Doppler shifts. This pattern propagates along the slit with a phase velocity of ∼ 15 km/s. Their interpretation of these observations is that instabilities that form in the current sheet region propagate down to the flare ribbons and cause oscillatory motions that appear as alternating Doppler shifts. An alternate view of the same flare was presented by Brosius and Daw (2015), who interpret the IRIS data as being evidence

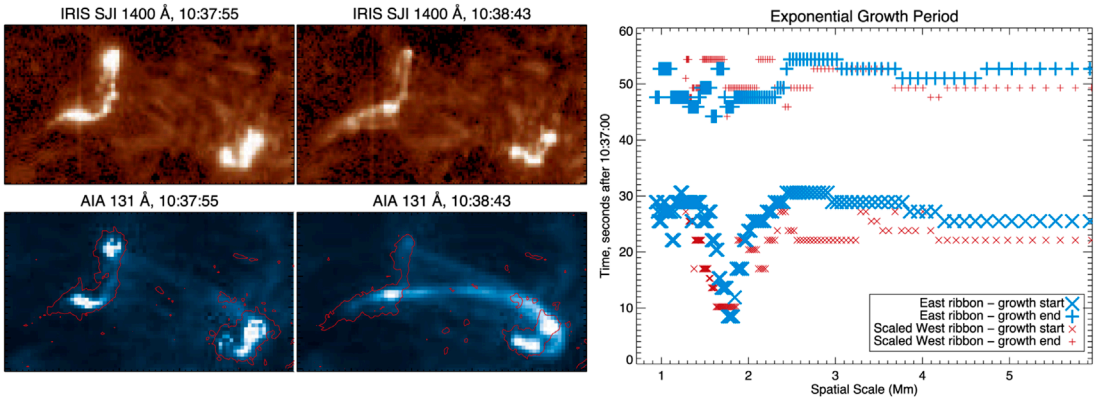

FIGURE 5
Left panels show the IRIS 1400 Å slit jaw images and SDO/AIA 131 Å images at two times during the 2016 December 6 flare. The right panel shows the start and end times of the period of exponential growth in power as a function of spatial scale. Adapted from French et al. (2021).

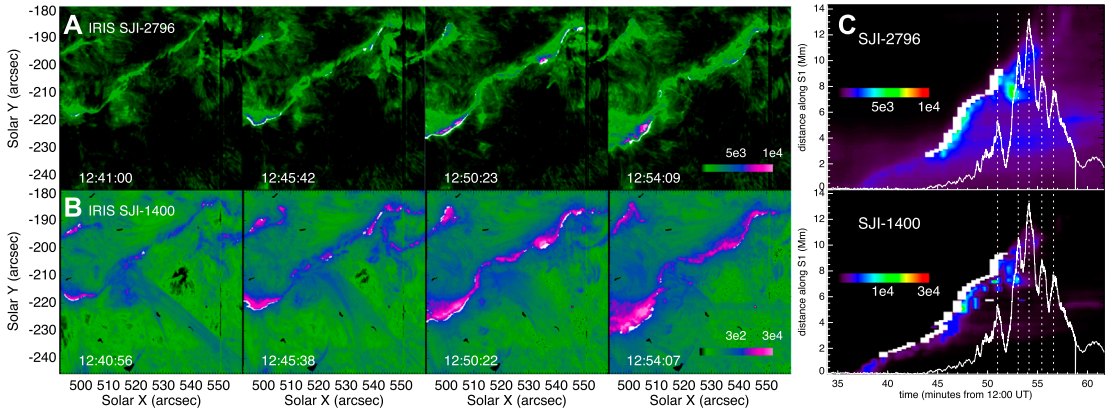

FIGURE 6
Panels **(A,B)** show the IRIS 2796 Å and 1400 Å slit jaw images, respectively, of the 2014 April 18 flare. White symbols indicate the newly brightened ribbon fronts. Panel **(C)** shows time distance diagrams of the ribbon intensity in the 2796 Å and 1400 Å images along a cut perpendicular to the ribbon. The height of the white bars corresponds to the width of the newly brightened part of the ribbon along the cut. The white line is the light curve of the hard X-ray emission in the 24–51 keV range from Fermi/GBM, and vertical dotted lines indicate the times of hard X-ray bursts. Adapted from Naus et al. (2022).

for bursty reconnection followed by subsequent deposition of energetic particles in the chromosphere. This interpretation accounts for the alternating Doppler shifts, but does not account for the phase velocity. Modeling indicates that a tearing mode instability in the current sheet with an asymmetric shear flow can explain both the oscillations and the phase velocity observed by IRIS (Parker and Longcope, 2017).

Another interesting example comes from French et al. (2021), who used high-cadence IRIS slit jaw images to examine the growth of the intensity in flare ribbons at different spatial scales in a B class flare that occurred on 2016 December 6. In this study, the intensity along the ribbon is used to calculate a fast Fourier transform (FFT), resulting in a power spectrum in the spatial domain for each time. As the ribbon intensity brightens to its peak, an exponential rise in power is seen at all spatial scales. The exponential growth starts initially at a spatial scale of 1.75 Mm, and then other shorter and longer spatial scales follow, indicating that both a cascade and an inverse cascade process are occurring. The start and end times of the exponential growth as a function of spatial scale is plotted in **Figure 5**. Models show that the cascade and reverse cascade occurring together can be caused by a tearing mode instability due to the simultaneous coalescence and collapse of plasmoids (Tenerani and Velli, 2020). Thus the flare ribbons may be mirroring the effects of a tearing mode instability in the flare current sheet. Exponential growth at the 1.75 Mm spatial scale begins before non-thermal velocities are detected, suggesting the tearing mode is the driver of plasma turbulence.

Naus et al. (2022) used the high resolution imaging of the IRIS Slit Jaw Imager (SJI) to examine the flare ribbons of the same flare observed by Brannon et al. (2015) and compared the results to hard X-ray footpoint emission observed by RHESSI and the Gamma-ray Burst Monitor (GBM) on Fermi. They find that in the later phase of this event the largest widths of the ribbon fronts and most intense bursts of UV emission are co-temporal and co-spatial with the hard X-ray emission, as shown in **Figure 6**. This observation implies that the hard X-rays are activated when the flare ribbon width is increasing quickly, an indication that the reconnection is bursty. The authors speculate that this burstiness could be caused by the formation of magnetic islands in the current sheet, consistent with the interpretation of Parker and Longcope (2017) that a tearing mode instability is present in this events. A model where particles are accelerated in magnetic islands would naturally lead to the close correlation between the UV brightness and the hard X-ray emission.

In the flare observed by Naus et al. (2022), the ribbon width enhancements precede the peaks in the UV emissions and hard X-rays by 30–120 s, indicating a timescale for the energy release process during reconnection, and that non-thermal electrons might be trapped in the corona before hitting the chromosphere. Several studies have found broadened Mg II profiles consistently appear at the leading edge of flare ribbons (Xu et al., 2016; Panos et al., 2018; Panos and Kleint, 2021). These spectral signatures similarly precede the brightest emission in the UV and X-rays, indicating that they are the near UV signature of the reconnection occurring in the current sheet. Some possible explanations for the broadened profiles are turbulence or to the superposition of unresolved downflows at different heights in the chromosphere. However, more modeling is needed in order to understand exactly what these profiles mean for the energy release in the current sheet.

5 Conclusion

Thanks to its high spatial and temporal resolution, IRIS observations have led to several advances in the study of reconnection. IRIS has conclusively shown that fast outflows of up to ~400 km/s occur during the reconnection process in flares, and the bi-directional outflows that are expected as part of the reconnection have also been clearly observed by IRIS. Some evidence for termination shocks in flares has also been found in IRIS observations, and it has become clear from IRIS observations that there are complicated dynamics occurring in the region above the flare loop tops. Flare ribbons are also proving to be a rich area of study, and IRIS observations of these regions are shedding light on the nature of the reconnection process.

While much progress in understanding the reconnection process has been made thanks to IRIS, there is still work to do. In particular, it is difficult to directly observe the region where reconnection is taking place with a spectroscopic instrument like IRIS simply because it is challenging to place the slit in the proper location at the right time during an eruption. Several serendipitous measurements of this region have occurred (e.g., Tian et al., 2014; Reeves et al., 2020), but much more progress will be made in understanding the reconnection process with the launch of the Multi-slit Solar Explorer (MUSE), which will combine high resolution (0.33 arcsec) context imaging with a 37-slit EUV spectrograph that has a resolution of 0.167 arcsec along the slits, covering the area of an active region with a cadence as fast as 12 s (Cheung et al., 2022). This configuration will guarantee that there will be spectroscopic coverage of areas of interest with both high spatial resolution and a fast cadence during flares, undoubtedly increasing our understanding of the reconnection region. Additionally, the upcoming EUV High-Throughput Spectroscopic Telescope (EUVST) on the Solar-C mission (Shimizu et al., 2020) will provide high spatial and temporal resolution spectroscopy in the EUV with a broad temperature coverage from the chromosphere (20,000 K) to hot plasma observed in flares (20 MK). This capability will provide data to discriminate between different models of energy deposition in flare ribbons and diagnostics of directly heated plasma in the reconnection region. High resolution spectropolarimetery of the photosphere, chromosphere, and low corona from the new Daniel K. Inoue Solar Telescope (Rimmele et al., 2020) will be able to diagnose changes in pre- and post-eruption magnetic fields, identifying flare triggering mechanisms and providing information about magnetic field changes as a function of height in the solar atmosphere (Rast et al., 2021). The future is indeed bright for studying reconnection physics in solar flares.

Author contributions

KR reviewed the papers summarized in this work and wrote the manuscript.

Funding

This work supported by contract 8100002705 from Lockheed-Martin to SAO and NASA grant NNX14AD43G.

Acknowledgments

The author would like to thank Dr. Graham Kerr for insightful comments that improved this paper. IRIS is a NASA small explorer mission developed and operated by LMSAL with mission operations executed at NASA Ames Research center and major contributions to downlink communications funded

by the Norwegian Space Center (NSC, Norway) through an ESA PRODEX contract.

Conflict of interest

The author declares that the research was conducted in the absence of any commercial or financial relationships that could be construed as a potential conflict of interest.

Publisher's note

References

Brannon, S. R., Longcope, D. W., and Qiu, J. (2015). Spectroscopic observations of an evolving flare ribbon substructure suggesting origin in current sheet waves. *Astrophys. J.* 810, 4. doi:10.1088/0004-637X/810/1/4

Brosius, J. W., and Daw, A. N. (2015). Quasi-periodic fluctuations and chromospheric evaporation in a solar flare ribbon observed by IRIS. *Astrophys. J.* 810, 45. doi:10.1088/0004-637X/810/1/45

Cai, Q., Shen, C., Raymond, J. C., Mei, Z., Warmuth, A., Roussev, I. I., et al. (2019). Investigations of a supra-arcade fan and termination shock above the top of the flare-loop system of the 2017 September 10 event. *MNRAS* 489, 3183–3199. doi:10.1093/mnras/stz2167

Cai, Q., Ye, J., Feng, H., and Zhao, G. (2022). Variations of the plasma environment revealed by the evolution of the supra-arcade fan in the 2017 september 10 flare. *Astrophys. J.* 929, 99. doi:10.3847/1538-4357/ac5fa4

Chen, H., Zhang, J., Li, L., and Ma, S. (2016). Tether-cutting reconnection between two solar filaments triggering outflows and a coronal mass ejection. *Astrophys. J.* 818, L27. doi:10.3847/2041-8205/818/2/L27

Cheung, M. C. M., Martínez-Sykora, J., Testa, P., De Pontieu, B., Chintzoglou, G., Rempel, M., et al. (2022). Probing the physics of the solar atmosphere with the multi-slit solar explorer (MUSE). II. Flares and eruptions. *Astrophys. J.* 926, 53. doi:10.3847/1538-4357/ac4223

Culhane, J. L., Harra, L. K., James, A. M., Al-Janabi, K., Bradley, L. J., Chaudry, R. A., et al. (2007). The EUV imaging spectrometer for Hinode. *Sol. Phys.* 243, 19–61. doi:10.1007/s01007-007-0293-1

De Pontieu, B., Polito, V., Hansteen, V., Testa, P., Reeves, K. K., Antolin, P., et al. (2021). A new view of the solar Interface region from the Interface region imaging spectrograph (IRIS). *Sol. Phys.* 296, 84. doi:10.1007/s11207-021-01826-0

De Pontieu, B., Title, A. M., Lemen, J. R., Kushner, G. D., Akin, D. J., Allard, B., et al. (2014). The Interface region imaging spectrograph (IRIS). *Sol. Phys.* 289, 2733–2779. doi:10.1007/s11207-014-0485-y

Forbes, T. G., Seaton, D. B., and Reeves, K. K. (2018). Reconnection in the post-impulsive phase of solar flares. *Astrophys. J.* 858, 70. doi:10.3847/1538-4357/aabad4

French, R. J., Matthews, S. A., Jonathan Rae, I., and Smith, A. W. (2021). Probing current sheet instabilities from flare ribbon dynamics. *Astrophys. J.* 922, 117. doi:10.3847/1538-4357/ac256f

Golub, L., Deluca, E., Austin, G., Bookbinder, J., Caldwell, D., Cheimets, P., et al. (2007). The X-ray telescope (XRT) for the Hinode mission. *Sol. Phys.* 243, 63–86. doi:10.1007/s11207-007-0182-1

Graham, D. R., and Cauzzi, G. (2015). Temporal evolution of multiple evaporating ribbon sources in a solar flare. *Astrophys. J.* 807, L22. doi:10.1088/2041-8205/807/2/L22

Graham, D. R., Cauzzi, G., Zangrilli, L., Kowalski, A., Simões, P., and Allred, J. (2020). Spectral signatures of chromospheric condensation in a major solar flare. *Astrophys. J.* 895, 6. doi:10.3847/1538-4357/ab88ad

Guo, L., Li, G., Reeves, K., and Raymond, J. (2017). Solar flare termination shock and synthetic emission line profiles of the Fe xxi 1354.08 Å line. *Astrophys. J.* 846, L12. doi:10.3847/2041-8213/aa866a

Hara, H., Watanabe, T., Harra, L. K., Culhane, J. L., and Young, P. R. (2011). Plasma motions and heating by magnetic reconnection in a 2007 may 19 flare. *Astrophys. J.* 741, 107. doi:10.1088/0004-637X/741/2/107

Imada, S., Aoki, K., Hara, H., Watanabe, T., Harra, L. K., and Shimizu, T. (2013). Evidence for hot fast flow above a solar flare arcade. *Astrophys. J.* 776, L11. doi:10.1088/2041-8205/776/1/L11

Innes, D. E., McKenzie, D. E., and Wang, T. (2003). Observations of 1000 km s^{-1} Doppler shifts in 10^7 K solar flare supra-arcade. *Sol. Phys.* 217, 267–279. doi:10.1023/B:SOLA.0000006874.31799.bc

Lemen, J. R., Title, A. M., Akin, D. J., Boerner, P. F., Chou, C., Drake, J. F., et al. (2012). The atmospheric imaging assembly (AIA) on the solar dynamics observatory (SDO). *Sol. Phys.* 275, 17–40. doi:10.1007/s11207-011-9776-8

Li, Y., Kelly, M., Ding, M. D., Qiu, J., Zhu, X. S., and Gan, W. Q. (2017). Spectroscopic observations of magnetic reconnection and chromospheric evaporation in an X-shaped solar flare. *Astrophys. J.* 848, 118. doi:10.3847/1538-4357/aa89e4

Lin, R. P., Dennis, B. R., Hurford, G. J., Smith, D. M., Zehnder, A., Harvey, P. R., et al. (2002). The reuven ramaty high-energy solar spectroscopic imager (RHESSI). *Sol. Phys.* 210, 3–32. doi:10.1023/A:1022428818870

Moore, R. L., Sterling, A. C., Hudson, H. S., and Lemen, J. R. (2001). Onset of the magnetic explosion in solar flares and coronal mass ejections. *Astrophys. J.* 552, 833–848. doi:10.1086/320559

Naus, S. J., Qiu, J., DeVore, C. R., Antiochos, S. K., Dahlin, J. T., Drake, J. F., et al. (2022). Correlated spatio-temporal evolution of extreme-ultraviolet ribbons and hard X-rays in a solar flare. *Astrophys. J.* 926, 218. doi:10.3847/1538-4357/ac4028

Panos, B., and Kleint, L. (2021). Exploring mutual information between IRIS spectral lines. II. Calculating the most probable response in all spectral windows. *Astrophys. J.* 915, 77. doi:10.3847/1538-4357/ac00c0

Panos, B., Kleint, L., Huwyler, C., Krucker, S., Melchior, M., Ullmann, D., et al. (2018). Identifying typical Mg II flare spectra using machine learning. *Astrophys. J.* 861, 62. doi:10.3847/1538-4357/aac779

Parker, J., and Longcope, D. (2017). Modeling a propagating sawtooth flare ribbon structure as a tearing mode in the presence of velocity shear. *Astrophys. J.* 847, 30. doi:10.3847/1538-4357/aa8908

Polito, V., Galan, G., Reeves, K. K., and Musset, S. (2018). Possible signatures of a termination shock in the 2014 March 29 X-class flare observed by IRIS. *Astrophys. J.* 865, 161. doi:10.3847/1538-4357/aadada

Polito, V., Reep, J. W., Reeves, K. K., Simões, P. J. A., Dudík, J., Del Zanna, G., et al. (2016). Simultaneous IRIS andhinode/eis observations and modeling of the 2014 october 27 X2.0 class flare. *Astrophys. J.* 816, 89. doi:10.3847/0004-637X/816/2/89

Polito, V., Reeves, K. K., Del Zanna, G., Golub, L., and Mason, H. E. (2015). Joint high temperature observation of a small C6.5 solar flare with Iris/Eis/Aia. *Astrophys. J.* 803, 84. doi:10.1088/0004-637X/803/2/84

Qiu, J., Liu, W., Hill, N., and Kazachenko, M. (2010). Reconnection and energetics in two-ribbon flares: A revisit of the bastille-day flare. *Astrophys. J.* 725, 319–330. doi:10.1088/0004-637X/725/1/319

Qiu, J., Wang, H., Cheng, C. Z., and Gary, D. E. (2004). Magnetic reconnection and mass acceleration in flare-coronal mass ejection events. *Astrophys. J.* 604, 900–905. doi:10.1086/382122

Rast, M. P., Bello González, N., Bellot Rubio, L., Cao, W., Cauzzi, G., Deluca, E., et al. (2021). Critical science plan for the Daniel K. Inouye solar telescope (DKIST). *Sol. Phys.* 296, 70. doi:10.1007/s11207-021-01789-2

Reeves, K. K., McCauley, P. I., and Tian, H. (2015). Direct observations of magnetic reconnection outflow and CME triggering in a small erupting solar prominence. *Astrophys. J.* 807, 7. doi:10.1088/0004-637X/807/1/7

Reeves, K. K., Polito, V., Chen, B., Galan, G., Yu, S., Liu, W., et al. (2020). Hot plasma flows and oscillations in the loop-top region during the 2017 september 10 X8.2 solar flare. *Astrophys. J.* 905, 165. doi:10.3847/1538-4357/abc4e0

Rimmele, T. R., Warner, M., Keil, S. L., Goode, P. R., Knölker, M., Kuhn, J. R., et al. (2020). The Daniel K. Inouye solar telescope - observatory overview. *Sol. Phys.* 295, 172. doi:10.1007/s11207-020-01736-7

Ruan, W., Yan, L., and Keppens, R. (2022). *MHD turbulence formation in solar flares: 3D simulation and synthetic observations.*

Savage, S. L., Holman, G., Reeves, K. K., Seaton, D. B., McKenzie, D. E., and Su, Y. (2012). Low-altitude reconnection inflow-outflow observations during a 2010 november 3 solar eruption. *Astrophys. J.* 754, 13. doi:10.1088/0004-637X/754/1/13

Savage, S. L., McKenzie, D. E., Reeves, K. K., Forbes, T. G., and Longcope, D. W. (2010). Reconnection outflows and current sheet observed with Hinode/XRT in the 2008 April 9 "cartwheel CME" flare. *Astrophys. J.* 722, 329–342. doi:10.1088/0004-637X/722/1/329

Shen, C., Polito, V., Reeves, K. K., Chen, B., Yu, S., and Xie, X. (2022). Non-thermal broadening of IRIS Fe XXI lines caused by plasma bulk flows in magnetic reconnection regions during solar eruptions. *Frontiers*.

Shibata, K., Takasao, S., and Reeves, K. K. (2022). Numerical study on excitation of turbulence and oscillation in above-the-loop-top region of a solar flare. *Astrophys. J.*

Shimizu, T., Imada, S., Kawate, T., Suematsu, Y., Hara, H., Tsuzuki, T., et al. (2020). The solar-C_EUVST mission: The latest status. *Soc. Photo-Optical Instrum. Eng. (SPIE) Conf. Ser.* 11444, 114440N. doi:10.1117/12.2560887

Takasao, S., and Shibata, K. (2016). Above-the-loop-top oscillation and quasi-periodic coronal wave generation in solar flares. *Astrophys. J.* 823, 150. doi:10.3847/0004-637X/823/2/150

Tenerani, A., and Velli, M. (2020). Spectral signatures of recursive magnetic field reconnection. *Mon. Not. R. Astron. Soc.* 491, 4267–4276. doi:10.1093/mnras/stz3310

Tian, H., and Chen, N. H. (2018). Multi-episode chromospheric evaporation observed in a solar flare. *Astrophys. J.* 856, 34. doi:10.3847/1538-4357/aab15a

Tian, H., Li, G., Reeves, K. K., Raymond, J. C., Guo, F., Liu, W., et al. (2014). Imaging and spectroscopic observations of magnetic reconnection and chromospheric evaporation in a solar flare. *Astrophys. J.* 797, L14. doi:10.1088/2041-8205/797/2/L14

Wang, T. J., Solanki, S. K., Curdt, W., Innes, D. E., Dammasch, I. E., and Kliem, B. (2003). Hot coronal loop oscillations observed with SUMER: Examples and statistics. *Astron. Astrophys.* 406, 1105–1121. doi:10.1051/0004-6361:20030858

Wang, T., Sui, L., and Qiu, J. (2007). Direct observation of high-speed plasma outflows produced by magnetic reconnection in solar impulsive events. *Astrophys. J.* 661, L207–L210. doi:10.1086/519004

Wilhelm, K., Curdt, W., Marsch, E., Schühle, U., Lemaire, P., Gabriel, A., et al. (1995). Sumer - solar ultraviolet measurements of emitted radiation. *Sol. Phys.* 162, 189–231. doi:10.1007/BF00733430

Xu, Y., Cao, W., Ding, M., Kleint, L., Su, J., Liu, C., et al. (2016). ULTRA-NARROW NEGATIVE FLARE FRONT OBSERVED IN HELIUM-10830 Å USING THE 1.6 m NEW SOLAR TELESCOPE. *Astrophys. J.* 819, 89. doi:10.3847/0004-637X/819/2/89

Xue, Z., Yan, X., Yang, L., Wang, J., Feng, S., Li, Q., et al. (2018). Spectral and imaging observations of a current sheet region in a small-scale magnetic reconnection event. *Astrophys. J.* 858, L4. doi:10.3847/2041-8213/aabe77

Yu, S., Chen, B., Reeves, K. K., Gary, D. E., Musset, S., Fleishman, G. D., et al. (2020). Magnetic reconnection during the post-impulsive phase of a long-duration solar flare: Bidirectional outflows as a cause of microwave and X-ray bursts. *Astrophys. J.* 900, 17. doi:10.3847/1538-4357/aba8a6

Zhang, Q. M., Huang, Z. H., Hou, Y. J., Li, D., Ning, Z. J., and Wu, Z. (2021). Spectroscopic observations of a flare-related coronal jet. *Astron. Astrophys.* 647, A113. doi:10.1051/0004-6361/202038924

frontiers | Frontiers in Astronomy and Space Sciences

TYPE Review
PUBLISHED 21 December 2022
DOI 10.3389/fspas.2022.1060856

OPEN ACCESS

EDITED BY
Scott William McIntosh,
National Center for Atmospheric Research (UCAR), United States

REVIEWED BY
Jeffrey Reep,
United States Naval Research Laboratory, United States
David Kuridze,
Aberystwyth University, United Kingdom

*CORRESPONDENCE
Graham S. Kerr,
kerrg@cua.edu

SPECIALTY SECTION
This article was submitted to Stellar and Solar Physics, a section of the journal Frontiers in Astronomy and Space Sciences

RECEIVED 03 October 2022
ACCEPTED 28 November 2022
PUBLISHED 21 December 2022

CITATION
Kerr GS (2022), Interrogating solar flare loop models with IRIS observations 1: Overview of the models, and mass flows. *Front. Astron. Space Sci.* 9:1060856. doi: 10.3389/fspas.2022.1060856

Interrogating solar flare loop models with IRIS observations 1: Overview of the models, and mass flows

Graham S. Kerr[1,2]*

[1]Department of Physics, The Catholic Univeristy of America, Washington, DC, United States, [2]NASA Goddard Space Flight Center, Heliophysics Sciences Division, Greenbelt, MD, United States

Solar flares are transient yet dramatic events in the atmosphere of the Sun, during which a vast amount of magnetic energy is liberated. This energy is subsequently transported through the solar atmosphere or into the heliosphere, and together with coronal mass ejections flares comprise a fundamental component of space weather. Thus, understanding the physical processes at play in flares is vital. That understanding often requires the use of forward modelling in order to predict the hydrodynamic and radiative response of the solar atmosphere. Those predictions must then be critiqued by observations to show us where our models are missing ingredients. While flares are of course 3D phenomenon, simulating the flaring atmosphere including an accurate chromosphere with the required spatial scales in 3D is largely beyond current computational capabilities, and certainly performing parameter studies of energy transport mechanisms is not yet tractable in 3D. Therefore, field-aligned 1D loop models that can resolve the relevant scales have a crucial role to play in advancing our knowledge of flares. In recent years, driven in part by the spectacular observations from the Interface Region Imaging Spectrograph (IRIS), flare loop models have revealed many interesting features of flares. For this review I highlight some important results that illustrate the utility of attacking the problem of solar flares with a combination of high quality observations, and state-of-the-art flare loop models, demonstrating: 1) how models help to interpret flare observations from IRIS, 2) how those observations show us where we are missing physics from our models, and 3) how the ever increasing quality of solar observations drives model improvements. Here in Paper one of this two part review I provide an overview of modern flare loop models, and of electron-beam driven mass flows during solar flares.

KEYWORDS

solar flares, solar atmosphere, solar chromosphere, UV radiation, sun, numerical modelling, radiation transfer

1 Introduction

Understanding the physical mechanisms responsible for, and at play during, solar flares still remains one of the most important open issues in astrophysics. These energetic events release a tremendous amount of magnetic energy, which can be $>10^{32}$ ergs, resulting in efficient particle acceleration and are often associated with the ejection of coronal material (e.g., Emslie et al., 2012). Flares and coronal mass ejections (CMEs), together solar eruptive events (SEEs), both strongly influence space weather making understanding flare processes a practical necessity as well as an interesting scientific problem. It is generally believed that the stressed magnetic field reconfigures *via* magnetic reconnection, liberating energy (e.g., Priest and Forbes, 2002; Shibata and Magara, 2011; Janvier et al., 2013). The primary energy release site is the solar corona, though it is possible that energy release also takes place elsewhere. Following reconnection, this energy manifests in various physical forms, such as the acceleration of vast numbers of particles (up to 10^{36} electrons per second!), direct heating of the corona, mass flows, coronal mass ejections (CMEs), and possibly magnetohydrodynamic (MHD) waves.

Ultimately, a significant fraction of this energy is transported to the lower solar atmosphere, that is the transition region, chromosphere, and potentially even deeper to the temperature minimum region and photosphere. Intense heating and ionisation occurs, producing the broadband enhancement to the Sun's radiative output that characterises the flare (e.g., Benz, 2008; Fletcher et al., 2011). An expansion of chromospheric layers occurs, driving mass flows both upwards into the corona (chromospheric evaporation) filling it with chromospheric material, and downwards to deeper layers (chromospheric condensation). The mass-loaded and heated coronal loops subsequently emit strongly, forming bright flare loops that often appear as part of a large scale arcade structure due to propagation of magnetic reconnection. The strength of a flare is defined by the flux of soft X-rays (primarily emitted from flare loops), as observed by the 1-min data from the X-ray Sensor B (1-8Å) on board NOAA's Geostationary Operational Environmental Satellite (GOES/XRSB) satellites. On a logarithmic scale flares are classified as [A, B, C, M, X], from weakest to strongest, with sub-divisions of, e.g. M1-10. Sub-A class (Glesener et al., 2017; Cooper et al., 2021) flares have been observed, as have flares > X10 (e.g., Emslie et al., 2012).

In the standard model of solar flares the dominant means by which energy is transported from the coronal release site to the chromosphere and transition region is thought to be by *via* directed beams of non-thermal particles, accelerated out of the thermal background. It is common to mainly consider non-thermal electrons in flare models given the volume of evidence of their presence in the lower atmosphere, but comparable energies (roughly within an order of magnitude) in flare accelerated protons have been observed (Emslie et al., 2012). Due in large part to the lack of physical constraints on the distribution of those protons they are typically omitted in flare models, and we concentrate primarily on electrons, however there is evidence in three flares of energetic protons near flare ribbons (Hurford et al., 2003; Hurford et al., 2006). Once in the denser chromosphere these energetic particles undergo Coulomb collisions, thermalising and heating the plasma, accompanied by the production of hard X-rays *via* bremsstrahlung (e.g., Brown, 1971; Emslie, 1978). A substantial body of evidence supports the important role that non-thermal electrons play in transporting flare energy, with a great many observations of hard X-rays, for example from the Reuven Ramaty High Energy Solar Spectroscopic Imager (RHESSI; Lin et al., 2002), that are co-spatial and co-temporal with other flare radiation (e.g., Fletcher et al., 2011; Krucker et al., 2011). From inversions of the X-ray energy spectrum it is possible to infer the spectral properties of the non-thermal electrons that bombard the chromosphere (see reviews by Holman et al., 2011; Kontar et al., 2011), which can subsequently be used to drive flare models of the type discussed in this review. It should be noted that there are caveats to this process, which can lead to uncertainties in the inferred non-thermal electron spectral properties. Uncertainties can be due to model assumptions (e.g., ignoring warm target or return current effects, Kontar et al., 2015; Jeffrey et al., 2019; Alaoui and Holman, 2017; Allred et al., 2020), or due to the particular difficulty in obtaining reliable estimates of the low-energy cutoff, E_c (where the spectrum transitions from thermal to non-thermal). In most fitting procedures this low-energy cutoff is taken to be the largest value consistent with the data (e.g., $\chi_{red}\sim1$) but, since the thermal emission masks the non-thermal emission at these small energies, E_c could in fact be much smaller, hence the derived estimate of the power carried by non-thermal electrons is essentially a lower-limit [see, for example, discussions in Holman et al. (2011), Kontar et al. (2011), Emslie et al. (2012), Kontar et al. (2015), Warmuth and Mann (2016), Warmuth and Mann (2020), Alaoui et al. (2021)]. The energy spectrum has an assumed power-law form, the parameters of which are generally the spectral index δ describing the slope of the power-law, and the total energy flux F, above some low-energy cutoff E_c and below some break energy. See the following reviews for in-depth discussions of the so-called "electron-beam" model: Holman et al. (2011), Kontar et al. (2011), Zharkova et al. (2011). Radio and microwaves can also give powerful diagnostics of non-thermal particles, for example recent studies using the Expanded Owens Valley Solar Array (EOVSA; Gary et al., 2018; Fleishman et al., 2020; Fleishman et al., 2022; Chen et al., 2020b; Chen et al., 2020a). Other mechanisms of energy transport in flares include non-thermal protons or heavier ions, thermal conduction following

direct heating of the corona, and Alfvénic waves, though it is not yet known under which circumstances each mechanism plays a significant role compared to the typically modelled non-thermal electrons. These are discussed in Paper two of this review (Kerr, submitted).

The flare impulsive phase describes the rapid release and deposition of energy that generally lasts a few minutes up to tens of minutes, and which is usually associated with the detection of hard X-rays. The flare gradual phase is the period during which flare emissions, as the moniker implies, gradually decrease and the flare plasma cools. This takes place over tens of minutes, or even hours in some long duration events. Due to the fact that flare models predict much shorter cooling timescales than are observed, and that there is evidence of late-phase evaporation (see e.g., Czaykowska et al., 1999; Czaykowska et al., 2001), there have been strong suggestions that there is some post-impulsive energy release of unknown form, perhaps even rivalling that of the impulsive phase [see discussions in Qiu and Longcope (2016), Kuhar et al. (2017), Zhu et al. (2018), Emslie and Bian (2018), Allred et al. (2022)]. There is evidence of yet further energy release up to several hours after the traditional gradual phase in some events, known as the "EUV late-phase" owing to their identification in EUV data (Woods et al., 2011; Woods, 2014), though they have since been studied in X-rays also (Kuhar et al., 2017). However, since this review concerns IRIS observations and flare loop models, not the global structure that might be responsible for the EUV late-phase (Woods, 2014), I focus mostly on the impulsive phase footpoints.

Flare emission can appear variously as compact kernels or footpoints (e.g., white light continua enhancements, hard X-rays, microwaves), extended ribbon-like structures (infrared, optical, UV, extreme-UV), or along the legs of coronal loops (EUV, soft X-rays). Looptop sources of hard X-rays, radio and microwaves are also observed, indicating populations of both very hot (up to tens of MK) thermal plasma, and non-thermal particles. The bulk of this review will focus on modelling of flare footpoints and ribbons, and what we can learn from that emission about flare energy transport and deposition mechanisms. I direct readers to the following detailed reviews of flare observations for a more general overview: Benz. (2008); Fletcher et al. (2011); Holman et al. (2011); Milligan. (2015).

The chromosphere and transition region, as well as being the locations where the bulk of flare energy is deposited, are where the bulk of the flare enhanced radiative output originates, and are thus excellent sources of diagnostic potential. However, the chromosphere and transition region are exceptionally complex environments, particularly so during dynamic events like flares. They are regions with strong gradients in temperature, density and velocity, that are partially ionised with a transition to being fully ionised over what can be vanishingly short distances. Further, the radiation field plays a signicant role in plasma heating and cooling, and in spectral line formation, such that non-local thermodynamic (NLTE) effects are present. Observations from the Interface Region Imaging Spectrograph (IRIS; De Pontieu et al., 2014) now provide an unprecedented view of the flaring chromosphere and transition region, yielding crucial new insights.

IRIS is a NASA Small Explorer mission that since its launch in 2013 has observed many hundreds of flares, including dozens of M and X class events, in the far-, and near-UV (FUV and NUV) offering a new window on the solar chromosphere, and transition region as well as hot flaring plasma *via* the Fe XXI 1,354.1 Å line. It is a slit scanning spectrograph, that offers high spatial resolution (0.33–0.4 arcseconds) spectra, at high cadences of a few to tens of seconds, but to down 1 s in some events, from a slit 175 arcseconds in length. IRIS can operate in either a sit-and-stare mode, or can raster over a field of view (FOV), so that the full FOV possible is 130×175 arcseconds. Observations probe many layers of the chromosphere and transition region in three passbands [1,332–1,358] Å [1,389–1,407] Å, and [2,783–2,834] Å, though it is rare to have full readout, with subsets of lines selected instead. The strongest lines are: Mg II h 2,803 Å and k 2,796 Å (chromosphere), C II 1,334 Å and 1,335 Å and Si IV 1,394 Å and 1,403 Å (transition region), and Fe XXI 1,354.1 Å (∼11 MK plasma), with numerous other weaker lines such as O I 1355.6A, lines of O IV, lines of Fe II, as well as lines of singly ionised species and even molecular H2 transitions. These lines are observable with resolutions of ∼53 mÅ in the NUV and ∼26 mÅ in the FUV. Alongside the spectrograph (SG) there is a slit-jaw imager (SJI) with four passbands available up to 175×175 arcseconds FOV at $2,796 \pm 4$ Å (Mg II k), $2,832 \pm 4$ Å (Mg II wing plus quasi-continuum), $1,330 \pm 55$ Å (C II), and $1,400 \pm 55$ Å (Si IV). IRIS has been an extraordinary mission that has brought about a renewed interest in chromospheric studies of both flare and quiescent phenomenon. A recent review provides an overview of the mission's successes: De Pontieu et al. (2021).

Major observational advancements can only be fully exploited if there is a parallel development and improvement of the theoretical models which are used to interpret those observations. This is particularly true when modelling the optically thick emission from the lower atmosphere, requiring advanced radiative transfer calculations, as well as the treatment of non-equilibrium conditions in the tenuous optically thin corona during dynamic events like flares. State-of-the-art modelling of the flare chromosphere and transition region is required to fully appreciate the information that the observations convey. In this review I discuss the interplay between recent chromospheric and transition region observations from IRIS, and flare loop modelling (with some digressions to coronal emission, mostly in the context of chromospheric evaporation). I demonstrate: 1) how modelling has helped interpret the IRIS observations; 2) how IRIS observations have been used

to interrogate and validate model predictions; and 3) how, when models fail to stand up to the stubborn reality of those observations, IRIS has led to model improvements. This review is in two parts. In this Paper 1 I discuss the codes themselves and flare-induced mass flows, and I discuss plasma properties, energy transport mechanisms, and future directions in Paper 2 (Kerr, submitted).

Field-aligned, 1D, (radiation-) hydrodynamic models are now routinely used to study the atmospheric plasma response to the heating in an individual flare loop. The advantage of such models is that they allow us to simulate the plasma dynamics at very small spatial scales. It is often required to resolve down to sub-metre scales due to sharp gradients and shocks that form following the injection of flare energy. It is also very important to adequately resolve the transition region, even in quiescent scenarios [e.g., see discussions in Johnston et al. (2017a), (2017b)], the exceptionally narrow interface between the flaring chromosphere and corona. Achieving the required temporal and spatial resolution for a flare simulation in a 2D or 3D model that includes an accurate NLTE chromosphere with appropriate radiative heating and cooling would be very computationally demanding. The 1D assumption is justified by the fact that in the low plasma β regime of the solar atmosphere, mass and energy transport across the magnetic field is highly inhibited, and it is therefore appropriate to treat each flare strand as an isolated plasma loop. Further, since they are much more computationally tractable, field-aligned models allow us to perform large parameter studies of flares driven by different energy transport mechanisms on reasonable timescales, which include the appropriate physical processes. It is essential that we understand the complex physics involved in a field-aligned model before progressing to 3D. There have now been 3D RMHD codes that have modelled the build up and release of flare energy, and subsequent atmospheric heating (e.g., Cheung et al., 2019). While impressive feats that give invaluable insight to flare energy release, those models do not yet include energetic particles, nor do they model chromospheres in as much as detail as the loop models discussed in this review. Also, large parameter studies of energy transport processes are currently precluded by the computational demands of 3D RMHD simulations.

The models discussed in detail in this review are all modern numerical codes that are now well-established but which have a rich heritage built upon efforts dating from the 1980s. I do not intend to provide an exhaustive list of historical field-aligned models, but direct the reader to consult the following literature, and references therein: Canfield and Ricchiazzi (1980), Ricchiazzi (1982), Cheng et al. (1983), Ricchiazzi and Canfield (1983), McClymont and Canfield (1983), Canfield et al. (1984), Fisher et al. (1985c), Fisher et al. (1985b), Fisher et al. (1985a), Fisher (1989), MacNeice (1986), Kopp (1984).

2 Overview of modern flare loop models

Here I introduce some flare loop models that have been used alongside IRIS data, namely: RADYN, HYDRAD, FLARIX, and PREFT. There are other flare loop models either currently in use, or that laid foundations, but which have not been used in conjunction with IRIS observations so are outwith the scope of this particular review. In particular I would like to draw the reader's attention to HYDRO2GEN, which has been used to study hydrogen line and continua emission in flares [e.g., Druett et al., 2017; Druett and Zharkova, 2018; Druett and Zharkova, 2019]. A natural question at the outset is "how well do these codes compare?" Each code has very different numerical schemes and approaches, but efforts to compare their predictions have shown that the flaring hydrodynamic response between RADYN and FLARIX is strikingly similar (Kašparová et al., 2019)! In that test the codes were stripped down to include as similar physics as possible, so that any major differences present were mostly due to the numerical approach. **Figure 1** shows the hydrodynamic variables at two snapshots from each code, illustrating their similarities, and that differences were relatively minor. Efforts to compare in detail the radiative predictions, and also to compare the predictions from HYDRAD to those from RADYN and FLARIX are actively underway as part of an International Space Science Institute team, with promising results thus far.

2.1 RADYN

RADYN (Carlsson and Stein, 1992; Carlsson and Stein, 1997; Carlsson and Stein, 2002; Abbett and Hawley, 1999; Allred et al., 2005; Allred et al., 2015) is a radiation hydrodynamic (RHD) code (written in Fortran) that solves the coupled non-linear equations of hydrodynamics, charge conservation, time-dependent (non-equilibrium) atomic level populations, and radiation transfer on a 1D field-aligned adaptive grid (Dorfi and Drury, 1987). This adaptive scheme allows RADYN to resolve the strong shocks and gradients that usually form in flare simulations, and typically has 191 or 300 grid points (though this changeable). A semi-circular loop geometry is assumed, with one-half of a symmetric flux tube modelled, and a reflecting boundary condition at the loop apex designed to mimic incoming disturbances from the other half of the loop. This loop spans the sub-photosphere, through the chromosphere, transition region, and corona. Equations are solved in the linearised form using a fully implicit scheme (Abbett, 1998).

Species important for chromospheric energy balance are computed in detail, solving the NLTE radiation transfer and atomic level populations with the methods of Scharmer (1981) and Scharmer and Carlsson (1985). Those species are a

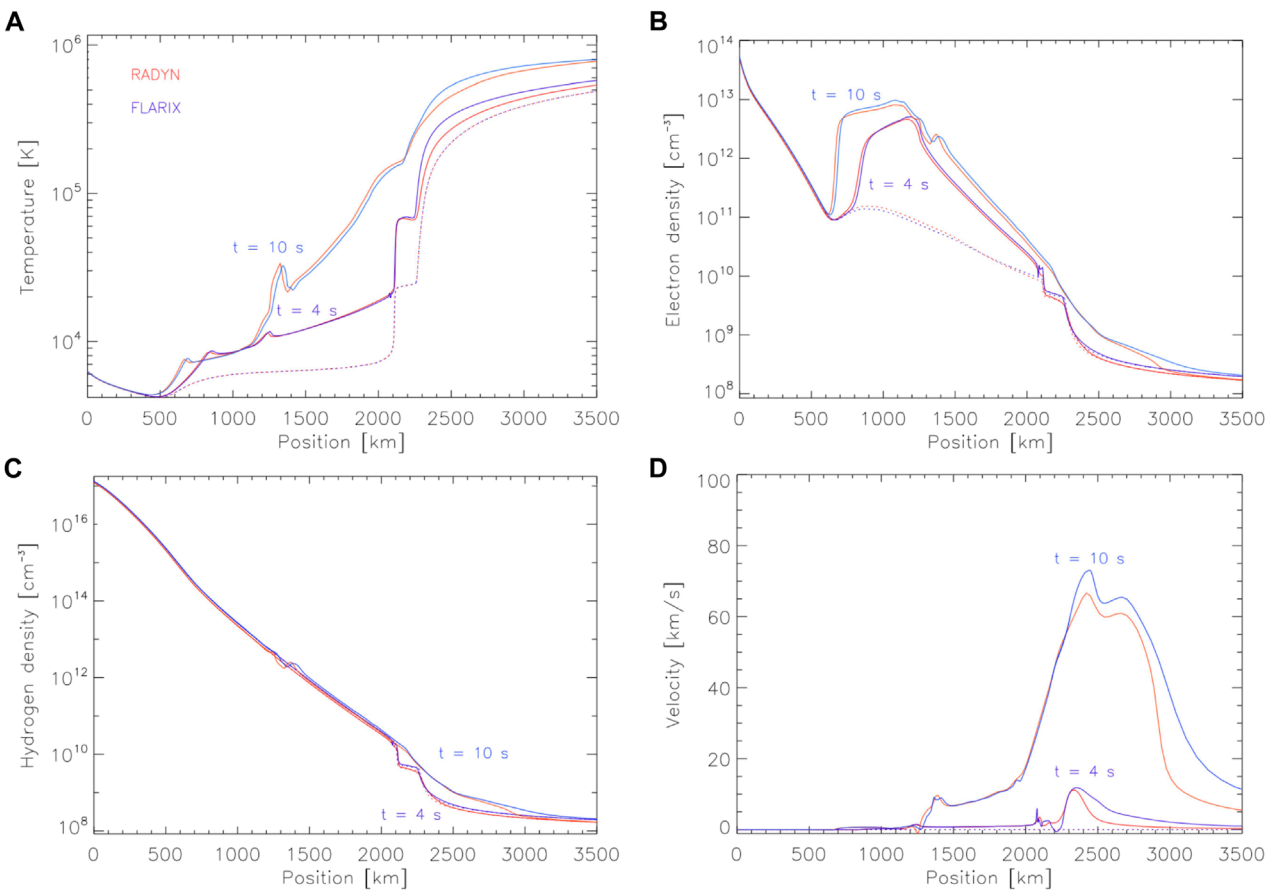

FIGURE 1
A comparison between RADYN and FLARIX, in which each code was purposefully stripped down to include as similar physics as possible. Despite very different numerical schemes, both codes produced strikingly similar results following injection of an electron beam. In each panel red is RADYN, blue is FLARIX, and the dotted lines are $t = 0$ s. Two snapshots during the flare are shown, at $t = 4$ s and $t = 10$ s. Panel **(A)** is temperature **(B)** is electron density **(C)** is hydrogen density, and **(D)** is velocity (upflows are positive). Figure adapted from Kašparová et al. (2019).

six-level-with-continuum H I atom, a six-level-with-continuum Ca II ion, and a nine-level-with-continuum helium atom/ion (with transitions of He I and He II). In some models a Mg II ion is also included. See Allred et al. (2015) for a list of the typical bound-bound and bound-free transitions. Bound-bound transitions are computed assuming complete frequency redistribution (CRD)[1]. To avoid overestimating radiative losses from the line wings, the Lyman lines mimic partial frequency redistribution (PRD) by either truncating at 10 Doppler widths, or modelling the line as a pure Doppler profile, depending on which version of the code is being used. Other species are included as a source of background continuum opacity *via* the Uppsala opacity package (Gustafsson, 1973). Optically thin losses are included by summing transitions from the CHIANTI atomic database (Dere et al., 1997; Del Zanna et al., 2015), excluding those transitions solved in detail. Downward directed incident radiation is included in the solution of the radiation transfer equation, so that photoionisations from X-ray, EUV and UV radiation are considered. This is achieved by calculating the sum of emissivities from transitions in CHIANTI, using the local temperature and density within each grid cell. Thermal conduction is a modified form of Spitzer conductivity, that saturates at the free-streaming limit, though, Allred et al. (2022) added the option to suppress thermal conduction using the method of Emslie and Bian (2018), which accounts for turbulence or non-local effects.

1 In brief, CRD assumes that the wavelength of a scattered/emitted photon is uncorrelated to the wavelength at which it was absorbed, due to collisions (e.g., photons absorbed in the line wings may be redistributed and emitted at a wavelength in the line core). However, in relatively low-density environments such as the chromosphere there may be an insufficient number of elastic collisions such that the scattered photon has a wavelength that is correlated to that of the absorbed photon. Photons absorbed in the line wings are re-emitted in the wings, where it easier to escape. This is the partial frequency redistribution (PRD) scenario. CRD has a frequency independent source function, whereas PRD has a frequency dependent source function and the absorption profile does not equal the emission profile. See discussions in Hubený (1982), and Uitenbroek. (2001); Uitenbroek. (2002).

Flares are typically simulated by injecting a beam of non-thermal electrons at the apex of the loop, which are then thermalised, heating the plasma. Pre-2015 this was achieved using the analytic expressions of Emslie (1978) and Hawley and Fisher (1994), but post (Allred et al., 2015) this is achieved using Fokker-Planck kinetic theory, following McTiernan and Petrosian (1990), that better captures scattering terms, and which is applicable no-matter the target temperature (that is, there is no need to make a cold or warm target assumption, both are modelled using the actual target temperature). More recently still, Allred et al. (2020) developed the standalone open-source FP[2] code to more accurately solve the non-thermal particle transport and energy dissipation, including the ability to include beam-neutralising return current effects, and to model the transport of non-thermal protons. FP has now been merged with RADYN. In all cases, non-thermal collisional ionisations and excitations of hydrogen by the particle beams are included, using the (Fang et al., 1993) approach, and post-(Allred et al., 2015), non-thermal ionisation of helium is included *via* data from Arnaud and Rothenflug (1985). Other options allow RADYN to model flare energy transport by mono-chromatic Alfvénic waves (Kerr et al., 2016) or by *ad hoc* time-dependent heating.

RADYN also allows us to calculate *a posteriori* (i.e., with no feedback on the plasma equations of mass, momentum, and energy) the time-dependent (non-equilibrium) populations and radiation transport of a desired ion *via* the minority species version of that code, MS_RADYN (Judge et al., 2003; Kerr et al., 2019b; 2019c). In this manner the hydrodynamic variables at each internal RADYN timestep, written separately from the main output file (that may have too low a cadence), can be used to calculate any additional species including non-equilibrium effects.

2.2 HYDRAD

The HYDrodynamics and RADiation (HYDRAD) code was originally developed to model the field-aligned plasma physics of solar coronal loops subject to impulsive thermal heating (Bradshaw and Mason, 2003a; 2003b). Particularly careful attention is paid to the time-dependent (non-equilibrium) evolution of any desired ion species and their radiative coupling to the plasma, and to dynamically capturing the small spatial scales that arise in the solar transition region.

HYDRAD solves the conservative form (mass, momentum, and energy density) of the hydrodynamic equations for a two-fluid plasma, on a grid that employs adaptive mesh refinement of arbitrary order. The loops can have any geometry, length, inclination, or cross-section, and span footpoint-to-footpoint (for flare runs, to date), or as an open field line configuration (e.g., Scott et al., 2022), with a corona, transition region, and stratified chromosphere. Prior to (Reep et al., 2019) the chromospheric ionisation fraction was calculated with LTE assumptions, but Reep et al. (2019) implemented an approach that aims to capture NTLE hydrogen effects by approximating the radiation field without solving the full radiation transfer problem. Radiative losses in the chromosphere make use of the lookup tables of Carlsson and Leenaarts (2012), which account for losses from hydrogen, calcium and magnesium. Coronal radiative losses are calculated by summing the emissivity of all transitions within the CHIANTI database, as a function of the ion population fraction, where the ionization state can be given in equilibrium or calculated out-of-equilibrium, and the emission measure in each grid cell.

Flares are simulated by injecting a power-law distribution of non-thermal electrons at the loop apex, following the analytic treatment of Emslie (1978) and Hawley and Fisher (1994), with a sharp low-energy cutoff. This was implemented in Reep et al. (2013), and non-thermal collisional ionisation and excitations of hydrogen were added in Reep et al. (2019) using the (Fang et al., 1993) expressions for those rates. Flares driven by mono-chromatic (i.e., a single frequency) Alfvénic waves have also be modelled (Reep and Russell, 2016; Reep et al., 2018b).

Over the years HYDRAD has evolved into a flexible and powerful code capable of modeling a broad variety of phenomena including: multi-species plasma confined to full-length, magnetic flux tubes of arbitrary geometrical and cross-section variation in the field-aligned direction (Bradshaw and Viall, 2016); solar flares driven by non-thermal electrons and mono-chromatic Alfvénic waves, and the non-equilibrium response of the chromosphere; coronal rain formed by condensations in thermal non-equilibrium where the adaptive grid is required to fully resolve and track multiple steep transition regions (Johnston et al., 2019); and ultracold, strongly coupled laboratory plasmas, composed of weakly-ionized strontium (McQuillen et al., 2013; 2015).

HYDRAD is written in C++ and is designed to be modular in its structure, such that new capabilities (e.g., physical processes) can be added in a relatively straightforward way and handled robustly by the numerical scheme. It is also intended to be fairly undemanding of computational resources, though its needs do depend strongly on the particular nature of each model run (e.g., physics requirements, spatial resolution). The recently implemented NLTE solver for a 6-level hydrogen atom in the optically-thick chromosphere necessitated parallelization of part of the code (the OpenMP standard is employed) to recover acceptable runtimes. A significant performance gain may also be obtained when solving for the time-dependent ionization state of a large number of elements coupled to the electron energy equation *via* the radiative loss term. Otherwise, if this functionality is not required, then HYDRAD is generally most

2 https://github.com/solarFP/FP.

efficiently executed in single-processor mode with multiple instances running in an "embarrassingly-parallel" exploration of a parameter space, for example.

The code has been extensively deployed, tested, and used for a large number of scientific investigations on Windows PC, Mac, and Linux platforms, and found to be stable and robust. HYDRAD can be freely downloaded from its GitHub repository[3].

2.3 Flarix

FLARIX is a hybrid radiation hydrodynamic code (written in Fortran), comprised of three parts (Heinzel et al., 2016). Each component can be run as standalone codes, but are fully integrated within FLARIX. They are 1) a test-particle code that models the transport and thermalisation of non-thermal particles (Varady et al., 2010; 2014), 2) a 1D field-aligned hydrodynamic code (e.g., Kašparová et al., 2009), and 3) a time-dependent (non-equilibrium) NLTE radiative transfer code (MALI; e.g., Heinzel, 1995; Kašparová et al., 2003). FLARIX solves the hydrodynamics and NLTE radiation transport equations separately, but with feedback between the two codes so that, like RADYN, radiative heating and cooling from chromospheric lines and continua are considered, as is an accurate time-dependent NLTE hydrogen ionisation fraction.

FLARIX solves the single fluid hydrodynamic equations along one leg of a symmetric magnetic loop, that is assumed to be semi-circular. When solving those equations the time-dependent hydrogen ionisation fraction is obtained from the NLTE radiation transport code MALI, with the coronal segment assumed to be fully ionised (the ionisation fraction explicitly set to 1). The conductive heat flux is the Spitzer classical formula, and mechanical heating is applied to assure stability of the pre-flare atmosphere, which is typically a VAL-C (Vernazza et al., 1981) type stratification. This atmosphere spans the sub-photosphere through corona, with a fixed grid of ~2000 cells that is optimised to resolve gradients and shocks in the flare chromosphere and transition region. Radiative losses in the chromosphere are computed at each timestep using MALI with the instantaneous values of temperature, electron density, hydrogen density, and non-thermal electron heating rate (to account for non-thermal collisional rates) from the hydrodynamics piece. The full plane-parallel radiation transfer problem is solved for appropriate bound-bound and bound-free transitions of H I, Ca II, and Mg II (with the addition of helium in progress), assuming CRD (with Lyman lines truncated at 10 Doppler widths), and ensuring charge and particle conservation. In the coronal part of the loop radiative losses are assumed optically thin, employing the loss function of Rosner et al. (1978).

Flares are simulated by injecting a distribution of non-thermal electrons or protons, which are propagated and thermalised by Coulomb collisions (subsequently heating the plasma) using test particle and Monte Carlo methods, following the approach of Bai (1982) and Karlicky and Henoux (1992). This includes the relevant scattering terms, and pitch angle effects, and is equivalent to solving directly the Fokker-Planck equations (MacKinnon and Craig, 1991), but also provides a flexible means to investigate many aspects of non-thermal electron or proton interactions, such as magnetic mirroring and return current effects (e.g., Varady et al., 2014). Alternatively, the analytic expressions of Emslie (1978) and Hawley and Fisher (1994) can also be used. Non-thermal rates follow the (Fang et al., 1993) approach. For full details see: Kašparová et al. (2009), Varady et al. (2010), and Heinzel et al. (2016).

Note that for the code-to-code comparison of Kašparová et al. (2019), shown in **Figure 1**, RADYN and FLARIX were made as similar as possible as concerns the physics included (e.g., the atoms treated in detail, the optically thick loss functions, the form of electron beam heating).

2.4 PREFT

Longcope and collaborators have developed a flare loop model which incorporates reconnection energy release by using thin flux tube (TFT; Spruit, 1981; Linton and Longcope, 2006) MHD equations. The axis of a thin flux tube evolves under a version of the ideal MHD equations expanded in small radius (Guidoni and Longcope, 2010). The tube is assumed to lay entirely within an equilibrium current sheet separating layers of magnetic flux with equal field strength but differing in direction by a shear angle $\Delta\theta$. The magnetic pressure from the external layers maintains the field strength of the tube, but otherwise exerts no force on the tube's axis. The tube evolves without reconnection under its own magnetic tension, and field-aligned pressure and viscosity. Energy transport is assumed to occur through thermal conduction, limited to the level of free-streaming electrons. The tube is initialized at the instant after a localized reconnection process within the current sheet has linked sections of equilibrium tubes from opposite sides of the current sheet. No further reconnection occurs, and any heating from the initializing event is neglected. In its subsequent evolution, the tube retracts under magnetic tension releasing magnetic energy and converting it to bulk kinetic energy in flows which include a component parallel to the tube. The collision between the parallel components generates a pair of propagating slow magnetosonic shocks, which resemble gas dynamic shocks as they must in the parallel limit. Absent thermal conduction, this evolution matches

3 https://github.com/rice-solar-physics/hydrad.

the classic models of Petschek reconnection including a guide field (i.e., component reconnection Longcope et al., 2009; Guidoni and Longcope, 2011; Longcope and Klimchuk, 2015). Solutions of the TFT equations show that thermal conduction carries heat away from the shocks, drastically altering the temperature and density of the post-flare plasma (Longcope and Guidoni, 2011; Longcope and Klimchuk, 2015; Longcope et al., 2016).

Guidoni and Longcope (2010) reported the first numerical implementation of the coronal TFT equations in a code called DEFT (Dynamical Evolution of a Flux Tube). A later implementation, called PREFT (Post-Reconnection Evolution of a Flux Tube; written in IDL), included optically thin radiative losses and a simplified chromosphere at each end of the reconnected flux tube, capable of reproducing chromospheric evaporation (Longcope and Klimchuk, 2015). Both versions have been adapted to include current sheets terminating in Y-points (Guidoni and Longcope, 2011; Unverferth and Longcope, 2020), although simulations are often done with a simpler uniform current sheet. Interactions with the current sheet plasma in the form of an aerodynamic drag force was later added (Unverferth and Longcope, 2021), and recent experiments impeded this drag force to investigate the role of MHD turbulence in prolonging heating into the flare gradual phase (Dr. William Ashfield, *private communication*, 2022). The chromosphere in PREFT is typically set to be isothermal (T∼10 kK) and gravitationally stratified according to some density scale height.

3 Forward modelling IRIS observables

Armed with the flaring atmospheres from the dynamic loop models we must then synthesise the emission that we predict IRIS would observe. This is true even in the case of RADYN and FLARIX where the radiation transfer of certain species is solved alongside the hydrodynamics, since the spectral lines observed by IRIS are not typically included in those solutions. This generally happens in one of two ways: 1) *via* an optically thin "coronal" assumption, using data from an atomic database such as CHIANTI alongside instantaneous properties of the flare atmospheres (e.g., emission measures, temperatures, and velocities); 2) *via* detailed NLTE radiation transfer calculations using snapshots from the dynamic simulations as input to post-processing code. Within the context of IRIS, the former is typically done for the Fe XXI, Si IV, and other optically thin transition region lines, and the latter for Mg II, C II, and other optically thick transitions or lines such as O I 1355.6 Å for which certain processes such as charge exchange require a radiation transport approach. Each approach has drawbacks and advantages.

In the optically thin line synthesis scenario the usual approach is to generate the contribution functions $G(n_e, T)$ (*via* a resource such as CHIANTI) that encapsulate the atomic physics processes that lead to the population and subsequent de-excitation of the transition in question. Normally this assumes ionisation equilibrium so that they peak at the equilibrium formation temperature of the ion in question. This may or not be a valid assumption in some scenarios. Codes like HYDRAD that track the non-equilibrium ionisation of minority species can instead use more realistic ionisation stratification. From these functions the emissivity in each grid cell can be calculated using the local plasma conditions within that cell:

$$j_{\lambda,z} = A_b G(n_e, T)\, n_e(z)\, n_H(z), \tag{1}$$

where A_b is the abundance of the species, $n_e(z)$ is the electron density at height z, and n_H, is the hydrogen density. The intensity in each grid cell is then $I_{\lambda,z} = j_{\lambda,z}\delta z$, for a grid cell width δz. Once the intensity is known the spectral lines can then broadened by the instrumental profile, by the Gaussian thermal width, and by any assumed non-thermal width (e.g., due to microturbulence). Non-thermal broadening is the catch all term for any width in excess of the quadrature sum of the thermal and instrumental widths, the source of which is an active area of study. This could be due to local turbulence, unresolved flows, or something more exotic. When modelling it is usually not included without some *apriori* information (or guess!) about what it should be. Often some scheme is used to sum the intensity in each cell through height to provide the total emergent intensity. For example, this can be as basic as integrating through the full loop, or we can isolate certain locations such as the footpoints to integrate over. Other techniques attempt to take into account instrument properties, for example we can assume a semi-circular loop at disk center, orientated perpendicular to the Sun's surface, and project each loop position onto an artificial pixel of some size inspired by the instrument we are trying to compare to (e.g., Bradshaw and Klimchuk, 2011, which is the norm for HYDRAD simulations).

When modelling optically thick lines by inputting snapshots from the flare simulations to radiation transport codes then it is usually the case that more advanced physics can be included in the solution that present in the original simulations, but at the expense of the dynamics. That is, non-equilbrium effects are often neglected and the statistical equilibrium population equations are solved instead. This can be mitigated somewhat by using in each atmospheric snapshot the electron density computed from a non-equilibrium solution, and in fact Kerr et al. (2019b) demonstrated using the minority species version of RADYN (MS_RADYN) that non-equilibrium effects can be, mostly, safely neglected when considering Mg II even in flares (as was previously shown to be the case in the quiet Sun Leenaarts et al., 2013). In that instance, the inclusion of more advanced physics afforded by codes such as RH15D (Uitenbroek, 2001; Pereira and Uitenbroek, 2015),

namely partial frequency redistribution (PRD), affected the line synthesis a great deal more than non-equilibrium effects. Post-processing flare snapshots through radiation transport codes typically involves providing the atmospheric stratification (e.g., height/column mass scale, temperature, electron density, velocity, microturbulence, H level populations or mass density) and a series of model atoms to solve (which in some cases form the basis of the non-hydrogen background opacities). The model atoms contain data about the atomic levels, the various transitions (oscillator strengths, damping terms *etc.*), thermal collisional excitation and ionisation rates, charge exchange rates, and the like. Thus, careful construction of the model atom is required to obtain a good result, including using the appropriate number of levels. There are three commonly used radiation transfer codes when processing flare atmospheres: RH, RH15D, and MALI. Of those, RH and RH15D are probably the most commonly used, and are in fact very similar to each other, the latter being a parallelised version of the former, allowing multiple snapshots to solved simultaneously. This greatly speeds up the problem as each 1D snapshot can take up to some tens of minutes or longer to solve if a very large number of transitions are desired, especially if PRD is being used.

Of the optically thick IRIS lines modelled in detail in flares, Mg II is the most common, likely because it offers exceptional (though still largely untapped) diagnostic potential. Kerr et al. (2019a) and Kerr et al. (2019b) explored the impact of various radiation transfer effects when considering Mg II in flares, partly in an attempt to determine if the large densities in flares meant that PRD could be neglected and the more computationally friendly complete frequency redistribution approach employed. Unfortunately it was the case that PRD was indeed required even in flares, but the hybrid angle averaged PRD approach of Leenaarts et al. (2012) was found to adequately approximate the full angle-dependent PRD solution and save an order of magnitude in computational time. Further, Kerr et al. (2019a) demonstrated that using a model atom with too few levels (e.g., 3-level-plus-continuum) produced different results than a larger model atom, in part due to the lack of cascades through upper levels present in larger model atoms (e.g., the 10-level-plus-continuum atom of Leenaarts et al., 2013). Aside from hydrogen, including other species in NLTE was found to not be required. A similar trade study has not yet been performed for other IRIS transitions in flares, though would be a worthwhile exercise.

Note that a new radiation transfer code capable of including time-dependent effects (if sufficiently high-cadence snapshots are available) and processes such as PRD and overlapping transitions has recently been developed: *Lightweaver* (Osborne and Milić, 2021). This exciting new resource has not yet been used to study IRIS observables (to my knowledge!) but should be employed in future efforts.

4 "Electron beam" driven mass flows

A major consequence of solar flare energy deposition is the driving of strong mass flows, which appear in spectral observations as Doppler shifted features either in the line core or as asymmetries in line wings. Both in early observations and modelling of flares (e.g., Fisher et al., 1985c; Fisher et al., 1985b; Fisher et al., 1985a; Fisher, 1989) a distinction was made between chromospheric evaporations that proceeded in a more "gentle" fashion and those that were "explosive". Gentle evaporation is subsonic, whereas explosive evaporation is supersonic, reaching 100s km s^{-1}, and is very impulsive in character, with a rapid rise to peak velocity. The overpressure and momentum balance from the explosive upflow scenario also produces downflows with speeds on the order a few $\times 10$ km s^{-1} (chromospheric condensations) that are denser and propagate deeper into the chromosphere, appearing as redshifts in spectral lines. The Fisher studies determined that the energy flux delivered to the chromosphere and transition region was the deciding factor, with $F = 1 \times 10$ erg s^{-1} cm^{-2} required to drive an explosive response. Those models used a fixed heating duration of $t = 5$ s, and a fixed $E_c = 20$ keV low-energy cutoff for the electron beam, and we know also that the low-energy cutoff can also an important parameter in determining the character of upflows/downflows (e.g., Reep et al., 2015). Note also that electron beams are not the only means to drive explosive chromospheric evaporation, and that they can be driven by a strong heat flux, for example.

As mentioned above, these upflows are produced by pressure gradients following flare heating, with momentum balance driving downflows. It is worth pointing out that the "dividing line" between upflows and downflows has been observationally identified in temperature space using *Hinode*/EIS data (e.g., Milligan and Dennis, 2009). In the footpoint of a C class flare, ions forming $T > \sim 1.5$ MK exhibited large blueshifts whereas $T < \sim 1.5$ MK exhibited redshifts (assuming ionisation equilibrium for their formation temperatures). Studying an X-class flare in which EIS observed several footpoint sources (Sellers et al., 2022) found similar results but with a range of flow reversal temperatures $T_{FR} \sim [1.35–1.82]$ MK. This flow reversal point is located within the flare transition region, and roughly identifies the location of a pressure imbalance, and therefore heating location. It is an important benchmark for models to meet, though only one study to my knowledge has used this to test the physical processes in models. Allred et al. (2022) modelled the flare observed by Milligan and Dennis (2009) using RADYN, where they explored the effects of turbulent and non-local suppression of thermal conduction. Comparing the synthetic EIS profiles they found that suppression factors between 0.3 and 0.5 times that of the Spitzer values were most consistent with the observed flow reversal temperature, the magnitudes of upflows as function of temperature, and the non-thermal widths [studied for the same flare by Milligan (2011)].

In their study Allred et al. (2022) included the turbulent mean free path in the line synthesis, acting as a source of non-thermal broadening. Sellers et al. (2022) performed a very detailed observational study of the flows from many lines as observed by EIS and IRIS, as well as analysing the hard X-ray observations from RHESSI. Modelling those various flare footpoints, driven by non-thermal electron distributions inferred from the RHESSI observations as a function of time [for example using the RADYN_Arcade framework of Kerr et al. (2020), see below] would be a worthwhile endeavour to explore the pattern of upflows *versus* downflows. The upcoming Solar-C/EUV High-Throughput Spectroscopic Telescope [EUVST; Shimizu et al., 2019] will provide capabilities comparable to IRIS but with a significantly broader temperature coverage, which should also be a valuable resource for such studies.

I will not review the wealth of observational evidence and analysis of chromospheric evaporations and condensations here but refer the reader to recent reviews of EUV (Milligan, 2015) and UV flare spectroscopy (De Pontieu et al., 2021), and reference therein. Instead, in this section I highlight a few studies in which loop models of flares driven by typical non-thermal electron distributions were used to interpret signatures of mass motions in IRIS spectra, and in which IRIS spectra challenge the models.

4.1 Long-lived flows

The high spatiotemporal resolution afforded by IRIS has led to a plethora of studies of the chromospheric evaporation and condensation processes in flares. An important spectral line that has been used extensively for studying hot flare plasma is Fe XXI 1,354.1 Å, forming at around T~11 MK (in equilibrium conditions). This line exhibits large Doppler motions both in flare ribbon footpoints, and along the legs of flare loops, in excess of $v_{Dopp} = 100$ km s^{-1} and up to v_{Dopp}~250–300 km s^{-1} (e.g., Tian et al., 2014; Tian et al., 2015; Young et al., 2015; Graham and Cauzzi, 2015; Polito et al., 2015; Sadykov et al., 2015; Polito et al., 2016). At the same time the lines are initially extremely broadened, narrowing as the line returns to rest. Importantly, this line is entirely blueshifted within an IRIS spatial pixel (e.g., Young et al., 2015). That is, it does not just have a blue wing asymmetry alongside a stationary component, as was generally the case with MK lines observed during flares with lower-resolution observatories, the implication being that IRIS is resolving the flare footpoint source (if the filling factor is ~1), or that there was only one source of footpoint emission within that pixel (if the filling factor <1).

To set these data in context I include a brief aside to discuss pre-IRIS observations of spectral lines produced in plasmas with a temperature in excess of several MK, though encourage the reader to see Milligan. (2015) for a fuller discussion. Blueshifts of up to a few hundred km s^{-1} from lines at >~8 MK temperatures in flares were initially observed to possess a dominant stationary component plus a blueshifted component, for example by Antonucci et al. (1982), Antonucci and Dennis. (1983), Mason et al. (1986), and Fludra et al., 1989 using SMM data. Further flare observations from *Yohkoh's* Bragg Crystal Spectrometer (BCS; Culhane et al., 1991) found similarly asymmetric profiles. Such observations were contrary to the expectations of fully blueshifted lines based on numerical models in which the whole flare was a monolithic loop[4] (see discussions in Hori et al., 1998; Doschek and Warren, 2005). These data lacked spatial information, so the total emission was the sum of all sources in the field of view. However, even with instruments that provided spatial information, for example SOHO's Coronal Diagnostic Explorer [CDS, with 4–5″ resolution; Harrison et al., 1995] or *Hinode's* EUV Imaging Spectrograph (EIS, with ~3″ resolution; Culhane et al., 2007), high-temperature lines still exhibited a stationary component alongside a blueshifted component. The dominance of each component varied, so that in some of those observations the blueshifted component was brighter than the stationary. Also, sometimes instead of being stationary, one component was actually just less blueshifted (still suggesting contributions from unresolved features). Some examples of studies that found multicomponent lines include: Teriaca et al. (2006), Milligan et al. (2006), Milligan and Dennis. (2009), Li and Ding (2011), Graham et al. (2011), Watanabe et al. (2010), Young et al. (2013), Doschek et al. (2013). There were, however, some flares in which fully blueshifted high-temperature lines was observed (e.g., del Zanna et al., 2006; Brosius, 2013; Doschek et al., 2015). So, prior to IRIS there was not a consistent picture. Now with the consistent presence of fully blueshifted Fe XXI 1,354.1 Å from IRIS we can more confidently isolate the hot flare footpoint emission to compare against predictions of mass flows in our numerical models.

A superposed epoch analysis of IRIS Fe XXI 1,354.1 Å Doppler motions during an X class flare revealed a remarkably uniform behaviour within each footpoint (Graham and Cauzzi, 2015). Along the flare ribbon each footpoint initially showed Fe XXI v_{Dopp}~250 km s^{-1}, with very little scatter, followed by a smooth decay in time back towards rest. Again with very little scatter, it took around 10 min for each source to return to rest (similar timescales have been seen in other flares). For various reasons (e.g., ribbon propagation timescales, rise times of UV or optical emission, duration of hard X-ray spikes) it is generally assumed that energy injection into each footpoint is more on the order of seconds to tens of seconds.

4 Note that when the codes discussed in detail in this review are used as single loops it is not believed that they represent the entire flare volume, rather that they are some portion of it.

In models that use those timescales the atmospheres undergo rapid global cooling, from flare temperatures towards quiescent temperatures, following cessation of energy injection and flows are quenched due to the collapse in chromospheric/transition region overpressure that drives the upflow of material. What then sustains these long lived upflows?

Similarly, in a number of flares the transition region Si IV resonance lines have been observed to exhibit redshifts lasting many minutes, in contrast to relatively shortlived chromospheric redshifts. Lifetimes of Si IV redshifts range from a few tens of seconds, to minutes, or even tens of minutes, seen in both high and low cadence observations (e.g., Brosius and Daw, 2015; Sadykov et al., 2015; Warren et al., 2016; Zhang et al., 2016; Li et al., 2015; 2017; 2019; Yu et al., 2020; Li et al., 2022; Ashfield et al., 2022). Pervasive net-redshifts, from $\sim 1-15$ km s^{-1}, with spatial fine structure, are not uncommon in the non-flaring mid-lower transition region (e.g., Hansteen, 1993; Brekke, 1993; Chae et al., 1998; Zacharias et al., 2018), and this may muddy the waters of identifying temporal signatures of condensations in transition region lines. For example several authors show observations of Si IV Doppler motions in which there is a consistent $v_{Dopp}\sim$10 km s^{-1} even adjacent to the main flaring region, on top of which briefer (a few seconds to tens of seconds) bursts of redshifts occur co-spatial with flare sources, with magnitudes $v_{Dopp}\sim$10–80 km s^{-1} (Li et al., 2019; Yu et al., 2020; Ashfield et al., 2022). Some do show smoother, less bursty Doppler shift lightcurves (e.g., Warren et al., 2016). Flare induced Doppler motions typically appeared as asymmetries in the red wing, with some instances exhibiting a fully shifted profile or even a transition from fully shifted to asymmetric (see discussions in Li et al., 2019; Yu et al., 2020). Quasi-periodic pulsations (QPPs) have been identified in the Si IV lines, with periods on the order $t\sim$32–42 s (Zhang et al., 2016), an interpretation of which could be so-called bursty reconnection with repeated energy injection (though the origin of QPPs is still a source of healthy debate). Other periodicities have been interpreted as being the result of current sheet dynamics (Brannon et al., 2015). Regarding the chromospheric redshifts, pre-IRIS observations suggested lifetimes of 2–3 min for the decay of H I α redshifts (e.g., the well-known results of Ichimoto and Kurokawa, 1984; Ding et al., 1995), but high spatiotemporal (so that effects of unresolved flows are reduced) observations of the Mg II lines from IRIS have suggested $\sim 30-60$ s decay time (e.g., Graham and Cauzzi, 2015; Kerr et al., 2015). In the IRIS Mg II observations, the redshifts rapidly fall on those short timescales, but there can be a residual low-magnitude redshift for a few minutes. The initial rapid decrease, though, is comparable to the theoretical predictions of Fisher (1989). A conceptual understanding of the briefer bursts of strong transition region redshifts as being due to the classical condensation picture is not difficult, but the cases with more sustained (over many minutes or tens of minutes), elevated, redshifted emission is rather more difficult to explain; especially as the chromospheric counterpart of the condensation does not tend to show such long periods.

In this section I discuss some attempts to address the long duration upflows and downflows identified in IRIS observations with loop modelling, that focussed on the Fe XXI and Si IV lines.

4.1.1 Single loop or arcade modelling

In an effort to facilitate a more realistic model-data comparison of optically thin flare emission, Kerr et al. (2020) produced a synthetic flare arcade model that used an observed active region magnetic skeleton and RADYN field-aligned models. This model takes into account the superposition of loops and geometric effects (e.g., loop inclination, viewing angles) so that line-of-sight effects in the synthetic optically thin images and spectra are accounted for. A RADYN model was grafted onto magnetic loops extrapolated from a non-flaring active region (Allred et al., 2018), and were set off in sequence to mimic ribbon propagation (5 loops every 3 s). Within each voxel of the 3D space the differential emission measures (DEM; a measure of how much material is present within a temperature bin) and Fe XXI 1,354.1 Å spectra were synthesised, and, from the former, observables from the Solar Dynamics Observatory's Atmospheric Imaging Assembly (SDO/AIA; Lemen et al., 2012) were synthesised. These were projected onto a 2D observational plane, with multiple voxels projected into a single pixel, so that superposition along the line-of-sight was included. This flare arcade model reproduced many aspects of Fe XXI Doppler shifts such as the magnitude of the blueshifts, the narrowing as they approached rest, and the localisation of the blueshifts to hot footpoints and lower legs of the loops. **Figure 2** shows some synthetic Fe XXI spectra and a map of the arcade in this model. However, this model significantly underpredicted the decay time. Constructing a superposed Doppler flow similar to Graham and Cauzzi. (2015) showed only a $t\sim$50 s decay time of footpoint Doppler shifts, more than an order of magnitude too fast. Each loop in the arcade was from the same RADYN simulation, with $t\sim$25 s injection time, but the projected velocity differed depending on the loop geometry. **Figure 3** illustrates the differences in decay time between the observations of Graham and Cauzzi. (2015) and the flare modelling.

This result was perhaps not unexpected. It is generally the case that flows subside not long after the cessation of energy injection, which alongside rapid global cooling removes the pressure imbalance in the absence of heating, quashing the upflows. Reep et al. (2018a) contains some detailed examples of this, where upflows in either a single model with bursty injection, or a multi-threaded model with simultaneous individual heating

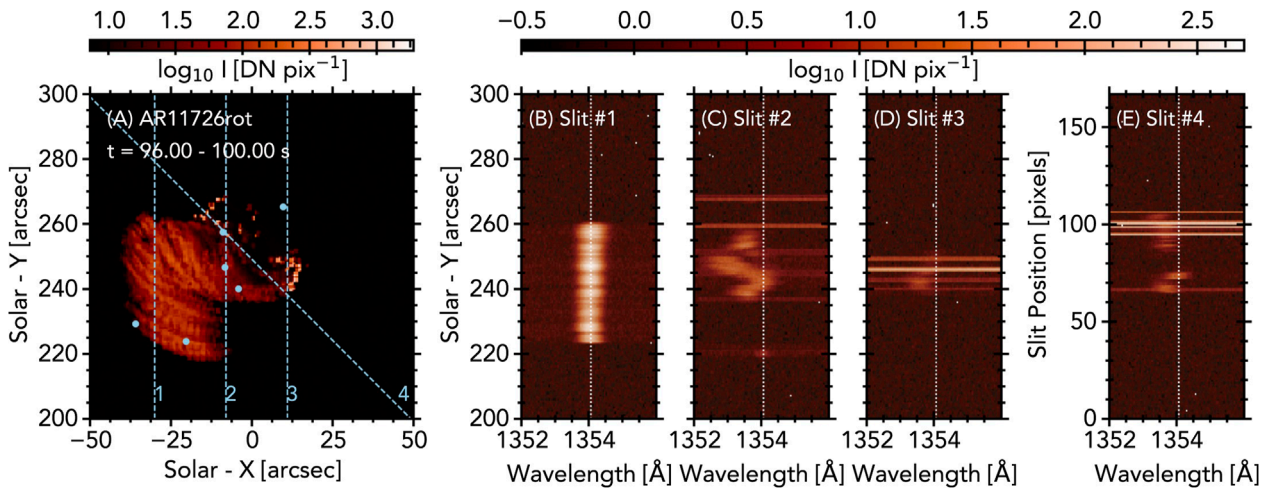

FIGURE 2
An example of RADYN_Arcade modelling of Fe XXI 1,354.1 Å, from Kerr et al. (2020). Panel **(A)** shows a map of the emission integrated over the Fe XXI line, with bright newly activated footpoints, and dense loops. Dashed lines are artificial slits, along which the spectra are shown in panels **(B–E)**, where Doppler shifts and broadening is present. Bright horizontal strips are intense continuum enhancements at loop footpoints. © AAS. Reproduced with permission.

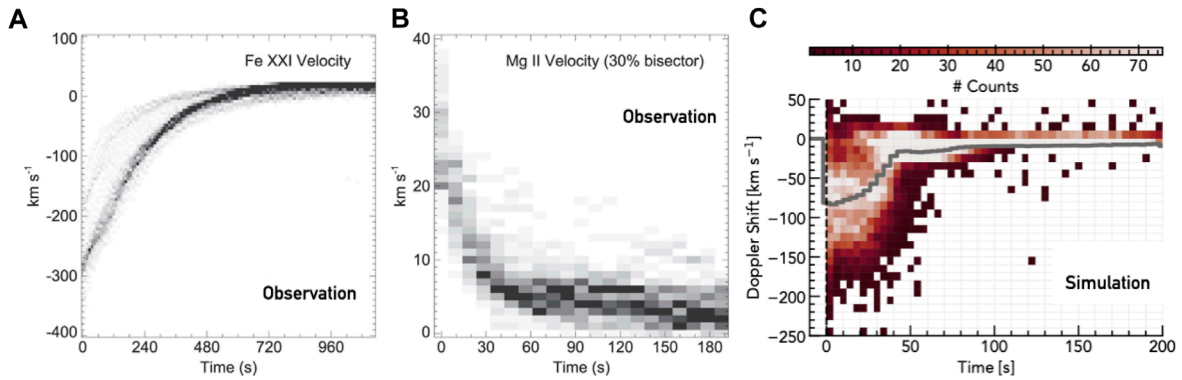

FIGURE 3
Comparing an observed superposed analysis of mass flows to the modelled upflows. Panel **(A)** shows the Fe XXI 1,354.1 Å Doppler shifts obtained from fitting Gaussians to IRIS observations of the 2014-September-10th X-class flare, and panel **(B)** shows the Mg II subordinate line Doppler shifts from that same flare, obtained *via* a bisector analysis (negative velocities are blueshifts, positive are redshifts). Both are adapted from Graham and Cauzzi. (2015). Panel **(C)** shows the synthetic Fe XXI 1,354.1 Å line Doppler shifts from the RADYN_Arcade model of Kerr et al. (2020), where the grey line represents the mean. Clearly the modelled upflows subside an order of magnitude too quickly. © AAS. Reproduced with permission.

events, disappeared shortly after the electron beams were switched off. As well as unexplained lengthy upflows we have a mix of short and long duration condensations as discussed above, which are also frustratingly hard to explain. The Fisher (1989) models of condensations predict that the downflows last t∼30–60 s, almost regardless of particle injection timescales. Once the chromosphere has been shocked out of equilibrium, the condensation propagates deeper, but accrues mass as it does so, and decelerates. Even if energy release is continuous over an extended time it seems hard to drive longer lived downflows as the chromosphere reaches a new equilibrium and is no longer shocked. The chromospheric timescales predicted by models are not as incongruous with observations as the upflows into the corona. Doppler shifts observed in Mg II and other chromsopheric lines have lifetimes not too dissimilar from the modelled 30–60 s (e.g., Graham and Cauzzi, 2015; Graham et al., 2020), shown in the middle panel of **Figure 3**.

One means to obtain long duration upflows of Fe XXI 1,354.1 Å is simply to bombard the atmosphere with an electron beam for an extended period of time. To reproduce the ∼1000 s of upflows observed in the 2014-Oct-27th X class flare, Polito et al. (2015) heated a single monolithic HYDRAD loop for 1000s of seconds. They synthesised Fe XXI, degraded to IRIS resolution, and were able to obtain Doppler shifts with a very similar decay profile (though it was necessary to divide the energy flux inferred from RHESSI observations by a factor of 10 to avoid excessively high temperatures and densities compared to their DEM analysis). Curiously, running with and without non-equilibrium effects turned on seemed to suggest an observed Doppler flow pattern somewhat more consistent with the loop being in equilibrium. This may indicate that the electron density during the actual flare was larger than the HYDRAD model. Polito et al. (2015) also tried asymmetric energy injection, where the electrons were injected somewhere along the loop, rather than the apex. The maximum of temperature and velocity occurred higher in the loop in that scenario, which may explain why the Fe XXI footpoint emission has been observed to appear 1″ from the enhanced FUV continuum, assumed to be the chromospheric footpoint (e.g., Young et al., 2015). So, continuous heating can drive extended durations of Doppler shift. However, it is unlikely that electron beams are injected into one loop for 10 min or more. A number of researchers assume it is actually closer to being on the order of <10 – 30 s into each footpoint. This has been inferred from rapid ribbon propagation, indicating energy injection into a new loop, motion of hard X-ray sources, the duration of individual spikes in hard X-ray lightcurves, and the rise time of UV and optical lightcurves from individual pixels.

4.1.2 Multi-threaded modelling

An alternative means to achieve long duration upflows, and to address similarly long lived transition region downflows is multi-threaded modelling in which each IRIS pixel is assumed to be comprised of many strands embedded within that volume, with one loop model representing just one of these strands. Warren et al. (2016) studied a B2 class flare, noting that whereas Mg II exhibited discrete bursts of intensity enhancements with associated redshifts, the Si IV and C II resonance line redshifts were more systematic, not returning to rest for many minutes. Their lightcurves were also sustained but showed more structure, with a few strong spikes. To explain these transition region observations (Reep et al. 2016) used HYDRAD loop models in a novel way. They ran 37 electron beam driven simulations, with the spectral index and low-energy cutoff inferred from RHESSI observations, and a range of energy fluxes spanning $F = 10^{8-11}$ erg s^{-1} cm^{-2}, applied for $t = 10$ s to each loop. From each loop, the Si IV spectra were synthesised, applying Doppler shifts as appropriate. They then randomly sample emission from N threads, activating randomly with an average rate of one per r unit time, and with a power law in energy flux space guided by the FUV intensity distribution from observations of Warren et al. (2016), dividing the total summed intensity by N. N and r are connected by the requirement that $N \times r > \tau$, for τ some observed duration, for example the duration of redshifts. Within each individual strand, weak energy deposition (<∼10^9 erg s^{-1} cm^{-2}) only produced blueshifts, due to gentle evaporation, consistent with the modelling of Testa et al. (2014). Stronger energy deposition quickly produced redshifts and high intensities.

Through trial and error to ensure smooth and longlived Si IV Doppler shift lightcurves, (Reep et al., 2016) determined that to reproduce the (Warren et al., 2016) observations, $N \geq 60$ threads were need per IRIS pixel, activating with a rate $r \leq 10$ s, and with a minimum flux of $F = 3 \times 10^9$ erg s^{-1} cm^{-2}. Burstier lightcurves resulted from decreasing the activation rate (increasing r), or allowing a smaller minimum energy so that large excursions resulting from the strongest threads were more prominent (recall that some observations of larger flares showed quite bursty Si IV Doppler motions). Comparing the observed and modelled slopes of the emission measure distributions (EMD) can help further constrain N and r. A smaller r forces a higher N, the consequence of which means there are many more cooling loops at any time, boosting the low temperature end, and thus the slope, of the EMD at those temperatures.

Building upon this framework, Reep et al. (2018a) performed similar modelling that could simultaneously address the long lived Fe XXI upflows and Si IV downflows. They again kept $\delta = 5$ and $E_c = 15$ keV of the non-thermal electron distribution fixed, but this time allowed the duration of energy injection onto each thread to vary. A triangular pulse with equal rise and fall times, with total durations ranging $t_{dur} = [1–1,000]$ s, in increments of 0.1 in log space was used, with peak energy fluxes ranging $F_{peak} = [10^8–10^{11}]$ erg s^{-1} cm^{-2} (providing 341 simulations total). Both Si IV and Fe XXI emission was synthesised from each loop model under optically thin conditions. Comparing two of their single loop models, Reep et al. (2018a) first demonstrated that with longer energy deposition timescales, the upflows persist, but that downflows diminish even before the energy deposition ceases, confirming earlier results from Fisher's models. Once the chromosphere has been shocked and produces a condensation, it is difficult to re-shock just with continuous energy deposition. Further, the weaker simulations did not produce sufficiently hot, sufficiently dense loops to emit strongly in Fe XXI (for intermediate energy fluxes non-equilibrium effects could lead to a delay in the formation Fe XXI). Comparisons of the peak densities, temperatures, and mass flows produced by the grid of individual loops demonstrated that in addition to the energy flux, and low-energy cutoff, the duration of energy deposition likely plays

a role in determining if evaporation proceeds explosively or not.

Performing the multi-threaded modelling with various setups (variously fixing or changing values of $N, r, F_{\rm min}, \alpha$, where α describes the slope of the energy flux distribution) using this HYDRAD grid, (Reep et al., 2018a) found the following general conclusions. Longer heating durations produce smoother lightcurves, as loops heated by shorter durations cool too fast. For a mix of heating durations, a median of t_{dur} = [50–100] s does a better job of reproducing the combination of long lived up- and downflows. More sustained past heating $t_{dur} > \sim$100 s results in the initial set of loops dominating the signal, but their downflows still subside after ∼1 min so that a persistent redshift is not seen. Much shorter durations make it difficult to produce detectable Fe XXI emission. Increasing the number of loops produces smoother lightcurves, which for the redshifts is due to the dominance of newly activated loops.

Applying this model to estimate the number of strands per IRIS pixel in an observed flare, the M class event on 2015-March-12, (Reep et al. (2018a)) find they can largely reproduce aspects of the observations with r = [3, 5] s, and heating durations between t_{dur} = [30–300] s. However, they note that the observed Si IV intensities decrease with time, possibly indicating that the maximum energy flux in the distribution of threads decreases over time. This comparison is shown in **Figure 4**, with the observations on the left, and the N = 200, r = 5 s multi-threaded HYDRAD model on the right. Comparing to **Figure 3**, the multi-threaded approach clearly does a better job at reproducing the extended Doppler shifts.

To tackle the chromospheric predictions in their multi-threaded modelling (Reep et al., 2019) synthesised O I 1355.6 Å and Mg II k line spectra *via* RH15D with HYDRAD flare atmospheres as input, after first modifying the treatment of the chromosphere in HYDRAD. Before Reep et al. (2019) the H ion fraction, and therefore estimates of radiative losses from the (Carlsson and Leenaarts, 2012) lookup tables, in the HYDRAD chromospheres were based on an LTE treatment that used the local temperature and electron density, assuming collisional rates dominated. To improve this, and to obtain better estimates of H ionisation stratification, electron density stratification, and radiative losses, they turned to the approach of Leenaarts et al. (2007), who followed the work of Sollum (1999).

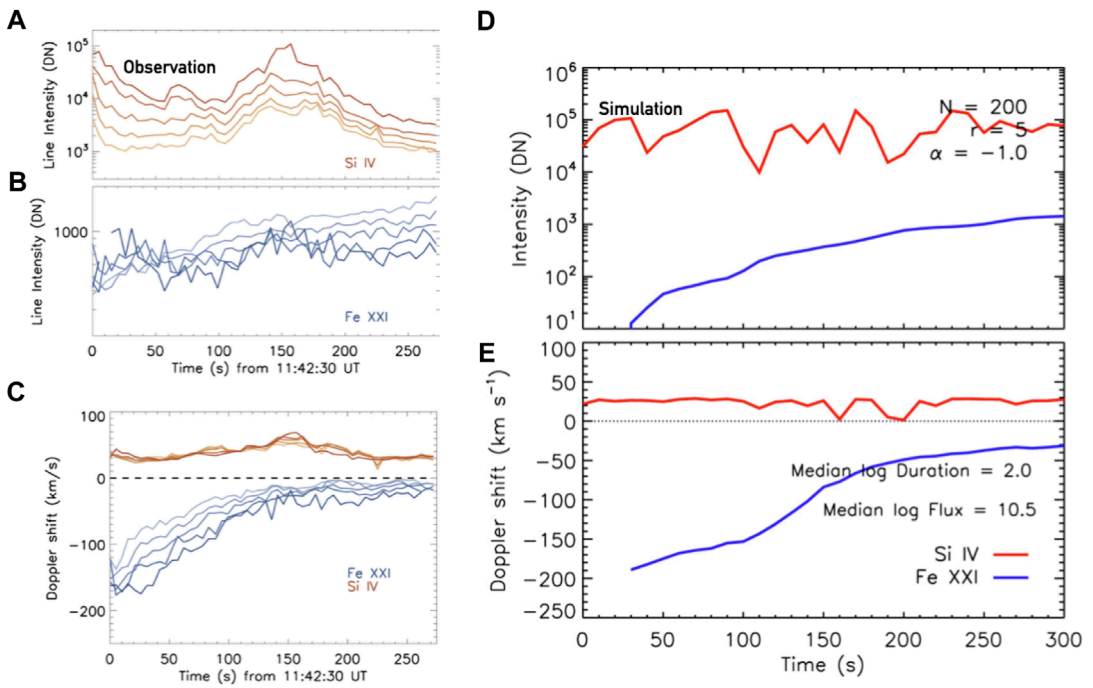

FIGURE 4
Explaining the observed long-duration flows with multi-threaded modelling. Panels **(A–C)** show observations of the M class 2015-March-12 solar flare, where from top to bottom we see the Si IV 1,403 Å intensity (yellow/brown colour scale), the Fe XXI 1,354.1 Å line intensities (blue colour scale), and the Doppler shift of each line (negative velocities are blueshifts, positive are redshift). The multiple lines shown for each quantity represent five different pixels in the flare ribbon. Panels **(D,E)** show the equivalent properties, but for a multi-threaded HYDRAD simulation, with N = 200 threads per IRIS pixel. In those panels red shows Si IV and blue shows Fe XXI. This model does a good job at capturing the duration of flows but does not exhibit the decrease in Si IV intensity towards the latter stage of the flare. Figure adapted from Reep et al. (2018a). © AAS. Reproduced with permission.

In this model the radiative and collisional rates for each transition of H were considered in order to obtain level populations for five levels of H plus the proton density. The collisional rate data were taken from standard sources. Obtaining the radiative rates without calculating the radiation field by solving the full NLTE radiation transfer problem required estimating the radiation field stratification above some critical height (below which the atmosphere could be assumed to be LTE), varying as a function of column mass above this height. Ultimately, the brightness temperatures were obtained as a function of height, and used to calculate the radiative rates. Reep et al. (2019) follow the Sollum (1999) results, but make some important modifications to account for the fact that the radiation field at the top of the chromosphere differs in flares. They note the relation between electron density and line intensity, using this to vary the brightness temperature at the top of the atmosphere as a function of electron density, with a grid of RADYN models serving as a guide.

Armed with this new model chromosphere, the parameter space of Reep et al. (2016) was re-run to model the observations of Warren et al. (2016), and multi-threaded models of the chromospheric lines calculated *via* processing HYDRAD flare atmospheres through RH15D and combining the emission in the same manner as Reep et al. (2016). Reep et al. (2019) argue that the single loop model cannot explain the O I emission, since it is strongly redshifted in the model but largely stationary in the observations. It was also far too bright in the models. Various setups of the multi-threaded approach managed to produce O I Doppler motions consistent with Warren et al. (2016) observations, but the ratio of O I to C I was not consistent (O I was too bright). The Mg II results were also consistent with the observations, showing bursty redshifts lasting throughout the heating phase. Something not addressed by Reep et al. (2019) is if we might really expect the chromospheric emission in a multi-threaded model to freely escape without radiation transfer effects between each closely space thread, which may confuse the picture of the very optically thick Mg II lines in this model (though O I is very likely optically thin in flares). Single loop models likely suffer similar issues with 2D/3D radiation transfer, though often the assumption is that they are embedded in a ribbon-like structure that evolves similarly, rather than having many tens or hundreds random energisation events within the small volume of an IRIS pixel. A recent study using RADYN flare models and *Lightweaver* has demonstrated the importance of including 2D and 3D radiation transfer (Osborne and Fletcher, 2022), though focussing on quiet Sun nearby a ribbon. A similar model that explores the effects *within* the ribbons or footpoints themselves (i.e., an inhomogenous ribbon) would be very interesting and worthwhile!

The application of multi-threaded modelling to the problem of long lived flows has been largely successful, with important implications if true, for example that individual threads may be smaller than 1/100 arcseconds for $N{\sim}60$, scaling inversely with N. While this model alleviates the demand of continuous energy injection into a single thread for many minutes, it still demands the injection for many minutes into an area the size of a single IRIS pixel (i.e., a single localised volume), and for up to ∼2 minutes on some threads. It remains to be seen if we actually have bombardment by energetic electrons into these areas for this long. Hard X-ray kernels, the proxy for non-thermal electrons, propagate in time during the flare, so don't necessarily always hover in a single location for many minutes (e.g., Fletcher et al., 2011; Cheng et al., 2012, among many studies), with the usual caveat that RHESSI's 1:10 dynamic range means that only the strongest sources are observed. Perhaps in the latter phase of multi-threaded modelling the upper range of the injected flux should be significantly reduced so that hard X-ray emission would be quite small, which is actually indicated by the pattern of Si IV intensities in Reep et al. (2018a). It would also be an interesting comparison to study the lifetime of flows in events in which hard X-rays quickly vary location, to those in which the hard X-ray motions are relatively stable. Further (and perhaps related), chromospheric redshifts do not seem to always exhibit the long lived decays seen in the B class event of Warren et al. (2016), and instead can show rapid decreases on the order of [30–120] s. It would be interesting to apply the multi-threaded approach to a flare observed with longlived transition region and coronal flows, but shorter duration chromospheric condensations, to determine if some parameter set can be constrained.

4.1.3 Area expansion in a single loop

An important facet of loop models that is typically ignored when modelling solar flares is area expansion along the loop. In most flare loop modelling the loop is assumed to be semi-circular with uniform cross-sectional area. However, given that the magnetic field decreases with height from photosphere to corona, in order to conserve magnetic flux, the area of the loops should presumably expand with height. This could also help alleviate the stark model-data discrepancies of transition region spectral line intensities (see the discussion in the detailed study of Reep et al., 2022a). Including area expansion in our models is relatively straightforward, but the questions are by how much should the area expand, where should this expansion begin, and does this have a strong effect?

The uncertainty here is not helped by the fact that it is observationally very tricky to identify the appropriate values to use. In fact, observations of both quiescent and flaring coronal loops do not seem to show significant expansion along their length, varying by only ∼30 % from midpoint to footpoint, (Klimchuk, 2000). Even observations at the highest spatial resolution yet achieved show similar results

(Klimchuk and DeForest, 2020). Nevertheless, it is important to gain an understanding of the effect on flare dynamics if we include area expansion. To that end, Reep et al., 2022b performed a systematic study of HYDRAD flare simulations that included area expansion. Although they did not synthesise IRIS observables in this particular study, their results are applicable to the problem of long-lived flows and to the fact that flare models typically cool much faster than observations suggest (see discussions in Qiu and Longcope, 2016; Emslie and Bian, 2018; Allred et al., 2022). Two scenarios were considered, one where expansion is limited to the transition region, and one where expansion occurs gradually and continuously through the loop, both implemented *via* a height varying factor $1/A(s)$ applied to the relevant hydrodynamic equations (where s is the position along the loop). This factor, that describes the relative area expansion, was obtained by imposing a magnetic field stratification, and using the fact that the area expansion is proportional to the magnetic field decrease.

In their continuous-expansion experiments, the expansion factors, from footpoint to loop apex, tested were $A_{\rm exp} = [1, 11, 43, 116]$. Each factor was used in an electron-beam driven flare simulation, with a deposition duration of 100 s. The time taken to reach peak density was delayed with increasing area expansion, producing much longer cooling phases than typically seen in flare simulations. There is an extended period of time where the peak densities remain roughly constant and the temperatures decrease slowly *via* radiation, with draining only occurring after the temperature drops below $T = 100$ kK. Area expansion modified the $T \sim n^2$ relation so that the dynamics of the radiative cooling phase of the flares were very different than a loop with uniform cross-section. Upflows through the high temperature coronal loops persist well beyond the energy injection phase, in contrast to results discussed previously. Sound waves that result from sloshing of material during the flare gradual phase are also suppressed with increasing area expansion, and the magnitude of evaporative upflows reduced as the plasma encounters larger cross-sections. Sun-as-a-star irradiances synthesised from these models were reduced for loops with increasing area expansion but equal total volume, and the longer draining and cooling timescales results in sustained emission. Similar results were found for area expansion localised near the transition region, but with smaller changes to the timescales compared to the continuous-expansion case when the expansion occurs closer to the flare footpoint in the transition region. Sounds waves were also less suppressed in this scenario.

The assumption of a semi-circular loop was also interrogated, with a modification made to the gravitational acceleration term parallel to the loop to make the loops more elliptical. This has a seemingly minor effect, mostly on the draining timescales due to slightly weaker gravitational acceleration.

It is not yet known what the appropriate values of area expansion to use are, but Reep et al. (2022b) has convincingly demonstrated that this factor should not be ignored, particularly for the gradual phase of each footpoint. Indeed, this may negate the requirement for continuous energisation of many threads within a single IRIS pixel in order to maintain long-lived flows. Hopefully further exploration of these impacts will shed light on the appropriate values to use.

4.2 Satellite component redshifts

Redshifted, broadened, emission appearing in the wings of strong chromospheric lines has been observed for many decades, for example famously in Hα (e.g., Ichimoto and Kurokawa, 1984) who found short-lived ($\sim$30 – 40 s) sources with H α red-wing asymmetry with implied velocities of 40–100 km s^{-1}. Other important studies of chromospheric redshifts from ground based observations of H α, Ca II and Na D lines include Canfield et al. (1990), Falchi et al. (1992), Falchi and Mauas. (2002), Falchi et al. (1997), and Zarro et al. (1988). Falchi et al. (1997) noted that redshifts tend to occur along the edge of propagating ribbons; that is, they occur at the feet of newly reconnected loops. Comparing the momentum in condensations observed in H α to that of upflows from SMM data, Canfield et al. (1990) found an order of magnitude consistency, bolstering the chromospheric evaporation models of Fisher et al. (1985c), and ruling out some alternate suggestions for the origin of upflows. The observational studies of Falchi et al. (1992) and Falchi and Mauas. (2002) found what appeared to be an extended spatial gradient in the condensation front, seemingly at odds with the models of Fisher et al. (1985c) and Fisher (1989), who predicted a narrow condensation. They do speculate, though, that if the condensations in fact originated from a smaller area (i.e., that flare footpoints are smaller than they were able to resolve) then the wing emission could originate from a high-lying condensation and not from the deeper region implied by the line core intensity. In that scenario, the condensation may still have a gradient, but this gradient would be sharp since the geometric extent of the feature is narrow. Indeed, most of the studies mentioned above, as well as others referenced by them, commented specifically on the need for improved spatial (sub-arcsecond) and temporal (the first few seconds of energy deposition) resolution of chromospheric flare footpoints. As noted by Graham et al. (2020), pre-IRIS, sufficiently resolved observations of the flare impulsive phase in the chromosphere were scarce (in part due to the difficulty of placing spectrograph slits in the correct place).

IRIS has now observed many example of chromospheric downflows in flares, especially in the Mg II NUV spectra, at sub-arcsecond resolution (e.g., Kerr et al., 2015; Liu et al., 2015; Graham and Cauzzi, 2015; Rubio da Costa et al., 2015;

Kowalski et al., 2017; Panos et al., 2018; Huang et al., 2019; Graham et al., 2020). Kowalski et al. (2017) identified similar features in weaker, more narrow chromospheric lines observed by IRIS, where they could appear as distinct components that persisted only for the duration of one 75 s raster. Modelling of the two brightest footpoints in that flare, using RADYN, revealed that a rather high energy flux of non-thermal electrons was required to be injected into each footpoint, but that the dwell time on each footpoint could be different. A short pulse ($\Delta t = 4$ s) and a longer pulse ($\Delta t = 8$ s) were necessary to produce consistent ratios of Fe II redshifted component intensity to line core intensity within each different footpoint. This bore similarities to the conclusions of Falchi and Mauas. (2002) who suspected that the red-asymmetry of certain line wings could originate from a condensation at a greater altitude than the usual line formation height.

Higher cadence ($\delta t = 9.4$ s) IRIS observations of the 2014-September-10th X-class flare revealed that in addition to spectra exhibiting redshifted cores and red-wing asymmetries in chromospheric species (Graham and Cauzzi, 2015), many spectra contained separate components with redshifts indicating downflows of the order 25–50 km s^{-1}. These components were at times sufficiently far from the strong, mostly stationary, components that they were dubbed "satellite" components (Graham et al., 2020). These were most apparent in singly ionised and neutral transitions that produce spectral lines that were generally more narrow than the very strong resonance lines observed by IRIS. For example, they were seen in Mg II 2,791.6 Å, Fe I 2,714.11 Å, Fe II 2,813.3 Å, Fe II 2,814.45 Å, C I 1,354.284 Å, and Si II 1,348.55 Å. The lefthand side of **Figure 5** shows examples of these satellite redshift components for the Fe II 2,814.45 Å lines, where it can be seen that the satellite components were broader than the primary more intense "stationary" component, and were observed to migrate towards, and ultimately merge with, the primary component over a period of ~30 s (that is, they decelerated).

Using *Fermi*/GBM (Meegan et al., 2009) hard X-ray data, Graham et al. (2020) performed data-driven modelling of the Fe II 2,814.45 Å line from that flare. The spectral properties of the non-thermal electron distribution were obtained ($\delta = 5$, $E_c = 15$ keV), along with the total instantaneous power carried as a function time, averaged over 10 s time bins to be consistent with the IRIS data. Crucially, the energy flux (power/area) was estimated by carefully measuring the newly brightened area of IRIS SJI images at each time, with the rationale being that this revealed the locations into which the non-thermal electrons observed in Sun-as-a-star *Fermi* data were being injected at any snapshot. Using different thresholdings to define

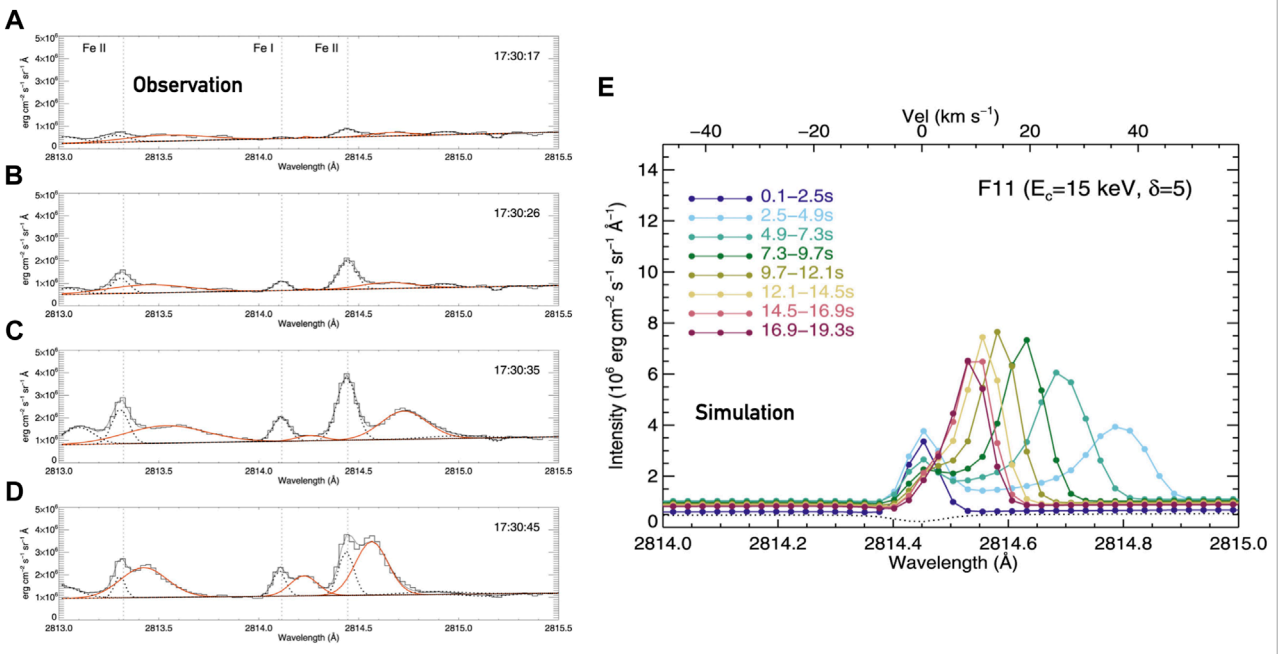

FIGURE 5
Modelling red wing asymmetries and satellite components. Panel **(A–D)** show a series of snapshots of the Fe II 2,814.5 Å line, observed by IRIS in the 2014-Sept-10 flare, where a stationary and satellite component are clear. The black solid histogram lines are the data, the black dotted line is the Gaussian fit to the stationary component, the red line is the Gaussian fit to the satellite component, and the thin grey line is the sum of the two components. Panel **(E)** shows RADYN modelling of the Fe II line from that flare, which was able to reproduce the satellite component, though with an overestimated intensity. Figure adapted from Graham et al. (2020). © AAS. Reproduced with permission.

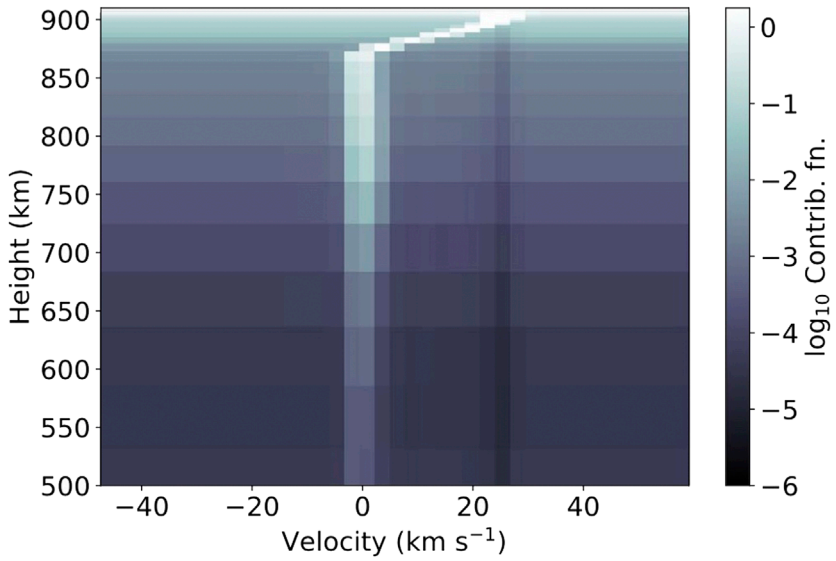

FIGURE 6
The contribution function to the emergent intensity of Fe II 2,814.45 Å. Integrating through height yields the emergent intensity. Note the intense, but narrow, condensation in the upper chromosphere producing bright, redshifted satellite component alongside the stationary component. Figure from Graham et al. (2020). © Copyright AAS. Reproduced with permission.

this area provided a range of energy flux densities on the order 10^{11-12} erg s^{-1} cm^{-2}. Finally, the duration of energy injection into each footpoint was estimated from the width of a half-Gaussian function fit to the rise time of the Fe II spectra [similar to the approach of Qiu et al., 2012], revealing a dwell time[5] of t_{inj}~20 s. RADYN modelling was performed with these derived parameters as input, in which a prominent condensation rapidly formed, with downflowing speed of up to 50 km s^{-1}, an electron density in excess of 10^{14} cm^{-3} and a width of only Δz = 30–40 km.

Modelling the Fe II lines, including averaging the synthetic spectra over the IRIS τ_{exp} = 2.4 s exposure time, revealed that this condensation did indeed result in a satellite component forming, that subsequently decelerated towards the stationary component as the condensation pushed deeper. Synthetic satellite components are shown in the righthand side of **Figure 5**, where colour represents time in the simulation. **Figure 6** shows the contribution function to the emergent intensity (i.e., where the line forms) of the Fe II line. The bright contribution from redshifted material is obvious, as is the narrowness of the condensation appearing in the upper chromosphere. From the formation properties of the lines, such as **Figure 6**, we can understand the origin of the satellite components. Flare heating in the chromosphere enhances the lines, but in a region without meaningful mass flows so that the near-stationary component is bright. Once the condensation develops at the top of the chromosphere/base of transition region and becomes dense it begins to produce Doppler shifted emission from those same ions. Since the stationary components are relatively narrow the very redshifted emission appears as a separate line. As the condensation accrues mass while it propagates deeper, it slows, such that the Doppler shift of the satellite component reduces and it merges with the stationary component, taking on the red-wing asymmetry appearance. The optical thickness of the lines comes into play as those lines that are very optically thick and form higher in altitude (e.g., the Mg II or C II resonance lines) will more quickly see the merging of the stationary and redshifted components (with the whole line appearing redshifted in many cases). In those cases the large opacity means that little light can escape the top of the condensation once enough density is accrued, and so the stationary component is not visible. For lines with smaller opacity both components can be seen. Further, the large opacity broadening of the resonance lines means that the redshifted component would likely not appear as a fully separate component, rather as a red wing asymmetry.

The intensity of both the surrounding continuum and the stationary components agreed with the observations, as did the magnitude of the Doppler shifts. However, several discrepancies did exist. The satellite component was much too intense, outshining the stationary component, and was much too narrow

5 Here the assumption is that the sharp rise time from background to peak intensity is an indication of the characteristic heating duration. From the histogram of Gaussian widths a typical heating time (dwell time of the electron beam in this case) was obtained.

(as discussed in Paper 2 Kerr submitted of this review line widths are a perennial problem). The onset and evolution of the satellite components also occurred on a more aggressive timescale compared to the observations, though not egregiously so (a factor 2–3× faster). Finally, varying the low-energy cutoff or energy flux illustrated how sensitive the properties and evolution of the condensation are. For example, increasing the energy flux to the upper range of the estimates in this particular case produced a condensation much too fast compared to the observations with a larger-than-observed continuum intensity. Similarly, increasing the low-energy cutoff meant that the condensation developed too late and was too slow. This demonstrates the possibility that such observations can be used to guide or constrain the range of plausible electron beam parameters consistent with the evolution of UV radiation in a particular flare (though I stress "guide"; I do not believe we are yet in a position to use them independent of X-ray observations).

Graham et al. (2020) explicitly demonstrated how useful high-cadence spectral characteristics are in confirming the inferred properties of the electron beam. They also demonstrated why we should pay attention to weaker lines in addition to the more commonly studied resonance lines. Similar condensations were shown in the models discussing the much broader Mg II h and k lines (Kerr et al., 2016; Kerr et al., 2019a; Kerr et al., 2019b) but in those cases instead of producing satellite components, they produced small asymmetries in the red wings. In comparison to the resonance lines of Mg II and C II, Fe II 2,814.45 Å has a much lower opacity, probing more easily the deeper layers of the chromosphere (Kowalski et al., 2017). Earlier modelling of condensation timescales found a similar discrepancy in the timescales compared to Hα observations (Fisher, 1989) as those noted by Graham et al. (2020). IRIS's very high spatial resolution suggests that the answer to this discrepancy does not lie in the superposition of flows from many unresolved elements (though note that the difference in timing is only a factor 2 or so, not the order of magnitude that is the case for evaporative upflows!). An overdense condensation could explain why the modelled satellite components were brighter than the stationary components. Though not focussing on red wing asymmetries, Kerr et al., 2019a shows Mg II 2,791 Å lines with a redshifted satellite component that is weaker than the stationary component. In that simulation the condensation is not very dense, hence the smaller intensity. A means to obtain an estimate of the electron density from the broadening of high-order Balmer lines was presented by Kowalski et al. (2022), and the effects of improved Stark broadening are now included in RADYN and RH. Coordinated DKIST and IRIS observations of the Balmer lines and FUV/NUV spectra would shed light on this discrepancy and condensation densities (see also the comprehensive discussion regarding model-data discrepancies in Kowalski et al. (2022), Section 5).

4.3 Flows in small scale heating events

It is not yet known if the physics of flares scales from the very large (M and X class events) to the very small (micro or nanoflares), but it is a reasonable assumption that electrons could be accelerated even in small events (see recent evidence from NuSTAR observations of (sub-) microflares Glesener et al., 2020; Cooper et al., 2021). Rapid variations in Doppler motions (both blue- and redshifts) and intensities have been observed at the base of coronal loops in the transition region, leading (Testa et al., 2014 and Polito et al., 2018) to investigate *via* RADYN modelling if non-thermal electron distributions injected into the transition region from the corona could explain these "nanoflare" signatures. The total energy deposited was estimated as being 6×10^{24} erg (based on Parker, 1988), compared to 10^{30-32} erg for moderate-to-large flares. This equated to an energy flux of 1.2×10^{9} erg s^{-1} cm^{-2} considering the area of the footpoint emission, and an assumed dwell time of 10 s based on lifetimes of short-lived brightenings in transition region moss. Note that the total energy, and the energy flux, associated with the nanoflares observed by Testa et al. (2014) and Polito et al. (2018), while fairly small, is not so different from an individual flare loop; it is the much greater number of flare loops/greater flare volume that leads to the larger total energy.

Polito et al. (2018) performed a parameter study sampling different non-thermal electron distributions, and injected those electrons into two pre-flare atmospheres, one initially cool and tenuous (a low density corona at 1 MK), and one hotter and dense (a high density corona at 3 MK). The latter represents an active region loop, the former being more quiet Sun-like, and both had extended plateaus of higher temperatures in the chromosphere compared to VAL-C type atmospheres, maintained in the model by artificial non-radiative heating. The electron energy spectra had low energy cutoffs in the range $E_c = [5, 10, 15]$ keV. The low-energy cutoff, E_c, had a strong impact on the subsequent dynamics. Flares with a small E_c efficiently heated the corona, driving the whole transition region to greater column mass, and therefore resulting in Si IV redshifts, along with explosive evaporation. The corona is very tenuous, so it is easy to drive fast flows even at these low energy fluxes if E_c is low such that energy is largely deposited in the upper transition region/lower corona. Larger values of E_c means that there are relatively more high energy electrons that thermalise somewhat deeper, so that gentle evaporation through the transition region occurred and upflows at the temperatures that form Si IV were present. Initially dense loops resulted in lower intensity emission and slower flows compared to initially tenuous loops. Loop length was also an important factor for the dense loops, with longer loops resulting in a larger portion of electrons thermalising in the corona.

The dynamics of the loops had a direct impact on the synthetic emission, allowing a straightforward comparison to

observations. Polito et al. (2018) synthesised Si IV resonance line emission, degrading the spectra to IRIS resolution and count rates. Tenuous loops result in a very intense Si IV response for all simulations, but reaching a peak in the 10 keV experiment. For the dense loops, the softest non-thermal electron distribution ($E_c = 5$ keV) did not produce an appreciable response of Si IV on rapid timescales. Blueshifts were seen in simulations with $E_c > 10$ keV, whereas redshifts were seen in simulations with $E_c = 5$ keV, as illustrated in **Figure 7** that shows the Si IV spectra and lightcurves for simulations with different values of E_c. Once the loops have filled following evaporation and become denser, electrons thermalise more easily in the corona where they cause further heating. Redshifts were also seen in experiments in which the same magnitude of energy was deposited directly in the corona and allowed to conduct through to the lower atmosphere. No blueshifts were seen in that scenario.

Polito et al. (2018) speculate that based on their loop modelling, the observations of impulsive brightenings in the transition region at the base of coronal loops are consistent with energy input to an initially cold, tenuous loop. Since observations show both blue and redshifted emission, this suggests that conduction driven heating of loop footpoints at the transition region alone is not consistent with the observations. That is, IRIS observations combined with RADYN modelling suggest that particles are accelerated even in small-scale brightenings, contributing to active region heating.

4.4 Exploring correlations between flare-induced upflows and downflows

Since the development of condensations and evaporations during flares is closely tied to the properties of energy injection, there could exist correlations between these flows inferred from spectral lines. Sadykov et al. (2019) explored the potential of such correlations using IRIS data, and also *via* RADYN modelling of electron beam driven flares. Seven flares were selected that conformed to a strict set of criteria, including fast scans (<90 s), flare ribbons crossing the slit, both simultaneous RHESSI observations with prominent non-thermal components *and* RHESSI hard X-ray sources that were co-spatial with the IRIS slit (to ensure that the spectra studied were more likely to arise from non-thermal electron precipitation), and a source no farther than 750″ from disk center to attempt to minimise projection effects. The Doppler motions of the C II 1,334.5 Å and Fe XXI 1,354.1 Å lines were determined, sampling the cooler layers more likely to experience a condensation and those more likely to experience upflows into the corona. A center-of-gravity approach was used

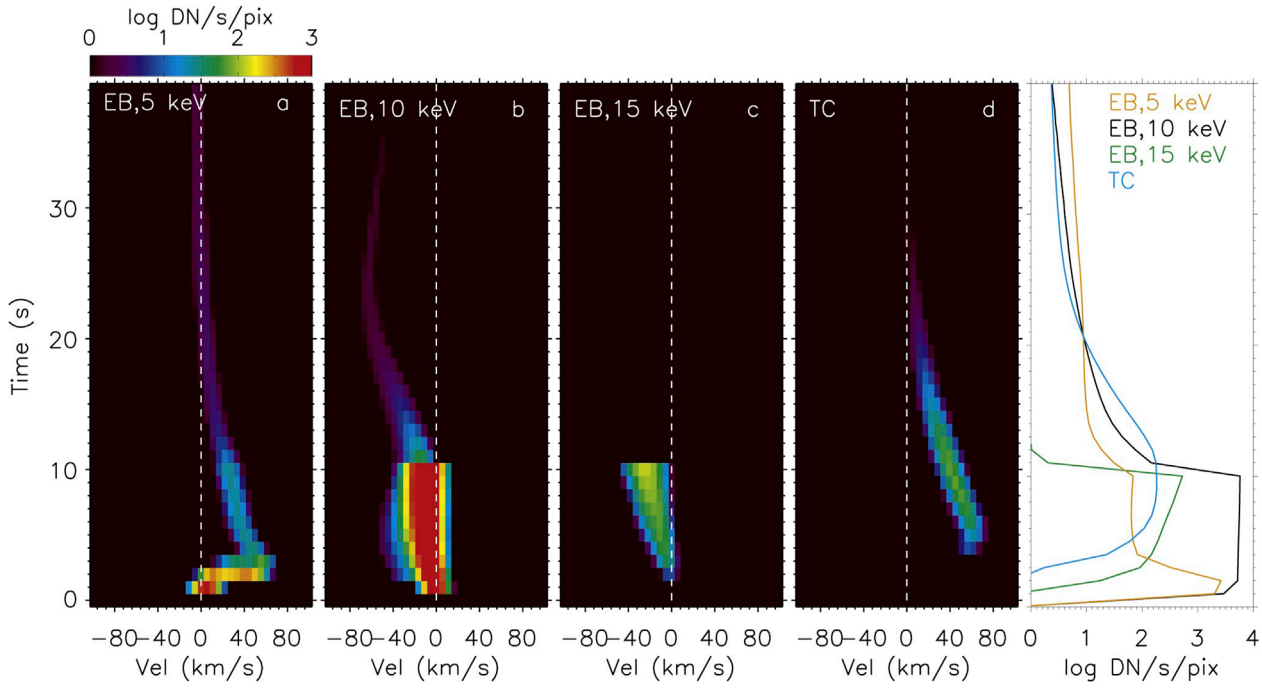

FIGURE 7
Demonstrating that non-thermal electron beams can produce blueshifted emission with $E_c > 10$ keV in nanoflare simulations using RADYN. Panels **(A–C)** show Si IV spectra for electron beams with different E_c, panel **(D)** shows the spectra in the case of a conduction driven flare, and the rightmost panel shows the lightcurves from each flare. Figure from Polito et al. (2018). © AAS. Reproduced with permission.

to obtain the Doppler shift of the optically thick[6] C II 1,334.5 Å Doppler shift, whereas Gaussian fitting was performed for the optically thin Fe XXI 1,354.1 Å line. For both lines, a mask of only the flaring sources was created, and the mean Doppler shifts in the area of the hard X-ray sources measured. Additionally, the maximum shifts were recorded.

These same lines were modelled from a grid of electron beam driven flare simulations produced by the F-CHROMA consortium using RADYN[7]. This grid samples a large parameter space of non-thermal electron distributions, that were injected into a VAL3C-like (Vernazza et al., 1981) pre-flare atmosphere. Energy was injected for $t = 20$ s, in a triangular profile peaking at $t = 10$ s. While most of the F-CHROMA grid represents relatively weak-to-moderate heating events, it is a very useful resource for studying flare processes and I encourage the reader to access it for their own research.

Sadykov et al. (2019) selected 20 flares from this grid that loosely were consistent with the observationally derived non-thermal electron distribution properties. For the observational analysis of hard X-rays, the area selected to determine the energy flux into the chromosphere was the 50% contour of the hard X-ray source. As I discuss in other sections, this very likely is an overestimate of the areas, and thus an underestimate of the actual energy flux. At a cadence of 1 s, synthetic C II and Fe XXI spectra were obtained from the RADYN atmospheres, using RH15D and data from CHIANTI, respectively. In the latter case, Fe xxi emission was summed through the full extent of the half-loop, so no geometric effects of extended emission regions were considered. The same Doppler shift metrics derived from the observations were then obtained from the models.

A statistical analysis revealed that there was no meaningful correlation between observed mean C II redshifts and non-thermal energy flux, but there was in the models. While still not very statistically significant, the observed maximum redshifts did show a correlation with the injected non-thermal energy flux. Similarly, there were no meaningful correlations between observed Fe XXI blueshifts and non-thermal energy flux, but there were in the models. Further discrepancies existed also. Unlike the observations, the models predicted that in some cases there should be modest C II blueshifts. Observed flows of Fe XXI were on the order 100 km s^{-1}, consistent with the range of reported values in other studies, but some of the models exceeded 500 km s^{-1}. The differences between the models and data suggest that either the flares being compared were not apples-to-apples (in the sense that the energy flux in the observed flares may have been underestimated due to the choice of using hard X-ray areas, and so larger than those used in the models), or that physics is missing from the models.

As an example of the latter, recent work by Allred et al. (2022) to include the suppression of thermal conduction in RADYN simulations due to turbulence and non-local effects revealed slower upflows, and a shift in the altitude at which the transition region forms. The latter results in the switch from upflow to downflow occurring at a different temperature for a given set of electron beam parameters [in this case, those observed by Milligan and Dennis (2009)]. That study focussed on EUV observations, but future work will include IRIS observables, which may address the discrepancies discovered by Sadykov et al. (2019).

5 Summary

In this first part of a two-part review of IRIS observations and flare loop modelling I have introduced the four main modern flare numerical models that have been used alongside IRIS data: RADYN, HYDRAD, FLARIX, and PREFT (though these latter two feature more in part two of this review). As well as this I have given an overview of how we synthesise IRIS observables from those models. With those models and the high spatial-, spectral-, and temporal resolution observations provided by IRIS we have learned much about flare-induced mass flows, that in the standard flare model assumed energy transport *via* directed beams of non-thermal electrons.

Though there are details to work out, recent modelling work performed in an attempt to explain long-lived mass flows induced in flare footpoints, at the scale of IRIS resolution elements (0.3–0.4″), has convincingly demonstrated that there is a seeming demand for continued energy deposition into each footpoint for up to several minutes. Multi-threaded modelling results also suggests that this energy deposition is not coherent; that is, not every thread is energised at the same time, different threads (of which there may be many hundreds within each 0.167″ pixel) are energised at different times, and for different durations. There are questions persisting here. We do not know if electrons are accelerated, and subsequently thermalised within the same small volume of an IRIS pixel for many minutes, nor even how long this would occur for on a single thread. Hard X-ray sources currently lack the high spatial resolution obtainable at UV wavelengths, and also have historically had low dynamic range so that only the strongest sources are observable. Still, hard X-ray sources are seen to move over time in a flare and not always linger for a long duration in a single location, and strong hard X-rays are not observed in the gradual phase.

IRIS observations of redshifted satellite components and red-wing asymmetries have been successfully modelled using field-aligned loop models in which non-thermal electron beams drive strong condensations. These condensations are narrow, and dense, producing redshifted emission that slows over time. Again, there are details to work out. For example the ratio of

6 Hence fitting with a Gaussian function is not appropriate.

7 https://star.pst.qub.ac.uk/wiki/public/solarmodels/start.html.

the redshifted to stationary component is not well-captured in models compared to observations. This could suggest an over-dense condensation in the model compared to the observation. The disparity between timescales of the redshifted components in the models compared to the observations is not as stark as those in the upflow scenario; condensation timescales in the models are more aggressive than in the observations, but do not reach the more than an order of magnitude differences that the modelled upflows suffer from.

Curiously, this means that we have different solutions to each problem: multi-threaded models with continued energy release is required to understand upflow behaviours, whereas single loop models with suitable non-thermal electron beam parameters that produce condensations can explain the chromospheric downflows. Transition region flows (e.g., Si IV) are somewhat of an in-between case, with some observations requiring multi-threaded observations, but individual bursts in other observations can be captured with single loop modelling (see also Paper 2 Kerr, submitted). It is important that we now work to reconcile this seeming contradiction between the need for multi-threaded *versus* single loop modelling for different parts of the atmosphere. One resolution may be to have continued energy deposition into the transition region and upper chromosphere but at a magnitude too weak to drive strong condensations. This was hinted at by the results of multi-threaded modelling which suggested that the intensity of Si IV emission should decrease towards the end of the energy deposition phase, whereas it remained rather flat for as long as energy was injected to the HYDRAD models (see **Figure 4**). Experiments with alternate forms of gradual phase energy deposition should be performed since there is not compelling evidence for non-thermal electrons towards the end of each small source's lifetime (i.e. towards the end of the lifetime of the footpoints modelled via multi-threaded simulations). Perhaps direct heating in the coronal portion of the loop following reconnection with a subsequent conductive heat flux carrying energy into the lower atmosphere. Of course, area expansion of loops and suppression of conduction *via* turbulence and non-local effects (e.g., Emslie and Bian, 2018; Zhu et al., 2018; Allred et al., 2022) mitigate the energetic requirements to sustain the temperature and density (and therefore line intensity) through the gradual phase, which might also indicate that after some time the energy flux in multi-threaded models should be decreased. Determining the appropriate parameters of suppression of conduction and the area expansion factors should also, therefore, be a priority.

Continued observations with IRIS will help here, but we must also look to future observations. IRIS demonstrated the benefits of detailed spectroscopy at high spatial and temporal resolution, and while it does sample different regions of the atmosphere it does have a fairly sparse temperature coverage. The upcoming Solar-C/EUVST instrument will have capabilities comparable to or slightly better than IRIS, but with a substantially denser temperature coverage, and a higher standard cadence[8]. Observations will be available from photosphere to corona, with several hot flare lines (5–15 MK). As such, EUVST is very well placed to perform detailed studies of mass flows during flares that encompass simultaneously the chromosphere, transition region, and corona (with each layer sampled by many lines). Comprehensive analyses such as those performed by Milligan and Dennis (2009) and Sellers et al. (2022) over this wide temperature range, and with higher spatiotemporal resolution, should be a priority to better understand the evolution of mass flows in flares. EUVST will be complemented by observations from the Multi-slit Solar Explorer (MUSE; De Pontieu et al., 2020; Cheung et al., 2022) which has a more limited temperature coverage, focussing on the corona and flare plasma, with one line sampling the transition region, but which has 37 slits, allowing imaging spectroscopy of an entire active region sized field of view to be performed in <12 s. MUSE observations of the flaring corona, covering the full flaring structure, will hopefully shed light on continued energy release in the post-impulsive phase. From the ground, the now-operating Daniel K. Inouye Solar Telescope (DKIST) will also provide coverage from photosphere through corona, with an unprecedented spatial resolution $\sim 0.1''$, which could reveal fine-structure in flare footpoints that guides future multi-threaded modelling.

I would also like to note that most of the flare modelling studies discussed here and in Paper 2 use standard pre-flare atmospheres (e.g., VALC, radiative equilibrium with different apex temperatures), but we know that the chromosphere is not homogenous. Real efforts should be made to 1) determine the large-scale impact on flare-induced flows of the choice of starting atmosphere, and to 2) perform bespoke modelling of flare footpoints where the pre-flare atmospheres are constrained by the observed chromosphere and corona. One means to guide the latter is the exciting advances in spectral inversions, including the IRIS2 resource (Sainz Dalda et al., 2019), in which machine learning techniques were used with the STiC inversion code (de la Cruz Rodríguez et al., 2019) and IRIS data to allow quick inversions of Mg II data to obtain the atmospheric satisfaction. (with updates to include other lines being actively worked on, A. Sainz Diaz *private communication*, 2022).

Finally, mass flows are but one manifestation of solar flares. In Paper 2 of this review (Kerr, submitted) I go on to discuss other plasma properties, energy transport mechanisms, and future directions of flare modelling.

8 IRIS has recently started performing ~1 s cadence flare observations, targeting the strongest lines.

Author contributions

GK performed the literature review and wrote the manuscript.

Funding

GK acknowledges funding *via* a NASA ROSES Early Career Investigator Award (Grant #80NSSC21K0460) and the NASA ROSES Heliophysics Supporting Research program (Grant # 80NSSC21K0010).

Acknowledgments

IRIS is a NASA small explorer mission developed and operated by LMSAL with mission operations executed at NASA Ames Research center and major contributions to downlink communications funded by the Norwegian Space Center (NSC, Norway) through an ESA PRODEX contract. This manuscript benefited from discussions held at a meeting of International Space Science Institute team: "Interrogating Field-Aligned Solar Flare Models: Comparing, Contrasting and Improving," led by GK and V. Polito. I also thank the following colleagues for their help, and patience, with answering questions related to RADYN, PREFT, FLARIX, and HYDRAD: Joel Allred, Mats Carlsson, Adam Kowalski, Vanessa Polito, Dana Longcope, William Ashfield, John Unverferth, Stephen Bradshaw, Jeffrey Reep, Jana Kašparová, Petr Heinzel, and Michal Varady. Finally, I am grateful to the referees, who's careful and thorough comments improved this review.

Conflict of interest

The author declares that the research was conducted in the absence of any commercial or financial relationships that could be construed as a potential conflict of interest.

Publisher's note

References

Abbett, W. P. (1998). A theoretical investigation of optical emission in solar flares. Ph.D. thesis. Ann Arbor: Michigan State University.

Abbett, W. P., and Hawley, S. L. (1999). Dynamic models of optical emission in impulsive solar flares. *Astrophys. J.* 521, 906–919. doi:10.1086/307576

Alaoui, M., Holman, G. D., Allred, J. C., and Eufrasio, R. T. (2021). Role of suprathermal runaway electrons returning to the acceleration region in solar flares. *Astrophys. J.* 917, 74. doi:10.3847/1538-4357/ac0820

Alaoui, M., and Holman, G. D. (2017). Understanding breaks in flare X-ray spectra: Evaluation of a cospatial collisional return-current model. *Astrophys. J.* 851, 78. doi:10.3847/1538-4357/aa98de

Allred, J. C., Alaoui, M., Kowalski, A. F., and Kerr, G. S. (2020). Modeling the transport of nonthermal particles in flares using fokker-planck kinetic theory. *Astrophys. J.* 902, 16. doi:10.3847/1538-4357/abb239

Allred, J. C., Hawley, S. L., Abbett, W. P., and Carlsson, M. (2005). Radiative hydrodynamic models of the optical and ultraviolet emission from solar flares. *Astrophys. J.* 630, 573–586. doi:10.1086/431751

Allred, J. C., Kerr, G. S., and Gordon Emslie, A. (2022). Solar flare heating with turbulent suppression of thermal conduction. *Astrophys. J.* 931, 60. doi:10.3847/1538-4357/ac69e8

Allred, J. C., Kowalski, A. F., and Carlsson, M. (2015). A unified computational model for solar and stellar flares. *Astrophys. J.* 809, 104. doi:10.1088/0004-637X/809/1/104

Allred, J., Daw, A., and Brosius, J. (2018). A 3D model of AR 11726 heated by nanoflares. arXiv:1807.00763.

Antonucci, E., and Dennis, B. R. (1983). Observation of chromospheric evaporation during the solar maximum mission. *Sol. Phys.* 86, 67–77. doi:10.1007/BF00157175

Antonucci, E., Gabriel, A. H., Acton, L. W., Culhane, J. L., Doyle, J. G., Leibacher, J. W., et al. (1982). Impulsive phase of flares in soft X-ray emission. *Sol. Phys.* 78, 107–123. doi:10.1007/BF00151147

Arnaud, M., and Rothenflug, R. (1985). An updated evaluation of recombination and ionization rates. *Astronomy Astrophysics Suppl.* 60, 425–457.

Ashfield, I., William, H., Longcope, D. W., Zhu, C., and Qiu, J. (2022). Connecting chromospheric condensation signatures to reconnection-driven heating rates in an observed flare. *Astrophys. J.* 926, 164. doi:10.3847/1538-4357/ac402d

Bai, T. (1982). Transport of energetic electrons in a fully ionized hydrogen plasma. *Astrophys. J.* 259, 341–349. doi:10.1086/160170

Benz, A. O. (2008). Flare observations. *Living Rev. Sol. Phys.* 5, 1. doi:10.12942/lrsp-2008-1

Bradshaw, S. J., and Klimchuk, J. A. (2011). What dominates the coronal emission spectrum during the cycle of impulsive heating and cooling? *Astrophys. J. Suppl. Ser.* 194, 26. doi:10.1088/0067-0049/194/2/26

Bradshaw, S. J., and Mason, H. E. (2003a). A self-consistent treatment of radiation in coronal loop modelling. *Astron. Astrophys.* 401, 699–709. doi:10.1051/0004-6361:20030089

Bradshaw, S. J., and Mason, H. E. (2003b). The radiative response of solar loop plasma subject to transient heating. *Astron. Astrophys.* 407, 1127–1138. doi:10.1051/0004-6361:20030986

Bradshaw, S. J., and Viall, N. M. (2016). Patterns of activity in a global model of a solar active region. *Astrophys. J.* 821, 63. doi:10.3847/0004-637X/821/1/63

Brannon, S. R., Longcope, D. W., and Qiu, J. (2015). Spectroscopic observations of an evolving flare ribbon substructure suggesting origin in current sheet waves. *Astrophys. J.* 810, 4. doi:10.1088/0004-637X/810/1/4

Brekke, P. (1993). Observed redshifts in O V and downflows in the solar transition region. *Astrophys. J.* 408, 735. doi:10.1086/172633

Brosius, J. W. (2013). Chromospheric evaporation in solar flare loop strands observed with the extreme-ultraviolet imaging spectrometer on board Hinode. *Astrophys. J.* 762, 133. doi:10.1088/0004-637X/762/2/133

Brosius, J. W., and Daw, A. N. (2015). Quasi-periodic fluctuations and chromospheric evaporation in a solar flare ribbon observed by IRIS. *Astrophys. J.* 810, 45. doi:10.1088/0004-637X/810/1/45

Brown, J. C. (1971). The deduction of energy spectra of non-thermal electrons in flares from the observed dynamic spectra of hard X-ray bursts. *Sol. Phys.* 18, 489–502. doi:10.1007/BF00149070

Canfield, R. C., Gunkler, T. A., and Ricchiazzi, P. J. (1984). The H-alpha spectral signatures of solar flare nonthermal electrons, conductive flux, and coronal pressure. *Astrophys. J.* 282, 296–307. doi:10.1086/162203

Canfield, R. C., and Ricchiazzi, P. J. (1980). A probabilistic approach to radiative energy loss calculations for optically thick atmospheres - hydrogen lines and continua. *Astrophys. J.* 239, 1036–1044. doi:10.1086/158193

Canfield, R. C., Zarro, D. M., Metcalf, T. R., and Lemen, J. R. (1990). Momentum balance in four solar flares. *Astrophys. J.* 348, 333. doi:10.1086/168240

Carlsson, M., and Leenaarts, J. (2012). Approximations for radiative cooling and heating in the solar chromosphere. *Astron. Astrophys.* 539, A39. doi:10.1051/0004-6361/201118366

Carlsson, M., and Stein, R. F. (2002). Dynamic hydrogen ionization. *Astrophys. J.* 572, 626–635. doi:10.1086/340293

Carlsson, M., and Stein, R. F. (1997). Formation of solar calcium H and K bright grains. *Astrophys. J.* 481, 500–514. doi:10.1086/304043

Carlsson, M., and Stein, R. F. (1992). Non-LTE radiating acoustic shocks and CA II K2V bright points. *Astrophys. J.* 397, L59–L62. doi:10.1086/186544

Chae, J., Yun, H. S., and Poland, A. I. (1998). Temperature dependence of ultraviolet line average Doppler shifts in the quiet sun. *Astrophys. J. Suppl. Ser.* 114, 151–164. doi:10.1086/313064

Chen, B., Shen, C., Gary, D. E., Reeves, K. K., Fleishman, G. D., Yu, S., et al. (2020a). Measurement of magnetic field and relativistic electrons along a solar flare current sheet. *Nat. Astron.* 4, 1140–1147. doi:10.1038/s41550-020-1147-7

Chen, B., Yu, S., Reeves, K. K., and Gary, D. E. (2020b). Microwave spectral imaging of an erupting magnetic flux rope: Implications for the standard solar flare model in three dimensions. *Astrophys. J.* 895, L50. doi:10.3847/2041-8213/ab901a

Cheng, C. C., Oran, E. S., Doschek, G. A., Boris, J. P., and Mariska, J. T. (1983). Numerical simulations of loops heated to solar flare temperatures. I - gasdynamics. II - X-ray and UV spectroscopy. *Astrophys. J.* 265, 1090–1119. doi:10.1086/160751

Cheng, J. X., Kerr, G., and Qiu, J. (2012). Hard X-ray and ultraviolet observations of the 2005 january 15 two-ribbon flare. *Astrophys. J.* 744, 48. doi:10.1088/0004-637X/744/1/48

Cheung, M. C. M., Martínez-Sykora, J., Testa, P., De Pontieu, B., Chintzoglou, G., Rempel, M., et al. (2022). Probing the physics of the solar atmosphere with the multi-slit solar explorer (MUSE). II. Flares and eruptions. *Astrophys. J.* 926, 53. doi:10.3847/1538-4357/ac4223

Cheung, M. C. M., Rempel, M., Chintzoglou, G., Chen, F., Testa, P., Martínez-Sykora, J., et al. (2019). A comprehensive three-dimensional radiative magnetohydrodynamic simulation of a solar flare. *Nat. Astron.* 3, 160–166. doi:10.1038/s41550-018-0629-3

Cooper, K., Hannah, I. G., Grefenstette, B. W., Glesener, L., Krucker, S., Hudson, H. S., et al. (2021). NuSTAR observations of a repeatedly microflaring active region. *Mon. Not. R. Astron. Soc.* 507, 3936–3951. doi:10.1093/mnras/stab2283

Culhane, J. L., Harra, L. K., James, A. M., Al-Janabi, K., Bradley, L. J., Chaudry, R. A., et al. (2007). The EUV imaging spectrometer for Hinode. *Sol. Phys.* 243, 19–61. doi:10.1007/s01007-007-0293-1

Culhane, J. L., Hiei, E., Doschek, G. A., Cruise, A. M., Ogawara, Y., Uchida, Y., et al. (1991). The Bragg crystal spectrometer for SOLAR-A. *Sol. Phys.* 136, 89–104. doi:10.1007/BF00151696

Czaykowska, A., Alexander, D., and De Pontieu, B. (2001). Chromospheric heating in the late phase of two-ribbon flares. *Astrophys. J.* 552, 849–857. doi:10.1086/320553

Czaykowska, A., De Pontieu, B., Alexander, D., and Rank, G. (1999). Evidence for chromospheric evaporation in the late gradual flare phase from [ITAL]SOHO[/ITAL]/CDS observations. *Astrophys. J.* 521, L75–L78. doi:10.1086/312176

de la Cruz Rodríguez, J., Leenaarts, J., Danilovic, S., and Uitenbroek, H. (2019). STiC: A multiatom non-LTE PRD inversion code for full-Stokes solar observations. *Astron. Astrophys.* 623, A74. doi:10.1051/0004-6361/201834464

De Pontieu, B., Martínez-Sykora, J., Testa, P., Winebarger, A. R., Daw, A., Hansteen, V., et al. (2020). The multi-slit approach to coronal spectroscopy with the multi-slit solar explorer (MUSE). *Astrophys. J.* 888, 3. doi:10.3847/1538-4357/ab5b03

De Pontieu, B., Polito, V., Hansteen, V., Testa, P., Reeves, K. K., Antolin, P., et al. (2021). A new view of the solar interface region from the interface region imaging spectrograph (IRIS). *Sol. Phys.* 296, 84. doi:10.1007/s11207-021-01826-0

De Pontieu, B., Title, A. M., Lemen, J. R., Kushner, G. D., Akin, D. J., Allard, B., et al. (2014). The interface region imaging spectrograph (IRIS). *Sol. Phys.* 289, 2733–2779. doi:10.1007/s11207-014-0485-y

del Zanna, G., Berlicki, A., Schmieder, B., and Mason, H. E. (2006). A multi-wavelength study of the compact M1 flare on october 22, 2002. *Sol. Phys.* 234, 95–113. doi:10.1007/s11207-006-0016-6

Del Zanna, G., Dere, K. P., Young, P. R., Landi, E., and Mason, H. E. (2015). Chianti - an atomic database for emission lines. Version 8. *Astron. Astrophys.* 582, A56. doi:10.1051/0004-6361/201526827

Dere, K. P., Landi, E., Mason, H. E., Monsignori Fossi, B. C., and Young, P. R. (1997). Chianti - an atomic database for emission lines. *Astron. Astrophys. Suppl. Ser.* 125, 149–173. doi:10.1051/aas:1997368

Ding, M. D., Fang, C., and Huang, Y. R. (1995). Analysis of 2-d flare spectra: Velocity fields derived from Hα line asymmetries. *Sol. Phys.* 158, 81–93. doi:10.1007/BF00680836

Dorfi, E. A., and Drury, L. O. (1987). Simple adaptive grids for 1-D initial value problems. *J. Comput. Phys.* 69, 175–195. doi:10.1016/0021-9991(87)90161-6

Doschek, G. A., and Warren, H. P. (2005). Chromospheric evaporation in solar flares revisited. *Astrophys. J.* 629, 1150–1163. doi:10.1086/431920

Doschek, G. A., Warren, H. P., Dennis, B. R., Reep, J. W., and Caspi, A. (2015). Flare footpoint regions and a surge observed by Hinode/EIS, RHESSI, and SDO/AIA. *Astrophys. J.* 813, 32. doi:10.1088/0004-637X/813/1/32

Doschek, G. A., Warren, H. P., and Young, P. R. (2013). Chromospheric evaporation in an M1.8 flare observed by the extreme-ultraviolet imaging spectrometer on Hinode. *Astrophys. J.* 767, 55. doi:10.1088/0004-637X/767/1/55

Druett, M. K., and Zharkova, V. V. (2018). HYDRO2GEN: Non-thermal hydrogen Balmer and Paschen emission in solar flares generated by electron beams. *Astron. Astrophys.* 610, A68. doi:10.1051/0004-6361/201731053

Druett, M. K., and Zharkova, V. V. (2019). Non-thermal hydrogen Lyman line and continuum emission in solar flares generated by electron beams. *Astron. Astrophys.* 623, A20. doi:10.1051/0004-6361/201732427

Druett, M., Scullion, E., Zharkova, V., Matthews, S., Zharkov, S., and Rouppe van der Voort, L. (2017). Beam electrons as a source of Hα flare ribbons. *Nat. Commun.* 8, 15905. doi:10.1038/ncomms15905

Emslie, A. G., and Bian, N. H. (2018). Reduction of thermal conductive flux by non-local effects in the presence of turbulent scattering. *Astrophys. J.* 865, 67. doi:10.3847/1538-4357/aad961

Emslie, A. G., Dennis, B. R., Shih, A. Y., Chamberlin, P. C., Mewaldt, R. A., Moore, C. S., et al. (2012). Global energetics of thirty-eight large solar eruptive events. *Astrophys. J.* 759, 71. doi:10.1088/0004-637X/759/1/71

Emslie, A. G. (1978). The collisional interaction of a beam of charged particles with a hydrogen target of arbitrary ionization level. *Astrophys. J.* 224, 241–246. doi:10.1086/156371

Falchi, A., Falciani, R., and Smaldone, L. A. (1992). Analysis of the optical spectra of the solar flares. VI. Velocity field in the 13 June 1980 flare area. *Astronomy Astrophysics* 256, 255–263.

Falchi, A., and Mauas, P. J. D. (2002). Chromospheric models of a solar flare including velocity fields. *Astron. Astrophys.* 387, 678–686. doi:10.1051/0004-6361:20020454

Falchi, A., Qiu, J., and Cauzzi, G. (1997). Chromospheric evidence for magnetic reconnection. *Astronomy Astrophysics* 328, 371–380.

Fang, C., Henoux, J. C., and Gan, W. Q. (1993). Diagnostics of non-thermal processes in chromospheric flares. 1. Hoe and Call K line profiles of an atmosphere bombarded by 10-500 keV electrons. *Astronomy Astrophysics* 274, 917.

Fisher, G. H., Canfield, R. C., and McClymont, A. N. (1985a). Flare loop radiative hydrodynamics - Part Seven - dynamics of the thick target heated chromosphere. *Astrophys. J.* 289, 434. doi:10.1086/162903

Fisher, G. H., Canfield, R. C., and McClymont, A. N. (1985b). Flare loop radiative hydrodynamics - Part Six - chromospheric evaporation due to heating by nonthermal electrons. *Astrophys. J.* 289, 425. doi:10.1086/162902

Fisher, G. H., Canfield, R. C., and McClymont, A. N. (1985c). Flare loop radiative hydrodynamics. V - response to thick-target heating. VI - chromospheric evaporation due to heating by nonthermal electrons. VII - dynamics of the thick-target heated chromosphere. *Astrophys. J.* 289, 414. doi:10.1086/162901

Fisher, G. H. (1989). Dynamics of flare-driven chromospheric condensations. *Astrophys. J.* 346, 1019–1029. doi:10.1086/168084

Fleishman, G. D., Gary, D. E., Chen, B., Kuroda, N., Yu, S., and Nita, G. M. (2020). Decay of the coronal magnetic field can release sufficient energy to power a solar flare. *Science* 367, 278–280. doi:10.1126/science.aax6874

Fleishman, G. D., Nita, G. M., Chen, B., Yu, S., and Gary, D. E. (2022). Solar flare accelerates nearly all electrons in a large coronal volume. *Nature* 606, 674–677. doi:10.1038/s41586-022-04728-8

Fletcher, L., Dennis, B. R., Hudson, H. S., Krucker, S., Phillips, K., Veronig, A., et al. (2011). An observational overview of solar flares. *Space Sci. Rev.* 159, 19–106. doi:10.1007/s11214-010-9701-8

Fludra, A., Lemen, J. R., Jakimiec, J., Bentley, R. D., and Sylwester, J. (1989). Turbulent and directed plasma motions in solar flares. *Astrophys. J.* 344, 991. doi:10.1086/167866

Gary, D. E., Chen, B., Dennis, B. R., Fleishman, G. D., Hurford, G. J., Krucker, S., et al. (2018). Microwave and hard X-ray observations of the 2017 september 10 solar limb flare. *Astrophys. J.* 863, 83. doi:10.3847/1538-4357/aad0ef

Glesener, L., Krucker, S., Duncan, J., Hannah, I. G., Grefenstette, B. W., Chen, B., et al. (2020). Accelerated electrons observed down to <7 keV in a NuSTAR solar microflare. *Astrophys. J.* 891, L34. doi:10.3847/2041-8213/ab7341

Glesener, L., Krucker, S., Hannah, I. G., Hudson, H., Grefenstette, B. W., White, S. M., et al. (2017). Nustar hard x-ray observation of a sub-a class solar flare. *Astrophys. J.* 845, 122. doi:10.3847/1538-4357/aa80e9

Graham, D. R., and Cauzzi, G. (2015). Temporal evolution of multiple evaporating ribbon sources in a solar flare. *Astrophys. J.* 807, L22. doi:10.1088/2041-8205/807/2/L22

Graham, D. R., Cauzzi, G., Zangrilli, L., Kowalski, A., Simões, P., and Allred, J. (2020). Spectral signatures of chromospheric condensation in a major solar flare. *Astrophys. J.* 895, 6. doi:10.3847/1538-4357/ab88ad

Graham, D. R., Fletcher, L., and Hannah, I. G. (2011). Hinode/EIS plasma diagnostics in the flaring solar chromosphere. *Astron. Astrophys.* 532, A27. doi:10.1051/0004-6361/201015416

Guidoni, S. E., and Longcope, D. W. (2011). Density enhancements and voids following patchy reconnection. *Astrophys. J.* 730, 90. doi:10.1088/0004-637X/730/2/90

Guidoni, S. E., and Longcope, D. W. (2010). Shocks and thermal conduction fronts in retracting reconnected flux tubes. *Astrophys. J.* 718, 1476–1490. doi:10.1088/0004-637X/718/2/1476

Gustafsson, B. (1973). A FORTRAN program for calculating "continuous" absorption coefficients of stellar atmospheres. *Upps. Astron. Obs. Ann.* 5, 1–85.

Hansteen, V. (1993). A new interpretation of the redshift observed in optically thin transition region lines. *Astrophys. J.* 402, 741. doi:10.1086/172174

Harrison, R. A., Sawyer, E. C., Carter, M. K., Cruise, A. M., Cutler, R. M., Fludra, A., et al. (1995). The coronal diagnostic spectrometer for the solar and heliospheric observatory. *Sol. Phys.* 162, 233–290. doi:10.1007/BF00733431

Hawley, S. L., and Fisher, G. H. (1994). Solar flare model atmospheres. *Astrophys. J.* 426, 387. doi:10.1086/174075

Heinzel, P., and Anzer, U. (1995). Prominence fine structures in a magnetic equilibrium: Two-dimensional models with multilevel radiative transfer. *Astron. Astrophys.* 299, 1082–1090. doi:10.1051/0004-6361:20010926

Heinzel, P., Kašparová, J., Varady, M., Karlický, M., and Moravec, Z. (2016). Numerical RHD simulations of flaring chromosphere with Flarix. *Proc. Int. Astron. Union* 320, 233–238. doi:10.1017/S1743921316000363

Holman, G. D., Aschwanden, M. J., Aurass, H., Battaglia, M., Grigis, P. C., Kontar, E. P., et al. (2011). Implications of X-ray observations for electron acceleration and propagation in solar flares. *Space Sci. Rev.* 159, 107–166. doi:10.1007/s11214-010-9680-9

Hori, K., Yokoyama, T., Kosugi, T., and Shibata, K. (1998). Single and multiple solar flare loops: Hydrodynamics and Ca XIX resonance line emission. *Astrophys. J.* 500, 492–506. doi:10.1086/305725

Huang, N., Xu, Y., Sadykov, V. M., Jing, J., and Wang, H. (2019). Spectral diagnosis of Mg II and Hα lines during the initial stage of an M6.5 solar flare. *Astrophys. J. Lett.* 878, L15. doi:10.3847/2041-8213/ab2330

Hubený, I. (1982). Non-coherent scattering in subordinate lines: III. Generalized redistribution functions. *J. Quantitative Spectrosc. Radiat. Transf.* 27, 593–609. doi:10.1016/0022-4073(82)90052-8

Hurford, G. J., Krucker, S., Lin, R. P., Schwartz, R. A., Share, G. H., and Smith, D. M. (2006). Gamma-ray imaging of the 2003 october/november solar flares. *Astrophysical J. Lett.* 644, L93–L96. doi:10.1086/505329

Hurford, G. J., Schwartz, R. A., Krucker, S., Lin, R. P., Smith, D. M., and Vilmer, N. (2003). First gamma-ray images of a solar flare. *Astrophys. J.* 595, L77–L80. doi:10.1086/378179

Ichimoto, K., and Kurokawa, H. (1984). Hα red asymmetry of solar flares. *Sol. Phys.* 93, 105–121. doi:10.1007/BF00156656

Janvier, M., Aulanier, G., Pariat, E., and Démoulin, P. (2013). The standard flare model in three dimensions. III. Slip-running reconnection properties. *Astron. Astrophys.* 555, A77. doi:10.1051/0004-6361/201321164

Jeffrey, N. L. S., Kontar, E. P., and Fletcher, L. (2019). The role of energy diffusion in the deposition of energetic electron energy in solar and stellar flares. *Astrophys. J.* 880, 136. doi:10.3847/1538-4357/ab2764

Johnston, C. D., Cargill, P. J., Antolin, P., Hood, A. W., De Moortel, I., and Bradshaw, S. J. (2019). The effects of numerical resolution, heating timescales and background heating on thermal non-equilibrium in coronal loops. *Astron. Astrophys.* 625, A149. doi:10.1051/0004-6361/201834742

Johnston, C. D., Hood, A. W., Cargill, P. J., and De Moortel, I. (2017b). A new approach for modelling chromospheric evaporation in response to enhanced coronal heating. II. Non-uniform heating. *Astron. Astrophys.* 605, A8. doi:10.1051/0004-6361/201730486

Johnston, C. D., Hood, A. W., Cargill, P. J., and De Moortel, I. (2017a). A new approach for modelling chromospheric evaporation in response to enhanced coronal heating. I. The method. *Astron. Astrophys.* 597, A81. doi:10.1051/0004-6361/201629153

Judge, P. G., Carlsson, M., and Stein, R. F. (2003). On the origin of the basal emission from stellar atmospheres: Analysis of solar C II lines. *Astrophys. J.* 597, 1158–1177. doi:10.1086/381222

Karlicky, M., and Henoux, J. C. (1992). Return current losses in pulse beam heating of the solar atmosphere. *Astronomy Astrophysics* 264, 679–685.

Kašparová, J., Carlsson, M., Varady, M., and Heinzel, P. (2019). "Modelling of flare processes: A comparison of two RHD codes FLARIX and RADYN," in Proceedings of astronomical society of the pacific conference series, Paris (Astronomical Society of the Pacific).

Kašparová, J., Heinzel, P., Varady, M., and Karlický, M. (2003). "Time-dependent flare models with Mali," in *Stellar atmosphere modeling*. Editors I. Hubeny, D. Mihalas, and K. Werner (Astronomical Society of the Pacific Conference Series), 544.

Kašparová, J., Varady, M., Heinzel, P., Karlický, M., and Moravec, Z. (2009). Response of optical hydrogen lines to beam heating. I. Electron beams. *Astron. Astrophys.* 499, 923–934. doi:10.1051/0004-6361/200811559

Kerr, G. (submitted). Interrogating solar flare loop models with IRIS observations 2: Plasma properties, energy transport, and future directions. *Frontiers*. doi:10.3389/fspas.2022.1060862

Kerr, G. S., Allred, J. C., and Carlsson, M. (2019a). Modeling Mg II during solar flares. I. Partial frequency redistribution, opacity, and coronal irradiation. *Astrophys. J.* 883, 57. doi:10.3847/1538-4357/ab3c24

Kerr, G. S., Allred, J. C., and Polito, V. (2020). Solar flare arcade modeling: Bridging the gap from 1D to 3D simulations of optically thin radiation. *Astrophys. J.* 900, 18. doi:10.3847/1538-4357/abaa46

Kerr, G. S., Carlsson, M., and Allred, J. C. (2019b). Modeling Mg II during solar flares. II. Nonequilibrium effects. *Astrophys. J.* 885, 119. doi:10.3847/1538-4357/ab48ea

Kerr, G. S., Carlsson, M., Allred, J. C., Young, P. R., and Daw, A. N. (2019c). SI IV resonance line emission during solar flares: Non-LTE, nonequilibrium, radiation transfer simulations. *Astrophys. J.* 871, 23. doi:10.3847/1538-4357/aaf46e

Kerr, G. S., Fletcher, L., Russell, A. J. B., and Allred, J. C. (2016). Simulations of the Mg II k and Ca II 8542 lines from an Alfvén wave-heated flare chromosphere. *Astrophys. J.* 827, 101. doi:10.3847/0004-637X/827/2/101

Kerr, G. S., Simões, P. J. A., Qiu, J., and Fletcher, L. (2015). IRIS observations of the Mg ii h and k lines during a solar flare. *Astron. Astrophys.* 582, A50. doi:10.1051/0004-6361/201526128

Klimchuk, J. A. (2000). Cross-sectional properties of coronal loops. *Sol. Phys.* 193, 53–75. doi:10.1023/A:1005210127703

Klimchuk, J. A., and DeForest, C. E. (2020). Cross sections of coronal loop flux tubes. *Astrophys. J.* 900, 167. doi:10.3847/1538-4357/abab09

Kontar, E. P., Brown, J. C., Emslie, A. G., Hajdas, W., Holman, G. D., Hurford, G. J., et al. (2011). Deducing electron properties from hard X-ray observations. *Space Sci. Rev.* 159, 301–355. doi:10.1007/s11214-011-9804-x

Kontar, E. P., Jeffrey, N. L. S., Emslie, A. G., and Bian, N. H. (2015). Collisional relaxation of electrons in a warm plasma and accelerated nonthermal electron spectra in solar flares. *Astrophys. J.* 809, 35. doi:10.1088/0004-637X/809/1/35

Kopp, R. A. (1984). Intercomparison of numerical flare-loop models during the NASA-SMM Workshop series on solar flares. *Mem. della Soc. Astron. Ital.* 55, 811.

Kowalski, A. F., Allred, J. C., Carlsson, M., Kerr, G. S., Tremblay, P.-E., Namekata, K., et al. (2022). The atmospheric response to high nonthermal electron-beam fluxes in solar flares. II. Hydrogen-Broadening predictions for solar flare observations with the Daniel K. Inouye solar telescope. *Astrophys. J.* 928, 190. doi:10.3847/1538-4357/ac5174

Kowalski, A. F., Allred, J. C., Daw, A., Cauzzi, G., and Carlsson, M. (2017). The atmospheric response to high nonthermal electron beam fluxes in solar flares. I. Modeling the brightest NUV footpoints in the X1 solar flare of 2014 march 29. *Astrophys. J.* 836, 12. doi:10.3847/1538-4357/836/1/12

Krucker, S., Hudson, H. S., Jeffrey, N. L. S., Battaglia, M., Kontar, E. P., Benz, A. O., et al. (2011). High-resolution imaging of solar flare ribbons and its implication on the thick-target beam model. *Astrophys. J.* 739, 96. doi:10.1088/0004-637X/739/2/96

Kuhar, M., Krucker, S., Hannah, I. G., Glesener, L., Saint-Hilaire, P., Grefenstette, B. W., et al. (2017). Evidence of significant energy input in the late phase of a solar flare from NuSTAR X-ray observations. *Astrophys. J.* 835, 6. doi:10.3847/1538-4357/835/1/6

Leenaarts, J., Carlsson, M., Hansteen, V., and Rutten, R. J. (2007). Non-equilibrium hydrogen ionization in 2D simulations of the solar atmosphere. *Astron. Astrophys.* 473, 625–632. doi:10.1051/0004-6361:20078161

Leenaarts, J., Pereira, T. M. D., Carlsson, M., Uitenbroek, H., and De Pontieu, B. (2013). The Formation of IRIS diagnostics. I. A quintessential model atom of Mg II and general formation properties of the Mg II h&k lines. *Astrophys. J.* 772, 89. doi:10.1088/0004-637X/772/2/89

Leenaarts, J., Pereira, T., and Uitenbroek, H. (2012). Fast approximation of angle-dependent partial redistribution in moving atmospheres. *Astron. Astrophys.* 543, A109. doi:10.1051/0004-6361/201219394

Lemen, J. R., Title, A. M., Akin, D. J., Boerner, P. F., Chou, C., Drake, J. F., et al. (2012). The atmospheric imaging assembly (AIA) on the solar dynamics observatory (SDO). *Sol. Phys.* 275, 17–40. doi:10.1007/s11207-011-9776-8

Li, D., Hong, Z., and Ning, Z. (2022). Simultaneous observations of chromospheric evaporation and condensation during a C-class flare. *Astrophys. J.* 926, 23. doi:10.3847/1538-4357/ac426b

Li, Y., and Ding, M. D. (2011). Different patterns of chromospheric evaporation in a flaring region observed with Hinode/EIS. *Astrophys. J.* 727, 98. doi:10.1088/0004-637X/727/2/98

Li, Y., Ding, M. D., Hong, J., Li, H., and Gan, W. Q. (2019). Different signatures of chromospheric evaporation in two solar flares observed with IRIS. *Astrophys. J.* 879, 30. doi:10.3847/1538-4357/ab245a

Li, Y., Ding, M. D., Qiu, J., and Cheng, J. X. (2015). Chromospheric evaporation in an X1.0 flare on 2014 march 29 observed with IRIS and EIS. *Astrophys. J.* 811, 7. doi:10.1088/0004-637X/811/1/7

Li, Y., Kelly, M., Ding, M. D., Qiu, J., Zhu, X. S., and Gan, W. Q. (2017). Spectroscopic observations of magnetic reconnection and chromospheric evaporation in an X-shaped solar flare. *Astrophys. J.* 848, 118. doi:10.3847/1538-4357/aa89e4

Lin, R. P., Dennis, B. R., Hurford, G. J., Smith, D. M., Zehnder, A., Harvey, P. R., et al. (2002). The reuven ramaty high-energy solar spectroscopic imager (RHESSI). *Sol. Phys.* 210, 3–32. doi:10.1023/A:1022428818870

Linton, M. G., and Longcope, D. W. (2006). A model for patchy reconnection in three dimensions. *Astrophys. J.* 642, 1177–1192. doi:10.1086/500965

Liu, W., Heinzel, P., Kleint, L., and Kašparová, J. (2015). Mg ii lines observed during the X-class flare on 29 march 2014 by the interface region imaging spectrograph. *Sol. Phys.* 290, 3525–3543. doi:10.1007/s11207-015-0814-9

Longcope, D., Qiu, J., and Brewer, J. (2016). A reconnection-driven model of the hard X-ray loop-top source from flare 2004-feb-26. *Astrophys. J.* 833, 211. doi:10.3847/1538-4357/833/2/211

Longcope, D. W., and Guidoni, S. E. (2011). A model for the origin of high density in looptop X-ray sources. *Astrophys. J.* 740, 73. doi:10.1088/0004-637X/740/2/73

Longcope, D. W., Guidoni, S. E., and Linton, M. G. (2009). Gas-dynamic shock heating of post-flare loops due to retraction following localized, impulsive reconnection. *Astrophys. J.* 690, L18–L22. doi:10.1088/0004-637X/690/1/L18

Longcope, D. W., and Klimchuk, J. A. (2015). How gas-dynamic flare models powered by Petschek reconnection differ from those with ad hoc energy sources. *Astrophys. J.* 813, 131. doi:10.1088/0004-637X/813/2/131

MacKinnon, A. L., and Craig, I. J. D. (1991). Stochastic simulation of fast particle diffusive transport. *Astronomy Astrophysics* 251, 693–699.

MacNeice, P. (1986). A numerical hydrodynamic model of a heated coronal loop. *Sol. Phys.* 103, 47–66. doi:10.1007/BF00154858

Mason, H. E., Shine, R. A., Gurman, J. B., and Harrison, R. A. (1986). Spectral line profiles of Fe xxi 1354.1 A from the solar maximum mission. *Astrophys. J.* 309, 435. doi:10.1086/164615

McClymont, A. N., and Canfield, R. C. (1983). Flare loop radiative hydrodynamics. I - basic methods. *Astrophys. J.* 265, 483–506. doi:10.1086/160692

McQuillen, P., Castro, J., Bradshaw, S. J., and Killian, T. C. (2015). Emergence of kinetic behavior in streaming ultracold neutral plasmas. *Phys. Plasmas* 22, 043514. doi:10.1063/1.4918705

McQuillen, P., Castro, J., Strickler, T., Bradshaw, S. J., and Killian, T. C. (2013). Ion holes in the hydrodynamic regime in ultracold neutral plasmas. *Phys. Plasmas* 20, 043516. doi:10.1063/1.4802813

McTiernan, J. M., and Petrosian, V. (1990). The behavior of beams of relativistic nonthermal electrons under the influence of collisions and synchrotron losses. *Astrophys. J.* 359, 524. doi:10.1086/169084

Meegan, C., Lichti, G., Bhat, P. N., Bissaldi, E., Briggs, M. S., Connaughton, V., et al. (2009). THE*FERMI*GAMMA-RAY burst monitor. *Astrophys. J.* 702, 791–804. doi:10.1088/0004-637X/702/1/791

Milligan, R. O., and Dennis, B. R. (2009). Velocity characteristics of evaporated plasma using Hinode/EUV imaging spectrometer. *Astrophys. J.* 699, 968–975. doi:10.1088/0004-637X/699/2/968

Milligan, R. O. (2015). Extreme ultra-violet spectroscopy of the lower solar atmosphere during solar flares (invited review). *Sol. Phys.* 290, 3399–3423. doi:10.1007/s11207-015-0748-2

Milligan, R. O., Gallagher, P. T., Mathioudakis, M., Bloomfield, D. S., Keenan, F. P., and Schwartz, R. A. (2006). RHESSI and SOHO CDS observations of explosive chromospheric evaporation. *Astrophys. J.* 638, L117–L120. doi:10.1086/500555

Milligan, R. O. (2011). Spatially resolved nonthermal line broadening during the impulsive phase of a solar flare. *Astrophys. J.* 740, 70. doi:10.1088/0004-637X/740/2/70

Osborne, C. M. J., and Fletcher, L. (2022). Flare kernels may be smaller than you think: Modelling the radiative response of chromospheric plasma adjacent to a solar flare. *Mon. Not. R. Astron. Soc.* 516, 6066–6074. doi:10.1093/mnras/stac2570

Osborne, C. M. J., and Milić, I. (2021). The lightweaver framework for nonlocal thermal equilibrium radiative transfer in Python. *Astrophys. J.* 917, 14. doi:10.3847/1538-4357/ac02be

Panos, B., Kleint, L., Huwyler, C., Krucker, S., Melchior, M., Ullmann, D., et al. (2018). Identifying typical Mg II flare spectra using machine learning. *Astrophys. J.* 861, 62. doi:10.3847/1538-4357/aac779

Parker, E. N. (1988). Nanoflares and the solar X-ray corona. *Astrophys. J.* 330, 474. doi:10.1086/166485

Pereira, T. M. D., and Uitenbroek, H. (2015). RH 1.5D: A massively parallel code for multi-level radiative transfer with partial frequency redistribution and zeeman polarisation. *Astron. Astrophys.* 574, A3. doi:10.1051/0004-6361/201424785

Polito, V., Reep, J. W., Reeves, K. K., Simões, P. J. A., Dudík, J., Del Zanna, G., et al. (2016). Simultaneous IRIS andhinode/eis observations and modeling of the 2014 october 27 X2.0 class flare. *Astrophys. J.* 816, 89. doi:10.3847/0004-637X/816/2/89

Polito, V., Reeves, K. K., Del Zanna, G., Golub, L., and Mason, H. E. (2015). Joint high temperature observation of a small C6.5 solar flare with Iris/Eis/Aia. *Astrophys. J.* 803, 84. doi:10.1088/0004-637X/803/2/84

Polito, V., Testa, P., Allred, J., De Pontieu, B., Carlsson, M., Pereira, T. M. D., et al. (2018). Investigating the response of loop plasma to nanoflare heating using RADYN simulations. *Astrophys. J.* 856, 178. doi:10.3847/1538-4357/aab49e

Priest, E. R., and Forbes, T. G. (2002). The magnetic nature of solar flares. *Astron. Astrophys. Rev.* 10, 313–377. doi:10.1007/s001590100013

Qiu, J., Liu, W.-J., and Longcope, D. W. (2012). Heating of flare loops with observationally constrained heating functions. *Astrophys. J.* 752, 124. doi:10.1088/0004-637X/752/2/124

Qiu, J., and Longcope, D. W. (2016). Long duration flare emission: Impulsive heating or gradual heating? *Astrophys. J.* 820, 14. doi:10.3847/0004-637X/820/1/14

Reep, J. W., Bradshaw, S. J., and Alexander, D. (2015). Optimal electron energies for driving chromospheric evaporation in solar flares. *Astrophys. J.* 808, 177. doi:10.1088/0004-637X/808/2/177

Reep, J. W., Bradshaw, S. J., Crump, N. A., and Warren, H. P. (2019). Efficient calculation of non-local thermodynamic equilibrium effects in multithreaded hydrodynamic simulations of solar flares. *Astrophys. J.* 871, 18. doi:10.3847/1538-4357/aaf580

Reep, J. W., Bradshaw, S. J., and McAteer, R. T. J. (2013). On the sensitivity of the GOES flare classification to properties of the electron beam in the thick-target model. *Astrophys. J.* 778, 76. doi:10.1088/0004-637X/778/1/76

Reep, J. W., Polito, V., Warren, H. P., and Crump, N. A. (2018a). The duration of energy deposition on unresolved flaring loops in the solar corona. *Astrophys. J.* 856, 149. doi:10.3847/1538-4357/aab273

Reep, J. W., and Russell, A. J. B. (2016). Alfvénic wave heating of the upper chromosphere in flares. *Astrophys. J.* 818, L20. doi:10.3847/2041-8205/818/1/L20

Reep, J. W., Russell, A. J. B., Tarr, L. A., and Leake, J. E. (2018b). A hydrodynamic model of alfvénic wave heating in a coronal loop and its chromospheric footpoints. *Astrophys. J.* 853, 101. doi:10.3847/1538-4357/aaa2fe

Reep, J. W., Siskind, D. E., and Warren, H. P. (2022a). Solar flare irradiance: Observations and physical modeling. *Astrophys. J.* 927, 103. doi:10.3847/1538-4357/ac4784

Reep, J. W., Ugarte-Urra, I., Warren, H. P., and Barnes, W. T. (2022b). Geometric assumptions in hydrodynamic modeling of coronal and flaring loops. *Astrophys. J.* 933, 106. doi:10.3847/1538-4357/ac7398

Reep, J. W., Warren, H. P., Crump, N. A., and Simões, P. J. A. (2016). Transition region and chromospheric signatures of impulsive heating events. II. Modeling. *Astrophys. J.* 827, 145. doi:10.3847/0004-637X/827/2/145

Ricchiazzi, P. J. (1982). A static model of chromospheric heating in solar flares. Ph.D. thesis. San Diego: University of California.

Ricchiazzi, P. J., and Canfield, R. C. (1983). A static model of chromospheric heating in solar flares. *Astrophys. J.* 272, 739–755. doi:10.1086/161336

Rosner, R., Tucker, W. H., and Vaiana, G. S. (1978). Dynamics of the quiescent solar corona. *Astrophys. J.* 220, 643–645. doi:10.1086/155949

Rubio da Costa, F., Kleint, L., Petrosian, V., Sainz Dalda, A., and Liu, W. (2015). Solar flare chromospheric line emission: Comparison between IBIS high-resolution observations and radiative hydrodynamic simulations. *Astrophys. J.* 804, 56. doi:10.1088/0004-637X/804/1/56

Sadykov, V. M., Kosovichev, A. G., Sharykin, I. N., and Kerr, G. S. (2019). Statistical study of chromospheric evaporation in impulsive phase of solar flares. *Astrophys. J.* 871, 2. doi:10.3847/1538-4357/aaf6b0

Sadykov, V. M., Vargas Dominguez, S., Kosovichev, A. G., Sharykin, I. N., Struminsky, A. B., and Zimovets, I. (2015). Properties of chromospheric evaporation and plasma dynamics of a solar flare fromirisobservations. *Astrophys. J.* 805, 167. doi:10.1088/0004-637X/805/2/167

Sainz Dalda, A., de la Cruz Rodríguez, J., De Pontieu, B., and Gošić, M. (2019). Recovering thermodynamics from spectral profiles observed by IRIS: A machine and deep learning approach. *Astrophys. J.* 875, L18. doi:10.3847/2041-8213/ab15d9

Scharmer, G. B., and Carlsson, M. (1985). A new approach to multi-level non-LTE radiative transfer problems. *J. Comput. Phys.* 59, 56–80. doi:10.1016/0021-9991(85)90107-X

Scharmer, G. B. (1981). Solutions to radiative transfer problems using approximate lambda operators. *Astrophys. J.* 249, 720–730. doi:10.1086/159333

Scott, R. B., Bradshaw, S. J., and Linton, M. G. (2022). The dynamic evolution of solar wind streams following interchange reconnection. *Astrophys. J.* 933, 72. doi:10.3847/1538-4357/ac7144

Sellers, S. G., Milligan, R. O., and McAteer, R. T. J. (2022). Call and response: A time-resolved study of chromospheric evaporation in a large solar flare. *Astrophys. J.* 936, 85. doi:10.3847/1538-4357/ac87a9

Shibata, K., and Magara, T. (2011). Solar flares: Magnetohydrodynamic processes. *Living Rev. Sol. Phys.* 8, 6. doi:10.12942/lrsp-2011-6

Shimizu, T., Imada, S., Kawate, T., Ichimoto, K., Suematsu, Y., Hara, H., et al. (2019). "The Solar-C_EUVST mission," in *UV, X-ray, and gamma-ray space instrumentation for Astronomy XXI of society of photo-optical instrumentation engineers (SPIE)* (San Diego: SPIE digital library), 1111807. doi:10.1117/12.2528240

Sollum, E. (1999). Hydrogen ionization in the solar atmosphere : Exact and simplified treatments. Master's thesis. Oslo: Univeristy of Oslo.

Spruit, H. C. (1981). Motion of magnetic flux tubes in the solar convection zone and chromosphere. *Astronomy Astrophysics* 98, 155–160.

Teriaca, L., Falchi, A., Falciani, R., Cauzzi, G., and Maltagliati, L. (2006). Dynamics and evolution of an eruptive flare. *Astron. Astrophys.* 455, 1123–1133. doi:10.1051/0004-6361:20065065

Testa, P., De Pontieu, B., Allred, J., Carlsson, M., Reale, F., Daw, A., et al. (2014). Evidence of nonthermal particles in coronal loops heated impulsively by nanoflares. *Science* 346, 1255724. doi:10.1126/science.1255724

Tian, H., Li, G., Reeves, K. K., Raymond, J. C., Guo, F., Liu, W., et al. (2014). Imaging and spectroscopic observations of magnetic reconnection and chromospheric evaporation in a solar flare. *Astrophys. J.* 797, L14. doi:10.1088/2041-8205/797/2/L14

Tian, H., Young, P. R., Reeves, K. K., Chen, B., Liu, W., and McKillop, S. (2015). Temporal evolution of chromospheric evaporation: Case studies of the M1.1 flare on 2014 september 6 and X1.6 flare on 2014 september 10. *Astrophys. J.* 811, 139. doi:10.1088/0004-637X/811/2/139

Uitenbroek, H. (2001). Multilevel radiative transfer with partial frequency redistribution. *Astrophys. J.* 557, 389–398. doi:10.1086/321659

Uitenbroek, H. (2002). The effect of coherent scattering on radiative losses in the solar Ca II K line. *Astrophys. J.* 565, 1312–1322. doi:10.1086/324698

Unverferth, J., and Longcope, D. (2021). Examining flux tube interactions as a cause of sub-alfvénic outflow. *Astrophys. J.* 923, 248. doi:10.3847/1538-4357/ac312e

Unverferth, J., and Longcope, D. (2020). Modeling observable differences in flare loop evolution due to reconnection location and current sheet structure. *Astrophys. J.* 894, 148. doi:10.3847/1538-4357/ab88cf

Varady, M., Karlický, M., Moravec, Z., and Kašparová, J. (2014). Modifications of thick-target model: Re-acceleration of electron beams by static and stochastic electric fields. *Astron. Astrophys.* 563, A51. doi:10.1051/0004-6361/201322391

Varady, M., Kasparova, J., Moravec, Z., Heinzel, P., and Karlicky, M. (2010). Modeling of solar flare plasma and its radiation. *IEEE Trans. Plasma Sci. IEEE Nucl. Plasma Sci. Soc.* 38, 2249–2253. doi:10.1109/TPS.2010.2057449

Vernazza, J. E., Avrett, E. H., and Loeser, R. (1981). Structure of the solar chromosphere. III. Models of the EUV brightness components of the quiet sun. *Astrophys. J. Suppl. Ser.* 45, 635–725. doi:10.1086/190731

Warmuth, A., and Mann, G. (2016). Constraints on energy release in solar flares from RHESSI and GOES X-ray observations. II. Energetics and energy partition. *Astron. Astrophys.* 588, A116. doi:10.1051/0004-6361/201527475

Warmuth, A., and Mann, G. (2020). Thermal-nonthermal energy partition in solar flares derived from X-ray, EUV, and bolometric observations. Discussion of recent studies. *Astron. Astrophys.* 644, A172. doi:10.1051/0004-6361/202039529

Warren, H. P., Reep, J. W., Crump, N. A., and Simões, P. J. A. (2016). Transition region and chromospheric signatures of impulsive heating events. I. Observations. *Astrophys. J.* 829, 35. doi:10.3847/0004-637X/829/1/35

Watanabe, T., Hara, H., Sterling, A. C., and Harra, L. K. (2010). Production of high-temperature plasmas during the early phases of a C9.7 flare. *Astrophys. J.* 719, 213–219. doi:10.1088/0004-637X/719/1/213

Woods, T. N. (2014). Extreme ultraviolet late-phase flares: Before and during the solar dynamics observatory mission. *Sol. Phys.* 289, 3391–3401. doi:10.1007/s11207-014-0483-0

Woods, T. N., Hock, R., Eparvier, F., Jones, A. R., Chamberlin, P. C., Klimchuk, J. A., et al. (2011). New solar extreme-ultraviolet irradiance observations during flares. *Astrophys. J.* 739, 59. doi:10.1088/0004-637X/739/2/59

Young, P. R., Doschek, G. A., Warren, H. P., and Hara, H. (2013). Properties of a solar flare kernel observed by Hinode and SDO. *Astrophys. J.* 766, 127. doi:10.1088/0004-637X/766/2/127

Young, P. R., Tian, H., and Jaeggli, S. (2015). The 2014 march 29 X-flare: Subarcsecond resolution observations of Fe XXI λ1354.1. *Astrophys. J.* 799, 218. doi:10.1088/0004-637X/799/2/218

Yu, K., Li, Y., Ding, M. D., Li, D., Zhou, Y.-A., and Hong, J. (2020). IRIS Si IV line profiles at flare ribbons as indications of chromospheric condensation. *Astrophys. J.* 896, 154. doi:10.3847/1538-4357/ab9014

Zacharias, P., Hansteen, V. H., Leenaarts, J., Carlsson, M., and Gudiksen, B. V. (2018). Disentangling flows in the solar transition region. *Astron. Astrophys.* 614, A110. doi:10.1051/0004-6361/201732055

Zarro, D. M., Canfield, R. C., Strong, K. T., and Metcalf, T. R. (1988). Explosive plasma flows in a solar flare. *Astrophys. J.* 324, 582. doi:10.1086/165919

Zhang, Q. M., Li, D., and Ning, Z. J. (2016). Chromospheric condensation and quasi-periodic pulsations in a circular-ribbon flare. *Astrophys. J.* 832, 65. doi:10.3847/0004-637X/832/1/65

Zharkova, V. V., Arzner, K., Benz, A. O., Browning, P., Dauphin, C., Emslie, A. G., et al. (2011). Recent advances in understanding particle acceleration processes in solar flares. *Space Sci. Rev.* 159, 357–420. doi:10.1007/s11214-011-9803-y

Zhu, C., Qiu, J., and Longcope, D. W. (2018). Two-phase heating in flaring loops. *Astrophys. J.* 856, 27. doi:10.3847/1538-4357/aaad10

frontiers | Frontiers in Astronomy and Space Sciences

TYPE Review
PUBLISHED 06 January 2023
DOI 10.3389/fspas.2022.1060862

OPEN ACCESS

EDITED BY
Fabio Reale,
University of Palermo, Italy

REVIEWED BY
Jeffrey Reep,
United States Naval Research Laboratory, United States
David Kuridze,
Aberystwyth University, United Kingdom

*CORRESPONDENCE
Graham S. Kerr,
graham.s.kerr@nasa.gov,
kerrg@cua.edu

SPECIALTY SECTION
This article was submitted to Stellar and Solar Physics, a section of the journal Frontiers in Astronomy and Space Sciences

RECEIVED 03 October 2022
ACCEPTED 12 December 2022
PUBLISHED 06 January 2023

CITATION
Kerr GS (2023), Interrogating solar flare loop models with IRIS observations 2: Plasma properties, energy transport, and future directions.
Front. Astron. Space Sci. 9:1060862.
doi: 10.3389/fspas.2022.1060862

Interrogating solar flare loop models with IRIS observations 2: Plasma properties, energy transport, and future directions

Graham S. Kerr[1,2]*

[1]Department of Physics the Catholic Univeristy of America, Washington, DC, United States, [2]NASA Goddard Space Flight Center Heliophysics Sciences Division Code 671, Greenbelt, MD, United States

During solar flares a tremendous amount of magnetic energy is released and transported through the Sun's atmosphere and out into the heliosphere. Despite over a century of study, many unresolved questions surrounding solar flares are still present. Among those are how does the solar plasma respond to flare energy deposition, and what are the important physical processes that transport that energy from the release site in the corona through the transition region and chromosphere? Attacking these questions requires the concert of advanced numerical simulations and high spatial-, temporal-, and spectral-resolution observations. While flares are 3D phenomenon, simulating the NLTE flaring chromosphere in 3D and performing parameter studies of 3D models is largely outwith our current computational capabilities. We instead rely on state-of-the-art 1D field-aligned simulations to study the physical processes that govern flares. Over the last decade, data from the Interface Region Imaging Spectrograph (IRIS) have provided the crucial observations with which we can critically interrogate the predictions of those flare loop models. Here in Paper 2 of a two-part review of IRIS and flare loop models, I discuss how forward modelling flares can help us understand the observations from IRIS, and how IRIS can reveal where our models do well and where we are likely missing important processes, focussing in particular on the plasma properties, energy transport mechanisms, and future directions of flare modelling.

KEYWORDS

solar flares, solar atmosphere, solar chromosphere, UV radiation, numerical methods, radiation transfer

1 Introduction

1.1 Solar flares

Solar flares are transient, broadband brightenings to the Sun's radiative output following the liberation of a tremendous amount of energy (up to 10^{32} erg, or larger: Emslie et al., 2012; Aschwanden et al., 2015) during magnetic reconnection (e.g.,

Priest and Forbes, 2002; Shibata and Magara, 2011; Janvier et al., 2013; Emslie et al., 2012). It is thought that this energy is subsequently transported predominately in the form of non-thermal particles. We primarily consider non-thermal electrons[1], accelerated during the reconnection process. Once they reach the denser lower solar atmosphere they thermalise *via* Coulomb collisions (e.g., Brown, 1971), heating and ionising the plasma and generating mass flows: chromospheric evaporation (upflowing material) and chromospheric condensations (downflowing material). Alternative mechanisms of energy transport in flares include non-thermal protons or heavier ions, thermal conduction following direct heating of the corona, and Alfvénic waves, discussed in more detail in **Section 3**.

There is unambiguous evidence for the presence of non-thermal particles in flares, due to the hard X-rays they produce *via* bremsstrahlung. Their ubiquitousness and the close spatial and temporal association with other flare emission (e.g., optical and UV) has bolstered the 'electron-beam' model of solar flares. Observations of hard X-rays, e.g., from the Reuven Ramaty High Energy Solar Spectroscopic Imager (RHESSI; Lin et al., 2002), can be used to infer the underlying non-thermal electron energy distribution, that itself can drive models of solar flares. There is a substantial body of literature describing the various characteristics of flares, and the means in which we observe them. I direct the reader towards the following reviews of flare observations, and flare particle acceleration and thermalisation: Benz (2008); Fletcher et al., 2011; Holman et al., 2011; Kontar et al., 2011; Zharkova et al., 2011; Milligan (2015). The bulk of the flare radiative output originates from the chromosphere and transition region, making those regions important areas of study for their diagnostic potential regarding the plasma response to energy injection, and the energy transport and release process themselves. However, speaking candidly, this potential has been somewhat squandered by the lack of routine high spatial-, temporal-, and spectral-observations of the chromosphere and transition region at UV wavelengths during flares (crucially, we lacked routine imaging spectroscopy of the flare chromosphere). That observational gap has fortunately been plugged following the launch of the Interface Region Imaging Spectrograph (IRIS; De Pontieu et al., 2014); in 2013, that now gives us an unprecedented view of the flaring chromosphere and transition region, yielding crucial new insights. Given the complex environment of these particular layers, parallel efforts to forward model the flaring lower atmosphere, and its impacts on the flaring corona, are required to make substantial progress in understanding the physics at play in flares.

This is the second paper in a two part review of how solar flare loop models in concert with IRIS observations have improved our understanding of solar flares. Between both parts I hope to emphasise that it is only by attacking the problem of flare physics *via* the combination of high quality observations and state-of-the-art models, that include the pertinent physical processes, that we can make rapid progress. Overall I aim to show: 1) how modelling has helped interpret the IRIS observations; 2) how IRIS observations have been used to interrogate and validate model predictions; and 3) how, when models fail to stand up to the stubborn reality of those observations, IRIS has led to model improvements. In Paper 1 of this review (Kerr, 2022) I provided a detailed overview of each numerical code, and discussed what we have learned from the study of Doppler motions from IRIS in the context of the non-thermal electron beam driven flare model. Also in Paper one is a more extensive introduction to solar flares. Here in Paper 2 I demonstrate how we have used the combination of IRIS and flare loop modelling to learn about plasma properties and flare energy transport mechanisms, and provide some thoughts on future directions.

IRIS is a NASA Small Explorer mission that has observed many hundreds of flares, including dozens of M and X class events. Both images (*via* the slit-jaw imager, SJI) and spectra (*via* the slit-scanning spectrograph, SG) are provided in the far- and near-UV (FUV and NUV), with a spatial resolution 0.33–0.4 arcseconds. High cadences are achievable, as low as 1 s but more generally a few seconds to tens of seconds. The strongest lines observed are Mg II h 2,803 Å and k 2,796 Å lines (chromosphere), C II 1,334 Å and 1,335 Å and Si IV 1,394 Å and 1,403 Å (transition region), and Fe XXI 1,354.1 Å (~11 MK plasma), with numerous other lines observed in the three passbands [1,332–1,358] Å [1,389–1,407] Å, and [2,783–2,834] Å. The spectral resolution is ~53 mÅ in the NUV and ~26 mÅ in the FUV. The SJI observes at $2,796 \pm 4$ Å (Mg II k), $2,832 \pm 4$ Å (Mg II wing plus quasi-continuum), $1,330 \pm 55$ Å (C II), and $1,400 \pm 55$ Å (Si IV). See De Pontieu et al., 2021 for a review of the various successes over the first near-decade of IRIS observations.

The models employed to study flares are generally field-aligned (1D) numerical codes (though there are some exceptions, e.g., the 3D radiative magnetohydrodynamic, MHD, model of Cheung et al., 2019). These codes are nimble enough to be run on timescales that make performing parameter studies of flare energy transport processes a tractable activity, and they allow us to include the relevant physical processes at the required spatial resolution (down to sub-metres) that is not yet feasible in 3D RMHD simulations. I focus on the RADYN, HYDRAD, FLARIX, and PREFT models here. A brief overview is presented below but see Paper 1 for a full description of each code.

1 Though ions likely carry significant amounts of energy (e.g., Emslie et al., 2012), the flare community primarily considers electrons since their signatures are easier to infer from hard X-rays. Flare accelerated protons and heavier ions are harder to constrain with current observational capabilities.

1.2 Summary of the models

The hydrodynamic field-aligned codes HYDRAD (Bradshaw and Mason, 2003a; Bradshaw and Mason, 2003b; Reep et al., 2013; Reep et al., 2019), RADYN (Carlsson and Stein, 1992; Carlsson and Stein, 1997; Carlsson and Stein, 2002; Abbett and Hawley, 1999; Allred et al., 2005; Allred et al., 2015), and FLARIX (Kašparová et al., 2009; Varady et al., 2010; Heinzel et al., 2016) are now well established and widely used by the solar flare community. These codes solve the equations describing the conservation of mass, momentum, charge, and energy in a single field-aligned magnetic strand rooted in the photosphere and stretching out to include the chromosphere, transition region, and corona. HYDRAD and RADYN use an adaptive grid where the size of the grid cells can vary to allow shocks and steep gradients in the atmosphere to be resolved as required (with HYDRAD varying the number of grid cells also), while FLARIX uses a fixed, but optimized, grid with ∼2000 points. The codes have various similarities and differences as regards treatment of radiation and flare energy transport, and with the numerical approaches themselves.

All three simulate the response of the atmosphere to injection of energy, typically *via* a beam of non-thermal electrons (but flare-accelerated ions can be included too). RADYN uses a Fokker-Plank treatment to model the evolution of the non-thermal electron distribution as a function of time (including return current effects), that was recently updated to use the standalone state-of-the-art non-thermal particle transport code FP[2] (Allred et al., 2020). HYDRAD uses the analytic treatment of Emslie (1978) and Hawley and Fisher (1994), and FLARIX uses a test-particle module that provides the time-dependent beam propagation including scattering terms. Dissipation of Alfvénic waves has also been implemented in both HYDRAD and RADYN (Reep and Russell, 2016; Reep et al., 2018b; Kerr et al., 2016), and all codes can include *ad hoc* time dependent heating.

Each code has been conceived and developed to focus on particular details of the flaring plasma physics problem. RADYN and FLARIX are radiation hydrodynamic codes which couple the hydrodynamic equations to the non-LTE (NLTE) 1D radiative transfer and time-dependent non-equilibrium atomic level population equations, for elements important for chromospheric energy balance. RADYN considers H, He and Ca, with Mg also sometimes included, whereas FLARIX considers H, Ca, and Mg (with plans to update the code to include He). Continua from other species are treated in LTE as background metal opacities. Optically thin losses are included by summing all transitions from the CHIANTI atomic database (Dere et al., 1997; Del Zanna et al., 2015; Del Zanna et al., 2021)[3] apart from those transitions solved in detail. Additional backwarming and photoionisations by soft X-ray, extreme ultraviolet, and ultraviolet radiation is included. Both currently use the assumption of complete frequency redistribution (CRD)[4] when solving the radiation transport problem, so that post-processing *via* other radiation transport codes such as RH (Uitenbroek, 2001), RH15D (Pereira and Uitenbroek, 2015), or MALI (Heinzel, 1995) is required. In RADYN and FLARIX the loop is modelled as one leg of a symmetric flux tube. RADYN also allows to calculate *aposteriori* (i.e. with no feedback on the plasma equations of mass, momentum, and energy) the time-dependent non-equilibrium populations and radiation transport of a desired ion *via* the minority species version of that code, MS_RADYN (Judge et al., 2003; Kerr et al., 2019b; Kerr et al., 2019c).

HYDRAD does not solve the detailed optically thick radiation transport and atomic level population equations, instead employing approximations of chromospheric radiation losses. Losses from H, Ca and Mg are included *via* the approach of Carlsson and Leenaarts (2012). The code has also recently adopted a more accurate method for computing NLTE H populations following the prescription of Sollum (1999) which approximates the radiation field in the chromosphere (Reep et al., 2019). Ion population equations, however, are solved self-consistently in full non-equilibrium ionization (NEI) for any desired element, returning a more accurate calculation of the optically thin radiative losses and spectral synthesis of optically thin lines using those ion fractions. While the treatment of optically thick radiation is less robust than in RADYN or FLARIX, HYDRAD has the advantage of being significantly less computationally demanding. Other important differences are that HYDRAD features a multi-fluid plasma that treats the electron and hydrogen temperatures separately, it solves a full length flux tube (foot-point to foot-point) of arbitrary geometry (e.g., based on a magnetic field extrapolation) and includes effects due to cross-sectional area expansion (varying inversely with the magnetic field strength), which has been shown to play an important role in dynamics (Reep et al., 2022).

2 https://github.com/solarFP/FP.

3 RADYN and FLARIX currently uses CHIANTI V8, and HYDRAD V10, but the version should be noted in the relevant studies.

4 As stated in Paper 1: CRD assumes that the wavelength of a scattered/emitted photon is uncorrelated to the wavelength at which it was absorbed, due to collisions (e.g., photons absorbed in the line wings may be redistributed and emitted at a wavelength in the line core). However, in relatively low-density environments such as the chromosphere there may be an insufficient number of elastic collisions such that the scattered photon has a wavelength that is correlated to that of the absorbed photon. Photons absorbed in the line wings are re-emitted in the wings, where it easier to escape. This is the partial frequency redistribution (PRD) scenario. CRD has a frequency independent source function, whereas PRD has a frequency dependent source function and the absorption profile does not equal the emission profile. See discussions in Hubený (1982), and Uitenbroek (2001), Uitenbroek (2002).

PREFT (Guidoni and Longcope, 2010; Longcope and Guidoni, 2011; Longcope and Klimchuk, 2015; Longcope et al., 2016) is a rather different code than the other three, and is a powerful tool to study the impact of magnetic loop dynamics during flares. It is a 1D MHD code that solves the thin flux tube (TFT) equations. The tube is initialized at the instant after a localized reconnection process within the current sheet has linked sections of equilibrium tubes from opposite sides of the current sheet. No further reconnection occurs, and any heating from the initializing event is neglected. In its subsequent evolution, the tube retracts under magnetic tension releasing magnetic energy and converting it to bulk kinetic energy in flows which include a component parallel to the tube. The collision between the parallel components generates a pair of propagating slow magnetosonic shocks, which resemble gas dynamic shocks as they must in the parallel limit. Radiative losses are optically thin, and normally an isothermal, but gravitationally stratified, chromosphere is included mostly as a mass reservoir. Solutions of the TFT equations show that thermal conduction carries heat away from the shocks, drastically altering the temperature and density of the post-flare plasma (Longcope and Guidoni, 2011; Longcope and Klimchuk, 2015; Longcope et al., 2016; Unverferth and Longcope, 2020).

2 Plasma properties in the flaring atmosphere

Since much of emission from the flaring chromosphere is optically thick, extracting meaningful information about the plasma properties is difficult and often requires forward modelling from flare simulations in order to interpret observations. Even in the corona where emission is optically thin, modelling is required. In this section I present some examples of where flare models have shed light on conditions in the flare atmosphere.

2.1 Understanding the flaring chromosphere via Mg II

The flare chromosphere has been studied extensively using optically thick lines, which while presenting challenges with respect to extracting useful information due to their complex formation properties, offer important diagnostics of how the plasma responds to flares. Most notably, the Hα line has been both observed and modelled in flare studies too numerous to exhaustively list or describe in detail here. Some examples include: Canfield and Ricchiazzi (1980), Canfield et al., 1984, Canfield and Gayley (1987), Canfield et al. (1991), Heinzel (1991), Gayley and Canfield (1991), Gan et al., 1992, Gan et al., 1993, Li et al., 2006, Kuridze et al., 2015, Rubio da Costa et al. (2015). Some important numerical results inform us about how conditions in the upper chromosphere result in varying characteristics of the line, such as the depth of central reversal, are related to plasma conditions. The coronal pressure, for example, was found to be an important factor in determining the depth of the central reversal, with a high coronal pressure (>100 dyne cm^{-2}) required to markedly reduce the depth or fill in the reversal (e.g., Canfield et al., 1984). The pressure is closely related to density at the formation region of Hα, such that increasing the pressure forces the transition region, and hence Hα formation height, deeper. As we will see in this section the Mg II central reversal depth is also seemingly related to conditions in the upper chromosphere. Additionally, exploring line widths and intensities could help constrain densities (*via* Stark wings) and temperatures (relative intensities of lines). Other lines have received significant attention in the past have included the Ca II H and K resonance lines, and the infrared triplet (e.g., Machado and Linsky, 1975; Fang et al., 1992; Falchi and Mauas, 2002; Kuridze et al., 2018; Ding, 1999). Non-thermal processes have also been studied numerically using chromospheric spectral lines. Non-thermal collisions between the particle beam and hydrogen or calcium have been shown to be a significant process, affecting the intensity and shape the lines (e.g., Fang et al., 1993; Druett and Zharkova, 2018; Kašparová et al., 2009), and charge exchange between ion beams and hydrogen, producing highly redshifted Lyman line emission, has been suggested as a means to diagnose the non-thermal proton distributions in the lower atmosphere (e.g. Orrall and Zirker, 1976; Canfield and Chang, 1985).

In this section I introduce the Mg II NUV spectra as observed by IRIS, which being one of the strongest lines in the IRIS passbands has become a workhorse for studying the chromosphere, including during flares. Like the spectral lines of hydrogen and calcium, their characteristics are very sensitive to atmospheric properties, with various flare effects changing both the formation location as well as local plasma conditions. Magnesium is 18 times more abundant than Calcium, consequently forming higher in altitude and sampling the upper chromosphere, a useful region for understanding energy deposition during flares. The Mg II h and k Doppler width is much smaller than that of Hα, offering advantages in sensitivity to both Doppler motions and turbulence.

2.1.1 Observational characteristics of Mg II emission

The Mg II NUV spectra, comprising the h and k resonance lines (λ2,803.52 Å and λ2,796.34 Å, respectively), the subordinate triplet (λ2,791.60 Å, λ2,798.75 Å and λ2,798.82 Å, the latter two of which are blended), and who's lower energy levels are the upper levels of the resonance lines, and the quasi-continuum that lies between them, offer a wealth of information about the chromosphere. As some of the strongest and most

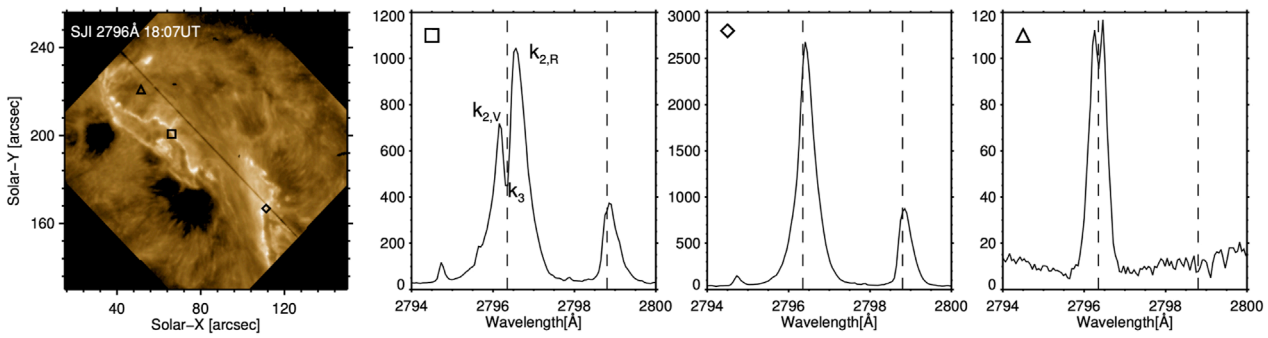

FIGURE 1
An illustration of the Mg II profiles as observed by IRIS. The map on the left shows a flare image from the SJI. The spectra in the other three panels come from the locations identified by symbols on the map. The square (second panel) is a profile from the leading edge of a flare ribbon, where the different line components are labelled. The diamond (third panel) is a source in the middle of a flare ribbon. The triangle (fourth panel) is a profile from the quiet Sun. Figure adapted from Polito et al., 2022. Reproduced with permission.

commonly observed lines in the IRIS dataset, they have been well studied both observationally and in models. They are, however, somewhat of a menace to interpret, requiring complicated radiation transfer modelling including partial frequency redistribution (PRD; meaning there is a coherency between incident and scattered photons, which effects conversion of photons from core to wing) to help extract the information they carry. Obtaining a strong almost one-to-one match even in the quiet Sun still proves very challenging, likely due to both the complexity of the radiation transfer involved, and the assumed model atmospheres (the main chronic problem is the line width, which is much too narrow in simulations). While we make progress in obtaining more consistent model-data comparisons we learn more about the formation properties of the lines and the flaring conditions that we can infer about the plasma.

The Mg II lines were comprehensively studied in the quiescent chromosphere most recently by Leenaarts et al. (2013a), Leenaarts et al. (2013b) and Pereira et al. (2013). While in active regions and flares their formation properties likely deviate from the description that follows, the quiescent studies form a basis for understanding these strong lines. These lines form throughout the chromosphere, with cores forming in the upper chromosphere, and wings forming from the upper photosphere through mid chromosphere. The resonance lines appear centrally reversed in most quiet Sun conditions (sunspots being the notable exception, though there the subordinate lines remain in absorption), with the core flanked by two emission peaks. The core is referred to as the k3 (or h3) component, and the emission peaks are collectively the k2 (or h2) components, with the blue peak referred to as k2v (or h2v) and the red peak as k2r (or h2r). **Figure 1** shows both a quiet Sun and flare Mg II k profile to illustrate these features. This central reversal forms because the line source function is decoupled from the Planck function (that is, the local temperature), and falls with increasing altitude, so intensity at the height at which optical depth is unity ($\tau_\lambda = 1$; the surface from which we see the emergent intensity at some λ) is smaller than the intensity of the emission peaks, which have a slightly smaller opacity and form somewhat deeper. Their width, the asymmetry of the strength of the flanking peaks, their intensity, the depth of the reversal, and the k/h intensity ratio all show variations depending on the source conditions (e.g., Lemaire and Skumanich, 1973; Kohl and Parkinson, 1976; Lemaire et al., 1981). The k/h intensity ratio[5], $R_{k:h}$, has a typical value around $R_{k:h} = 1.2$, indicative of optically thick line formation ($R_{k:h} = 2$, the ratio of their oscillator strengths, in optically thin formation conditions). The subordinate lines are generally in absorption, unless there is additional heating at large column depth where they typically form (e.g., Pereira et al., 2015). Note that modelling suggests that in the flaring case, the subordinate lines form much higher in altitude, and so subordinate line emission in flares is likely not a signature of deep heating, instead representing a heated mid-upper chromosphere (see, e.g., Kerr et al., 2019c; Zhu et al., 2019).

In flares the Mg II h and k profiles are seen to significantly increase their intensity (by several factors to greater than an order of magnitude), broaden (with $FWHM > 1$ Å, compared to $FWHM < \sim 0.5$ Å pre-flare), exhibit redshifted cores (several tens of km s^{-1}) and/or extreme red wing asymmetries, and to fill in their central reversal, appearing single peaked or with only a very shallow reversal (e.g., Kerr et al., 2015; Liu et al., 2015; Panos et al., 2018). These lines can appear rather Lorentzian in shape in many flare spectra. The subordinate lines come into emission and display many of the same

5 This is typically the integrated intensity, but recently Zhou et al., 2022 showed in their study of the Si IV resonance lines it can be instructive to consider the ratio as a function of wavelength.

characteristics as the resonance lines. In some cases, blue wing asymmetries are observed (e.g., Kerr et al., 2015; Tei et al., 2018; Huang et al., 2019). The k/h line intensity ratios during flares still indicate optically thick emission, and have been reported to decrease slightly. Kerr et al., 2015 found $R_{k:h}$ = 1.07–1.19 in an M-class flare, and Panos et al., 2018 found an average of $R_{k:h}$ = 1.16 from their larger survey. The range of observed $R_{k:h}$ values seems smaller in the flaring region (Kerr et al., 2015). Finally, Xu et al. (2016) and Panos et al., 2018 found that profiles located at the leading edge of some flare ribbons appeared very different to the profiles located in the bright ribbon segments. They contained deep central reversals, were much broader, had slightly blueshifted cores, and asymmetric emission peaks. The Mg II profiles from flares can vary on short timescales and small spatial scales (sometimes frame-to-frame, and pixel-by-pixel), suggesting they are extremely sensitive to plasma conditions, and therefore flare energy input.

2.1.2 Flare modelling of Mg II

Efforts to model the Mg II spectra with electron beam driven flare simulations generally leads to profiles that behave qualitatively as we might expect, but contain important quantitative issues (e.g., Liu et al., 2015; Kerr, 2017; Kerr et al., 2016; Rubio da Costa et al., 2016; Kerr et al., 2019a; Kerr et al., 2019b). For example results from RADYN + RH or using semi-empirical flare atmospheres shows that the Mg II spectra have an intensity increase (but are usually *too* intense, by up to approximately an order of magnitude or more), have redshifts and red-wing asymmetries (but the occasionally observed blue-wing asymmetries are harder to explain in the models), are broadened (but are significantly more narrow in the mid-far wings than observations, with observations in the range $FWMH \sim [0.5–2]$ Å but in typical modelling $FWHM < 0.5$ Å), have subordinate lines in emission (but which are also too narrow and too weak relative to the resonance lines, by up to several factors), and have shallower central reversals (but it is difficult to synthesise the single peaked spectra that are observed). Understanding the source of these differences can lead us to better understanding of plasma conditions and how to improve our modelling efforts to obtain those conditions.

In a data-driven study of the 2014-March-29th X-class flare Rubio da Costa et al. (2016) analysed Mg II k line observations, comparing them to forward modelling using RADYN + RH. RHESSI hard X-ray observations were used to obtain the non-thermal electron distribution over time, using 2,796 Å IRIS SJI flare source areas to estimate the energy fluxes (which ranged $F \sim [4 \times 10^{10}–10^{11}]$ erg s^{-1} cm^{-2}), and were split into 16 'threads', the timings of which were defined by the derivative of the GOES X-ray Sensor-B channel (XRS-B; 1-8Å soft X-rays). Each individual peak in the soft X-ray derivative was proposed to represent the injection of particles into the chromosphere, and the duration of the heating phase of each thread was taken from the duration of each soft X-ray peak. These threads were individually processed through RH to synthesise Mg II spectra, and were subsequently averaged in time to mimic the contribution from multiple threads over the flaring area (the heating and relaxation times of some threads overlapped). IRIS spectra were averaged over the source region of hard X-rays, and compared to the thread-averaged synthetic spectra. As hinted above, this comparison was less than ideal, with synthetic Mg II spectra having central reversals in the cores, that were much too narrow, and which at times exhibited blueshifts. There were some qualitative matches, however, with strong intensity enhancements and downflows producing redshifted line cores of up to a few tens of km s^{-1}. Contrary to what is suggested by Rubio da Costa et al. (2016), I think that the presence of a strong k2v peak in the synthetic spectra is indicative of a strong *downflow* in the upper chromosphere in the model, rather than upflows. In their Figure 13, it can be seen that the line core (the centrally reversed part of the line) is redshifted, indicating a downflow. This would shift the absorption profile to the red, meaning that k2r photons from the red peak are more strongly absorbed than k2v blue peak photons that can more easily escape. The result is a brighter blue peak relative to red peak, producing an asymmetry. The effect of mass flows on the absorption of emission in optically thick lines has been discussion in detail in the context of Ca II, Hα, and Mg II in both acoustic shocks and flares: Carlsson and Stein (1992); Kuridze et al., 2015; Kerr et al., 2016.

To address the sources of these model-data discrepancies Rubio da Costa et al. (2016) studied the line formation properties and manually varied a snapshot of the RADYN atmosphere input to RH, introducing microturbulence. They found that introducing a large microturbulent velocity (v_{turb} = 27 km s^{-1}, compared to the v_{turb} = 10 km s^{-1} assumed in the original model) could broaden the line core, but could not model the extended wings. A similar conclusion was reached by Huang et al., 2019, who performed a model-data study comparing a flare jointly observed by IRIS and Big Bear Solar Observatory/Goode Solar Telescope (BBSO/GST; Goode and Cao, 2012) to an F-CHROMA RADYN model database[6] with inputs most closely aligned with non-thermal electron distribution parameters discerned from RHESSI hard X-rays. They processed snapshots of that simulation through RH1 5D, with different values of $v_{turb} = [10, 20, 30]$ km s^{-1}, and while it seems that a single value of turbulent velocity was not able to appropriately model the line, a weighted combination was more successful at capturing the width at the time a blue-wing asymmetry appeared, which was the main focus of that work. A means to estimate the actual turbulent velocity in flares that contributes to line broadening is to measure the non-thermal line width of an optically thin line (or ideally multiple lines),

6 https://star.pst.qub.ac.uk/wiki/public/solarmodels/start.html.

which does not suffer from opacity broadening effects that muddy the waters. There are not many strong optically thin lines originating and often observed in the chromosphere so obtaining this value at multiple formation temperatures is difficult, but even a rough guide would be very useful. The O I 1,355.6 Å line observed by IRIS is optically thin in the quiet Sun (Lin and Carlsson, 2015), and preliminary modelling results suggests that it remains so during flares (e.g. Kerr et al., 2019c, plus Prof. M. Carlsson *private communication 2022*). This line has been relatively little studied observationally, but some estimates of v_{nthm}~9–10 km s^{-1} were obtained in an M class flare (Kerr, 2017), and similar values have been seen in C-class flares (Dr. Sargam Mulay, *private communication 2022*), a slight increase from the ~7 km s^{-1} measured in plage (Carlsson et al., 2015). More flare observations of this important line should be studied, especially in relation to Mg II line widths. The value required by Rubio da Costa et al. (2016) is rather high compared to the (albeit, limited) estimates courtesy of O I 1,355.6, and could be unfeasibly large, approaching the sound speed of the chromosphere. Though, flares are very complex environments and it remains to be seen what a full survey of O I reveals, and understanding how much of the missing width is due to turbulence is important to constrain the requirements of other sources to explain the deficit.

Returning to Rubio da Costa et al. (2016), they also experimented with manually raising the electron density by a factor of 10 (to $n_e > 10^{14}$ cm^{-3}) in a narrow region at the base of the transition region (though not in a self-consistent manner so that the temperature and other properties were fixed), which had the effect of filling in the central reversal. This was because the larger density allowed a greater degree of collisional coupling to local conditions[7], and the Mg II k line core source function increased with height, tracking the rise of the Planck function more closely, past the point at which the $\tau_\lambda = 1$. This suggests that in actual flares, extremely large densities are present in the upper chromosphere/lower transition region, to drive the line to appearing single peaked.

Given the discrepancies identified by Rubio da Costa et al. (2016) and other authors Rubio da Costa and Kleint (2017), decided to perform a much larger parametric study to determine what aspects of the flaring atmosphere had to change in order to produce Mg II NUV spectra more consistent with observations. They took a snapshot from one of the RADYN simulations from Rubio da Costa et al. (2016), and manually varied the temperature, electron density, and velocity structure of the flaring chromosphere in a systematic way, that were processed through RH. They varied one parameter at a time, and did not re-solve the atmosphere to hydrostatic equilibrium given the updated parameter, in order to discern the direct impact of, for example, temperature variations by itself. This means that charge was not conserved in their models, and the atmospheres investigated were not self-consistent. Still Rubio da Costa and Kleint (2017), provided great insights into plasma conditions that could be producing the observed profiles.

Introducing a steeper temperature rise in the upper chromosphere through the transition region [8], the formation region of the Mg II h and k line cores, led to weaker (by a factor ~1.5 – 2), single peaked profiles, but did not sufficiently enhance the subordinate lines so that the k:subordinate line ratio was much too high compared to the observations ($R_{k:sub}$~15 compared to the observed $R_{k:sub}$~4). Here, introducing higher temperatures forces Mg II to a deeper formation region due to thermal ionisation. At those deeper altitudes, there is a greater average electron density where the line core forms, thus stronger coupling to the local conditions that acts to fill in the central reversal. Increasing the mid chromosphere temperature did not lead to single peaked profiles but did decrease the k:subordinate line ratio closer to the observed values ($R_{k:sub}$~8). Adding temperature spikes of several thousand kelvin in the lower atmosphere (peaking at a column mass $\log_{10}\sim -2.2$ [g cm^{-3}]) resulted in prominent spikes in the blue wings of both resonance and subordinate lines that are not observed (presumably the redshifted absorption profile results in the absorption of a similar feature in the red wing).

Enhancing the electron density by a factor of ten through the formation region of the resonance line cores[9] produced single peaked profiles, and actually drove the k:subordinate line ratio closer to observations ($R_{k:sub}$~8, so within a factor two of the observations), though also increased the line intensity by around a factor of two. This is illustrated in the lefthand

7 The line source function is, roughly, a measure of the ratio of the upper and lower level populations, which depends on local conditions *via* collisions, and non-local conditions *via* the radiation field. The dominance of radiative processes over collisions, and the escape of radiation near $\tau_\lambda = 1$, means that the source function deviates from the Planck function. In fact, this is what creates the central reversal in optically thick lines. While the Planck function increases with height due to larger temperatures, the source function decreases as it deviates from the Planck function. The line core source function is smaller at the height where the line core k3 photons can escape ($z(\tau_{\lambda,core} = 1)$) than the source function at a deeper altitudes where the photons that create the flanking k2 peaks escape ($z(\tau_{\lambda,k3} = 1) > z(\tau_{\lambda,k2} = 1)$). Increasing collisions (e.g., *via* a larger density and temperature) helps to maintain or increase the population of the upper level *via* collisional transitions, and the source function more closely tracks the local Planck function, reducing the difference between the k2 and k3 source functions, such that the central reversal can reduce in depth or disappear.

8 Temperatures originally climbed from $log_{10}T$~4.1 [K] to $log_{10}T$~4.6 [K] between column mass of log_{10}~[−3.6, −4.3] [g cm^{-3}], before then rapidly attaining transition region/coronal temperatures a column mass of $log_{10} > -4.4$ [g cm^{-3}]. They were modified to instead increase from $log_{10}T$~4.1 [K] to $log_{10}T$~4.9 [K] at a column mass of log_{10}~[−3.4, −3.6] [g cm^{-3}], before more gradually increasing to $log_{10}T > 5.5$ [K] between column mass of log_{10} = [−3.6, −4.3] [g cm^{-3}].

9 Roughly, increasing the electron density by an order of magnitude though column masses of log_{10}~[−3.6, −3.8] [g cm^{-3}], peaking at $log_{10}n_e$~14.8 [cm^{-3}].

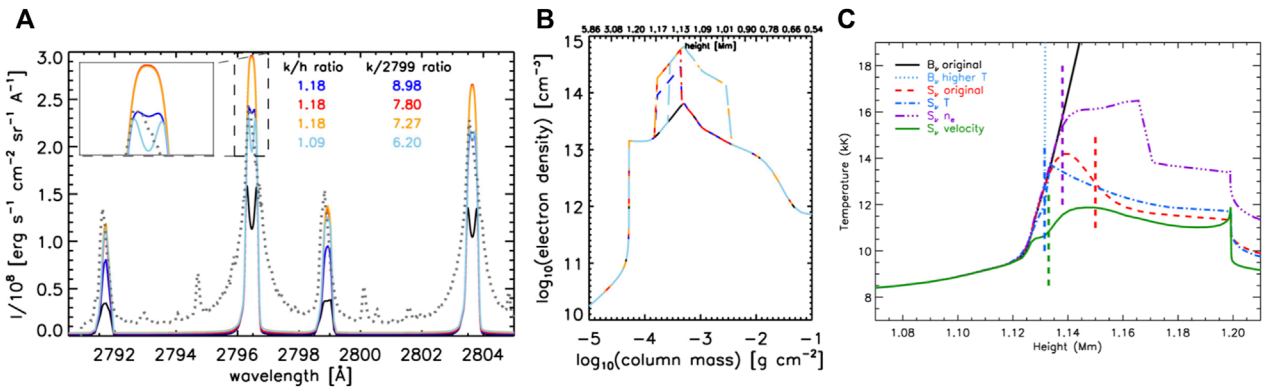

FIGURE 2
Illustrating the effect of increased electron density in the upper chromosphere on the Mg II NUV spectrum. Panel **(A)** shows the Mg II spectra synthesised from a RADYN simulation, using RH, where each colour represents a different modification to the electron density, the stratification of which is shown in panel **(B)**. The black line is the original, and the dotted line is a sample observed flare spectrum from IRIS. The resonance to subordinate line ratios are indicated. An order of magnitude increase in the electron density to $>5\times10^{14}$ cm^{-3} is required to produce a single peaked profile. **(C)** shows that increasing the electron density (purple line, compared to all others) results in a stronger coupling to the Planck function (black line), hence the lack of central reversal in that instance. The vertical lines in that panel are the formation heights of the Mg II k line core for each model atmosphere. Figure adapted from Rubio da Costa and Kleint, (2017). © AAS. Reproduced with permission.

side of **Figure 2**, which shows the Mg II NUV spectra for different electron density stratifications with fixed temperature stratification. Here the enhanced electron density resulted in stronger collisional coupling to the local temperature, that is the Planck function, which can be seen the righthand panel of **Figure 2**. Raising the electron density below the core formation heights also drove the k:subordinate ratio lower, but did not produce single peaked resonance lines. In that scenario, the electron density increases the coupling of the subordinate lines to local conditions so that the source functions, and ultimately the emergent intensities, were larger. Seemingly, increasing the electron density deeper into the atmosphere affects the subordinate lines whereas the resonance lines largely require an increased upper chromospheric density.

Varying the temperature and electron density independently could not recover the very broad line wings. Instead, experiments with introducing extremely large downflows of $v\sim200$ km s^{-1} were attempted, in concert with weaker upflows $v\sim75$–100 km s^{-1}. Combining unresolved flows did produce very broad resonance lines, but also too-weak subordinate lines. The blending of the far wings of the resonance lines with the quasi-continuum between them, and with the subordinate lines, was not well captured in those static models. While there is *prima facie* evidence from the modelling work of Rubio da Costa and Kleint (2017) that unresolved bi-directional flows can broaden the lines, my own opinion is that extreme macrovelocity 'smearing' of the lines is not the source of the missing widths far into the line wings. Such extreme flows are a difficult proposition. Downflows are typically modelled (and inferred from observations) as being much more modest, on the order of $v\sim$ a few$\times10$ km s^{-1}, and concentrated in narrow, dense condensations. While complex flows often form in loop models, even sometimes with transient downflows of $v\sim150$ km s^{-1} in extended transition regions (e.g. Zhu et al., 2019), by the time the condensations reach the chromosphere they have cooled, accrued mass and decelerated to be $v<100$ km s^{-1} (more often slower, to a few $\times10$ km s^{-1}). That is not to say that extreme bi-directional flows are not what is happening in the actual chromosphere, but we therefore must determine a means to produce such large downflows in simulations that can capture the complex interplay between flows, the subsequent accrual and evacuation of mass, and the associated changes to opacity. One observational sanity check here could be to determine the k:h line ratio as a function of wavelength over the line, which may help determine the relative opacity of the secondary blueshifted component, which formed higher in the atmosphere.

To summarise, the experiments of Rubio da Costa and Kleint (2017) suggest that increasing the upper chromosphere temperature pushes the formation height of the Mg II lines deeper, but that perhaps we are missing a temperature increase through the chromosphere to enhance the subordinate lines. The likely culprit behind filling in the central reversal is an enhanced electron density in the upper chromosphere, perhaps (in my view: certainly!) related to the dense condensations produced in RHD models and studied extensively by Prof. Kowalski and collaborators (see Paper 1). While extreme bi-directional velocity flows that are unresolved within an IRIS pixel appear to produce some of the missing line widths in their modelling, I am a bit more sceptical that these conditions can appear in the actual chromosphere. Rubio da Costa and Kleint (2017) clearly indicate that unresolved flows do play some role, but the flow magnitude required has not, to my knowledge, been inferred from typical

observations of chromospheric spectral lines. A key focus for future flare modelling should be to 1) self-consistently combine several aspects of these important findings, e.g. a temperature rise through the lower-mid chromosphere would also raise the electron density and likely generate flows, and 2) to produce a flare model driven by some energy input that naturally produces the plasma conditions required by Rubio da Costa and Kleint (2017). We must also assess if the conditions that produce a closer match to Mg II observations do not produce conditions that results in a discordant match to other spectral lines (e.g Hα, Ca II 8,542 or Ca II H and K).

One alternative potential resolution to the question of the missing line widths in the models is that we have been underestimating quadratic Stark broadening (electron pressure broadening). Though not terribly important for the Mg II NUV spectral lines in the quiet Sun, the many orders of magnitude enhancement of the electron density in flares could result in pressure broadening playing an outsized role[10], due to the fact that quadratic Stark broadening is a function of the electron density. In RH the quadratic Stark effect is typically computed following classical Impact Theory with various approximations (see discussion in Zhu et al., 2019), including the adiabatic approximation. As Zhu et al., 2019 demonstrate, the adiabatic approximation is likely not valid for Mg II. Instead, impact-semiclassical-theory provides a better estimate, which is included in the STARK-B database[11]. Zhu et al., 2019 modified RH to model Mg II Stark widths based on the STARK-B database, where the Stark width is a polynomial function of temperature and density. At the temperatures relevant for Mg II the STARK-B results have an order of magnitude greater value than is typically modelled by RH. A RADYN simulation was produced with a very high peak electron beam flux of $F_{peak} = 5 \times 10^{11}$ erg s^{-1} cm^{-2}, that was ramped up and down with FWHM of 20 s. Snapshots were processed through RH with and without the improved Stark broadening. The inclusion of increased Stark broadening resulted in broader profiles compared to the typical flare loop models (though only the h and k lines were strongly affected). Still, however, they remained too narrow compared to observations, and through experimentation it was found that a factor ×30 additional stark broadening was required over and above the STARK-B estimates to sufficiently broaden the lines. In that case, lines and quasi-continuum between the lines, were well reproduced, albeit with a factor ∼36 too high an intensity (which was the case with and without improved treatments of Stark broadening[12]). **Figure 3** shows the results of improving Stark broadening, and that an additional broadening factor is still required to match the far wings. Zhu et al. (2019) followed Rubio da Costa and Kleint (2017) by experimenting with different microturbulence stratifications but found that if the h and k line cores were suitably broadened *via* microturbulence, the subordinate lines had the wrong shape.

Additionally, single-peaked profiles were produced naturally by their model at several times. A detailed examination of the formation properties revealed that this happened when the electron density in the line formation region was exceptionally high (a result of the merging of several compressive flows), on the order of $n_e \simeq 8 \times 10^{14}$ cm^{-3}. The formation region was very narrow ($\Delta z = 32$ m, compared to $\Delta z \sim 100$ s m at other times), with a constantly increasing temperature. These results confirmed the findings of Rubio da Costa and Kleint (2017) that the electron density in the formation region is a key factor in understanding the typically observed Mg II lines. Zhu et al., 2019 also note that unresolved flows in their simulations did broaden lines, but not to the extent required as the flows had slowed to <50 km s^{-1} in the chromosphere, and to <10 km s^{-1} at the time of single peaked profiles. They also had difficulty producing very asymmetric red wings, instead producing transient secondary components when the flows were still strong. It could be case that smearing over an exposure time typical of IRIS observations (up to a few seconds), and to IRIS resolution, would merge the shifted and stationary components into a more asymmetric type profile. Nevertheless, Zhu et al. (2019) successfully produced a single peaked profiles, and made progress towards understanding the missing line widths. Questions remain: 1) how do we explain the factor ×∼30 still required to model the far wings? Could this be addressed by temperature/electron density enhancements in the lower atmosphere above that which we currently model with electron beams? Since the far wings are Lorenztian this seems like a plausible line of investigation; 2) how can we produce such high densities in flares in which the non-thermal electron flux derived from hard X-rays appears to be $<5 \times 10^{11}$ erg s^{-1} cm^{-2}. Have we perhaps been underestimating the energy fluxes so far, either of electron beams alone, or non-thermal electrons in conjunction with other sources of energy (for example non-thermal ions, conductive fluxes, MHD waves)?; 3) what is the impact of the pre-flare atmosphere in producing such high densities and in the overall evolution in general?

There have been a few reports of blue wing asymmetries that are concentrated early in the development of flare sources

10 Note that this is in contrast to the lower density flaring corona and transition region. Milligan (2011) found that pressure broadening played a negligible role in the broadening of optically thin lines in the corona and transition region.

11 A database of Stark widths for various atoms/ions: http://stark-b.obspm.fr/.

12 This intensity discrepancy is likely a combination of the atmospheric stratification, and other factors such as 3D radiation transfer and the assumed filling factors of the observations. While this is a large intensity offset, such exploratory studies of chromospheric observables still teach us about important physical processes, even if we do not yet simultaneously solve both the problem of intensity and broadening here.

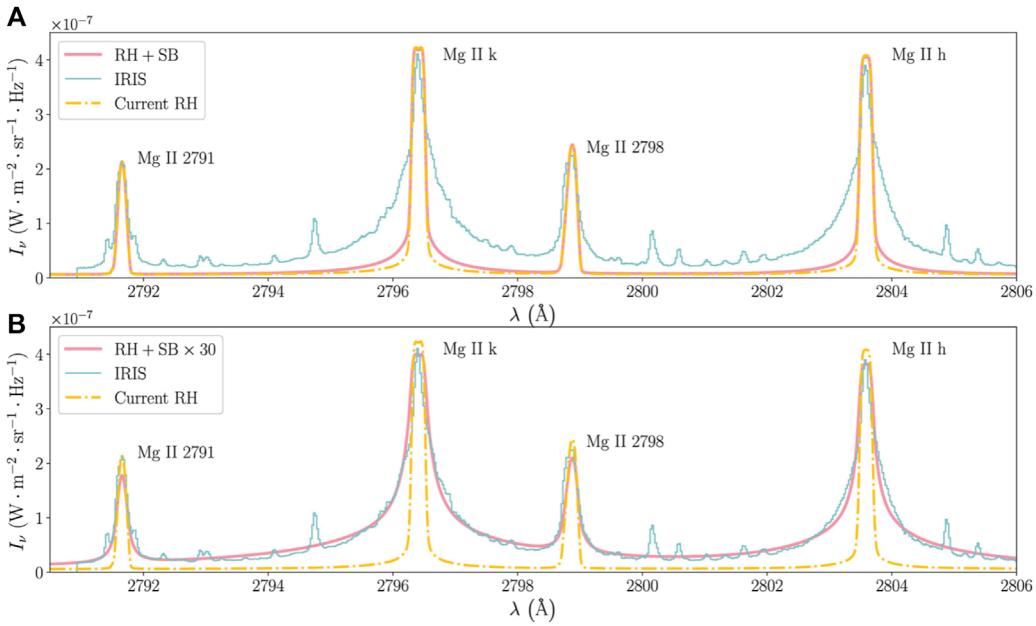

FIGURE 3
Improved treatment of Stark broadening for Mg II lines results in broader line wings. **(A)** compares a RADYN simulation processed through RH, where yellow dot-dashed is the synthetic Mg II line with standard Stark broadening, and the salmon coloured line is the line with improved Stark broadening of Zhu et al., 2019. The blue line is the observation, scaled in intensity. **(B)** illustrates that even with this improvement a further factor of ×30 Stark broadening would be required to produce a width consistent with the observation, indicating that we are still missing something in our models. Figure adapted from Zhu et al., 2019. © AAS. Reproduced with permission.

(e.g., Kerr et al., 2015; Tei et al., 2018; Huang et al., 2019). A suggestion was put forward by Tei et al., 2018 that blue wing asymmetries at ribbon fronts were produced by gentle evaporation of cool, dense chromospheric material into the corona, ahead of a hot bubble of material. This cool material is heated and dissipates. They created a cloud model that could produce Mg II h line blue wing asymmetries, along with the peak asymmetries observed. To my knowledge this has not been modelled in detail using flare loop models. A similar, but seemingly more extreme phenomenon, is the appearance of Mg II profiles that have unique shapes that only appear in the leading edge of flare ribbons (so-called ribbon fronts), found by Xu et al., 2016 and Panos et al., 2018. As mentioned above, these exhibit quite different properties to brighter flare sources (namely blueshifted line cores, deep central reversals, and very broad profiles). When present, these profiles are located along the leading edge of propagating flare ribbons, and thus represent the very initial stages of energy deposition. Other ribbon front spectral behaviour includes the *dimming* of He I 10,830 Å before it brightens during the main part of the ribbons (e.g., Xu et al., 2016). Kerr et al. (2021) demonstrated using RADYN flare modelling that this dimming is caused by the presence of non-thermal particles in the chromosphere, and that a weaker flux with a harder distribution (that is, greater proportion of high energy electrons than low energy electrons) resulted in stronger dimming that was sustained for slightly longer. However, observed ribbon front behaviour can persist for up to 120–180 s (though they can also be shorter in duration), whereas the models of Kerr et al., 2021 predicted only a few seconds. Once the chromosphere was hot enough in those simulations, the He I 10,830 Å line was driven into emission. The causes of flare ribbon fronts (which do not appear uniformly along the ribbon), and how they transition to the more typical bright ribbons we have historically studied, is not known. Work is in-progress to address the ribbon front problem using RADYN modelling of electron beam driven flares: Polito et al., 2022 investigates the relation between the magnitude of energy flux deposited and response of the Mg II ribbon front-like profiles, finding that weak energy fluxes are more consistent with ribbon-front like profiles and that stronger energy fluxes produce more 'standard' ribbon profiles. That study used the same simulations from Kerr et al., 2021, and those simulations that were most consistent with He I 10,830 Å ribbon front observations also resulted in Mg II spectra that were comparable to ribbon-front observations. The implication here is that there are potentially different stages of energy deposition to explain the evolution from ribbon-front to ribbon spectral profiles, and follow on work from Polito et al., 2022, led by myself, is investigating how to obtain longer lived ribbon fronts in both He I and Mg II. From these two on-going studies it is clear that the Mg II

ribbon front profiles can strongly constrain the characteristics of initial energy deposition into the chromosphere, and that high spatial-, temporal-, and spectral resolution observations in other wavelengths should focus on ribbon leading edges.

2.2 Hot flare plasma observed by IRIS

Prior EUV observations of hot flare lines have shown anomalously broad lines, of unknown origin (e.g., Milligan, 2011; Milligan, 2015). While several suggestions have been made, a definitive solution remains elusive (as you have no doubt realised by now, line widths are a sore spot for flare modellers). As discussed in Paper 1 in relation to probing the duration and magnitudes of chromospheric evaporation, the Fe XXI 1,354.1 Å line observed by IRIS offers a window at high spatial, temporal, and spectral resolution on hot flare plasma at ~11 MK. Here I discuss a few studies that attempted to model Fe XXI 1,354.1 Å emission in flares, concentrating on line broadening. This is a different problem than the Mg II missing width, as opacity effects play no role for Fe XXI 1,354.1 Å emission, which is a forbidden line.

The Fe XXI 1,354.1 Å line has been observed in numerous flares by IRIS (e.g., Graham and Cauzzi, 2015; Polito et al., 2015; Polito et al., 2016; Young et al., 2015; Tian et al., 2015). It is observed to be largely symmetric, with significantly enhanced line widths. It is initially weak and broad, and becomes more narrow and intense over time. The line widths during flares have ranged from the instrumental + thermal width W~0.43 Å (assuming ionisation equilibrium) at loop tops to W~[0.5–1] Å or larger in ribbons. Kerr et al., 2020 performed a superposed epoch analysis similar to Graham and Cauzzi (2015)'s Doppler shift analysis, to understand the typical evolution of Fe XXI line widths over time in the 2014-September-10th X-class flare. That event showed a large amount of scatter during the impulsive phase of the flare, but with W~[0.6–1.2] Å, peaking after t~200 s, before gradually returning to pre-flare values over the subsequent 500 s or so.

A popular suggestion for the origin of the broad line profiles of hot lines is the superposition of flows along the line of sight from numerous Doppler shifted line components. Using the RADYN code, Polito et al., 2019 explored this idea. They produced several field-aligned flare simulations, with a $t = 60$ s heating duration. Synthetic Fe XXI emission was produced, with Doppler shifts applied as appropriate as a function of height along the loop. From those simulations they constructed both single and multi-stranded loop models, which for the latter had 100 identical threads each with a randomly selected start time within 15 s of the first thread start time. Other loop lengths and energy fluxes was also tested, but no change to the overall conclusions was found. The threads were then orientated in several ways that investigated the effects of loops being co-spatial or along a ribbon-like structure within 20 IRIS pixels, either aligned in the same angle or at different orientations. Emission from each set-up was summed to mimic different scenarios of IRIS looking through different lines of sight. Polito et al., 2019 found that there was a non-negligible asymmetry, with an anti-correlation between broadening and asymmetry (broader lines were more asymmetric), in contrast to observations which showed largely symmetric lines no matter the width, in each of their scenarios. Narrow profiles were quite symmetric, and were largely due to superposition of several upflows that had similar magnitudes, but the superposition of loops was unable to characterise the broad, symmetric Fe XXI profiles in this case. **Figure 4** shows a sample of these experiments, for a single loop model with different orientations. The synthetic spectra and resulting broadening are shown, where it is clear that asymmetries are present.

Kerr et al., 2020 also studied synthetic Fe XXI line widths using RADYN simulations. The model framework they developed, RADYN_Arcade, is described in Paper 1. From the field-aligned loops grafted onto the observed magnetic field skeleton, the superposition along the line of sight, and loop geometry was automatically taken into account. Qualitatively they produced synthetic Fe XXI emission that largely followed the observations. There was line broadening that was strongest at flare footpoints, and which narrowed along the loops towards looptops. However, while some profiles exceeded W~0.8 Å the majority of the Fe XXI lines only reached W~[0.5–0.6] Å, much narrower than observed. There was not a very strong correlation between asymmetry and line width (broad profiles could be both symmetric or asymmetric), but the largest asymmetries were associated with the broadest profiles. The majority of the profiles were fit well with a single Gaussian, with only a subset requiring multiple components. There was also not a strong correlation between line width and Doppler shift, in contrast to some observations of hot flare lines studied by Milligan (2011). Finally, a synthetic superposed epoch analysis showed again a qualitative similarity to observations, but with profiles that were too narrow (with synthetic FWHM ~[0.4–0.8] Å, clustered around FWHM~0.5 Å, compared to observations with a range of FWHM ~[0.4–1.4] Å, clustered around FWHM~0.8 Å), and profiles that both peaked and narrowed in width too quickly (in observations the profiles took several hundred seconds to narrow towards pre-flare values, compared to $t < 100$ s in the model). **Figure 5** shows a map of Fe XXI from the RADYN_Arcade model at various snapshots, alongside the synthetic superposed widths, and the asymmetries *versus* line widths, illustrating the discrepancies. These results agree with the earlier findings of Polito et al., 2019.

As set out nicely by Polito et al., 2019, there are several possible physical conditions that the RADYN modelling did not account for, which might explain how to obtain a closer match to the IRIS observations. Turbulence (including MHD wave turbulence) could broaden lines symmetrically. In fact,

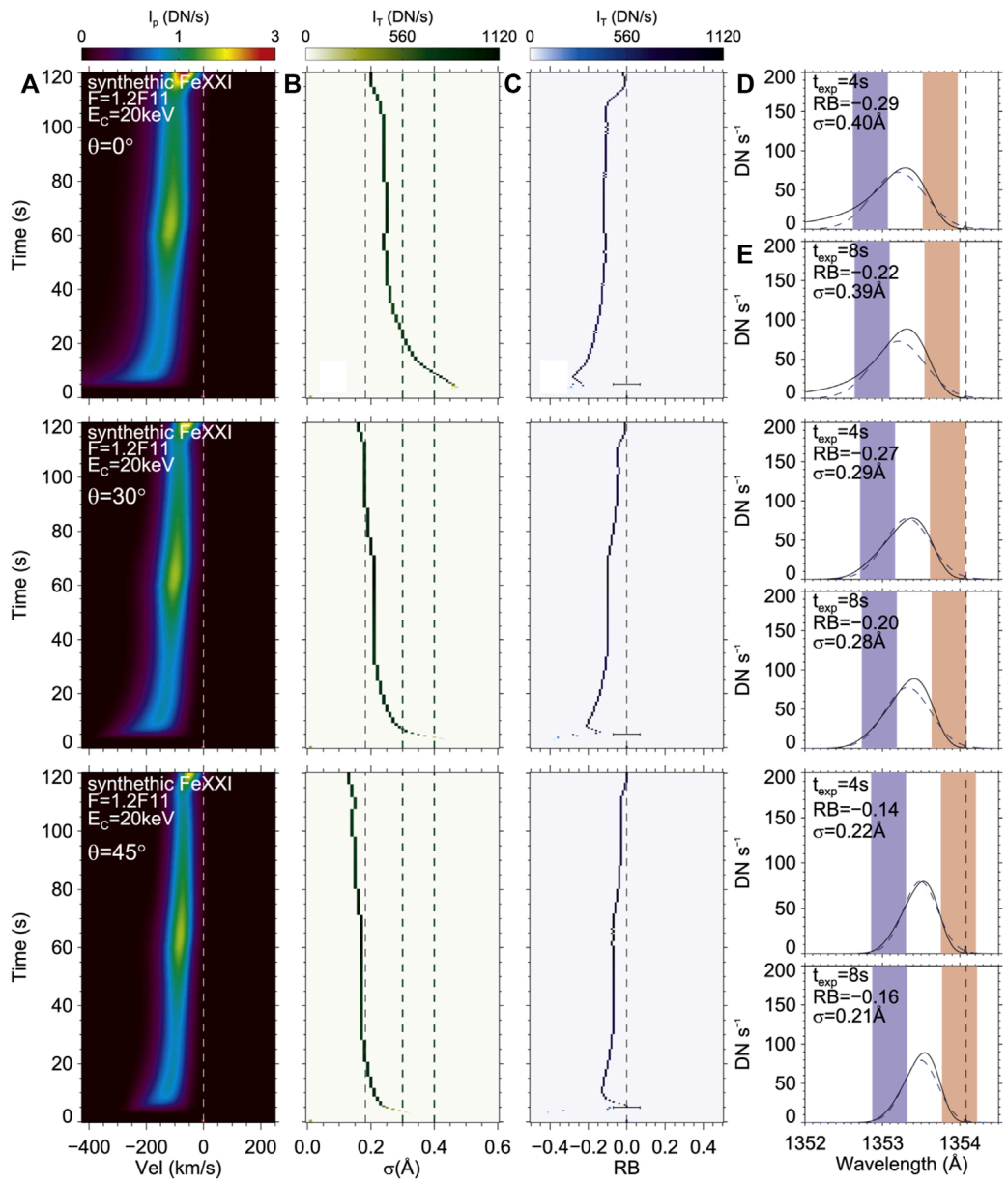

FIGURE 4
Synthetic Fe XXI 1,354.1 Å line profiles from a RADYN simulation that modelled the superposition of loops to attempt to explain line broadening. **(A)** shows the spectra as a function of time. **(B)** is the line width as a function of time, where the vertical lines are the minimum width (leftmost) and typical ranges from observations (two rightmost). **(C)** is the red-blue wing asymmetry as a function of time, where the horizontal line shows the typically observed values. **(D–E)** are synthetic spectra showing the difference in assumed exposure times. The coloured bands represent the areas used to calculate the red-blue wing asymmetry and the dashed curve is a single Gaussian fit to the spectra. The vertical line is the rest wavelength. The remaining panels show the same, but for different inclination angles of the loop to the solar surface. Figure adapted from Polito et al., 2019. © AAS. Reproduced with permission.

Allred et al., 2022 recently demonstrated that by suppressing thermal conduction in a RADYN simulation, *via* non-local effects or turbulence (e.g. Emslie and Bian, 2018), could lengthen the gradual phase of a flare, and produce a flow pattern more consistent with observations (e.g. Milligan and Dennis, 2009). Taking the turbulent mean free path of the best fit model, Allred et al., 2022 were able to estimate the broadening associated with turbulence for numerous lines (including hot lines from high charge states of Fe), finding that they were broadened substantially and symmetrically. There

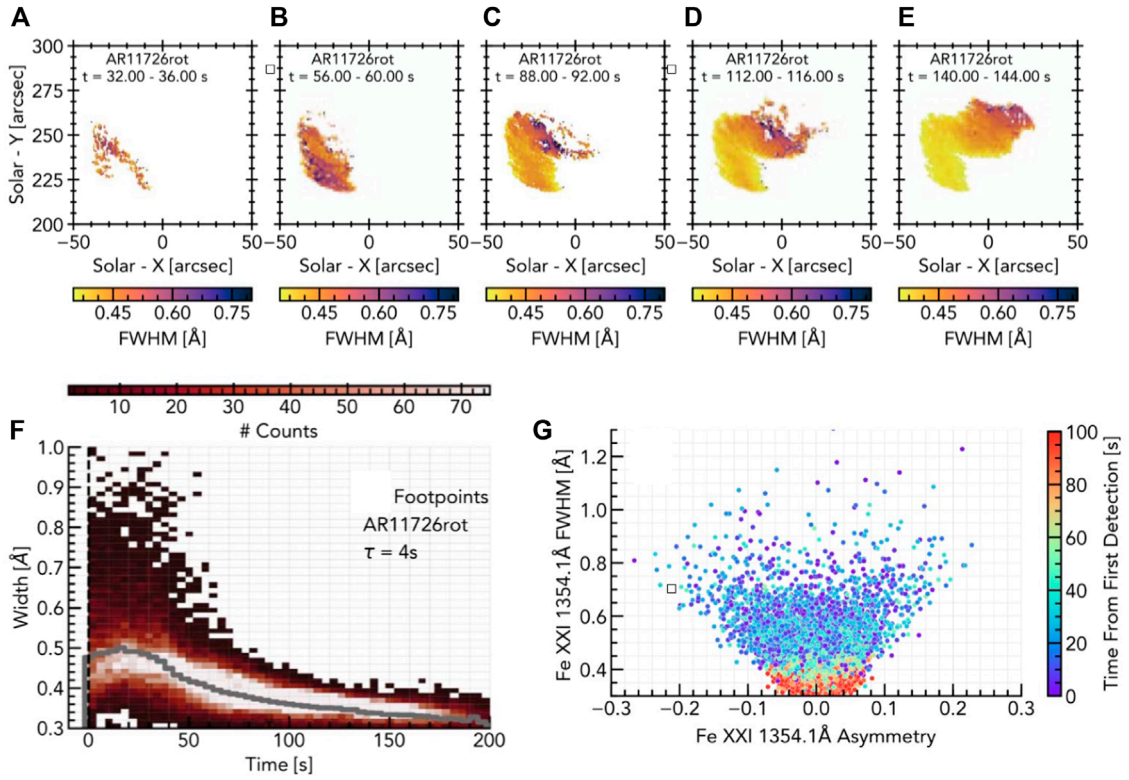

FIGURE 5
Evolution of Fe XXI widths in a RADYN_Arcade model. The top row **(A–E)** show maps of the line widths at various snapshots, illustrating that the footpoints and lower legs exhibit broader profiles. Taking all these pixels and producing a superposed epoch analysis **(F)** indicates that in comparison to an observations the line widths are too narrow. Panel **(G)** further illustrates that the profiles are too narrow, and that larger-than-observed asymmetries appear for some of the broadest profiles (colour represents elapsed time from the first moment that Fe XXI was detected in that pixel). Figure adapted from Kerr et al., 2020. © AAS. Reproduced with permission.

are plans to perform follow on studies to the modelling of Kerr et al., 2020, using these RADYN updates, and with the observed line widths from IRIS and the *Hinode*/EUV Imaging Spectrograph (EIS) observations as constraints on the degree of suppression to include. Using PREFT, Dr. William Ashfield and Dr. Dana Longcope are exploring the creation of MHD turbulence following loop retraction with added drag (*private communication 2022*). I eagerly await the application of their modelling to the formation of Fe XXI. Another source of broadening could be non-equilibrium effects, such that the ion temperature is very much larger than the equilibrium value of 11.2 MK. This would require an ion temperature on the order 40–60 MK, which also likely requires decoupling of the ion and electron temperatures (see also de Jager, 1985; Polito et al., 2018a). Given the high densities in flare footpoints, it is not clear if such extreme non-equilibrium processes apply, but the HYDRAD code is the ideal resource to study this in flares. Finally, Alfvénic waves propagating downwards from the magnetic reconnection site could broaden spectral lines *via* ion motions (see **Section 3**).

2.3 The transition region observed by IRIS

The extreme gradients through the transition region make it an important interface for mass and energy transport during flares. Strong lines produced in the transition region that are observed by IRIS are the Si IV and C II resonance lines. Aside from study of their Doppler shifts, C II has been relatively little studied in flare loop models. Si IV 1,394 Å and 1,402 Å, however, have been modelled in a few studies. I discuss their Doppler shifts in Paper 1, but here focus on their intensity ratio, and what that might tell us about temperatures and densities in the flaring transition region.

These lines have been used to infer flows in flares from their Doppler shifts, under the assumption that they are optically thin. They increase in intensity, broaden to a line width of similar magnitude to Mg II, and exhibit red wing asymmetries indicative of mass flows on the order of a few ×10–100 km s^{-1} (e.g., Tian et al., 2015; Li et al., 2017; Yu et al., 2020). Non-Gaussian line shapes have been observed in flare ribbons, but most

observations suggest optically thin formation from the ratio of the 1,394 Å/1,402 Å intensities ($R_{1394/1402} = 2$; though it is often the case that only one of the lines is included in the IRIS lineslists), with exceptions discussed later in this section. Given the optically thin assumption, most flare modelling of this line was performed by computing the emissivity from CHIANTI atomic data alongside the stratification of physical variables from flare loop model atmospheres, and summing through height in some fashion to obtain the total intensity. However, some quiescent Sun studies suggested that effects of non-equilibrium radiation transfer, photoexcitation, or charge exchange may be important in setting the Si ion fraction stratification (e.g., Dudík et al., 2017; Dzifčáková et al., 2017; Dzifčáková and Dudík, 2018; Kerr et al., 2019c). Observations of line ratios in stellar flares have also suggested that the resonance lines of Si IV, and also of C IV, exhibit opacity effects (e.g., Bloomfield et al., 2002; Mathioudakis et al., 1999) and form under optically thick conditions, or, at least with some non-negligible optical depth $\tau > 0.1$.

To determine the importance of radiation transfer effects on the formation of Si IV resonance lines during flares, Kerr et al., 2019c simulated a large number of electron beam driven flares using RADYN, and then generated the synthetic Si IV emission in two ways. The first was the standard optically thin synthesis using CHIANTI contribution functions and ionisation fractions, assuming equilibrium. The second was to use the minority species version of RADYN, MS_RADYN, to synthesise the two Si IV lines including the effects of photoionisation and photoexcitation, non-equilibrium ionisation, opacity, and charge exchange. MS_RADYN takes as input certain hydrodynamic variables at the cadence of RADYN's internal timestep (i.e. the relevant timescales to capture dynamics, not simply the output cadence), and then solves just the NLTE non-equilibrium radiation transfer for a given minority species. That is, there is no feedback of the radiation from the minority species on the atmosphere itself. The line profiles from each method were quite different, even from the pre-flare where charge exchange broadened the Si IV ion fraction stratification, which peaked slightly cooler in temperature than it does in ionisation equilibrium (T~66 kK *versus* T~80 kK). Charge exchange is generally not considered in transition region line modelling, but both the results of Kerr et al., 2019c, and recent quiet Sun modelling of Dufresne et al. (2021a), Dufresne et al. (2021b) highlight its importance. Weaker simulated flares generally produced similar results from both synthesis methods. However, in stronger flares they differed. The peak intensities of MS_RADYN Si IV profiles were smaller, but the lines broader overall due to opacity effects so that the integrated line intensities were higher. Those profiles also showed stronger asymmetries, and self-absorption features. Crucially, the intensity ratio deviated from the optically thin ratio of $R_{1394/1402} = 2$. Opacity effects were present in all simulations with an energy injection $F > 5 \times 10^{10}$ erg s^{-1} cm^{-2}, and for some weaker flares with softer electron distributions since they more easily heated the upper chromosphere and lower transition region. Some of these flares only exhibited opacity effects for a transient period, since the transition region and upper chromosphere compressed quickly, meaning there was not a sufficient column mass of Si IV to build up opacity. When there was an extended flaring lower-transition region (that is temperatures climbing through 30 kK$<T<$ 100 kK over a large height range before sharply rising to MK coronal temperatures), opacity effects were present. Roughly, opacity effects were present when the temperatures were enhanced to $40 < T < 100$ kK above a column mass 5×10^{-6} g cm^{-2}.

There have since been a number of observations of $R_{1394/1402}$ deviating from the optically thin limit $R_{1394/1402} = 2$ (e.g., Mulay and Fletcher, 2021; Zhou et al., 2022). Mulay and Fletcher (2021) found $R_{1394/1402} \neq 2$ at several locations along flare ribbons in an M7.3 flare. Zhou et al., 2022 report similar results, noting also that the ratio varies across the line profile, with stronger opacity in the core so that photons scattered from an optically thick core can easily escape through optically thin line wings. In those observations, we might infer that the flaring atmosphere produced the extended region of $40 < T < 100$ kK at sufficiently high density. It is important to note that if we do not see much observational evidence for these potentially short lived opacity effects, then our models may be predicting too much density at these intermediate temperatures. Further RT modelling, particularly of other transition region lines in conjunction with Si IV is sorely required, as are high cadence observations to catch potentially transient opacity effects. Another impact of potential opacity effects in transition region lines, and motivation for their further study, is that these are important contributors to the (assumed) optically thin radiative loss functions, which are a major component energy loss in the simulations, governing the plasma response in our models.

Panos et al., 2021 and Panos and Kleint (2021) explored, using machine learning techniques based around mutual information theory (MI; Li, 1990)[13], the correlation between the various spectral lines of IRIS through the transition region and chromosphere. I encourage the reader to read their detailed analysis carefully, in particular the subtleties surrounding selecting flaring areas and how this might impact

13 MI captures statistical dependencies, in this case between various features of different spectral lines. If the information in one spectral lines is independent from the other spectral line, the joint probability of obtaining a certain property of line X alongside a property of line Y is the product of the individual probabilities. If however the probabilities are related due to some correlation between the properties of lines X and Y then the joint probability is a more complicated evaluation. The specific elements of "information" are many and varied (for example the probability that a Mg II line has a single peak or central reversal at the same time that Si IV is doppler shifted). As applied by Panos et al., 2021 and Panos and Kleint (2021) MI aggregates the many properties and outputs a single score that describes how correlated the lines appear to be overall, which can be studied spatially and temporally.

correlations, but note the headline results here. They find weak correlations between spectral line pairs during quiescent periods, but substantially enhanced correlations of those pairs during solar flares. Mg II and C II have the strongest correlation, followed by their correlations with Si IV. Other lines (e.g. O IV) are more weakly correlated, and others such as Fe II only show strong correlations directly over flare ribbons. This coupling meant that Panos and Kleint (2021) were able to predict the most probable spectrum of a certain IRIS observable given an input Mg II spectra, for example. The strong correlation of Si IV to the chromospheric lines, despite the weak correlation of other transition region lines such as O IV, could be due to the deeper formation height suggested during the Kerr et al., 2019c simulations. Further, the coherency that flares introduce could be a result of the strong compression of the chromosphere and transition that occurs in many flare simulations. For example, Figure 11 in Kerr et al., 2019c shows that over time the range of formation height of the IRIS line cores can shrink to a very small Δz. The "big data" studies of Dr. Panos and collaborators provide an excellent test bed against which models can be critiqued—our models should be able to produce similar coherency between the various lines observed by IRIS, and this should be a target of our efforts in the near future.

Finally, I note briefly that it is typical in flare simulations from HYDRAD, RADYN, and FLARIX to produce large enhancements in electron density through the chromosphere and into the corona. These can be in excess of $n_e > 10^{13-14}$ cm^{-3} in the chromosphere, and $n_e > 10^{10-12}$ cm^{-3} through the transition region and lower corona. Indeed, as discussed in the preceding sections, a very large electron density at the Mg II formation temperatures is required to explain the single peaked profiles. IRIS and *Hinode*/EIS density sensitive lines from the corona and transition region can demonstrate if these densities are consistent with observations. Polito et al., 2016 measured the ratio of the O IV 1,399.77 Å and O IV 1,401.16 Å line pair, which form at T∼158 kK, during the impulsive phase of the X2-class flare that occurred on 2014-October-27th. The ratio reached the high-density limit, indicating that the density of the flare transition region reached $n_e > 10^{12}$ cm^{-3}. A caveat here is the assumption of ionisation equilibrium, so that the observed ratio may be in part due to non-equilibrium effects. Other assumptions are that the lines are free of unknown blends, and that the plasma is a Maxwellian, which may not be the case in solar flares, or even active regions, which have been seen to exhibit κ distributions (e,g, Jeffrey et al., 2016; Dzifčáková et al., 2018; Del Zanna et al., 2022). Similar analysis using EUV spectral lines from EIS indicated a coronal density at 2 MK of $n_e > 10^{10-11}$ cm^{-3}. Polito et al., 2016 then modelled this flare using HYDRAD, finding that the electron density in the synthetic flaring atmosphere (both flare footpoints and the transition region/lower corona) were consistent with the observationally derived values.

Pivoting slightly to white light observations, the IRIS NUV Balmer continuum modelling and observations seem to suggest that there is likely some contribution to the optical continuum excess in flares from recombination radiation in the upper chromosphere (see **Section 3.3**). Given the dependence of bound-free (and also free-free) emission on electron density, NUV and optical continuum observations of the chromosphere can give us some means to investigate the density there, and off-limb observations allow us to isolate the chromospheric portion. Off-limb observations of white light flares have revealed both the typical footpoint sources at the base of flare loops as well as bright loop structures (also referred to as prominence loop systems in some literature). The former was discussed by Heinzel et al., 2017, who analysed SDO/HMI continuum data of off-limb flares that revealed co-spatial HMI 6173 Å and RHESSI hard X-ray emission, with a characteristic height of ∼1000 km (see also Krucker et al., 2015). Using an analytical argument of the relative strength of white-light continuum emission mechanisms, Heinzel et al., 2017 determined that for electron densities above $n_e > 10^{12}$ cm^{-3} Balmer bound-free recombination emission dominated over Thomson scattering of incident radiation from the solar disk, with some contribution from free-free emission. Further comparisons using FLARIX electron-beam driven flares confirmed their supposition, with the simulations containing a high electron density ($n_e > 10^{12-13}$ cm^{-3}) at the height range of the observed HMI emission, and with an intensity as a function of height resembling the HMI observations (with some assumed loop thickness). These results are consistent with the IRIS NUV continuum flare footpoint observations. To my knowledge no off-limb IRIS NUV flare observations have been reported, and it is likely they would be fairly weak unless a long exposure time was used, but those would be very interesting to compare to the HMI sources. Looptop structures that are readily apparent in optical continuum observations pose a bit more of a challenge to models to reproduce, namely due to the very high coronal densities they imply. Several studies of very strong flares have inferred looptop electron densities between $n_e = 10^{12}$–10^{13} cm^{-3}, usually in the gradual phase of flares, presumably once loops have cooled. For example, Hiei et al., 1992 studied both footpoint and loop sources in the 16 August 1989 flare that was estimated to be an X20 class event. They predicted the intensity of emission from Thomson scattering, free-free, or recombination radiation for a range of temperatures given an assumed emitting volume, inferring from the observed intensity that $n_e = [\,5 \times 10^{11}, 2 \times 10^{12}, 1 \times 10^{13}$ cm^{-3} for $T = [10^4, 10^5, 10^6]$ K, respectively, in a loop source several hundred km above the white-light footpoint sources. A similar analysis was performed by Jejčič et al., 2018 using HMI observations from the X8.2 10 September 2017 event, finding $n_e = 10^{12}$–10^{13} cm^{-3} were the most likely values in a large parameter space of temperatures and emitting thicknesses. Inverting Ca II 8,542 Å and H β data taken by the Swedish Solar

Telescope of that same flare, Koza et al., 2019 found consistent values in the cool loops. By studying polarisation of HMI data from the X2.8 flare on 13 May 2013, Saint-Hilaire et al., 2014 determined that the emission could not be solely due to Thomson scattering and estimated an electron density in the range $n_e = 3.5 \times 10^{11}$–1.8×10^{12} cm^{-3}. While flare models can readily explain electron densities up to a few $\times 10^{11}$ cm^{-3} in the upper portion of the corona, obtaining higher electron densities at looptops is less straightforward and demands an explanation.

3 Energy transport in flares

In this section I discuss how IRIS observations are aiding our efforts to not only refine and challenge the details of the electron beam model, but also in our efforts to explore additional energy transport mechanisms. Alternative mechanisms, that may act in concert with, or instead of, non-thermal electrons (likely varying in dominance in different spatial locations) that are under active study are: non-thermal protons or ions, downward propagating Alfvénic waves, and conductive heat flux resulting from direct *in situ* heating of the corona. There are possibly others too! I do not touch on non-thermal protons or heavier ions here, other than to say it that these accelerated ions are undoubtedly produced during solar flares and that they may carry energy equivalent to that of electrons (Ramaty and Mandzhavidze, 2000; Shih et al., 2009; Emslie et al., 2012; Aschwanden et al., 2017). That means we could be missing up to half of the energy delivered to the lower atmosphere in flares! Allred et al., 2020 recently updated the FP code, which has been merged with RADYN, to model the propagation of these suprathermal ions, and initial results have demonstrated that protons can penetrate much deeper into the lower atmosphere than electrons, aided by warm target effects (e.g., Allred and Kerr, 2021). I look forward to studies that use RADYN+FP proton-beam driven flares to forward model IRIS observables.

3.1 Coronally-generated Alfvénic waves in flares

First proposed as a means of heating the temperature minimum region where non-thermal electrons likely could not reach, but which observational evidence suggested experienced a modest temperature rise in flares, Emslie and Sturrock (1982) constructed a simple but informative model of energy transport *via* downward propagating, coronally-generated, Alfvénic waves. In this model, waves would be produced from the reconnection site, propagating through the corona into the lower atmosphere to the temperature minimum region where they were damped by resistivity. These simulations assumed Mono-chromatic (single frequency) waves, employed the WKB approximation (that is, waves were not reflected by density gradients), and assumed an instantaneous travel time. These assumptions allowed a straightforward formulation of a damping length to model the dissipation.

This notion was revisited by Fletcher and Hudson (2008) who investigated the possibility that Alfvénic waves could not only deliver the energy liberated by magnetic reconnection to the chromosphere, and accelerate electrons in the corona *via* field-aligned electric fields but could also potentially locally accelerate electrons in the chromosphere *via* mode-conversion to high wave-numbers resulting in turbulent acceleration. More work is required to understand the role of these waves in particle acceleration. The thought experiments of Fletcher and Hudson (2008) explored Alfvénic waves as an alternative to the electron beam model as a means to deliver flare energy and explain observations of both hard X-rays and broadband enhancements of the UV/optical/infrared. This was motivated by perceived issues with the coronal acceleration problem, namely the vast numbers of electrons required ($>10^{36}$ elec s^{-1}), which can quickly deplete the coronal volume of ambient electrons. Return currents can resupply the corona with electrons, however, mitigating this problem.

Even if they are not required as a complete replacement to electron beams (which is still a source of vigorous debate), it is important that we continue to properly consider the role of Alfvénic waves in flares. Flares are, fundamentally, a violent restructuring of the magnetic field, meaning that MHD waves are undoubtedly produced. The question is, do they carry sufficient energy to play a non-negligible role in transporting energy compared to coronally accelerated electrons, and can they efficiently heat the chromosphere (either alongside or instead of those electrons). Additionally, we do not see hard X-rays all along the flare ribbons. Perhaps different parts of ribbons are heated by different mechanisms. Some MHD simulations by Russell and Fletcher (2013) and Russell and Stackhouse (2013) revealed that Alfvénic waves could penetrate the transition region density boundary if they had a high enough frequency, $f > 1$ Hz, meaning the WKB approximation could be used within loop models to further investigate high-frequency Alfvénic waves. They also noted that ion-neutral interactions were important, alongside electron resistivity, in damping the Alfvén waves.

Inspired by these results Reep and Russell (2016) modified HYDRAD to model Alfvén waves using the WKB approach of Emslie and Sturrock (1982), but with an updated treatment of damping which included ambipolar effects. Thus, the waves were damped by ion-neutral, neutral-electron, and electron-ion collisions. Modelling a range of Alfvén wave parameters, including the injected Poynting flux, mono-chromatic frequency, and wave number they found that they could strongly heat the chromosphere, and that they could drive explosive chromospheric evaporation. This model was further improved in HYDRAD by Reep et al., 2018b, to include the wave travel time, *via* ray-tracing so that the waves propagate at the local Alfvén

speed. They show that in addition to certain wave parameters being damped more effectively in the lower atmosphere than in the upper chromosphere, that leading waves can effectively bore a hole through the chromosphere allowing following rays to penetrate deeper into the lower atmosphere. This occurred due to ionisation by the leading waves, reducing the local damping.

Following the approach of Reep and Russell (2016), Kerr et al., 2016 included Alfvén waves as a mode of energy transport into RADYN. This initial work employed the instant-travel approximation where the wave propagation was ignored. I have since updated RADYN to include the travel time of the wave in the same manner as Reep et al., 2018b. For the remainder of this section I mostly discuss the results using the Kerr et al., 2016 model, since those are the published results relevant to IRIS, but work modelling the IRIS observables including travel time is underway *via* both HYDRAD and RADYN.

Kerr et al., 2016 compared the atmospheric dynamics and radiative output of two RADYN simulations, 1) an electron beam, and 2) a mono-chromatic Alfvén wave. The energy flux of each was set to be 1×10^{11} erg s^{-1} cm^{-2}, and the Alfvén wave parameters set to most effectively heat the upper chromosphere. A magnetic field stratification was imposed for the purpose of defining the Alfvén speed and damping lengths; it did not evolve during the simulations. Two spectral lines were compared, the Ca II 8,542 Å and Mg II k line, the latter synthesised using RADYN atmospheres with RH. While the atmospheres showed some striking similarities in each model's ability to heat the chromosphere and drive strong upflows, as was first seen in Reep and Russell (2016), there were intriguing differences in the chromospheric stratification. These differences revealed themselves in the spectral lines also.

The Alfvén waves produced a flatter, more spatially extended energy deposition profile compared to the electron-beam heating profile, resulting in temperature rises at deeper heights than the electron beam simulation. Despite this, it did take time for the electron density in the lower atmosphere to catch up to the electron beam simulation because of the absence of non-thermal collisional ionisation due to the beam itself. Runaway helium ionisation due to the more concentrated electron beam heating removed the 304 Å line as a radiator, resulting in a high temperature bubble forming, flanked by narrow cool high density regions. These flanking regions expanded as a high velocity upflow, and slower downflow (in addition to the initial explosive evaporation). While this did not form in the Alfvén wave simulation, a secondary upflow appeared in the Alfvén wave simulation also, but was more gentle with a shallower spatial gradient. In the electron beam simulation the Mg II k line had a central reversal that was redshifted during most of the heating phase. The line wings had small optically thin contributions due to the flow patterns. In the Alfvén wave simulation, however, the line formed in a gentle upflowing region of the chromosphere, shifting the absorption profile strongly to the blue. Since the densities in the upflow were relatively weak this did not fully shift the line but instead pushed the core and blue k2v peak closer in formation height until they merged. The upflow produced optically thin contributions through the blue wing. Fewer absorptions due to shifting the absorption profile boosted the red k2r peak in comparison to the heavily suppressed k2v peak, meaning that the whole profile took on a very asymmetric form. The k line could be mistaken as being single peaked with a large blue wing asymmetry. Differences in the shape of the Mg II k line cores were a direct result of the different flows, that themselves were due to the different stratifications of damping in either the electron beam or Alfvén wave energy transport mechanisms. Kerr et al., 2016 demonstrated that Mg II can help discriminate between energy transport models, but much more work needs to be done here, particularly studying multiple IRIS spectral lines forming in a wider array of Alfvén wave driven simulations that include the wave travel time. The predictions from each model should also be compared to the *k*-means classifications of Panos et al., 2018, and we must work to improve the models to include a spectrum of wave frequencies, and to constrain the properties of the waves.

While Alfvén waves are certainly produced during magnetic reconnection they have been detected *in situ* in the magnetosphere, (e.g., Chaston et al., 2005; Wygant et al., 2002; Gershman et al., 2017), a vital question is how much energy do they carry to the lower atmosphere? Is it enough to compete with electron beams as an important contributor to the flare energy budget, or is it negligible and thus safely ignorable? Thus far, the simulations of Reep and Russell (2016), Reep et al. (2018b) and Kerr et al. (2016) injected a Poynting flux of the level that we know from electron beam driven flare simulations, and bolometric flare observations, is required to significantly heat the chromosphere. An observational constraint on the Poynting flux is required. An upper limit could be placed on this by investigating the width of lines formed at different temperatures (i.e., altitudes). The non-thermal component of the width could result from ion motion in response to an Alfvén wave. To demonstrate what the upcoming EUV observations from the Multi-Slit Solar Explorer (MUSE, scheduled for launch in 2026; De Pontieu et al., 2020) would reveal about solar eruptive events, many flare models synthesised MUSE observables and demonstrated how MUSE might discriminate between model predictions (Cheung et al., 2022). As part of that effort we modelled the broadening that would be induced due to an Alfvén wave propagating down the loops in our RADYN_Arcade model, noting that the line was indeed substantially broadened. This is demonstrated in **Figure 6** which shows the RADYN_Arcade model before and after Alfvén wave broadening is included. Coordinated high spatiotemporal resolution observations between MUSE and the High Throughput EUV Solar Telescope (EUVST, also scheduled for a ∼2026 launch) could track the development of

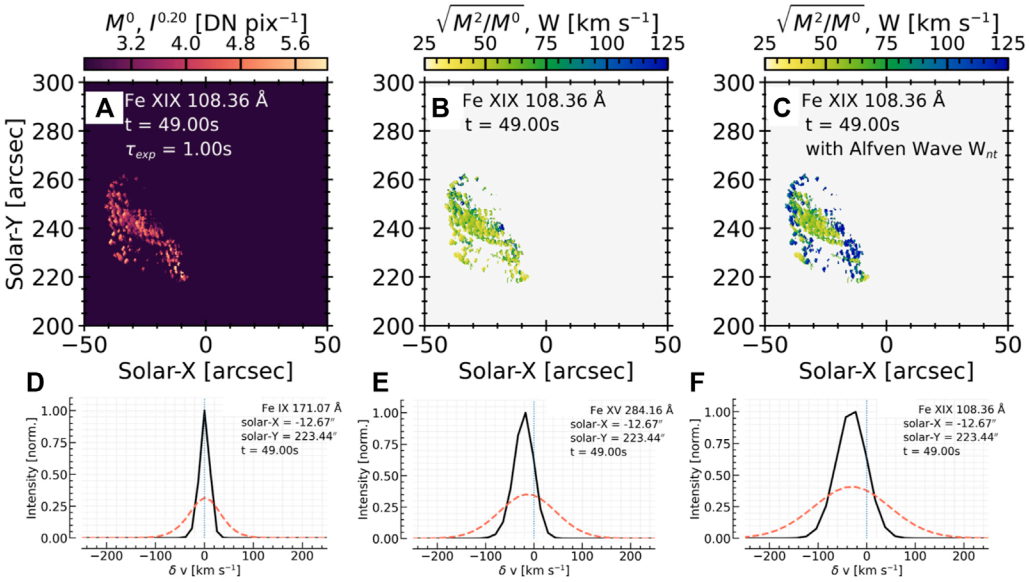

FIGURE 6
Demonstrating how Alfvén waves may explain some of the anomalous broadening of hot flare lines. In this RADYN_Arcade flare simulation predictions were made of the MUSE 108 Å line, forming at 10 MK. **(A)** shows the a map of the line intensity (zeroth spectral moment), scaled to the 1/5th power to show both weak and strong sources, at $t = 49$ s into the simulation, where hot footpoints and loop legs are apparent. **(B)** shows a map of the line widths (second spectral moment) where broadening is solely due to thermal and instrumental effects and the superposition of sources along the line of sight. **(C)** also shows a map of line width, but also includes broadening due to an Alfvén wave propagating along each loop, with a Poynting flux of 1×10^{10} erg s^{-1} cm^{-2} (a magnetic field was assumed for the purposes of calculating the Alfvén speed). Clearly the line was much broader. **(D–F)** show individual spectra, where black is the original, and the red-dashed is the Alfvén wave broadened version. Figure adapted from Cheung et al., 2022. © AAS. Reproduced with permission.

non-thermal widths during a flare, placing constraints on the Poynting flux. Knowledge of the coronal magnetic field would also be very advantageous here, to help set the Alfvén speed and damping lengths, and to determine the amplitude of magnetic field perturbations. Finally, it is worth noting that Alfvénic waves have been proposed as the mechanism responsible for the observed elemental fractionation between the photosphere and corona. Low-first ionisation potential (FIP; <10 eV) species generally have a coronal abundance that is 4 or so times that of the photosphere. The ponderomotive force generated in MHD waves has been suggested as a potential cause of the so-called FIP effect (e.g., Laming, 2015). Observations of the FIP effect in flares (e.g., Doschek et al., 2018) may then shed light on the properties of Alfvénic waves produced during flare reconnection.

3.2 High non-thermal electron energy fluxes

The energy flux injected to dynamic flare simulations has typically ranged on the order $F = 10^{9-11}$ erg s^{-1} cm^{-2}, driven in part, admittedly, because of the computational expense and difficulty of injecting very much stronger values of F into time-dependent models until fairly recently ($F > 10^{12}$ erg s^{-1} cm^{-2} fluxes, while computationally demanding, are now possible). This range has been inferred from numerous studies of flares in both the RHESSI era and before, but we are now realising that in some of the strongest flare sources we may be underestimating F, perhaps by an order of magnitude in some cases! The physical rationale and implications behind this, with regard to non-thermal particle production and transport, are beyond the scope of this review, but an important factor in tying down the existence of very high beam fluxes are the modern observations at high spatiotemporal resolution of UV and optical flare sources. IRIS, *Hinode*/Solar Optical Telescope (SOT), and ground based observatories have revealed flare sources are smaller that typically assumed from older data (particularly so if looking at white light flare data)[14]. A detailed

14 An assumption here is that the white light flare area represents the same area into which electrons are deposited. While the hard X-ray sources sizes are large due to the relatively poor spatial resolution of those instruments, we do not know with certainty that the small white light areas represent the true areas from which hard X-rays originate. There is some ambiguity as to the relative heights at which hard X-rays and white light emission is produced, though as we will see models do suggest they are close. Observations of limb flares also suggest that some white light emission and the hard X-rays come from the same volume (e.g., Krucker et al., 2015). Additionally, there could be area expansion through the loop affecting source areas. All this is to say that while we now believe that white light and UV source areas are truer representations of the area into which non-thermal electrons are deposited, it is perhaps best to say that they are a lower limit, with the upper limit coming from the hard X-rays.

study comparing source sizes from flare ribbons observed by *Hinode*/SOT to hard X-ray imaging spectroscopy suggested that the beam flux may very well be $F > 10^{12}$ erg s^{-1} cm^{-2} in that flare (Krucker et al., 2011). Further, some groups have started looking at newly activated sources to define the areas into which energy is being injected within some observational window. Newly activated sources might be as small as to be on the order 10^{16} cm^{-2} or below (Krucker et al., 2011; Sharykin and Kosovichev, 2014; Milligan et al., 2014; Kleint et al., 2016; Kowalski et al., 2017; Graham et al., 2020). IRIS observations can both guide the magnitude to inject based on high resolution observations of source areas, and act as a validation.

Kowalski et al., 2017 injected fluxes of $F = [1 \times 10^{11}, 5 \times 10^{11}]$ erg s^{-1} cm^{-2} to simulate the two brightest sources in the 2014-March-29th X-class flare, focussing on modelling the NUV continuum response. These fluxes were guided by the hard X-ray analyses of Kleint et al., 2016 and Battaglia et al., 2015, with the range based on arguments of the continuum emitting areas identified by Kowalski et al., 2017. Portions of the NUV continuum in the region $\lambda \sim$ [2,814–2,832] Å, observed by IRIS, were first identified by Heinzel and Kleint (2014), who extracted patches of continua free from lines. They determined these line-free regions as likely being part of the Balmer continuum that remained optically thin during the flare and which formed in the mid-upper chromosphere. This means the continuum response would be very sensitive to the electron density throughout the flare chromosphere. Kowalski et al., 2017's numerical experiments showed that the NUV continuum was too weak in the lower energy flux simulation, and *much* too weak in a set of experiments in which similar energy flux was instead deposited directly in the corona and allowed to conduct down to the chromosphere (potentially due to the lack of non-thermal collisional ionisations in the conduction-only simulations, though this was not commented on by the authors). In the high energy flux simulation the continuum did reach a sufficient level to match observations by t∼2 s, peaked a few seconds later, before declining thereafter (but still remaining 100–200% above the pre-flare). Thus, a high energy flux was in fact required to produce conditions to raise the continuum intensity to the observed level. An in-depth analysis found that the NUV continuum was formed by hydrogen recombination emission from two distinct layers, both optically thin: a stationary chromospheric layer and a dense condensation that rapidly forms and accrues mass. As time progressed the condensation became responsible for the bulk of the emission, due to the fact that as the density increased an increasing proportion of the non-thermal electrons thermalised in the condensation itself, and consequently the stationary layer cooled somewhat. The conditions inside this condensation were found to be comparable to those of earlier slab model explanations of Balmer continuum enhancements (e.g. Donati-Falchi et al., 1985), suggesting that condensations (and high beam fluxes) are required to explain the brightest continua enhancements.

Various effects should be accounted for when considering very large non-thermal electron flux densities, such as the beam-neutralising return current including the effects of runaways (Zharkova and Gordovskyy, 2005; Holman, 2012; Allred et al., 2020; Alaoui and Holman, 2017; Alaoui et al., 2021), and instabilities that affect the beam propagation (e.g. Hannah et al., 2009; Lee et al., 2008; Li et al., 2014). A discussion of those is included in Kowalski et al., 2017, but are beyond the scope of this review, though I note that the careful model-data analysis of the type performed by Kowalski et al., 2017 is crucial as we explore the impact of these effect in flare loop models.

3.3 Constraining flare energetics with balmer continuum observations

In the standard flare model there is typically not enough power carried by the highest energy electrons to meaningfully heat the deepest chromospheric/photospheric layers. However, there are some strands of evidence that suggest we do indeed require heating deeper than models currently predict. Listing some examples: excess line widths of chromospheric transitions (e.g., Mg II h and k) cannot be accounted for; there is evidence of heating at the temperature minimum region (e.g., from inversions of Mg I $\lambda\lambda$4571Å and $\lambda\lambda$5173Å, Metcalf et al., 1990a; Metcalf et al., 1990b); there is speculation that white light flares (WLFs) may originate from the photosphere *via* enhanced H^- emission following a local temperature increase, or contain significant contributions from the lower atmosphere (see discussions in Neidig, 1989; Machado et al., 1989; Neidig et al., 1993; Martínez Oliveros et al., 2014; Kerr and Fletcher, 2014; Kleint et al., 2016; Jurčák et al., 2018). An alternative explanation to the WLF problem is optically thin bound-free (recombination) radiation resulting from overionisation of the mid-upper chromosphere (e.g., Hudson, 1972). This would produce a Balmer jump at 3,646 Å. Of course, likely both of those mechanisms play a role. If we do need heating to great depth, then we must identify the agent capable of doing so, and constrain how much energy is required.

Given the scarcity of white light continuum observations, the NUV continuum as observed by IRIS is one such means to constrain the need for deep heating (the NUV is thought to be closely related to the optical continuum, albeit we do not yet know if they always originate from the same volume during flares). Heinzel and Kleint (2014) first determined that the Balmer continuum could be observed by IRIS, using observing windows in the NUV near λ = [2,813–2,816, 2,825–2,828, 2,831–2,834] Å. They carefully

extracted narrow, line free, portions of the spectrum, finding ∼100 – 200 % contrast compared to the pre-flare values, with an impulsive rise and more gradual decay. Comparing to bright, non-flaring features, they note that the continuum rose but lines did not (as in the flare case) suggesting that the continuum patches between the lines are unaffected by the line emission. Using the static flare models of Ricchiazzi and Canfield (1983), processed with the radiation transfer code MALI, they inferred from the similarity in model-to-data intensities and from the formation properties in the model, that the observed NUV spectra did represent the Balmer continuum, and that it was due to optically thin recombination emission in the upper chromosphere. This represented the first detection of the Balmer continuum from space based instruments, and provides a constraint on flare models due its proximity to the Balmer jump.

Following on from this initial detection, Kleint et al., 2016 studied the IRIS Balmer continuum emission alongside other continuum enhancements from both space and ground observatories, spanning the UV through infrared. They performed blackbody fits to data (including modifying the blackbody intensity due to opacity effects) to determine the viability of an upper photospheric origin to the continuum emission, finding that the NUV lay well above the blackbody curve predicted by the optical and IR emission (as expected if the NUV emission was indeed recombination radiation, producing a Balmer jump). Building upon the modelling work started by Heinzel and Kleint (2014), Kleint et al., 2016 selected a few models from Ricchiazzi and Canfield (1983) and calculated the non-LTE hydrogen recombination continuum using the MALI code. Several were consistent with the observed NUV continuum enhancements (with a non-thermal electron flux close to that derived from RHESSI observations for that flare), but those models under-predicted the optical and IR enhancements from SDO/HMI and the Facility Infrared Spectropolarimeter at the Dunn Solar Telescope (DST/FIRS). Instead, a semi-empirical model atmosphere with photospheric temperature rise was required to achieve consistency with the optical/IR observations. Finally, they manually modified atmospheres that were input to RH in an attempt to find a stratification consistent with all three regimes (UV, optical and IR). A model with a modest photospheric temperature increase alongside a strongly heated chromosphere was required, as shown in **Figure 7**. Thus, IRIS in combination with ground based observations demonstrated that in some events we may indeed need both chromospheric and photospheric heating. To my knowledge no time-dependent flare model has self-consistently produced such an atmosphere (electrons beams typically do not carry enough power to such depths), and this should be a focus of our continuing efforts. However, it should also be noted that since an optically thin source at T∼10 kK produces optical emission with a radiation temperature of 4–6 kK (see e.g. Kowalski and Allred, 2018), some ambiguity remains. At the same time as attempting to model self-consistently the heating throughout the chromosphere and photosphere to determine how to obtain atmospheres similar to the empirical models of Kleint et al., 2016, we should endeavour to obtain IRIS observations in the NUV alongside a broad spectral coverage of the optical (e.g. from DKIST) to determine the spectral shape more accurately, which would help resolve the ambiguity over emission mechanisms.

Since it will likely remain challenging to obtain observations covering the Balmer jump (and thus a guide as to the formation of the optical continuum), Kowalski et al., 2019 have begun to search for alternative metrics that can gauge the extent to which the lower atmosphere is strongly heated. Using the fact that Fe II lines observed by IRIS form under similar physical conditions as the NUV Balmer continuum (T∼8–18 kK but mostly towards the cooler end, discerned from their earlier modelling work regarding high beam fluxes; Kowalski et al., 2017), they explored the ratio of wavelength-integrated flare excess Fe II 2,814.45 Å intensity to the average continuum intensity in the region $\lambda = [2,824.5–2,825.9]$ Å. This ratio was observed to be $R_{Fe:NUV}$∼7–8 at the peak of very bright flare sources located in a sunspot umbra during the 2014-Oct-25th X class flare, significantly higher than the prediction from slab models with low-to-moderate densities of $\rho < 10^{-9}$ g cm^{-3} which had values $R_{Fe:NUV}$∼1. They speculate that this means there is significant heating (to T∼10 kK) at high column depth ($\log m \sim -2$ [g cm^{-2}]) where Fe II can be optically thick. They are currently modelling this ratio in a range of RADYN flares (*private communication 2022*), but noted that their earlier study of the 2014-March-29th X class flare (Kowalski et al., 2017) only produced an observed ratio of $R_{Fe:NUV}$∼1, with a modelled ratio of $R_{Fe:NUV}$∼1–1.8. Clearly there is something quite different at work during the 2014-Oct-25th flare. This could be due to the pre-flare atmospheres, since the 2014-October-25th flare sources propagated into the sunspot umbra, allowing a colossal 1,000% NUV contrast, and an excess intensity 20× that of the 2014-March-29th flare. Hopefully further observations from a variety of flares, and modelling of a variety of energy inputs (including varying the pre-flare atmosphere) will lead to a firm diagnostic of deep heating during IRIS flares.

The NUV continuum was forward modelled by Heinzel et al., 2016, using one of the short-pulse experiments of Kašparová et al., 2009. In those FLARIX simulations, a non-thermal energy flux was injected in a trapezoidal form over time, with peak flux $F = 4.5 \times 10^{10}$ erg s^{-1} cm^{-2}. The whole pulse was very short, only lasting 3 s. The resulting Balmer continuum intensity was quite small compared to the observations of Kleint et al., 2016. This was attributed to the magnitude of energy flux deposited in the chromosphere. It was an order of magnitude smaller than that of the flare studied by Kleint et al., 2016. Further, the short duration of this relatively moderate injection meant that evaporation was weak and the pressure in the upper chromosphere did not increase to the level inferred

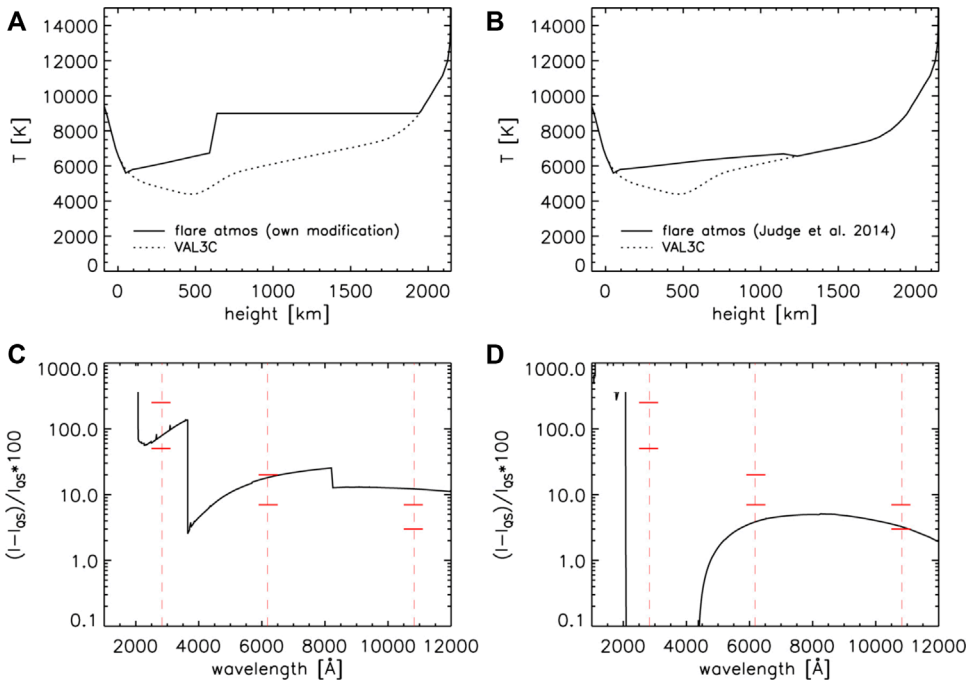

FIGURE 7
Synthetic continuum spectra from flare atmospheres processed using RH. Here Kleint et al., 2016 manually modified the temperature in the lower atmosphere to demonstrate that both a chromospheric temperature enhancement, and a temperature enhancement at greater depth **(A)** was required to synthesise the NUV and optical continuum (black line in **(C)**) that was consistent with the IRIS and SDO/HMI observations (red symbols on **(C)**). A lower atmosphere increase on its own **(B)** was not able to explain the Balmer continuum observations from IRIS **(D)**. Figure adapted from Kleint et al., 2016. © AAS. Reproduced with permission.

from the best-match Ricchiazzi and Canfield (1983) analysed by Kleint et al., 2016. This could point to the need for either longer electron beam dwell times in large flares, or for a train of short pulses. In those models the hydrogen subordinate continua, in particular the Balmer continuum, were the dominant source of radiative losses throughout the chromosphere, overtaking losses from singly ionised metals such as Ca II and Mg II, underscoring the importance of IRIS Balmer continuum observations. Since the Balmer continuum is seemingly optically thin, the radiative losses integrated through the continuum formation heights are directly related to the emergent intensity. Thus, the observed excess intensities impose strict constraints on flare energetics.

The Balmer continuum is also a useful constraint for smaller events where heating is, largely, confined to the upper chromosphere. A 'mini-flare' event accompanying a jet was studied by Joshi et al., 2020 who determined that a reconnection event occurred at the base of the jet. A small Balmer continuum excess was present in very localised sources, from both IRIS SG spectra, and the SJI 2832 Å images (Joshi et al., 2021). Comparing to the analysis of Kleint et al., 2016, who had processed the Ricchiazzi and Canfield (1983) atmospheric models using MALI to obtain predictions for the hydrogen recombination continuum, Joshi et al., 2021 found that a few simulations were consistent with their observations. This balanced the continuum intensity, as well as the brightness of the Mg II line cores. The most well matched models had non-thermal electron energy fluxes $F = 1 \times 10^{9-10}$ erg s^{-1} cm^{-2}, with $\delta = 5$ and $E_c = 20$ keV (note that the Ricchiazzi and Canfield 1983 did not sample other values of E_c and only a few values of δ for more energetic flares). From the *Fermi*/GBM (Meegan et al., 2009) hard X-ray observations, the injected non-thermal electron distribution was calculated as having an energy flux $F = 6.5 \times 10^9$ erg s^{-1} cm^{-2} for $E > 20$ keV, assuming the area into which the electrons were injected was the same as the continuum enhancement source. While there is some uncertainty in the low-energy cutoff, the parameters derived from the hard X-ray observations are consistent with those models that also provide a well-matched Balmer continuum excess intensity. Joshi et al., 2021 estimate that 82% of the intensity in the IRIS SJI 2832 Å images is continuum emission, contrasting the result from similar analysis of an X-class flare that found significant line emission (Kleint et al., 2017), which makes sense if we consider the weak energy flux involved that was unable to sufficiently excite the many lines within that part of the spectrum. In summary, small-scale reconnection at the base of a jet seemingly was able to accelerate enough electrons to bombard the upper chromosphere, enhancing the Balmer continuum, but was unable to really effect the lower chromosphere.

3.4 Flares driven by conductive heat fluxes

While there is unambiguous observational evidence for the presence of non-thermal electrons in a great many solar flares, they are not ubiquitously present. This is true both in the global sense, meaning there are some "thermal" flares that do not exhibit strong evidence of hard X-rays or microwaves of non-thermal origin, and the local sense meaning that hard X-rays sources do not appear uniformly along optical/UV flare ribbons (though this latter case may be related to the dynamic range of most hard X-ray observatories that precludes detection of weak sources alongside strong footpoints). In such flares *in situ* heating of the corona results in a conductive heat flux that transports energy to the lower atmosphere, generating the strong heating and mass flows (e.g. Zarro and Lemen, 1988; Battaglia et al., 2009; Fletcher et al., 2011; Brosius, 2012; Brosius and Holman, 2012; López et al., 2022). This is often referred to as 'direct heating', a somewhat nebulous term that refers generally to any heating of the corona (either looptops or along the legs of the loop) following the release of energy during magnetic reconnection[15], including the retraction of magnetic loops that produce shocks such as those modelled by PREFT. It is indeed likely that some form of direct coronal heating acts alongside non-thermal electrons even in flares with clear evidence of particle acceleration, but the dominance of each mechanism varies from flare to flare and with spatial location. For example, recent results using GOES soft X-ray observations suggest that in a number of flares the corona is rapidly heated to $T\sim$10–15 MK before the onset of evaporation (so-called "hot onsets" Hudson et al., 2021). Several studies have either modelled flares as being purely driven by thermal conduction (e.g., Cheng et al., 1983; MacNeice, 1986; Gan et al., 1991, to name but a few) or have contrasted predictions between electron beam and conduction driven flares (e.g., Polito et al., 2018b; Kerr et al., 2021; Cheung et al., 2022). This latter exercise should be performed more often, as it is likely that both mechanisms act but the direct heating in the corona is often ignored. As shown in Cheung et al., 2022, the inclusion of direct heating can have impacts on the predicted intensities and Doppler motions of coronal and transition region lines. Some of those effects can only be seen at very high spatial and temporal resolution, such as will be afforded by the MUSE mission (see **Section 4**).

I summarise in detail here two recent examples of modelling flares driven purely by a conductive heat flux, and what we can learn about the nature of condensations from those simulations and IRIS observations.

The seminal studies of mass flows in flare models by Fisher et al. (1985a), Fisher et al. (1985b), and Fisher (1989) revealed the relationship between flare energy input and the development of both upflows and downflows in the chromosphere. Of those, Fisher (1989) concentrated on chromospheric condensations, developing an analytical model that described the timescales and magnitudes of flare-induced downflows. Fisher (1989) built that equation of motion from generalising various properties that occurred in flare loop models. Notably, Fisher, (1989) discovered that the lifetime of the condensations depend only on the chromospheric conditions, not the energy input, and is $\tau_{life} \approx 2(H/g)^{1/2}$, where H is the chromospheric density scale height and g is gravitational acceleration. For reasonable values of H, $\tau_{life}\sim$60 s. The half-life of the condensation was $\tau_{1/2} \approx 2(H/g)^{1/2}/M_{peak}$, where M_{peak} is the ratio of the peak downflow velocity to the sound speed in the pre-flare chromosphere. Though τ_{life} does not depend on properties of the energy injection, the peak downflow velocity (and thus $\tau_{1/2}$) does, varying as $u_0 \propto F^{1/3}$, with some dependence on whether energy was transported *via* non-thermal electrons or was conducted down from a hot corona.

Ashfield and Longcope (2021) used the PREFT gas-dynamic code to study conduction-only driven chromospheric condensations, building upon and complementing the work of Fisher (1989). They found similar relationships, with some differences as described below, but using an alternative approach. They set up a simplified set of physical parameters to explore the dynamics of shocks in the chromosphere using jump conditions, and compared those predictions to numerical experiments. The analytical model informed a subsequent analysis and interpretation of numerical results from PREFT. Unlike Fisher (1989), Ashfield and Longcope (2021) allowed H to be a free parameter in their model, from which they found a similar scaling for the half-life, but with a different factor (2.8 *versus* 2). Casting in terms of u_0 this was: $\tau_{1/2} \approx 2.8H/u_0$. PREFT was set up as a rigid flux tube so that the only energy transport was *via* energy injected to the loop to mimic direct flare heating, and conduction-driven flares were simulated. Using those simulations with various values of pre-flare H and injected energy flux F, the velocity as a function of time $u(t)$ was fit with a similar functional form as that from their analytical model. The best-fit values suggested that the relationship was instead $\tau_{1/2} \approx 1.67H/u_0$, with the discrepancy attributed to at least one of the simplifying assumptions in their analytical model not being satisfied. The results of Fisher (1989) and Ashfield and Longcope (2021) demonstrate that both analytically and numerically the pre-flare chromospheric density scale height $H \propto u_0\tau_{1/2}$, with the numerical results of Ashfield and Longcope (2021) pointing to $H \approx 0.6u_0\tau_{1/2}$. The slight difference between the results of Ashfield and Longcope (2021) and the earlier work of Fisher (1989) could be due in part to the heating

15 This does not include potential heating of the corona by very low-energy non-thermal electrons that are thermalised in the lower corona, which are already captured by the models. In such cases, a conductive heat flux is present due to this coronal heating, but in this section we refer to coronal heating in flares in the absence of non-thermal particles.

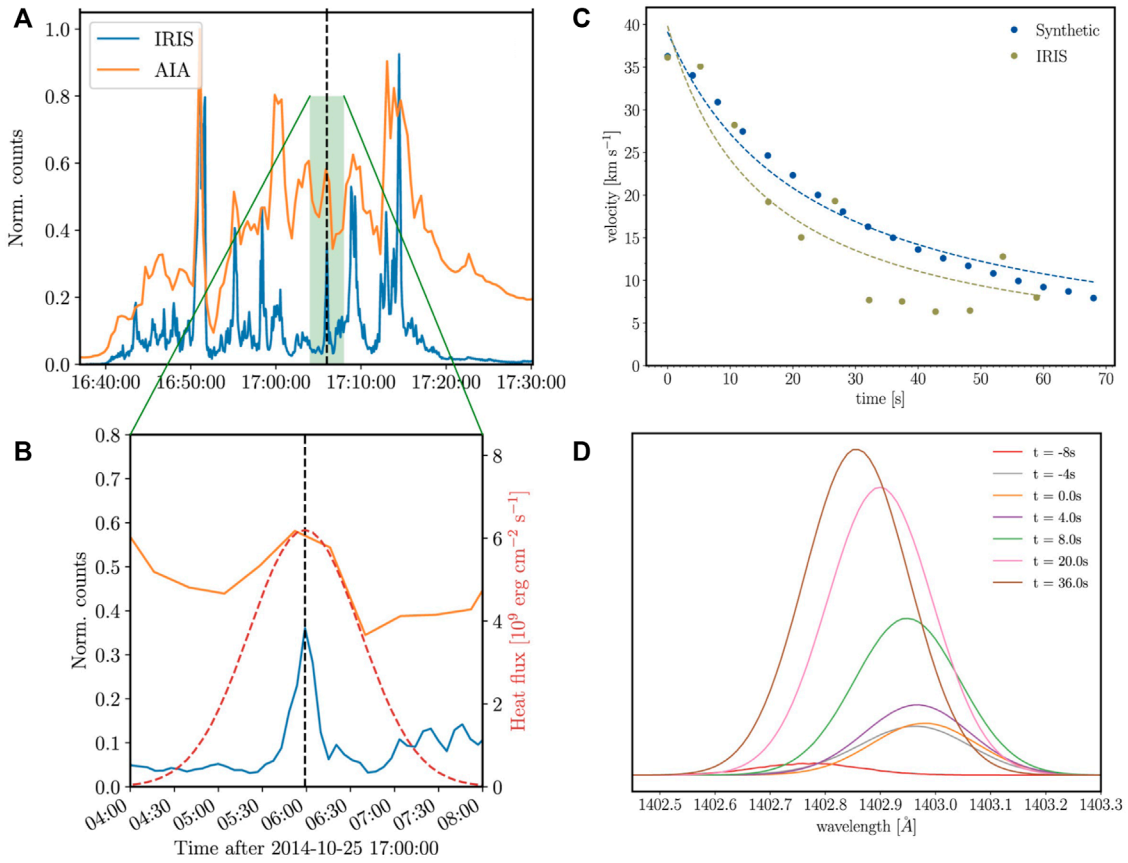

FIGURE 8
A thermal conduction driven flare simulation using PREFT. **(A)** shows observations of a single pixel in the 2014-Oct-25th X class flare. The Si IV 1402 line lightcurve is shown in blue, and the SDO/AIA 1600 Å lightcurve is shown in orange. The dashed line shows the peak of the individual condensation event studied. **(B)** shows a zoomed in view, where the injected heat flux is shown also, which was derived *via* the UFC method (red, dashed line). The resulting Si IV redshifts due to the condensation are shown in **(C)** where blue symbols are the PREFT results and green are the IRIS observations of that pixel. The dashed lines are fits to the decay of the condensation according to the model described in Ashfield and Longcope (2021). **(D)** shows the synthetic line profiles on an arbitrary intensity axis. Figure adapted from Ashfield et al., 2022. © AAS. Reproduced with permission.

profile assumed. Fisher (1989) assumed short pulses of non-thermal electrons in the models which the analytical expressions used a base, whereas Ashfield and Longcope (2021) assumed direct heating in the corona. Nevertheless, this is a rather powerful diagnostic that suggests variations in the lifetime of condensations could be related to variations in the pre-flare chromospheric densities into which shocks propagate, and that variations along a flare ribbon could reveal corrugation of the pre-flare atmosphere. Note that the condensations referred to here are the relatively strong, transient, downflows that may appear on top of a longer-lived envelope as discussed Paper 1. The peak velocity, u_0, itself scaled with the input energy flux, without much reliance on H, going as $u_0 \propto F^{1/2}$ for weaker energy fluxes ($F < 2 \times 10^{10}$ erg s^{-1} cm^{-2}), and $u_0 \propto F^{1/3}$ for stronger fluxes. The latter was predicted by Fisher (1989), and the former by Longcope (2014) for low-energy fluxes.

Applying their findings to an actual flare, Ashfield et al., 2022 analysed the 2014-October-25th X-class event. During the flare there were persistent redshifts of Si IV, with v_{Dopp}~10 km s^{-1}, but on top of which were many transient (<1 minute) redshifts of several tens of km s^{-1}. After carefully analysing the IRIS Si IV spectra to extract a candidate condensation event to model, they used SDO/AIA and HMI data to trace a magnetic loop. Imaging the hard X-rays from RHESSI in the range 25–50 keV revealed only a coronal source, with no evidence of non-thermal particles at the footpoints. Thus, they used PREFT to model this event as a 'thermal' flare, to confirm that the observationally derived energy flux could drive the observed condensation. The density scale height was estimated from u_0 and $\tau_{1/2}$ as $H = 369$ km, which was used to initialise a rigid flux tube of length 85 Mm. Since no evidence of electron precipitation into that footpoint was present, Ashfield et al., 2022 used the UV Footpoint Calorimeter

method (UFC; Qiu et al., 2012; Liu et al., 2013; Zhu et al., 2018; Qiu, 2021) to determine the time-dependent energy flux injected into the loop. In that method, the energy flux is proportional to the intensity in the SDO/AIA 1600 Å passband, with a scaling factor constrained by the SDO/AIA EUV channels and GOES Soft X-ray channels. The Enthalpy-Based Thermal Evolution of Loops (EBTEL; Klimchuk et al., 2008) model was used to synthesise the EUV and soft X-ray intensities for different energy fluxes, from which the best-fit match to the observations is used to define the scaling constant. EBTEL is a 0D model, and thus very quick to run, allowing many thousands of possible solutions to be generated efficiently to obtain the best-fit match. The 1,600 Å peak was fit by a Gaussian function, to obtain an energy flux profile with peak flux $F = 6.2 \times 10^9$ erg s^{-1} cm^{-2}, and duration of a few minutes. The heating profile and observed lightcurves are shown in the lefthand column of **Figure 8**.

Injecting this derived energy flux profile into the PREFT loop resulted in the formation of a condensation, peaking prior to the peak of the energy input, and reaching a maximum of velocity 45 km s^{-1}, before decreasing to 10 km s^{-1}, again prior to the peak energy input. Only a small fraction of the input energy flux was required to drive the condensation, leading to the conclusion that the timescales of condensations do not necessarily impart knowledge of the duration of energy input, in agreement with the analytical work of Fisher (1989). From the dynamic PREFT simulation, the Si IV spectral lines were synthesised assuming optically thin emission, and summed through the extent of each leg of the loop. Non-equilibrium effects were considered by tracking the change in ionisation state for each Lagrangian grid cell. While qualitatively consistent with the observed Si IV emission from the footpoint, with similar redshifts produced (see the righthand column of **Figure 8**), the synthetic intensities did not track the condensation evolution and were over an order of magnitude too high. The synthetic profiles were also fully redshifted rather than showing two component behaviour, possibly pointing to the need for many strands along the lines of Reep et al., 2018a's multi-threaded modelling. Since the synthetic profiles continued to increase in intensity after their peak redshift, it is possible that the Gaussian form assumed for energy input was not correct. Keeping the total energy from the UFC method, but having a more impulsive initial energy release could decrease the energy deposited later in the event, reducing the line's intensity. Prior experiments with PREFT that included the loop retraction exhibited much more rapid energy release (Longcope and Klimchuk, 2015). Of particular importance here, aside from testing the work of Ashfield and Longcope (2021), and demonstrating that the observed conductions could be produced in a thermal conduction-driven flare, was that this was the first simulation of a flare in which the energy input to the chromosphere was inferred from coronal observations.

4 Future directions

In this extensive review (including Paper 1) I have illustrated how the powerful combination of high spatial-, temporal-, and spectral-resolution observations of the chromosphere, transition region and corona, coupled with state-of-the-art numerical loop models can greatly further our understanding of the physics of solar flares. IRIS observations have been used to challenge the predictions of models, requiring us to update the physics we include in our models, as well as the ways in which we perform model-data comparisons. The models, on the other hand, have been used to assist in the interpretation of IRIS observations, particularly of the complex formation properties of the optically thick chromospheric and transition region spectral lines. Through study of Doppler shifts and line asymmetries, both their magnitude and lifetimes, we have come to understand the likely requirement of muti-threaded modelling to understand upflows. Chromospheric condensations, on the contrary, seemingly do not require multi-threaded modelling, presenting a discrepancy. Detailed comparisons of synthetic optically thick lines, and the NUV and optical continua, have demonstrated that while flare models can capture the upper chromospheric response to flare energy injection, we are perhaps missing heating deeper in the atmosphere. If higher energy fluxes are required, as suggested by some model-data comparisons, do those originate solely from non-thermal electrons or do we need other agents by which flare energy can be transported to the chromosphere? We must seriously consider Alfvénic waves, and non-thermal ions, and work to characterise the magnitude of energy directly deposited into the corona that is subsequently conducted down. Recent model improvements have included incorporating area expansion and suppression of thermal conduction, but more work on those features is required in particular to tie down the appropriate parameter spaces to use in general flare models (e.g. when producing grids of models). Modelling IRIS observables has also revealed that opacity effects could occur for transition region lines, which are important contributors to the "optically thin" radiative loss functions in the models. A re-evaluation of the loss tables would be a worthwhile enterprise considering their importance, with HYDRAD NEI results helping to assess which species are also likely to suffer from non-equilibrium effects.

There still remain open questions, likely pointing to missing ingredients in our models. While they are many, I take the liberty to note the questions that capture my own focus at the present moment: 1) What causes the very broad chromospheric spectral lines? Could this point to the need for deeper heating through the lower atmosphere, and if so what transports that energy? 2) What is the nature of white light flares? Are they largely of chromospheric origin like the Balmer continuum that IRIS has observations have suggested, or do we need additional heating

through the lower atmosphere? 3) What is the source of post-impulsive phase energy transport that maintains the flare gradual phase? 4) What is the nature and magnitude of turbulence throughout the flaring atmosphere? Turbulence could explain broadening of coronal lines and the suppression of thermal conduction, as well causing heating in its own right and particle acceleration. Continued coupling of flare loop modelling and high quality observations, can help address, and close, these questions. A powerful method to both guide and evaluate the models is the atmospheric stratification obtained from spectral inversions, for example using the IRIS2 database of Mg II inversions (Sainz Dalda et al., 2019) and subsequent updates to further constrain the atmospheres using other IRIS lines. These should be compared to the output of flare models, with the results of both critically compared and interrogated to determine when they agree, when they disagree and in that event, crucially, why they disagree.

IRIS continues to deliver excellent observations. Both from observational analysis, and from numerical modelling it has become clear that flare processes can occur at rapid cadence, on the order of seconds to sub-second. In the present solar cycle there will be concerted efforts to obtain flare observations of the main IRIS lines (Mg II k, Si IV 1,402 Å, C II resonance lines, and sometimes O I 1,356 Å) with very high cadences of $t < 1.5$ s or even at sub-second cadence. This observing campaign has already caught many flares[16]. Additionally, we can look ahead to future missions that build upon the heritage of IRIS, both technologically and from the methodological approach of strongly coupling modelling and observations. Those missions include the Solar-C EUV High-Throughput Spectroscopic Telescope (EUVST; Shimizu et al., 2019), and the Multi-slit Solar Explorer (MUSE; De Pontieu et al., 2020). EUVST is a single-slit spectrometer with a huge temperature coverage spanning the chromosphere through hot flare plasma ($T = 0.02$–15 MK), observing with spatial resolution of 0.4 arcsec and temporal resolution down to ∼2 s in sit-and-stare mode (of course lower cadence longer if rastering). MUSE is an also an EUV observatory, but is specifically designed with temporal cadence in mind, such that it has 37 slits enabling rastering over an active region field of view in only 12s with 0.4 arcsec spatial resolution, and 1 s cadence in sit-and-stare mode. Fewer lines are observed by MUSE given the complexity of its 37 slit design, but those that are observed sample the transition region and corona. With 37 slits we will no longer have the frustration of missing the interesting features because the slit was pointed in the 'wrong' place. We will instead have transition region and coronal imaging spectroscopy over much larger areas than ever achieved. Recent modelling efforts demonstrated the transformative science that MUSE will achieve in the area of solar flares and eruptions (Cheung et al., 2022). Coordination of these space based missions with ground-based observatories such as Big Bear Solar Observatory (BBSO), the Swedish Solar Telescope (SST), GREGOR, and the Daniel K. Inouye Solar Telescope (DKIST) should provide coverage from photosphere through corona, to observe the full flaring atmosphere.

At the same time as obtaining ever higher quality observations we must strive to improve our modelling ability and frameworks. To make rapid and serious progress not only in solar flare physics, but in modern space physics more generally, we must have significant investment of time and resources in models. This involves continued improvements of our existing field-aligned models (some examples are discussed in Section 5.2 of Kowalski et al., 2022), but also to attempt to bridge the gap to multi-dimensional models. A fully 3D radiative-MHD model capable of simulating an NLTE chromosphere to sub-metre scales following flare energy injection is a daunting task that may not be fully realised for many years, but certainly we must attempt to include multi-dimensional effects. Efforts are already underway to study 2D/3D RT effects. For example, Osborne and Fletcher (2022) are exploring the effects of 2D radiation transfer, using 1D field-aligned RADYN models embedded within regions of quiet-Sun, finding significant differences may be present (including on the intensity of transition region lines, *private communication*). Additionally, non-thermal electrons have now been included in 3D radiative-MHD simulations, with very low fluxes to explore nano-flare heating (Bakke et al., 2018), and hopefully larger fluxes typical of flares may be explored in the future. However, we must also think about how to handle horizontal expansion of plasma in flare footpoints in the field-aligned models that can handle the vertical scales required in the chromosphere.

Recently, Dr. Joel Allred and co-authors proposed an end-to-end modelling framework of solar eruptive events in a white paper titled "Next-Generation Comprehensive Data-Driven Models of Solar Eruptive Events" [17] submitted to the National Academy of Science Solar and Space Physics Decadal Survey. In this framework, models that target different aspects of solar eruptive events should be linked such that the output of one is either the input to the next link in the chain, or strongly guides/constrains the next link, ideally in a data-driven or data-constrained manner. Field-aligned models would be an essential component. An example of such a chain could be: 1) an MHD model of the build up and release of magnetic energy, that then drives 2) a model of particle

16 https://iris.lmsal.com/data.html.

17 White papers will appear in the Bulletin of the American Astronomical Society, but are for now hosted by the NAS on their website: https://www.nationalacademies.org/our-work/decadal-survey-for-solar-and-space-physics-heliophysics-2024-2033. A link to Dr. Allred's white paper is: http://surveygizmoresponseuploads.s3.amazonaws.com/fileuploads/623127/6920789/140-a8d175a52b5836b620abf6d961febf97_AllredJoelC.pdf.

acceleration, the energy spectrum of which drives, 3) a model that propagates and dissipates non-thermal particles, producing 4) the radiative hydrodynamic response of the atmosphere, that 5), ultimately predicts observables, including geometry of the original magnetic field/loops (e.g., *via* a RADYN_Arcade type framework). The latter three steps are of course already being done with the models discussed in this review (e.g., RADYN + FP). Joined up modelling such as that described by Allred et al., interrogated by high-resolution observations, is perhaps the best way to make rapid progress whilst covering the vast range of scales, from MHD to kinetic, present in solar flares.

Author contributions

GK performed the literature review and wrote the manuscript.

Funding

GK acknowledges funding *via* a NASA ROSES Early Career Investigator Award (Grant# 80NSSC21K0460), and the Heliophysics Supporting Research program (Grant# 80NSSC21K0010).

Acknowledgments

IRIS is a NASA small explorer mission developed and operated by LMSAL with mission operations executed at NASA Ames Research center and major contributions to downlink communications funded by the Norwegian Space Center (NSC, Norway) through an ESA PRODEX contract. This manuscript benefited from discussions held at a meeting of International Space Science Institute team: "Interrogating Field-Aligned Solar Flare Models: Comparing, Contrasting and Improving," led by GK and V. Polito. I also thank the following colleagues for their help, and patience, with answering questions related to RADYN, PREFT, FLARIX, and HYDRAD: Joel Allred, Mats Carlsson, Adam Kowalski, Vanessa Polito, Dana Longcope, William Ashfield, John Unverferth, Stephen Bradshaw, Jeffrey Reep, Jana Kašparová, Petr Heinzel, and Michal Varady. Finally, I thank the referees for their diligent reading and useful comments which improved both content and clarity of this review.

Conflict of interest

The author declares that the research was conducted in the absence of any commercial or financial relationships that could be construed as a potential conflict of interest.

Publisher's note

References

Abbett, W. P., and Hawley, S. L. (1999). Dynamic models of optical emission in impulsive solar flares. *Astrophysical J.* 521, 906–919. doi:10.1086/307576

Alaoui, M., Holman, G. D., Allred, J. C., and Eufrasio, R. T. (2021). Role of suprathermal runaway electrons returning to the acceleration region in solar flares. *Astrophysical J.* 917, 74. doi:10.3847/1538-4357/ac0820

Alaoui, M., and Holman, G. D. (2017). Understanding breaks in flare X-ray spectra: Evaluation of a cospatial collisional return-current model. *Astrophysical J.* 851, 78. doi:10.3847/1538-4357/aa98de

Allred, J. C., Alaoui, M., Kowalski, A. F., and Kerr, G. S. (2020). Modeling the transport of nonthermal particles in flares using fokker-planck kinetic theory. *Astrophysical J.* 902, 16. doi:10.3847/1538-4357/abb239

Allred, J. C., Hawley, S. L., Abbett, W. P., and Carlsson, M. (2005). Radiative hydrodynamic models of the optical and ultraviolet emission from solar flares. *Astrophysical J.* 630, 573–586. doi:10.1086/431751

Allred, J. C., Kerr, G. S., and Gordon Emslie, A. (2022). Solar flare heating with turbulent suppression of thermal conduction. *Astrophysical J.* 931, 60. doi:10.3847/1538-4357/ac69e8

Allred, J. C., Kowalski, A. F., and Carlsson, M. (2015). A unified computational model for solar and stellar flares. *Astrophysical J.* 809, 104. doi:10.1088/0004-637x/809/1/104

Allred, J., and Kerr, G. (2021). "Modeling the transport and heating resulting from nonthermal ions in solar flares," in AGU Fall Meeting Abstracts, SH24B–04.2021

Aschwanden, M. J., Boerner, P., Ryan, D., Caspi, A., McTiernan, J. M., and Warren, H. P. (2015). Global energetics of solar flares: II. Thermal energies. *Astrophysical J.* 802, 53. doi:10.1088/0004-637X/802/1/53802

Aschwanden, M. J., Caspi, A., Cohen, C. M. S., Holman, G., Jing, J., Kretzschmar, M., et al. (2017). Global energetics of solar flares. V. Energy closure in flares and coronal mass ejections. *ApJ* 836, 17. doi:10.3847/1538-4357/836/1/17

Ashfield, I., William, H., Longcope, D. W., Zhu, C., and Qiu, J. (2022). Connecting chromospheric condensation signatures to reconnection-driven heating rates in an observed flare. *Astrophysical J.* 926, 164. doi:10.3847/1538-4357/ac402d

Ashfield, W. H., and Longcope, D. W. (2021). Relating the properties of chromospheric condensation to flare energy transported by thermal conduction. *Astrophysical J.* 912, 25. doi:10.3847/1538-4357/abedb4

Bakke, H., Frogner, L., and Gudiksen, B. V. (2018). Non-thermal electrons from solar nanoflares. In a 3D radiative MHD simulation. *Astronomy Astrophysics* 620, L5. doi:10.1051/0004-6361/201834129

Battaglia, M., Fletcher, L., and Benz, A. O. (2009). Observations of conduction driven evaporation in the early rise phase of solar flares. *Astronomy Astrophysics* 498, 891–900. doi:10.1051/0004-6361/200811196

Battaglia, M., Kleint, L., Krucker, S., and Graham, D. (2015). How important are electron beams in driving chromospheric evaporation in the 2014 march 29 flare? *Astrophysical J.* 813, 113. doi:10.1088/0004-637x/813/2/113

Benz, A. O. (2008). Flare observations. *Living Rev. Sol. Phys.* 5, 1. doi:10.12942/lrsp-2008-1

Bloomfield, D. S., Mathioudakis, M., Christian, D. J., Keenan, F. P., and Linsky, J. L. (2002). Opacity in the upper atmosphere of AU Mic. *Astronomy Astrophysics* 390, 219–224. doi:10.1051/0004-6361:20020690

Bradshaw, S. J., and Mason, H. E. (2003a). A self-consistent treatment of radiation in coronal loop modelling. *Astronomy Astrophysics* 401, 699–709. doi:10.1051/0004-6361:20030089

Bradshaw, S. J., and Mason, H. E. (2003b). The radiative response of solar loop plasma subject to transient heating. *Astronomy Astrophysics* 407, 1127–1138. doi:10.1051/0004-6361:20030986

Brosius, J. W. (2012). Extreme-ultraviolet spectroscopic observation of direct coronal heating during a C-class solar flare. *Astrophysical J.* 754, 54. doi:10.1088/0004-637x/754/1/54

Brosius, J. W., and Holman, G. D. (2012). Using SDO's AIA to investigate energy transport from a flare's energy release site to the chromosphere. *Astronomy Astrophysics* 540, A24. doi:10.1051/0004-6361/201118144

Brown, J. C. (1971). The deduction of energy spectra of non-thermal electrons in flares from the observed dynamic spectra of hard X-ray bursts. *Sol. Physcs* 18, 489–502. doi:10.1007/bf00149070

Canfield, R. C., and Chang, C. R. (1985). Ly-alpha and H-alpha emission by superthermal proton beams. *Astrophysical J.* 295, 275–284. doi:10.1086/163371

Canfield, R. C., and Gayley, K. G. (1987). Impulsive H alpha diagnostics of electron-beam–heated solar flare model chromospheres. *Astrophysical J.* 322, 999. doi:10.1086/165795

Canfield, R. C., Gunkler, T. A., and Ricchiazzi, P. J. (1984). The H-alpha spectral signatures of solar flare nonthermal electrons, conductive flux, and coronal pressure. *Astrophysical J.* 282, 296–307. doi:10.1086/162203

Canfield, R. C., and Ricchiazzi, P. J. (1980). A probabilistic approach to radiative energy loss calculations for optically thick atmospheres - hydrogen lines and continua. *Astrophysical J.* 239, 1036–1044. doi:10.1086/158193

Canfield, R. C., Wulser, J.-P., Zarro, D. M., and Dennis, B. R. (1991). A study of solar flare energy transport based on coordinated H alpha and X-ray observations. *Astrophysical J.* 367, 671. doi:10.1086/169663

Carlsson, M., and Leenaarts, J. (2012). Approximations for radiative cooling and heating in the solar chromosphere. *Astronomy Astrophysics* 539, A39. doi:10.1051/0004-6361/201118366

Carlsson, M., Leenaarts, J., and De Pontieu, B. (2015). What do IRIS observations of Mg II k tell us about the solar plage chromosphere? *Astrophysical J. Lett.* 809, L30. doi:10.1088/2041-8205/809/2/L30

Carlsson, M., and Stein, R. F. (2002). Dynamic hydrogen ionization. *Astrophysical J.* 572, 626–635. doi:10.1086/340293

Carlsson, M., and Stein, R. F. (1997). formation of solar calcium H and K bright grains. *Astrophysical J. Lett.* 481, 500–514. doi:10.1086/304043

Carlsson, M., and Stein, R. F. (1992). Non-LTE radiating acoustic shocks and CA II K2V bright points. *Astrophysical J. Lett.* 397, L59–L62. doi:10.1086/186544

Chaston, C. C., Phan, T. D., Bonnell, J. W., Mozer, F. S., Acuña, M., Goldstein, M. L., et al. (2005). Drift-kinetic Alfvén waves observed near a reconnection X line in the earth's magnetopause. *Phys. Rev. Lett.* 95, 065002. doi:10.1103/PhysRevLett.95.065002

Cheng, C. C., Oran, E. S., Doschek, G. A., Boris, J. P., and Mariska, J. T. (1983). Numerical simulations of loops heated to solar flare temperatures. I - gasdynamics. II - X-ray and UV spectroscopy. *Astrophysical J.* 265, 1090–1119. doi:10.1086/160751

Cheung, M. C. M., Martínez-Sykora, J., Testa, P., De Pontieu, B., Chintzoglou, G., Rempel, M., et al. (2022). Probing the physics of the solar atmosphere with the multi-slit solar explorer (MUSE). II. Flares and eruptions. *Astrophysical J.* 926, 53. doi:10.3847/1538-4357/ac4223

Cheung, M. C. M., Rempel, M., Chintzoglou, G., Chen, F., Testa, P., Martínez-Sykora, J., et al. (2019). A comprehensive three-dimensional radiative magnetohydrodynamic simulation of a solar flare. *Nat. Astron.* 3, 160–166. doi:10.1038/s41550-018-0629-3

de Jager, C. (1985). Kernel heating and ablation in the impulsive phase of two solar flares. *Sol. Physcs* 98, 267–280. doi:10.1007/bf00152460

De Pontieu, B., Martínez-Sykora, J., Testa, P., Winebarger, A. R., Daw, A., Hansteen, V., et al. (2020). The multi-slit approach to coronal spectroscopy with the multi-slit solar explorer (MUSE). *Astrophysical J.* 888, 3. doi:10.3847/1538-4357/ab5b03

De Pontieu, B., Polito, V., Hansteen, V., Testa, P., Reeves, K. K., Antolin, P., et al. (2021). A new view of the solar interface region from the interface region imaging spectrograph (IRIS). *Sol. Physcs* 296, 84. doi:10.1007/s11207-021-01826-0

De Pontieu, B., Title, A. M., Lemen, J. R., Kushner, G. D., Akin, D. J., Allard, B., et al. (2014). The interface region imaging spectrograph (IRIS). *Sol. Physcs* 289, 2733–2779. doi:10.1007/s11207-014-0485-y

Del Zanna, G., Dere, K. P., Young, P. R., and Landi, E. (2021). CHIANTI—an atomic database for emission lines. XVI. Version 10, further extensions. *Astrophysical J.* 909, 38. doi:10.3847/1538-4357/abd8ce

Del Zanna, G., Dere, K. P., Young, P. R., Landi, E., and Mason, H. E. (2015). Chianti - an atomic database for emission lines. Version 8. *Astronomy Astrophysics* 582, A56. doi:10.1051/0004-6361/201526827

Del Zanna, G., Polito, V., Dudík, J., Testa, P., Mason, H. E., and Dzifčáková, E. (2022). *Diagnostics of non-Maxwellian electron distributions in solar active regions from Fe XII lines observed by Hinode/EIS and IRIS*. arXiv e-prints , arXiv:2207.07026.

Dere, K. P., Landi, E., Mason, H. E., Monsignori Fossi, B. C., and Young, P. R. (1997). Chianti - an atomic database for emission lines. *Astronomy Astrophysics Suppl.* 125, 149–173. doi:10.1051/aas:1997368

Ding, M. D. (1999). An unusually intense CA II K line wing: Possible role of particle acceleration in the lower atmosphere. *Astronomy Astrophysics* 351, 368–372.

Donati-Falchi, A., Falciani, R., and Smaldone, L. A. (1985). Analysis of the optical spectra of solar flares. IV - the 'blue' continuum of white light flares. *Astronomy Astrophysics* 152, 165–169.

Doschek, G. A., Warren, H. P., Harra, L. K., Culhane, J. L., Watanabe, T., and Hara, H. (2018). Photospheric and coronal abundances in an X8.3 class limb flare. *Astrophysical J.* 853, 178. doi:10.3847/1538-4357/aaa4f5

Druett, M. K., and Zharkova, V. V. (2018). HYDRO2GEN: Non-thermal hydrogen Balmer and Paschen emission in solar flares generated by electron beams. *Astronomy Astrophysics* 610, A68. doi:10.1051/0004-6361/201731053

Dudík, J., Polito, V., Dzifčáková, E., Del Zanna, G., and Testa, P. (2017). Non-maxwellian analysis of the transition-region line profiles observed by the interface region imaging spectrograph. *Astrophysical J.* 842, 19. doi:10.3847/1538-4357/aa71a8

Dufresne, R. P., Del Zanna, G., and Badnell, N. R. (2021a). The influence of photo-induced processes and charge transfer on carbon and oxygen in the lower solar atmosphere. *Mon. Notices R. Astronomical Soc.* 503, 1976–1986. doi:10.1093/mnras/stab514

Dufresne, R. P., Del Zanna, G., and Storey, P. J. (2021b). Modelling low charge ions in the solar atmosphere. *Mon. Notices R. Astronomical Soc.* 505, 3968–3981. doi:10.1093/mnras/stab1498

Dzifčáková, E., and Dudík, J. (2018). Non-equilibrium ionization by a periodic electron beam. II. Synthetic Si IV and O IV transition region spectra. *Astronomy Astrophysics* 610, A67. doi:10.1051/0004-6361/201731744

Dzifčáková, E., Vocks, C., and Dudík, J. (2017). Synthetic IRIS spectra of the solar transition region: Effect of high-energy tails. *Astronomy Astrophysics* 603, A14. doi:10.1051/0004-6361/201629205

Dzifčáková, E., Zemanová, A., Dudík, J., and Mackovjak, Š. (2018). Spectroscopic diagnostics of the non-maxwellian κ-distributions using SDO/EVE observations of the 2012 march 7 X-class flare. *Astrophysical J.* 853, 158. doi:10.3847/1538-4357/aaa426

Emslie, A. G., and Bian, N. H. (2018). Reduction of thermal conductive flux by non-local effects in the presence of turbulent scattering. *Astrophysical J.* 865, 67. doi:10.3847/1538-4357/aad961

Emslie, A. G., Dennis, B. R., Shih, A. Y., Chamberlin, P. C., Mewaldt, R. A., Moore, C. S., et al. (2012). Global energetics of thirty-eight large solar eruptive events. *ApJ* 759, 71. doi:10.1088/0004-637x/759/1/71

Emslie, A. G., and Sturrock, P. A. (1982). Temperature minimum heating in solar flares by resistive dissipation of Alfvn waves. *Sol. Physcs* 80, 99–112. doi:10.1007/bf00153426

Emslie, A. G. (1978). The collisional interaction of a beam of charged particles with a hydrogen target of arbitrary ionization level. *Astrophysical J.* 224, 241–246. doi:10.1086/156371

Falchi, A., and Mauas, P. J. D. (2002). Chromospheric models of a solar flare including velocity fields. *Astronomy Astrophysics* 387, 678–686. doi:10.1051/0004-6361:20020454

Fang, C., Henoux, J. C., and Gan, W. Q. (1993). Diagnostics of non-thermal processes in chromospheric flares. 1. Hoe and Call K line profiles of an atmosphere bombarded by 10-500 keV electrons. *Astronomy Astrophysics* 274, 917.

Fang, C., Hiei, E., Yin, S.-Y., and Gan, W.-Q. (1992). *CA II K line diagnostics of the dynamics of the solar flare atmosphere*, 44. Publications of the Astronomical Society of Japan, 63–72.

Fisher, G. H., Canfield, R. C., and McClymont, A. N. (1985a). Flare loop radiative hydrodynamics - Part Seven - dynamics of the thick target heated chromosphere. *Astrophysical J.* 289, 434. doi:10.1086/162903

Fisher, G. H., Canfield, R. C., and McClymont, A. N. (1985b). Flare loop radiative hydrodynamics. V - response to thick-target heating. VI - chromospheric evaporation due to heating by nonthermal electrons. VII - dynamics of the thick-target heated chromosphere. *Astrophysical J.* 289, 414. doi:10.1086/162901

Fisher, G. H. (1989). Dynamics of flare-driven chromospheric condensations. *Astrophysical J.* 346, 1019–1029. doi:10.1086/168084

Fletcher, L., Dennis, B. R., Hudson, H. S., Krucker, S., Phillips, K., Veronig, A., et al. (2011). An observational overview of solar flares. *Space Sci. Rev.* 159, 19–106. doi:10.1007/s11214-010-9701-8

Fletcher, L., and Hudson, H. S. (2008). Impulsive phase flare energy transport by large-scale Alfvén waves and the electron acceleration problem. *Astrophysical J.* 675, 1645–1655. doi:10.1086/527044

Gan, W. Q., Rieger, E., Fang, C., and Zhang, H. Q. (1992). Spectral diagnostics for a thermal hydrodynamical model of a solar flare loop. *Astronomy Astrophysics* 266, 573–580.

Gan, W. Q., Rieger, E., Fang, C., and Zhang, H. Q. (1993). The influence of chromospheric condensation on Hα line profiles. *Sol. Physcs* 143, 141–149. doi:10.1007/BF00619101

Gan, W. Q., Zhang, H. Q., and Fang, C. (1991). A hydrodynamic model of the impulsive phase of a solar flare loop. *Astronomy Astrophysics* 241, 618–624.

Gayley, K. G., and Canfield, R. C. (1991). Inferring chromospheric flare heating from hydrogen-line wings. *Astrophysical J.* 380, 660. doi:10.1086/170621

Gershman, D. J., F-Viñas, A., Dorelli, J. C., Boardsen, S. A., Avanov, L. A., Bellan, P. M., et al. (2017). Wave-particle energy exchange directly observed in a kinetic Alfvén-branch wave. *Nat. Commun.* 8, 14719. doi:10.1038/ncomms14719

Goode, P. R., and Cao, W. (2012). "The 1.6 m off-Axis new solar telescope (NST) in big bear," in *Second ATST-EAST meeting: Magnetic fields from the photosphere to the corona of astronomical society of the pacific conference series*. Editors T. R. Rimmele, A. Tritschler, F. Wöger, M. Collados Vera, H. Socas-Navarro, and R. Schlichenmaier, 463, 357.

Graham, D. R., and Cauzzi, G. (2015). Temporal evolution of multiple evaporating ribbon sources in a solar flare. *Astrophysical J. Lett.* 807, L22. doi:10.1088/2041-8205/807/2/l22

Graham, D. R., Cauzzi, G., Zangrilli, L., Kowalski, A., Simões, P., and Allred, J. (2020). Spectral signatures of chromospheric condensation in a major solar flare. *Astrophysical J.* 895, 6. doi:10.3847/1538-4357/ab88ad

Guidoni, S. E., and Longcope, D. W. (2010). Shocks and thermal conduction fronts in retracting reconnected flux tubes. *Astrophysical J.* 718, 1476–1490. doi:10.1088/0004-637x/718/2/1476

Hannah, I. G., Kontar, E. P., and Sirenko, O. K. (2009). The effect of wave-particle interactions on low-energy cutoffs in solar flare electron spectra. *Astrophysical J. Lett.* 707, L45–L50. doi:10.1088/0004-637x/707/1/l45

Hawley, S. L., and Fisher, G. H. (1994). Solar flare model atmospheres. *Astrophysical J.* 426, 387. doi:10.1086/174075

Heinzel, P. (1991). A chromospheric response to pulse beam heating. *Sol. Physcs* 135, 65–88. doi:10.1007/bf00146699

Heinzel, P. (1995). Multilevel radiative transfer with partial frequency redistribution. *Astrophys. J.* 299, 563. doi:10.1086/321659

Heinzel, P., Kašparová, J., Varady, M., Karlický, M., and Moravec, Z. (2016). "Numerical RHD simulations of flaring chromosphere with Flarix," in *Solar and stellar flares and their effects on planets*. Editors A. G. Kosovichev, S. L. Hawley, and P. Heinzel., 320, 233–238. doi:10.1017/S1743921316000363

Heinzel, P., and Kleint, L. (2014). Hydrogen balmer continuum in solar flares detected by the interface region imaging spectrograph (IRIS). *Astrophysical J. Lett.* 794, L23. doi:10.1088/2041-8205/794/2/l23

Heinzel, P., Kleint, L., Kašparová, J., and Krucker, S. (2017). On the nature of off-limb flare continuum sources detected by SDO/HMI. *Astrophysical J.* 847, 48. doi:10.3847/1538-4357/aa86ef

Hiei, E., Nakagomi, Y., and Takuma, H. (1992). *White-light flare observed at the solar limb*, 44. Publications of the Astronomical Society of Japan, 55–6244.

Holman, G. D., Aschwanden, M. J., Aurass, H., Battaglia, M., Grigis, P. C., Kontar, E. P., et al. (2011). Implications of X-ray observations for electron acceleration and propagation in solar flares. *Space Sci. Rev.* 159, 107–166. doi:10.1007/s11214-010-9680-9

Holman, G. D. (2012). Understanding the impact of return-current losses on the X-ray emission from solar flares. *Astrophysical J.* 745, 52. doi:10.1088/0004-637x/745/1/52

Huang, N., Xu, Y., Sadykov, V. M., Jing, J., and Wang, H. (2019). Spectral diagnosis of Mg II and Hα lines during the initial stage of an M6.5 solar flare. *Astrophysical J. Lett.* 878, L15. doi:10.3847/2041-8213/ab2330

Hubený, I. (1982). Non-coherent scattering in subordinate lines: III. Generalized redistribution functions. *J. Quantitative Spectrosc. Radiat. Transf.* 27, 593–609. doi:10.1016/0022-4073(82)90052-8

Hudson, H. S., Simões, P. J. A., Fletcher, L., Hayes, L. A., and Hannah, I. G. (2021). Hot X-ray onsets of solar flares. *Mon. Notices R. Astronomical Soc.* 501, 1273–1281. doi:10.1093/mnras/staa3664

Hudson, H. S. (1972). Thick-target processes and white-light flares. *Sol. Physcs* 24, 414–428. doi:10.1007/BF0015338424.414H

Janvier, M., Aulanier, G., Pariat, E., and Démoulin, P. (2013). The standard flare model in three dimensions. III. Slip-running reconnection properties. *Astronomy Astrophysics* 555, A77. doi:10.1051/0004-6361/201321164

Jeffrey, N. L. S., Fletcher, L., and Labrosse, N. (2016). First evidence of non-Gaussian solar flare EUV spectral line profiles and accelerated non-thermal ion motion. *Astronomy Astrophysics* 590, A99. doi:10.1051/0004-6361/201527986

Jejčič, S., Kleint, L., and Heinzel, P. (2018). High-density off-limb flare loops observed by SDO. *Astrophysical J.* 867, 134. doi:10.3847/1538-4357/aae650

Joshi, R., Schmieder, B., Aulanier, G., Bommier, V., and Chandra, R. (2020). The role of small-scale surface motions in the transfer of twist to a solar jet from a remote stable flux rope. *Astronomy Astrophysics* 642, A169. doi:10.1051/0004-6361/202038562

Joshi, R., Schmieder, B., Heinzel, P., Tomin, J., Chandra, R., and Vilmer, N. (2021). Balmer continuum enhancement detected in a mini flare observed with IRIS. *Astronomy Astrophysics* 654, A31. doi:10.1051/0004-6361/202141172

Judge, P. G., Carlsson, M., and Stein, R. F. (2003). On the origin of the basal emission from stellar atmospheres: Analysis of solar C II lines. *Astrophysical J.* 597, 1158–1177. doi:10.1086/381222

Jurčák, J., Kašparová, J., Švanda, M., and Kleint, L. (2018). Heating of the solar photosphere during a white-light flare. *Astronomy Astrophysics* 620, A183. doi:10.1051/0004-6361/201833946

Kašparová, J., Varady, M., Heinzel, P., Karlický, M., and Moravec, Z. (2009). Response of optical hydrogen lines to beam heating. I. Electron beams. *Astronomy Astrophysics* 499, 923–934. doi:10.1051/0004-6361/200811559

Kerr, G. (2022). Interrogating solar flare loop models with IRIS observations 1: Overview of the models, and mass flows. *Front. Astron. Space Sci.* 9, 1060856. doi:10.3389/fspas.2022.1060856

Kerr, G. S., Allred, J. C., and Carlsson, M. (2019a). Modeling Mg II during solar flares. I. Partial frequency redistribution, opacity, and coronal irradiation. *Astrophysical J.* 883, 57. doi:10.3847/1538-4357/ab3c24

Kerr, G. S., Allred, J. C., and Polito, V. (2020). Solar flare arcade modeling: Bridging the gap from 1D to 3D simulations of optically thin radiation. *Astrophysical J.* 900, 18. doi:10.3847/1538-4357/abaa46

Kerr, G. S., Carlsson, M., and Allred, J. C. (2019b). Modeling Mg II during solar flares. II. Nonequilibrium effects. *Astrophysical J.* 885, 119. doi:10.3847/1538-4357/ab48ea

Kerr, G. S., Carlsson, M., Allred, J. C., Young, P. R., and Daw, A. N. (2019c). SI IV resonance line emission during solar flares: Non-LTE, nonequilibrium, radiation transfer simulations. *Astrophysical J.* 871, 23. doi:10.3847/1538-4357/aaf46e

Kerr, G. S., and Fletcher, L. (2014). Physical properties of white-light sources in the 2011 february 15 solar flare. *Astrophysical J.* 783, 98. doi:10.1088/0004-637x/783/2/98

Kerr, G. S., Fletcher, L., Russell, A. J. B., and Allred, J. C. (2016). Simulations of the Mg II k and Ca II 8542 lines from an AlfvÊn wave-heated flare chromosphere. *Astrophysical J.* 827, 101. doi:10.3847/0004-637x/827/2/101

Kerr, G. S. (2017). *Observations and modelling of the chromosphere during solar flares*. UK 423K: University of Glasgow. Ph.D. thesis.

Kerr, G. S., Simões, P. J. A., Qiu, J., and Fletcher, L. (2015). IRIS observations of the Mg ii h and k lines during a solar flare. *Astronomy Astrophysics* 582, A50. doi:10.1051/0004-6361/201526128

Kerr, G. S., Xu, Y., Allred, J. C., Polito, V., Sadykov, V. M., Huang, N., et al. (2021). He I 10830 Å dimming during solar flares. I. The crucial role of nonthermal collisional ionizations. *Astrophysical J.* 912, 153. doi:10.3847/1538-4357/abf42d

Kleint, L., Heinzel, P., Judge, P., and Krucker, S. (2016). Continuum enhancements in the ultraviolet, the visible and the infrared during the X1 flare on 2014 march 29. *Astrophysical J.* 816, 88. doi:10.3847/0004-637x/816/2/88

Kleint, L., Heinzel, P., and Krucker, S. (2017). On the origin of the flare emission in IRIS' SJI 2832 filter:balmer continuum or spectral lines? *Astrophysical J.* 837, 160. doi:10.3847/1538-4357/aa62fe

Klimchuk, J. A., Patsourakos, S., and Cargill, P. J. (2008). Highly efficient modeling of dynamic coronal loops. *Astrophysical J.* 682, 1351–1362. doi:10.1086/589426

Kohl, J. L., and Parkinson, W. H. (1976). The Mg II h and k lines. I. Absolute center and limb measurements of the solar profiles. *Astrophysical J.* 205, 599–611. doi:10.1086/154317

Kontar, E. P., Brown, J. C., Emslie, A. G., Hajdas, W., Holman, G. D., Hurford, G. J., et al. (2011). Deducing electron properties from hard X-ray observations. *Space Sci. Rev.* 159, 301–355. doi:10.1007/s11214-011-9804-x

Kowalski, A. F., Allred, J. C., Carlsson, M., Kerr, G. S., Tremblay, P.-E., Namekata, K., et al. (2022). The atmospheric response to high nonthermal electron-beam fluxes in solar flares. II. Hydrogen-Broadening predictions for solar flare observations with the Daniel K. Inouye solar telescope. *Astrophysical J.* 928, 190. doi:10.3847/1538-4357/ac5174

Kowalski, A. F., Allred, J. C., Daw, A., Cauzzi, G., and Carlsson, M. (2017). The atmospheric response to high nonthermal electron beam fluxes in solar flares. I. Modeling the brightest NUV footpoints in the X1 solar flare of 2014 march 29. *Astrophysical J.* 836, 12. doi:10.3847/1538-4357/836/1/12

Kowalski, A. F., and Allred, J. C. (2018). Parameterizations of chromospheric condensations in dG and dMe model flare atmospheres. *Astrophysical J.* 852, 61. doi:10.3847/1538-4357/aa9d91

Kowalski, A. F., Butler, E., Daw, A. N., Fletcher, L., Allred, J. C., De Pontieu, B., et al. (2019). Spectral evidence for heating at large column mass in umbral solar flare kernels. I. IRIS near-UV spectra of the X1 solar flare of 2014 october 25. *Astrophysical J.* 878, 135. doi:10.3847/1538-4357/ab1f8b

Koza, J., Kuridze, D., Heinzel, P., Jejčič, S., Morgan, H., and Zapiór, M. (2019). Spectral diagnostics of cool flare loops observed by the SST. I. Inversion of the Ca II 8542 Å and hβ lines. *Astrophysical J.* 885, 154. doi:10.3847/1538-4357/ab4426

Krucker, S., Hudson, H. S., Jeffrey, N. L. S., Battaglia, M., Kontar, E. P., Benz, A. O., et al. (2011). High-resolution imaging of solar flare ribbons and its implication on the thick-target beam model. *Astrophysical J.* 739, 96. doi:10.1088/0004-637x/739/2/96

Krucker, S., Saint-Hilaire, P., Hudson, H. S., Haberreiter, M., Martinez-Oliveros, J. C., Fivian, M. D., et al. (2015). Co-spatial white light and hard X-ray flare footpoints seen above the solar limb. *Astrophysical J.* 802, 19. doi:10.1088/0004-637x/802/1/19

Kuridze, D., Henriques, V. M. J., Mathioudakis, M., van der Voort, L. R., de la Cruz Rodríguez, J., and Carlsson, M. (2018). Spectropolarimetric inversions of the Ca ii 8542 Å line in an M-class solar flare. *Astrophysical J.* 860, 10. doi:10.3847/1538-4357/aac26d

Kuridze, D., Mathioudakis, M., Simões, P. J. A., Rouppe van der Voort, L., Carlsson, M., Jafarzadeh, S., et al. (2015). Hα line profile asymmetries and the chromospheric flare velocity field. *Astrophysical J.* 813, 125. doi:10.1088/0004-637x/813/2/125

Laming, J. M. (2015). The FIP and inverse FIP effects in solar and stellar coronae. *Living Rev. Sol. Phys.* 12, 2. doi:10.1007/lrsp-2015-2

Lee, K. W., Büchner, J., and Elkina, N. (2008). Collisionless transport of energetic electrons in the solar corona at current-free double layers. *Astronomy Astrophysics* 478, 889–895. doi:10.1051/0004-6361:20078419

Leenaarts, J., Pereira, T. M. D., Carlsson, M., Uitenbroek, H., and De Pontieu, B. (2013a). The Formation of iris diagnostics. I. A quintessential model atom of Mg II and general formation properties of the Mg II h&k lines. *Astrophysical J.* 772, 89. doi:10.1088/0004-637x/772/2/89

Leenaarts, J., Pereira, T. M. D., Carlsson, M., Uitenbroek, H., and De Pontieu, B. (2013b). The Formation of IRIS diagnostics. II. The formation of the Mg II h&k lines in the solar atmosphere. *Astrophysical J.* 772, 90. doi:10.1088/0004-637x/772/2/90

Lemaire, P., Gouttebroze, P., Vial, J. C., and Artzner, G. E. (1981). Physical properties of the solar chromosphere deduced from optically thick lines. I - observations, data reductio3, and modelling of an average plage. *Astronomy Astrophysics* 103, 160–176.

Lemaire, P., and Skumanich, A. (1973). Magnesium II doublet profiles of chromospheric inhomogeneities at the center of the solar disk. *Astronomy Astrophysics* 22, 61–22.

Li, H., You, J., and Du, Q. (2006). Spectroscopic properties of dynamical chromospheric processes in a confined solar flare. *Sol. Physcs* 235, 107–123. doi:10.1007/s11207-006-2094-x

Li, T. C., Drake, J. F., and Swisdak, M. (2014). Dynamics of double layers, ion acceleration, and heat flux suppression during solar flares. *Astrophysical J.* 793, 7. doi:10.1088/0004-637x/793/1/7

Li, W. (1990). Mutual information functions versus correlation functions. *J. Stat. Phys.* 60, 823–837. doi:10.1007/bf01025996

Li, Y., Kelly, M., Ding, M. D., Qiu, J., Zhu, X. S., and Gan, W. Q. (2017). Spectroscopic observations of magnetic reconnection and chromospheric evaporation in an X-shaped solar flare. *Astrophysical J.* 848, 118. doi:10.3847/1538-4357/aa89e4

Lin, H.-H., and Carlsson, M. (2015). The Formation of IRIS diagnostics. VII. The formation of the OI 135.56 NM line in the solar atmosphere. *Astrophysical J.* 813, 34. doi:10.1088/0004-637x/813/1/34

Lin, R. P., Dennis, B. R., Hurford, G. J., Smith, D. M., Zehnder, A., Harvey, P. R., et al. (2002). The reuven ramaty high-energy solar spectroscopic imager (RHESSI). *Sol. Physcs* 210, 3–32. doi:10.1023/A:1022428818870.3L

Liu, W.-J., Qiu, J., Longcope, D. W., and Caspi, A. (2013). Determining heating rates in reconnection formed flare loops of the M8.0 flare on 2005 may 13. *Astrophysical J.* 770, 111. doi:10.1088/0004-637x/770/2/111

Liu, W., Heinzel, P., Kleint, L., and Kašparová, J. (2015). Mg ii lines observed during the X-class flare on 29 march 2014 by the interface region imaging spectrograph. *Sol. Physcs* 290, 3525–3543. doi:10.1007/s11207-015-0814-9

Longcope, D., Qiu, J., and Brewer, J. (2016). A reconnection-driven model of the hard X-ray loop-top source from flare 2004-feb-26. *Astrophysical J.* 833, 211. doi:10.3847/1538-4357/833/2/211

Longcope, D. W. (2014). A simple model of chromospheric evaporation and condensation driven conductively in a solar flare. *Astrophysical J.* 795, 10. doi:10.1088/0004-637x/795/1/10

Longcope, D. W., and Guidoni, S. E. (2011). A model for the origin of high density in looptop X-ray sources. *Astrophysical J.* 740, 73. doi:10.1088/0004-637x/740/2/73

Longcope, D. W., and Klimchuk, J. A. (2015). How gas-dynamic flare models powered by petschek reconnection differ from those with ad hoc energy sources. *Astrophysical J.* 813, 131. doi:10.1088/0004-637x/813/2/131

López, F. M., Giménez de Castro, C. G., Mandrini, C. H., Simões, P. J. A., Cristiani, G. D., Gary, D. E., et al. (2022). A solar flare driven by thermal conduction observed in mid-infrared. *Astronomy Astrophysics* 657, A51. doi:10.1051/0004-6361/202141967

Machado, M. E., Emslie, A. G., and Avrett, E. H. (1989). Radiative backwarming in white-light flares. *Sol. Physcs* 124, 303–317. doi:10.1007/BF00156272

Machado, M. E., and Linsky, J. L. (1975). Flare model chromospheres and photospheres. *Sol. Physcs* 42, 395–420. doi:10.1007/bf00149921

MacNeice, P. (1986). A numerical hydrodynamic model of a heated coronal loop. *Sol. Physcs* 103, 47–66. doi:10.1007/bf00154858

Martínez Oliveros, J.-C., Krucker, S., Hudson, H. S., Saint-Hilaire, P., Bain, H., Lindsey, C., et al. (2014). Chromospheric and coronal observations of solar flares with the helioseismic and magnetic imager. *Astrophysical J. Lett.* 780, L28. doi:10.1088/2041-8205/780/2/l28

Mathioudakis, M., McKenny, J., Keenan, F. P., Williams, D. R., and Phillips, K. J. H. (1999). The effects of opacity in the transition region of YZ CMi. *Astronomy Astrophysics* 351, L23–L26.

Meegan, C., Lichti, G., Bhat, P. N., Bissaldi, E., Briggs, M. S., Connaughton, V., et al. (2009). THE*FERMI*GAMMA-RAY burst monitor. *Astrophysical J.* 702, 791–804. doi:10.1088/0004-637x/702/1/791

Metcalf, T. R., Canfield, R. C., Avrett, E. H., and Metcalf, F. T. (1990a). Flare heating and ionization of the low solar chromosphere. I - inversion methods for MG I 4571 and 5173. *Astrophysical J.* 350, 463. doi:10.1086/168400

Metcalf, T. R., Canfield, R. C., and Saba, J. L. R. (1990b). Flare heating and ionization of the low solar chromosphere. II. Observations of five solar flares. *Astrophysical J.* 365, 391. doi:10.1086/169494

Milligan, R. O., and Dennis, B. R. (2009). Velocity characteristics of evaporated plasma using Hinode/EUV imaging spectrometer. *Astrophysical J.* 699, 968–975. doi:10.1088/0004-637x/699/2/968

Milligan, R. O. (2015). Extreme ultra-violet spectroscopy of the lower solar atmosphere during solar flares (invited review). *Sol. Physcs* 290, 3399–3423. doi:10.1007/s11207-015-0748-2

Milligan, R. O., Kerr, G. S., Dennis, B. R., Hudson, H. S., Fletcher, L., Allred, J. C., et al. (2014). The radiated energy budget of chromospheric plasma in a major solar flare deduced from multi-wavelength observations. *Astrophysical J.* 793, 70. doi:10.1088/0004-637x/793/2/70

Milligan, R. O. (2011). Spatially resolved nonthermal line broadening during the impulsive phase of a solar flare. *Astrophysical J.* 740, 70. doi:10.1088/0004-637x/740/2/70

Mulay, S. M., and Fletcher, L. (2021). Evidence of chromospheric molecular hydrogen emission in a solar flare observed by the IRIS satellite. *Mon. Notices R. Astronomical Soc.* 504, 2842–2852. doi:10.1093/mnras/stab367

Neidig, D. F. (1989). The importance of solar white-light flares. *Sol. Physcs* 121, 261–269. doi:10.1007/BF00161699

Neidig, D. F., Wiborg, P. H., and Gilliam, L. B. (1993). Physical properties of white-light flares derived from their center-to-limb distribution. *Sol. Physcs* 144, 169–194. doi:10.1007/BF00667990

Orrall, F. Q., and Zirker, J. B. (1976). Lyman-alpha emission from nonthermal proton beams. *Astrophysical J.* 208, 618–632. doi:10.1086/154642

Osborne, C. M. J., and Fletcher, L. (2022). Flare kernels may be smaller than you think: Modelling the radiative response of chromospheric plasma adjacent to a solar flare. *Mon. Notices R. Astronomical Soc.* 516, 6066–6074. doi:10.1093/mnras/stac2570

Panos, B., and Kleint, L. (2021). Exploring mutual information between IRIS spectral lines. II. Calculating the most probable response in all spectral windows. *Astrophysical J.* 915, 77. doi:10.3847/1538-4357/ac00c0

Panos, B., Kleint, L., Huwyler, C., Krucker, S., Melchior, M., Ullmann, D., et al. (2018). Identifying typical Mg II flare spectra using machine learning. *Astrophysical J.* 861, 62. doi:10.3847/1538-4357/aac779

Panos, B., Kleint, L., and Voloshynovskiy, S. (2021). Exploring mutual information between IRIS spectral lines. I. Correlations between spectral lines during solar flares and within the quiet sun. *Astrophysical J.* 912, 121. doi:10.3847/1538-4357/abf11b

Pereira, T. M. D., and Uitenbroek, H. (2015). RH 1.5D: A massively parallel code for multi-level radiative transfer with partial frequency redistribution and Zeeman polarisation. *Astron. Astrophys.* 574, A3. doi:10.1051/0004-6361/201424785

Pereira, T. M. D., Carlsson, M., De Pontieu, B., and Hansteen, V. (2015). The Formation of IRIS diagnostics. IV. The Mg II triplet lines as a new diagnostic for lower chromospheric heating. *Astrophysical J.* 806, 14. doi:10.1088/0004-637x/806/1/14

Pereira, T. M. D., Leenaarts, J., De Pontieu, B., Carlsson, M., and Uitenbroek, H. (2013). The Formation of IRIS diagnostics. III. Near-Ultraviolet spectra and images. *Astrophysical J.* 778, 143. doi:10.1088/0004-637x/778/2/143

Polito, V., Dudík, J., Kašparová, J., Dzifčáková, E., Reeves, K. K., Testa, P., et al. (2018a). Broad non-Gaussian Fe XXIV line profiles in the impulsive phase of the 2017 september 10 X8.3-class flare observed by Hinode/EIS. *Astrophysical J.* 864, 63. doi:10.3847/1538-4357/aad62d

Polito, V., Kerr, G. S., Xu, Y., Sadykov, V. M., and Lorincik, J. (2022). *Solar flare ribbon fronts I: Constraining flare energy deposition with IRIS spectroscopy*. arXiv e-prints , arXiv:2211.05333.

Polito, V., Reep, J. W., Reeves, K. K., Simões, P. J. A., Dudík, J., Del Zanna, G., et al. (2016). Simultaneous iris andhinode/eis observations and modeling of the 2014 october 27 X2.0 class flare. *Astrophysical J.* 816, 89. doi:10.3847/0004-637x/816/2/89

Polito, V., Reeves, K. K., Del Zanna, G., Golub, L., and Mason, H. E. (2015). Joint high temperature observation of a small C6.5 solar flare with Iris/Eis/Aia. *Astrophysical J.* 803, 84. doi:10.1088/0004-637x/803/2/84

Polito, V., Testa, P., Allred, J., De Pontieu, B., Carlsson, M., Pereira, T. M. D., et al. (2018b). Investigating the response of loop plasma to nanoflare heating using RADYN simulations. *Astrophysical J.* 856, 178. doi:10.3847/1538-4357/aab49e

Polito, V., Testa, P., and De Pontieu, B. (2019). Can the superposition of evaporative flows explain broad Fe XXI profiles during solar flares? *Astrophysical J. Lett.* 879, L17. doi:10.3847/2041-8213/ab290b

Priest, E. R., and Forbes, T. G. (2002). The magnetic nature of solar flares. *Astronomy Astrophysics Rev.* 10, 313–377. doi:10.1007/s001590100013

Qiu, J., Liu, W.-J., and Longcope, D. W. (2012). Heating of flare loops with observationally constrained heating functions. *Astrophysical J.* 752, 124. doi:10.1088/0004-637x/752/2/124

Qiu, J. (2021). The neupert effect of flare ultraviolet and soft X-ray emissions. *Astrophysical J.* 909, 99. doi:10.3847/1538-4357/abe0b3

Ramaty, R., and Mandzhavidze, N. (2000). High energy processes in solar flares. *Amer. Inst. Phy. Conf.Series.* 522, 401–410. doi:10.1063/1.1291742

Reep, J. W., Bradshaw, S. J., Crump, N. A., and Warren, H. P. (2019). Efficient calculation of non-local thermodynamic equilibrium effects in multithreaded hydrodynamic simulations of solar flares. *ApJ* 871, 18. doi:10.3847/1538-4357/aaf580

Reep, J. W., Bradshaw, S. J., and McAteer, R. T. J. (2013). On the sensitivity of the GOES flare classification to properties of the electron beam in the thick-target model. *Astrophysical J.* 778, 76. doi:10.1088/0004-637x/778/1/76

Reep, J. W., Polito, V., Warren, H. P., and Crump, N. A. (2018a). The duration of energy deposition on unresolved flaring loops in the solar corona. *Astrophysical J.* 856, 149. doi:10.3847/1538-4357/aab273

Reep, J. W., and Russell, A. J. B. (2016). Alfvénic wave heating of the upper chromosphere in flares. *ApJL* 818, L20. doi:10.3847/2041-8205/818/1/l20

Reep, J. W., Russell, A. J. B., Tarr, L. A., and Leake, J. E. (2018b). A hydrodynamic model of alfvénic wave heating in a coronal loop and its chromospheric footpoints. *ApJ* 853, 101. doi:10.3847/1538-4357/aaa2fe

Reep, J. W., Siskind, D. E., and Warren, H. P. (2022). Solar flare irradiance: Observations and physical modeling. *Astrophysical J.* 927, 103. doi:10.3847/1538-4357/ac4784

Ricchiazzi, P. J., and Canfield, R. C. (1983). A static model of chromospheric heating in solar flares. *Astrophysical J.* 272, 739–755. doi:10.1086/161336

Rubio da Costa, F., and Kleint, L. (2017). A parameter study for modeling Mg II h and k emission during solar flares. *ApJ* 842, 82. doi:10.3847/1538-4357/aa6eaf

Rubio da Costa, F., Kleint, L., Petrosian, V., Liu, W., and Allred, J. C. (2016). Data-driven radiative hydrodynamic modeling of the 2014 march 29 X1.0 solar flare. *Astrophysical J.* 827, 38. doi:10.3847/0004-637x/827/1/38

Rubio da Costa, F., Kleint, L., Petrosian, V., Sainz Dalda, A., and Liu, W. (2015). Solar flare chromospheric line emission: Comparison between IBIS high-resolution observations and radiative hydrodynamic simulations. *Astrophysical J.* 804, 56. doi:10.1088/0004-637x/804/1/56

Russell, A. J. B., and Fletcher, L. (2013). Propagation of alfvénic waves from corona to chromosphere and consequences for solar flares. *Astrophysical J.* 765, 81. doi:10.1088/0004-637x/765/2/81

Russell, A. J. B., and Stackhouse, D. J. (2013). Solar flares and focused energy transport by MHD waves. *Astronomy Astrophysics* 558, A76. doi:10.1051/0004-6361/201321916

Saint-Hilaire, P., Schou, J., Martínez Oliveros, J.-C., Hudson, H. S., Krucker, S., Bain, H., et al. (2014). Observations of linear polarization in a solar coronal loop prominence system observed near 6173 Å. *Astrophysical J. Lett.* 786, L19. doi:10.1088/2041-8205/786/2/l19

Sainz Dalda, A., de la Cruz Rodríguez, J., De Pontieu, B., and Gošić, M. (2019). Recovering thermodynamics from spectral profiles observed by iris: A machine and deep learning approach. *Astrophysical J. Lett.* 875, L18. doi:10.3847/2041-8213/ab15d9

Sharykin, I. N., and Kosovichev, A. G. (2014). Fine structure of flare ribbons and evolution of electric currents. *Astrophysical J. Lett.* 788, L18. doi:10.1088/2041-8205/788/1/l18

Shibata, K., and Magara, T. (2011). Solar flares: Magnetohydrodynamic processes. *Living Rev. Sol. Phys.* 8, 6. doi:10.12942/lrsp-2011-6

Shih, A. Y., Lin, R. P., and Smith, D. M. (2009). RHESSI observations of the proportional acceleration of relativistic >0.3 MeV electrons and >30 MeV protons in solar flares. *ApJL* 698, L152–L157. doi:10.1088/0004-637x/698/2/l152

Shimizu, T., Imada, S., Kawate, T., Ichimoto, K., Suematsu, Y., Hara, H., et al. (2019). "The Solar-C_EUVST mission," in UV, X-Ray, and Gamma-Ray Space Instrumentation for Astronomy XXI of Society of Photo-Optical Instrumentation Engineers (SPIE) Conference Series, 1111807. doi:10.1117/12.2528240

Sollum, E. (1999). *Hydrogen ionization in the solar atmosphere : Exact and simplified treatments*. Master's thesis. Oslo: University of Oslo, Institute of Theoretical Astrophysics, 1S.

Tei, A., Sakaue, T., Okamoto, T. J., Kawate, T., Heinzel, P., UeNo, S., et al. (2018). *Blue-wing enhancement of the chromospheric Mg II h and k lines in a solar flare*, 70. Publications of the Astronomical Society of Japan, 100. doi:10.1093/pasj/psy04770.100T

Tian, H., Young, P. R., Reeves, K. K., Chen, B., Liu, W., and McKillop, S. (2015). Temporal evolution of chromospheric evaporation: Case studies of the M1.1 flare on 2014 september 6 and X1.6 flare on 2014 september 10. *Astrophysical J.* 811, 139. doi:10.1088/0004-637x/811/2/139

Uitenbroek, H. (2001). Multilevel radiative transfer with partial frequency redistribution. *Astrophysical J.* 557, 389–398. doi:10.1086/321659

Uitenbroek, H. (2002). The effect of coherent scattering on radiative losses in the solar Ca II K line. *Astrophysical J.* 565, 1312–1322. doi:10.1086/324698

Unverferth, J., and Longcope, D. (2020). Modeling observable differences in flare loop evolution due to reconnection location and current sheet structure. *Astrophysical J.* 894, 148. doi:10.3847/1538-4357/ab88cf

Varady, M., Kasparova, J., Moravec, Z., Heinzel, P., and Karlicky, M. (2010). Modeling of solar flare plasma and its radiation. *IEEE Trans. Plasma Sci.* 38, 2249–2253. doi:10.1109/tps.2010.2057449

Wygant, J. R., Keiling, A., Cattell, C. A., Lysak, R. L., Temerin, M., Mozer, F. S., et al. (2002). Evidence for kinetic Alfvén waves and parallel electron energization at 4-6 R_E altitudes in the plasma sheet boundary layer. *J. Geophys. Res. (Space Phys.* 107, SMP24-1–SMP24-15. doi:10.1029/2001JA900113

Xu, Y., Cao, W., Ding, M., Kleint, L., Su, J., Liu, C., et al. (2016). Ultra-Narrow Negative Flare Front Observed in Helium-10830 Å Using the 1.6 m New Solar Telescope. *Astrophysical J.* 819, 89. doi:10.3847/0004-637x/819/2/89

Young, P. R., Tian, H., and Jaeggli, S. (2015). The 2014 march 29 X-flare: Subarcsecond resolution observations of Fe XXI λ1354.1. *Astrophysical J.* 799, 218. doi:10.1088/0004-637x/799/2/218

Yu, K., Li, Y., Ding, M. D., Li, D., Zhou, Y.-A., and Hong, J. (2020). IRIS Si IV line profiles at flare ribbons as indications of chromospheric condensation. *Astrophysical J.* 896, 154. doi:10.3847/1538-4357/ab9014

Zarro, D. M., and Lemen, J. R. (1988). Conduction-driven chromospheric evaporation in a solar flare. *Astrophysical J.* 329, 456. doi:10.1086/166391

Zharkova, V. V., Arzner, K., Benz, A. O., Browning, P., Dauphin, C., Emslie, A. G., et al. (2011). Recent advances in understanding particle acceleration processes in solar flares. *Space Sci. Rev.* 159, 357–420. doi:10.1007/s11214-011-9803-y

Zharkova, V. V., and Gordovskyy, M. (2005). The kinetic effects of electron beam precipitation and resulting hard X-ray intensity in solar flares. *Astronomy Astrophysics* 432, 1033–1047. doi:10.1051/0004-6361:20041102

Zhou, Y.-A., Hong, J., Li, Y., and Ding, M. D. (2022). Diagnosing the optically thick/thin features using the intensity ratio of Si IV resonance lines in solar flares. *Astrophysical J.* 926, 223. doi:10.3847/1538-4357/ac497e

Zhu, C., Qiu, J., and Longcope, D. W. (2018). Two-phase heating in flaring loops. *ApJ* 856, 27. doi:10.3847/1538-4357/aaad10

Zhu, Y., Kowalski, A. F., Tian, H., Uitenbroek, H., Carlsson, M., and Allred, J. C. (2019). Modeling Mg II h, k and triplet lines at solar flare ribbons. *Astrophysical J.* 879, 19. doi:10.3847/1538-4357/ab2238

frontiers | Frontiers in Astronomy and Space Sciences

TYPE Original Research
PUBLISHED 02 February 2023
DOI 10.3389/fspas.2023.1096133

OPEN ACCESS

EDITED BY
Mihalis Mathioudakis,
Queen's University Belfast, United Kingdom

REVIEWED BY
Damian Christian,
California State University, Northridge, United States
Alexey A. Kuznetsov,
Institute of Solar-Terrestrial Physics (RAS), Russia

*CORRESPONDENCE
Chengcai Shen,
chengcaishen@cfa.harvard.edu

SPECIALTY SECTION
This article was submitted to Stellar and Solar Physics, a section of the journal Frontiers in Astronomy and Space Sciences

RECEIVED 11 November 2022
ACCEPTED 16 January 2023
PUBLISHED 02 February 2023

CITATION
Shen C, Polito V, Reeves KK, Chen B, Yu S and Xie X (2023), Non-thermal broadening of IRIS Fe XXI line caused by turbulent plasma flows in the magnetic reconnection region during solar eruptions.
Front. Astron. Space Sci. 10:1096133.
doi: 10.3389/fspas.2023.1096133

Non-thermal broadening of IRIS Fe XXI line caused by turbulent plasma flows in the magnetic reconnection region during solar eruptions

Chengcai Shen[1]*, Vanessa Polito[2,3,4], Katharine K. Reeves[1], Bin Chen[5], Sijie Yu[5] and Xiaoyan Xie[1]

[1]Center for Astrophysics | Harvard & Smithsonian, Cambridge, MA, United States, [2]Bay Area Environmental Research Institute, NASA Research Park, Moffett Field, CA, United States, [3]Lockheed Martin Solar and Astrophysics Laboratory, Palo Alto, CA, United States, [4]Department of Physics, Oregon State University, Corvallis, OR, United States, [5]Center for Solar-Terrestrial Research, New Jersey Institute of Technology, University Heights, Newark, NJ, United States

Magnetic reconnection is the key mechanism for energy release in solar eruptions, where the high-temperature emission is the primary diagnostic for investigating the plasma properties during the reconnection process. Non-thermal broadening of high-temperature lines has been observed in both the reconnection current sheet (CS) and flare loop-top regions by UV spectrometers, but its origin remains unclear. In this work, we use a recently developed three-dimensional magnetohydrodynamic (MHD) simulation to model magnetic reconnection in the standard solar flare geometry and reveal highly dynamic plasma flows in the reconnection regions. We calculate the synthetic profiles of the Fe XXI 1354 Å line observed by the Interface Region Imaging Spectrograph (IRIS) spacecraft by using parameters of the MHD model, including plasma density, temperature, and velocity. Our model shows that the turbulent bulk plasma flows in the CS and flare loop-top regions are responsible for the non-thermal broadening of the Fe XXI emission line. The modeled non-thermal velocity ranges from tens of km s^{-1} to more than two hundred km s^{-1}, which is consistent with the IRIS observations. Simulated 2D spectral line maps around the reconnection region also reveal highly dynamic downwflow structures where the high non-thermal velocity is large, which is consistent with the observations as well.

KEYWORDS

solar corona, spectroscopic, magnetohydrodynamical simulations, magnetic reconnection (MR), solar eruption

1 Introduction

Magnetic reconnection, or the breaking and rejoining of magnetic field lines in a highly conducting plasma, is commonly believed to be a fundamental process during solar eruptions, and it plays a key role in rapid magnetic energy release (*e.g.*, Shibata and Magara, 2011). During a solar eruption, the magnetic energy can be quickly transported to kinetic and thermal energy in the reconnection diffusion and exhausting regions, and generate energetic particles. The spectroscopic investigations of ultraviolet (UV) emission lines serve as an important diagnostic tool because these diagnostics include physical information about the high-temperature plasma, such as the dynamic evolution properties and the heating and

particle acceleration mechanisms. Various parameters, such as temperature, thickness, density, turbulent velocity, and reconnection rate are interpreted from the observations of the CS. One of the most interesting features is the broadening of high temperature emission lines formed during flares. The theoretical explanation for such broadening includes microscopic ion motions and macroscopic plasma motions of the emitting ion. Therefore, it is important to investigate the impacts and contribution of the turbulent flows on observable emission lines to understand the reconnection process during solar eruptions. Recently, high-temperature plasma due to magnetic reconnection has been widely observed in UV and Extreme-UV (EUV) emission lines, including observations of the entire reconnection site from the large scale-reconnection current sheet down to the flare loop-top region (e.g., Ciaravella et al., 2002; Warren et al., 2018).

In post coronal mass ejection (CME) plasma sheets, the spectroscopic observations from the Ultraviolet Coronagraph Spectrometer (UVCS) on the Solar and Heliospheric Observatory (SoHO) are well studied from large heights above the solar surface (*e.g.*, reviewed in Lin et al., 2015). Among them, turbulent motions inside these hot plasma sheets have been reported by many authors based on the observations of UV/EUV spectral lines. For instance, Ciaravella et al. (2002) deduced that the turbulent motion had a speed less than 60 km s^{-1} in the CS; Ciaravella and Raymond (2008) reported large non-thermal [Fe XVIII] line width in the CS, which at the early stage of the CS is as high as 380 km s^{-1} and later ranges between 50 and 200 km s^{-1}. The combination of bulk motions (*e.g.*, the flow along a fan-shaped CS if the fan is seen edge-on) and turbulence (*e.g.*, Lazarian and Vishniac, 1999) are suggested to be the main contributions to the line broadening. In a long duration, CS studied by Bemporad (2008), the derived non-thermal speeds in the Fe XVIII 974.8 Å spectral lines are of the order of ∼60 km s^{-1} a few hours after the CME and slowly decay down to about 30 km s^{-1} in the following 2 days.

At lower heights of CME/flare plasma sheets (up to about 1.15 R_{sun} from the center of Sun), the EUV Imaging Spectrometer (EIS) on Hinode (Kosugi et al., 2007) has reported a large amount of spectroscopic observations of the plasma sheet region. Warren et al. (2018) analyzed the EIS Fe XXIV lines and found that strong broadening of the 192.04 Å line occurs at the largest observed heights along the CS in a large X-class CME/flare eruption on 2017 September 10th. For instance, the measured non-thermal velocity rises from about 87 km s^{-1} to about 152 km s^{-1} over the observed length of the current sheet in a short time period (the 16:09 UT raster). Furthermore, the line broadening is strong very early in the flare and diminishes over time. Large non-thermal velocities up to 200 km s^{-1} in EIS Fe XXIV line are also analyzed by Li et al. (2018) during this eruption. In addition, the presence of non-Maxwellian electron distributions with enhanced high-energy tails has also been reported by Polito et al. (2018a) during the impulsive phase of this event. The observed line widths of the Fe XXIII and Fe XXIV EIS lines still imply considerable non-thermal broadening in excess of ∼200 km s^{-1} above the flare loop-top region.

The non-thermal features are also be found in other high-temperature Fe XXI lines (*e.g.*, 11 MK). Using the Interface Region Imaging Spectrograph (IRIS De Pontieu et al., 2015), Tian et al. (2014) reported the red-shifted features of Fe XXI that coincided with an X-ray source as observed by RHESSI above flare loops. They obtained greatly redshifted velocities (∼125 km s^{-1} along the line of sight, LOS) on the Fe XXI 1354.08 Å emission line with large non-thermal widths (∼100 km s^{-1}) at the reconnection region.

In recent flare fan observations (seen faceon), the non-thermal widths of the Fe XXI line observed by IRIS were also measured by Reeves et al. (2020). In this work, they found that the pixels at the fan top have broader non-thermal widths than the rest of the emission, especially for the later rasters. By comparing the spectral results of the IRIS and Hinode/EIS observations with the synthetic results of 2D MHD simulations; Cai et al. (2022) suggested that a compressed interface with apparent changes in intensity and Doppler velocities of the spectral lines exist above the flare loops, possibly related to termination shocks. The temporal variation of non-thermal velocity was also studied in flare fan regions; Cai et al. (2019) showed that the non-thermal velocity ranged from 19 to 64 km s^{-1} during a particular period (between 16:00 UT and 16:26 UT, on 2017 September 10th) by analyzing the IRIS Fe XXI 1354.08 Å spectral lines. It is worth mentioning that the observed line width in their work decreased with time as well, though the time period (∼ half an hour) was shorter than these studies in long durations post-CME current sheets (*e.g.*, Bemporad, 2008). The spatial variation of non-thermal velocities is reported by Doschek et al. (2014) in which, they found that the non-thermal motions in the multimillion-degree regions increase with height above flare loops. The deduced non-thermal velocity ranges from 40 to 60 km s^{-1} in the EIS Fe XXIII and Fe XXIV lines spectra.

The broadening of spectral line profiles is commonly thought to be the result mainly due to turbulent and bulk flows in solar flares. In theory, the plasma sheet and flare loop-top regions (which are generally referenced as flare fans when viewed face-on) are predicted to contain substantial turbulence in a set of theoretical models. For example, the tearing current sheet and multiple plasma instabilities (*e.g.,* the plasmoid instability) may cause a set of small-scale turbulent structures which has been widely found in recent numerical models (*e.g.*, Huang and Bhattacharjee, 2016; Ye et al., 2020). Once the Alfvénic reconnection downflows have collided with the closed magnetic loops, the dramatic variation of plasma β also creates favorable environments for generating turbulent flows in these interface regions, where the β can change from high-beta values in the current sheet region to low-beta states in the potential flare loops (*e.g.*, Shen et al., 2022). Bulk plasma flows may significantly contribute to line profiles as well (Ciaravella and Raymond, 2008). For instance, Guo et al. (2017) calculated synthetic spectral line profiles of the IRIS Fe XXI 1354 Å line at the reconnection site with the presence of termination shocks (TS) in an MHD model of a solar flare. The significant shifts of these synthetic IRIS spectral lines suggested that the synthetic line profile of Fe XXI and its time evolution may serve as a possible guide for observational signatures of a flare TS. Possible Doppler shift signatures of such termination shocks have been subsequently reported by Polito et al. (2018b) using IRIS Fe XXI observations. Further, in a comprehensive radiative 3D model of solar flare (Cheung et al., 2019), synthetic non-Gaussian (κ) distributions of EUV emission-line profiles result from temperature and velocity gradients along the line of sight.

In observations, various dynamic flows at multiple scales have also been found in a set of image observations above flare loops. For instance, McKenzie (2013) reported turbulent dynamic flows observed by the X-ray Telescope (XRT; Golub et al., 2007) on board Hinode and the Atmospheric Image Assembly (AIA; Lemen et al., 2012) on board the solar dynamic observatory (SDO; Pesnell et al., 2012). The flows were found above the post-eruption arcades and

measured with local correlation tracking. These results also show significant shears in velocity, giving the appearance of vortices and stagnations. More plasma downflows, now referred to as supra-arcade downflows (SADs), have often been investigated in the flare fan regions above the post-flare loops (e.g., Xie et al., 2022). However, studies focusing on how these turbulent flows affect the EUV line profiles and the non-thermal broad features above the post-flare loops remain sparse.

In this study, we focus on the properties of Fe XXI lines in the plasma sheet and flare-loop top regions. The high-temperature plasma in flare cusp regions is well observed in the 2015–03-07 flare by IRIS, Hinode/XRT, and SDO/AIA. In **Section 2**, we will briefly review the main observational features and show the non-thermal broadening and Doppler velocity variations observed by the Fe XXI line. On the modeling side, in our recent state-of-the-art MHD model of solar flares Shen et al. (2022), a turbulent interface region below the flare termination shock is revealed in the classic solar flare geometry. The highly dynamic flows are also found in the CS regions. Therefore, we aim to investigate the emission lines based on this 3D model and discuss the origin of line broadening to be compared with observations. We describe the numerical models and the calculation method for simulating Fe XXI lines in **Section 2**, and show the synthetic spectral lines in Section 3. We then investigate the spatial and temporal distribution of the non-thermal spectral line broadening by combining 3D MHD modeling and IRIS spectral observations. Finally, discussions and conclusions are given in **Section 4**.

2 Materials and methods

2.1 Observations

The flare event under study is a long-duration M9.2 solar flare located at the east limb, that occurred on March 7, 2015. We mostly focus on observations from the IRIS satellite, which, since its launch in 2013, has been providing unprecedented high-resolution images and spectra of the lower atmosphere and corona (De Pontieu et al., 2014; 2021). IRIS consists of: (1) a Slit-Jaw Imager (SJI) channel, acquiring images in four different filters showing plasma at photospheric, chromospheric and transition region temperatures with a 0.167″ resolution; and (2) a spectrograph channel, observing emission lines and continua formed over a broad range of temperatures (from the photosphere to the flaring corona), at very high spatial (0.33–0.4″), temporal (down to ≈ 1s) and spectral (2.7 km s^{-1} pixels) resolution. The level 2 IRIS data used here are already calibrated and prepped, as described in the IRIS' documentation and instrument papers (De Pontieu et al., 2014; Wülser et al., 2018).

The *Hinode* X-Ray Telescope (Golub et al., 2007; Kano et al., 2008) observed the flare with its flare response, using the Be-Thin and Be-Med filters and a resolution of 1.028″ per pixel. A two-filter observing program consisting of the Al-poly and Be-thin filters was taken before and after the flare response. The XRT data is calibrated and prepped using the xrt_prep routine, available in the SolarSoft suite of IDL programs (Freeland and Handy, 1998), which does the dark subtraction, and removes the pedestal and vignetting effects (Kobelski et al., 2014). The current version of xrt_prep also aligns the XRT images with AIA images by calibrating the time-dependent offsets between XRT and the *Hinode* Ultra Fine Sun Sensors (Yoshimura and McKenzie, 2015).

AIA (Lemen et al., 2012) provides full-Sun images with a resolution of ∼0.6″ per pixel and a cadence of 12 seconds for the EUV passbands. The AIA data are processed using the SolarSoft routine aia_prep, which de-rotates the images from the different AIA telescopes, aligns them, and gives them all the same plate scale.

Figure 1 shows an overview of the flare as observed by XRT in the Be-Thin filter (left columns), AIA in the 131Å filter (dominated by Fe XXI emission at ≈ 10MK, middle column) and in the IRIS SJI centered at 1330Å (right column). This SJI channel is dominated by emission from C II plasma at around 10–40kK, but it is also sensitive to hot plasma from Fe XXI during flares. The vertical lines in the XRT images indicate the location of the IRIS spectrograph slit during the observation. The white box in the middle images indicates the field of view of the IRIS SJI images on the right.

Figure 2 shows two images from the XRT flare response using the Al-Thick and Be-Thin filters. The right two panels of **Figure 2** shows the temperature and emission measure, calculated from the filter ratio of the XRT two filters using the IDL routine xrt_teem_ch. We use coronal abundances to calculate the XRT temperature response functions because we are interested in the above-the-looptop plasma, which is likely directly heated, instead of resulting from chromospheric evaporation. Spectroscopic measurements in this region during another flare indicate that abundances are likely coronal (Warren et al., 2018).

In this work, we focus on the analysis of the Fe XXI observed by IRIS in high-temperature ≈10 MK plasma during flares. The IRIS observations during the flare event under study consist of an 8-step sparse raster (where the distance between consecutive slit positions is 1″), with a ≈30s exposure time, a raster cadence of ≈250s and a factor of two summing along the slit position. **Figure 3** shows the intensity map of Fe XXI and spectra profiles at different times. For each slit position and time we averaged the Fe XXI spectra over 50 slit pixels to increase the signal-to-noise ratio. The centroid position (or Doppler velocity) of spectral lines and width (or FWHM) are obtained by using Gaussian fitting at each time. In fact, the line is very weak in the cusp/reconnection region, which is not surprising given the low density of the plasma there and the fact that the IRIS Fe XXI 1354.08Å line is a forbidden transition (*e.g.*, Young et al., 2015). The non-thermal velocity was obtained by using the following formula:

$$v_{nth} = \frac{\lambda_0}{c} \cdot 2\sqrt{ln2} \cdot \sqrt{FWHM^2 - FWHM_{th}^2 - FWHM_{instr}^2}. \quad (1)$$

where λ_0 is 1354.08 Å, the rest wavelength of the line (e.g. Polito et al., 2015), c is 3×10^{10} cm s^{-1}, $FWHM_{instr}$ is the IRIS instrumental width (26 mÅ) and $FWHM_{th}$ is the thermal broadening of the line (≈0.43Å) assuming a formation temperature of $\log T$[K] = 7.05.

Figure 4A shows that the non-thermal velocity gradually decreases over time from more than 100 km s^{-1} to about 30 km s^{-1} in around 2 hours. **Figure 4B** shows that the Doppler shift velocity appears to be close to a mean value(∼4 km^{-1}) for most of the time. The only exception is the first few minutes of the observation, where the Doppler velocity reaches larger values up to almost 40 km s^{-1}. We note that there is a lot of scattering between the values obtained in different IRIS slits. The IRIS level 2 data used in this work are already corrected for both the orbital and absolute calibration of the wavelength array, with an accuracy that is estimated to be ≈1 km s^{-1} for most databases (Wülser et al., 2018). However, it is usually recommended to double-check the calibration manually using the centroids of strong neutral lines in case a small residual drift is still present. Such a sanity check

10.3389/fspas.2023.1096133

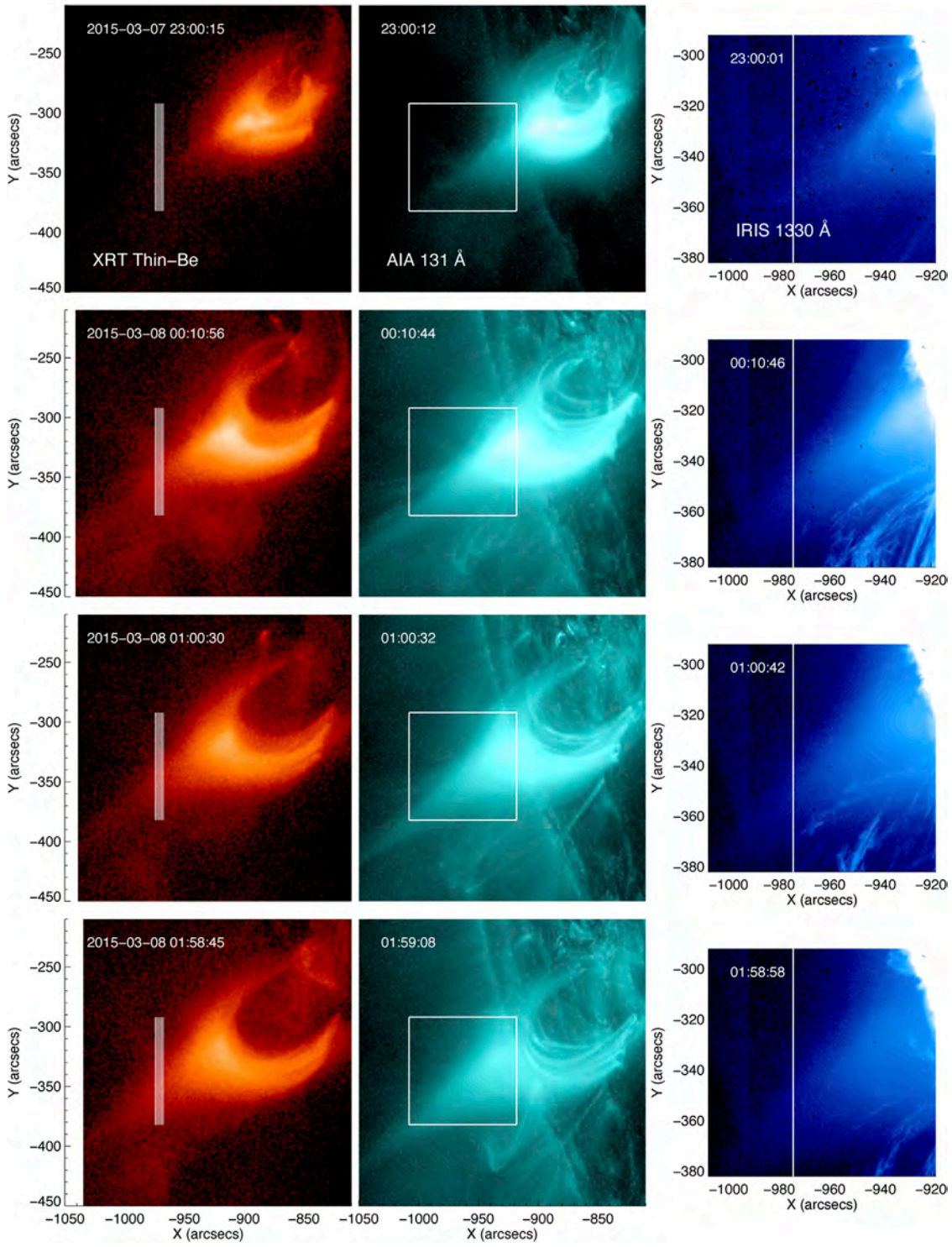

FIGURE 1
Overview of the 2015–03-07 flare between 23:00:15 UT to 01:58:45 UT on March 8th. The panels from left to right are observed images from *Hinode*/XRT, *SDO*/AIA 131Å, and *IRIS* 1330 Å SJI. The vertical white lines on XRT images indicate the slit position of *IRIS* Fe XXI spectra observations. The white box on AIA 131 maps shows the SJI FOV.

cannot be performed in our data set because the raster is located off-limb and neutral lines are not observed.

Further, we note that the peak time of the M class flare occurred at about 22:22UT, but IRIS did not detect sufficient signals in the Fe XXI line before ~22:55UT shown by the dashed line in **Figure 4C**. As shown by the light curves of GOES X-ray, RHESSI, SDO/AIA 131Å and Fe XXI flux in this figure, the eruption starts from about 22:00UT and continues for more than 4 h. On the other hand, high temperature plasma is already observed before this time in the AIA 131 Å channel, showing plasma at ~10 MK. This lack of emission in the IRIS Fe XXI

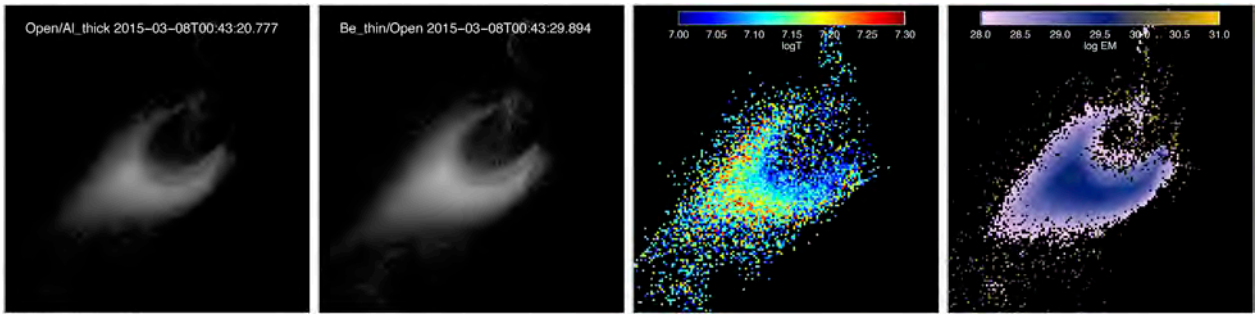

FIGURE 2
Left two images: XRT Al-Thick and Be-Thin, respectively, at about 00:43 UT on March 8. Right two images: Temperature and emission measure, respectively, calculated from the Al-Thick/Be-Thin filter ratio.

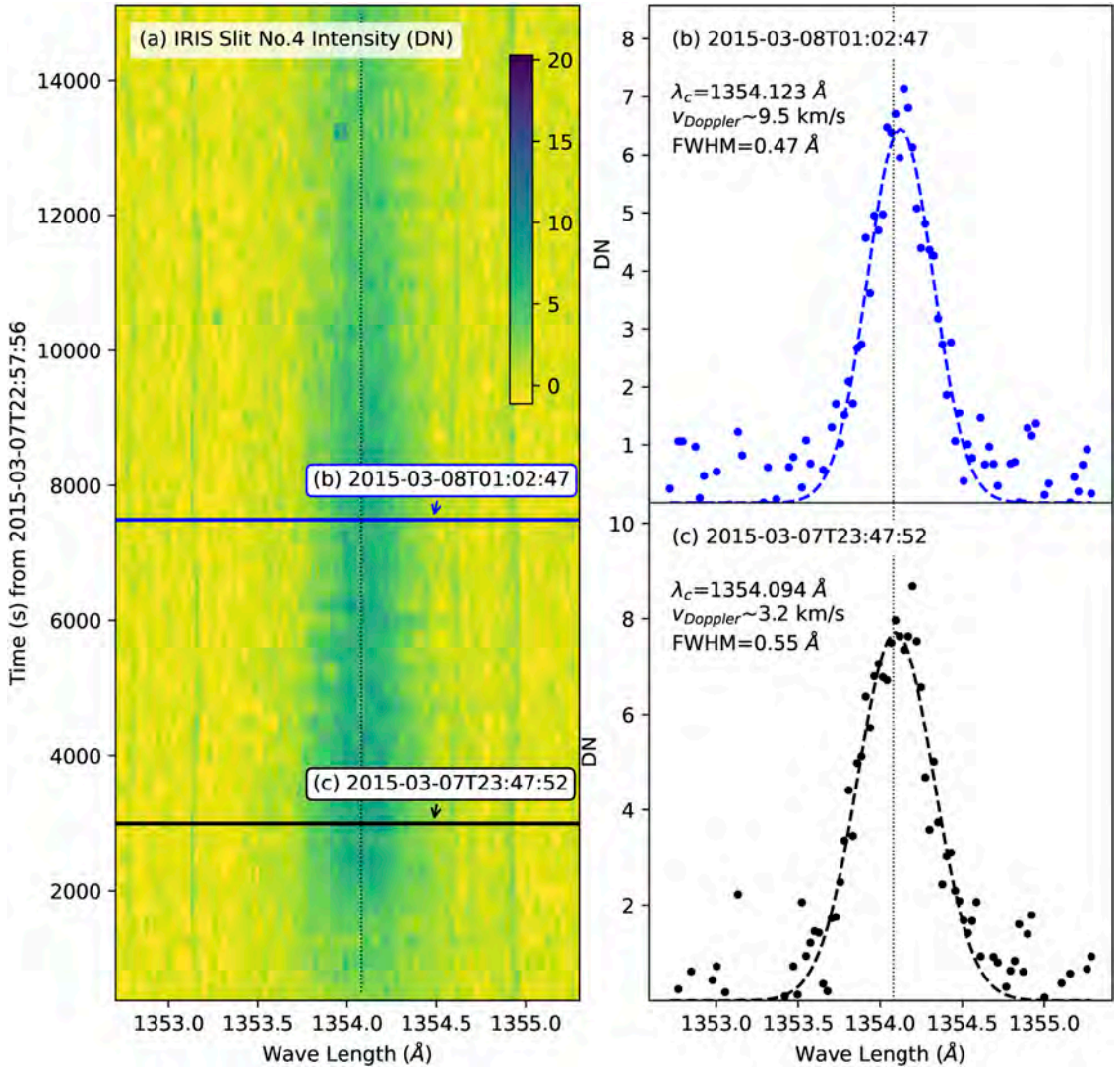

FIGURE 3
Fe XXI observations from IRIS during the 2015–03-07 flare. Panel **(A)** is the 2D spectral map as a function of time observed by IRIS slit No. 4. Panels **(B–C)** show Fe XXI spectral profiles at the chosen times indicated by blue and black lines in panel **(A)**. The dashed curves show Gaussian fitting results with fit parameters (the central wavelength (λ_c) and FWHM). The vertical dotted lines indicate the position of λ_0=1354.08 Å.

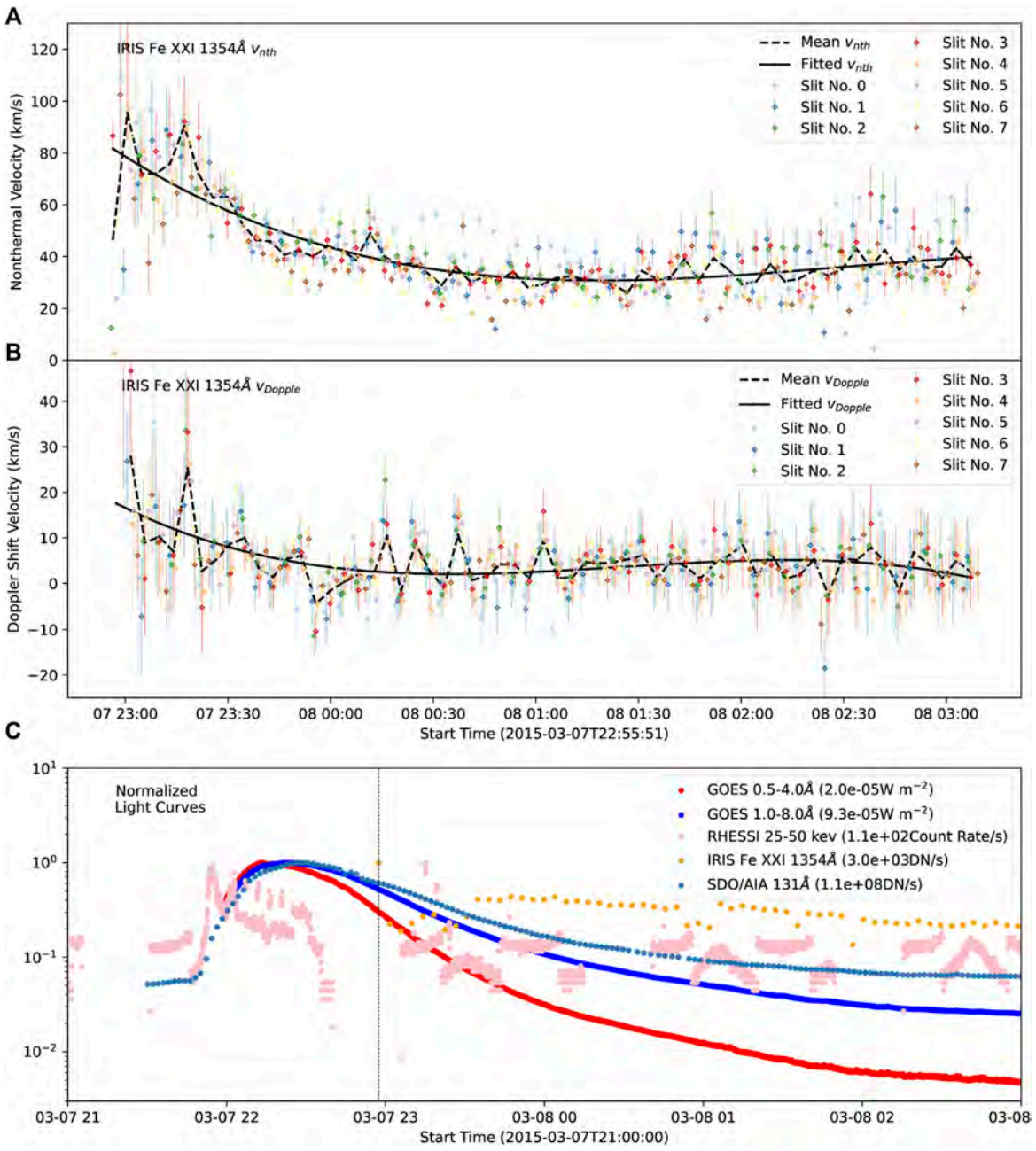

FIGURE 4
Panel **(A)**: non-thermal velocity of the Fe XXI 1354 Å line observed by the eight IRIS raster slits over time during the 2015–03–07 flare. The error bar indicates measurement errors based on the statistical error estimation. The dashed black line is for the mean values over eight slits, and the solid black line shows the third-order polynomial fitting profile based on the mean values. Panel **(B)** is for the Doppler shifting velocity of Fe XXI 1354 Å line in the same event. Panel **(C)**: normalized light curves of GOES and RHESSI, and the IRIS Fe XXI and SDO/AIA 131 flux in the chosen regions as shown in **Figure 1**. The dashed vertical line indicates the starting time for the following analysis on IRIS Fe XXI 1354 Å lines.

line may be caused by the fact that this line is particularly faint, as mentioned above. This also suggests that the non-thermal velocity might have been higher during the early impulsive phase of the flare, before we can observe any Fe XXI emission in IRIS.

2.2 Model Setup

We use the same 3D solar flare model as shown in Shen et al. (2022), which follows the classic CHSKP configuration of two-ribbon flares. In this model, we solve the initial and boundary value problem governed by resistive MHD equations using the public code Athena (Stone et al., 2008). We use the non-dimensional form of MHD equations and set the primary characteristic parameters as follows: length $L_0 = 1.5 \times 10^8$m, magnetic field strength $B_0 = 0.001$T, density $\rho_0 = 2.5 \times 10^{14}$m^{-3}, temperature $T_0 = 1.13 \times 10^8$K, velocity $V_0 = 1.366 \times 10^6$ m s^{-1}, and time $t_0 = 109.8$s according to the general coronal environments. At the beginning of the MHD simulations, the magnetic field strength is uniform (~10 Gauss) in the background region, and the plasma number density is around 8×10^{14}m^{-3} near

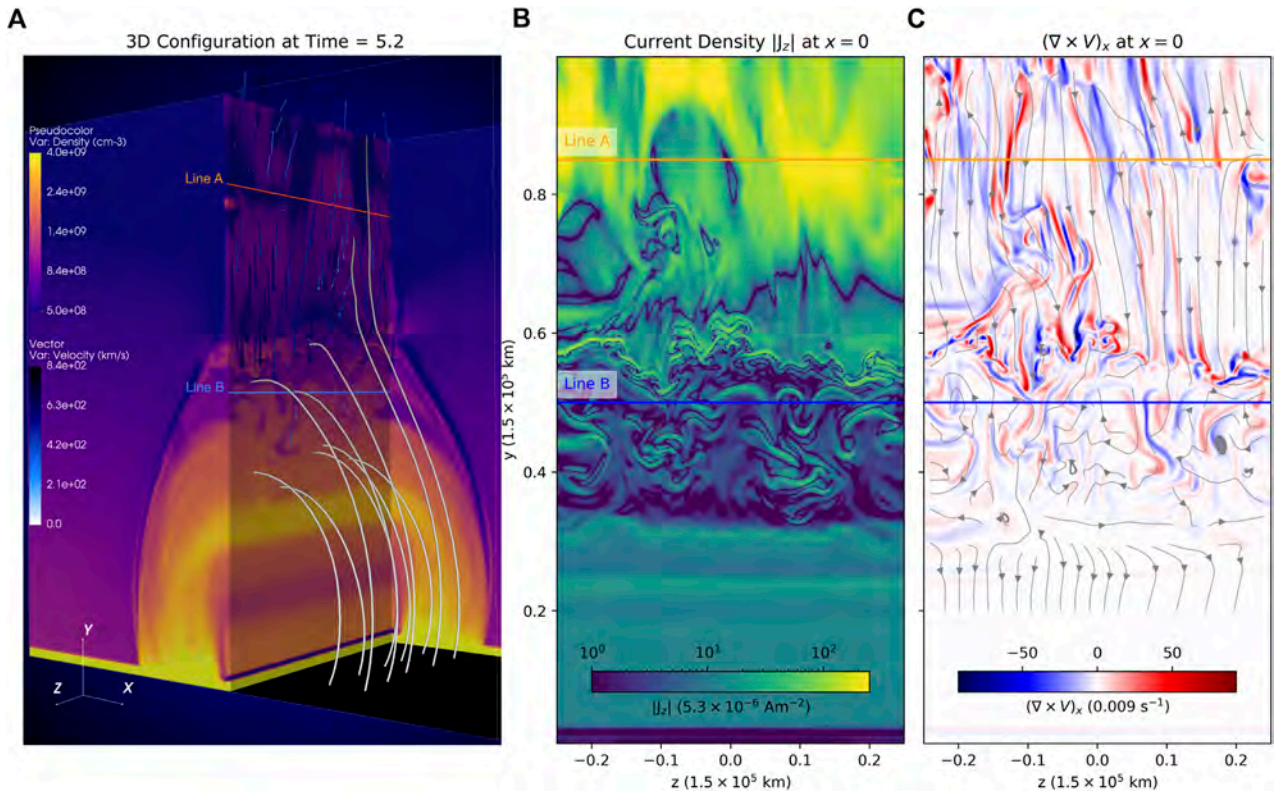

FIGURE 5
Distribution of primary variables in a 3D flare model at *time* = $5.2t_0$. **(A)** Density and velocity distribution on the chosen planes in 3D. The gray tubes indicate magnetic field lines, and the black/blue arrows are for plasma flows. Along the LOS direction, two sampling lines A and B are chosen on the central plane ($x = 0$). **(B)** Current density at the central plane. **(C)** Velocity vorticity component $(\nabla \times V)_x$ on the central plane. The streamlines show velocity fields (V_y, V_z).

the bottom of the corona, above a denser layer representing the chromosphere. In the later time as shown in the following sections (e.g., **Figure 5**), the magnetic field strength slightly enhanced by ∼1.3 times in both flare foot-points and loop-top regions following the magnetic loops shrinking, while the plasma density can be ∼10 and ∼6 times higher in foot-points and loop-top regions, compared with the background corona. As the magnetic reconnection continually takes place, the plasma in the reconnection region and flare loop-top regions can be heated to higher than 10^7 K at the most bursty phases and maintain the relatively high temperature (>∼8 MK) during the whole simulation period. It is worth mentioning that the plasma β, the ratio of the gas pressure to the magnetic pressure, is another dominant parameter in the MHD simulations and is set to about 0.1 in the background corona. The characteristics (such as magnetic strength and plasma density) are then scaleable variables by maintaining a constant β.

We perform combined 2D and 3D models in which the 2D simulation runs first to build the classic flare geometry and then the 3D model is started based on the resulting 2D configuration. In 2D cases, the system is initialized from a pre-existing vertical Harris-type CS along the y direction in mechanical and thermal equilibrium. Driven by the initial perturbation on magnetic fields (also see Shen et al., 2022), the CS becomes thinner due to the Lorentz-force attraction, and a pair of reconnection jets flow away from the reconnection X-point close to the initial perturbation center. The closed magnetic loops then appear as the reconnected magnetic flux accumulated at the bottom due to the line-tied boundary, in which the magnetic field lines are rooted at the boundary. Once the flare loops are well-formed after about $t = 17.5t_0$, we start the 3D simulations by symmetrically extending all primary variables from the 2D domain to the third direction ($z-$). We then apply this time as the starting-point of evolution in the following analysis. The system then self-consistently evolves, and a set of reconnection-driven flare phenomena are seen, including Alfvénic bi-directional reconnection outflows, the termination shocks, and the turbulent interface region below the extended reconnection current sheet and above the flare loops (**Figure 5A**).

To compare our models with observations, we calculate synthetic Fe XXI 1354 Å line profiles that are observable by IRIS in high-temperature flare plasma (e.g., ∼11 MK). Once we compute the plasma properties (temperature, density, and velocity) on each cell from the 3D MHD simulation, the synthetic emission can be obtained along any chosen LOS (e.g., Lines A and B in **Figure 5**) by using the formula (e.g., Guo et al., 2017):

$$I_\nu = \frac{h\nu}{4\pi} \int f_\nu n_e n_H g(T_e)\ dl \tag{2}$$

where ν indicates the frequency of emission lines, and l is the integration path. $n_e, n_H \sim 0.83 n_e$ are the electron and proton densities, which are obtained from MHD plasma density in the following calculations. $g\ (T_e)$ is the contribution function, which can be obtained from the CHIANTI database (Del Zanna et al., 2021) but needs

account for proper element abundance (e.g., Feldman, 1992, in this paper). f_v indicates the variation of velocity distribution function due to plasma flows along the LOS, given by

$$f_v = \frac{1}{\pi^{1/2}\Delta v} exp\left(-\left(\frac{\Delta v + v_0 v_l/c}{\Delta v_D}\right)^2\right). \quad (3)$$

Here v_l is the plasma flow speed along the LOS, c is the speed of light. v_0 is the rest frequency, and $\Delta = v - v_0$ means the offset frequency accordingly. The thermal broadening can be calculated by

$$\Delta v_D = \frac{v_0}{c}\sqrt{\frac{2kT}{m}}, \quad (4)$$

where k is the Boltzmann constant, T is the temperature, m is the atomic mass of the chosen ion (e.g., Fe in this work).

3 Results

We calculate the synthetic emission line profiles of the Fe XXI 1354 Å line when the dynamic flows are well-developed in both the CS and flare cusp regions. It is noticed that Fe XXI 1354 Å is one of the strongest emission line from high-temperature plasma (e.g., ~10MK) in IRIS observations. The emission from other cool lines (e.g., C I (Li et al., 2015)) is expected to be rare from an edge-on viewing direction, so we will only focus on Fe XXI 1354 Å in this paper but exclude other IRIS lines. **Figure 5** shows the magnetic field lines and the distribution of primary variables (density and velocity) at the chosen time (time = $5.2t_0$, with the chosen characteristic timescale t_0~110 s). Above y~$0.6L_0$, the reconnection downward outflows can be clearly seen from the velocity vectors (**Figure 5A**) and streamlines (**Figure 5C**). The turbulent structures in the interface regions below the CS are well illustrated on the current density map, as shown in **Figure 5B**. The high shearing and vortex flow, indicated by the large curl of the velocity field ($\nabla \times V$) and randomly rounding streamlines, are easily found around the chosen sampling Lines A and B as well.

3.1 Emission line profiles

We first analyze the spectral properties along the sampling Lines A and B. As shown in **Figure 5**, Line A is located at a relatively higher altitude along the CS, which is close to the primary reconnection X-points indicated by the strongest current density (J_z, in **Figure 5B**) and flow stagnation regions (**Figure 5C**). On the other hand, Line B is chosen to go through highly turbulent above loop-top regions, where the SADs-like tenuous down flow features are well-developed as reported by Shen et al. (2022). At this time ($5.2t_0$), Line A shows slightly higher temperature and lower density than that of Line B overall (**Figure 6**). Along the LOS, we note that the plasma is appreciably cooler than the expected Fe XXI 1354 Å line temperature (e.g., Log T~7.05 K). This effect occurs because the LOS path is outside the high-temperature CS at some positions. Due to the highly turbulent plasma flows, the temperature, density, and velocity along the sampling lines all show various perturbations. The domain perturbation velocity ranges from ~ + 100 to ~ − 100 km s^{-1} as shown in **Figure 6C**.

Figure 6D shows the synthetic line profiles of the Fe XXI 1354 Å lines for the above two sampling lines. We assume that LOS is from $z = -0.25L_0$ to $z = +0.25L_0$ along each sampling line, and the Doppler shift velocity is then plotted based on this geometry accordingly. We note that the LOS direction may also be reversed in the observations, so the red and blue shifted Doppler velocity is a relative value in this plot. In this case, Line A shows a larger Doppler shift velocity (about 18 km s^{-1}) than that of Line B because the Alfvénic downward reconnection outflows around Line A dominate the overall flow behavior. We measure the line broadening width using the full width at half maximum (FWHM) of the synthetic emission profiles. Then the non-thermal velocity (v_{nth}) can be obtained according to the following equation:

$$\mathrm{FWHM} = \sqrt{4\ln 2\left(\frac{\lambda_0}{c}\right)\left(\frac{2kT_{eq}}{m} + v_{nth}^2\right)}, \quad (5)$$

where the λ_0 is the central wavelength of Fe XXI 1354 Å line, $\log T_{eq}$ = 7.05 K is the typical formation temperature of this line. In this particular position, the non-thermal velocity of Lines A (~95 km s^{-1}) and B (~37 km s^{-1}) are consistent with the deduced values in recent observations (e.g., Warren et al., 2018), but the line A value is slightly larger than those found by Doschek et al. (2014). However, the synthetic line profile strongly depends on the space and time evolution of the solar flare system, which will be addressed in the next section. In the current analysis in this paper, we only focus on non-thermal broadening features but leave the Doppler shifts for future works because the integration depth along the LOS is limited to the simulation box scale, which is surely shorter than the realistic CME/flare scale. Thus, the synthetic Doppler shift of Fe XXI 1354 Å line can be significantly affected by several locally large momentum components (e.g., the well-developed flux ropes), and the model-deduced Doppler velocity can largely depart from the common observational results by IRIS (**Figure 4B**). Therefore, large-scale solar eruption models are required to make a detailed comparison with the observable Doppler velocity in the future.

In general, the actual temperature on each pixel (or cell) along the LOS cannot always be exactly at the T_{eq}, in either the observations and MHD models. Therefore, the deduced non-thermal velocity is unavoidably affected by the thermal broadening due to different temperatures, especially for high-temperature plasmas with $\log T$ > 7.05 K. In the following sections, we will follow this approach (where the equilibrium temperature is usually assumed when calculating the non-thermal broadening) to match the observational data analysis but give a more detailed discussion in **Section 3.3**.

We analyze the perturbation properties of primary variables along the LOS by using the Fourier transform method to investigate the nature of the broadening of spectral lines. In **Figure 7**, we perform the one-dimensional Fourier transform for density (ρ), velocity square (v^2), and kinetic energy (E_k) along the Lines A and B. It is clear that these perturbations appear on all scales (or wave number (k) ranges), and the kinetic energy cascades from the large scale to the small scale as well. Furthermore, the spectrum matches the power-law tendency as the prediction in the classic turbulence theories, which could naturally result in the line broadening. Due to the limitation of the MHD grid sizes, we do not show here the spectrum distribution in high-k ranges where the possible inertial range is expected in turbulence theories. However, we can estimate the turbulence properties in the intermediate ranges quantitatively by fitting a power-law spectrum ($\sim k^{-\gamma}$) in **Figure 7C**. We also check the temperature

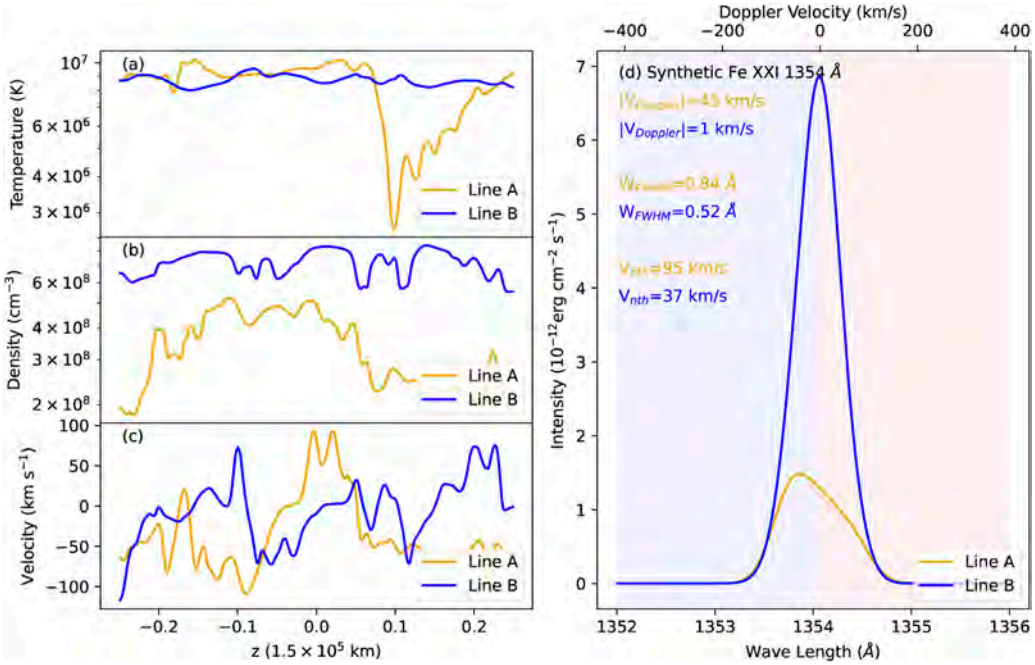

FIGURE 6
Synthetic Fe XXI 1354.08 Å emission along the sampling lines A and B shown in **Figure 5**. **(A–C)** Temperature, density, and velocity profiles along the two sampling lines. **(D)** Synthetic spectra for lines A and B $v_{Doppler}$ and v_{nth} indicate the Doppler shift velocity and non-thermal velocity, respectively. W_{FWHM} are the line broadenings of each spectral line obtained by measuring the full width at half maximum (FWHM).

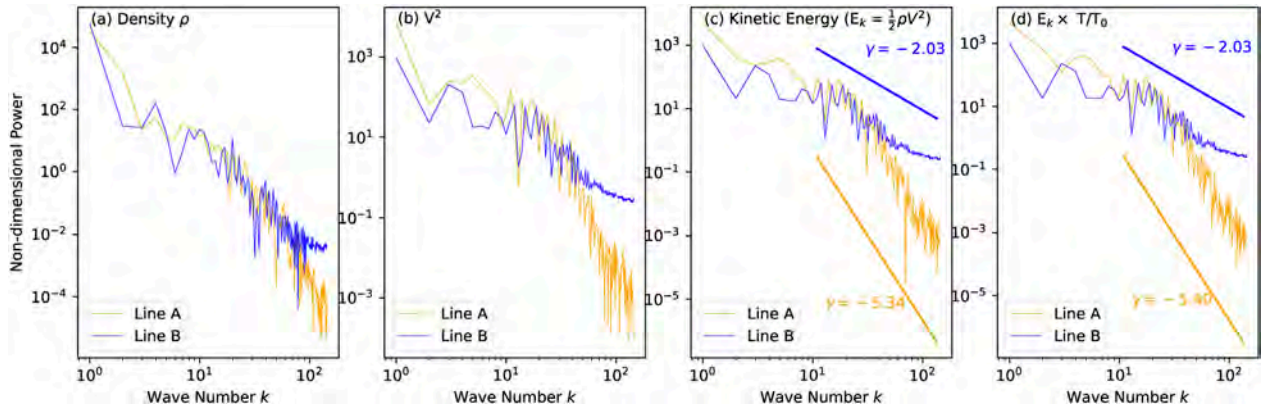

FIGURE 7
Fourier power spectrum along the sampling lines A and B for **(A)** density perturbations, **(B)** velocity power, **(C)** kinetic energy perturbations, and **(D)** temperature-weighted kinetic energy. The peak formation temperature T_0 for Fe XXI lines is about 11.5 MK in panel **(D)**. The horizontal axis is wave numbers, and the vertical axis is non-dimensional power. The γ indicates the power index by fitting the spectrum profiles with power-law functions ($\sim k^{-\gamma}$).

weighted E_k in according to the chosen temperature (log$T$~7.05 K) for the Fe XXI 1354 Å line. A similar power law distribution pattern can be seen clearly, as shown in **Figure 7D**. We notice that Line A with larger Fe XXI 1354 Å line broadening shows a higher index (γ~5.34) as compared with the shallower line B (γ~2). This result indicates that large bulk flows can significantly contribute to the line broadening as shown by the velocity spectrum of Line A, in which the more turbulent flows remain in the low-k (or large scale) ranges.

3.2 Spatial and temporal evolution

In **Figure 8**, we plot the distribution and temporal evolution of synthetic Fe XXI 1354 Å emissions with a viewpoint such that the plasma sheet is viewed edge-on. At each MHD simulation cell on the $x-y$ plane, we obtain the synthetic spectral lines assuming that the LOS is along the $z-$ direction. The maximum intensity of the obtained Fe XXI 1354 Å spectra line at each MHD grid is shown in **Figure 8A**, in which the bright sheet structure and flare cusp regions can be clearly

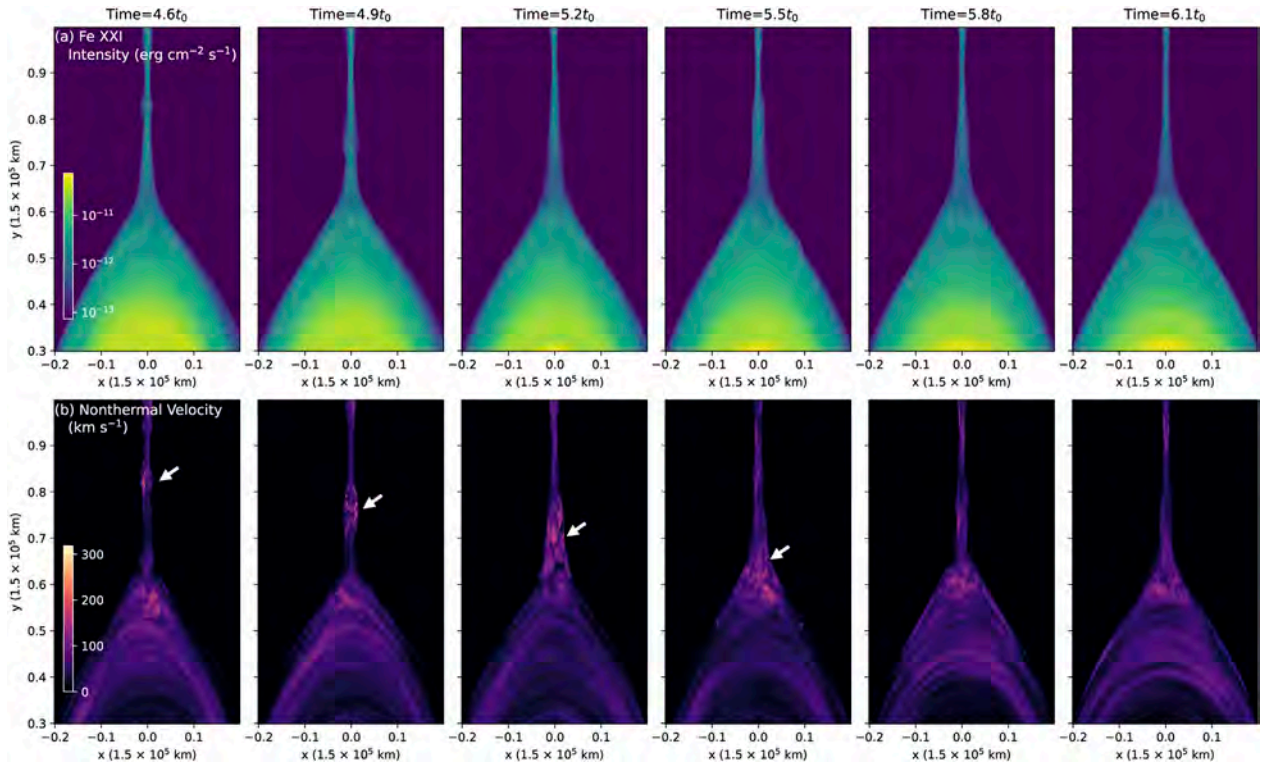

FIGURE 8
Synthetic Fe XXI 1354 Å emission maps at different times. **(A)** The peak intensity of 1354 Å spectra line during time $t = 4.6t_0$ to $6.1t_0$, **(B)** The deduced non-thermal velocity (v_{nth}). The white arrows annotate the downward moving high v_{nth} structures.

seen as predicted by the standard solar flare model. The non-thermal velocity is calculated and shown in Figure 8B.

Figure 8 shows that the region where there is strong non-thermal line broadening (up to ~300 km s^{-1}) is dynamically evolving in both the CS and flare cusp regions. The region of high non-thermal broadening flows downwards along the CS from the primary reconnection X-point region to the flare cusp region. The white arrows in Figure 8B illustrate this process during about one characteristic timescale from $t = 4.6t_0$ to $5.5t_0$. The downward-moving patch of high non-thermal broadening finally consolidates into the cusp region after t~$5.5t_0$, and causes extended regions of high non-thermal broadening above the flare loop-top.

In order to understand the magnetic field topology and plasma flow properties in these high-v_{nth} regions, we plot out the horizontal momentum component (ρV_z) and magnetic component (B_z) in Figure 9. Because the emission intensity of the Fe XXI line is proportional to ρ^2 and is primarily affected by horizontal flow V_z, the plasma momentum (ρV_z) should be a sensitive factor to distinguish the effects of different structures on emission line profiles and line broadening. As shown in Figure 9A, the dashed lines and arrows highlight the heights characterized by enhanced v_{nth}, similarly to Figure 8B. It is clear that the position of the strong horizontal momentum component coincides with such heights. The strongest momentum regions are usually associated with well-developed magnetic flux-ropes. At time = $4.6t_0$, two of these flux-ropes are highlighted by plotting the chosen helical magnetic field lines where the strongest momentum component appears. At later times ($4.9 \sim 5.2t_0$), these two flux-ropes are associated with strong ρV_z components that move downwards to lower heights. In fact, the strong momentum components (ρV_z) are due to the appearance of a guide field B_z in such a turbulent reconnection current sheet. As shown in the second row of Figure 9, the guide field B_z widely appears with a very turbulent behavior inside the whole current sheet. The typical relative strength of B_z to the total background (B) ranges from ~5%–10%, and can be larger than ~30% at particular positions and times (indicated by the dark-blue color in Figure 9). It is then not surprising that the well-developed flux-ropes with strong momentum components (ρV_z) are generally found in high B_z regions. In addition, other structures all have significant contributions to the momentum component ρV_z, including the growing flux-ropes and very turbulent reconnection outflows with remarkable horizontal flow components along the $z-$ direction. As shown in Figure 9, well-developed flux-ropes are relatively rare in the whole current sheet region. The fluctuations in ρV_z can be commonly found around the growing flux-ropes and turbulent reconnection outflow patches as well. For example, a large number of growing flux-ropes appear at the center region at time = $5.2t_0$, which is consistent with the high v_{nth} region above $y = 0.7L_0$. Meanwhile, the nearby fully developed flux rope is located at a much lower altitude (y~$0.65L_0$).

The downward high-v_{nth} features commonly exist for a longer duration in the reconnection process. Figure 10 displays the time–distance map (or "stack plot"), showing the distribution of the non-thermal velocity of Fe XXI 1354 Å line along at the CS center ($x = 0$) as a function of time. The high-v_{nth} emission flows away from the primary X-point regions nearby y~0.9, as can be clearly seen in Figure 10B. These high-v_{nth} patches are most like to originate from

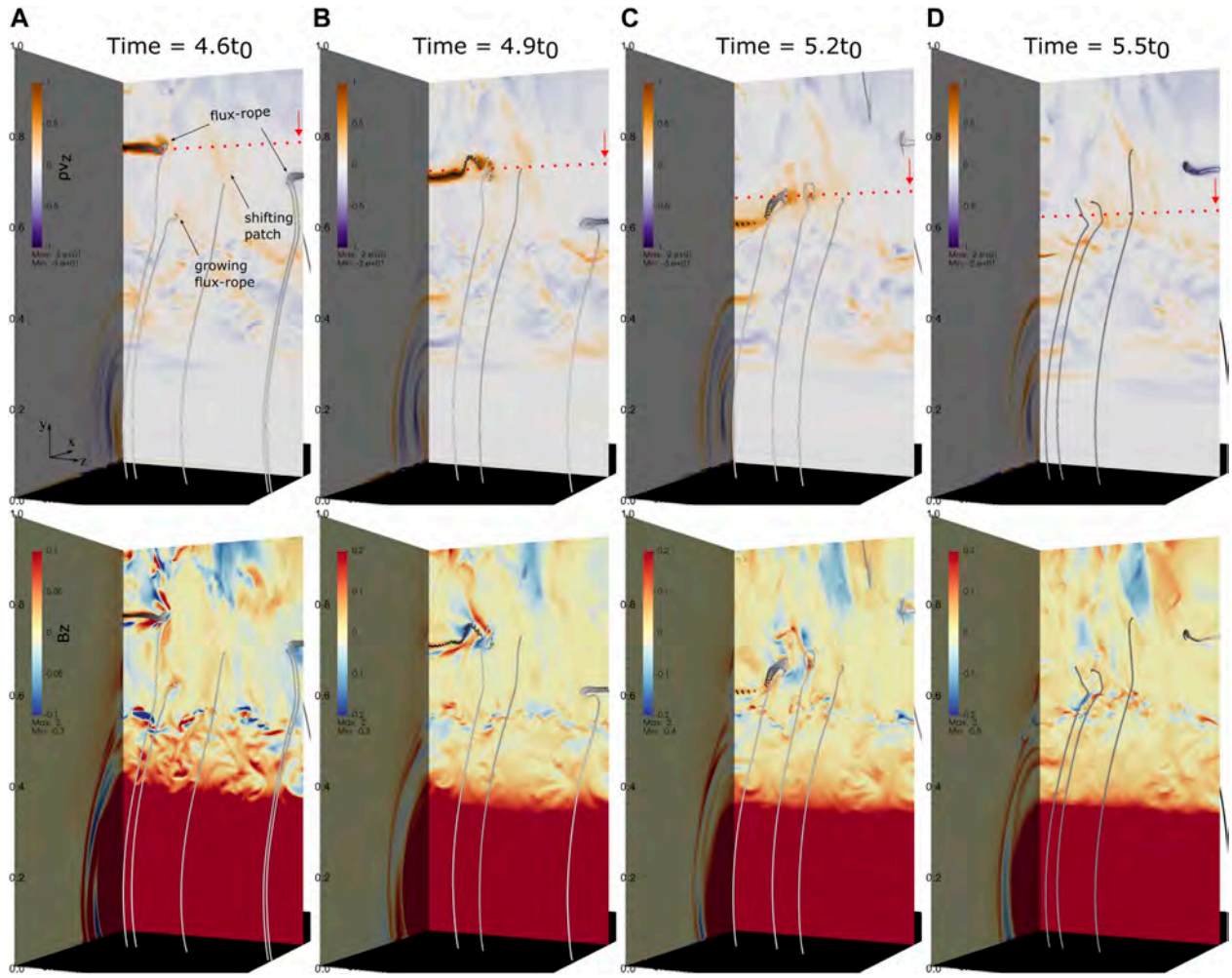

FIGURE 9
Distribution of momentum component (ρV_z) and magnetic component B_z on the center plane ($x = 0$) at different times. Panels **(A–D)** are for Time = 4.6, 4.9, 5.2, and 5.5 t_0, respectively. The upper row is for (ρV_z) in which the gray tubes show magnetic field lines around the well-developed magnetic flux-ropes, the growing magnetic flux-rope, and shift-moving reconnection outflow patches in z–direction. The red dotted lines and arrows indicate the same heights annotated in **Figure 8**. The low panels are for B_z with the same magnetic field lines.

the reconnection X-point sites (around y~$0.9L_0$), and spread with the reconnection outflows to the lower end of the CS. At different altitudes along the CS, there are two obvious regions of high non-thermal broadening: one is close to the primary reconnection X-point site and another is located above the flare loop-top. Above the flare loop-top region, the non-thermal velocity is strong but highly depends on the more complex plasma dynamics in this interface region. It could be roughly the same or decrease with height, as shown in **Figure 10**. We also notice that high non-thermal-broadenings also appear in upward flowing plasma near the upper boundary (y~1.0).

3.3 Relations between v_{nth} and plasma turbulence strength

In general, both plasma turbulence and bulk flows can contribute to the non-thermal widening (e.g., Ciaravella and Raymond, 2008), and it is hard to quantitatively explore the turbulent strength based on the observational line profiles due to complex plasma environments along the LOS direction. On the other hand, the numerical models allow us to obtain detailed information about the local plasma flows and integrated effects on spectral line profiles. Therefore, it is interesting to examine the correlation between the non-thermal velocity and plasma turbulence over a sample of locations in both the CS and flare loop-top regions during a relatively long period from 4.6 ~ 7.4 $\boldsymbol{t_0}$ in this model. We introduce a non-dimensional parameter $V_{turb} \equiv \sqrt{\frac{1}{n_z}\sum {v_{zi}}^2}/V_A$ to describe the turbulence strength of plasma flows along the LOS. Here, $v_{zi} \equiv v_z - \bar{v}_z$ is the turbulent fluctuation of each cell to the mean velocity $\bar{v}_z$, V_A is the characteristic Alfven speed, and n_z is the total cell number along the LOS. **Figure 11** plots the two-dimensional population histogram of V_{turb} and non-thermal velocity (v_{nth}). In **Figure 11A**, the background colors indicate the population of samples on the v_{nth} - V_{turb} map. An overarching feature of these plots is that the v_{nth} distribution is clearly proportional to the turbulence strength (V_{turb}) because stronger plasma turbulent flows can naturally cause larger line-broadening, as discussed in the previous sections.

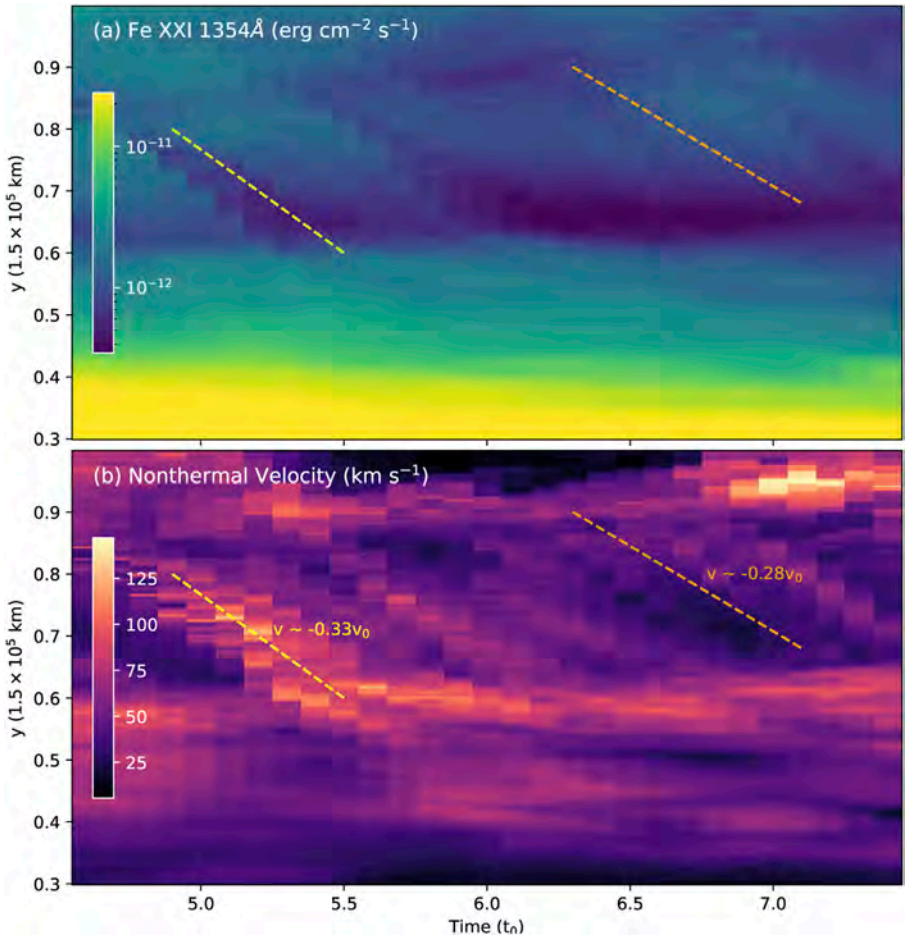

FIGURE 10
Time-distance maps along the CS direction at the system center ($x = 0$). Panel **(A)** is for maximum Fe XXI 1354 Å intensity, **(B)** is for the non-thermal velocity (v_{nth}) as functions of time. At each height, the median values over all non-zero values are shown here. The red and gray dashed lines indicate the downwards moving features with the speed of ~0.33 and ~0.28v_0, respectively.

However, the detailed distribution is more widely distributed with the increase of V_{turb}, and will not likely be fitted by using one simple linear line. Here, we annotate one typical growth direction using a red dashed line and a deviation direction using a black dashed line in **Figure 11A**, where the most dominant samples appear. The samples around the red line show higher non-thermal velocities with comparable turbulence strength compared with those around the black line.

The deviation among the black and red dashed lines in **Figure 11A** could be due to the variation of plasma flows and turbulence properties at different heights, especially in the CS region and flare cusp regions where the plasma density and plasma β environments are largely different. Therefore, we display all samples on the v_{nth}-V_{turb} map with their height information, in which colors indicate y– position of each sample in **Figures 11B–D**. We separate all samples into three groups ($y \leq 0.5L_0$, $0.5L_0 < y < 0.65L_0$, and $y \geq 0.65L_0$) to make the difference more visible.

Figure 11B shows the first group of samples with the lowest heights below y~$0.5L_0$, in which both the v_{nth} and V_{turb} are small. Because this group of samples is close to the more dense flare loop-top regions, where the turbulent flows are expected to be relatively lower than those in the above-the-looptop regions, v_{nth} is naturally small (e.g., <~100 km/s). The samples in the second group (**Figure 11C**) in the very turbulent flare cusp regions have stronger turbulence and larger non-thermal velocities.

Similar high-v_{nth} and high-V_{turb} can be seen in the CS region as shown in **Figure 11D** as well. Samples in both the CS and the above loop-top regions tend to follow the growth direction marked by the red dashed line in **Figure 11A**, except small abnormal patches with low v_{nth} and high V_{turb} that usually appear in the low end of the CS ($y < \sim 0.8L_0$) and upper the loop top region ($y > \sim 0.57L_0$). In fact, these abnormal samples that have departed from the red line direction may indicate strong bulk flows which will be discussed in the following section.

It is worth noticing that thermal broadening also contributes to the emission line broadening and has an impact on the corresponding v_{nth} distribution, especially when the plasma is hotter than the equilibrium temperature of Fe XXI 1354 Å at $\log T_{eq}$~ 7.05 K. In the above investigations, there is a set of samples in our model that are slightly lower in temperature than the Fe XXI 1354 Å temperature (T_{eq}) (e.g., see **Figure 6A**). Therefore, we investigate the v_{nth} distribution in different temperature environments. We maintain the plasma density the same as in the above analysis but scale the temperature to match

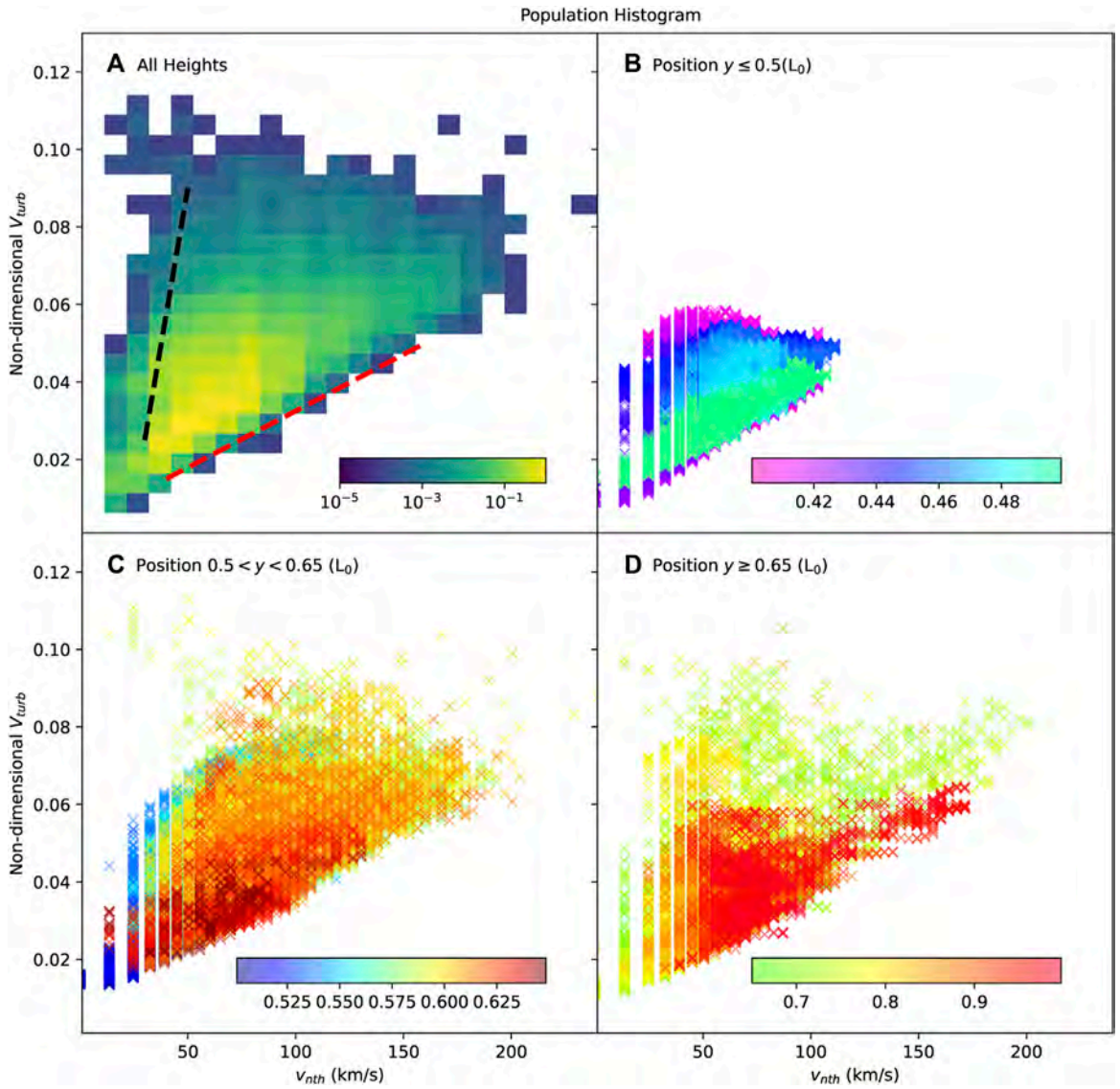

FIGURE 11
Distribution of plasma turbulence strength V_{turb} *versus* non-thermal velocity v_{nth}. Panel **(A)** is the 2D histogram of v_{nth}-V_{turb} map, which shows the population of samples in all heights from $y \sim 0.4L_0$ **to** $y \sim 1.0L_0$. The red and black dashed lines indicate two typical monotone correlations between v_{nth} and V_{turb}. Panels **(B) (C) (D)** show each sample on the v_{nth}-V_{turb} maps at different heights: near the flare loop-top region ($y \leq 0.5L_0$), the above-the-looptop region ($0.5L_0 < y < 0.65L_0$), and CS regions ($y \geq 0.65L_0$), respectively.

the observations (e.g., log$T$ 7.0 ~ 7.2 K shown in Figure 2). In the non-dimensional MHD models, the characteristic temperature can be expressed by $T_0 = B_0^2\beta_0/(2\mu\rho_0\tilde{R})$ and Alfvén velocity is $V_A = \sqrt{B_0^2/(\mu\rho_0)}$. Here, β_0, $\tilde{R}$, and μ are background plasma β, gas constant, and magnetic permeability, respectively. Thus, the scaling of temperature (T_0) with corresponding changes in characteristic velocity (V_A) allows the MHD model to be scalable by maintaining the plasma β_0 as the same. Therefore, we increased the simulated temperature to a factor of 1.4× higher than that in the original MHD model result, and the velocity is also increased by a factor of $\sqrt{1.4}$ accordingly. As a result, the samples in the model can cover a higher temperature range from log$T$~6.9 to ~7.2K.

Figure 12A shows the population histogram of V_{turb} and v_{nth} in the scaled temperature case. The red and black dashed lines are exactly the same as in Figure 11A as well. The distribution feature of v_{nth} is consistent with the above results in the original MHD temperature case (T_{MHD}), though the absolute values of v_{nth} are slightly larger by about 10% ~ 20%. These larger v_{nth} are partially caused by the scaling process of MHD models, because the characteristic velocity increased by about ~18%, which could lead to larger Doppler shift velocities and corresponding larger line broadenings. The mean temperature of each sample is displayed by different colors in Figure 12B. It is interesting to note that the highest temperature (log$T$~7.2K) does not necessarily indicate the largest v_{nth} if the turbulence strength remains low (the dark-red samples), which suggests that the plasma perturbation behaviors have more crucial impacts on the non-thermal velocity distribution than the thermal broadening itself.

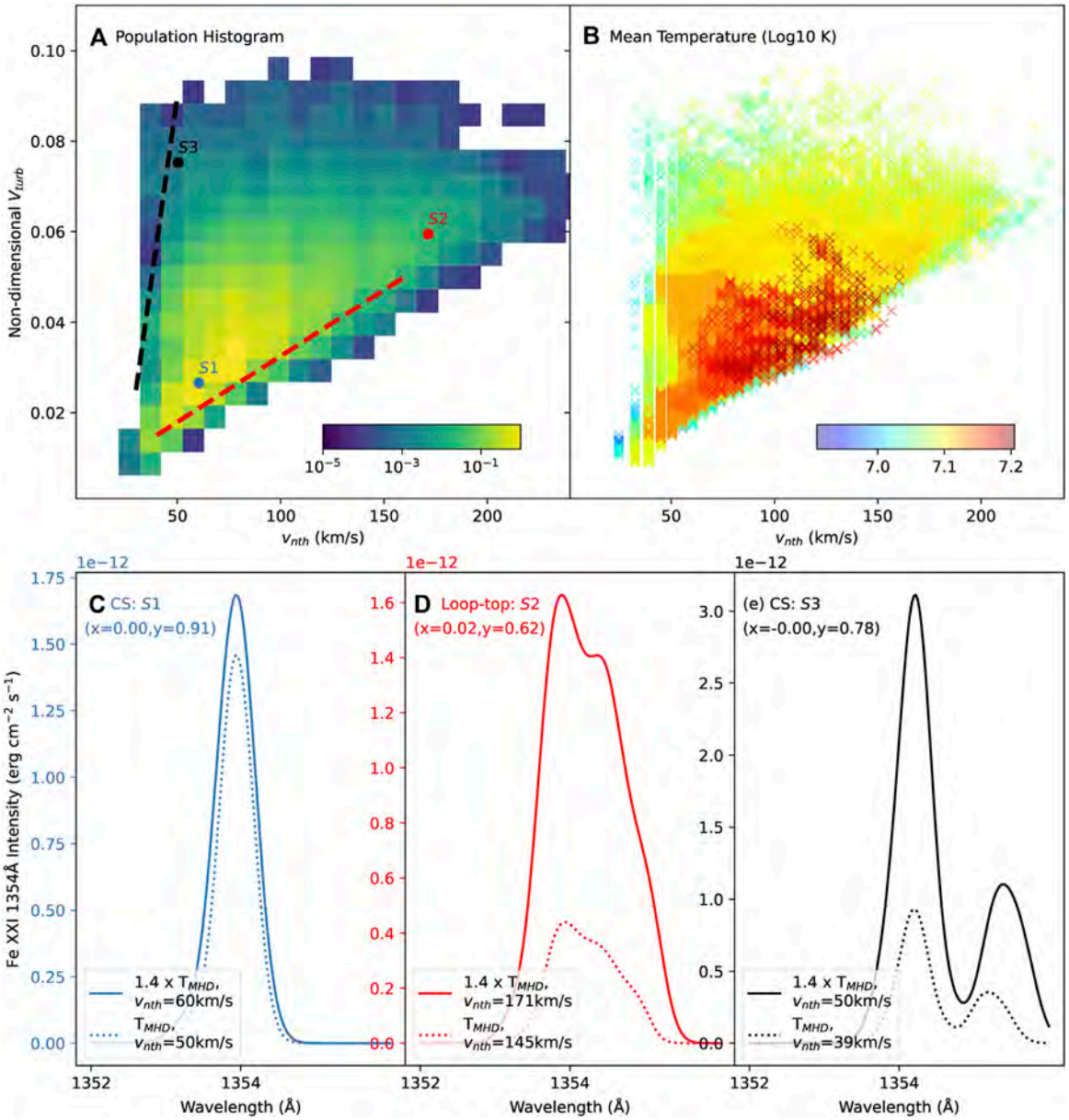

FIGURE 12
Distribution of the deduced non-thermal velocity v_{nth} in the scaled temperature case. Panels **(A) (B)** show v_{nth}-V_{turb} map in a 1.4× higher temperature situation compared with the original temperature (T_{MHD}). The red and black dashed lines are the same as in **Figure 11A**. Panels **(C–E)** show synthetic Fe XXI 1354 Å line profiles at the marked sampling points in panel **(A)**: *S1* and *S3* are located in the reconnection current sheet (CS) region, and *S2* is above the flare loop-top region. Their projected position on the *xoy* plane are marked by (*x*,*y*) accordingly. The solid lines are for 1.4× scaled temperature cases and the dotted lines are for T_{MHD} cases.

Figures 12C–E shows Fe XXI 1354 Å line profiles in two typical regions: CS region (*S*1, *S*3), and the above flare loop-top region (*S*2). Sample *S*1 represents the most dominant features with low turbulence strength and low non-thermal velocity. The line profile basically matches the Gaussian-type shape with minor line broadening due to the relatively weak turbulent flows. Sample *S*2 is at the high v_{nth} end with strong V_{turb}, where the strong plasma perturbations contribute to a remarkable line-broadening in both the 1.4× higher and slightly lower T_{MHD} cases. In addition, the plasma bulk flows also cause the second emission peak at ∼1354.4 Å which makes the line profile depart from a Gaussian distribution and causes a wider v_{nth}. Sample *S*3 indicates the abnormally high V_{turb} with low non-thermal velocity. The reason can be found in the line profiles which show two separate emission peaks: one is for the dominant Fe XXI 1354 Å with a smaller Doppler velocity and the other one is centered at ∼1355.4 Å due to the enormous plasma bulk flow, such as the well-developed flux-ropes as shown in **Figure 9**. In general, the turbulence strength (V_{turb}) only refers to mean perturbation features, and it could be too simple to represent complex flow properties including randomly turbulent flows and large bulk flows. Therefore, the appearance of these abnormal samples around the black dashed line in **Figure 12** suggests that the investigation of plasma turbulence based on the emission line

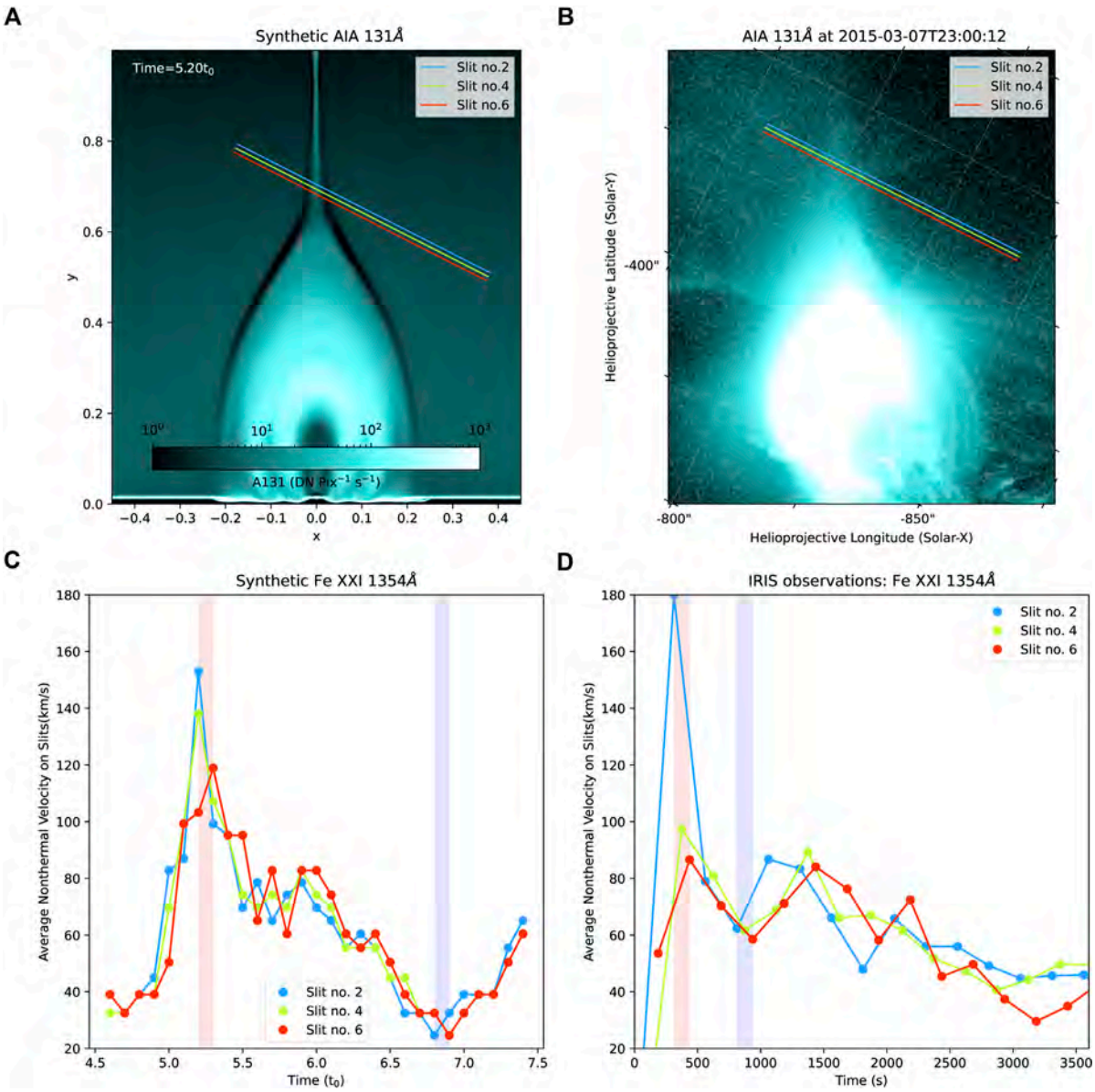

FIGURE 13
Modeled and observed non-thermal velocity of IRIS Fe XXI line. The left panels show: **(A)** the synthetic SDO/AIA 131 image, and **(C)** the non-thermal velocity calculated by using the averaged Fe XXI 1354 Å profiles along each IRIS slit. The colored solid lines in panels **(A)** and **(C)** indicate the IRIS slits with the length of ~9.3×10^4 km (or ~ 128 arcsec). The right panels **(B)** and **(D)** are for SDO/AIA 131 observations at 2015–03–07T23:00:12 and IRIS raster results, respectively. The start time on the horizontal axis in panel **(D)** is 2015-03–07T22:55:51. The red and blue shadowed regions display the evolution of the non-thermal velocity on different slits.

broadening features must consider the different fine structures in the CS (e.g., plasma blobs or flux-ropes) and flare loop-top regions (e.g., macro plasma instabilities or SADs in Shen et al. (2022)).

3.4 Non-thermal velocity across the CS

In this section, we investigate the averaged Fe XXI lines profiles across the CS and compare them to the IRIS observations during the 2015–03–07 flare. We set the position of the simulated IRIS slits above the flare loop top region in the MHD model as shown by **Figure 13A**. The synthetic SDO/AIA 131 image in this plot is obtained by assuming that the LOS is along the $z-$ direction. The synthetic bright flare loops, cusp region, and extending CS regions all match well the SDO/AIA images of the solar flare under study (**Figure 13A**) well. It is clear that the IRIS slits are located just above the bright flare arches in AIA 131 during this eruption event (also see **Figure 1**). Therefore, we chose a height of y~$0.62L_0$ in the MHD model to simulate the IRIS raster in the following analysis. As the reconnected magnetic flux is accumulated at the solar surface, the flare loop system gradually grows in both vertical and horizontal directions. Thus, the relative position of the IRIS slits to the flare cusp region gradually changes as a function of time. Because our MHD model is focused on the fast magnetic reconnection process in solar flares, it is reasonable to

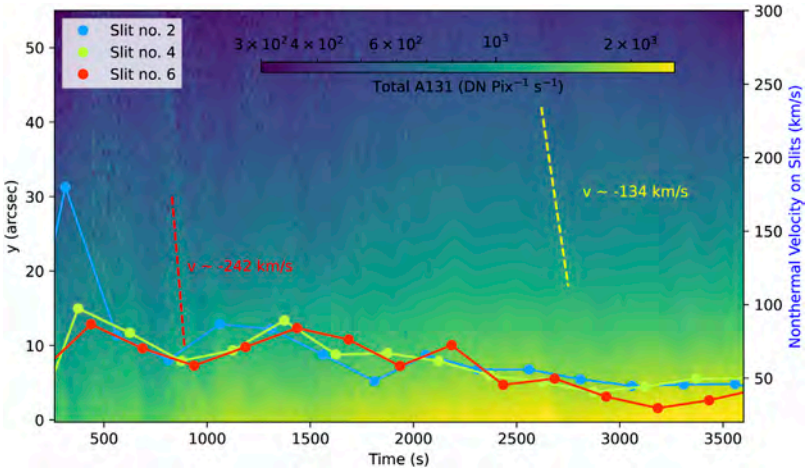

FIGURE 14
Time-distance map of SDO/AIA 131Å images in the reconnection region. The total AIA 131Å intensity is calculated by counting 16 pixels at each height around the brightest region above the flare loop top. The two dashed lines indicate the typical downwards-moving features with velocities of ~242 km/s and ~134 km/s. The right *y*-axes are for the v_{nth} of the Fe XXI 1354 Å spectra (solid-dots lines) from the IRIS observations in the same range as that of **Figure 13D**.

compare the predicted SDO/AIA emissions with the observed flare just after the impulsive phase when the post-flare loops are well-formed but the bursty magnetic energy release is still on-going. To simplify the analysis, we show a particular SDO/AIA observation at the starting time of IRIS observations (2015–03–07T23:00) in **Figure 13B**, and keep the simulated IRIS slits in the same position in this work.

Along each slit in **Figure 13A**, we average the Fe XXI 1354 Å line profiles over all MHD cells with $I > \frac{I_{peak}}{e}$. Here I is the maximum intensity of the Fe XXI line at each cell, and I_{peak} indicates the peak I across the CS on this slit. The non-thermal velocity of each slit is then calculated using the averaged line profile, assuming $\log T = 7.05$K for the strongest Fe XXI emission. **Figure 13C** shows the non-thermal velocity variation with time on the chosen slits, No. 2, 4, and 6. An overall feature is that the v_{nth} variation tendency on these three slits is consistent with each other. For example, the local maximum v_{nth} peak (red shadowed region) appears initially at times 5.2 on slit two and then at $5.4t_0$ for slit 6. A similar tendency is also clear around time $6.8t_0$, as highlighted by the blue shadowed region. By comparing the v_{nth} trends above with **Figure 10**, one can see that the first v_{nth} peak (around times $5.3t_0$) is consistent with downwards moving structures with enhanced Fe XXI line widths between $t = 4.6$ to $t = 5.5t_0$, as indicated by the yellow dashed line. In the later times ($t = 5.5$ to $t = 7.4t_0$), the relatively weaker downward structures also caused the second local v_{nth} peak at $5.9t_0$ and possibly the third peak at $7.4t_0$ on **Figure 13C**.

In the ideal situation when the non-thermal velocity variation is due to the passing downward structures, the characteristic size of detectable downward patches can be estimated as follows:

$$\delta l + \frac{d_{slit}}{cos(\theta)} \sim v_d \times \delta t. \quad (6)$$

Here δl is the length of moving patches, d_{slit} is the interval of the IRIS slits, θ is the intersection angle between slits and the solar surface, v_d is the moving speed of patches, and δt is the exposure time of each slit (or interval time between two slits). For instance, $\delta t \sim 30$ s for the IRIS Fe XXI observations, d_{slit} is about 726 km, and $\theta \sim 30°$. Assuming the downward moving structures are in sub-Alfvénic speed (e.g., 300 km/s), a moving enhanced v_{nth} patch with the size of $\delta l \geq \sim 8000$ km should be well recognized. The above estimated δl equals $\sim 0.05 L_0$, which is reasonable and matches the modeling structures as shown in **Figure 10**.

Similar to the synthetic results in MHD models, we also see very similar v_{nth} evolution trends in the IRIS observations (**Figure 13D**). The red and blue shadowed regions show one example where the local maximum and minimum v_{nth} has been recognized first on slit 2, then on the following slits 4, and 6. Remarkably, the evolution of v_{nth} of the Fe XXI line is comparable between MHD model predictions and IRIS observations, which range from ~20 km/s to 180 km/s during this particular period. We note that the time-resolution of the deduced v_{nth} variation from the IRIS is limited by the relatively long exposure time (~30s). Therefore, **Figure 13D** may unavoidably smooth out fine structures and cannot display the short-period perturbations that are visible in the synthetic modeling results.

Due to the similar variations in the MHD predictions and the IRIS observations described above, it is likely that the v_{nth} variation on IRIS Fe XXI lines is due to intermittent downwards moving structures along with the reconnection outflows as shown in the above models. In fact, we find very similar intermittent downwards-moving signals on SDO/AIA 131Å images. **Figure 14** shows the time-distance map of AIA 131Å intensity above the flare loop top regions. In this plot, we count all emissions over 16 pixels around the CS region (the bright plasma sheet on AIA 131Å maps) at each height to increase the signal-to-noise ratio. Two typical downward features are fitted by using red and yellow dashed lines. These downflow features range from ~ 250 km/s to ~ 100 km/s, which is consistent with the model-predicted moving speed of turbulent structures as shown in **Figure 10**. We also overlay the non-thermal velocity trends on the AIA 131Å stack map as shown by the solid-dots lines. There is no clear correlation between the brightest AIA features and the highest v_{nth} because the AIA intensity is mainly dominated by plasma density in the CS

region, while the v_{nth} values are more affected by the turbulent plasma flows.

We notice that the variation feature of non-thermal velocity above the flare loops (e.g., in **Figures 11**, **14**) are consistent with the previous observational studies. The increasing behaviors on non-thermal velocity from the flare loops to higher altitudes have been reported in the past. For example, Doschek et al. (2014) found that the non-thermal velocity in the multimillion-degree regions increases with height above the bright coronal flare loops from Hinode/EIS observations. Our simulation results also match their explanation, in which the strong newly contracting hot and turbulent plasma mainly contributes to these high non-thermal motions.

4 Discussion and conclusion

Using our three-dimensional MHD model based on the classic solar flare configuration, we calculate the synthetic emission profiles of the Fe XXI 1354 Å line observed by the Interface Region Imaging Spectrograph (IRIS) spacecraft. The synthetic line broadening and non-thermal velocities (v_{nth}) are obtained around the whole magnetic reconnection regions including the current sheet (CS) and flare loop-top regions. We compare the predicted non-thermal velocities due to the turbulent flows with the IRIS observations during the 2015–03–07 flare.

The main results are summarized as follows.

1. Our MHD model reveals highly turbulent plasma flows both in the CS where the magnetic reconnection sites are located, and in the flare loop top region, an interface region below the CS where the reconnection outflows mix into the flare arcade. Fourier transform analysis of plasma density, velocity, and kinetic energy show that the plasma perturbation spectrum along the LOS ($z-$ direction in this model) follows the power-law tendency of the classic turbulence scenarios.
2. Using the modeled plasma density, temperature, and velocity distribution in 3D, we calculate the emission line profiles in CS and flare loop-top regions in an edge viewing. We found that the non-thermal broadening of Fe XXI 1354 Å is mainly due to the plasma bulk flows in high turbulence states. The dominant non-thermal velocity ranges from ∼20 km/s to ∼180 km/s, and could be up to ∼300 km/s in some particular position and times.
3. We obtain a two-dimensional synthetic non-thermal velocity (v_{nth}) map and investigate the spatial and temporal evolution features. We find that v_{nth} is dynamically evolving in both the CS and flare loop-top regions. The high v_{nth} structures flow down with a typical speed of $\sim 0.3 v_A$ along the CS from the primary reconnection X-point sites to the flare cusp. By revealing the 3D magnetic field configuration and studying the plasma perturbation amplitude for velocity and density, we confirm that these downwards high v_{nth} structures are due to highly turbulent plasma which is usually associated with complex fine structures inside the CS, such as the growing/well-developed magnetic flux ropes and shifting reconnection outflows with in high guide field (B_z) region.
4. We study synthetic v_{nth} distribution *versus* plasma turbulence strength V_{trub} during a relatively long period. The two-dimensional population histogram map shows that v_{nth} is basically proportional to V_{trub}, but with a set of abnormal points due to the large plasma bulk flows. This result indicates that the investigation of plasma turbulence properties based on the emission line broadening features must consider the different fine structures in the CS and flare loop-top regions.
5. We investigate the Fe XXI lines profiles across the CS and make a detailed comparison with the IRIS observations. The deduced v_{nth} obtained by averaging the Fe XXI emission over the IRIS slit and exposure time ranges from ∼20 km/s to ∼160 km/s, which is consistent with the IRIS observations. Consistent v_{nth} features on different IRIS slits were found in both the synthetic results and the IRIS observations. By comparing the down-flowing high v_{nth} structures and SDO/AIA observations, our results suggest that these downwards-moving fine structures inside the CS could be identified by IRIS due to the variation of the line width of the high-temperature Fe XXI 1354 Å line.

It is worth mentioning that the magnetic configuration of our MHD model may be largely different from the 2015–03–07 flare event. Therefore, we can not exactly compare the model synthetic results with IRIS observations over a very long interval (e.g., ∼ 4 h observation as shown in **Figure 4**). However, the down-flowing high v_{nth} structures can be expected to exist in the model commonly (also see **Figure 10**). Thus, it is reasonable that to choose one short period evolution from the model ($4.6 \sim 7.4\ t_0$) during the magnetic reconnection process to compare with the IRIS observations. The speed of down-flowing high v_{nth} structures are predicted to be less than one-third of the Afvénic speed in the reconnection region 10), which matches the downflow features observed by SDO/AIA if we assume that the local background Alfvén speed is reduced by a factor of two as compared with the characteristic speed in the model. Due to the lack of accurate magnetic field information around the CS, further accurate studies on v_{nth} variation require more effort on both the MHD modeling and observational side. In particular, the Multi-Slit Explorer (MUSE), which will be launched in 2027, will be ideal for observing the current sheet and above the loop-top region given its multi-slit configuration and will provide groundbreaking observations of this region as a whole.

Data availability statement

The original contributions presented in the study are included in the article/supplementary material, further inquiries can be directed to the corresponding author.

Author contributions

CS performed the MHD simulations and visualized the results. VP and KR performed IRIS, XRT, and SDO/AIA data analysis. BC contributed to spectrum prediction for IRIS. SY and XX contributed to the synthetic SDO/AIA image modeling. All authors contributed to the model development, discussed the results, and commented on the manuscript.

Funding

This work was supported by NSF grants AGS1723313 and AST2108438 to the Smithsonian Astrophysical Observatory. CS

acknowledges the support of NASA grants 80NSSC21K2044, 80NSSC19K0853, 80NSSC18K1129, and 80NSSC20K1318. VP acknowledges financial support from the NASA grants 80NSSC20K0716 and NNG09FA40C (*IRIS*). KR and XX are supported by NASA grant 80NSSC18K0732. SY and BC are supported by NSF grant AST-2108853 and NASA grants 80NSSC20K1318 and 80NSSC20K1283/SV0-09025 to NJIT.

Acknowledgments

The computations in this paper were conducted on the Smithsonian High-Performance Cluster, Smithsonian Institution (https://doi.org/10.25572/SIHPC). CHIANTI is a collaborative project involving George Mason University, the University of Michigan (United States), and the University of Cambridge (United Kingdom). AIA data are courtesy of NASA/SDO and the AIA science team. IRIS is a NASA small explorer mission developed and operated by LMSAL with mission operations executed at NASA Ames Research center and major contributions to downlink communications funded by ESA and the Norwegian Space Centre.

Conflict of interest

The authors declare that the research was conducted in the absence of any commercial or financial relationships that could be construed as a potential conflict of interest.

Publisher's note

References

Astropy Collaboration, Robitaille, T. P., Tollerud, E. J., Greenfield, P., Droettboom, M., Bray, E., et al. (2013). Astropy: A community Python package for astronomy. *A&A* 558, A33. doi:10.1051/0004-6361/201322068

Bemporad, A. (2008). Spectroscopic detection of turbulence in post-CME current sheets. *Astrophysical J.* 689, 572–584. doi:10.1086/592377

Cai, Q., Shen, C., Raymond, J. C., Mei, Z., Warmuth, A., Roussev, I. I., et al. (2019). Investigations of a supra-arcade fan and termination shock above the top of the flare-loop system of the 2017 September 10 event. *MNRAS* 489, 3183–3199. doi:10.1093/mnras/stz2167

Cai, Q., Ye, J., Feng, H., and Zhao, G. (2022). Variations of the plasma environment revealed by the evolution of the supra-arcade fan in the 2017 september 10 flare. *ApJ* 929, 99. doi:10.3847/1538-4357/ac5fa4

Cheung, M. C. M., Rempel, M., Chintzoglou, G., Chen, F., Testa, P., Martínez-Sykora, J., et al. (2019). A comprehensive three-dimensional radiative magnetohydrodynamic simulation of a solar flare. *Nat. Astron.* 3, 160–166. doi:10.1038/s41550-018-0629-3

Ciaravella, A., and Raymond, J. C. (2008). The current sheet associated with the 2003 november 4 coronal mass ejection: Density, temperature, thickness, and line width. *Astrophysical J.* 686, 1372–1382. doi:10.1086/590655

Ciaravella, A., Raymond, J. C., Li, J., Reiser, P., Gardner, L. D., Ko, Y. K., et al. (2002). Elemental abundances and post-coronal mass ejection current sheet in a very hot active region. *Astrophysical J.* 575, 1116–1130. doi:10.1086/341473

De Pontieu, B., Title, A. M., Lemen, J. R., Kushner, G. D., Akin, D. J., Allard, B., et al. (2014). The interface region imaging spectrograph (IRIS). *Sol. Phys.* 289, 2733–2779. doi:10.1007/s11207-014-0485-y

De Pontieu, B., Polito, V., Hansteen, V., Testa, P., Reeves, K. K., Antolin, P., et al. (2021). A new view of the solar interface region from the interface region imaging spectrograph (IRIS). *Sol. Phys.* 296, 84. doi:10.1007/s11207-021-01826-0

Del Zanna, G., Dere, K. P., Young, P. R., and Landi, E. (2021). CHIANTI—an atomic database for emission lines. XVI. Version 10, further extensions. *ApJ* 909, 38. doi:10.3847/1538-4357/abd8ce

Doschek, G. A., McKenzie, D. E., and Warren, H. P. (2014). Plasma dynamics above solar flare soft X-ray loop tops. *ApJ* 788, 26. doi:10.1088/0004-637x/788/1/26

Feldman, U. (1992). Elemental abundances in the upper solar atmosphere. *Phys. Scr.* 46, 202–220. doi:10.1088/0031-8949/46/3/002

Freeland, S. L., and Handy, B. N. (1998). Data analysis with the SolarSoft system. *Sol. Phys.* 182, 497–500. doi:10.1023/A:1005038224881

Golub, L., Deluca, E., Austin, G., Bookbinder, J., Caldwell, D., Cheimets, P., et al. (2007). The X-ray telescope (XRT) for the Hinode mission. *Sol. Phys.* 243, 63–86. doi:10.1007/s11207-007-0182-1

Guo, L., Li, G., Reeves, K., and Raymond, J. (2017). Solar flare termination shock and synthetic emission line profiles of the Fe xxi 1354.08 - line. *Astrophysical J.* 846, L12. doi:10.3847/2041-8213/aa866a

Huang, Y.-M., and Bhattacharjee, A. (2016). Turbulent magnetohydrodynamic reconnection mediated by the plasmoid instability. *ApJ* 818, 20. doi:10.3847/0004-637x/818/1/20

Kano, R., Sakao, T., Hara, H., Tsuneta, S., Matsuzaki, K., Kumagai, K., et al. (2008). The Hinode X-ray telescope (XRT): Camera design, performance and operations. *Sol. Phys.* 249, 263–279. doi:10.1007/s11207-007-9058-7

Kobelski, A. R., Saar, S. H., Weber, M. A., McKenzie, D. E., and Reeves, K. K. (2014). Calibrating data from the hinode/X-ray telescope and associated uncertainties. *Sol. Phys.* 289, 2781–2802. doi:10.1007/s11207-014-0487-9

Kosugi, T., Matsuzaki, K., Sakao, T., Shimizu, T., Sone, Y., Tachikawa, S., et al. (2007). The Hinode (solar-B) mission: An overview. *Sol. Phys.* 243, 3–17. doi:10.1007/s11207-007-9014-6

Lazarian, A., and Vishniac, E. T. (1999). Reconnection in a weakly stochastic field. *Astrophysical J.* 517, 700–718. doi:10.1086/307233

Lemen, J. R., Title, A. M., Akin, D. J., Boerner, P. F., Chou, C., Drake, J. F., et al. (2012). The atmospheric imaging assembly (AIA) on the solar dynamics observatory (SDO). *Sol. Phys.* 275, 17–40. doi:10.1007/s11207-011-9776-8

Li, Y., Ding, M. D., Qiu, J., and Cheng, J. X. (2015). Chromospheric evaporation in an X1.0 flare on 2014 March 29 observed with IRIS and EIS. *Astrophysical J.* 811, 7. doi:10.1088/0004-637x/811/1/7

Li, Y., Xue, J. C., Ding, M. D., Cheng, X., Su, Y., Feng, L., et al. (2018). Spectroscopic observations of a current sheet in a solar flare. *Astrophysical J.* 853, L15. doi:10.3847/2041-8213/aaa6c0

Lin, J., Murphy, N. A., Shen, C., Raymond, J. C., Reeves, K. K., Zhong, J., et al. (2015). Review on current sheets in CME development: Theories and observations. *Space Sci. Rev.* 194, 237–302. doi:10.1007/s11214-015-0209-0

McKenzie, D. E. (2013). Turbulent dynamics in solar flare sheet structures measured with local correlation tracking. *Astrophysical J.* 766, 39. doi:10.1088/0004-637x/766/1/39

Mumford, S. J., Freij, N., Christe, S., Ireland, J., Mayer, F., Stansby, D., et al. (2022). SunPy. *Zenodo*. doi:10.5281/zenodo.591887

Pesnell, W. D., Thompson, B. J., and Chamberlin, P. C. (2012). The solar dynamics observatory (SDO). *Sol. Phys.* 275, 3–15. doi:10.1007/s11207-011-9841-3

Polito, V., Reeves, K. K., Del Zanna, G., Golub, L., and Mason, H. E. (2015). Joint high temperature observation of a small C6.5 solar flare with Iris/Eis/Aia. *ApJ* 803, 84. doi:10.1088/0004-637X/803/2/84

Polito, V., Dudík, J., Kašparová, J., Dzifčáková, E., Reeves, K. K., Testa, P., et al. (2018a). Broad non-Gaussian Fe XXIV line profiles in the impulsive phase of the 2017 september 10 X8.3-class flare observed by Hinode/EIS. *Astrophysical J.* 864, 63. doi:10.3847/1538-4357/aad62d

Polito, V., Galan, G., Reeves, K. K., and Musset, S. (2018b). Possible signatures of a termination shock in the 2014 March 29 X-class flare observed by IRIS. *ApJ* 865, 161. doi:10.3847/1538-4357/aadada

Reeves, K. K., Polito, V., Chen, B., Galan, G., Yu, S., Liu, W., et al. (2020). Hot plasma flows and oscillations in the loop-top region during the 2017 september 10 X8.2 solar flare. *Astrophysical J.* 905, 165. doi:10.3847/1538-4357/abc4e0

Shen, C., Chen, B., Reeves, K. K., Yu, S., Polito, V., and Xie, X. (2022). The origin of underdense plasma downflows associated with magnetic reconnection in solar flares. *Nat. Astron.* 6, 317–324. doi:10.1038/s41550-021-01570-2

Shibata, K., and Magara, T. (2011). Solar flares: Magnetohydrodynamic processes. *Living Rev. Sol. Phys.* 8, 6. doi:10.12942/lrsp-2011-6

Stone, J. M., Gardiner, T. A., Teuben, P., Hawley, J. F., and Simon, J. B. (2008). Athena: A new code for astrophysical MHD. *ApJS* 178, 137–177. doi:10.1086/588755

Tian, H., Li, G., Reeves, K. K., Raymond, J. C., Guo, F., Liu, W., et al. (2014). Imaging and spectroscopic observations of magnetic reconnection and chromospheric evaporation in a solar flare. *Astrophysical J.* 797, L14. doi:10.1088/2041-8205/797/2/l14

Warren, H. P., Brooks, D. H., Ugarte-Urra, I., Reep, J. W., Crump, N. A., and Doschek, G. A. (2018). Spectroscopic observations of current sheet formation and evolution. *Astrophysical J.* 854, 122. doi:10.3847/1538-4357/aaa9b8

Wülser, J. P., Jaeggli, S., De Pontieu, B., Tarbell, T., Boerner, P., Freeland, S., et al. (2018). Instrument calibration of the interface region imaging spectrograph (IRIS) mission. *Sol. Phys.* 293, 149. doi:10.1007/s11207-018-1364-8

Xie, X., Reeves, K. K., Shen, C., and Ingram, J. D. (2022). Statistical study of the kinetic features of supra-arcade downflows detected from multiple solar flares. *ApJ* 933, 15. doi:10.3847/1538-4357/ac695d

Ye, J., Cai, Q., Shen, C., Raymond, J. C., Lin, J., Roussev, I. I., et al. (2020). The role of turbulence for heating plasmas in eruptive solar flares. *ApJ* 897, 64. doi:10.3847/1538-4357/ab93b5

Yoshimura, K., and McKenzie, D. E. (2015). Calibration of Hinode/XRT for coalignment. *Sol. Phys.* 290, 2355–2372. doi:10.1007/s11207-015-0746-4

Young, P. R., Tian, H., and Jaeggli, S. (2015). The 2014 March 29 X-flare: Subarcsecond resolution observations of Fe XXI λ1354.1. *ApJ* 799, 218. doi:10.1088/0004-637X/799/2/218

frontiers | Frontiers in Astronomy and Space Sciences

TYPE Original Research
PUBLISHED 16 March 2023
DOI 10.3389/fspas.2023.1099346

OPEN ACCESS

EDITED BY
Adam Kowalski,
University of Colorado Boulder, United States

REVIEWED BY
Paul Charbonneau,
Montreal University, Canada
Gianna Cauzzi,
National Solar Observatory, United States

*CORRESPONDENCE
Markus J. Aschwanden,
aschwanden@lmsal.com

SPECIALTY SECTION
This article was submitted to Stellar and Solar Physics, a section of the journal Frontiers in Astronomy and Space Sciences

RECEIVED 15 November 2022
ACCEPTED 15 February 2023
PUBLISHED 16 March 2023

CITATION
Aschwanden MJ and Nhalil NV (2023), The universality of power law slopes in the solar photosphere and transition region observed with HMI and IRIS. *Front. Astron. Space Sci.* 10:1099346. doi: 10.3389/fspas.2023.1099346

The universality of power law slopes in the solar photosphere and transition region observed with HMI and IRIS

Markus J. Aschwanden[1]* and Nived Vilangot Nhalil[2]

[1]Lockheed Martin, Solar and Astrophysics Laboratory (LMSAL), Advanced Technology Center (ATC), Palo Alto, CA, United States, [2]Armagh Observatory and Planetarium, Armagh, United Kingdom

We compare the size distributions of *self-organized criticality (SOC)* systems in the solar photosphere and the transition region, using magnetogram data from *Helioseismic and Magnetic Imager (HMI)* and *Interface Region Imaging Spectrograph (IRIS)* data. For each dataset we fit a combination of a Gaussian and a power law size distribution function, which yields information on four different physical processes: (i) Gaussian random noise in IRIS data; (ii) spicular events in the plages of the transition region (described by power law size distribution in IRIS data); (iii) salt-and-pepper small-scale magnetic structures (described by the random noise in HMI magnetograms); and (iv) magnetic reconnection processes in flares and nanoflares (described by power law size distributions in HMI data). We find a high correlation (CCC = 0.90) between IRIS and HMI data. Datasets with magnetic flux balance are generally found to match the SOC-predicted power law slope $\alpha_F = 1.80$ (for mean fluxes F), but exceptions occur due to arbitrary choices of the HMI field-of-view. The matching cases confirm the universality of SOC-inferred flux size distributions, and agree with the results of Parnell et al. (ApJ, 2009, 698, 75–82), $\alpha_F = 1.85 \pm 0.14$.

KEYWORDS

methods, statistics, fractal dimension, sun, transition region, solar granulation, solar photosphere

1 Introduction

Self-Organized Criticality (SOC) is a critical state of a non-linear energy dissipation system that is slowly and continuously driven towards a critical value of a system-wide instability threshold, producing scale-free, fractal-diffusive, and intermittent avalanches with power law-like size distributions (Aschwanden, 2011). The original paradigm and characteristic behavior of SOC systems was studied from sandpile avalanches, based on the next-neighbor interactions in microscopic lattice grids (Bak et al., 1987; Bak et al., 1988; Bak 1996, Lu and Hamilton 1991), also called cellular automaton algorithms. However, alternative macroscopic models can mimic the same system behavior also, based on macroscopic power law scaling laws of correlated physical parameters. For instance, the hard X-ray flux radiated in a solar flare was found to scale with the (fractal) spatial volume of the flare. The exponentially growing instability that produces the flare predicts a well-defined power law size distribution function, which applies also to a host of other non-linear systems, such as earthquakes or stock market fluctuations, in contrast to linear

systems, such as Gaussian noise. Thus, modeling of SOC systems helps us to discriminate between linear and non-linear systems. Knowledge of the correct size distributions yields us statistical predictions of the largest catastrophic events in SOC systems. Besides flaring and heating of the solar corona, we hope to obtain also new insights into nanoflaring in the atmosphere of the Quiet Sun, which we pursue here.

The atmospheric structure of the Sun consists of the photospheric layer on the solar surface, the chromosphere, the transition region, the corona, and solar wind regions, which all host different physical processes, characterized by the electron density, the electron temperature, and the magnetic field strength. In this study we sample very diverse temperature structures, from $T_e \approx 5,800$ K observed in photospheric magnetograms with the *Helioseismic and Magnetic Imager (HMI)*, to $T_e \approx 10^4$–10^5 K, observed in Slitjaw images (SJI) of the 1,400 Å channel of IRIS, which are dominated by the Si IV 1,394 Å and 1,403 Å resonance line, and form in the transition region (Rathore and Carlsson, 2015; Rathore et al., 2015). Due to this huge temperature range, different physical processes are dominant in the various temperature regimes (Gallagher et al., 1998; Warren et al., 2016), and thus we do not know *a priori* whether the concept of *self-organized criticality (SOC)* systems (Aschwanden, 2011; Aschwanden, 2014; Aschwanden et al., 2016; McAteer et al., 2016; Warren et al., 2016) is applicable. More specifically, we want to understand the functional shapes of observed occurrence frequency (size) distributions, and whether they exhibit power law function (slopes) with universal validity in different temperature and wavelength regimes.

There is an ongoing debate on the functional form of size distributions in avalanching SOC processes, such as: a power law function, a log-normal distribution (Verbeeck et al., 2019), a Pareto distribution (Hosking and Wallis, 1987), a Lomax distribution (Lomax, 1954; Giles et al., 2011), or a Weibull distribution (Weibull, 1951), for instance. Since all these functional forms are close to a power law function on the right-hand side of the size distribution, which is also called the "fat-tail", various linear combinations of these functional forms have been found to fit the observed size distributions with comparable accuracy (Munoz-Jaramillo et al., 2015). In this study we use a combination of (Gaussian) incoherent random and (power law-like) coherent random structures. Gaussian statistics reflect the operation of a memoryless stationary (incoherent) random process; while avalanching (coherent) processes such as occurring in SOC systems are characterized by extended spatial and temporal correlations (i.e., the unfolding of an avalanche is influenced by the imprint of earlier avalanches on the system; see Jensen, 1998, chapter 2).

Here, the incoherent component describes the Gaussian noise (visible in IRIS data), as well as the salt-and-pepper structure (visible in HMI magnetograms). On the other side, the coherent noise of the power law component may be produced by the spicular dynamics (visible in IRIS data), or by magnetic reconnection dynamics of small-scale features and nanoflares (visible in HMI magnetograms). Gaussian noise distributions have been tested with Yohkoh soft X-ray data (Katsukawa and Tsuneta, 2001). Log-normal distributions, which are closest to our Gaussian-plus-power-law method used here, have been previously studied for Quiet-Sun FUV emission (Fontenla et al., 2007), solar flares (Verbeeck et al., 2019), the solar wind (Burlaga and Lazarus, 2000), accretion disks (Kunjaya et al., 2011), and are discussed also in Ceva and Luzuriaga (1998), Mitzenmacher (2004), and Scargle (2020).

A new aspect of this study is the invention of a single-image algorithm to derive "pixelized" size distributions $N(F) \propto F^{-\alpha_F}$. A major test consists of comparing the observed power law slopes α_F with the theoretical SOC-predicted values. Another crucial test is the power law slope α_E of nanoflare energies, which is decisive for testing the coronal heating energetics (Hudson, 1991; Krucker and Benz, 1998; Vilangot Nhalil et al., 2020; Aschwanden, 2022b). Numerous studies have inferred SOC parameter correlations of impulsive events in the outer solar atmosphere, in an attempt to understand the predominant energy supply mechanism in the corona (Vilangot Nhalil et al., 2020), which motivates us to pursue a follow-on study, using data from sunspots and plages to further investigate bright impulsive events in the transition region. Ultimately, we strive for a unification of small-scale phenomena in the solar corona and transition region (e.g., Harrison et al., 2003; Rutten, 2020), but this is beyond the scope of this study.

The content of this paper includes data analysis (**Section 2**), a discussion (**Section 3**), and conclusions (**Section 4**).

2 Data analysis

When we observe solar emission at *near ultra-violet (NUV)* and *far ultra-violet (FUV)* wavelengths, we may gather photons from spicules in plages in the transition region (at formation temperatures of $T_e \approx 10^4$–10^5). In order to study both coherent and incoherent processes, we have to deal with multiple size distribution functions, including incoherent random (Gaussian) noise, as well as coherent avalanche processes with power law-like distribution functions, also known as "fat-tail" distribution functions, which occur natually in *self-organized criticality (SOC)* systems.

2.1 Definitions of flux distributions

In the following we attempt to model event statistics with a combination of (i) a Gaussian distribution (originating from incoherent random processes), and (ii) a power law distribution, e.g., created by spicular activity in the transition region, (**Figure 1**). The Gaussian noise is defined in the standard way,

$$N(F)\ dF = N_0 \exp\left(-\frac{(F-F_0)^2}{2\sigma_F^2}\right) dF, \tag{1}$$

where F is the flux averaged over the duration of an event (measured here at a wavelength of 1,400 Å), $N(F)$ is the histogram of observed structures, F_0 is the mean value, σ_F is one standard deviation, and N_0 is the normalized number of events.

The second distribution we use in our analysis is a power law distribution function, which is defined in the simplest way by,

$$N(F)\ dF = N_0 \left(\frac{F}{F_0}\right)^{-\alpha_F} dF, \tag{2}$$

where α_F is the power law slope of the relevant part of the distribution function.

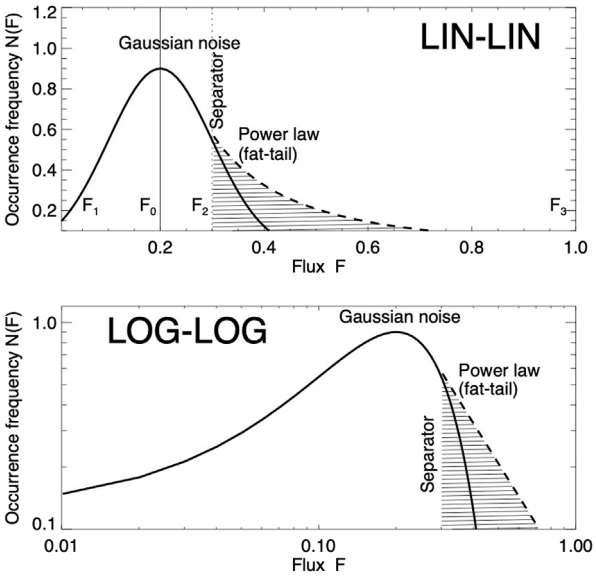

FIGURE 1
A schematic of the two size distributions is shown: a Gaussian function for the incoherent random statistics, and a power law function (also called fat-tail) for the statistics of coherent avalanche events, separated at a critical value F_2. The upper panel shows a linear (LIN-LIN) representation, the lower panel a logarithmic (LOG-LOG) representation.

The flux $F_{\rm IRIS}$ of an **IRIS pixel** is defined by,

$$F_{\rm IRIS} = \frac{4\ \pi\ f\ E_\lambda\ k}{A\ \Omega}, \quad [\text{erg cm}^{-2}\text{s}^{-1}] \tag{3}$$

where f is the observed flux in [DN] (data number per second), E_λ is the energy of the photon, k is the factor that converts the DN to the number of photons, Ω is the pixel size in units of steradians, A [cm^2] is the effective area of IRIS, and the unrelated background is subtracted (Vilangot Nhalil et al., 2020).

2.2 Pixelized method of size distribution

In this study we use a "pixelized" size distribution method that is more efficient and easier to calculate than standard size distributions. The standard method to sample size distributions $N(F)$ of SOC avalanches is generally carried out by an algorithm that detects fluxes of an avalanche event above some given threshold $F > F_{thr}$, traces its spatial $A(t)$ and temporal evolution $F(t)$, and infers the size of an avalanche from the spatio-temporal evolution after saturation. Such avalanche detections have been accomplished for 12 IRIS datasets in the study of Vilangot Nhalil et al., 2020. Because the development of an automated feature recognition code is a complex and a time-consuming task, which needs extensive testing, we explore here a new method that is much simpler to apply and requires much less data to determine the underlying power law slope α_F.

We can parameterize a pixelized IRIS image with a Cartesian grid, i.e., $\mathcal{F}_{i,j} = \mathcal{F}(x_i, y_j), \quad i = 0, \ldots, n_x, \quad j = 0, \ldots, n_y$, where n_x and n_y are the dimensions of the image, and $\Delta x = \Delta y$ is the pixel size. We can model a 2-D image with a superposition of n_k spatial structures with avalanche areas A_k and average fluxes $\mathcal{F}_k$, where the size distributions follow a power law distribution, i.e., $N(\mathcal{F}) \propto \mathcal{F}^{-\alpha_\mathcal{F}}$ (Eq. 2). The total flux $\mathcal{F}_{\rm tot}$ of such a 2-D distribution, which serves here as an analytical model of a 2-D (IRIS) image, can then be written as,

$$\mathcal{F}_{\rm tot} = \Sigma_{k=1}^{n_k}\ \mathcal{F}_k^{-\alpha_\mathcal{F}}\ A_k, \tag{4}$$

where the avalanche areas A_k are required to be non-overlapping, but area-filling. Areas without significant avalanche structures, ($\mathcal{F} < \mathcal{F}_{thr}$), can be included, in order to fulfill flux conservation, or can be neglected if the flux maximum is much larger than the threshold value, i.e., $\mathcal{F}_{max} \gg \mathcal{F}_{thr}$.

In our new method we decompose the flux $\mathcal{F}_k$ and area A_k of all avalanche components down to the pixel size level, Δx. The two requirements of non-overlapping and area-filling topology yield a unique mapping of the avalanche number k to the pixel ranges $i = [i_1(k), i_2(k)]$ and $j = [j_1(k), j_2(k)]$, i.e., $k \mapsto i_1(k), \ldots, i, \ldots\ i_2(k)$ and $j_1(k), \ldots j, \ldots\ , j_2(k)$. For instance, in the case of a rectangular area A_k, the avalanche area A_k is then defined by,

$$A_k = [i_2(k) - i_1(k)] \star [j_2(k) - j_1(k)]\ \Delta x^2 \tag{5}$$

Adding the areas A and fluxes $\mathcal{F}$ of all k avalanche components, we obtain then the following total flux $\mathcal{F}_{\rm tot,pix}$,

$$\mathcal{F}_{\rm tot,pix} = \Sigma_{i=1}^{n_x} \Sigma_{j=1}^{n_y}\ \mathcal{F}_{i,j}^{-\alpha_\mathcal{F}}\ \Delta x^2, \tag{6}$$

which can be set equal to the value of $\mathcal{F}_{\rm tot}$ of the standard method (Eq. 4) and proves this way that the power law slopes $\alpha_\mathcal{F}$ of the two methods are identical. Thus, our new method is parameterized just by a different decomposition of elementary components than in the standard size distribution sampling.

As a caveat, we have to be aware that the method determines size distribution from a single image. If the used 2-D image is not representative, additional 2-D images need to be included.

The new pixelation method is used in the calculations of the values $\alpha_{\mathcal{F}_1}$ listed in **Table 1** and **Figure 4**.

2.3 Analysis of IRIS data

The 12 analyzed 1,400 Å SJI images $F(x, y)$ of IRIS are shown in **Figure 2**, which are identical in time and FOV (field-of-view) with those of Vilangot Nhalil et al., 2020, and are also identical with those used in the study on fractal dimension measurements (Aschwanden and Vilangot Nhalil, 2022). Note that events #6 and #7; are almost identical, except for a time difference of 20 min, which can be used for stability tests.

The 12 IRIS maps shown in **Figure 2** have the following color code: The Gaussian distribution with values $F(x, y) < F_{thr}$ below a threshold of F_{thr} is rendered with orange-to-red colors, while the power law function with the fat-tail $F(x, y) > F_{thr}$ is masked out with white color. In other words, all the orange-to-red regions in the IRIS maps visualize the locations of incoherent random noise while the white regions mark the location of SOC-driven coherent avalanches (probably produced by spicular dynamics in the transition region). An even crispier representation of the spicular component $F(x, y) > F_{thr}$, is displayed with a black-and-white rendering (**Figure 3**), where black depicts locations with

TABLE 1 Results of 12 datasets obtained with IRIS 1,400 Å: the power law slope α_F of the flux distribution, the separator flux F_2, and the maximum flux F_{max}. Note that the power law slope α_F agrees with the theoretical prediction of $\alpha_F = 9/5 = 1.8$ in 5 cases, whenever there is no sunspot and the maximum flux F_{max} amounts to less than a critical value of $F_{max} \lesssim 50$ DN. The values α_F in parenthesis are ignored in the calculation of the averages (second-last line).

Number Dataset IRIS #	Phenomenon 1,400 Å	Power law slope fit α_F	Agrees with prediction $\alpha_F \approx 1.8$	Separator flux F_2 [DN]	Maximum flux F_{max} [DN]	Max.flux criterion <50 DN
1	Sunspot	(1.51 ± 0.04)	NO	21	121	NO
2	Sunspot	(1.23 ± 0.02)	NO	32	190	NO
3	Sunspot	(2.13 ± 0.06)	NO	128	243	NO
4	Plage	(0.94 ± 0.02)	NO	20	108	NO
5	Plage	(1.02 ± 0.01)	NO	36	199	NO
6	Plage	1.59 ± 0.02	YES	17	50	YES
7	Plage	1.59 ± 0.03	YES	9	26	YES
8	Plage	1.92 ± 0.03	YES	8	28	YES
9	Plage	1.81 ± 0.01	YES	13	42	YES
10	Sunspot	(1.25 ± 0.02)	NO	120	501	NO
11	Plage	1.61 ± 0.02	YES	9	31	YES
12	Plage	(1.40 ± 0.05)	NO	22	54	NO
	Observations	1.70 ± 0.15				
	Theory	1.80				

power law distributions, and white demarcates locations with Gaussian distributions.

The information content of an IRIS image can be described with a 2-D array of flux values $F(x,y)$ at a given time t, or alternatively with a 1-D histogram $N(F)$. Since we want to fit a two-component distribution function (i.e., with a Gaussian and a power law), we need to introduce a separator between the two distributions, which we derive from the full width at half maximum (see F_2 in **Figure 1**). We fit then both distribution functions (Eqs **1**, **2**) separately, the Gaussian function in the range of $[F_1,F_2]$, and the power law function in the range of $[F_2,F_3]$, as depicted in **Figure 1**. The minimum flux (F_1) and maximum flux (F_3) are determined from the minimum and maximum flux value in the image. We are fitting the distribution functions with a standard Gaussian fit method, and with a standard linear regression fit for the logarithmic flux function. Note that the power law function $N(S)$ appears to be a straight line in a logarithmic display only (**Figure 1** bottom panel), i.e., log(N)-log(S), but not in a linear representation (**Figure 1** top panel), i.e., lin(N)-lin(S), as used here.

The results of the fitting of the observed histograms are shown for all 12 datasets in **Figure 4**, where the Gaussian fit is rendered with a blue color, and the power law fit with a red color. We see that our two-component model for the distribution function produces accurate fits to the analyzed IRIS data (histograms in **Figure 4**) for seven datasets (# 4–9, 11), while it fails in 5 cases (# 1–3, 10, 12). On the other hand, 4 cases contain sunspots (# 1–3, 10) and coincide with the cases with power law fit failures.

If we would assume that all fluxes are generated by incoherent random noise, we would not be able to fit the histogrammed data at all. Obviously, we would under-predict most of the fluxes substantially (blue dashed curves in **Figure 4**), which underscores that the "fat-tail" power law function, a hallmark of SOC processes, is highly relevant for fitting the observed IRIS 1400 Å data here.

In a next step we investigate the numerical values of the power law slopes α_F of the flux distribution parameters F, which are listed in the third column of **Table 1**. At a first glance, it appears that these values vary wildly in a range of $\alpha_F = 0.94$ to 2.13. However, Vilangot Nhalil et al., 2020 classified the 12 analyzed datasets into 4 cases containing sunspots, and 8 cases containing plages in the transition region without sunspots. From this bimodal behavior it was concluded that the power law index of the energy distribution is larger in plages ($\alpha_E > 2$), compared with sunspot-dominated active regions ($\alpha_E < 2$), (Vilangot Nhalil et al., 2020). In our investigation here, the 4 cases with sunspots exhibit substantially flatter power law slopes α_F (except #3), which indicates that sunspot-dominant distributions are indeed significantly different from those without sunspots (**Table 1**). Actually, we find an even better predictor of this bimodal behavior, by using the maximum flux F_{max} (Column 6 in **Table 1**). We find that flux distributions $N(F) \propto F^{-\alpha_F}$ with maximum fluxes less than $F_{max} \lesssim 50$ [DN] exhibit a power law value of

$$\alpha_F^{obs} \approx 1.70 \pm 0.15, \quad F_{max} < 50 \text{ DN}, \tag{7}$$

which includes the five datasets #6–9, 11. In contrast, the seven other datasets #1–5, 10, 12 have consistently higher maximum values, $F_{max} \gtrsim 50$ DN. Instead of using the maximum values F_{max}, we can also use the average fluxes and find the same bimodal behavior.

Even more significant is that this power law value is consistent with the theoretical prediction of the power law slopes

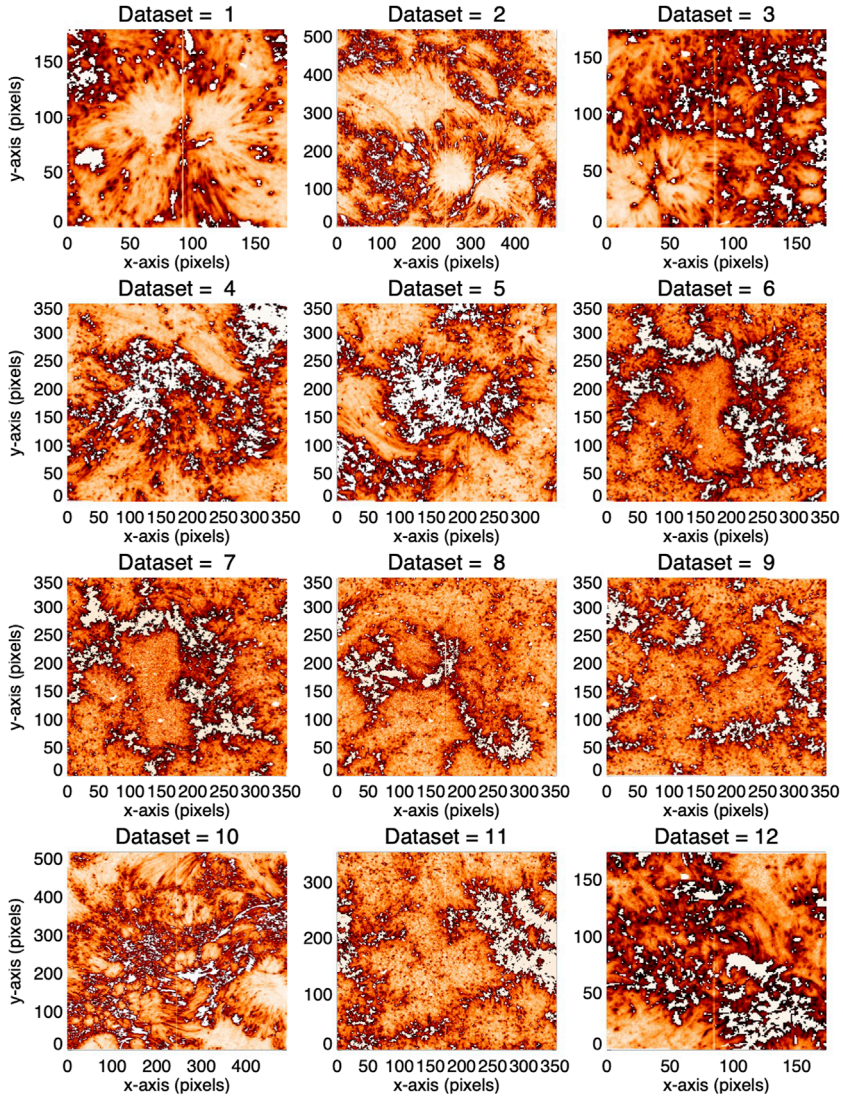

FIGURE 2
Intensity maps of 12 different active regions and Quiet-Sun regions, observed with IRIS SJI 1400 Å. Gaussian random noise is rendered in orange-to-red color, while spicules and network cells are masked out with white color.

(Aschwanden, 2012; Aschwanden, 2022a; Aschwanden et al., 2016),

$$\alpha_{\mathrm{F,SOC}} = \frac{9}{5} = 1.80. \tag{8}$$

Thus we conclude that flux distributions have a power law slope that agree with the theoretial prediction under special conditions, such as for small maximum fluxes. Moreover we find that magnetic flux distributions with sunspots and large magnetic flux imbalances produce flatter slopes and failed power law fits (**Tables 1** and **2**), see **Section 2.4**.

2.4 HMI magnetogram analysis

In order to test the universality of the results we repeat the same analysis for 12 coincident HMI magnetograms onboard the Solar Dynamics Observatory (SDO), which have simultaneous times and identical spatial field-of-views. The 12 analyzed HMI images are shown in **Figure 5**, where black features indicate negative magnetic polarity, and white features indicate positive magnetic polarity. We see sunspots in at least four magnetograms (#1–3, 10), with two sunspots having a negative magnetic polarity (#1, 2), and two cases with positive magnetic polarity (#3, 10). All 12 magnetograms show mixed polarities, but some are heavily unbalanced (#1–5, 10–12).

We quantify the magnetic flux balance with the ratio q_{pos},

$$q_{pos} = \left(\frac{\sum_{pos} F_{ij}}{\sum_{pos} F_{ij} + |\sum_{neg} F_{ij}|} \right). \tag{9}$$

If the magnetic flux (line-of-sight) component is well-balanced, we would expect a value of $q_{pos} = 0.5$, assuming $\Sigma_{pos} = |\Sigma_{neg}|$. Only 4 cases have approximately balanced fluxes (#6–9), namely, $q_{pos} = [0.44, 0.43, 0.38, 0.44]$, while the other 6 cases have large flux imbalances, from $q_{pos} = 0.04$ to 0.99 (**Table 2**; **Figure 6**). The

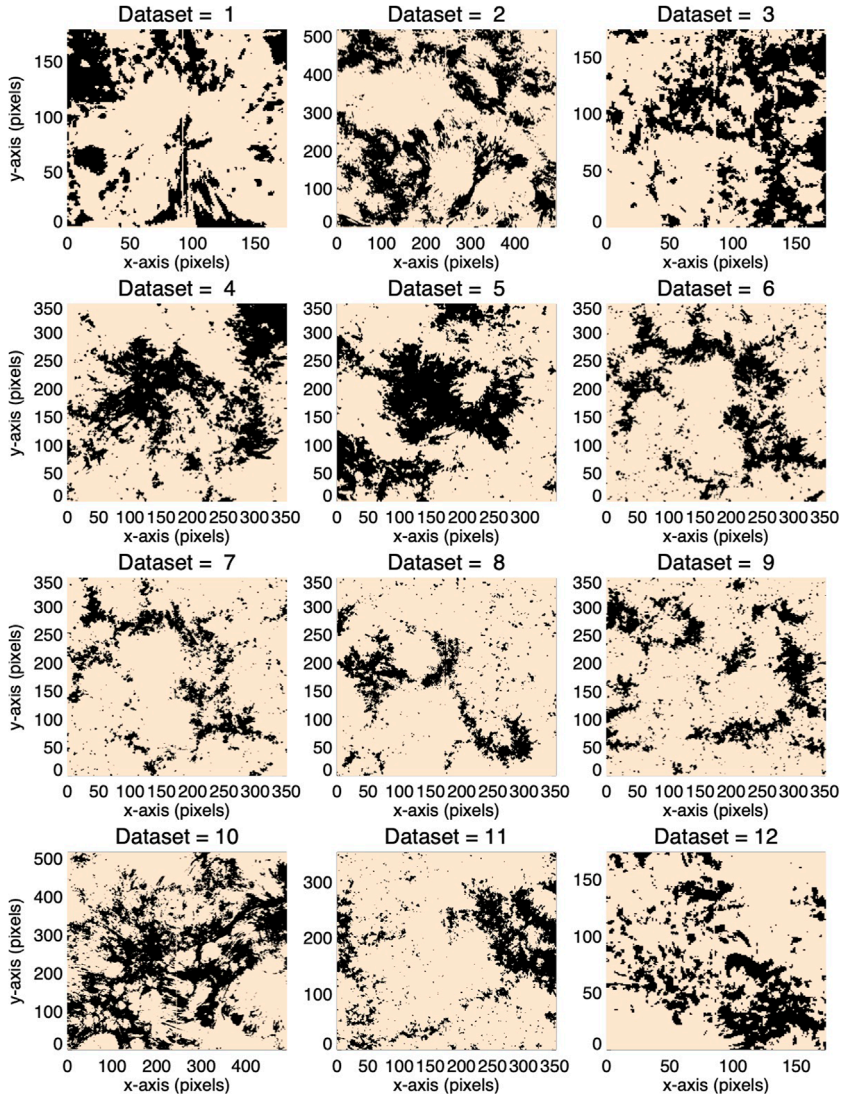

FIGURE 3
Intensity maps of 12 different active regions and Quiet-Sun regions, observed with IRIS SJI 1400 Å. Gaussian random noise is masked out (with peak fluxes $F(x,y) < F_{thr}$), while network cells and spicules are rendered in black.

associated power law slopes of the four well-balanced cases are $\alpha_F = [1.67, 1.64, 1.79, 1.78] = 1.72 \pm 0.07$, which closely coincide with the theoretical SOC-prediction of $\alpha_F \approx 1.80$ (Aschwanden, 2012; Aschwanden, 2022a; Aschwanden et al., 2016).

We analyze the HMI data in the same way as the IRIS data, by fitting Gaussian distributions (blue curves in **Figure 6**) and power law distribution functions (red curves in **Figure 6**), which clearly show a "fat-tail" feature that is far in excess of the Gaussian function (blue dashed curves in **Figure 6**). We compare the power law slopes α_F obtained with the two completely different datasets from IRIS and HMI in **Figure 7**, using the "pixelation" method. The two datasets are found to be highly correlated (with CCC = 0.90, if we ignore the outlier #3). Nevertheless, the power law slopes α_F shown in **Figure 7** are concentrated in two regimes, one that is consistent with our theoretical SOC prediction of $\alpha_{F,IRIS} = \alpha_{F,HMI} \approx 1.80$, while a second cluster is centered around $\alpha_{F,IRIS} \approx 1.0$–$1.5$ and $\alpha_{F,HMI} \approx 1.0$–$1.5$ (**Figure 7**). In essence, we find four datasets (# 6–9) that are consistent with the SOC prediction for events with well-balanced flux $q_{pos} \approx 0.5$, while a second group cannot reproduce the SOC model, but can be characterized with large unbalanced magnetic fluxes (# 1–5, 10–12). The flux imbalance, however, is not always decisive. Tests with variations of the FOV reveal that the arbitrary choice of the FOV (in HMI data) can be more important in deciding whether the calculated power law slope is universally consistent with SOC models, e.g., see event #11.

The physical interpretation of the HMI data is, of course, different for the IRIS data. In the previous analysis of IRIS data we interpreted the coherent statistics (in terms of SOC-controlled power law functions) due to spicular activity in the transition region. In contrast, using the HMI data, which provides the magnetic field line-of-sight component B_z, we can interpret the statistics of incoherent random distributions in terms of

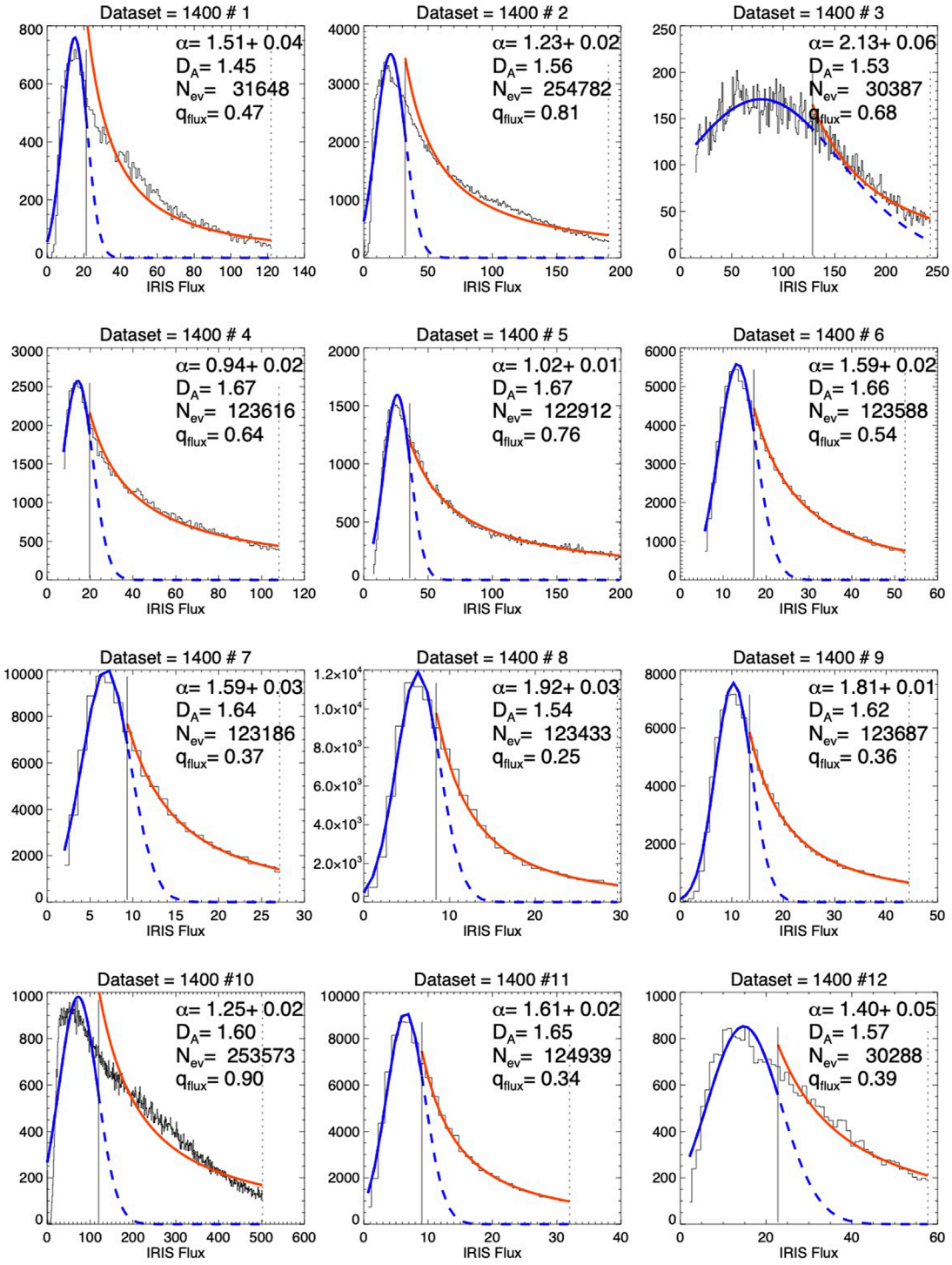

FIGURE 4
Flux histograms of 12 different regions in plages of transition regions, observed with IRIS SJI 1,400 Å. The flux distribution of granules is fitted with a Gaussian function (blue curve, $F < F_2$), and extrapolated with dashed blue curves. The flux distribution of spicules is fitted with a power law distribution function (thick red curve. The separation of the two distributions at F_2 is marked with a vertical thin line.

"salt-and-pepper" small-scale magnetic fields in the photosphere, and the coherent avalanche statistics in terms of SOC-controlled magnetic reconnection processes in nanoflares and larger flares (Table 3). Note that the two parameters $\alpha_{\rm F,IRIS}$ amd $\alpha_{\rm F,HMI}$ are observed independently from different spacecraft, as well as in markedly different wavelength bands, i.e., $\lambda \approx 1,400$ Å for IRIS, and $\lambda = 6,173$ Å for HMI/SDO magnetograms, which measures the mean flux F from the line-of-sight magnetic field component $B_z(x, y)$. Despite of the very different instruments and wavelengths, the power law slope α_F of the mean flux appears to be universally

TABLE 2 Results of 12 datasets obtained with HMI/SDO, showing the power law slope α_F of the flux distribution, the separator flux F_2, the magnetic flux balance q_{pos}, the magnetic field strength B_z, the magnetic flux balance q_{pos}, and the fractal dimension D_A. Note that the power law slope α_F agrees with the theoretical prediction of $\alpha_F = 9/5 \approx 1.8$ in 5 cases approximately, when there is no sunspot and the magnetic flux is balanced. The values of α_F in parenthesis are ignored in the calculation of the averages.

Number Dataset HMI #	Phenomenon	Power law slope fit α_F	Matching prediction $\alpha_F \approx 1.8$	Separator flux F_2 [DN]	Magnetic field B_z [G]	Magnetic flux balance q_{pos}	Matching balance $q_{pos} \approx 0.50$	Fractal dimension D_A
1	Sunspot	(1.32 ± 0.03)	NO	8	+1,073	(0.04)	NO	1.54
2	Sunspot	(1.27 ± 0.01)	NO	6	−1729	(0.16)	NO	1.55
3	Sunspot	(0.92 ± 0.02)	NO	5	−2076	(0.99)	NO	1.59
4	Plage	(1.32 ± 0.01)	NO	5	+1785	(0.29)	NO	1.58
5	Plage	(1.33 ± 0.02)	NO	5	−1,186	(0.81)	NO	1.57
6	Plage	1.67 ± 0.02	YES	4	+1854	0.44	YES	1.51
7	Plage	1.64 ± 0.02	YES	4	−1,011	0.43	YES	1.51
8	Plage	1.79 ± 0.03	YES	4	−1,022	0.38	YES	1.49
9	Plage	1.78 ± 0.03	YES	5	+955	0.44	YES	1.50
10	Sunspot	(0.94 ± 0.01)	NO	7	−1,055	(0.34)	NO	1.66
11	Plage	1.72 ± 0.02	YES	5	+2058	(0.92)	NO	1.51
12	Plage	(1.22 ± 0.03)	NO	4	+1,036	(0.88)	NO	1.52
	Observations	1.72 ± 0.07				0.42 ± 0.03		1.54 ± 0.05
	Theory	1.80				0.50		1.50

valid and consistent with the theoretical SOC prediction for datasets with approximate magnetic flux balance (**Figure 7**). However we learned that the magnetic flux balance and the absence of sunspots represent additional requirements to warrant the universality of the SOC slopes. This yields a testable prediction: If the field-of-view of each HMI magnetogram is readjusted so that the enclosed magnetic flux becomes more balanced and no sunspot appears in the FOV, the power law slope is expected to approach the theoretical universal value of $\alpha_{F,IRIS} \approx \alpha_{F,HMI} \approx 1.80$.

3 Discussion

In the following we discuss an incoherent random process (e.g., salt-and-pepper small-scale magnetic elements), and two coherent random processes (e.g., spicular dynamics, and magnetic reconnection), which relate to each other as shown in the diagram of **Table 3**.

3.1 Magnetic flux distribution

The most extensive statistical study on the size distribution of magnetic field features on the solar surface has been undertaken by Parnell et al. (2009). Combining magnetic field data from three instruments (SOT/Hinode, MDI/NFI, and MDI/FD on SOHO, a combined occurrence frequency size distribution was synthesized that extends over 5 decades, in the range of $\Phi = 2 \times 10^{17}$–10^{23} Mx (Parnell et al., 2009),

$$N(\Phi) \propto (\Phi_0)^{-1.85\pm0.14} \quad [\mathrm{Mx}^{-1}\mathrm{cm}^{-2}], \tag{10}$$

where the magnetic flux Φ is obtained from integration of the magnetic field $B(x,y)$ over a thresholded area $A = \int dx\, dy$,

$$\Phi = \int B(x,y)\; dx\; dy \quad [\mathrm{Mx}]. \tag{11}$$

If we equate the magnetic flux Φ with the mean flux F of an event in standard SOC models, we predict a power law slope of (Aschwanden, 2012; Aschwanden, 2022a; Aschwanden et al., 2016), using $d = 3$, $D_V = 5/2$, and $\gamma = 1$,

$$\alpha_{F,SOC} = 1 + \frac{(d-1)}{(\gamma D_V)} = \frac{9}{5} = 1.80, \tag{12}$$

which agree well with the result (Eq. **10**) observed by Parnell et al. (2009). A lower value was found from cellular automaton simulations, $N(\Phi) \approx \Phi^{-1.5\pm0.05}$ (Fragos et al., 2004), where flux emergence is driven by a percolation rule, similar to the percolation model of Seiden and Wentzel (1996), or Balke et al. (1993). Mathematical models have been developed to model the percolation phenomenon, based on combinatorial and statistical concepts of connectedness that exhibit universality in form of powerlaw distributions.

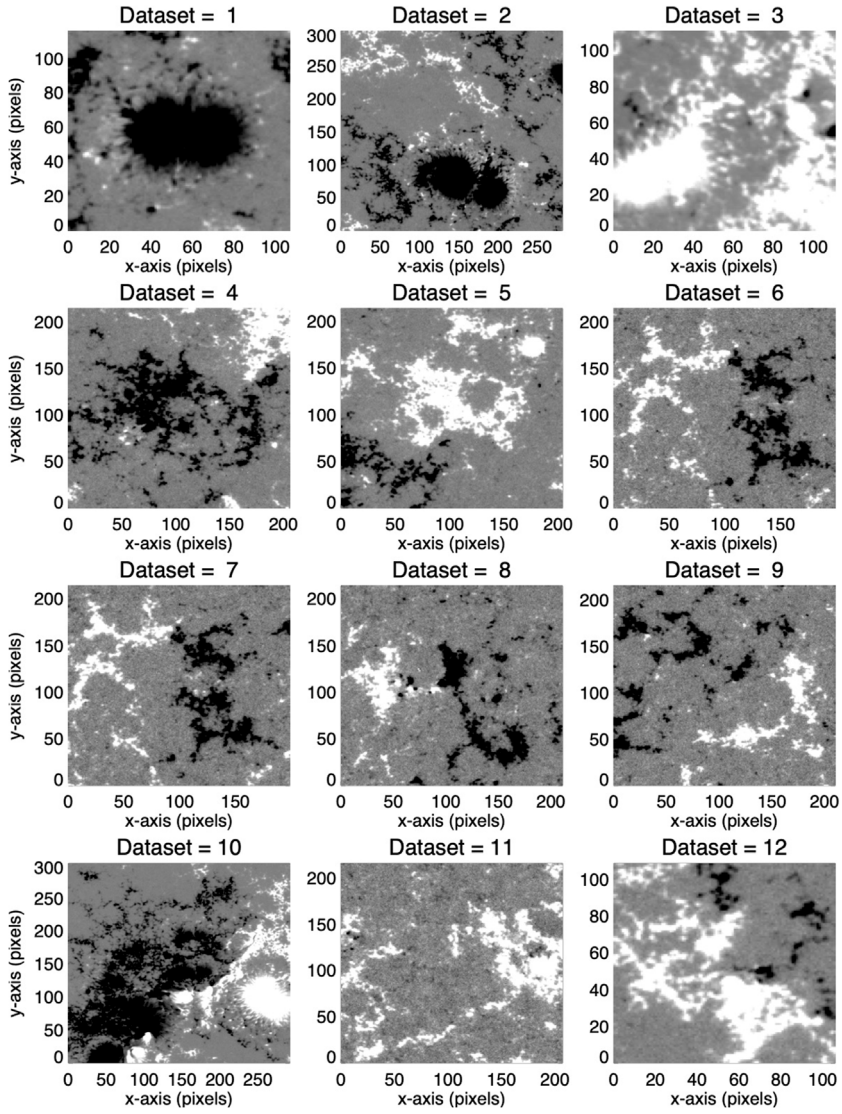

FIGURE 5
Magnetograms of 12 different active regions and plage regions, observed with HMI/SDO. The black color indicates negative magnetic polarity, and the white color represents positive magnetic polarity.

3.2 Universality of SOC size distributions

Power law-like size distributions are the hallmark of self-organized criticality systems. Statistical studies in the past have collected SOC parameters such as length scales L, time scales T, peak flux rates P, mean fluxes F, fluences and energies $E = F \times T$, mono-fractal and multi-fractal dimensions (Mandelbrot, 1977), in order to test whether the theoretically expected power law size distributions, or the power law slopes of waiting times, agree with the observed distributions (mostly observed in astrophysical systems). The universality of SOC models (Aschwanden, 2012; Aschwanden, 2022a; Aschwanden et al., 2016) is based on four scaling laws: the scale-free probability conjecture $N(L) \propto L^{-d}$, classical diffusion $L \propto T^{\beta/2}$, the flux-volume relationship $F \propto V^{\gamma}$, and the Euclidean scaling law, $P \propto L^{\gamma d}$, where $d = 3$ is the Euclidean dimension, $\beta \approx 1$ is the classical diffusion coefficient, $\gamma \approx 1$ the flux-volume proportionality, while $D_A = 3/2$ and $D_V = 5/2$ are the mean fractal dimensions in 2-D and 3-D Euclidean space. The standard SOC model is expressed in terms of these universal constants: $d = 3$, $\gamma = 1$, $\beta = 1$. Consequently, the four basic scaling laws reduce to $N(L) \propto L^{-3}$, $L \propto T^{1/2}$, $F \propto L^{2.5}$, and $P \propto L^3$. Since we measure the mean flux F in this study, our main test of the universality of SOC models if formulated in terms of the flux-volume relationship $F \propto V^{\gamma}$, leading to the power law slope $\alpha_{\mathrm{F,SOC}} = 1.80$ (Eq. 12).

The SOC-inferred scaling laws hold for a large number of phenomena. This implies that our SOC formalism is universal in the sense that the statistical size distributions are identical for each phenomenon, displaying a universal power law slope of $\alpha_{\mathrm{F,SOC}} = 1.80$. When we conclude that the power law slope α_F is universal, the SOC model implies that the flux-volume proportionality ($\gamma \approx 1$) as well as the mean fractal dimension ($d = 3$, $D_V \approx 2.5$) are universal too.

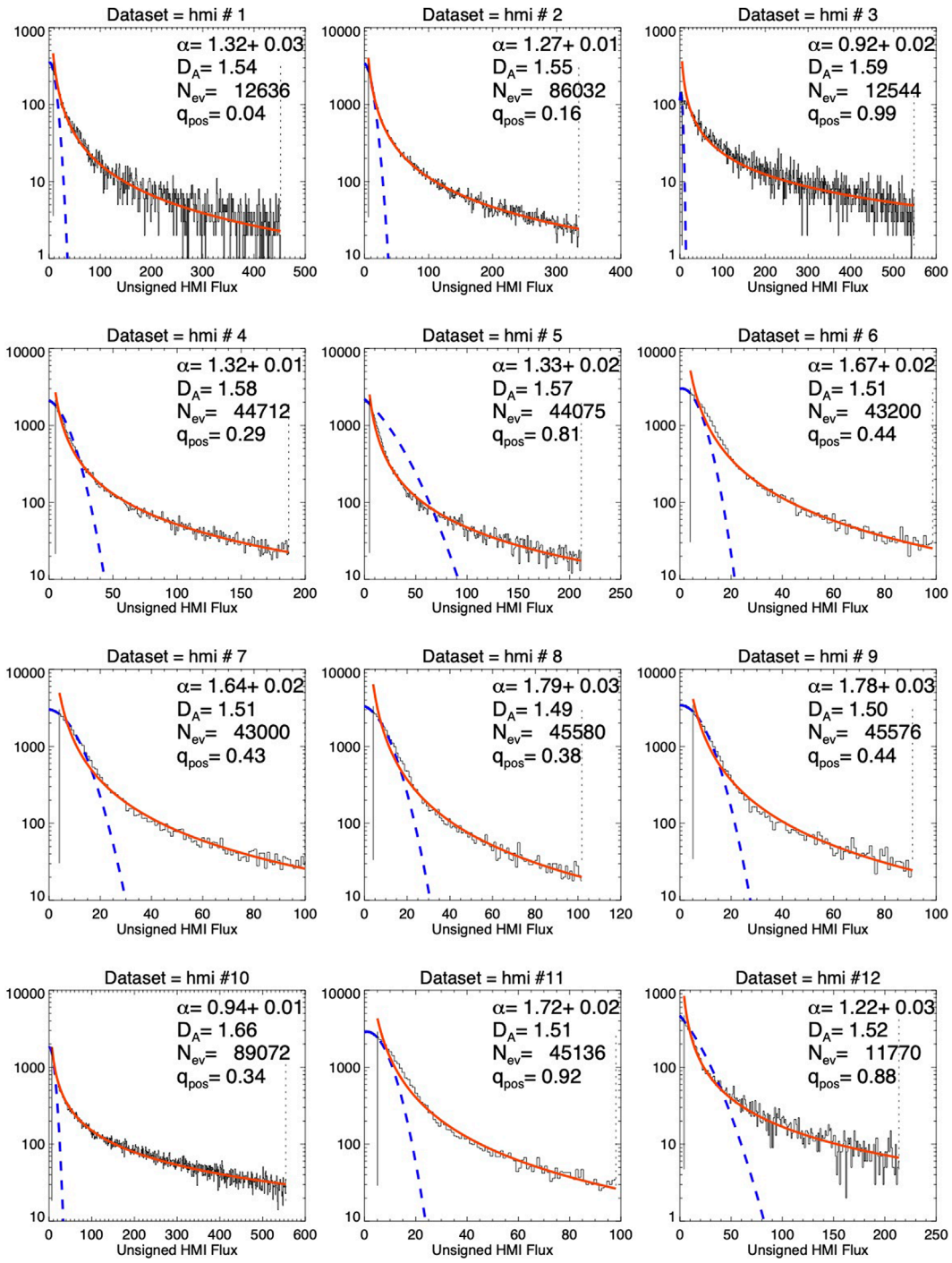

FIGURE 6
Histograms of different solar regions, observed in magnetograms with HMI/SDO. The size distribution of salt-and-pepper magnetic noise is fitted with a Gaussian function (blue curve), the extrapolation of the Gaussian (dashed blue curve), while the distribution of magnetic features are fitted with power law functions (red curves).

3.3 Phenomena with SOC

Once we establish the self-consistency of power law slopes between theoretical (SOC) and observed size distributions, the next question is what physical processes are at work. We envision four different types of phenomena (Table 3): (i) Gaussian random noise in IRIS data); (ii) spicular plage events in the transition region (described by the power law size distribution in IRIS data); (iii) salt-and-pepper small-scale magnetic structures (described by the random noise distributions in HMI magnetograms); and (iv) magnetic reconnection processes in flares and nanoflares (described by the power law size distribution in HMI data).

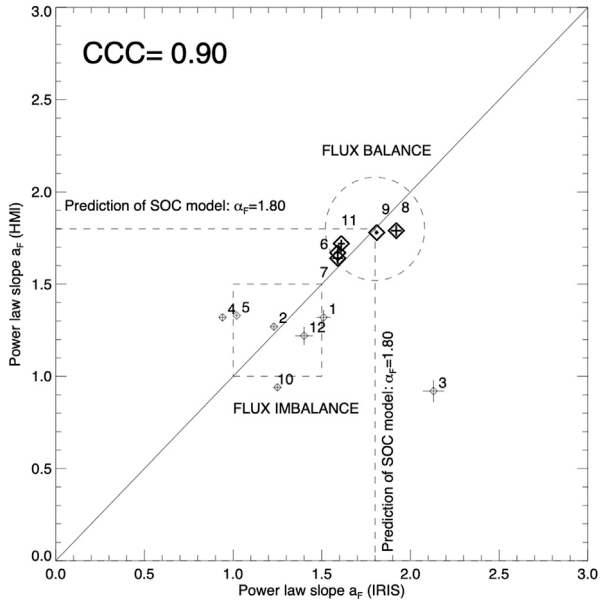

FIGURE 7
The power law slopes α_F are calculated for 12 datasets for two independent instruments and wavelengths: from IRIS data (*x*-axis) and from HMI/SDO data (*y*-axis). Note that five datasets (#6–9, 11) coincide approximately with the theoretically expected value $\alpha_F = 1.80$ (marked with a circle). The other 7 cases (shown in rectangle) are subject to sunspots, relatively large peak fluxes, and large magnetic flux imbalances.

TABLE 3 Diagram of phenomena observed with different instruments (IRIS, HMI), different wavelengths (columns), for incoherent and coherent random processes (rows).

	IRIS 1,400 Å	HMI 6,173 Å
incoherent random process (Gaussian function)	?	salt-and-pepper small-scale magnetic fields
coherent random process (power law function)	spicules	flares, nanoflares magnetic reconnection

However, there are deviations from these rules. We found that the power law distributions are modified in the presence of sunspots, when the magnetic flux is unbalanced, or when the FOV is arbitrarily chosen. Under ideal conditions, the SOC scaling laws are fulfilled universally, independent of the wavelength or plasma temperature. Magnetic field data (from HMI/SDO) or $\lambda \approx 1,400$ Å (from IRIS) appear to produce emission in volumes that are proportional in the photosphere or transition zone, even when they are formed at quite different temperatures, i.e., $T_{\rm phot} \approx 5,800$ K in the photosphere and $T_{\rm TR} \approx 10^4$–10^5 K in the transition region.

Another ingredient of the SOC model is the scale-free probability conjecture, i.e., $N(L) \propto L^{-d} = L^{-3}$, which cannot be uniquely linked to a particular physical process. Parnell et al. (2009) conclude that a combination of emergence, coalescence, cancellation, and fragmentation may possibly produce power law size distributions of spatial scales *L*. Alternative models include the turbulence and the Weibull distributions (Parnell, 2002). Munoz-Jaramillo et al. (2015) study the best-fitting distribution functions for 11 different databases of sunspot areas, sunspot group areas, sunspot umbral areas, and magnetic fluxes. They find that a linear combination of Weibull and log-normal distributions fit the data best (Munoz-Jaramillo et al., 2015). Weibull and log-normal distributions combine two distribution functions, similar to our synthesis of a Gaussian-plus-power-law distribution.

A general physical scenario of a power law size distribution is the evolution of avalanches by exponential growth (Rosner and Vaiana, 1978), with subsequent saturation (logistic growth) after a random time interval, which produces an exact power law function (Aschwanden et al., 1998). Our approach to model the size distribution of solar phenomena with two different functions, employing a Gaussian noise and a power law tail, reflects the duality of incoherent and coherent random components, in both the data from IRIS and HMI (**Table 3**). In summary, incoherent random components include salt-and-pepper small-scale magnetic features, while coherent components include spicular avalanches, and magnetic reconnection avalanches from nanoflares to large flares.

3.4 Granular dynamics

The physical understanding of solar (or stellar) granulation has been advanced by numerical magneto-convection models and N-body dynamic simulations, which predict the evolution of small-scale (granules) into large-scale features (meso- or super-granulation), organized by surface flows that sweep up small-scale structures and form clusters of recurrent and stable granular features (Berrilli et al., 1998; Berrilli et al., 2005; Hathaway et al., 2000; Martinez-Sykora et al., 2008; Rieutord et al., 2008; Rieutord et al., 2010; Cheung and Isobe, 2014). An analytical model of convection-driven generation of ubiquitous coronal waves is considered in Aschwanden et al. (2018b). The fractal multi-scale dynamics has been found to be operational in the Quiet-Sun photosphere, in quiescent non-flaring states, as well as during flares (Uritsky et al., 2007; Uritsky et al., 2013; Uritsky and Davila, 2012). The fractal structure of the solar granulation is obviously a self-organizing pattern that is created by a combination of subphotospheric magneto-convection and surface flows, which are turbulence-type phenomena.

The interpretation of granulation as the cause of the Gaussian "noise" in IRIS data is controversial for two reasons: (i) The intensity measured by IRIS 1400 in non-magnetic areas has densities that originate from the middle chromosphere, rather than from the underlying photosphere. (ii) No convective signal propagates to these heights and densities, and thus the scale of granulation cannot be probed at these heights (Martinez-Sykora et al., 2015).

3.5 Spicular dynamics

One prominent feature in the transition region is the phenomenon of *"moss"*, which appears as a bright dynamic pattern with dark inclusions, on spatial scales of $L \approx 1$–3 Mm, which has been interpreted as the upper transition region above active region plages, and below relatively hot loops (De Pontieu et al., 1999; De Pontieu et al., 2014). Our measurement of structures in the IRIS 1,400 Å channel is sensitive to a temperature range of $T_e \approx 10^4$–10^5 K, and thus is likely to include chromospheric and transition region phenomena such as: spicules II (De Pontieu et al., 2007), macro-spicules, dark mottles, dynamic fibrils, surges, miniature filament eruptions, *etc.* Theoretical models include the rebound shock model (Sterling and Hollweg, 1988), pressure-pulses in the high atmosphere (Singh et al., 2019), Alfvénic resonances (Sterling, 1998), magnetic reconnection models for type II spicules (De Pontieu et al., 2007), ion-neutral collisional damping (De Pontieu, 1999), leakage of global p-mode oscillations (De Pontieu et al., 2004), MHD kink waves (Zaqarashvili and Erdelyi, 2009), vortical flow models (Kitiashvili et al., 2013), and magneto-convective driving by shock waves (De Pontieu et al., 2007).

The fact that we obtain a power law size distribution ($\alpha_F = 1.70 \pm 0.15$, **Table 1**), which is very similar to solar flares in general, $\alpha_{F,SOC} = 1.80$, implies the universality of the SOC framework. Furthermore we find power law-like size distributions for spicular events, rather than a Gaussian distribution, which tells us that spicule events need to be modeled in terms of SOC-driven avalanches, instead of Gaussian random distributions. As mentioned above, the difference between incoherent and coherent random processes is the following: Gaussian statistics reflect the operation of a memoryless stationary random process; while avalanche processes such as occurring in SOC systems are characterized by extended spatial and temporal correlations, i.e., the unfolding of an avalanche is influenced by the imprint of earlier avalanches on the system.

We propose that spicules around magnetic elements are responsible for the power law slope α_F observed in those areas. This appears to be a plausible interpretation since these dynamical phenomena are very relevant in plage and network areas. For instance, event #11 shows a fully unbalanced magnetic configuration, which supports the idea that strong magnetic fields, fragmented in small-scale elements in plage and/or network seems to be the relevant characteristics, rather than flux balance over an arbitrary FOV.

3.6 Salt-and-pepper magnetic field

We interepret the random noise Gaussian distribution of magnetic fluxes in Quiet-Sun regions as small-scale magnetic field "pepper-and-salt" structures, also called *magnetic carpet* (Priest et al., 2002), where the black and white color in magnetograms (**Figure 5**) corresponds to negative and positive polarity. The fact that we obtain two distinctly different size distributions (Gaussian vs power law) indicates at least two different physical mechanisms, one being an incoherent random (Gaussian) process, the other one being a coherent (power law-like) avalanche process. The salt-and-pepper structure is generated apparently by an incoherent random process, rather than by a coherent avalanching process, according to our fits. This may constrain the origin of the solar magnetic field, being created by emergence, submergence, coalescence, cancellation, fragmentation, and/or small-scale dynamos, *etc.* Not all would be expected to yield Gaussian statistics (e.g., fragmentation processses often yield log-normal distributions; Verbeeck et al., 2019).

3.7 Magnetic reconnection

The re-arrangement of the stress-induced solar magnetic field requires ubiquitous and permanent (but intermittent) magnetic reconnection processes on all spatial and temporal scales. Our study finds power law size distributions, with a slope of $\alpha_F = 1.72 \pm 0.07$ from HMI magnetograms, which is similar to flares in general (see Aschwanden et al., 2016 for a review of all wavelengths (e.g., gamma-rays, hard X-rays, soft X-rays, UV, EUV, FUV, etc.). This tells us that there is a strong correlation between the photospheric field (in HMI images) and the transition region (in IRIS images), as evident from the cross-correlation coefficient of CCC = 0.90 shown in **Figure 7**. The fractal multi-scale dynamics apparently operates in the quiet photosphere, in the quiescent non-flaring state, as well as during flares in active regions (Uritsky and Davila, 2012).

4 Conclusion

Solar and stellar flares, pulsar glitches, auroras, lunar craters, as well as earthquakes, landslides, wildfires, snow avalanches, and sandpile avalanches are all driven by self-organized criticality (SOC), which predicts power law-like occurrence frequency (size) distributions and waiting time distribution functions. What is new in our studies of SOC systems is that we are now able to calculate the slope α_x of power law functions, which allows us to test SOC models by comparing the observed (and fitted) distribution functions with the theoretically predicted values. In this study we compare statistical distributions of SOC parameters from different wavelengths and different instruments (UV emission observed with IRIS and magnetograms with HMI). The results of our study are:

1. The histogrammed distribution of fluxes $N(F)$ obtained from an IRIS 1,400 Å image, or from a HMI magnetogram, cannot be fitted solely by a Gaussian function, but requires a two-component function, such as a combination of a Gaussian and a power law function, a "fat-tail" extension above some threshold. We define a separator between the two functions above the full width at half maximum. We obtain power law slopes of $\alpha_F = 1.70 \pm 0.15$ from the IRIS data, and $\alpha_F = 1.72 \pm 0.07$ from the HMI data, which agree with the theoretical SOC prediction of $\alpha_F = 1.80$, and thus demonstrate universality across UV wavelengths and magnetograms. Moreover, it agrees with the five order of magnitude extending power law distribution sampled by Parnell et al. (2009), $\alpha_F = 1.85 \pm 0.14$.
2. **Tables 1, 2** show the following characterizations of the 12 selected datasets: 4 cases with sunspots, 5 cases that have a max flux

<50 DN, 4 cases with a magnetic flux balance of $q_{pos} \approx 0.4$, and 5 cases that agree with the theortical prediction $a_F = 1.8$ (see values flagged with YES/NO in **Tables 1**, **2**). In summary, the universality of the flux power law slope ($a_F = 1.80$) depends on the absence of sunspots, small maximum fluxes, magnetic flux balance, and the choice of the field-of-view of an active region. In other words, the scale-free probability inherent to SOC models requires some special conditions for magnetic field parameters. Strong magnetic fields, fragmented in small-scale elements in plage and/or network seems to be the relevant characteristics, rather than flux balance over an arbitrary FOV.

3. We designed an algorithm that produces "pixelized" size distributions from a single image (e.g., from a UV image or a magnetogram). In this method, the flux and area of each avalanche event is decomposed down to the pixel size level, which allows us to calculate the power law slope of the size flux distibution without requiring an automated feature recognition code. The method is computationally very fast and does not require any particular automated pattern recognition code.
4. We can characterize the analyzed size distributions in terms of four distinctly different physical interpretations: (i) the Gaussian random noise distribution in IRIS data; (ii) spicular plage events in the transition region (described by the power law size distribution in IRIS data); (iii) salt-and-pepper small-scale magnetic structures (described by the random noise distributions in HMI magnetograms); and (iv) magnetic reconnection processes in flares and nanoflares (described by the power law size distribution in HMI data).

Future work may include: (i) Testing of the SOC-predicted size distributions with power law slopes α_F for all available (mean) fluxes F (in HXR, SXR, EUV, *etc.*); (ii) testing the selection of different FOV sizes in the absence or existence of sunspots, and magnetic flux balance; (iii) and cross-comparing the "pixelization" method with the standard method. Ultimately these methods should help us to converge the numerical values in SOC models.

Data availability statement

The raw data supporting the conclusions of this article will be made available by the authors, without undue reservation.

Author contributions

All authors listed have made a substantial, direct, and intellectual contribution to the work and approved it for publication.

Funding

IRIS mission support. This work was partially supported by NASA contract NNX11A099G "Self-organized criticality in solar physics", NASA contract NNG04EA00C of the SDO/AIA instrument, and the IRIS contract NNG09FA40C to LMSAL. IRIS is a NASA small explorer mission developed and operated by LMSAL with mission operations executed at NASA Ames Research Center and major contributions to downlink communications funded by ESA and the Norwegian Space Centre.

Acknowledgments

The author is indebted to data contributions and data preparation. We acknowledge constructive and insightful comments of two reviewers and stimulating discussions (in alphabetical order), with Paul Charbonneau, Adam Kowalski, Karel Schrijver, and Vadim Uritsky.

Conflict of interest

The authors declare that the research was conducted in the absence of any commercial or financial relationships that could be construed as a potential conflict of interest.

Publisher's note

References

Aschwanden, M. J. (2014). A macroscopic description of self-organized systems and astrophysical applications. *ApJ* 782, 54. doi:10.1088/0004-637x/782/1/54

Aschwanden, M. J. (2012). A statistical fractal-diffusive avalanche model of a slowly-driven self-organized criticality system. *A&AA2* 539, A2. doi:10.1051/0004-6361/201118237

Aschwanden, M. J., Crosby, N., Dimitropoulou, M., Georgoulis, M. K., Hergarten, S., McAteer, J., et al. (2016). 25 Years of self-organized criticality: Solar and astrophysics. *Space Sci. Rev.* 198, 47–166. doi:10.1007/s11214-014-0054-6

Aschwanden, M. J., Dennis, B. R., and Benz, A. O. (1998). Logistic avalanche processes, elementary time structures, and frequency distributions in solar flares. *ApJ* 497, 972–993. doi:10.1086/305484

Aschwanden, M. J., Gosic, M., Hurlburt, N. E., and Scullion, E. (2018b). Convection-driven generation of ubiquitous coronal waves. *ApJ* 866 (13), 73. doi:10.3847/1538-4357/aae08b

Aschwanden, M. J. (2022b). Reconciling power-law slopes in solar flare and nanoflare size distributions. *ApJL* 934, L3. doi:10.3847/2041-8213/ac7b8d

Aschwanden, M. J. (2011). *Self-organized criticality in astrophysics. The statistics of nonlinear processes in the universe*. New York: Springer-Praxis, 416p. ISBN 978-3-642-15000-5.

Aschwanden, M. J. (2022a). The fractality and size distributions of astrophysical self-organized criticality systems. *ApJ* 934, 33. doi:10.3847/1538-4357/ac6bf2

Aschwanden, M. J., and Vilangot Nhalil, N. (2022). Interface region imaging spectrograph (IRIS) observations of the fractal dimension in the solar atmosphere. *Front. Astronomy Space Sci.* Manuscript ID 999329.

Bak, P. (1996). *How nature works*. New York: The Science of Self-Organized Criticality. Copernicus.

Bak, P., Tang, C., and Wiesenfeld, K. (1988). Self-organized criticality. *Phys. Rev. A* 38 (1), 364–374. doi:10.1103/physreva.38.364

Bak, P., Tang, C., and Wiesenfeld, K. (1987). Self-organized criticality: An explanation of the 1/*f* noise. *Phys. Rev. Lett.* 59 (27), 381–384. doi:10.1103/physrevlett.59.381

Balke, A. C., Schrijver, C. J., Zwaan, C., and Tarbell, T. D. (1993). Percolation theory and the geometry of photospheric magnetic flux concentrations. *Sol. Phys.* 143, 215–227. doi:10.1007/bf00646483

Berrilli, F., Del Moro, D., Russo, S., Consolini, G., and Straus, T. (2005). Spatial clustering of photospheric structures. *ApJ* 632, 677–683. doi:10.1086/432708

Berrilli, F., Florio, A., and Ermolli, I. (1998). On the geometrical properties of the chromospheric network. *Sol. Phys.* 180, 29–45. doi:10.1023/a:1005023819431

Burlaga, L. F., and Lazarus, A. J. (2000). Lognormal distributions and spectra of solar wind plasma fluctuations: Wind 1995-1998. *JGR* 105, 2357–2364. doi:10.1029/1999ja900442

Ceva, H., and Luzuriaga, J. (1998). Correlations in the sand pile model: From the log-normal distribution to self-organized criticality. *Phys. Lett. A* 250, 275–280. doi:10.1016/s0375-9601(98)00848-2

Cheung, M. C. M., and Isobe, H. (2014). Flux emergence (theory). *LRSP* 11, 3. doi:10.12942/lrsp-2014-3

De Pontieu, B., Berger, T. E., Schrijver, C. J., and Title, A. M. (1999). Dynamics of transition region 'moss' at high time resolution. *Sol. Phys.* 190, 419–435. doi:10.1023/a:1005220606223

De Pontieu, B., Erdelyi, R., and James, S. P. (2004). Solar chromospheric spicules from the leakage of photospheric oscillations and flows. *Nature* 430, 536–539. doi:10.1038/nature02749

De Pontieu, B., McIntosh, S., Hansteen, V. H., Carlsson, M., Schrijver, C. J., Tarbell, T. D., et al. (2007). A tale of two spicules: The impact of spicules on the magnetic chromosphere. *PASJ* 59, S655–S652. doi:10.1093/pasj/59.sp3.s655

De Pontieu, B. (1999). Numerical simulations of spicules driven by weakly-damped Alfvén waves I. WKB approach. *A&A* 347, 696.

De Pontieu, B., Title, A. M., Lemen, J. R., Kushner, G. D., Akin, D. J., Allard, B., et al. (2014). The Interface region imaging spectrograph (IRIS). *Sol. Phys.* 289, 2733.

Fontenla, J. M., Curdt, W., Avrett, E. H., and Harder, J. (2007). Log-normal intensity distribution of the quiet-Sun FUV continuum observed by SUMER. *A&A* 468, 695–699. doi:10.1051/0004-6361:20066854

Fragos, T., Rantsiou, E., and Vlahos, L. (2004). On the distribution of magnetic energy storage in solar active regions. *A&A* 420, 719–728. doi:10.1051/0004-6361:20034570

Gallagher, P. T., Phillips, K. J. H., Harra-Murnion, L. K., et al. (1998). Properties of the quiet Sun EUV network. *A&A* 335, 733.

Giles, D. E., Feng, H., and Godwin, R. T. (2011). *On the bias of the maximum likelihood estimator for the two-parameter Lomax distribution*. Econometrics Workshop Paper EWP1104, ISSN 1485.

Harrison, R. A., Harra, L. K., Brkovic, A., and Parnell, C. E. (2003). A Study of the unification of quiet-Sun transient-event phenomena. *A&A* 409, 755–764. doi:10.1051/0004-6361:20031072

Hathaway, D. H., Beck, J. G., Bogart, R. S., Bachmann, K., Khatri, G., Petitto, J., et al. (2000). *photospheric Convect. Spectr. SoPh* 193, 299–312. doi:10.1023/a:1005200809766

Hosking, J. R. M., and Wallis, J. R. (1987). Parameter and quantile estimation for the generalized Pareto distribution. *Technometrics* 29 (3), 339–349. doi:10.1080/00401706.1987.10488243

Hudson, H. S. (1991). Solar flares, microflares, nanoflares, and coronal heating. *Sol. Phys.* 133, 357–369. doi:10.1007/bf00149894

Jensen, H. J. (1998). *Self-Organized Criticality: Emergent complex behaviour in physical and biological systems*. Cambridge University Press.

Katsukawa, Y., and Tsuneta, S. (2001). Small fluctuation of coronal X-ray intensity and a signature of nanoflares. *ApJ* 557, 343–350. doi:10.1086/321636

Kitiashvili, I. N., Kosovichev, A. G., Lele, S. K., Mansour, N. N., and Wray, A. A. (2013). Ubiquitous solar eruptions driven by magnetized vortex tubes. *ApJ* 770, 37. doi:10.1088/0004-637x/770/1/37

Krucker, S., and Benz, A. O. (1998). Energy distribution of heating processes in the quiet solar corona. *ApJ* 501, L213–L216. doi:10.1086/311474

Kunjaya, C., Mahasena, P., Vierdayanti, K., and Herlie, S. (2011). Can self-organized critical accretion disks generate a log-normal emission variability in AGN? *ApSS* 336, 455–460. doi:10.1007/s10509-011-0790-y

Lomax, K. S. (1954). Business failures: Another example of the analysis of failure data. *J. Am. Stat. Assoc.* 49, 847–852. doi:10.1080/01621459.1954.10501239

Lu, E. T., and Hamilton, R. J. (1991). Avalanches and the distribution of solar flares. *ApJ* 380, L89. doi:10.1086/186180

Mandelbrot, B. B. (1977). *The fractal geometry of nature*. New York: W.H.Freeman and Company.

Martinez-Sykora, J., Hansteen, V., and Carlsson, M. (2008). Twisted flux tube emergence from the convection zone to the corona. *ApJ* 679, 871–888. doi:10.1086/587028

Martinez-Sykora, J., Rouppe van der Voort, L., Carlsson, M., De Pontieu, B., Pereira, T. M. D., Boerner, P., et al. (2015). Internetwork chromospheric bright grains observed with IRIS and SST. *ApJ* 803, 44. doi:10.1088/0004-637x/803/1/44

McAteer, R. T. J., Aschwanden, M. J., Dimitropoulou, M., Georgoulis, M. K., Pruessner, G., Morales, L., et al. (2016). 25 Years of self-organized criticality: Numerical detection methods. *SSRv* 198, 217–266. doi:10.1007/s11214-015-0158-7

Mitzenmacher, M. (2004). A brief history of generative models for power law and lognormal distributions. *Internet Math.* 1 (2), 226–251. doi:10.1080/15427951.2004.10129088

Munoz-Jaramillo, A., Senkpeil, R. R., Windmueller, J. C., Amouzou, E. C., Longcope, D. W., Tlatov, A. G., et al. (2015). Small-scale and global dynamos and the area and flux distributions of active regions, sunspot groups, and sunspots: A multi-database study. *ApJ* 800, 48. doi:10.1088/0004-637x/800/1/48

Parnell, C. E., DeForest, C. E., Hagenaar, H. J., Johnston, B. A., Lamb, D. A., and Welsch, B. T. (2009). A power-law distribution of solar magnetic fields over more than five decades in flux. *ApJ* 698, 75–82. doi:10.1088/0004-637x/698/1/75

Parnell, C. E. (2002). Nature of the magnetic carpet - 1. Distribution of magnetic fluxes. *MNRAS* 335/2, 398.

Priest, E. R., Heyvaerts, J. F., and Title, A. M. (2002). A flux-tube tectonics model for solar coronal heating driven by the magnetic carpet. *ApJ* 576, 533–551. doi:10.1086/341539

Rathore, B., Carlsson, M., Leenaarts, J., and De Pontieu, B. (2015). The Formation of Iris diagnostics. VIII. Iris observations in the C II 133.5 nm multiplet. *ApJ* 811, 70. doi:10.1088/0004-637x/814/1/70

Rathore, B., Carlsson, M., Leenaarts, J., and Pontieu, B. D. (2015). The Formation of IRIS diagnostics. VI. The diagnostic potential of the C II lines at 133.5 nm in the solar atmosphere. *ApJ* 811, 81. doi:10.1088/0004-637x/811/2/81

Rieutord, M., Meunier, N., Roudier, T., Rondi, S., Beigbeder, F., and Pares, L. (2008). Solar super-granulation revealed by granule tracking. *A&A* 479, L17–L20. doi:10.1051/0004-6361:20079077

Rieutord, M., Roudier, T., Rincon, F., Malherbe, J. M., Meunier, N., Berger, T., et al. (2010). On the power spectrum of solar surface flows. *A&A* 512, A4. doi:10.1051/0004-6361/200913303

Rosner, R., and Vaiana, G. S. (1978). Cosmic flare transients: Constraints upon models for energy storage and release derived from the event frequency distribution. *ApJ* 222, 1104. doi:10.1086/156227

Rutten, R. J. (2020). *SoHO campfires in SDO images*. arXiv:2009.00376v1, astro-ph.SR.

Scargle, J. D. (2020). Studies in astronomical time-series analysis. VII. An enquiry concerning nonlinearity, the rms-mean flux relation, and lognormal flux distributions. *ApJ* 895, 90. doi:10.3847/1538-4357/ab8d38

Seiden, P. E., and Wentzel, D. G. (1996). Solar active regions as a percolation phenomenon II. *ApJ* 460, 522. doi:10.1086/176989

Singh, B., Sharma, K., and Srivastava, A. K. (2019). On modelling the kinematics and evolutionary properties of pressure pulse-driven impulsive solar jets. *Ann. Geophys.* 37, 891–902. doi:10.5194/angeo-37-891-2019

Sterling, A. C. (1998). Alfvénic resonances on ultraviolet spicules. *ApJ* 508, 916–924. doi:10.1086/306433

Sterling, A. C., and Hollweg, J. V. (1988). The rebound shock model for solar spicules: Dynamics at long times. *ApJ* 327, 950. doi:10.1086/166252

Uritsky, V. M., and Davila, J. M. (2012). Multiscale dynamics of solar magnetic structures. *ApJ* 748, 60. doi:10.1088/0004-637x/748/1/60

Uritsky, V. M., Davila, J. M., Ofman, L., and Coyner, A. J. (2013). Stochastic coupling of solar photosphere and corona. *ApJ* 769, 62. doi:10.1088/0004-637x/769/1/62

Uritsky, V. M., Paczuski, M., Davila, J. M., and Jones, S. I. (2007). Coexistence of self-organized criticality and intermittent turbulence in the solar corona. *Phys. Rev. Lett.* 99 (2), 025001. doi:10.1103/physrevlett.99.025001

Verbeeck, C., Kraaikamp, E., Ryan, D. F., and Podladchikova, O. (2019). Solar flare distributions: Lognormal instead of power law? *ApJ* 884, 50. doi:10.3847/1538-4357/ab3425

Vilangot Nhalil, N. V., Nelson, C. J., Mathioudakis, M., Doyle, G. J., and Ramsay, G. (2020). Power-law energy distributions of small-scale impulsive events on the active Sun: Results from IRIS. *MNRAS* 499, 1385–1394. doi:10.1093/mnras/staa2897

Warren, H. P., Reep, J. W., Crump, N. A., and Simoes, P. J. A. (2016). Transition region and chromospheric signatures of impulsive heating events. *I. Obs. ApJ* 829, 35. doi:10.3847/0004-637x/829/1/35

Weibull, W. (1951). A statistical distribution function of wide applicability. *J. Appl. Mech.* 18 (3), 293–297. doi:10.1115/1.4010337

Zaqarashvili, T. V., and Erdelyi, R. (2009). Oscillations and waves in solar spicules. *SSRv* 149, 355–388. doi:10.1007/s11214-009-9549-y

frontiers | Frontiers in Astronomy and Space Sciences

TYPE Original Research
PUBLISHED 20 June 2023
DOI 10.3389/fspas.2023.1133429

OPEN ACCESS

EDITED BY
Adam Kowalski,
University of Colorado Boulder, United States

REVIEWED BY
Jorrit Leenaarts,
Stockholm University, Sweden
Petr Heinzel,
Academy of Sciences of the Czech Republic (ASCR), Czechia

*CORRESPONDENCE
Alberto Sainz Dalda,
sainzdalda@baeri.org

RECEIVED 28 December 2022
ACCEPTED 16 May 2023
PUBLISHED 20 June 2023

CITATION
Sainz Dalda A and De Pontieu B (2023), Chromospheric thermodynamic conditions from inversions of complex Mg II h & k profiles observed in flares. *Front. Astron. Space Sci.* 10:1133429. doi: 10.3389/fspas.2023.1133429

Chromospheric thermodynamic conditions from inversions of complex Mg II h & k profiles observed in flares

Alberto Sainz Dalda[1,2]* and Bart De Pontieu[2,3,4]

[1]Bay Area Environmental Research Institute, NASA Research Park, Moffett Field, CA, United States, [2]Lockheed Martin Solar and Astrophysics Laboratory, Palo Alto, CA, United States, [3]Rosseland Center for Solar Physics, University of Oslo, Oslo, Norway, [4]Institute of Theoretical Astrophysics, University of Oslo, Oslo, Norway

The flare activity of the Sun has been studied for decades, using both space- and ground-based telescopes. The former have mainly focused on the corona, while the latter have mostly been used to investigate the conditions in the chromosphere and photosphere. The Interface Region Imaging Spectrograph (IRIS) instrument has served as a gateway between these two cases, given its capability to observe quasi-simultaneously the corona, the transition region, and the chromosphere using different spectral lines in the near- and far-ultraviolet ranges. IRIS thus provides unique diagnostics to investigate the thermodynamics of flares in the solar atmosphere. In particular, the Mg II h&k and the Mg II UV triplet lines provide key information about the thermodynamics of low to upper chromosphere, while the C II 1334 & 1335 Å lines cover the upper-chromosphere and low transition region. The Mg II h&k and the Mg II UV triplet lines show a peculiar, pointy shape before and during the flare activity. The physical interpretation, i.e., the physical conditions in the chromosphere, that can explain these profiles has remained elusive. In this paper, we show the results of a non-LTE inversion of such peculiar profiles. To better constrain the atmospheric conditions, the Mg II h&k and the Mg II UV triplet lines are simultaneously inverted with the C II 1334 & 1335 Å lines. This combined inversion leads to more accurate derived thermodynamic parameters, especially the temperature and the turbulent motions (micro-turbulence velocity). We use an iterative process that looks for the best fit between the observed profile and a synthetic profile obtained by considering non-local thermodynamic equilibrium and partial frequency redistribution of the radiation due to scattered photons. This method is computationally rather expensive (≈6 CPU-hour/profile). Therefore, we use the k-means clustering technique to identify representative profiles and associated representative model atmospheres. By inverting the representative profiles with the most advanced inversion code (STiC), in addition to recover the main physical parameters, we are able to conclude that these unique, pointy profiles are associated with a large gradient in the line-of-sight velocity along the optical depth in the high chromosphere.

KEYWORDS

Sun, chromosphere, flares, thermodynamics, inversion

1 Introduction

A flare is the release of magnetic energy as a consequence of reconnection in magnetically stressed coronal loops. The magnetic energy stored in these loops comes from the low solar atmosphere. Once it is released, it is transferred to both the outer and the lower solar atmosphere in a variety of energy forms: radiation, thermal energy, kinetic energy associated to non-thermal phenomena (accelerated particles and turbulence), magnetic energy (large-scale Alfvén waves), and others. The most evident observational counterpart of this sudden release of energy is an enhancement in the specific intensity in almost any spectral range. This description, although simplistic, allow us to picture the basic flare phenomena. Many complex physical processes however occur and need to be properly studied for a full understanding of this type of solar event. This complexity is also reflected in the observational data we have of flares.

In the last few decades, with the advance of instrumentation, especially instrumentation onboard space-based observatories, we have largely improved our access to a steady flow of high-quality flare data. In this paper, we focus our attention on the interpretation of the thermodynamics conditions during the maximum of the X1.0-class flare of SOL2014-03-29T17:48 (see **Figure 1**). To this aim, we have inverted the Mg II h&k and C II 1334 & 1335 Å lines observed by the Interface Region Imaging Spectrograph (IRIS, De Pontieu et al., 2014).

The resonance Mg II h&k profiles have been used in the past for the study of the chromosphere (Lemaire and Skumanich, 1973; Kohl and Parkinson, 1976; Kneer et al., 1981; Lites and Skumanich, 1982), including the study of flares (Lemaire et al., 1984). The theoretical modeling and interpretation of these lines have been an active topic for decades (e.g., Feldman and Doschek, 1977; Lites and Skumanich, 1982; Lemaire and Gouttebroze, 1983; Uitenbroek, 1997). More recently, thanks to the advance in the computational resources and triggered by the huge amount of data provided by IRIS, these lines have been investigated using more realistic assumptions when solving the radiative transfer equation (RTE) (e.g., Leenaarts et al., 2013a; Leenaarts et al., 2013b; Pereira et al., 2013; Pereira et al., 2015; Sukhorukov and Leenaarts, 2017), including treatment of polarized radiation (del Pino Alemán et al., 2016; Manso Sainz et al., 2019). Kerr et al. (2019a) and Kerr et al. (2019b) have investigated the effect of the physics included in the radiation transport to forward-model these Mg II h&k lines from radiative hydrodynamic flare simulations. These authors conclude that to properly reproduce these lines we need to consider: i) partial frequency redistribution of the scattered photons (PRD), ii) only hydrogen and Mg II need to be included in non-local thermodynamic equilibrium (non-LTE), iii) nonequilibrium hydrogen populations, with nonthermal collisional rates, iv) an atom model with more levels than the ones involving the resonance Mg II h&k lines, and v) the irradiation from hot, dense flaring transition region, which can affect the formation of Mg II. Kerr et al. (2019b) also suggest to consider the nonequilibrium (NEQ) ionization when the atomic level populations are calculated, instead of the statistical equilibrium (SE), for most of the stages of the flare. However, these authors also acknowledge the computational cost of considering this approach, and for most of the duration of the flare, especially the stronger ones, the SE approach is valid. Nevertheless, a careful treatment of the hydrogen lines and the electron densities, prior the calculation of the Mg II h&k lines, is also important for the proper synthesis of these lines, as (Liu et al., 2015) have demonstrated.

The formation and behavior of the C II 1334 & 1335 Å have been investigated by Rathore and Carlsson (2015) and Rathore et al. (2015). Using state-of-the-art numerical models and the most advanced radiative transfer methods, these authors found that these lines can behave as optically thick or as optically thin, and the range of the temperature and height where they are formed can vary significantly, from 6 to 40kK, i.e., from the chromosphere to the transition region.

In this work, we have analyzed the profiles of these lines corresponding to the flare ribbons during the maximum of the flare. In this location, at that time, the Mg II h&k profiles are characterized by a pointy, broad-on-the-base shape[1]. **Figure 2** shows a typical Mg II h&k profile in the quiet Sun. The main features of the lines and their rest wavelength positions are indicated by labels and vertical lines respectively. In each of these lines, we can distinguish two peaks (the $k_{2v,r}$ and $h_{2v,r}$ features) and a central depression or self-reversal in the core of the lines (the k_3 and h_3 features). However, in the profiles studied in this investigation the central depression has disappeared and the top of the profiles is defined by an inverted-V shape in just a few spectral samples. Note that some authors refer to *single-peaked* Mg II h&k profiles as those profiles that show k_3 and h_3 in emission, but at the same intensity or slightly higher or lower than the k_2 and h_2 spectral features. Such profiles, while being single-peaked, are mostly characterized by being *flat-topped*, as they were described by Carlsson et al. (2015). The central depression is also reduced when high coronal pressures (10–100 dyn cm^{-2}), associated to chromespheric evaporation, are considered (Liu et al., 2015). In contrast, the Mg II h&k profiles discussed in this paper are *single-peaked* as well, but their main characteristics are: i) their very pointy top, as a consequence of the lack of k_3 and h_3 features and of having the violet and red components of the k_2 and h_2 almost totally blended in one pointy feature, ii) extended broad wings, which renders indistinguishable the k_1 and/or h_1 spectral features; and iii) the subordinated Mg II UV triplet lines are in emission, often also showing a pointy, broad shape, albeit not as extremely pointy, since the top of these lines shows an inverted-U shape.

The C II 1334 & 1335 Å lines also show a pointy shape, and in many cases, it is red-shifted or showing a strong red-shifted component. These extreme profiles are difficult to invert, and, therefore, the interpretation of the results at values with optical depth $\log(\tau) < -6.5$ presented in this investigation has to be carefully considered.

Because of this pointy aspect, we refer to these profiles as *extreme* and *very pointy* profiles (see **Figures 3**, **4**), and to an intermediate case as *combined pointy* profile (see **Figure 5**). A more detailed explanation of this classification is given in **Section 2.2**.

These kinds of pointy spectral line profiles, especially the Mg II h&k, were identified in IRIS data as soon as the instrument started

1 By shape of a profile or a line, we mean the spectral distribution of the intensity (specifically, the spectral radiance) with respect to the wavelength in a given spectral range.

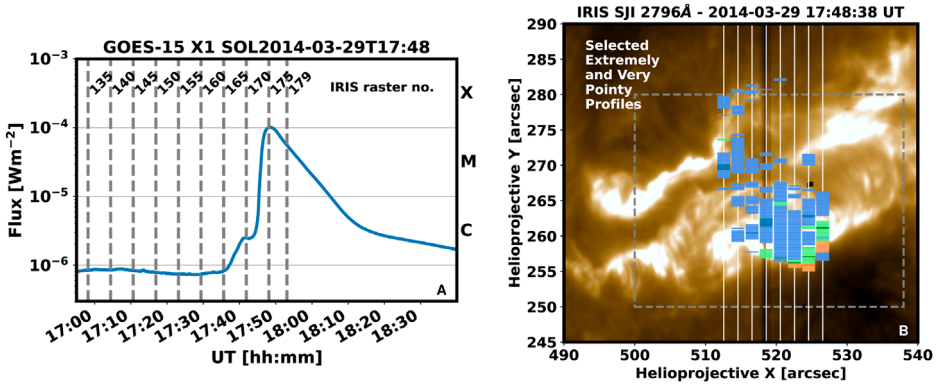

FIGURE 1
Panel **(A)** Temporal evolution of the X-ray flux during the X1-class flare at SOL2014-04-29T17:48. The vertical lines indicate the number of some IRIS rasters that recorded this flare. Panel **(B)** The image taken by the SJI instrument at IRIS during the maximum of the X1-class flare SOL2014-03-20T17:48 at 2796 Å, that corresponds to the chromosphere. The time indicated at the top of the panel corresponds to the step number 4 of the raster. The location of the slits of all the steps of this raster (no. 175) are indicated with vertical lines. The colored squares mark the location of the extremely pointy profiles of the type A (blue) and the type B (orange), and of the very pointy or combined profiles (green). The locations in dark colors correspond to the profiles shown in **Figures 3**–**5** respectively. The grey rectangle delimits the area shown in **Figure 14**.

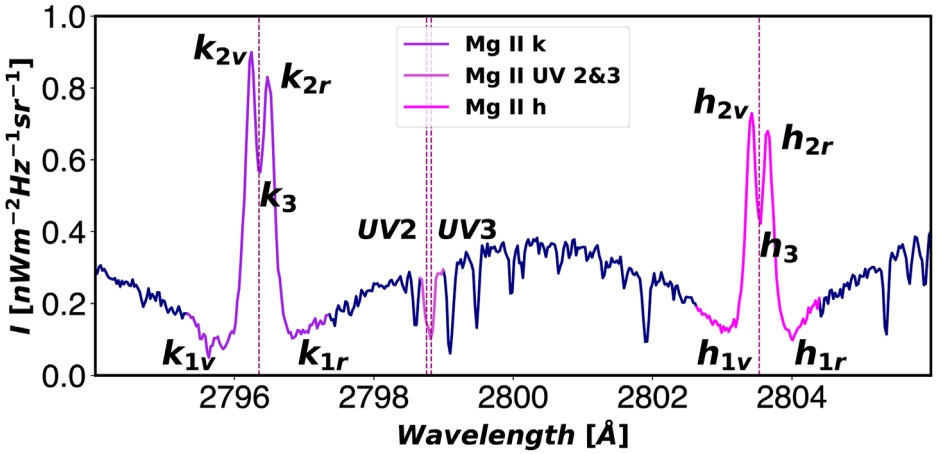

FIGURE 2
Mg II h&k and Mg II UV2&3 lines - the latter belonging to the Mg II UV triplet - as observed by IRIS in the quiet-sun. Spectral sampling is 0.025 Å. The rest position for the core of the lines is indicated by the vertical dashed lines. The main features of the *h* and *k* lines are indicated with labels. The wavelength values are given in vacuum wavelength.

to observe flares. Kerr et al. (2015) reported strong emission in the Mg II h&k and the Mg II UV2&3 lines in the ribbons of the M class flare SOL2014-02-13T01:40 observed by IRIS. The authors noted the absence of the depression in the core of the Mg II h&k lines, i.e., the lack of the k_3 and h_3 features. They also concluded, based on the ratio of the intensity between the *k* and the *h* lines, that these lines are optically thick during the flare. As we just mentioned above, this may not be the case for the C II 1334 & 1335 Å lines. The profiles shown by Kerr et al. (2015) are inverted-U pointy profiles. **Figure 6** in Liu et al. (2015) shows a selection of Mg II h&k profiles belonging to the flare studied in the current paper. As we will discuss later, some of the profiles shown in that figure are pointy profiles. Xu et al. (2016) identified extremely pointy Mg II h&k and C II 1334 & 1335 Å profiles in the positive polarity part of the ribbon of the M1.4-class SOL2013-08-17T18:43 flare, but not in the negative polarity part (decrease in the contrast of the intensity).

Several models have been proposed to explain the pointy profiles, particularly the ones observed by IRIS on SOL2014-03-29T17:48. Rubio da Costa et al. (2016) and Rubio da Costa and Kleint (2017) studied the parameters needed to model the Mg II h&k profiles observed during the maximum of this flare. The authors modified the thermodynamics parameters in hydrodynamic simulations (RADYN, Carlsson and Stein, 1995; Carlsson and Stein, 1997; Allred et al., 2015), and then they obtained the synthetic profiles of these lines using the RH code (Uitenbroek, 2001) considering non-LTE and PRD. The authors obtained inverted-U, single Mg II h&k profiles by increasing the temperature and density

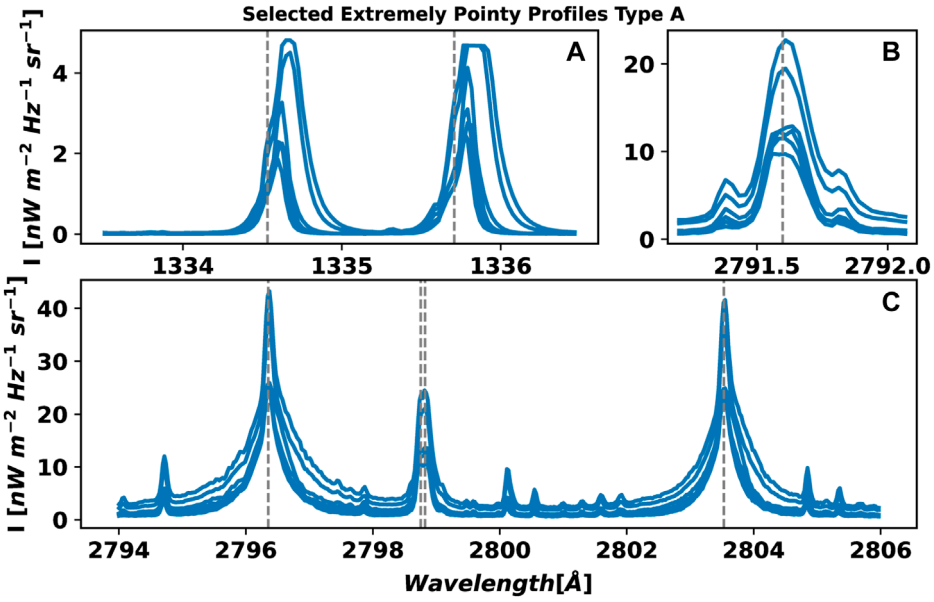

FIGURE 3
Examples of the type A extremely pointy profiles. Panel **(A)** shows the C II 1,334 & 1,335 Å lines, panel **(B)** the Mg II UV1 line, and panel **(C)** the Mg II UV triplet lines, including the Mg II UV2&3 between them. The dashed vertical lines indicate the rest wavelength of these lines.

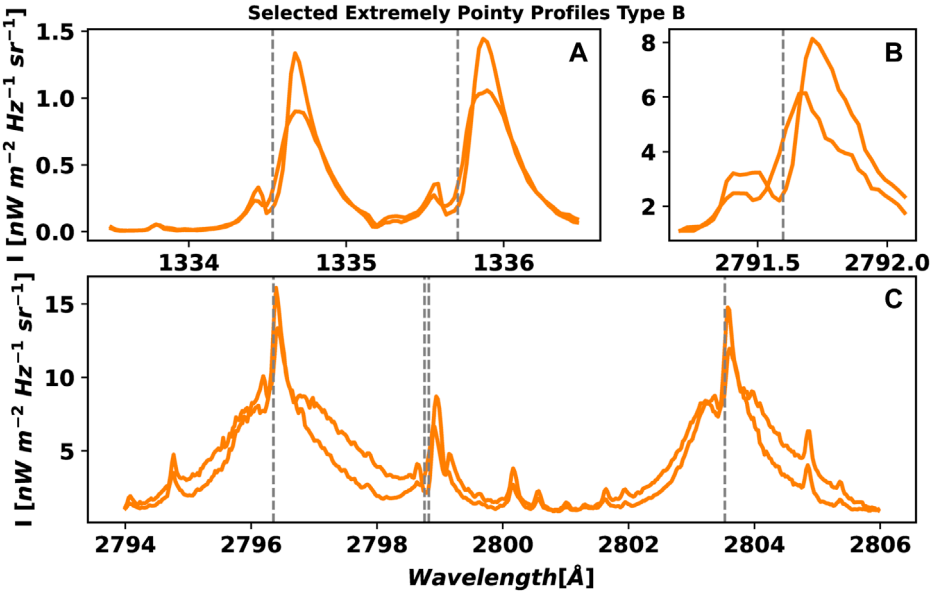

FIGURE 4
Examples of the type B extremely pointy profiles. See caption of **Figure 3** for details.

in the formation region of these lines. However, the intensity of these profiles is larger than the intensity in the observed profiles. They were only able to match intensity profiles with inverted-U, single-peak profiles when they considered a strong gradient in the line-of-sight velocity (v_{los}). These calculated profiles show however a significant asymmetry. In addition, their calculated profiles were not able to properly reproduce the large broad wings observed in the IRIS observations, except when they introduced micro-turbulent velocities (v_{mic}) values as large as 40 km s^{-1}, which they considered to be an unrealistic value. Zhu et al. (2019) followed a similar approach to that of Rubio da Costa et al. (2016), i.e., forward modeling using RADYN and RH, to interpret the Mg

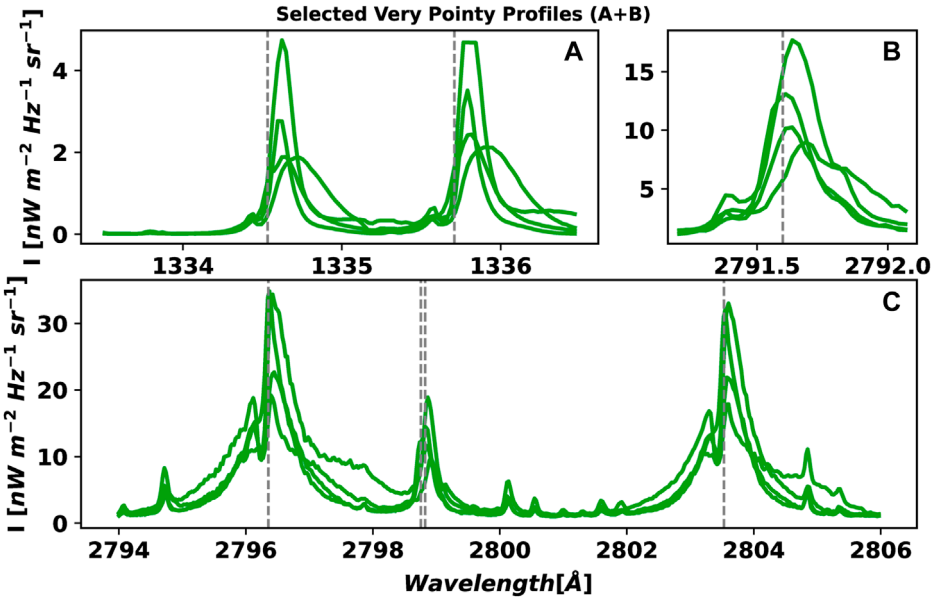

FIGURE 5
Examples of the combined type of pointy profile. See caption of Figure 3 for details.

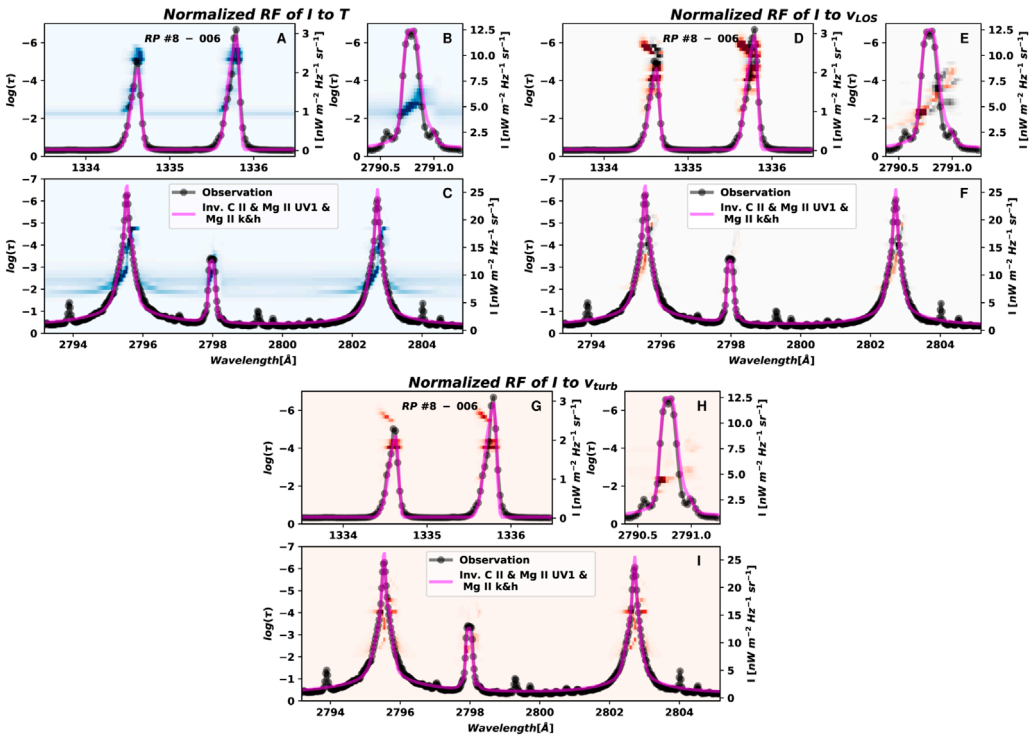

FIGURE 6
Response functions of the intensity (I) to the temperature [panels **(A–C)**], the v_{los} **(D–F)**, and the v_{turb} **(G–I)** for the atmosphere model corresponding to the extremely pointy profile type A shown in Figure 7 are shown in the background of the panels. The pointy profile and the fit are over-plotted as a reference.

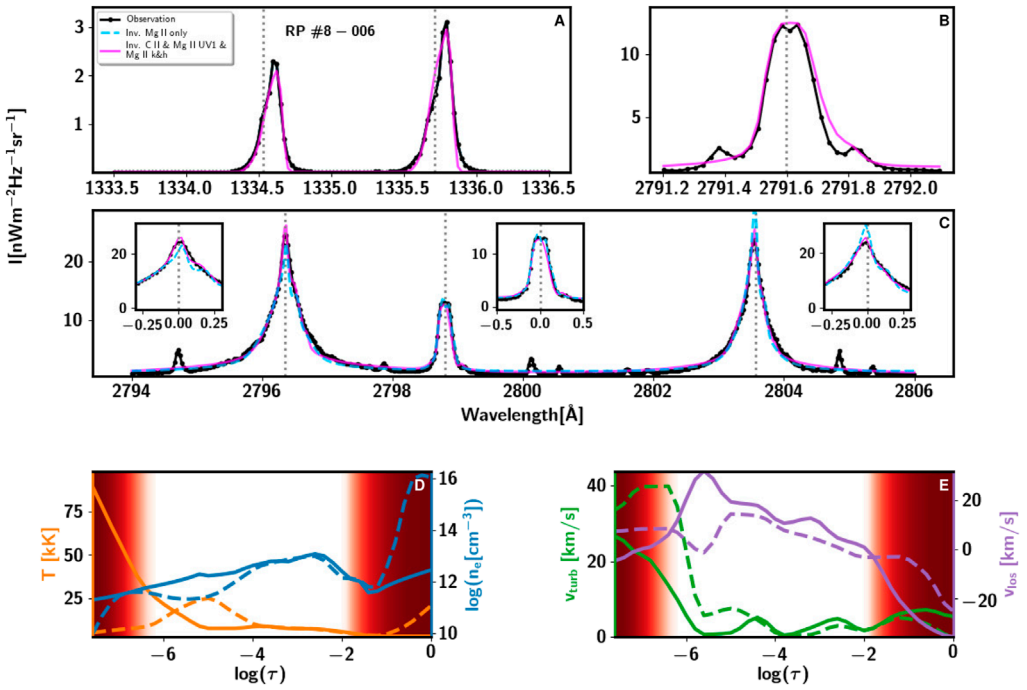

FIGURE 7
Inversion (fit) of the C II 1334 & 1335 Å panel **(A)**, Mg II UV1 **(B)**, Mg II h&k [**(C)** and left and right sub-panels in panel **(C)**], and Mg II UV2&3 [**(C)** and center sub-panel in panel **(C)**] lines of an extremely pointy profile type A, and the model recovered from the inversion. The three first panels show the inversion of an extremely pointy profile type A (in dotted, black line). The dashed, blue line corresponds to the inversion only taking into account the Mg II h&k lines. The fuchsia line corresponds to the inversion considering simultaneously the C II 1,334 & 1,335 Å lines, the Mg II UV1 line, and the Mg II h&k lines - including the Mg II UV2&3 lines. The last two panels show the thermodynamic variables obtained from the inversions: temperature (T, in orange), logarithm of the electron density (n_e, in blue), velocity of turbulent motions or micro-turbulence (v_{turb}, in green), and line-of-sight velocity (v_{los}, in violet). The dashed lines correspond to model recovered from the inversion considering only the Mg II h&k lines, while the solid lines correspond to the inversion considering all the spectral lines mentioned above. The red shade areas in the model atmosphere panels **(D,E)** indicates the optical depth range that we should not consider as reliable.

II h&k lines of the same flare studied by Rubio da Costa et al. (2016) and Rubio da Costa and Kleint (2017), and by us in the current paper. In this case, the authors considered the impact of the Stark effect on line broadening. They used the STARK-B database - in which line broadening is calculated based on a semi-classical impact-perturbation theory Dimitrijević and Sahal-Bréchot (1995; 1998)–for the treatment of the quadratic Stark effect by RH. This is because the Stark effect was previously implemented in RH considers the adiabatic approximation to calculate the quadratic Stark effect, and this approximation may underestimate the broadening for the Mg II h&k lines during flares (Rubio da Costa and Kleint, 2017). In summary, Zhu et al. (2019) were able to fit the extremely pointy Mg II h&k profiles observed by IRIS in the flare but only by considering an *ad hoc* contribution of 30 times of the quadratic Stark effect obtained by using STARK-B in RH. This *ad hoc* assumption allowed them to properly fit the very broad wings of these profiles. However, the authors were unable to provide a physical justification for the large *ad hoc* enhancement of the Stark effect. They also tried to fit the broad wings by considering the STARK-B database value and various values of $v_{\rm turb}$. They found an unrealistic value of $v_{\rm turb}$≈30 km s^{-1} below the formation region of the line core of the Mg II h&k lines, and even in this case, the fit in the part of the wings furthest from line core is not good both for Mg II h&k and the Mg II UV triplet. In this paper, we focus our attention on the study of both the extremely pointy and the very pointy profiles observed by IRIS during the maximum of the flare. This kind of profile is mostly present during the maximum of the flare. We note that while single-peaked profiles can also be seen in the pre-flare stage and they may help us to predict the flare onset with about 30–50 min advance notice (Panos et al., 2018; Woods et al., 2021), these are quite different: the peak of the latter Mg II h&k profiles shows an inverted-U shape, the Mg II UV triplet is barely in emission, and the C II 1334 & 1335 Å lines show a wide inverted-U shape. The thermodynamics along the optical depth of pre-flare profiles was for the first time described by Woods et al. (2021). In contrast, in the current investigation, we will reveal the thermodynamics of the most intriguing and peculiar profiles emitted at the maximum of the flare.

The interpretation of these extremely pointy profiles during the maximum of flares has presented a challenge for modelers and observers. In this paper, we present a solution - in good agreement with several possibilities speculated in previous work—that is able to reproduce these complex profiles. This solution provides reasonable values of the thermodynamics parameters involved in the problem, i.e., gives a realistic view of the conditions in the chromosphere of flare during its maximum.

2 Materials and methods

The data analyzed in this paper correspond to the maximum of the X1-class flare at SOL2014-03-29T17:48. This data are part of the multi-instrument observations that we led from the Dunn Solar Telescope at Sacramento Peak Observatory in coordination with IRIS and Hinode (Kosugi et al., 2007). Moreover, this flare was simultaneously observed by other observatories such as the *Reuven Ramaty High-Energy Solar Spectroscopic Imager* (RHESSI, Lin et al., 2002), the *Solar Dynamics Observatory* (SDO, Pesnell et al., 2012), and the *Solar Terrestrial Relations Observatory* (STEREO, Kaiser et al., 2008). A description of this unique observation and the evolution of the flare is provided by Kleint et al. (2015), and of the observed Mg II h&k lines by Liu et al. (2015) and Rubio da Costa et al. (2016).

The rasters obtained by IRIS of the region where this flare occurred - NOAA AR 12017—span from 2014-03-29T14:09:39 UT to 2014-03-29T17:54:16 UT. This active region was located at $\mu = 0.78$, with $\mu = \cos\theta$, and θ the heliocentric viewing angle. The maximum X-ray flux measured by GOES-15 during the flare took place at 2014-03-29T17:48, which corresponds to raster no. 175 of the series of rasters taken by IRIS (see **Figure 1**). Each raster consisted of an 8-step scan with the slit crossing the two ribbons of the flare. Each step of the raster is $2''$ in the direction perpendicular to the slit, covering a field-of-view (FoV) of $14'' \times 174''$, with $174''$ the length of the slit. The exposure time was nominally 8*s* (but was reduced during the flare in response to the onboard automatic exposure control algorithm), the spectral sampling was 0.025 Å (in the NUV passband), and the spatial sampling along the slit was $0''.16$. At each step of the raster the IRIS Slit-jaw Imager (SJI) took an image. In this observation, during the acquisition at steps number 1, 5, and 7 the SJI took an image at 1400 Å, at step number 3 an image at 2832 Å, and steps number 2, 4, 6 and 8 images at 2796 Å. The FoV covered by the SJI was $167'' \times 174''$. The right panel in **Figure 1** shows the SJI image taken by IRIS during the maximum of the flare at 2796 Å.

Since we are mostly interested in understanding, as accurately as possible, the thermodynamics in the chromosphere, we decided to investigate simultaneously the C II 1334 & 1335 Å and the Mg II h&k lines. It has been shown that these lines are sensitive to thermodynamics in roughly the same region of the chromosphere, both by solving the radiative transfer equation in 3D magnetohydrodynamics models (Rathore and Carlsson, 2015), and by looking into the *mutual information* shared by these lines (Panos et al., 2021). Having this simultaneous information is a great advantage to decouple the T and $v_{\rm turb}$ encoded in the width of the spectral lines (see Section 4.6 in Jefferies, 1968).

In this paper we proceed in a similar fashion as Woods et al. (2021) and invert simultaneously the C II 1,334 & 1,335 Å lines, the Mg II h&k lines, and the blended Mg II UV2&3 line. In addition, in this paper, we invert the other line of the triplet, Mg II UV1. Thus, following the analysis made by Pereira and Uitenbroek (2015) and Pereira et al. (2015) on the formation region of the Mg II h&k and the Mg II UV triplet respectively, and by Rathore and Carlsson (2015) on the C II 1334 & 1335 Å lines, we are in principle sampling the solar atmosphere from the low chromosphere to the top of the chromosphere. The caveat here is that some of the previous work focused on quiet Sun, and it is known that during flares the formation height of the line can sometimes be significantly different. This is mostly due to the change of the electron density and temperature along the optical depth during a flare, as several semi-empirical models indicate (e.g., Lites and Cook, 1979; Machado et al., 1980; Avrett et al., 1986; Hawley and Fisher, 1994; Allred et al., 2015).

2.1 Data treatment: clustering and inversions

To simultaneously invert these lines we have taken advantage of the capabilities of the *STockholm inversion Code* (STiC, de la Cruz Rodríguez et al., 2016; 2019) to solve the radiative transfer equation for multiple lines and multiple atoms, considering non-local thermodynamic equilibrium and partial frequency redistribution of the radiation of the scattered photons. STiC uses the RH code Uitenbroek (2001) at the backend to self-consistently solve the RTE and the statistical equilibrium equations (SEE) for the atomic level populations. STiC is the only code with the ability to properly treat the Mg II h&k, Mg II UV triplet, and C II 1334 & 1335 Å lines to recover the thermodynamics encoded in these lines. However, to invert a single *concatenated profile* of these lines takes between 6 and 8 CPU-hour - depending of the complexity of the profiles. Because of this computational burden, we have followed the strategy introduced by Sainz Dalda et al. (2019), i.e., to invert the *Representative Profile* (RP) and recover its corresponding *Representative Model Atmosphere* (RMA) by the inversion of the former. The RP is the averaged profile of a cluster of profiles that share the same shape, i.e., the same atmospheric conditions, since the shape of a profile is an encoded representation of the conditions of the matter and the radiation in the region where the lines are formed. To cluster the profiles we use the $k-means$ technique (Steinhaus, 1957; MacQueen, 1967). This technique, due to its simplicity and robustness, has become very popular in Machine Learning, and more recently in solar physics. However, clustering in solar data (Stokes V profiles) was already used in 2000 by Sánchez Almeida and Lites (2000). The core of the code is to find the centroids of clusters of elements so that the elements within a cluster are closer to its centroid than to any other centroid. For that, the code calculates the Euclidean distance between an initial number of elements randomly selected (in the original $k-means$ version) and all the elements in the data set. Then, all the closest elements to a centroid form a cluster. A new centroid is calculated as the average of all the elements of that cluster. And again, the distance between all the elements in the data set and the centroids are calculated, then, new centroids are calculated as the average of the new cluster. This process is repeated until the total sum of the squared distance between the within-cluster samples and their corresponding centroid is minimized, that is:

$$\underset{\{C_i\}_1^K}{arg\ min} \sum_{i=1}^{K} \sum_{x_j \in C_i} \|x_j - \mu_i\|_2^2 \tag{1}$$

with $\|\cdot\|_2$ the ℓ_2 norm, $\{C_i\}_1^K$ is a set of K clusters C, x_j the $j^{\rm th}$ sample belonging to the $i^{\rm th}$ cluster C_i, and μ_i the average of the samples x belonging to the cluster C_i, i.e., the *centroid*. One of the challenges of this method is how to determine the number of clusters K that

are needed to properly cluster the data set. Several methods have been proposed to minimize the impact of this choice on the resulting clustering. We have selected the *elbow method* (Thorndike, 1953) to determine this number. It has been shown that a number of clusters larger than 100 is typically enough to cluster properly, in general, for IRIS Mg II h&k data sets (see Section 1.2 of *IRIS*[2] tutorial web page[2]). Based on the results of the elbow plot[3], we have decided to cluster our data set in 320 RPs. Thus, we optimize the representation of the data by taking into account our computational resources (320 CPU cores). For the case studied here, the number of profiles is ≈ 8,000 px per raster. Hence, to invert that number of profiles with STiC would take at least ≈ 48, 000 CPU-hour. Nowadays, this number is not too large in terms of computation time. It would however turn computationally expensive if we wanted to invert the 175 available rasters of this flare (≈8.4 MCPU-hour). Fortunately, we can reduce these numbers very significantly through the use of representative profiles. As mentioned, a number of 320 RPs per raster is enough to cluster this kind of data, and they can be inverted with a mid-size server (≈1050 CPU-hour for the 175 rasters).

An important issue of working with Euclidean distance is the scale of the features. If some features have very large values with respect to others, the smaller values will have a small impact on or significance in the distance. One way to solve this situation is to normalize each feature, for instance between 0 and 1. This is what we did for the cropped, joint profiles. These are the profiles that we have clustered. In this way, we give equal weight to all the involved spectral lines. After the $k-means$ is run over this new data set of concatenated profiles, the elements of a cluster are identified, that is, they are labeled with the number corresponding to that cluster. Finally, the RP of that cluster is calculated as the average of the original, joint profiles within the cluster.

This would be the standard way to proceed. But it is not the procedure we followed. During the maximum of the flare, the ratio between the maximum intensity in the Mg II h&k lines and the C II 1,334 & 1,335 Å lines varies from ~100 in the pseudo-quiet-sun (the closest area to the quiet in the FoV of our data) to just ~10 in the ribbons. A significant variation also exists between the ratio of the integrated intensity of the Mg II UV triplet lines and the Mg II h&k although not as large. This is not important for clustering the data, since, as we mentioned above, we scale all the features between 0 and 1, but it represents a problem for the inversion. STiC tries iteratively to minimize the Euclidean distance between a synthetic profile - resulting from the synthesis of a model atmosphere- and the observed profile, slightly modifying the model atmosphere at each iteration. Again, since we are using the Euclidean distance as a metric, we will have a problem if the scales of the features are very different. But now, due to coding practicality, we cannot scale the profiles individually. In this case, we use a set of weights at the sample wavelengths to scale all the profiles. These weighted profiles are then inverted. In our case, we weigh the C II 1,334 & 1,335 Å lines, Mg II UV triplet lines with respect to Mg II h&k lines. However, given the large variation in the ratio of the integrated intensity of C II 1,334 & 1,335 Å lines with respect to the Mg II h&k lines, we decided to stratify the data in 8 percentiles, with the 8 parts dividing the number density distribution. The 3 or 4 first portions have many original profiles, representing the pseudo-quiet-sun (the closest region to the quiet-sun in the field of view). Then, the rest of the portions are associated with the flare ribbons. Each of these portions has its own weight ratio $w_{\mathrm{MgIIh\&k}}$: w_{CII}: $w_{\mathrm{MgIIUVtriplet}}$. Once the portions are defined, 40 RPs are calculated following the procedure explained above: the creation of joint, concatenated profile, scaling between 0 and 1, k-means calculation, rebuild the k-means with the original data. Then, the 40 RPs of each portion are inverted considering their chosen weights. Note that in the first portions, since they are the most populated ones, the RPs are clustering a large number of profiles, while the rest of the portions are clustering a significantly smaller number of profiles. This is beneficial to our investigation, since we will have a better representation by the RPs of the original profiles in the flaring areas.

TABLE 1 Number of nodes at each cycle for the thermodynamics variables considered during the inversions.

No. Cycle	1	2	3	4
T	4	7	9	13
v_{turb}	2	4	8	13
v_{los}	2	4	8	13

Table 1 shows the number of nodes for each cycle considered during the inversions. These numbers are obtained after a careful inspection of selected inversions. It is important to find a good balance between the number of nodes and cycles used and the computational time required to invert the RPs, in addition to obtaining a model physically meaningful, and at the same time avoid overfitting. The inversion uses the model for the C atom described in Rathore and Carlsson (2015). This model includes 8 energy levels plus the continuum, and it was created by Mats Carlsson. The model for Mg II includes 10 energy levels plus the continuum, and it is described in Leenaarts et al. (2013a). At each cycle, the inversion is initialized 3 times, at each initialization, if the selected χ^2 threshold is not reached, a maximum of 5 inversions are allowed. The values of these inversion setup parameters are usually larger when the inversion considers simpler assumptions (e.g., LTE and CRD), that means, when the convergence is quickly reached. In our case, these values are low due to the long time needed to self-consistently solve the RTE and the SE considering PRD.

2.2 Selected pointy profiles

The selection of the extremely pointy profiles and the very pointy profiles was made through visual inspection. Thanks to the clustering of the data, this task is easily doable: we look for these peculiar profiles in a set of 320 RPs instead of ≈ 8,000 profiles. We have selected the most clear cases of these profiles to show their main characteristics. We can distinguish two main groups among the extremely pointy profiles that we have classified as Type A and Type B (see **Figures 3**, **4**). The core of the Mg II h&k extremely pointy profiles Type A (panel C) resembles the core of a Lorenztian distribution, while the wings look like the wings of a Laplacian distribution. The C II 1,334 & 1,335 Å lines are pointy, red-shifted, and in most cases their shape shows a negative skew (panel A). In

2 https://iris.lmsal.com/iris2/iris2_chapter01.html#limitations-of-iris2-inversions

3 https://www.youtube.com/watch?v=55sT144u5ag

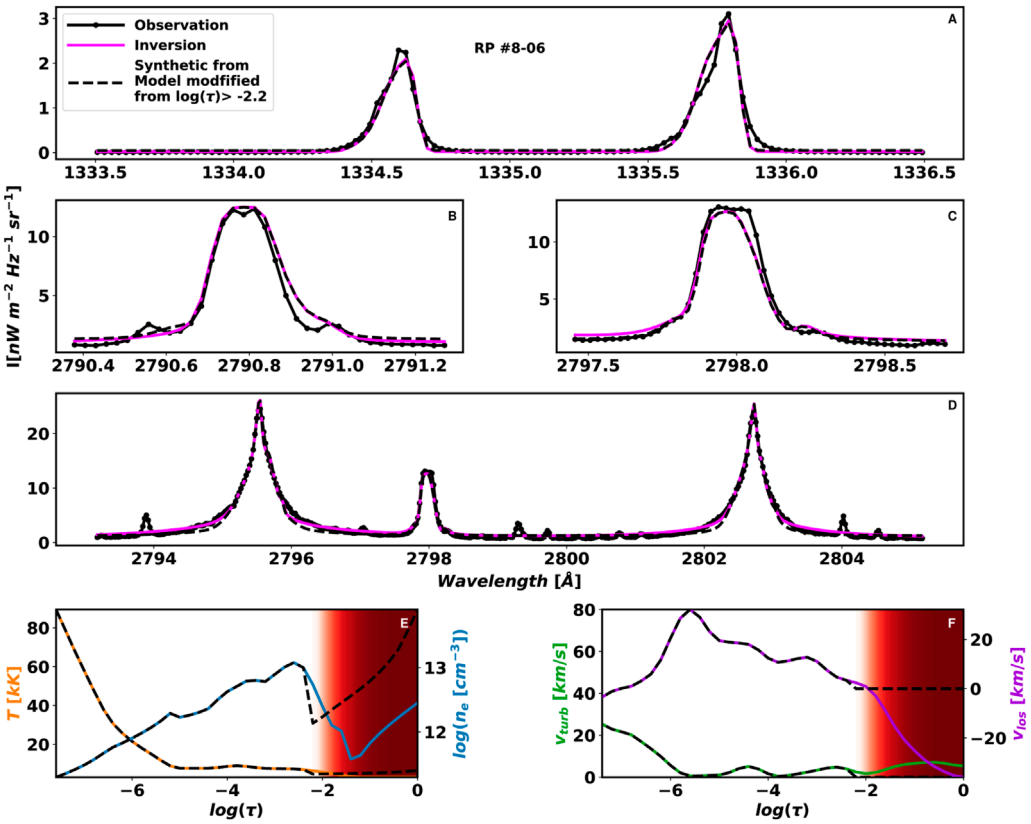

FIGURE 8
Deviation from the inverted profile corresponding to the extremely pointy type A profile (in fuchsia) shown in the **Figure 7** that shows how sensitive the synthetic profile [dashed black line, panels from **(A–D)**] is along the solar atmosphere the model atmosphere [panels **(E,F)**]. The profile in dashed black line shows the resulting profile by considering a modified version [in dashed black lines, panels **(E,F)**] of the original model [in colors in the lower panels, panels **(E,F)**] from $-2.2 < \log(\tau) < 0$. See details in the main text.

some cases, the C II 1,334 & 1,335 Å lines saturate the response of the detector.

The Mg II h&k extremely pointy profiles type B (see panel C in **Figure 4**), in addition to having the pointy core, show very enhanced wings. Sometimes, the blue wing is slightly more enhanced than the red wing, making the k_3 and the h_3 features identifiable. The Mg II h&k lines are a bit shifted to the red. The Mg II UV triplet lines are clearly shifted to the red, and they have a blue component (panel B). Interestingly, the same happens for the C II 1,334 & 1,335 Å lines (panel A).

The last type of profile seems to be a combination of types A and B (see **Figure 5**). The main difference is the presence of a well-defined, stronger blue component, and the peak of the line is now well-centered. Note that the blue component is well distinguished, and the profile can be clearly described in terms of the $2v, 2r$, and 3 features, that means, in terms of 2 peaks and the central depression. In this case, the $2r$ feature largely dominates over the $2v$ one, and it is located on the rest spectral position of the line. On the other hand, the 3 feature is present, and it is slightly blue-shifted. The wings of these profiles are not as enhanced as those of the extremely pointy profile of type B. As we will see in **Section 4**, the subtle differences between the profiles belonging to the combination type and the ones belonging to the type B are related to the slightly different stages of the flare's evolution.

In all the types, the Mg II UV triplet lines show either a blue or red component, or both (see **Figure 3**). These components appear, in most cases, both in the Mg II UV1 line and the Mg II UV2&3 lines. This behavior indicates that these components are actually belonging to these lines and not to nearby lines in emission.

The spatial distribution of these profiles is shown in the right panel of **Figure 1**. The Type A profiles are mostly located in the ribbon (dark blue ticks), the type B profiles are located in the leading edge (dark orange ticks), and the combination type profiles are mostly located close to (and just trailing) the leading edge (dark green ticks). The locations displayed in light colors show all the profiles of the various types not shown in **Figures 3–5**. The profiles associated with these locations have a range of gradually changing appearances within their corresponding type. For instance, a profile in a light blue location is an extremely pointy type A profile but the wings of the Mg II h&k lines look more Lorentzian than Laplacian, in contrast to the most intense ones shown in **Figure 3**, which have more Laplacian wings.

The pointy profiles almost always occur in the flare ribbons. Pointy profiles have also been observed during the pre-flare phase, as we have already mentioned. However, it is during the maximum of the flare that the extreme and very pointy profiles appear.

2.3 Where in the solar atmosphere we can trust the model atmosphere associated to the pointy profiles

The main characteristic of the profiles studied in this paper is the pointy aspect in the core of the Mg II h&k lines, to some extent in the C II 1,334 & 1,335 Å lines, and a strong emission of the Mg II UV triplet lines. Another important feature of these profiles is the broad width of the lines, especially in their wings. This broadening affects all the lines mentioned above. Because the radiation of the wings comes from deeper in the atmosphere, we have investigated how deep in the model atmosphere the information recovered from the inversion is still reliable.

The traditional method to recover this information is by using the *response function* (RF, Mein, 1971; Landi Degl'Innocenti and Landi Degl'Innocenti, 1977) of the profile to a small variation of a physical parameter in the model atmosphere associated with the synthetic profile. In our case, this synthetic profile is the one that best fits the observation (inverted profile, in fuchsia line in all the figures of this paper). The background image of the panels in **Figure 6** shows the normalized RF of the intensity (I) to changes in the temperature (panels A–C), v_{los} (D–F), and v_{turb} (G–I) for the extremely pointy *inverted* profile type shown in fuchsia in **Figure 7**. The observed and inverted profiles are shown as a reference for a better location in wavelength of the spectral features of the profile. In the RF background image, the stronger the color is the stronger the response of I at that wavelength is to a variation of the physical parameter at that optical depth. Note that the RFs are evaluated for each physical parameter independently.

In this paper, we have considered another approach: to determine at what optical depth the synthetic profile obtained from the modified model associated with the inverted profile deviates from that inverted profile. We have modified the T and the n_e by changing these values with the FALC model values, starting from $\log(\tau) = 0$ to $\log(\tau) = -7$ with steps of $\Delta\tau = 0.2$. Similarly, we have changed the v_{turb} and the v_{los} to 0 km s^{-1} in the same optical range. This method has the advantage that considers simultaneously the 4 physical parameters, while the RFs quantify the impact of the perturbation of only one physical variable in the profile.

In most of the cases analyzed, the inverted profile remains as it is, ignoring the modifications we have made to the atmosphere, up to $\log(\tau) \approx -2.0$, which means: any change in the model atmosphere at $-2 \lesssim \log(\tau)$ has no effect on the shape in the associated synthetic profile. **Figure 8** shows the extremely pointy profile shown in **Figure 7** in the dotted solid black line and the inverted profile in fuchsia in panels A to D, and the model atmosphere in solid colored lines in the last row of the figure in panels E and F. The profile in the dashed black line in panels A to D corresponds to the synthesis of the model shown in the last row in dashed black line as well. This modified model differs from the model atmosphere (in colors) associated to the inverted profile (in fuchsia) between $-2.2 < \log(\tau) < 0$, but it is just after $\log(\tau) \approx -2.0$ when the new synthetic profile (dashed black line) starts to be different with respect to the original inverted profile (in fuchsia). As we can see, the wings of the Mg II h&k lines obtained from the modified model atmosphere start to deviate from the inverted profile. This also happens in the extended wings of the Mg II UV triplet lines. We have to mention that this deviation occurs at $\log(\tau) \approx -1.8$ in other pointy profiles, such is the case for the profile shown in **Figure 11**. Any perturbation in the model at $\log(\tau) < -2.2$ produces a dramatic deviation from the inverted profile. Thus, those profiles showing extended, enhanced broad wings, either in the Mg II h&k lines or the Mg II UV triplet lines, are sensitive to the variations in the high-photosphere. This is also observed in the RFs shown in **Figure 6**, with the significant response at the extended wings of the Mg II h&k at $\log(\tau) < -2.2$ for T, v_{los}, and v_{turb}, while for the Mg II UV1 the response to variation of these parameters is still important at $\log(\tau) < -2.2$, but it is at as low as $\log(\tau) < -1.8$ for the v_{los} and at $\log(\tau) < -2.0$ for the v_{turb}. As a result, we should be cautious with the values of the model atmosphere between $-2.0 < \log(\tau) < -1.8$, and completely discard the values for $-1.8 < \log(\tau) < 0$ shown in the figures of this paper. Because of this, the values in this optical depth range are gradually shaded in red.

To support this statement more strongly, we have verified that the photospheric lines available in the IRIS Mg II h&k spectral range do not show a high Doppler shift. We will use photospheric lines to recover the information from this optical depth range in a following investigation.

As it has been already mentioned, the values at $\log(\tau) < -6.5$ should be taken with caution. This is because the current inversion scheme is not able to capture changes in the thermodynamics - if any - in that optical depth range, i.e., well inside the transition region, from the C II 1,334 & 1,335 Å lines. None of the lines in this study are sensitive to changes in the thermodynamics at $-1 < \log(\tau)$. Therefore, the values shown at these two ranges are due to the interpolation used by the inversion code in the nodes at that optical depths, and we have tested that changing those values in these ranges has no effect on the inverted profiles.

3 Results

Figures 7, **9**, **10**, **11** show the results from the inversions of two profiles of type A, one of type B, and a combination profile, respectively. These figures show the fit of the C II 1,334 & 1,335 Å lines, Mg II UV1 line, and the Mg II handk lines, including the Mg II UV2&3 blended lines. They show both the inversion considering only the latter lines and all together. Thus, we can better appreciate the impact in the model atmosphere by including the C II 1,334 & 1,335 Å lines and the Mg II UV1line. The physical parameters are shown along the logarithm of the optical depth, $\log(\tau)$[4].

The model atmosphere obtained differs for the different types of pointy profiles. We first discuss the main behavior of the extremely pointy profiles A (**Figures 7**, **9**), then the type B (**Figure 10**), and finally the combined type (**Figure 11**).

The fit of the spectral lines in **Figure 7**, while not perfect, is rather good in all the lines. In the high chromosphere[5], the T shows large

4 In this paper, log actually means $\log_{10}$, and $\log(\tau)$ means $\log_{10}(\tau_{500})$, being τ_{500} the reference of the optical depth unity corresponding to the continuum at 500 nm.

5 Roughly speaking, in this paper, we refer to the high chromosphere as the optical depth range $-6.5 < \log(\tau) < -5$, the mid chromosphere is $-5 < \log(\tau) < -4$, the low chromosphere is $-4 < \log(\tau) < -2$, the high photosphere is $-2 < \log(\tau) < -1$, and the low photosphere is $-1 < \log(\tau) < 0$. These ranges are dynamically changing, especially for events such as flares. Throughout

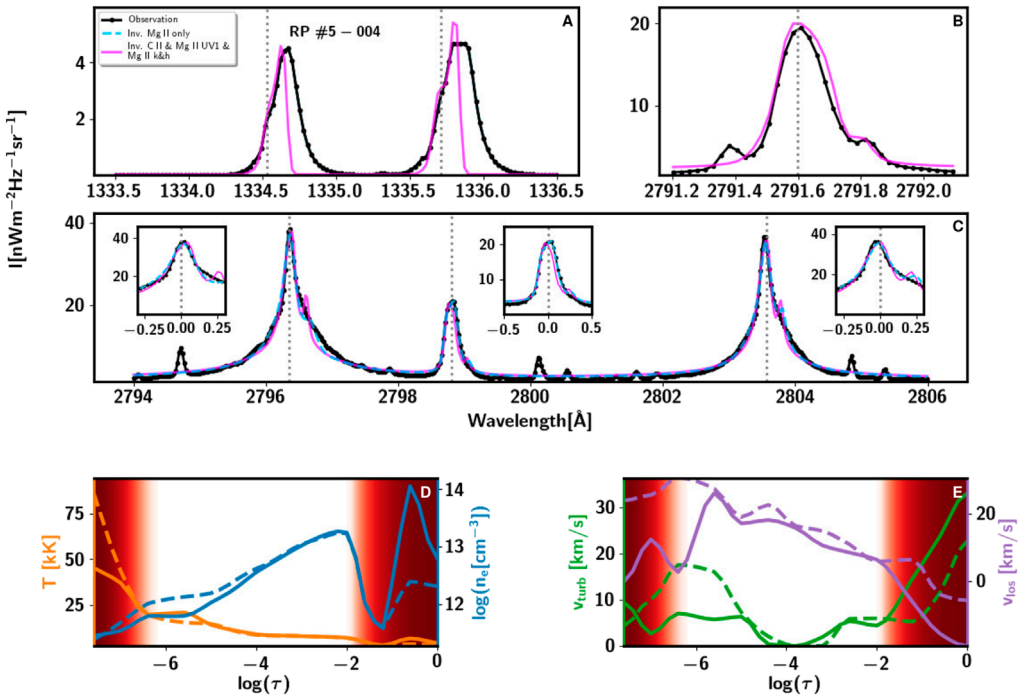

FIGURE 9
Inversion (fit) of the C II 1,334 & 1,335 Å, Mg II UV1 Mg II h&k, and Mg II UV2&3 lines of another extremely pointy profile type A, and the model recovered from the inversion. See caption of **Figure 7** for details.

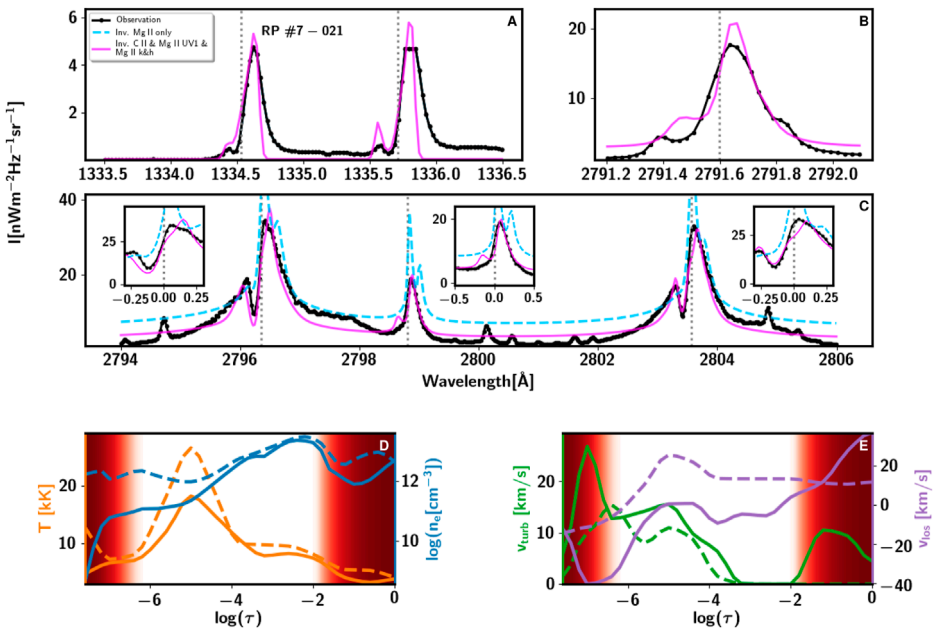

FIGURE 10
Inversion (fit) of the C II 1,334 & 1,335 Å, Mg II UV1 Mg II h&k, and Mg II UV2&3 lines of an extremely pointy profile type B, and the model recovered from the inversion. See caption of **Figure 7** for details.

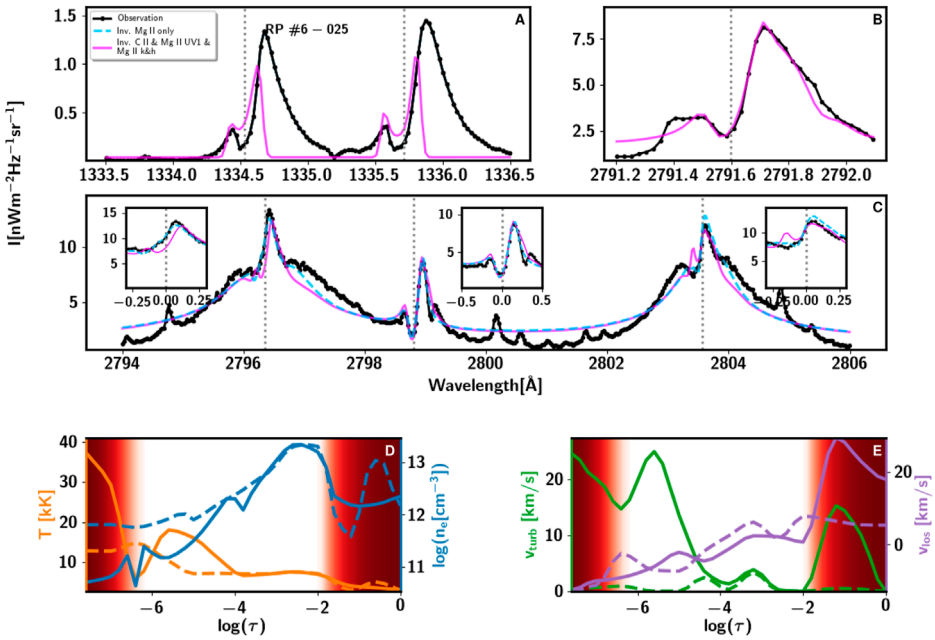

FIGURE 11
Inversion (fit) of the C II 1,334 & 1,335 Å, Mg II UV1 Mg II h&k, and Mg II UV2&3 lines of a combined pointy profile type, and the model recovered from the inversion. See caption of Figure 7 for details.

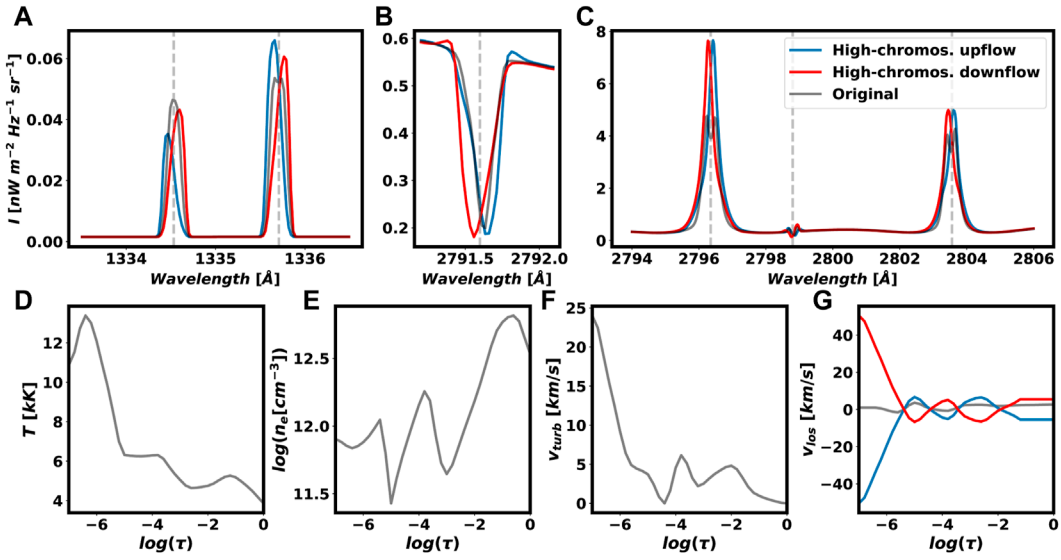

FIGURE 12
Creating an Mg II h&k extremely pointy profile type A [red or blue, in panels **(A–C)**] from a double-peaked Mg II h&k profile (grey) by considering an extreme gradient downflow (red) or upflow (blue) in the high chromosphere [panel **(G)**].

values, between 25 kK and 7.5 kK, as the optical depth increases. The n_e shows a steady, small increase around $\log(n_e) \approx 12$. The v_{los} goes from 0 km s^{-1} to $\approx +30$ km s^{-1}, that is, a downflow with a strong gradient in the v_{los}. These values are very similar to the ones obtained in the inversion of the profiles shown in Figure 9. The v_{turb} however, shows a difference. In the first case (Figure 7), the v_{turb} is close to 0 between $-6 < \log(\tau) < -5$, then increases up to 15–20 km s^{-1} at $\log(\tau) = -6.5$. In the second case of pointy profile type A (Figure 9) the value is almost constant around $v_{turb} = 5$ km s^{-1}. Because the fit,

such changes, the region just above the temperature minimum is referred to as the low chromosphere, while the steep, large increase of the temperature at small log(τ) values is the top of the chromosphere.

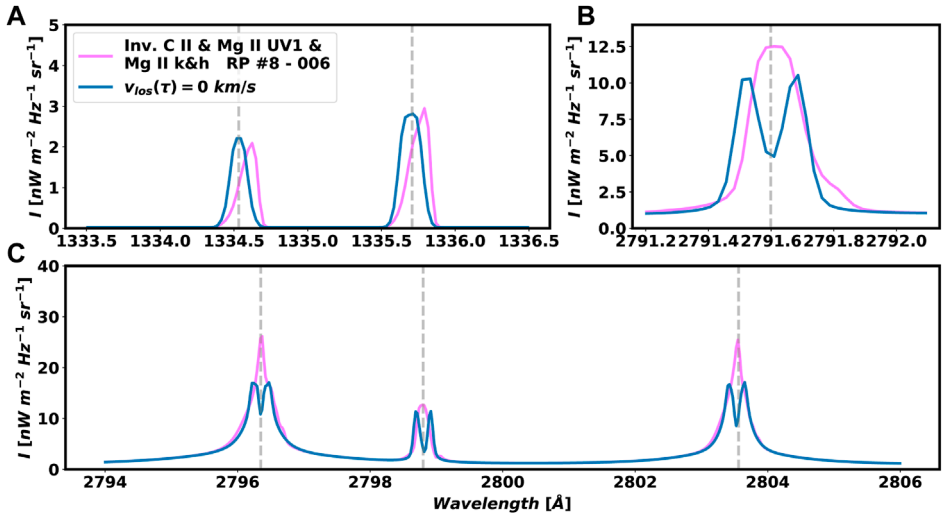

FIGURE 13
Deconstruction of the synthetic extremely pointy type A profile (in fuchsia) shown in the **Figure 7** that shows the role played by the v_{los}. Panels A, B and C show the C II 1334 & 1335 Å, Mg II UV1, and the Mg II h&k lines (including Mg II UV2&3 lines) respectively. The profile in blues shows the resulting profile by considering v_{los} = 0 km s^{-1} in the atmosphere associated to the profile mentioned above (two bottom panels in the **Figure 7**).

especially the width of the lines, in the first case is good in all the lines - including the C II 1,334 & 1,335 Å an lines, we consider the v_{turb} ≈15 – 20 km s^{-1} as a valid value. In the second case, the fit of the C II 1,334 & 1,335 Å lines is not good, failing to fit the width of these lines. This, as it has been mentioned above, may be due to the dual optical behavior of these lines. Therefore, the values of v_{turb} must be considered carefully, especially in the higher part of the chromosphere, i.e., at log(τ)< – 6. In the mid and low chromosphere, both cases behave very similarly: i) the and T decreases gradually, reaching its minimum value at log(τ) = 1, ii) the n_e increases up to log (n_e) = 13 at log(τ) = −2, then it drops off to 13 < log (n_e) < 12 at log(τ) = −1, iii) the v_{los} decreases gradually from 30 km s^{-1} to 0 km s^{-1}, and iv) the v_{turb} shows a wavy behavior around 5 km s^{-1}.

The profiles in **Figure 10** show an extremely pointy profile of type B. The T is lower in the high chromosphere (≈10 kK) than in the mid chromosphere (≈15 kK). The n_e in the high chromosphere has a lower value (log(n_e) ≈ 11) than for the pointy type A profiles. The T and n_e reach their minimum value at log(τ) = −1. The v_{turb} is ≈15 km s^{-1} in the high chromosphere, decreasing rapidly to 0 in the low chromosphere. The v_{los} shows a steep gradient in the upflow velocity at the high chromosphere, from −40 km s^{-1} to 0 km s^{-1}, becoming and a downflow of ≈ + 5 km s^{-1} in the low chromosphere.

The atmosphere corresponding to the combined type (**Figure 11**) is more similar to the one corresponding to type B than to type A. The most significant difference with respect to type B results are: i) the large value of the v_{turb} in the high chromosphere, with a value as high as 20–25 km s^{-1}, which explains by the very broad, enhanced wings, and ii) the smaller, more gradual upflow v_{los} varying from −10 km s^{-1} to 0 km s^{-1} from the high to the low chromosphere.

The fits of the C II 1334 & 1335 Å lines in 10, 11, and 12 are not good. To model and invert the C II 1334 & 1335 Å lines, especially in explosive events, is challenging. The fit of these lines is satisfactory in many cases, e.g., in active regions (Sainz Dalda et al., 2022), and even during pre-flare conditions (Woods et al., 2021). However, during the maximum of a flare, the physical conditions may be too complex to model and invert these lines properly with the currently available tools. As we mentioned above, these lines can be also formed in the transition region. Therefore, the inversion code must have the capability to reproduce the large jump in the temperature from the chromosphere to the transition region in very few optical depths. This is not possible with the current inversion scheme. As a consequence, the fit of the C II 1334 & 1335 Å lines in **Figures 9**, **10**, **11** is not as satisfactory as in simpler conditions. A deeper investigation into the C atom model and an improved inversion code will likely help to fit these complex profiles, but this falls out of the scope of this paper.

3.1 How the extremely pointy profiles are formed

A simple way to create an extremely pointy type A profile in the Mg II h&k lines is by considering an extreme gradient in the high chromosphere. **Figure 12** shows how to get an extremely pointy profile type A from a double-peaked Mg II h&k profile. The red and blue profiles are the result of considering the T, v_{turb}, and n_e of the double-peaked profile (panels D to F) with v_{los} shown in red and blue lines respectively (panel G) of **Figure 12**. In this example, the steep gradient is located between −7 < log(τ) < – 5.5 and goes from ±50 to 0 km s^{-1}. We have done several tests and we have also obtained extremely pointy profiles for lower values of v_{los}. Note that the C II 1,334 & 1,335 Å lines (panel A) are shifted to the red and blue wavelengths for the downflow and upflow gradients respectively, and they show the skewness previously observed in the IRIS data.

Another way of studying what can cause pointy profiles is by studying the contribution of v_{los} to the synthetic profile obtained by the inversion of the extremely pointy type A profile shown in **Figure 7** (in fuchsia). We have taken the same thermodynamics atmosphere associated with that profile (see bottom panels in the 6) and imposed a zero velocity at all optical depths ($v_{los}(\tau) = 0$ km s^{-1}), and then synthesized that new atmosphere. Again, we obtain a double-peaked profile (panels B and C), which is shown in blue in **Figure 13**.

The role played by the v_{los} in the enhancement or diminution of emission peaks in the line was first studied by Scharmer (1984), and more recently by de la Cruz Rodríguez et al. (2015). Thus, a v_{los} to the blue (red) is able to reduce the line opacity in the red wing, and as a result an enhancement in the red (blue) wing of the line is produced. In addition, in the presence of a strong gradient of v_{los} the core of the line (k_3) is shifted with respect to the wings, making it able to *vanish* one of the peaks of the line (k_{2r} or k_{2v}). Therefore, the enhancement of one of the peaks at the same time that the other peak is hidden by the shifted core produces an extremely pointy profile or a combined pointy profile.

In summary, the extremely pointy shape of these profiles is the signature of an extreme gradient in the v_{los} in the chromosphere. In the context of a flare, the downflows and upflows are associated with the *chromospheric condensation* and *evaporation* respectively. In this case, these flows have extreme gradients along the optical depth and take place in a well-determined optical depth range: the high chromosphere. Thus the difference between type A and type B is mainly due to the difference in the temperature in the high chromosphere, being smaller for the type B with respect to the type A.

4 Discussion

The inversion and interpretation of the profiles presented in this paper entail a significant challenge. The highly dynamic event studied - the maximum of an X1.0-class flare, is reflected both in the associated profiles and the thermodynamics recovered from the inversions of these profiles. The extremely pointy and combined type profiles belong to the same solar feature - the ribbon, including its leading and trailing edge. However, they are related to slightly different stages of the same event, which happen simultaneously in different locations in the ribbon. We should understand that both the variation in the appearance of the profiles and their associated thermodynamics is gradual. Thus, while we have focused our attention on the most significant of each type, the following interpretation captures the main physical properties during the maximum of the flare. **Figure 14** is particularly helpful for this interpretation.

For the positions scanned by the IRIS slit, the location of the trailing edge of the upper ribbon is at $[X, Y] = [512, 268]$, and in the lower ribbon at $[X, Y] = [517–526, 263]$. It is in these locations where the extremely pointy type A profiles such as the ones shown in **Figure 3** are found, while the rest of the profiles of this type are mostly located within the ribbon itself. The location for the leading edge of the upper ribbon is at $[X, Y] = [512, 277]$ and in the lower ribbon at $[X, Y] = [512–526, 257–255]$. Most of the type B pointy profiles are located at the leading edge of the lower ribbon, while the combination profiles are located within the ribbon on the trailing side immediately adjacent to the leading edge and the ribbon of the ribbon (some are also located in the region just leading the trailing edge of the ribbon). Thus, as the ribbon is energized, starting from the trailing edge towards the leading edge, the profiles go from extremely pointy type A to the combination type and finally to type B.

Because ribbons propagate across the solar surface as the flare evolves, the spatial distribution of the thermodynamic parameters from trailing to leading edge of the ribbon provides a window into the typical temporal evolution within a single location. From the temporal evolution observed in the IRIS SJI data, we know that the trailing edge has been energized longer than the leading edge in the single snapshot shown in **Figure 14**. That could explain why in these locations the temperature is so high in the high chromosphere ($\log(\tau) = -5.8$, the first panel in the first row of **Figure 14**), while in the rest of the ribbon the high chromosphere temperature is lower. The trailing edge also differs from the rest of the ribbon when we consider the temperature difference between the high and middle chromosphere. In the trailing edge, the temperature of the high chromosphere is higher than in the mid chromosphere. In contrast, the mid chromosphere temperature ($\log(\tau) = -4.2$, the first panel of the second row of **Figure 14**) is higher than in the high chromosphere for the leading edge and interior of the ribbon itself. Thus, the bump in the temperature at $\log(\tau) \approx -5$ observed in **Figure 10** has not reached yet the high-chromosphere, as it does in **Figure 9** and even higher in **Figure 7**. This spatial pattern of a somewhat reduced temperature in the high chromosphere accompanied by an increase in the mid chromosphere is seen in both flare ribbons but most clearly in the lower ribbon as IRIS scanned this ribbon more fully. This pattern has been obtained in some numerical models of flare energy deposition in the chromosphere by Allred et al., 2015. These observations support a scenario in which energy is deposited in the middle chromosphere, with an associated increase in the local temperature. This energy deposition affects the high chromosphere at later times, as the flare evolves.

The most critical physical parameter that contributes to the very distinctive profiles studied in this paper is the line-of-sight velocity. As we have demonstrated, the extremely pointy profiles of the Mg II h&k lines, but also of the C II 1,334 & 1,335 Å lines, need the presence of a strong, divergent velocity gradient located between the high and middle chromosphere. Therefore, the main thermodynamic phenomenon in the chromosphere happening in the ribbons during the maximum of the flare is a divergent flow hosting strong velocity gradients.

In addition, the Mg II UV triplet lines have signatures associated with strong velocities in the high photosphere. The divergent flow located between the high and mid chromosphere can be appreciated between the first (i.e., top) and the second panel of the second column of **Figure 14**. There, we can observe predominantly an upflow in the ribbon in the high chromosphere ($\log(\tau) = -5.8$), while in the middle chromosphere and lower regions in the atmosphere ($-4.2 < \log(\tau)$) the ribbon shows a downflow. Note that in the trailing edge, there are some locations where the velocities in the high chromosphere are positive, i.e., they host downflows. Again, these locations are likely *ahead in time* (i.e., have evolved for the longest time since the start of the flare), so it is possible they may

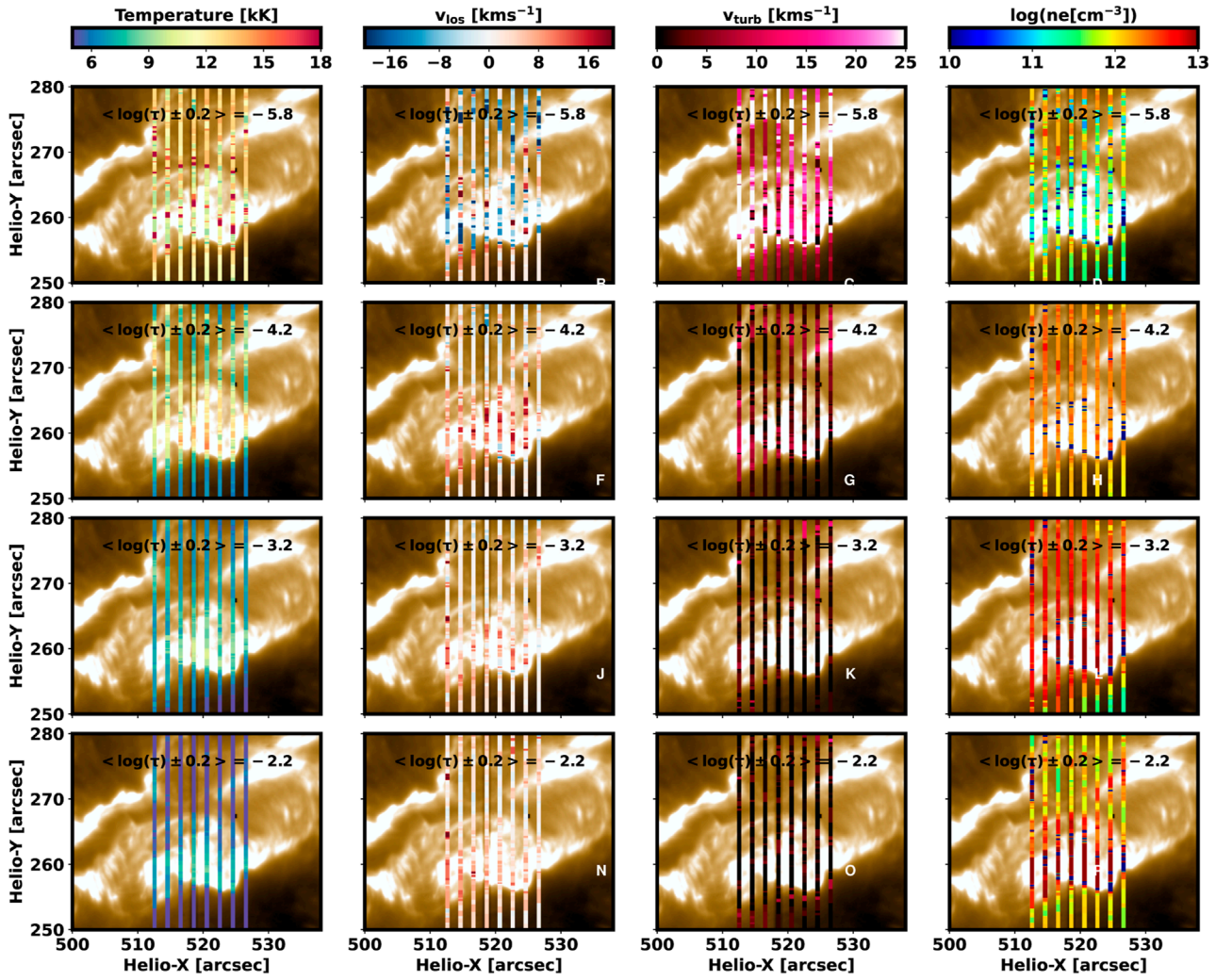

FIGURE 14
Maps of thermodynamic values (columns) during the maximum of the X1.0-class flare SOL2014-03-29T17:48, for various optical depths (rows). The image in the background of the panels corresponds to IRIS SJI 2796 Å shown in the dashed grey square in **Figure 1**.

have experienced the upflows at an earlier stage of their evolution. The presence of a divergent flow is compatible with a scenario where an electron beam propagating downwards from the flare reconnection site in the corona impacts the dense chromosphere (thick-target model, Hudson and Ohki, 1972). Such divergent flows have also been obtained in radiation hydrodynamic experiments by Kerr et al., 2016 and Kowalski et al., 2017 who studied the same flare that we analyzed in the current paper. However, the synthetic Mg II h&k profiles obtained by Kerr et al., 2016 show the k_3 feature in absorption, which indicates that their models are missing some ingredient(s) needed to reproduce the observed profiles. Similarly, the temperature increase where the divergent flows occur in Kowalski et al., 2017 is much higher ($T \approx 10$ MK) than the one we obtain. What can explain the strong velocity flows that we observe in the high photosphere? Several results suggest that these can be explained by the different penetration of the different energy regimes of the electron beams. Graham et al., 2020 demonstrated that low-energy electrons ($E \approx 25$–50 keV) are responsible for the evaporation-condensation in the high chromosphere, while very high-energy electrons ($E \geq 50$ keV) can penetrate deeper into the atmosphere and produce a similar situation in the high photosphere. These authors used, in addition to the Mg II UV1 line, the optically thin lines Fe I 2814.11 Å, and Fe II 2813.3 and 2814.45 Å. In their study all these lines show a strong red component. However, in the flare we study here no red components are present in the Fe I and Fe II lines, and the Mg II UV1 line shows on occasion a strong red component, but also blue and red components in other cases. Likely, the situation shown in **Figure 14** is compatible with the scenario described by Graham et al., 2020 and the one previously suggested by Libbrecht et al., 2019 (see Figure 14 of their paper). Here, in agreement with Graham et al., 2020, we interpret that the bounce-back motion that Libbrecht et al., 2019 locates in the chromosphere is lower in our case, reaching the high photosphere. In summary, there are two slabs, one

located between the high and mid chromosphere and the other in the high photosphere, that are suffering the impact from energized electron coming from the corona, and producing explosive, divergent upflows and downflows. These slabs are not necessarily located in the same feature of the ribbon at the same time, and their location evolves as the ribbon is energized by the flare.

Finally, in the ribbons the velocity associated turbulent motions is large, v_{turb}≈10 – 20 km s^{-1}, in the high and mid chromosphere in the ribbons. It is in these regions where the core of both the C II 1,334 & 1,335 Å lines and the Mg II handk lines is sensitive to this parameter. The values presented in this investigation are more realistic than the ones obtained by Rubio da Costa and Kleint (2017) (40 km s^{-1}) or Zhu et al. (2019) (40–50 km s^{-1}). In the low chromosphere and the high photosphere the *vturb* in the ribbons is negligible. The extended, broad wings of the Mg II h&k are sensitive to changes in $v_{\rm turb}$ in the mid chromosphere, while the Mg II UV triplet lines are sensitive to turbulence in the low chromosphere. We also note that the electron density in the ribbons is $12 < \log(n_e) < 13$ in the chromosphere, reaches its maximum in the low chromosphere with a value of $\log(n_e) \approx 15$, just before the temperature minimum, which is *pushed down* (in terms of the optical depth) towards the low-photosphere ($\log(\tau) \approx -1$). Thus, the extended wings of the Mg II h&k lines are mostly due to the thermodynamics conditions in the chromosphere. This region is where the contribution function of these lines is prominent when a flare model F2 (Machado et al., 1980) and non-LTE are considered, as it is shown in Figure 16 of Liu et al. (2015). This authors found that the contribution to the winds of the Mg II h&k lines in a F2 flare model extends in a region of ≈ 1,000 km in the chromosphere, in comparison to a ≈ 200 km when the VALC quiet-sun model (Vernazza et al., 1981) is considered. However, because in their model the $v_{\rm turb}$≈0 – 10 km s^{-1}, and it is uniform in the formation region of the Mg II h&k lines, the authors justify the large broadening of the observed wings to an enhanced line source function rather than an extra broadening. Our results prove that reasonable $v_{\rm turb}$ values varying along the optical depth are able to reproduce the width of the Mg II h&k lines.

The spectral profiles studied in this article are challenging to model and interpret due to the complexity of the physical conditions that generate them. In addition to belonging to an extreme event (an X1-class flare), we note that several physical processes such as upflows and downflows, or heating and cooling, occur simultaneously in the same structure—the ribbon. We are analyzing the maximum of the flare, but that does not mean all regions in the ribbon show the same behavior. For example, the trailing edge experiences different physical conditions than the ribbon itself. The interpretation of the peculiar profiles clearly will depend on where and when they are observed in the macroscopic spatiotemporal evolution of the flare. Until now there have not been any theoretical or numerical models that are able to properly reproduce these profiles. In this context, our investigation and results provide strict observational constraints to these models and suggest a reasonable physical scenario.

Data availability statement

Publicly available datasets were analyzed in this study. This data can be found to strictly the following text: https://www.lmsal.com/hek/hcr?cmd=view-event&event-id=ivo%3A%2F%2Fsot.lmsal.com%2FVOEvent%23VOEvent_IRIS_20140329_140938_3860258481_2014-03-29T14%3A09%3A382014-03-29T14%3A09%3A38.xml.

Author contributions

This paper has been led by ASD. He has made the analysis of the IRIS spectra, and the interpretation of the inversions and the models recovered from them, as well as the main contain of the manuscript. BDP has contributed with meaningful ideas, enlightening discussions with AD, and with critical comments and improvements to the manuscript. All authors contributed to the article and approved the submitted version.

Funding

ASD was supported in part by the NASA contract NNG09FA40C (IRIS) and the NASA grant 80NSSC21K0726 "Understanding the role played by the turbulence in the chromosphere during flares". BDP was supported by NASA contract NNG09FA40C (IRIS).

Acknowledgments

IRIS is a NASA small explorer mission developed and operated by LMSAL with mission operations executed at NASA Ames Research Center and major contributions to downlink communications funded by ESA and the Norwegian Space Agency. The authors thank the helpful discussions and clarifications made by J. de la Cruz Rodríguez. We also thanks him for sharing the state-of-the-art inversion code STiC, which is available to the public.

Conflict of interest

The authors declare that the research was conducted in the absence of any commercial or financial relationships that could be construed as a potential conflict of interest.

Publisher's note

References

Allred, J. C., Kowalski, A. F., and Carlsson, M. (2015). A unified computational model for solar and stellar flares. *Astrophysical J.* 809, 104. doi:10.1088/0004-637X/809/1/104

Avrett, E. H., Machado, M. E., and Kurucz, R. L. (1986). "Chromospheric flare models," in *The lower atmosphere of solar flares* Editors D. F. Neidig, and M. E. Machado (United States: National Solar Observatory), 216–281.

Carlsson, M., Leenaarts, J., and De Pontieu, B. (2015). What do IRIS observations of Mg II k tell us about the solar plage chromosphere? *Astrophysical J.* 809, L30. doi:10.1088/2041-8205/809/2/L30

Carlsson, M., and Stein, R. F. (1995). Does a nonmagnetic solar chromosphere exist? *Astrophysical J.* 440, L29. doi:10.1086/187753

Carlsson, M., and Stein, R. F. (1997). formation of solar calcium H and K bright grains. *Astrophysical J.* 481, 500–514. doi:10.1086/304-043

de la Cruz Rodríguez, J., Hansteen, V., Bellot-Rubio, L., and Ortiz, A. (2015). Emergence of granular-sized magnetic bubbles through the solar atmosphere. II. Non-LTE chromospheric diagnostics and inversions. *Astrophysical J.* 810, 145. doi:10.1088/0004-637X/810/2/145

de la Cruz Rodríguez, J., Leenaarts, J., and Asensio Ramos, A. (2016). Non-LTE inversions of the Mg II h & k and UV triplet lines. *Astrophysical J.* 830, L30. doi:10.3847/2041-8205/830/2/L30

de la Cruz Rodríguez, J., Leenaarts, J., Danilovic, S., and Uitenbroek, H. (2019). STiC: A multiatom non-LTE PRD inversion code for full-Stokes solar observations. *A&A* 623, A74. doi:10.1051/0004-6361/201834464

De Pontieu, B., Title, A. M., Lemen, J. R., Kushner, G. D., Akin, D. J., Allard, B., et al. (2014). The Interface region imaging Spectrograph (IRIS). *Sol. Phys.* 289, 2733–2779. doi:10.1007/s11207-014-0485-y

del Pino Alemán, T., Casini, R., and Manso Sainz, R. (2016). Magnetic diagnostics of the solar chromosphere with the Mg II h-k lines. *Astrophysical J.* 830, L24. doi:10.3847/2041-8205/830/2/L24

Dimitrijević, M. S., and Sahal-Bréchot, S. (1998). Electron-impact broadening of MgII spectral lines for astrophysical and laboratory plasma research. *Phys. Scr.* 58, 61–71. doi:10.1088/0031-8949/58/1/009

Dimitrijević, M. S., and Sahal-Bréchot, S. (1995). Stark broadening parameter tables for Mg II. *Bull. Astron. Belgr.* 151, 101–114.

Feldman, U., and Doschek, G. A. (1977). The 3s-3p and 3p-3d lines of Mg II observed above the solar limb from Skylab. *Astrophysical J.* 212, L147. doi:10.1086/182395

Graham, D. R., Cauzzi, G., Zangrilli, L., Kowalski, A., Simões, P., and Allred, J. (2020). Spectral signatures of chromospheric condensation in a major solar flare. *Astrophysical J.* 895, 6. doi:10.3847/1538-4357/ab88ad

Hawley, S. L., and Fisher, G. H. (1994). Solar flare model atmospheres. *Astrophysical J.* 426, 387. doi:10.1086/174075

Hudson, H. S., and Ohki, K. (1972). Soft X-ray and microwave observations of hot regions in solar flares. *Sol. Phys.* 23, 155–168. doi:10.1007/BF00153899

Jefferies, J. T. (1968). Spectral line formation. *A Blaisdell Book Pure Appl. Sci.* 1968.

Kaiser, M. L., Kucera, T. A., Davila, J. M., Cyr, St.O. C., Guhathakurta, M., and Christian, E. (2008). The STEREO mission: An introduction. *Space Sci. Rev.* 136, 5–16. doi:10.1007/s11214-007-9277-0

Kerr, G. S., Allred, J. C., and Carlsson, M. (2019a). Modeling Mg II during solar flares. I. Partial frequency redistribution, opacity, and coronal irradiation. *ApJ* 883, 57. doi:10.3847/1538-4357/ab3c24

Kerr, G. S., Carlsson, M., and Allred, J. C. (2019b). Modeling Mg II during solar flares. II. Nonequilibrium effects. *Astrophysical J.* 885, 119. doi:10.3847/1538-4357/ab48ea

Kerr, G. S., Fletcher, L., Russell, A. J. B., and Allred, J. C. (2016). Simulations of the Mg II k and Ca II 8542 lines from an AlfvÉn wave-heated flare chromosphere. *Astrophysical J.* 827, 101. doi:10.3847/0004-637X/827/2/101

Kerr, G. S., Simões, P. J. A., Qiu, J., and Fletcher, L. (2015). IRIS observations of the Mg ii h and k lines during a solar flare. *A&A* 582, A50. doi:10.1051/0004-6361/201526128

Kleint, L., Battaglia, M., Reardon, K., Sainz Dalda, A., Young, P. R., and Krucker, S. (2015). The fast filament eruption leading to the X-flare on 2014 march 29. *Astrophysical J.* 806, 9. doi:10.1088/0004-637X/806/1/9

Kneer, F., Scharmer, G., Mattig, W., Wyller, A., Artzner, G., Lemaire, P., et al. (1981). OSO-8 observations of CAII H and K MGII H and K lyman-alpha and lyman-beta above a sunspot. *Sol. Phys.* 69, 289–300. doi:10.1007/BF00149995

Kohl, J. L., and Parkinson, W. H. (1976). The Mg II h and k lines. I. Absolute center and limb measurements of the solar profiles. *Astrophysical J.* 205, 599–611. doi:10.1086/154317

Kosugi, T., Matsuzaki, K., Sakao, T., Shimizu, T., Sone, Y., Tachikawa, S., et al. (2007). The Hinode (solar-B) mission: An overview. *Sol. Phys.* 243, 3–17. doi:10.1007/s11207-007-9014-6

Kowalski, A. F., Allred, J. C., Uitenbroek, H., Tremblay, P.-E., Brown, S., Carlsson, M., et al. (2017). Hydrogen balmer line broadening in solar and stellar flares. *Astrophysical J.* 837, 125. doi:10.3847/1538-4357/aa603e

Landi Degl'Innocenti, E., and Landi Degl'Innocenti, M. (1977). Response function for magnetic lines. *A&A* 56, 111–115.

Leenaarts, J., Pereira, T. M. D., Carlsson, M., Uitenbroek, H., and De Pontieu, B. (2013a). The Formation of iris diagnostics. I. A quintessential model atom of Mg II and general formation properties of the Mg II h&k lines. *Astrophysical J.* 772, 89. doi:10.1088/0004-637X/772/2/89

Leenaarts, J., Pereira, T. M. D., Carlsson, M., Uitenbroek, H., and De Pontieu, B. (2013b). The Formation of IRIS diagnostics. II. The formation of the Mg II h&k lines in the solar atmosphere. *Astrophysical J.* 772, 90. doi:10.1088/0004-637X/772/2/90

Lemaire, P., Choucq-Bruston, M., and Vial, J. C. (1984). Simultaneous H and K Ca ii, h and k Mg ii, Lα and Lβ H i profiles of the April 15, 1978 solar flare observed with the OSO-8/L.P.S.P. experiment. *Sol. Phys.* 90, 63–82. doi:10.1007/BF00153785

Lemaire, P., and Gouttebroze, P. (1983). Magnesium II line formation - the contribution of high atomic levels to the resonance lines. *A&A* 125, 241–245.

Lemaire, P., and Skumanich, A. (1973). Magnesium II doublet profiles of chromospheric inhomogeneities at the center of the solar disk. *A&A* 22, 61.

Libbrecht, T., de la Cruz Rodríguez, J., Danilovic, S., Leenaarts, J., and Pazira, H. (2019). Chromospheric condensations and magnetic field in a C3.6-class flare studied via He I D_3 spectro-polarimetry. *A&A* 621, A35. doi:10.1051/0004-6361/201833610

Lin, R. P., Dennis, B. R., Hurford, G. J., Smith, D. M., Zehnder, A., Harvey, P. R., et al. (2002). The reuven ramaty high-energy solar spectroscopic imager (RHESSI). *Sol. Phys.* 210, 3–32. doi:10.1023/A:1022428818870

Lites, B. W., and Cook, J. W. (1979). A semiempirical model of the upper flare chromosphere. *Astrophysical J.* 228, 598–609. doi:10.1086/156884

Lites, B. W., and Skumanich, A. (1982). A model of a sunspot chromosphere based on OSO 8 observations. *Astrophysical J.* 49, 293–315. doi:10.1086/190800

Liu, W., Heinzel, P., Kleint, L., and Kašparová, J. (2015). Mg II lines observed during the X-class flare on 29 march 2014 by the Interface region imaging Spectrograph. *Sol. Phys.* 290, 3525–3543. doi:10.1007/s11207-015-0814-9

Machado, M. E., Avrett, E. H., Vernazza, J. E., and Noyes, R. W. (1980). Semiempirical models of chromospheric flare regions. *Astrophysical J.* 242, 336–351. doi:10.1086/158467

MacQueen, J. (1967). "Some methods for classification and analysis of multivariate observations," in *Proc. Of the fifth berkeley symposium on mathematical statistics and probability* Editors L. M. Le Cam, and J. Neyman (California: University of California Press), 281–297.

Manso Sainz, R., del Pino Alemán, T., Casini, R., and McIntosh, S. (2019). Spectropolarimetry of the solar Mg II h and k lines. *Astrophysical J.* 883, L30. doi:10.3847/2041-8213/ab412c

Mein, P. (1971). Inhomogeneities in the solar atmosphere from the Ca II infra-red lines. *Sol. Phys.* 20, 3–18. doi:10.1007/BF00146089

Panos, B., Kleint, L., Huwyler, C., Krucker, S., Melchior, M., Ullmann, D., et al. (2018). Identifying typical Mg II flare spectra using machine learning. *Astrophysical J.* 861, 62. doi:10.3847/1538-4357/aac779

Panos, B., Kleint, L., and Voloshynovskiy, S. (2021). Exploring mutual information between IRIS spectral lines. I. Correlations between spectral lines during solar flares and within the quiet sun. *Astrophysical J.* 912, 121. doi:10.3847/1538-4357/abf11b

Pereira, T. M. D., Carlsson, M., De Pontieu, B., and Hansteen, V. (2015). The Formation of IRIS diagnostics. IV. The Mg II triplet lines as a new diagnostic for lower chromospheric heating. *Astrophysical J.* 806, 14. doi:10.1088/0004-637X/806/1/14

Pereira, T. M. D., Leenaarts, J., De Pontieu, B., Carlsson, M., and Uitenbroek, H. (2013). The Formation of IRIS diagnostics. III. Near-Ultraviolet spectra and images. *Astrophysical J.* 778, 143. doi:10.1088/0004-637X/778/2/143

Pereira, T. M. D., and Uitenbroek, H. (2015). RH 1.5D: A massively parallel code for multi-level radiative transfer with partial frequency redistribution and zeeman polarisation. *A&A* 574, A3. doi:10.1051/0004-6361/201424785

Pesnell, W. D., Thompson, B. J., and Chamberlin, P. C. (2012). The solar dynamics observatory (SDO). *Sol. Phys.* 275, 3–15. doi:10.1007/s11207-011-9841-3

Rathore, B., Carlsson, M., Leenaarts, J., and De Pontieu, B. (2015). The Formation of IRIS diagnostics. VI. The diagnostic potential of the C II lines at 133.5 nm in the solar atmosphere. *Astrophysical J.* 811, 81. doi:10.1088/0004-637X/811/2/81

Rathore, B., and Carlsson, M. (2015). The Formation of iris diagnostics. V. A quintessential model atom of C II and general formation properties of the C II lines at 133.5 nm. *Astrophysical J.* 811, 80. doi:10.1088/0004-637X/811/2/80

Rubio da Costa, F., and Kleint, L. (2017). A parameter study for modeling Mg II h and k emission during solar flares. *Astrophysical J.* 842, 82. doi:10.3847/1538-4357/aa6eaf

Rubio da Costa, F., Kleint, L., Petrosian, V., Liu, W., and Allred, J. C. (2016). Data-driven radiative hydrodynamic modeling of the 2014 march 29 X1.0 solar flare. *Astrophysical J.* 827, 38. doi:10.3847/0004-637X/827/1/38

Sainz Dalda, A., Agrawal, A., De Pontieu, B., and Gosic, M. (2022). *IRIS^{2+}: A comprehensive database of stratified thermodynamic models in the low solar atmosphere*. arXiv e-prints , arXiv:2211.

Sainz Dalda, A., de la Cruz Rodríguez, J., De Pontieu, B., and Gošić, M. (2019). Recovering thermodynamics from spectral profiles observed by iris: A machine and deep learning approach. *Astrophysical J.* 875, L18. doi:10.3847/2041-8213/ab15d9

Sánchez Almeida, J., and Lites, B. W. (2000). Physical properties of the solar magnetic photosphere under the MISMA hypothesis. II. Network and internetwork fields at the disk center. *Astrophysical J.* 532, 1215–1229. doi:10.1086/308603

Scharmer, G. B. (1984). "Accurate solutions to non-LTE problems using approximate Lambda operators," in *Methods in radiative transfer* (Cambridge: Cambridge University Press), 173–210.

Steinhaus, H. (1957). Sur la division des corps matériels en parties. *Bull. Acad. Pol. Sci.* 4, 801.

Sukhorukov, A. V., and Leenaarts, J. (2017). Partial redistribution in 3D non-LTE radiative transfer in solar-atmosphere models. *A&A* 597, A46. doi:10.1051/0004-6361/201629086

Thorndike, R. L. (1953). Who belongs in the family? *Psychometrika* 18, 267–276. doi:10.1007/BF02289263

Uitenbroek, H. (2001). Multilevel radiative transfer with partial frequency redistribution. *Astrophysical J.* 557, 389–398. doi:10.1086/321659

Uitenbroek, H. (1997). THE solar Mg II h and k lines - observations and radiative transfer modeling. *Sol. Phys.* 172, 109–116. doi:10.1023/A:1004981412889

Vernazza, J. E., Avrett, E. H., and Loeser, R. (1981). Structure of the solar chromosphere. III. Models of the EUV brightness components of the quiet sun. *Astrophysical J.* 45, 635–725. doi:10.1086/190731

Woods, M. M., Sainz Dalda, A., and De Pontieu, B. (2021). Unsupervised machine learning for the identification of preflare spectroscopic signatures. *Astrophysical J.* 922, 137. doi:10.3847/1538-4357/ac2667

Xu, Y., Cao, W., Ding, M., Kleint, L., Su, J., Liu, C., et al. (2016). Ultra-narrow negative flare front observed in helium-10830 Å using the 1.6 m new solar telescope. *ApJ* 819, 89. doi:10.3847/0004-637X/819/2/89

Zhu, Y., Kowalski, A. F., Tian, H., Uitenbroek, H., Carlsson, M., and Allred, J. C. (2019). Modeling Mg II h, k and triplet lines at solar flare ribbons. *Astrophysical J.* 879, 19. doi:10.3847/1538-4357/ab2238

frontiers | Frontiers in Astronomy and Space Sciences

TYPE Original Research
PUBLISHED 21 September 2023
DOI 10.3389/fspas.2023.1214901

OPEN ACCESS

EDITED BY
Qiang Hu,
University of Alabama in Huntsville,
United States

REVIEWED BY
P. S. Athiray,
University of Alabama in Huntsville,
United States
Yingna Su,
Chinese Academy of Sciences (CAS),
China

*CORRESPONDENCE
Vanessa Polito,
polito@baeri.org

RECEIVED 30 April 2023
ACCEPTED 21 July 2023
PUBLISHED 21 September 2023

CITATION
Polito V, Peterson M, Glesener L, Testa P, Yu S, Reeves KK, Sun X and Duncan J (2023), Multi-wavelength observations and modeling of a microflare: constraining non-thermal particle acceleration.
Front. Astron. Space Sci. 10:1214901.
doi: 10.3389/fspas.2023.1214901

Multi-wavelength observations and modeling of a microflare: constraining non-thermal particle acceleration

Vanessa Polito[1,2]*, Marianne Peterson[3], Lindsay Glesener[3], Paola Testa[4], Sijie Yu[5], Katharine K. Reeves[4], Xudong Sun[6] and Jessie Duncan[7]

[1]Bay Area Environmental Research Institute, NASA Research Park, Moffett Field, CA, United States, [2]Department of Physics, Oregon State University, Corvallis, OR, United States, [3]School of Physics and Astronomy, University of Minnesota—Twin Cities, Minneapolis, MN, United States, [4]Harvard-Smithsonian Center for Astrophysics, Cambridge, MA, United States, [5]Center for Solar-Terrestrial Research, New Jersey Institute of Technology, Newark, NJ, United States, [6]Institute for Astronomy, University of Hawaii at Manoa, Honolulu, HI, United States, [7]Goddard Space Flight Center, Greenbelt, MD, United States

In this work we analyze a small B-class flare that occurred on 29 April 2021 and was observed simultaneously by the Interface Region Imaging Spectrograph (IRIS) and the Nuclear Spectroscopic Telescope Array (NuSTAR) X-ray instrument. The IRIS observations of the ribbon of the flare show peculiar spectral characteristics that are typical signatures of energy deposition by non-thermal electrons in the lower atmosphere. The presence of the non-thermal particles is also confirmed directly by fitting the NuSTAR spectral observations. We show that, by combining IRIS and NuSTAR multi-wavelength observations from the corona to the lower atmosphere with hydrodynamic simulations using the RADYN code, we can provide strict constraints on electron-beam heated flare models. This work presents the first NuSTAR, IRIS and RADYN joint analysis of a non-thermal microflare, and presents a self-consistent picture of the flare-accelerated electrons in the corona and the chromospheric response to those electrons.

KEYWORDS

solar flare, solar atmosphere, UV spectroscopy, hard X-ray, hydrodynamic simulations

1 Introduction

Flares result from the rapid release of large amounts of energy via the magnetic reconnection process in the solar corona (e.g., Benz, 2008; Shibata and Magara, 2011; Testa and Reale, 2022). Such energy release efficiently accelerates particles, heats ambient plasma and generates magnetohydrodynamic (MHD) waves (e.g., Fletcher et al., 2011). Solar flares are typically catalogued in terms of their soft X-ray energy flux as measured by the Geostationary Orbiting Environmental Satellites (GOES). For example, microflares in the GOES A- or B-class range emit ≈6 orders of magnitude less energy than the largest GOES X-class flares. An increasing amount of evidence seems to suggest that smaller microflare or even nanoflare (even fainter, as-yet unresolvable events predicted by Parker (1988)) size events found in the core of active regions are in many aspects scaled-down versions of large flares, e.g., characterized by high temperatures (up to ~10 MK, Reale et al., 2019a; Reale et al.,

2019b; Glesener et al., 2020; Testa et al., 2020; Testa and Reale, 2020; Cooper et al., 2020), and particle acceleration (Hannah et al., 2008; Testa et al., 2014; Wright et al., 2017; Testa et al., 2020; Glesener et al., 2020; Cooper et al., 2021). In addition, small flares occur much more frequently, possibly contributing to coronal heating (Hudson, 1991; Hannah et al., 2008).

Observations in the hard X-ray (HXR) range are a primary tool for studying particle acceleration. HXRs are emitted mainly via bremsstrahlung, with higher HXRs dominated by non-thermal bremsstrahlung, providing important observational signatures of the accelerated electron spectrum. A statistical study of approximately 25,000 microflares was conducted using the Reuven Ramaty High-Energy Solar Spectroscopic Imager (RHESSI), utilizing indirect Fourier imaging techniques (Christe et al., 2008; Hannah et al., 2008). RHESSI was sensitive to energies between 3 keV and 17 MeV, but experienced lower sensitivity to faint events due to high background from large detector volume (Lin et al., 2002). The Nuclear Spectroscopic Telescope ARray (NuSTAR) instrument (Harrison et al., 2013) is an astrophysical-focused mission which utilizes direct-focusing HXR telescopes, capable of achieving greater sensitivity to fainter events. NuSTAR solar observations are performed rarely (a few times per year), usually consisting of a few to several hours for each observation. Previous NuSTAR studies include analysis of both GOES sub-A-class quiet Sun brightenings (Glesener et al., 2017) and GOES A-class flares from active regions (Wright et al., 2017; Hannah et al., 2019; Glesener et al., 2020; Cooper et al., 2021). NuSTAR's enhanced sensitivity has notably shown evidence of accelerated electrons below 7 keV, previously indistinguishable by RHESSI (Glesener et al., 2020). However, NuSTAR observations of non-thermal microflares are still somewhat rare, with Duncan et al. (2021) only definitively labeling one of the eleven studied A-class flares as exhibiting non-thermal emission. In both RHESSI and NuSTAR microflare studies, steeper non-thermal spectra have often been observed as compared to larger solar flares, resulting in more difficulty distinguishing an accelerated electron spectrum from thermal emission. Such work can be complemented by a multi-wavelength approach to analysis, particularly by including the chromospheric response to such accelerated electrons.

Our understanding of both large and small flare events has greatly improved since the launch of the Interface Region Imaging Spectrograph (IRIS; De Pontieu et al., 2014) in 2013. We refer the readers to Sections 4.6 and 5 of De Pontieu et al. (2021) for a recent review of the most significant results from IRIS in these topics. For instance, IRIS observations of footpoint brightenings associated with coronal nano to microflares has provided unexpected new indirect diagnostics of the presence of non-thermal particles in small heating events (e.g., Testa et al., 2014). These small coronal heating events induce rapid variability in the lower atmospheric (transition region and chromosphere) emission (e.g., Testa et al., 2013), and early IRIS observations, combined with simulations, showed that their spectral properties are crucially dependent on the mechanism of energy transport (e.g., thermal conduction vs non-thermal particles), and duration of the heating. In particular, IRIS Si IV blueshifts and Mg II triplet emission are signatures of non-thermal particles, and the IRIS spectral properties also provide valuable diagnostics of the properties of the non-thermal particles, such as the low-energy cutoff (E_C) of their power-law distributions and total energy (Testa et al., 2014; Polito et al., 2018; Testa et al., 2020; Cho et al., 2023). These new IRIS indirect diagnostics of accelerated particles in small events are particularly interesting because of their sensitivity to small events which are typically difficult to observe in HXRs, and because of their diagnostics of the non-thermal particles properties (especially E_C), which are often difficult to tightly constrain with HXR spectra because of the overlap of thermal and non-thermal spectra.

Joint analysis has previously been performed combining IRIS, RHESSI and modeling for large flares (e.g., Polito et al., 2016; Rubio da Costa et al., 2016), achieving a more detailed understanding of flare energy release processes. The only previously combined NuSTAR and IRIS analysis is presented in Hannah et al. (2019), which analyzed a microflare with a background-subtracted GOES class of A1. Non-thermal emission was not detected, but the ability to connect NuSTAR's HXR detection of 5 MK flare-heated plasma to transition region and chromospheric signatures with IRIS provided evidence for the usefulness of joint analysis between the two instruments.

In this paper we analyze coordinated observations with IRIS and NuSTAR of a B-class flare, which provide a rare opportunity to study non-thermal particles in a small flare using two independent diagnostics. NuSTAR observations provide a direct measure of flare-accelerated electrons, while IRIS reveals, with great sensitivity, the chromospheric response to those electrons. Hydrodynamic modeling performed using the RADYN model connect these observables. As discussed above, the IRIS diagnostics are indirect diagnostics, based on the predictions of state-of-the-art RADYN modeling. The analysis presented here therefore serves as a validation of our previous interpretation of the IRIS observations based on hydrodynamic modeling.

The paper is organized as follows. In Section 2 we describe the SDO, IRIS and NuSTAR observations analyzed in this work. Sections 3 and 4 present the details of the IRIS and NuSTAR spectroscopic observations for the event under study, while Section 5 and 6 present the results of the hydrodynamic modeling and three-dimensional magnetic field extrapolation. Finally, in Section 7 we summarise and discuss our results.

2 Observations of the 29 April 2021 B-class flare

The small B-class flare under study was part of a series of B-class flares that occurred on 29 April 2021 in the active region (AR) complex 12820/12821 from around 14 UT and that culminated in a C-class flare around 22:30 UT. Some of these small flares were observed by a combination of instruments, including Hinode, IRIS and NuSTAR, as part of the coordinated IRIS–Hinode Operation Plan (IHOP) 409 "Energetics of solar eruptions from the chromosphere to the inner heliosphere"[1]. Figure 1 shows the evolution of the energy flux for the flares as observed by the GOES satellite in soft X-rays. The light blue curve and blue, magenta, and green arrows highlight the time intervals of the NuSTAR, IRIS, Hinode/EIS and VLA observational coverage respectively. In this

1 https://www.isas.jaxa.jp/home/solar/hinode_op/hop.php?hop=0409

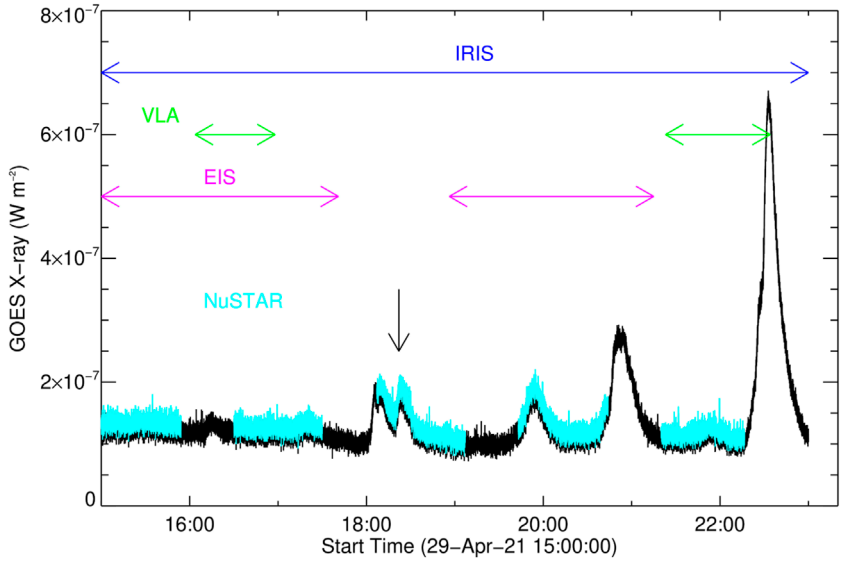

FIGURE 1
Overview of the 29 April 2021 flare observations and instrument coverage. The blue color indicates the NuSTAR observing time, and the horizontal arrows indicate the start and end time of the spectroscopic observations by IRIS and EIS, as well as VLA. The black vertical arrow indicates roughly the time of the microflare understudy. Unfortunately this flare was not observed by EIS and VLA.

work we focus on studying the small flare around 18:20 UT, that was observed by both IRIS and NuSTAR. While NuSTAR also observed the previous B-class flare around 18 UT, which occurred in the same active region (see Sect. 2.3), as well as a larger flare around 20 UT, these two events were not observed under the IRIS spectrograph slit. Unfortunately, the 18:20 UT microflare was not observed by Hinode/EIS and VLA, so we do not focus on these instruments in this work.

Figure 2 shows an overview of the B-class flare under study as observed by the Atmospheric Imaging Assembly (AIA) 304 Å (panel a) and 94 Å (panel b) filters, showing plasma formed at around $7 \cdot 10^6$ K (7 MK, respectively O'Dwyer et al., 2010; Martínez-Sykora et al., 2011; Boerner et al., 2012; Testa and Reale, 2012, see Sect. 2.1). The 94 Å images have been processed to isolate the contribution from the Fe XVIII line, using an established linear combination of the flux observed in AIA's 94, 171 and 211 Å channels (Del Zanna, 2013). An animation associated with Figure 2 shows the evolution of the plasma emission over time. The larger and smaller boxes overlaid on the AIA images indicate the field-of-view (FOV) of the IRIS Slit-Jaw Imager (SJI) and spectrograph respectively. Panel c) shows an image from the IRIS SJI C II 1,330 Å filter, dominated by plasma formed at $T \approx 10–40 \cdot 10^3$ K (10–40 kK). The bright structure visible in both the 304 Å and the IRIS SJI images is the mini-ribbon of the B flare, where we observe interesting spectral features in the IRIS data. We describe these features in detail in Section 2.2. The analysis of the NuSTAR hard X-ray observations is described in Section 2.3.

2.1 SDO observations

Extreme ultraviolet (EUV) context data from the Atmospheric Imaging Assembly (AIA; Lemen et al., 2012) on-board the Solar Dynamics Observatory spacecraft (Pesnell et al., 2012, SDO) is utilized as a large FOV context to our spectroscopic observations, for co-alignment between IRIS and NuSTAR observations, and to account for NuSTAR's inherent pointing uncertainty when performing solar observations, as discussed in Section 2.3. The AIA 94 Å channel contains two temperature response peaks. The higher of the two is centered around 7 MK (e.g., O'Dwyer et al., 2010; Boerner et al., 2012; Testa and Reale, 2012), making it sensitive to temperatures measured by NuSTAR for flaring plasma. AIA 94 Å context images were made for the 18:20 UT flare, as well as the background time utilized in NuSTAR analysis. We isolate the higher temperature response peak in the 94 Å channel due to Fe XVIII via a linear combination of observed flux from AIA's 94, 171, and 211 Å channels (Del Zanna, 2013). We have also used AIA 304 Å and 1600 Å images as context to our observations and to co-align the IRIS and AIA observations. Both filters show the cooler emission from the small ribbon that is also visible in the SJI images (see Figure 2).

We also analyze photospheric vector magnetograms and line-of-sight magnetic field intensities provided by the Helioseismic and Magnetic Imager (Scherrer et al., 2012, HMI) on board SDO. We use HMI data to derive a magnetic field extrapolation and obtain information about the magnetic connectivity of the flare loops under study (Sect. 6), which is useful to compare the results of the spectroscopic observations and models (Sect. 7). Both AIA images and HMI line-of-sight magnetic field intensity maps were processed and corrected for instrumental effects by using the standard *SolarSoft* routine `aia_prep.pro`.

2.2 IRIS observations

Since July 2013, IRIS has been providing far ultraviolet (FUV) and near ultraviolet (NUV) images and spectra of the solar

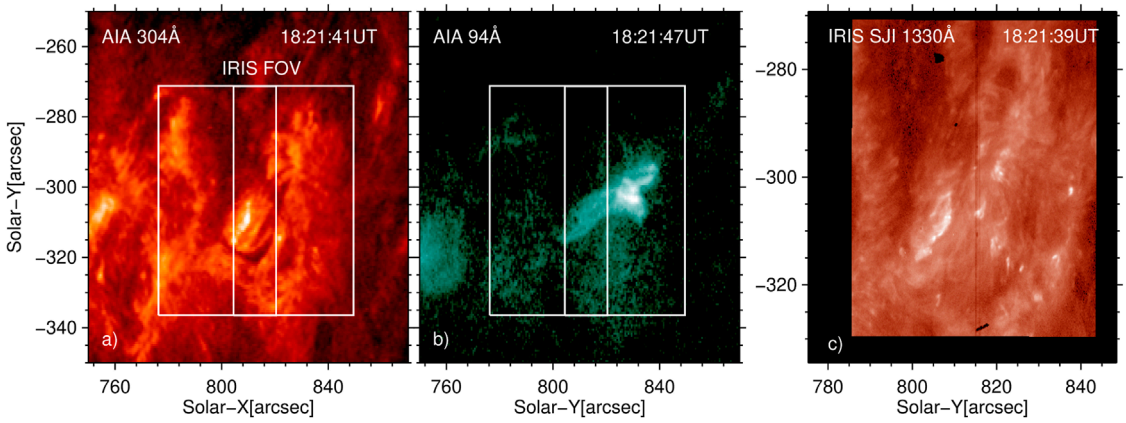

FIGURE 2
B-class flares around 18:20 UT as observed by the AIA 304 Å (Panel **A**), 94Å (Panel **B**) channels and the IRIS SJI 1330 Å (Panel **C**) channel. The IRIS FOV is also overlaid on the AIA images. An animation of this figure is available.

atmosphere, from the photosphere to low corona, at very high spatial (0.33–0.4″), spectral (2.7 km s^{-1} per pixel) and temporal resolution (down to 1s or less in high-cadence flare mode, De Pontieu et al., 2014). The IRIS spectrograph channel observes line and continua formed over a broad range of temperatures, from logT [K] ≈ 3.5–7. Simultaneously, the IRIS Slit-Jaw Imager (SJI) provides high-resolution (0.33″) context images in four individual filters (C II 1330 Å, Si IV 1400 Å, Mg II k 2796 Å and Mg II h wing 2803 Å). Thanks to its unique instrumental capabilities, IRIS has significantly improved our understanding of the energy deposition in the lower atmosphere during flares (e.g., see De Pontieu et al., 2021, for a recent review).

The IRIS dataset under study was a part of a medium coarse 8-step raster observation, that ran between 13:59:21–22:58:59UT on 29 April 2021. A "coarse" raster means that there is a 2″ separation between consecutive IRIS slit positions. The medium raster FOV was ≈4″× 60″, and the raster cadence was ≈75s, with an average raster step cadence of 8 s. IRIS SJI images in the 1330 Å filter were also taken with a cadence of 10 s over a ≈59″× 60″ FOV. In this work, we use level 2 IRIS data, which have been corrected for a number of instrumental issues, including geometric, dark and flat-field calibration, and correction for the wavelength orbital variation (De Pontieu et al., 2014; Wülser et al., 2018).

2.3 NuSTAR observations

The Nuclear Spectroscopic Telescope ARray (NuSTAR), is a NASA small explorer mission launched in 2012. The instrument consists of two co-aligned direct-focusing HXR telescopes, with a 12′× 12′ FOV and angular resolution FWHM of 18″ (Harrison et al., 2013). The identical CdZnTe solid-state focal plane detectors are made up of four pixel detector arrays (Madsen et al., 2015). Both detectors are used to improve sensitivity, and are defined as focal plane module A (FPMA) and focal plane module B (FPMB). NuSTAR is primarily an astrophysical observatory, with a total observation range of 3–79 keV. When used for solar observations, NuSTAR is limited to observing between 2.5–13 keV due to high count rates at low energies dominating the livetime during solar observations (Grefenstette et al., 2016). NuSTAR also experiences an uncertainty in absolute pointing of one to two arcmin when performing solar observations, which is accounted for by co-aligning NuSTAR data to AIA 94 Å images utilizing Sunpy's `calculate_match_template_shift` function.

NuSTAR's spatial data during this orbit is complex, with the active region producing two flares in different locations during a relatively short timescale. The first flare, occurring at 18:08 UT, is located at the eastern side of the active region. After this flare, the second flare occurs at 18:20 UT in the west, as shown in Figure 3. A background emission was measured at 18:40 UT after the second flare, with a background temperature of 4.4 MK found. Due to the quick succession of the flares, plasma heated above the background temperature is still present in the eastern region during the impulsive phase of the second flare. Because of this circumstance, we have carefully chosen source and background regions for spectroscopy, which will be further discussed in Sect. 4.2.

3 IRIS spectral observations in the small flare ribbon

We focus on the spectroscopic analysis of the small flare ribbon observed by IRIS under the slit in the Si IV (T ≈ 80 kK) line, formed in the transition region, as well as the C II, Mg II k and Mg II triplet lines, formed at different heights across the chromosphere (Leenaarts et al., 2013a; b; Pereira et al., 2015).

Figure 4 shows an overview of the IRIS spectral observations during the B-class flare around 18:20 UT. Panels a) and f) show context images from the IRIS SJI 1330 Å (dominated by C II emission) and AIA 94 Å filters respectively, with the IRIS raster FOV overlaid. The 94 Å images were processed to isolate the Fe XVIII emission, as mentioned earlier in the text. A movie associated with Figure 4 and 6 shows the evolution of the emission and spectral parameters as a function of time. Panels b)–e) and g)–l) show the IRIS spectrograph data in the same FOV. In particular, panels b)–d) show the Si IV line intensity, Doppler shift velocity and

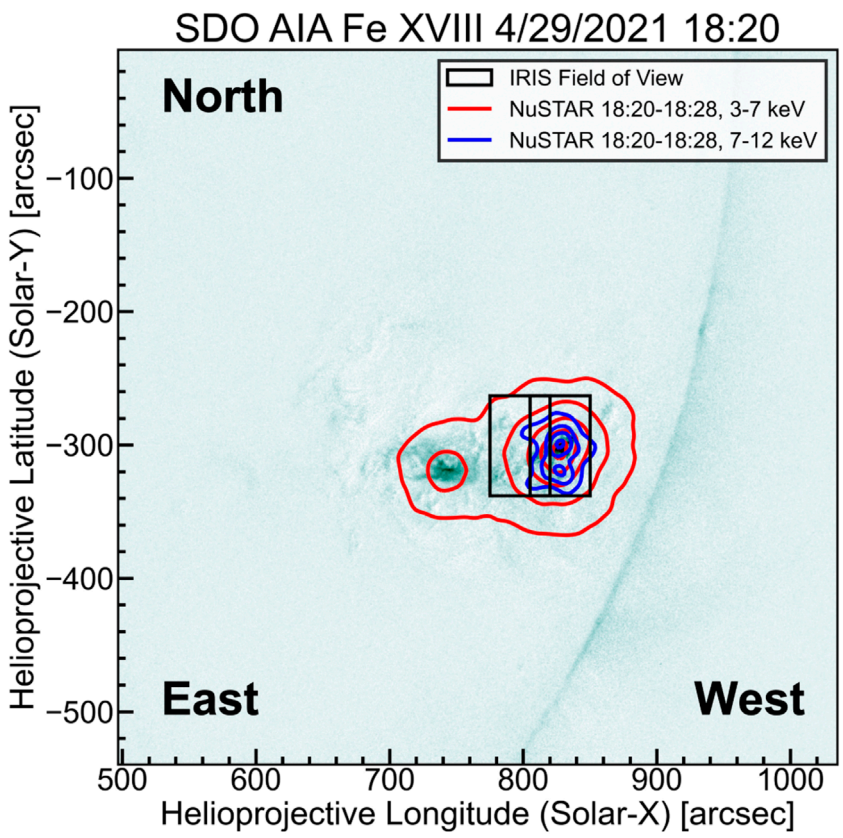

FIGURE 3
NuSTAR 25, 50, 75 and 95 percent contours of 3–7 keV (red) and 7–12 keV (blue) cross-correlated to AIA 94 Å to account for NuSTAR's pointing uncertainty during solar observations. The IRIS FOV is shown in black, with the thin middle rectangle representing IRIS's slit capable of spectroscopy. The western flare occurring at 18:20 UTC, shown on the right, is the primary subject of this study.

full-width at half maximum (FWHM) as calculated by performing a single Gaussian fit image of the raster pixels, while panel e) shows the red-blue asymmetry (RB) of the Si IV line. The RB asymmetry describes the level of asymmetry of the line wings as compared to the peak and was calculated using the IDL routine `gen_rb_profile_err.pro`, available within the IRIS *SolarSoft* distribution and described by Tian et al. (2011). In this figure, we are showing the asymmetry calculated between ±30 km s^{-1} from the line peak assuming a velocity interval of 5 km s^{-1}. In addition, panels g)–i) show the Mg II k3 intensity, k2 peak difference and separation, respectively. The location of k3 and the k2 peaks for a typical Mg II k reversed profile are shown in Figure 5G) for convenience. For the optically thick Mg II line, Figure 4G) provides measurements of either the intensity of the reversed line core, when the line exhibits the typically central reverse profile (e.g., Figure 5G), or the peak intensity, when the line has a "single-peaked" type of profile (e.g., Figure 5C). The k2 peak difference and separation are calculated following formulas described in Polito et al. (2023), and they are ≈0 in case of single peaked type of profiles. Finally, panel l) shows the intensity of the Mg II triplet line, calculated by integrating the intensity across the line profile between 2798.57 Å and 2799.1 Å, after subtracting a background taken between 2798 Å and 2798.3 Å (following Polito et al., 2023). Stronger intensities in panel l) (reversed color scale) indicate that the line is in emission, in contrast to a typical quiet Sun profile, where the lines would be mostly in absorption (Pereira et al., 2015).

Figure 4 shows that the Si IV line is either blue shifted or red shifted in the ribbons. The cross and diamond symbols in the IRIS rasters indicate pixels where we observe a Si IV blueshift (of the order of 20–30 km s^{-1}) and a gentle redshift (less than 5 km s^{-1}) respectively. The Si IV, C II, Mg II and Mg II triplet spectra in these positions are shown in the top and bottom panels of Figure 5, respectively. In the same location as that of the Si IV blueshifted spectra we also see an increase in the FWHM and blue asymmetry of the line, as well as a decrease in the peak difference and separation of the Mg II k line. A closer look to the spectra in Figure 5 reveals that the chromospheric lines in the locations of the Si IV blue shift within the small ribbon are characterized by a small line center reversal, with spectra that more closely resemble single peaked profiles, with no or small centroid Doppler shift for Mg II (but a small blueshift for C II), as well as an increased Mg II triplet emission. For comparison, the spectra observed in the location indicated by the diamond symbol exhibit Mg II and C II chromospheric spectra with a stronger center reversal, but similarly enhanced Mg II triplet emission. The variability in the behavior of these lines is consistent with the wide range of spectral features found in the statistical study of Testa et al. (2020) and the follow-up work by Cho et al. (2023), and with the predictions of RADYN simulations by Polito et al. (2018).

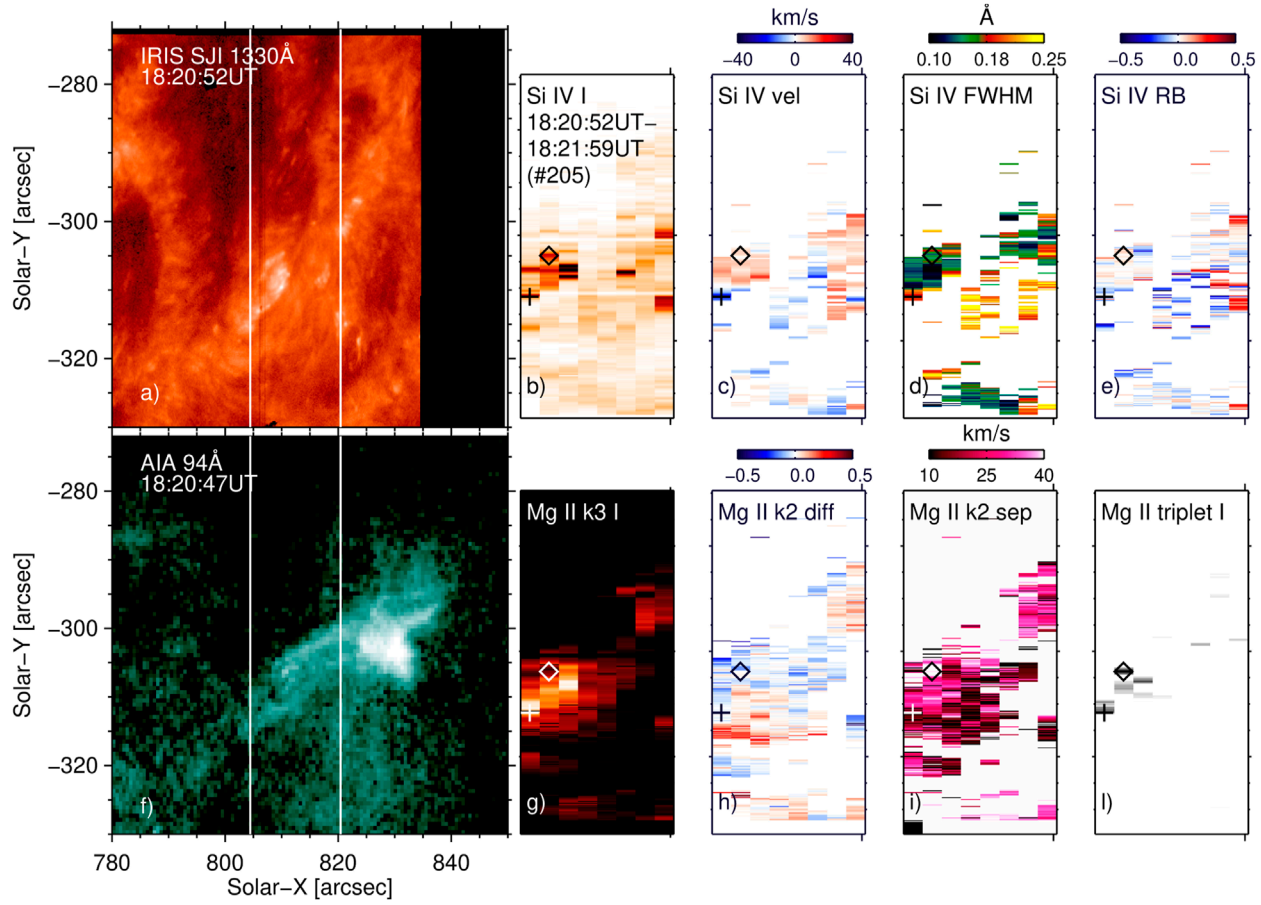

FIGURE 4
Observation of the B class flare around 18:20:50UT. Panel **(A)** IRIS SJI image in 1330 Å filter with the spectrograph FOV overlaid. Panels **(B–E)** IRIS spectroscopic observations in the Si IV line (intensity, Doppler shift velocity, FWHM and red-blue asymmetry. Panel **(F)** AIA 94 Å image with the IRIS spectrograph FOV overlaid. Panels **(G–L)** IRIS spectroscopic observations in the Mg II line (intensity, k_2 peak difference and separation) and intensity of the Mg II triplet line. The cross and diamond symbols in the IRIS spectroscopic rasters indicates a position where we observe respectively blueshifts and redshifts in the Si IV line in the mini-ribbon. An animation of this figure is available.

Figure 6 shows the same quantities as those of Figure 4 for the following IRIS raster (about 1 min later). The triangle symbol in this panel shows the location of a Si IV blue shift (also ≈25–30 km s^{-1}) that occurs in the same IRIS pixel as in the previous raster. The blue shift in this location is observed for 3 consecutive IRIS rasters, or about 4 min. This time period is significantly longer than for the events analyzed by Testa et al. (2020) who have presented statistical studies of IRIS brightenings in the ribbons for small nano or microflare events, and found Si IV brightenings with lifetime between 5 and 40s. However, for a significantly larger statistical sample (~1100 events) of these small AR core heating events, Cho et al. (2023) find a somewhat uniform distribution of durations of Si IV brightenings up to 60 s, which was used as an upper limit of their selection criteria, therefore strongly suggesting a broad distribution of brightness duration for these events, and the presence of similar longer-lived events like the one studied here. Also, since the cadence of the raster in our observation is approximately 75 s, it is not clear whether the Si IV blueshift might have a shorter lifetime and simply appear and disappear in the same pixel within consecutive rasters as a consequence of recurring heating events in the same IRIS pixel (although possibly in separate field lines). The spectra shown in Figure 7 for the later blueshift indicated by the diamond symbol are relatively similar to those in Figure 5. Further, we note that the C II line tends to be blueshifted (or with a blueshifted center reversal) in all 3 locations.

As mentioned in Sect. 1, it has been shown that Si IV blueshifts and Mg II triplet enhanced emission are crucial indirect signatures for the presence of non-thermal electrons (Testa et al., 2014; Polito et al., 2018; Testa et al., 2020). In this observation, for the first time in this type of study, we also have direct measurements of the accelerated electrons from NuSTAR, as described in the next Section.

4 Direct measurement of the accelerated electron distribution

In this section, we describe the spectral analysis of the NuSTAR data. Such analysis is crucial to confirm whether accelerated electrons are present in the small flare (as suggested by the IRIS

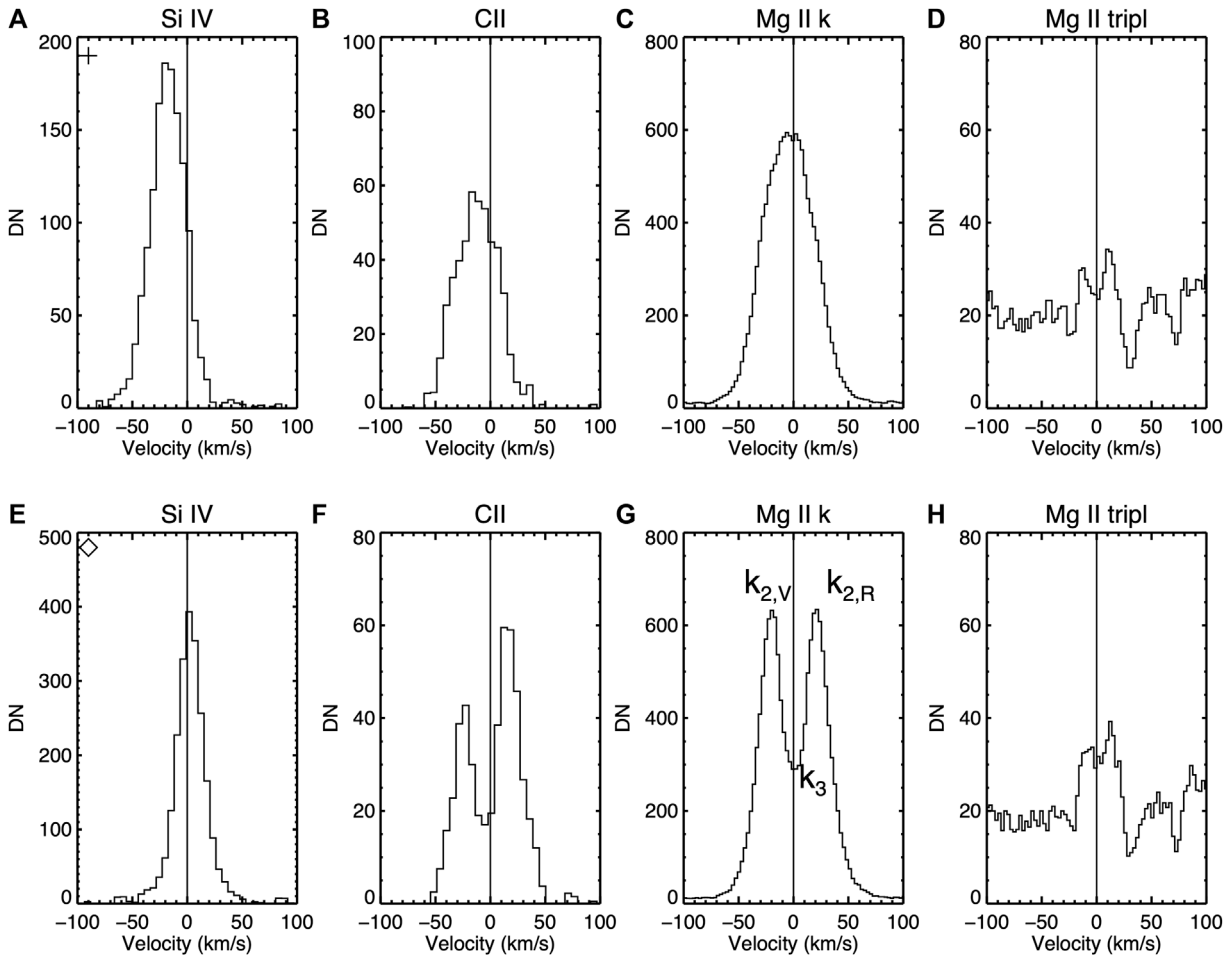

FIGURE 5
Spectra of IRIS lines : Si IV, CII, Mg II k and Mg II triplet in the location indicated by the cross **(A–D)** and diamond **(E–H)** in panels **(B–E)** and **(G–L)** of Figure 4.

spectral observations), and to provide measurements of the electron-beam distribution to guide the models (Sect. 5).

4.1 Temporal analysis

The lightcurves for this NuSTAR observation are shown in Figure 8. The middle two panels are livetime-corrected count rates for NuSTAR, separated into low and high energies. The top panel shows the total GOES short- and long-wavelength X-ray Sensor (XRS) SXR flux. The bottom panel includes both the high and low energy NuSTAR lightcurves, normalized to arbitrary units to best compare their time profiles. The derivatives of the NuSTAR 3–7 keV count rate and the long-wavelength GOES XRS flux, with a 2-min boxcar average to account for noise, are also included.

The NuSTAR lightcurve displays noticeable similarities to those of larger flares and the standard flare model. The higher energy NuSTAR lightcurve shows an earlier peak time and greater impulsivity than the lower energy range. The change in lightcurve profile is at ~7keV, which matches well to the found cutoff energies for accelerated electrons in spectral fitting (discussed in Section 4.2). Notably, the NuSTAR low energy and GOES SXR derivatives match the profile of the higher energy HXR lightcurve, exhibiting the Neupert effect (Neupert, 1968). The Neupert effect is often used to address the potential for non-thermal signatures. The derivative of SXR or EUV emission matching that of the higher energy HXRs suggests that thermal emission results from heating by accelerated electron beams (Neupert, 1968; Veronig et al., 2002; Dennis et al., 2003).

4.2 Spectral analysis

Spectroscopy of the 18:20 UT flare was performed using the X-ray spectral fitting package OSPEX and was independently confirmed using the package XSPEC. A 2-min window during the impulsive phase of the flare, highlighted in red in Figure 8, was used for spectral fitting. This early-flare phase was used in order to best search for signatures of accelerated electrons.

Solar observations result in significantly higher count rates than those experienced by NuSTAR when observing its astrophysical targets. Therefore, the detectors must be checked for pileup (discussed in Grefenstette et al., 2016; Appendix C). Detector pileup may occur when multiple photons enter a single pixel within a

10.3389/fspas.2023.1214901

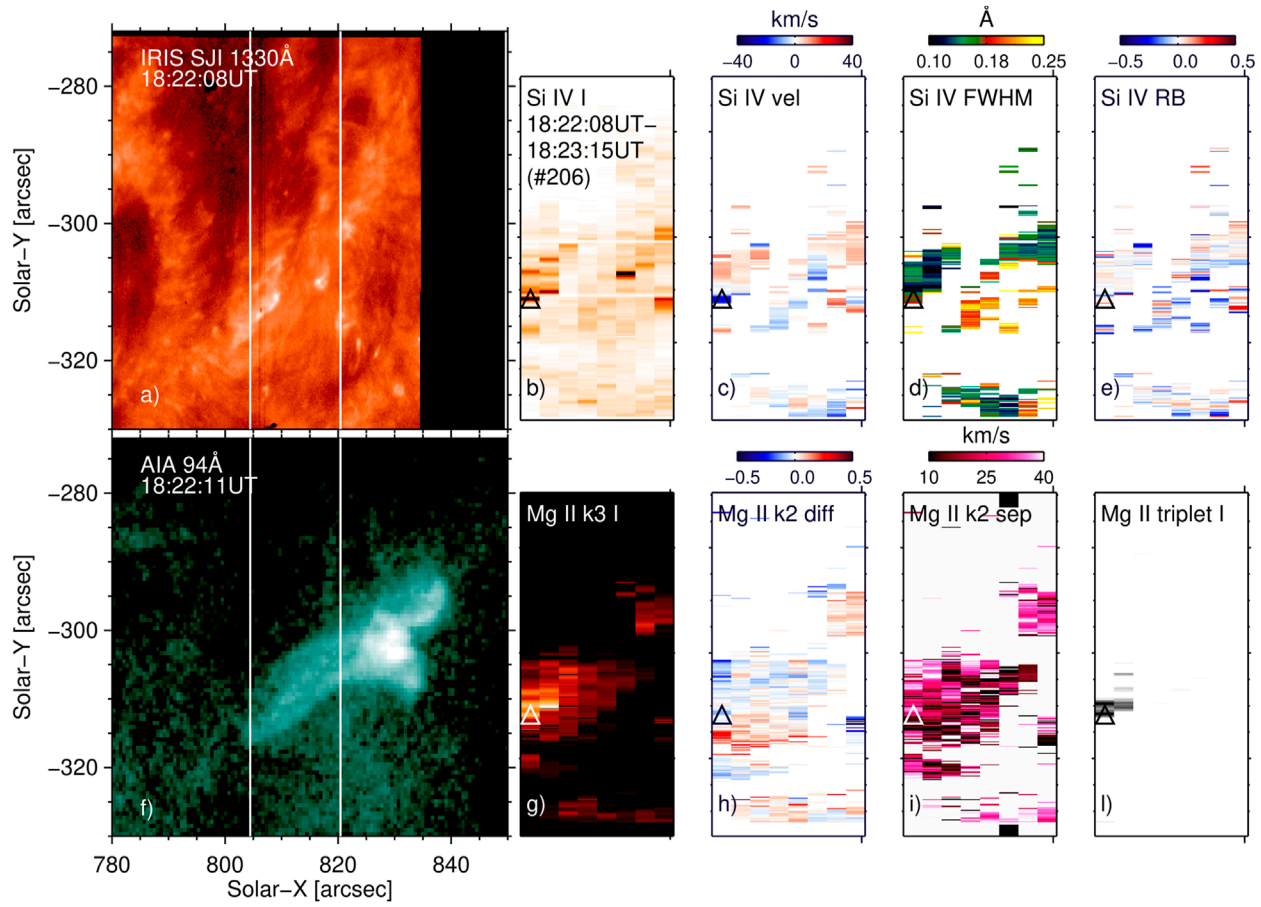

FIGURE 6
Observation of the B class flare around 18:22UT. For a description of the panels, see Figure 4. The triangle symbol in the IRIS spectroscopic rasters indicates a position where we observe blueshifts in the Si IV line in the mini-ribbon. An animation of this figure is available.

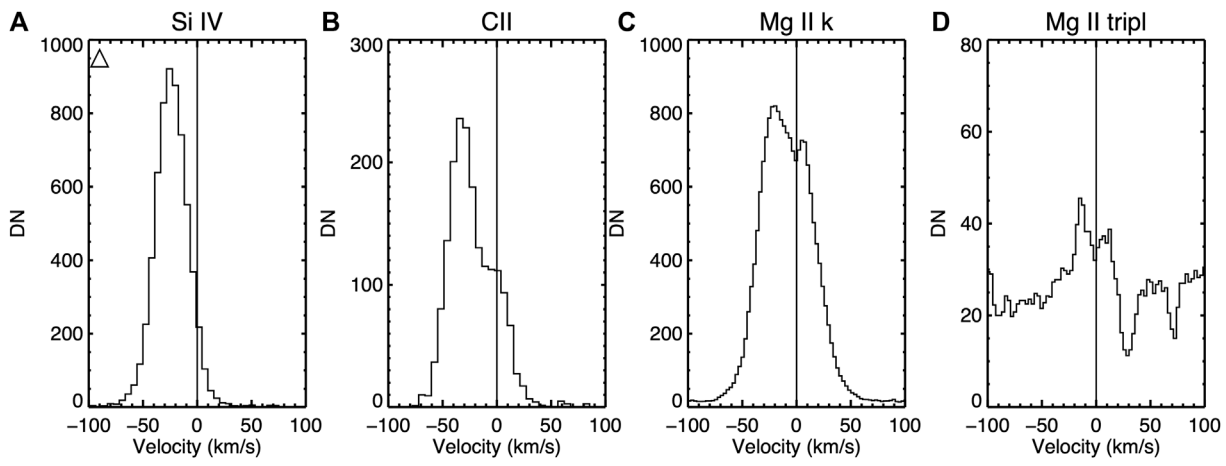

FIGURE 7
Spectra of IRIS lines : Si IV, CII, Mg II k and Mg II triplet in the location indicated by the triangle **(A–D)** in panels **(B–E)** and **(G–L)** of Figure 6.

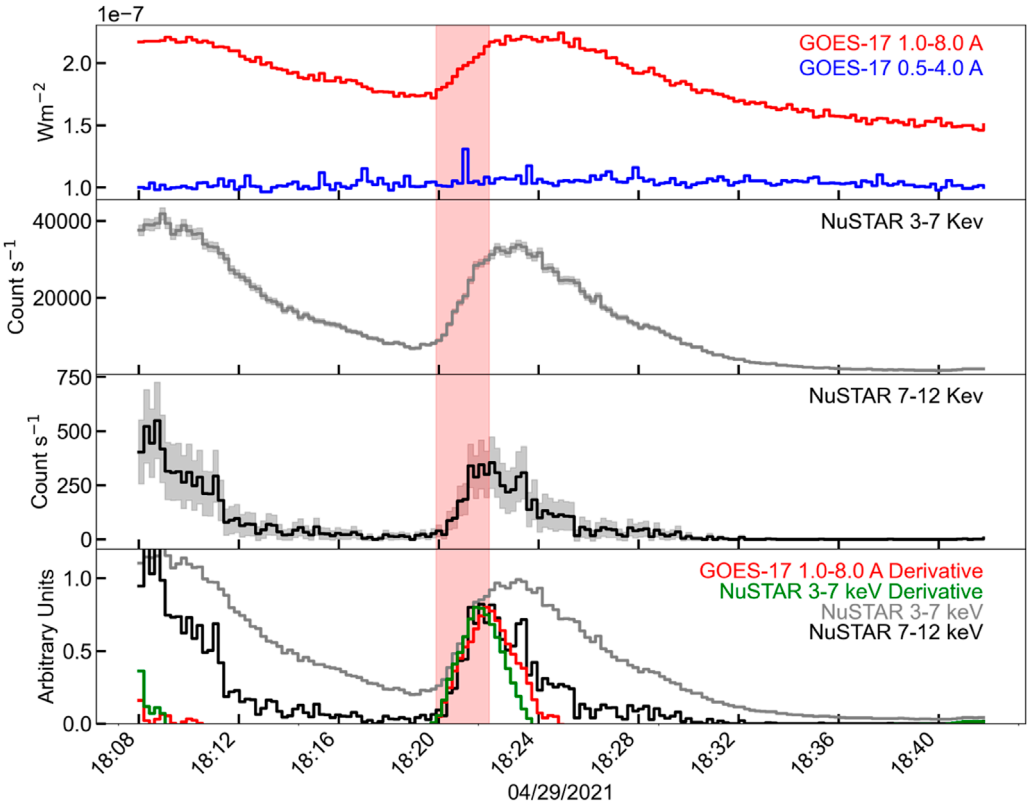

FIGURE 8
GOES and NuSTAR lightcurves, with the red shaded region representing the 2-min interval used for spectroscopy. Panel 1 shows the GOES XRS long and short-wavelength soft-xray flux. Panels 2 and 3 show the NuSTAR livetime-corrected lightcurves, separating the lower (3–7 keV) and higher (7–12 keV) energies. Panel 4 shows both NuSTAR lightcurves, and both the NuSTAR 3–7 keV and GOES 1.0–8.0 A derivatives (with 2-min boxcar averages) normalized to arbitrary units. The earlier peak of the higher energy NuSTAR lightcurve, with the NuSTAR low energy and GOES SXR derivatives matching that lightcurve, is indicative of the Neupert effect and suggests that the highest-energy NuSTAR emission is non-thermal.

single measurement time, but are only recorded as a single event Harrison et al. (2013). NuSTAR events track the pattern of pixels in which charge was measured, or "grade." Pulse pileup conditions may be checked by looking at the event rate of "unphysical grades"—combinations that are impossible to achieve from a single photon. The number of events per grade was calculated for the unphysical grades, and found to be a negligible fraction of the total events. Therefore, pileup effects are considered to be negligible in this analysis. Due to the significantly low detector livetimes (<1%), a gain calibration correction must be performed when doing spectroscopy on NuSTAR solar events. This gain correction is performed by allowing the gain slope of FPMA and FPMB to be independent free parameters during a spectral fit, and is discussed in detail in the Appendix of Duncan et al. (2021). For this event, the gain correction was performed using the XSPEC spectroscopy package.

In this microflare, a thermal background of temperature 4.4 MK was measured at 18:40–18:42 UT and utilized in spectral fitting. The 4.4 MK background temperature is similar to thermal temperatures found when performing spectral fitting on the same region during other non-flaring intervals on the same day. No gain correction was performed for the background interval, as it was not found to be necessary based on the criteria described in Duncan et al. (2021).

Counts used for spectral fitting of both the flare and the background were limited to the western side of the active region, in order to eliminate emission from the previous eastern 18:08 UT flare. The eastern NuSTAR source lies ~100 arcsec from the source of interest. Given that NuSTAR's PSF drops by at least an order of magnitude at a distance of ~100 arcsec (Koglin et al., 2011; Madsen et al., 2015), and given that the eastern source is much fainter than our source of interest, the contamination from the eastern source at our flare site is negligible. Spectral fitting over the 2-min window was performed for this eastern post-flare region, in order to assess the physical implications of excluding emission from that side. A double thermal model, including a temperature very close to the 4.4 MK background and a higher temperature component, was found to be the best fit for the eastern area. This indicates that this additional thermal component is leftover cooling plasma from the 18:08 UT flare and is unrelated to the western flare. Since the eastern region showed no non-thermal signatures and is outside of IRIS's FOV, the area was excluded from NuSTAR spectral fitting in order to best compare the results with IRIS observations and RADYN simulations.

Spectral fitting in XSPEC (Arnaud, 1996) was used to ascertain the gain correction and for an initial assessment of whether

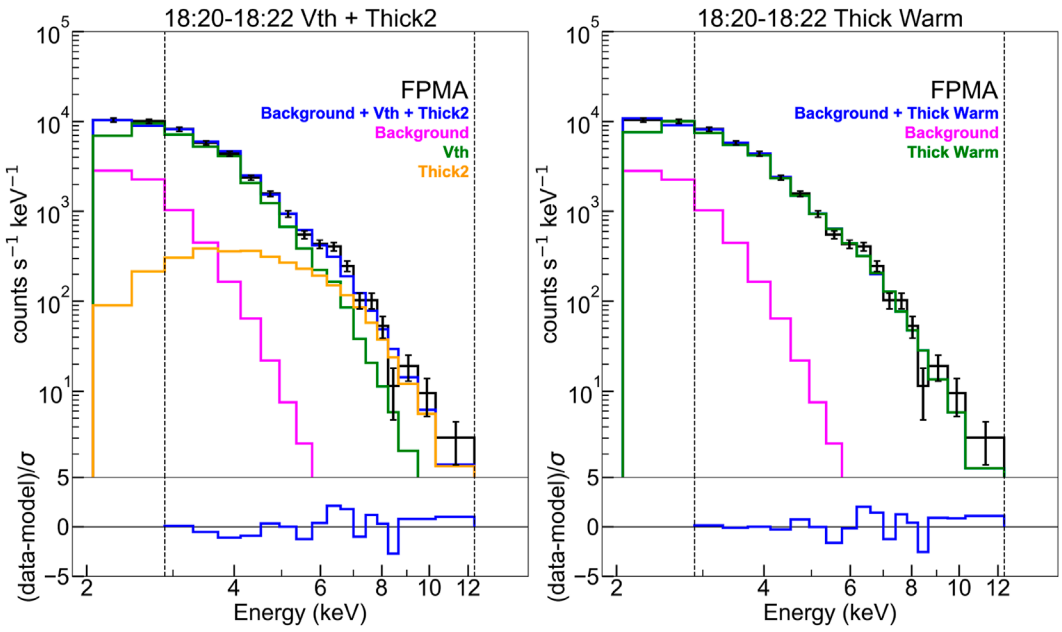

FIGURE 9
NuSTAR data from telescope FPMA was fit in OSPEX to model the electron distribution directly using the vth + thick2 (left) and thick warm (right) models. The thermal background taken at 18:40 UT is included, the fit is corrected for gain, and the count spectrum is pileup corrected. Modeling the electron distribution allows for a direct measurement of the cutoff energy parameter, which was found to be ≈8 keV.

non-thermal electrons were present in this microflare. Finding that particle acceleration was indeed present, we then used the OSPEX fitting tool for the rest of the analysis. OSPEX allows to directly fit a thick-target non-thermal electron distribution to the X-ray data. NuSTAR non-thermal flares are assumed to be thick-target sources in that all electrons presumably lose their suprathermal energy to collisions with the ambient plasma within the observation region.

The best fit statistic is achieved by the model that includes a non-thermal component, indicating the presence of accelerated electrons. A double thermal fit was also considered, but the double thermal model requires the higher temperature plasma component to have a superhot temperature of ~50 MK, a temperature that has only been observed in large M or X class flares (Caspi et al., 2014).

The OSPEX thermal plus non-thermal model results are shown in Figure 9, and their parameter results are listed in Table 1. Both a cold thick target model (background + vth + thick2) and a warm thick target model (background + thick warm) were fit. The warm thick target fit did not require an additional thermal component, and the plasma temperature and density were set as free parameters. The fit parameters obtained by the warm thick target model closely resemble those achieved using the cold thick target model, affirming the use of the cold thick target model as an accurate approximation of this flare.

Thermal and non-thermal energies are calculated for the cold thick target model. The thermal energy may be calculated by assuming an isothermal plasma for each vth component. The thermal energy may be up to a few times greater than this isothermal approximation due to cooler components NuSTAR is not sensitive to (Aschwanden et al., 2015). The thermal energy is given by.

$$U_T = 3k_B T\sqrt{\mathrm{EM}fV} \quad [\mathrm{erg}] \tag{1}$$

$$U_T \approx 1\times 10^{28} \quad [\mathrm{erg}] \tag{2}$$

with the emission measure EM and temperature T taken from the vth fit. The filling factor f is assumed to be unity. The thermal energy is an order of magnitude estimate. For the thick warm calculation, $\sqrt{\mathrm{EM}fV}$ is replaced with nV, with n representing the emission measure. The volume V was calculated from the AIA 94 Å images, solving for the area and converting to volume via $A^{3/2} = V$. The AIA 94 Å data was cropped to the region used for spectroscopy, and thresholded to only the flaring region by subtracting the 18:40 UT background.

The non-thermal energy is found by multiplying the non-thermal power by the spectral observation window, in this case 2 minutes. If the electron spectrum F(ϵ) above the cutoff energy is assumed to be a power law of index δ, the non-thermal energy for the vth + thick2 model may be calculated as.

$$U_N(E>E_C) = P(E>E_C)\Delta t = \int_{E_C}^{\infty} \mathrm{F}(\epsilon)\,\mathrm{E}dE\Delta t$$

$$\approx 1.6\times 10^{-9}\frac{\delta-1}{\delta-2}NE_C\Delta t \quad [\mathrm{erg}] \tag{3}$$

$$U_N(E>E_C) = 2.3^{+0.9}_{-0.9}\times 10^{28} \quad [\mathrm{erg}] \tag{4}$$

with N representing the number of electrons per second, δ the electron spectral index, and E_C the cutoff energy—all parameters fit by OSPEX.

TABLE 1 Fit parameters for the background and OSPEX models, as well as the gain correction and fit statistic. All fits, including the background, include only the Western flaring region. The background was taken at 18:40 UT, after the flare. The thermal background component was held fixed for all spectral fitting of the source.

Background: vth					
vth					
Temperature	Emission Measure [cm^{-3}]	Gain Correction			
$4.4^{+0.1}_{-0.1}$	$1.4^{+0.2}_{-0.2} \times 10^{46}$	No Gain Correction			
Microflare model: OSPEX background + vth + thick2					
vth		thick2			
Temperature [MK]	Emission Measure [cm^{-3}]	Electron Index δ	Cutoff Energy [keV]	Gain Correction	χ^2
$8.3^{+0.5}_{-0.5}$	$5.3^{+1.1}_{-1.1} \times 10^{45}$	$9.4^{+1.9}_{-1.9}$	$7.7^{+0.6}_{-0.6}$	0.96	1.84
Microflare model: OSPEX background + thick warm					
thick warm					
Plasma Temperature [MK]	Plasma Density [cm^{-3}]	Electron Index δ	Cutoff Energy [keV]	Gain Correction	χ^2
$7.7^{+0.6}_{-0.6}$	$1.44^{+0.3}_{-0.3}$	$9.9^{+1.4}_{-1.4}$	$7.3^{+0.5}_{-0.5}$	0.96	2.00

5 Modeling

5.1 RADYN simulations

The IRIS observations provide crucial information about the response of the plasma to the energy release in the lower atmosphere. At the same time, NuSTAR observations provide direct constraints on the energy distributions of the accelerated electrons in the corona. In order to find evidence for the physical mechanisms driving the flare, we run hydrodynamic simulations using the RADYN code (e.g., Carlsson and Stein, 1992; Allred et al., 2005; 2015; Carlsson et al., 2015), which solves the equation of radiative hydrodynamics on a 1-dimensional (1D) adaptive grid (Dorfi and Drury, 1987). A key property of RADYN is the ability to perform non-local thermodynamic equilibrium (non-LTE) radiative transfer for species which are important for chromospheric energy balance (e.g., H, He and Ca). Other atomic species are included as background continuum opacity sources (in LTE) using the Uppsala opacity package (Gustafsson, 1973). The radiative losses for optically thin lines are calculated using the CHIANTI 7.1 (Dere et al., 1997; Landi et al., 2013) database assuming ionization and thermal equilibrium.

RADYN simulates flare heating assuming different possible physical mechanisms: accelerated non-thermal electrons streaming from the corona to the chromosphere, whose propagation is treated using the Fokker-Planck equation (Allred et al., 2015); *in-situ* heating in the corona and consequent energy transport to the lower atmosphere via thermal conduction; or dissipation of Alfvén waves (Kerr et al., 2016). Since we have direct observations of accelerated electrons from NuSTAR, here we focus on the first mechanism.

We run simulations which covered a range of electron beam parameters and initial conditions of the flare loops, as summarized below.

- Energy flux (F) = $3 \cdot 10^8$–$5 \cdot 10^9$ ergs s^{-1} cm^{-2} (3F8–5F9)
- Energy cut-off (E_C) = 4–9 keV
- Spectral index (δ) = 9–11
- Initial temperature at loop apex = 1MK and 3 MK (with apex densities = $10^{8.7}$ and $10^{9.6}$ cm^{-3} respectively)

We use values of E_C and δ which are close to those provided by the NuSTAR spectral analysis, within uncertainties. We simulate a broader range of values for the energy flux, since this parameter is not completely constrained by NuSTAR, as it depends also on the area over which the electrons deposit their energy (as discussed in Sect. 6). We use the same "plage-like" atmospheres presented in Polito et al. (2018), and we also assume half-loop lengths of 15 Mm. Our choice of loop length and initial temperatures is motivated by the larger parameter studies presented in Polito et al. (2018) and Testa et al. (2020). In particular, these studies have demonstrated that simulations with different loop lengths and the same initial temperature provide very similar trends (e.g., Figure A1 of Polito et al., 2018). Testa et al. (2014) and Polito et al. (2018) also showed that using hotter and denser initial loop atmospheres (e.g., 5 MK loop with apex density of ≈ 10^{10} cm^3) results in less heating of the lower atmosphere for smaller events such as this B1 flare under study. Finally, given the uncertainty in the duration of the blue shifts in individual IRIS pixels due to the relatively long raster cadence of this observation, we assume here a heating duration of 10 s for simplicity, and we refer to future work for a more extended investigation of the effects of longer duration heating on the models (e.g., Testa et al., 2020; Cho et al., 2023).

5.2 Synthesis of IRIS spectral lines

We synthesize the emission of the IRIS Si IV spectral line using the values of density, temperature, and bulk velocity at each grid point and timestep from the RADYN simulations and atomic data from CHIANTI v.10 (Dere et al., 1997; Del Zanna et al.,

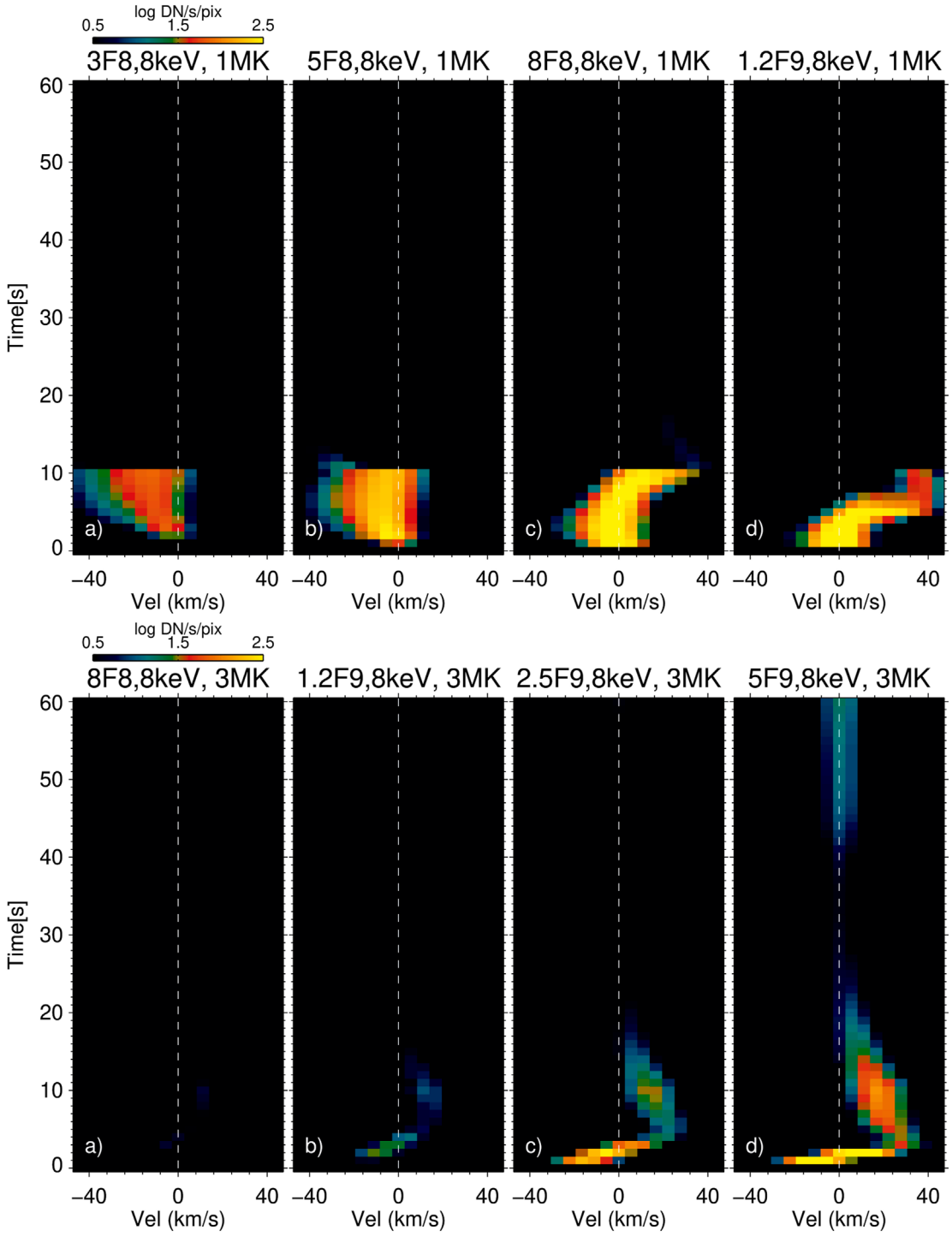

FIGURE 10
Time-velocity synthetic spectra of Si IV for different RADYN flare simulations. Top panels: simulations with an apex temperature of 1 MK, E_C = 8keV, δ = 10 keV, in different F = 3F8 **(A)**, 5F8 **(B)**, 8F8 **(C)** and 1.2F9 **(D)**. Bottom panels: same as top panels, with initial apex temperature of 3 MK, and F = 8F8 **(A)**, 1.2F9 **(B)**, 2.5F9 **(C)** and 5F9 **(D)**.

2021), assuming photospheric abundances (Asplund et al., 2009) and equilibrium ionization. We follow Eq 1 of Polito et al. (2018) to convert the synthetic spectra to units of DN s^{-1} $pixel^{-1}$. The time-velocity spectra described in Sect. 5.3 are then obtained by integrating the synthetic emission in each RADYN grid point along the loop as a function of time, assuming an exposure time of 1s and taking into account the instrumental broadening of 0.026 Å.

To synthesize the optically thick Mg II and C II spectra, we provide the input from our RADYN flare atmospheres (temperature, electron density, bulk velocity, hydrogen atomic level populations) as a function of time to the radiation transport code RH15D (Pereira and Uitenbroek, 2015). RH15D solves the equation of non-LTE radiation transport and atomic level populations and allows us to take into account the effects of partial redistribution (PRD), which can be important for the Mg II lines (Leenaarts et al., 2013a). The NLTE radiation transport equations were solved for H, Mg II and C II, with additional species solved in LTE as sources of background opacity. We add a microturbulence of 7 km s^{-1} as an additional source of line broadening mechanism in the chromosphere, consistent with the values reported in Carlsson et al. (2015), as well as a recent study by Sainz Dalda and De Pontieu (2022) based on inversions of IRIS Mg II profiles during flares. The synthetic Mg II and C II NUV spectra were converted to IRIS count rates using the same procedure described in Polito et al. (2018); Testa et al. (2020); Polito et al. (2023).

5.3 Comparison between observations and models

Figure 10 (top panel) shows Si IV synthetic spectra as a function of velocity (x-axis) and time (y-axis) for different RADYN flare simulations, assuming an initial apex temperature of 1 MK, E_C = 8keV, δ = 10, and different values of energy flux, according to the legend. The vertical dotted white lines indicate the position of the line at rest (assuming the reference wavelength available in CHIANTI v.10), and negative values here indicate blueshifts. The time-velocity plots show that when the energy flux is below $5 \cdot 10^8$ ergs s^{-1} cm^{-2} (5F8), the line is mostly blueshifted over time. On the other hand, as the flux energy increases, the line becomes more at-rest or red shifted. As described in detail in Polito et al. (2018), this different behavior is due to the fact that, in case of more gentle fluxes, the electrons can deposit their energy below the height formation of Si IV–and thus driving the Si IV evaporation–for a longer time. In these simulations it takes longer for the loop density to rise, meaning that the electrons can deposit energy in the lower atmosphere for a longer time. In fact, when the density is high enough, the electrons get stopped at higher heights and eventually drive a downflow of Si IV plasma. This shift from upflow to downflow happens much quicker in simulations with stronger energy flux (see Polito et al., 2018, for more details).

Figure 10 (bottom panels) shows Si IV synthetic spectra for models with an initial apex temperature of 3 MK. As also discussed in Polito et al. (2018), this hotter initial atmosphere is also denser (with apex density $10^{9.6}$ cm^{-3} compared to $10^{8.7}$ cm^{-3} for the 1MK loop), meaning that the electrons need comparatively higher energy to be able to heat the transition region and therefore drive an increase of intensity and brightenings in the Si IV line. This phenomenon is illustrated in Figure 10A), which shows that an energy flux of at least $1.2 \cdot 10^9$ ergs s^{-1} cm^{-2} (1.2F9) is needed to drive a response in the Si IV line. These results demonstrate that in order to reproduce the Si IV blueshift, one needs a certain combination of parameters for the electron beam distribution, which will also depend on the initial conditions.

Figure 11 shows a summary of Si IV Doppler shift velocities based on moment calculation for different models. Panel a) summarizes the Si IV Doppler shift velocity at the maximum intensity during the simulation, while panel b) shows the maximum blue shift velocity during the simulation. For both panels, we only consider spectra where the Si IV line is above a detection threshold of 10 DN for the total intensity of the line. For some simulations there is no associated data point in Figure 11B), which means that the Si IV line does not exhibit blue shifts in the detectable spectra. Figure 11 also shows that, in order to reproduce a significant (of 10 km s^{-1} or larger) Si IV blueshift for the range of E_C obtained from the NuSTAR observations, including uncertainties (i.e. 7–9 keV), we need an energy below $\approx 8 \cdot 10^8$ ergs s^{-1} cm^{-2} (8F8) for the 1MK loop or $\approx 5 \cdot 10^9$ ergs s^{-1} cm^{-2} (5F9) for the 3MK loop. Further, we note that for the 5F9 model, the maximum blueshift does not occur in the brightest spectrum of the simulation. Finally, Figure 11B) shows the impact of the initial temperature (and density) of the

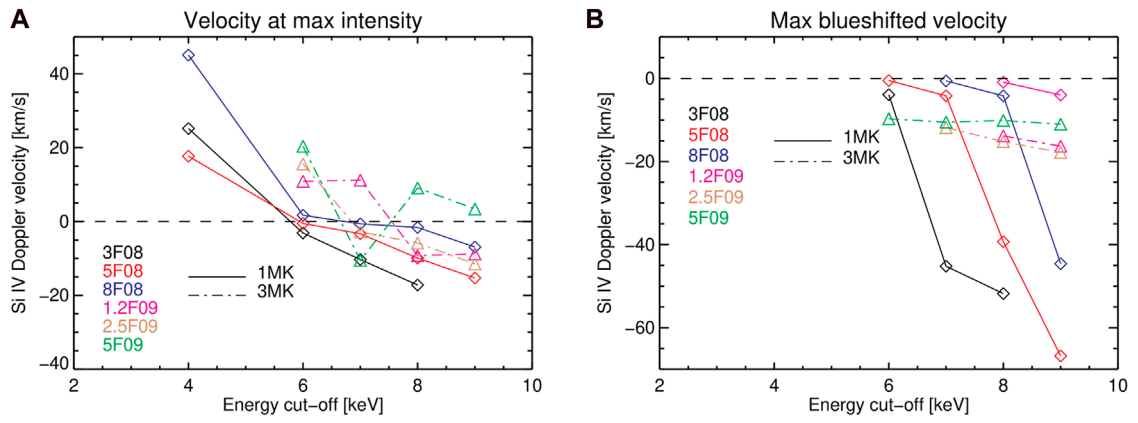

FIGURE 11
Summary of Si IV Doppler shifts as a function of E_C for different RADYN models. Panel **(A)** shows the line Doppler shifts at the time of maximum Si IV intensity during the simulation. Panel **(B)** shows the largest blueshift for each simulation. In both cases, we only analyze spectra which are strong enough to be observed (with total intensity greater than 10DN).

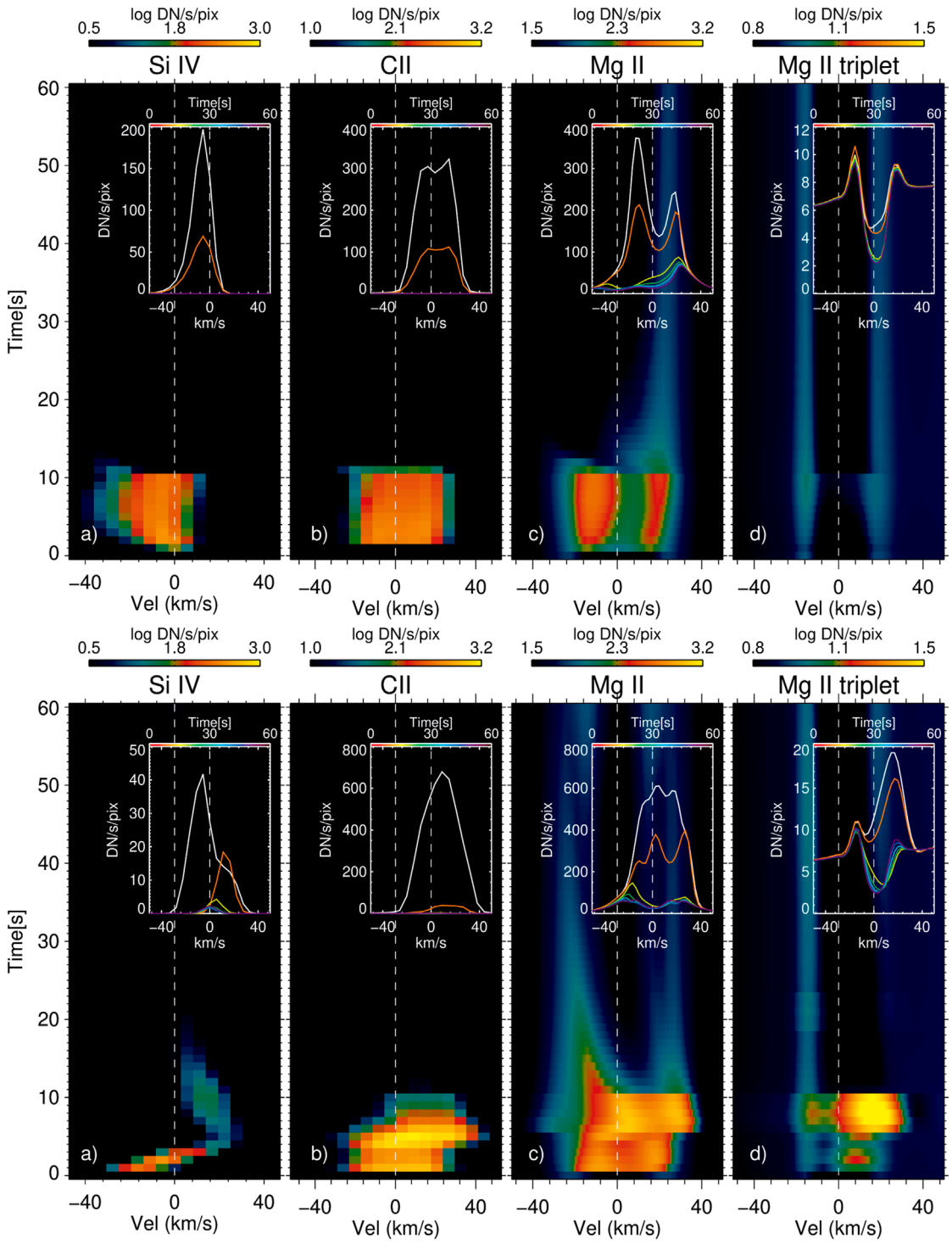

FIGURE 12
Top panels: Synthetic spectra from RADYN and RH simulations for the 5F8 flare model with E_C = 8 keV, δ = 10 and initial loop apex temperature of 1MK. The four panels show the: Si IV (Panel **A**), C II (Panel **B**), Mg II (Panel **C**) and Mg II triplet (Panel **D**) lines as a function of velocity and time. The insert on each panel shows the spectra averaged in time with a cadence of 8s, as indicated by the legend. Bottom panels: Same plots for the 2.5F9 flare model with E_C = 8 keV, δ = 10 and initial loop apex temperature of 3MK.

loop atmosphere on the magnitude of the Doppler shifts, with stronger Si IV blueshift values being observed in simulations with an initial lower temperature loop. This behavior was also discussed in Polito et al. (2018) and suggests that, although the observed values of blueshifts are slightly larger (≈-25–30 km s^{-1}) than the maximum blueshifts observed in the simulations with the 3MK loop, this might be due to some extent to the details of the initial physical conditions of the loops.

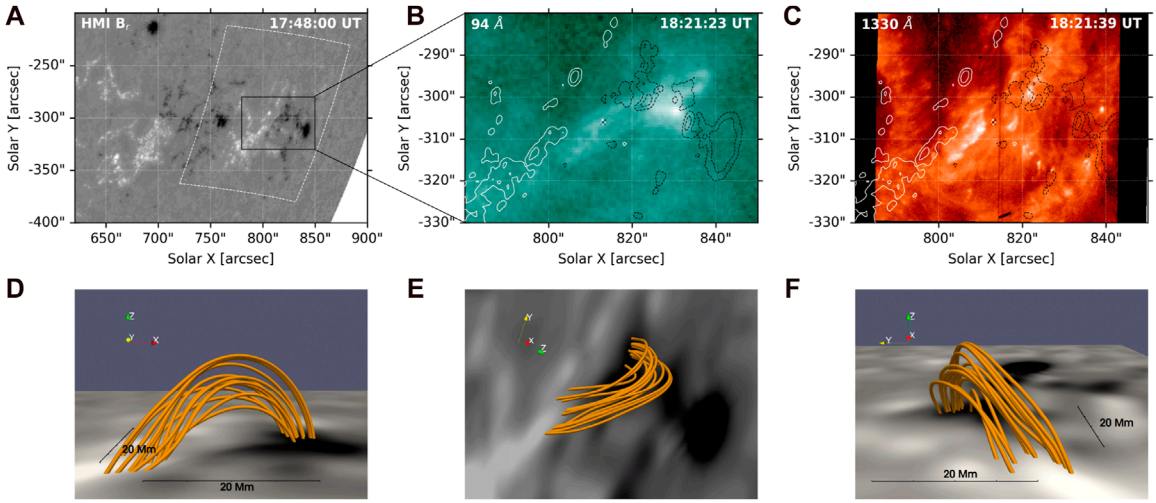

FIGURE 13
3D modeling of the NOAA 12821 Active region. Panel **(A)** Radial component of the photospheric magnetic field strength obtained at 17:48 UT, with the boundary data region for magnetic field extrapolation denoted by a white dashed box. Panel **(B–C)** AIA 94 Å image and IRIS SJI image in 1,330 Å filter, with their FOV indicated by a black solid box in panel **(A)**. Magnetic field strength contours of ±500 and ±1,000 Gauss overlaid, with the positive and negative polarity shown as white and black lines, respectively. Panel **(D–F)** Nonlinear force-free field (NLFFF) extrapolation model of the AR, viewed from Y-axis, line-of-sight, and X-axis perspectives. X- and Y-axes represent heliographic longitude and latitude on the solar disk, respectively, while Z-axis points radially from the solar center.

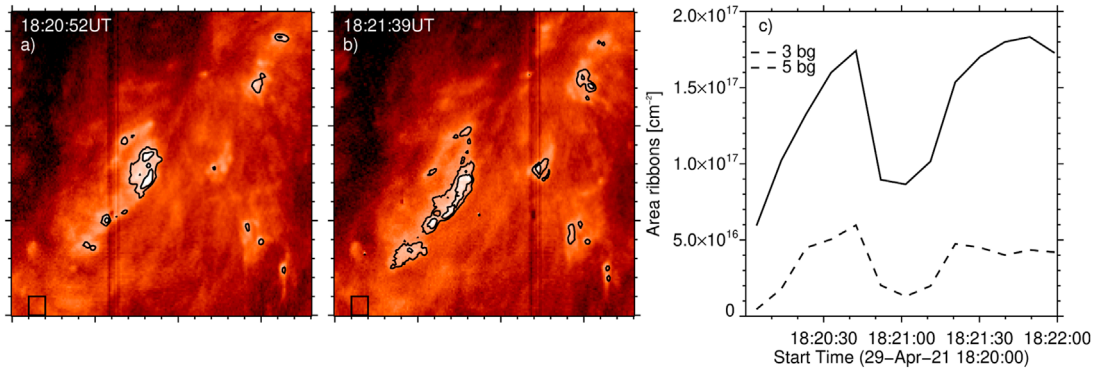

FIGURE 14
Estimation of the ribbon area from the IRIS UV images. Panel **(A, B)** show the SJI 1330 Å images at two time intervals during the flare. The contours show the intensity above 3 and 5 (dotted line) times the intensity of a chosen background area within the active region, which is highlighted by the small black boxes. Panel **(C)** shows the same contour areas as a function of time during the NuSTAR observation.

Previous work has shown that studying the response of the atmosphere to the flare heating by combining IRIS spectral lines formed at different heights from the chromosphere to the transition region, we can obtain even stricter constraints on the models (Polito et al., 2018; Testa et al., 2020). With this motivation in mind, we investigate in more detail the behavior of the chromospheric lines for those models where we succeed in reproducing the Si IV blueshifts. Figure 12 (top panels) shows synthetic spectra for the Si IV (Panel a), C II (Panel b), Mg II (Panel c) and Mg II triplet (Panel d) lines as a function of velocity and time for the 5F8 model with E_C = 8 keV, δ = 10 and initial loop apex temperature of 3MK. The bottom panels show the same quantities for the 2.5F9 flare model with E_C = 8 keV, δ = 10 and initial loop apex temperature of 3MK. Figure A2 in the Appendix also show the synthetic spectra of the IRIS lines for the 1.2F9 model and 3 MK loop. While these three models can to some extent explain the observed Si IV blueshifts, they are characterized by different behaviors in the synthetic spectra of the chromospheric lines. In particular, the Mg II k and triplet chromospheric lines in the simulations with the 1 MK loop are characterized by a deeper central reversal (Figure 12,

top panels c) and d)). A less pronounced center reversal (which is still deeper than that in the observed spectra) is also seen in the 1.2F9 model and 3 MK loop (Figure A2). On the other hand, the chromospheric spectra in the 2.5F9 flare model with the 3MK loop (Figure 12, bottom panels c) and d)) more closely resemble the key characteristics of the observed spectra. One main difference that remains is that, in all of the three models, the C II line appears to be red shifted or stationary, while in the observations the line is blueshifted. Another difference between models and observations is in the values of line width, which are smaller in the models than the observations. Such discrepancies are well-known and were discussed in detail in e.g. Testa et al. (2020), Cho et al. (2023). In particular, these previous studies pointed out the difficulty associated with comparing the results of a single loop model with observed spectral lines in one IRIS pixel, where heating episodes from many individual loop strands (possibly also with different physical conditions) might overlap. In addition, physical mechanisms such as turbulence and waves, which are missing from our models, may contribute to the discrepancy between the observed and simulated line widths.

In summary, despite their limitations, the models with an initial temperature of 3MK and energy flux in the range of 1.2–2.5F9 are capable of reproducing qualitative observational characteristics of the flare spectra (e.g., Si IV blueshift, lack of Mg II k deep central reversal and presence of increased Mg II triplet emission). We note that the initial higher temperature for the flare loops is more consistent also with the background temperature observed by NuSTAR of ≈ 4MK.

The comparison discussed here demonstrates how the models can provide a useful tool to constrain the properties of the heating. In order to compare the simulations with the results of the NuSTAR X-ray spectral analysis, we need to estimate the area over which the electrons might deposit their energy in the lower atmosphere. In Sect.6 we discuss how to derive this value using magnetic field extrapolations, while in Sect. 7 we compare both UV and X-ray observations with the predictions of the models and summarize our conclusions.

6 Magnetic field extrapolation

Figure 13 shows an overview of the three-dimensional (3D) magnetic field modeling of the AR 12821 under study. In particular, panels a), b) and c) show: the radial component of the photospheric magnetic field from HMI, AIA 94 Å and IRIS SJI 1330 Å images respectively for context to the magnetic field extrapolation. Panels d), e) and f) show a nonlinear force-free field (NLFFF) extrapolation model of the active region with different line-of-sight views. The HMI radial magnetic field in panel a) and vector magnetogram data used for the extrapolation are taken just before the beginning of the flare activity in the AR complex 12820/12821 as to minimize the possible impact on the photosphere. The images in panels b) and c) are taken at the same time as that in Figure 14. The extrapolation was performed using the optimization algorithm from Wiegelmann et al. (2012), with a Cartesian grid of 970 km per pixel.

The comparison between the extrapolation and the AIA and IRIS SJI images confirms that the event under study occurs in the eastern part of the active region. This comparison has enabled us to determine the magnetic connectivity of the loops visible in the AIA 94 Å images and the ribbons observed by IRIS. The extrapolation also suggests that the flare loops are rooted between the larger and more elongated ribbon observed in the IRIS SJI images at approximately 810″ in solar X direction, and the more fragmented brightenings located to the west at around 820″.

Figure 14 (panels a) and b)) shows the IRIS SJI 1330 Å images at two time intervals during the flare, with overlaid contours highlighting the image intensity above 3 and 5 (dotted line) times a background intensity. The location where we measure the background is indicated by the small black boxes in panels a) and b) and is chosen to be within the AR but outside the ribbons. After comparison between these images and Figure 13 we suggest that the ribbon area identified by the contours roughly represents the region where the flare loops are rooted. Further, panel c) shows the time evolution of the contour areas. We take these values as an approximation of the area over which the electrons may deposit their energy over time. Such assumption is not perfect and provides just an order of magnitude estimate, but we cannot obtain a more accurate estimate since the NuSTAR spatial resolution does not allow us to measure the area of the X-ray footpoints. Using this method, we find that the estimated area $A_{min/max}$ for the ribbons is $\approx 4.6 \cdot 10^{15}$ to $1.8 \cdot 10^{17}$ cm^2.

7 Discussion and conclusion

We have analyzed rare coordinated IRIS and NuSTAR observations of a small B-class microflare on 29 April 2021, which provide independent diagnostics of non-thermal particles and therefore a unique opportunity to constrain the properties of accelerated particles in small heating events. The IRIS slit observes the largest flare ribbon, and analysis of the IRIS spectral lines show peculiar spectral characteristics in some of the pixels (e.g., Si IV blueshift and enhanced Mg II triplet emission), which, as extensively described in our previous works (e.g., Testa et al., 2014; Polito et al., 2018; Testa et al., 2020; Cho et al., 2023), are indirect signatures of the presence of non-thermal electrons in the lower atmosphere. Here we focus on the spectra characterized by Si IV blueshifts because those are the unique spectral signatures of non-thermal particles, but we note that Si IV redshifts are also observed in other locations along the ribbon (and can be also due to non-thermal particles under certain conditions; see, e.g., Testa et al., 2014; Polito et al., 2018; Testa et al., 2020). Direct confirmation for the presence of accelerated electrons in the corona is independently provided by the NuSTAR spectral investigation which observes the hard X-ray emission.

We compare the IRIS spectral observations with the predictions of RADYN hydrodynamic models assuming flare heating by accelerated electron beams, and use the measurements of the electron beam parameters from NuSTAR to guide our parameter space of the simulations. In particular, we simulate models with a range of low-energy cutoff and spectral index values that are consistent with those observed with NuSTAR. As mentioned earlier, the only parameter that we cannot directly compare with the models is the electron energy flux, as that requires an estimation of the

area over which the electrons deposit their energy, which is not known with great accuracy. In Sect. 6, we provide some order of magnitude estimates for such area based on the IRIS UV images. Using those values and the energy flux measured by NuSTAR, we obtain the following values of energy flux F for the electron beams:

$$E_{NuSTAR} = 1.9 \cdot 10^{26}\ ergs\ s^{-1} \tag{5}$$

$$F = \frac{E_{NuSTAR}}{A_{min/max}} = \frac{1.9 \cdot 10^{26}}{4.6 \cdot 10^{15}/1.8 \cdot 10^{17}}\ ergs\ s^{-1} cm^{-2}$$
$$= 1.0 \cdot 10^{9} - 4.1 \cdot 10^{10}\ ergs\ s^{-1}\ cm^{-2} \tag{6}$$

The comparison between the IRIS transition region and chromospheric line spectra and the RADYN simulations suggest that the best candidate models to explain the observations are electron-beam heating models with $F \approx 1.2–2.5 \cdot 10^{9}$ ergs s^{-1} cm^{-2} and an initial apex temperature of 3MK. These values are consistent with the lower range of F independently estimated from NuSTAR in Eq. 6. If non-thermal energy calculations for the warm thick target model are used, the computed NuSTAR energy flux range is $1.6 \cdot 10^{9}$–$9.0 \cdot 10^{10}$, which still overlaps the energy flux range of the electron-beam heating models. A direct comparison of the energy estimate from the RADYN simulations that best reproduce the IRIS observations and that obtained by NuSTAR can be affected by a number of factors, including but not limited to: (1) the uncertainty in the estimate of the ribbon area, as discussed in Sect. 6; (2) difference between energy released in the corona (measured by NuSTAR) and energy dissipated in the ribbons (where IRIS is observing); (3) inhomogeneities on how the energy is distributed in different locations along the ribbons (also suggested by the different behavior of the Si IV Doppler shifts). We should also mention the different timescales involved in our analysis: we integrated the NuSTAR spectra over a period of about 2 min to increase the signal-to-noise ratio, while the IRIS exposure time is 8 s with a raster cadence of ≈ 75 s. Therefore, it is possible that the energy release varies during the 2 min of the NuSTAR observations. HXR observations with high enough sensitivity to detect small energetic events at significantly higher cadence are not available at the moment and would be highly desirable in the future. Despite these possible sources of uncertainty, we find a reasonable agreement between the energy estimate between different methods.

In conclusion, this work demonstrates that combining UV and X-ray spectral observations from IRIS and NuSTAR with state-of-art simulations can provide crucial diagnostics of flare heating models. We have also presented a consistent picture based on independent measurements of non-thermal particle acceleration in the corona and the response of the lower atmospheric plasma to the non-thermal energy deposition.

Given the difficulty associated with coordinating different instruments, including a single-slit spectrograph, catching a flare in the right location and at the same time, it is not surprising that this is the first of such studies that we were able to perform. We hope to expand this work in the near future by obtaining larger statistics of IRIS and NuSTAR coordinated events and by comparing the observations with an extended range of models, including longer duration heating and different initial conditions for the loops (following other recent broader investigations such as that of Testa et al., 2020; Cho et al., 2023).

Data availability statement

Publicly available datasets were analyzed in this study. This data can be found here: https://iris.lmsal.com, https://heasarc.gsfc.nasa.gov/docs/nustar/nustar_archive.html, https://sdo.gsfc.nasa.gov/data/aiahmi/.

Author contributions

VP led the analysis of the IRIS observations and modeling and MP led the analysis of the NuSTAR observations. LG assisted MP on the NuSTAR analysis. PT and Dr. Kathy KR assisted VP on the IRIS and AIA analysis, and PT also assisted with the interpretation of RADYN models and their comparison with the observations. XS performed the magnetic field extrapolation, and SY worked on the 3D visualization of the extrapolation results. JD acquired the NuSTAR data used in this manuscript. All authors contributed to the article and approved the submitted version.

Funding

VP, SY, KR and XS acknowledge support from NASA Heliophysics System Observatory Connect Grant # 80NSSC20K1283. VP also acknowledges support from NASA ROSES Heliophysics Guest Investigator program (Grant# NASA 80NSSC20K0716) and from NASA under contract NNG09FA40C(*IRIS*). LG and MP acknowledge the NSF CAREER grant AGS1752268 and NASA Guest Observer grant 80NSSC21K0135. PT was supported by contract 8100002705 (*IRIS*) to the Smithsonian Astrophysical Observatory, and NASA grant 80NSSC20K1272. SY and VP acknowledge support from NASA Early Career Investigator Program (Grant# NASA 80NSSC21K0623). JD's research was supported by an appointment to the NASA Postdoctoral Program at the NASA Goddard Space Flight Center, administered by Oak Ridge Associated Universities under contract with NASA. Resources supporting this work were provided by the NASA High-End Computing (HEC) Program through the NASA Advanced Supercomputing (NAS) Division at Ames Research Center.

Acknowledgments

CHIANTI is a collaborative project involving George Mason University, the University of Michigan (United States), and the University of Cambridge (United Kingdom). AIA and HMI data are courtesy of NASA/SDO and the AIA and HMI science team. IRIS is a NASA small explorer mission developed and

operated by LMSAL with mission operations executed at NASA Ames Research center and major contributions to downlink communications funded by ESA and the Norwegian Space Centre. This paper made use of data from the NuSTAR mission, a project led by the California Institute of Technology, managed by the Jet Propulsion Laboratory, funded by the National Aeronautics and Space Administration.

Conflict of interest

The authors declare that the research was conducted in the absence of any commercial or financial relationships that could be construed as a potential conflict of interest.

Publisher's note

Supplementary material

The Supplementary Material for this article can be found online at: https://www.frontiersin.org/articles/10.3389/fspas.2023.1214901/full#supplementary-material

References

Allred, J. C., Hawley, S. L., Abbett, W. P., and Carlsson, M. (2005). Radiative hydrodynamic models of the optical and ultraviolet emission from solar flares. *Apj* 630, 573–586. doi:10.1086/431751

Allred, J. C., Kowalski, A. F., and Carlsson, M. (2015). A unified computational model for solar and stellar flares. *Apj* 809, 104. doi:10.1088/0004-637X/809/1/104

Arnaud, K. A. (1996). "Xspec: the first ten years," in *Astronomical data analysis software and systems V of astronomical society of the pacific conference series*. Editors G. H. Jacoby, and J. Barnes, 101, 17.

Aschwanden, M. J., Boerner, P., Ryan, D., Caspi, A., McTiernan, J. M., and Warren, H. P. (2015). Global energetics of solar flares: II. Thermal energies. *Apj* 802, 53. doi:10.1088/0004-637X/802/1/53

Asplund, M., Grevesse, N., Sauval, A. J., and Scott, P. (2009). The chemical composition of the Sun. *ARA&A* 47, 481–522. doi:10.1146/annurev.astro.46.060407.145222

Benz, A. O. (2008). Flare observations. *Living Rev. Sol. Phys.* 5, 1. doi:10.12942/lrsp-2008-1

Boerner, P., Edwards, C., Lemen, J., Rausch, A., Schrijver, C., Shine, R., et al. (2012). Initial calibration of the atmospheric imaging assembly (AIA) on the solar Dynamics observatory (SDO). *Sol. Phys.* 275, 41–66. doi:10.1007/s11207-011-9804-8

Carlsson, M., Leenaarts, J., and De Pontieu, B. (2015). What do IRIS observations of Mg II k tell us about the solar plage chromosphere? *ApJ* 809, L30. doi:10.1088/2041-8205/809/2/L30

Carlsson, M., and Stein, R. F. (1992). Non-LTE radiating acoustic shocks and CA II K2V bright points. *ApJ* 397, L59–L62. doi:10.1086/186544

Caspi, A., Krucker, S., and Lin, R. P. (2014). Statistical properties of super-hot solar flares. *ApJ* 781, 43. doi:10.1088/0004-637X/781/1/43

Cho, K., Testa, P., De Pontieu, B., and Polito, V. (2023). A statistical study of IRIS observational signatures of nanoflares and nonthermal particles. *ApJ* 945, 143. doi:10.3847/1538-4357/acb7da

Christe, S., Hannah, I. G., Krucker, S., McTiernan, J., and Lin, R. P. (2008). RHESSI microflare statistics. I. Flare-finding and frequency distributions. *ApJ* 677, 1385–1394. doi:10.1086/529011

Cooper, K., Hannah, I. G., Grefenstette, B. W., Glesener, L., Krucker, S., Hudson, H. S., et al. (2020). NuSTAR observation of a minuscule microflare in a solar active region. *ApJ* 893, L40. doi:10.3847/2041-8213/ab873e

Cooper, K., Hannah, I. G., Grefenstette, B. W., Glesener, L., Krucker, S., Hudson, H. S., et al. (2021). NuSTAR observations of a repeatedly microflaring active region. *MNRAS* 507, 3936–3951. doi:10.1093/mnras/stab2283

De Pontieu, B., Polito, V., Hansteen, V., Testa, P., Reeves, K. K., Antolin, P., et al. (2021). A new view of the solar Interface region from the Interface region imaging spectrograph (IRIS). *Sol. Phys.* 296, 84. doi:10.1007/s11207-021-01826-0

De Pontieu, B., Title, A. M., Lemen, J. R., Kushner, G. D., Akin, D. J., Allard, B., et al. (2014). The Interface region imaging spectrograph (IRIS). *Sol. Phys.* 289, 2733–2779. doi:10.1007/s11207-014-0485-y

Del Zanna, G., Dere, K. P., Young, P. R., and Landi, E. (2021). CHIANTI—an atomic database for emission lines. XVI. Version 10, further extensions. *ApJ* 909, 38. doi:10.3847/1538-4357/abd8ce

Del Zanna, G. (2013). The multi-thermal emission in solar active regions. *A&A* 558, A73. doi:10.1051/0004-6361/201321653

Dennis, B. R., Veronig, A., Schwartz, R. A., Sui, L., Tolbert, A. K., Zarro, D. M., et al. (2003). The neupert effect and new RHESSI measures of the total energy in electrons accelerated in solar flares. *Adv. Space Res.* 32, 2459–2464. doi:10.1016/S0273-1177(03)00884-6

Dere, K. P., Landi, E., Mason, H. E., Monsignori Fossi, B. C., and Young, P. R. (1997). Chianti - an atomic database for emission lines. *A&AS* 125, 149–173. doi:10.1051/aas:1997368

Dorfi, E. A., and Drury, L. O. (1987). Simple adaptive grids for 1-D initial value problems. *J. Comput. Phys.* 69, 175–195. doi:10.1016/0021-9991(87)90161-6

Duncan, J., Glesener, L., Grefenstette, B. W., Vievering, J., Hannah, I. G., Smith, D. M., et al. (2021). NuSTAR observation of energy release in 11 solar microflares. *ApJ* 908, 29. doi:10.3847/1538-4357/abca3d

Fletcher, L., Dennis, B. R., Hudson, H. S., Krucker, S., Phillips, K., Veronig, A., et al. (2011). An observational overview of solar flares. *Space Sci. Rev.* 159, 19–106. doi:10.1007/s11214-010-9701-8

Glesener, L., Krucker, S., Duncan, J., Hannah, I. G., Grefenstette, B. W., Chen, B., et al. (2020). Accelerated electrons observed down to <7 keV in a NuSTAR solar microflare. *ApJ* 891, L34. doi:10.3847/2041-8213/ab7341

Glesener, L., Krucker, S., Hannah, I. G., Hudson, H., Grefenstette, B. W., White, S. M., et al. (2017). NuSTAR hard X-ray observation of a sub-A class solar flare. *ApJ* 845, 122. doi:10.3847/1538-4357/aa80e9

Grefenstette, B. W., Glesener, L., Krucker, S., Hudson, H., Hannah, I. G., Smith, D. M., et al. (2016). The first focused hard X-ray images of the Sun with NuSTAR. *ApJ* 826, 20. doi:10.3847/0004-637X/826/1/20

Gustafsson, B. (1973). Uppsala astron. *Obs. Ann.* 5.

Hannah, I. G., Christe, S., Krucker, S., Hurford, G. J., Hudson, H. S., and Lin, R. P. (2008). RHESSI microflare statistics. II. X-ray imaging, spectroscopy, and energy distributions. *ApJ* 677, 704–718. doi:10.1086/529012

Hannah, I. G., Kleint, L., Krucker, S., Grefenstette, B. W., Glesener, L., Hudson, H. S., et al. (2019). Joint X-ray, EUV, and UV observations of a small microflare. *ApJ* 881, 109. doi:10.3847/1538-4357/ab2dfa

Harrison, F. A., Craig, W. W., Christensen, F. E., Hailey, C. J., Zhang, W. W., Boggs, S. E., et al. (2013). The nuclear spectroscopic telescope array (NuSTAR) high-energy X-ray mission. *ApJ* 770, 103. doi:10.1088/0004-637X/770/2/103

Hudson, H. S. (1991). Solar flares, microflares, nanoflares, and coronal heating. *Sol. Phys.* 133, 357–369. doi:10.1007/BF00149894

Kerr, G. S., Fletcher, L., Russell, A. J. B., and Allred, J. C. (2016). Simulations of the Mg II k and Ca II 8542 lines from an AlfvÉn wave-heated flare chromosphere. *ApJ* 827, 101. doi:10.3847/0004-637X/827/2/101

Koglin, J. E., An, H., Barrière, N., Brejnholt, N. F., Christensen, F. E., Craig, W. W., et al. (2011). "First results from the ground calibration of the NuSTAR flight optics," in *Society of photo-optical instrumentation engineers (SPIE) conference series of society of photo-optical instrumentation engineers (SPIE) conference series*. Editors S. L. O'Dell, and G. Pareschi, 8147, 81470J. doi:10.1117/12.895279

Landi, E., Young, P. R., Dere, K. P., Del Zanna, G., and Mason, H. E. (2013). CHIANTI—an atomic database for emission lines. XIII. Soft X-ray improvements and other changes. *ApJ* 763, 86. doi:10.1088/0004-637X/763/2/86

Leenaarts, J., a, T. M. D., Carlsson, M., Uitenbroek, H., and De Pontieu, B. (2013a). The Formation of iris diagnostics. I. A quintessential model atom of Mg II and general formation properties of the Mg II h&k lines. *ApJ* 772, 89. doi:10.1088/0004-637X/772/2/89

Leenaarts, J., Pereira, T. M. D., Carlsson, M., Uitenbroek, H., and De Pontieu, B. (2013b). The Formation of IRIS diagnostics. II. The formation of the Mg II h&k lines in the solar atmosphere. *ApJ* 772, 90. doi:10.1088/0004-637X/772/2/90

Lemen, J. R., Title, A. M., Akin, D. J., Boerner, P. F., Chou, C., Drake, J. F., et al. (2012). The atmospheric imaging assembly (AIA) on the solar Dynamics observatory (SDO). *Sol. Phys.* 275, 17–40. doi:10.1007/s11207-011-9776-8

Lin, R. P., Dennis, B. R., Hurford, G. J., Smith, D. M., Zehnder, A., Harvey, P. R., et al. (2002). The reuven ramaty high-energy solar spectroscopic imager (RHESSI). *Sol. Phys.* 210, 3–32. doi:10.1023/A:1022428818870

Madsen, K. K., Harrison, F. A., Markwardt, C. B., An, H., Grefenstette, B. W., Bachetti, M., et al. (2015). Calibration of the NuSTAR high-energy focusing X-ray telescope. *ApJS* 220, 8. doi:10.1088/0067-0049/220/1/8

Martínez-Sykora, J., De Pontieu, B., Testa, P., and Hansteen, V. (2011). Forward modeling of emission in solar Dynamics observatory/atmospheric imaging assembly passbands from dynamic three-dimensional simulations. *ApJ* 743, 23. doi:10.1088/0004-637X/743/1/23

Neupert, W. M. (1968). Comparison of solar X-ray line emission with microwave emission during flares. *ApJ* 153, L59. doi:10.1086/180220

O'Dwyer, B., Del Zanna, G., Mason, H. E., Weber, M. A., and Tripathi, D. (2010). SDO/AIA response to coronal hole, quiet Sun, active region, and flare plasma. *A&A* 521, A21. doi:10.1051/0004-6361/201014872

Parker, E. N. (1988). Nanoflares and the solar X-ray corona. *ApJ* 330, 474. doi:10.1086/166485

Pereira, T. M. D., Carlsson, M., De Pontieu, B., and Hansteen, V. (2015). The Formation of IRIS diagnostics. IV. The Mg II triplet lines as a new diagnostic for lower chromospheric heating. *ApJ* 806, 14. doi:10.1088/0004-637X/806/1/14

Pereira, T. M. D., and Uitenbroek, H. (2015). RH 1.5D: a massively parallel code for multi-level radiative transfer with partial frequency redistribution and zeeman polarisation. *A&A* 574, A3. doi:10.1051/0004-6361/201424785

Pesnell, W. D., Thompson, B. J., and Chamberlin, P. C. (2012). The solar Dynamics observatory (SDO). *Sol. Phys.* 275, 3–15. doi:10.1007/s11207-011-9841-3

Polito, V., Kerr, G. S., Xu, Y., Sadykov, V. M., and Lorincik, J. (2023). Solar flare ribbon fronts. I. Constraining flare energy deposition with IRIS spectroscopy. *ApJ* 944, 104. doi:10.3847/1538-4357/acaf7c

Polito, V., Reep, J. W., Reeves, K. K., Simões, P. J. A., Dudík, J., Del Zanna, G., et al. (2016). Simultaneous iris andhinode/eis observations and modeling of the 2014 october 27 X2.0 class flare. *Astrophysical J.* 816, 89. doi:10.3847/0004-637X/816/2/89

Polito, V., Testa, P., Allred, J., De Pontieu, B., Carlsson, M., Pereira, T. M. D., et al. (2018). Investigating the response of loop plasma to nanoflare heating using RADYN simulations. *ApJ* 856, 178. doi:10.3847/1538-4357/aab49e

Reale, F., Testa, P., Petralia, A., and Graham, D. R. (2019a). Impulsive coronal heating from large-scale magnetic rearrangements: from IRIS to SDO/AIA. *ApJ* 882, 7. doi:10.3847/1538-4357/ab304f

Reale, F., Testa, P., Petralia, A., and Kolotkov, D. Y. (2019b). Large-amplitude quasiperiodic pulsations as evidence of impulsive heating in hot transient loop systems detected in the EUV with SDO/AIA. *ApJ* 884, 131. doi:10.3847/1538-4357/ab4270

Rubio da Costa, F., Kleint, L., Petrosian, V., Liu, W., and Allred, J. C. (2016). Data-driven radiative hydrodynamic modeling of the 2014 march 29 X1.0 solar flare. *ApJ* 827, 38. doi:10.3847/0004-637X/827/1/38

Sainz Dalda, A., and De Pontieu, B. (2022). *Chromospheric thermodynamic conditions from inversions of complex Mg II h&k profiles observed in flares*. arXiv e-prints , arXiv:2211.05459.

Scherrer, P. H., Schou, J., Bush, R. I., Kosovichev, A. G., Bogart, R. S., Hoeksema, J. T., et al. (2012). The helioseismic and magnetic imager (HMI) investigation for the solar Dynamics observatory (SDO). *Sol. Phys.* 275, 207–227. doi:10.1007/s11207-011-9834-2

Shibata, K., and Magara, T. (2011). Solar flares: magnetohydrodynamic processes. *Living Rev. Sol. Phys.* 8, 6. doi:10.12942/lrsp-2011-6

Testa, P., De Pontieu, B., Allred, J., Carlsson, M., Reale, F., Daw, A., et al. (2014). Evidence of nonthermal particles in coronal loops heated impulsively by nanoflares. *Science* 346, 1255724. doi:10.1126/science.1255724

Testa, P., De Pontieu, B., Martínez-Sykora, J., DeLuca, E., Hansteen, V., Cirtain, J., et al. (2013). Observing coronal nanoflares in active region moss. *ApJ* 770, L1. doi:10.1088/2041-8205/770/1/L1

Testa, P., Polito, V., and De Pontieu, B. (2020). IRIS observations of short-term variability in moss associated with transient hot coronal loops. *ApJ* 889, 124. doi:10.3847/1538-4357/ab63cf

Testa, P., and Reale, F. (2012). Hinode/EIS spectroscopic validation of very hot plasma imaged with the solar Dynamics observatory in non-flaring active region cores. *ApJ* 750, L10. doi:10.1088/2041-8205/750/1/L10

Testa, P., and Reale, F. (2020). On the coronal temperature in solar microflares. *ApJ* 902, 31. doi:10.3847/1538-4357/abb36e

Testa, P., and Reale, F. (2022). *The solar X-ray corona*. arXiv e-prints , arXiv:2206.03530. doi:10.48550/arXiv.2206.03530

Tian, H., McIntosh, S. W., De Pontieu, B., Martínez-Sykora, J., Sechler, M., and Wang, X. (2011). Two components of the solar coronal emission revealed by extreme-ultraviolet spectroscopic observations. *ApJ* 738, 18. doi:10.1088/0004-637X/738/1/18

Veronig, A., Vršnak, B., Dennis, B. R., Temmer, M., Hanslmeier, A., and Magdalenić, J. (2002). Investigation of the Neupert effect in solar flares. I. Statistical properties and the evaporation model. *A&A* 392, 699–712. doi:10.1051/0004-6361:20020947

Wiegelmann, T., Thalmann, J. K., Inhester, B., Tadesse, T., Sun, X., and Hoeksema, J. T. (2012). How should one optimize nonlinear force-free coronal magnetic field extrapolations from SDO/HMI vector magnetograms? *Sol. Phys.* 281, 37–51. doi:10.1007/s11207-012-9966-z

Wright, P. J., Hannah, I. G., Grefenstette, B. W., Glesener, L., Krucker, S., Hudson, H. S., et al. (2017). Microflare heating of a solar active region observed with NuSTAR, Hinode/XRT, and SDO/AIA. *ApJ* 844, 132. doi:10.3847/1538-4357/aa7a59

Wülser, J. P., Jaeggli, S., De Pontieu, B., Tarbell, T., Boerner, P., Freeland, S., et al. (2018). Instrument calibration of the Interface region imaging spectrograph (IRIS) mission. *Sol. Phys.* 293, 149. doi:10.1007/s11207-018-1364-8

Appendix: Additional RADYN simulations

In this section we include synthetic spectra for additional RADYN simulations that were not essential to the main text. In particular, Figure A1 shows Si IV spectra for simulations with the same parameters but different values for the spectral index δ. Further, Figure A2 show synthetic spectra of all the IRIS lines for the 1.2F9 model with initial temperature of 3MK. See Section 5 for more details.

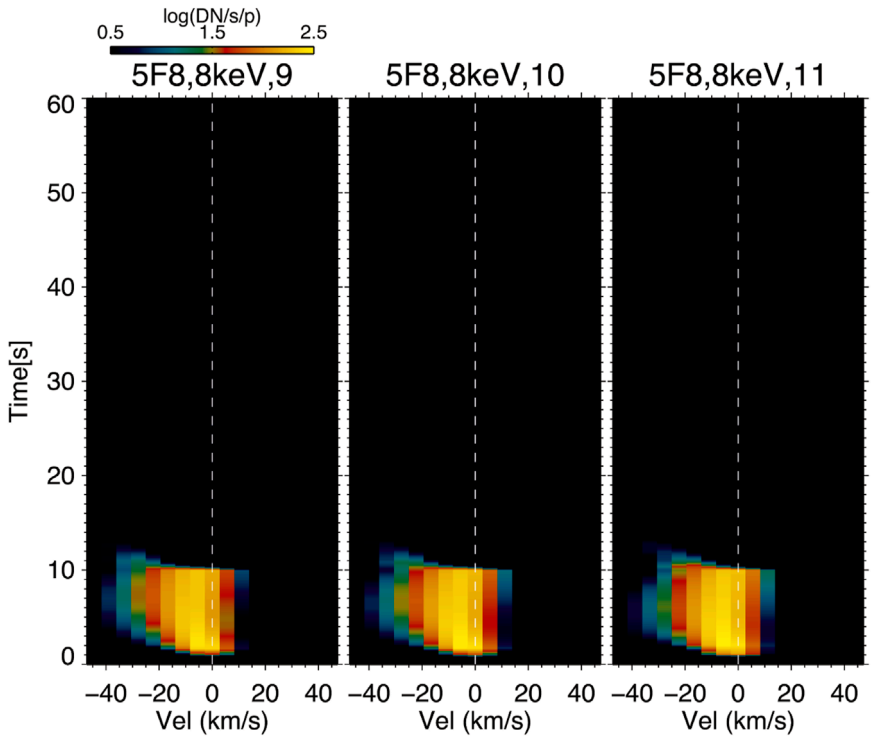

FIGURE A1
Time-velocity synthetic spectra of Si IV for RADYN flare simulations with initial apex temperature of 1 MK, F = 5F8, E_C = 8keV, and δ = 9,10 and 11. This image shows that different values of spectral index, within the constraints we obtained from NuSTAR, do not affect the results significantly.

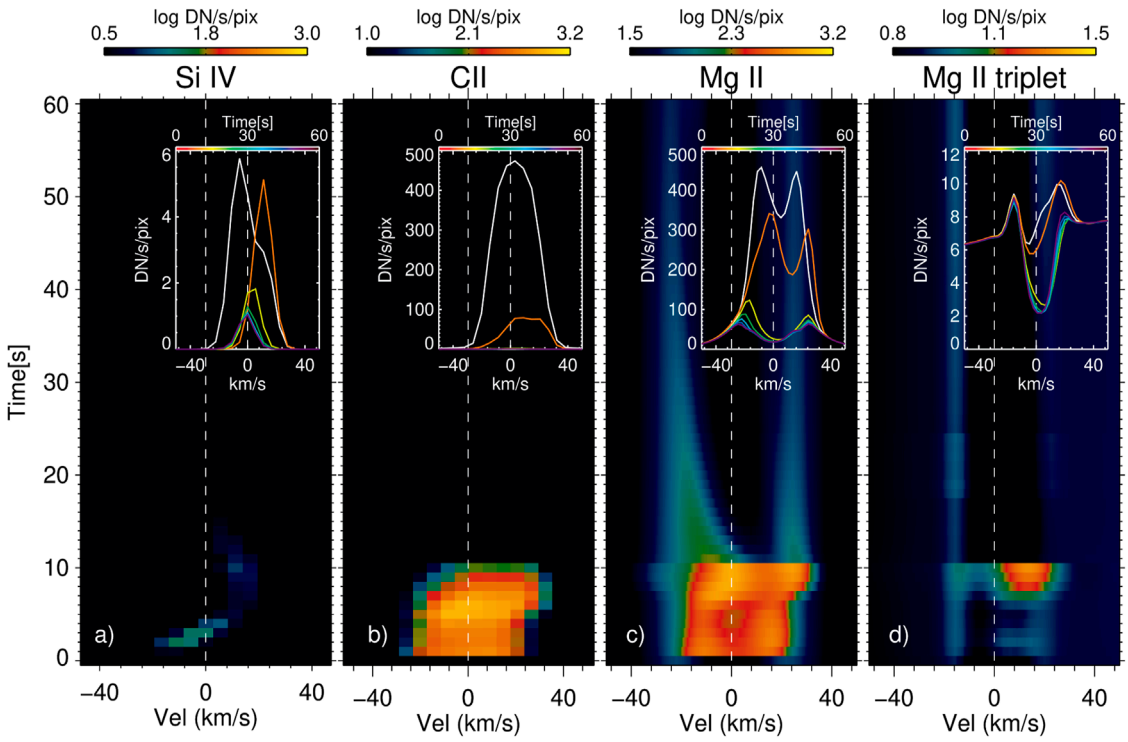

FIGURE A2
Top panels: Synthetic spectra from RADYN and RH simulations for the 1.2F9 flare model with E_C = 8 keV, δ = 10 and initial loop apex temperature of 3MK. The four panels show the: Si IV (Panel **A**), C II (Panel **B**), Mg II (Panel **C**) and Mg II triplet (Panel **D**) lines as a function of velocity and time. The insert on each panel shows the spectra averaged in time with a cadence of 8s, as indicated by the legend.

Frontiers in
Astronomy and Space Sciences

Explores planetary science and extragalactic astronomy in all wavelengths

Advances the understanding of our universe - from planetary science to extragalactic astronomy, to high-energy and astroparticle physics.

Discover the latest Research Topics

See more →

Frontiers

Avenue du Tribunal-Fédéral 34
1005 Lausanne, Switzerland
frontiersin.org

Contact us

+41 (0)21 510 17 00
frontiersin.org/about/contact